Petrochronology of monazite and zircon in ultra-high temperature granulite from Rogaland, Norway

Antonin Laurent

Université Fédérale
Toulouse Midi-Pyrénées

THÈSE

En vue de l'obtention du

DOCTORAT DE L'UNIVERSITÉ DE TOULOUSE

Délivré par :

Université Toulouse 3 Paul Sabatier (UT3 Paul Sabatier)

Présentée et soutenue par :
Antonin LAURENT

le mardi 8 novembre 2016

Titre :

Étude pétrologique et chronométrique (U–Th–Pb) de la monazite et du zircon dans les granulites de ultra-haute température du Rogaland, Norvège

---

École doctorale et discipline ou spécialité :
ED SDU2E : Sciences de la Terre et des Planètes Solides

Unité de recherche :
Géosciences Environnement Toulouse – UMR 5563

Directeur/trice(s) de Thèse :
Mme Stéphanie Duchene (Directrice)
Mme Anne-Magali Seydoux-Guillaume (Co-directrice)
M. Bernard Bingen (Co-encadrant)

Jury :

M. Philippe GONCALVES	Maître de conférences	Rapporteur
M. Simon HARLEY	Professeur des universités	Rapporteur
M. Fernando CORFU	Professeur des universités	Examinateur
M. Jean-Marc MONTEL	Professeur des universités	Examinateur
M. Olivier VANDERHAEGHE	Professeur des universités	Président du jury
Mme Valérie BOSSE	Maître de conférences	Invitée

Sommaire

Liste des figures

Introduction

Chapitre 1

Chapitre 2

Chapitre 3

Chapitre 4

Chapitre 5

Liste des tableaux

Introduction

Chapitre 1

Chapitre 2

Chapitre 3

Chapitre 4

Chapitre 5

Liste des annexes

Chapitre 2

Chapitre 3

Chapitre 4

Chapitre 5

Introduction Générale

Les processus physiques et chimiques accompagnant la construction des chaînes de montagnes laissent des traces plus ou moins durables dans les roches affectées. Parmi les indices permettant de comprendre la dynamique terrestre, le métamorphisme, c'est à dire l'ensemble des changements se produisant dans une roche soumise à des conditions physiques différentes de celles où elle s'est formée, est un phénomène de premier ordre (Miyashiro 1961 ; Ernst 1975 ; England et Thompson 1984). Au cours de l'orogenèse, les roches voient les minéraux qui les composent recristalliser à l'état solide mais aussi en présence d'un fluide hydraté ou encore sous l'influence d'un liquide silicaté à plus haute température (Austrheim 1987). Les mécanismes permettant aux minéraux d'atteindre l'équilibre thermodynamique sont en effet activés par la présence d'une phase fluide ou encore par la déformation plastique dans les cristaux (Putnis 1992 ; Passchier et Trouw 1996). Comprendre la complexité du comportement des minéraux en réponse aux changements de pression (*P*), de température (*T*), de composition du fluide ou de la déformation permet ensuite d'inverser les observations de terrain pour mieux quantifier les objets naturels.

Historiquement, les minéraux silicatés dits majeurs, formant plus de 95 % des roches métamorphiques acides, ont été la cible privilégiée de la pétrologie métamorphique (Haüy 1822 ; Daubrée 1857 ; Eskola 1920 ; Turner 1948 ; Thompson 1957). Des bases de données thermodynamiques autocohérentes ont été patiemment construites à partir de données expérimentales et systématiquement testées par les données de terrain (Helgeson 1978 ; Berman 1988 ; Holland et Powell 1990, 1998). La quantification du chemin pression–température (*P–T*) suivi par les roches est aujourd'hui accessible pour une large gamme de roches via l'approche des pseudosections (Korzhinskii 1959 ; Hensen 1971 ; Connolly 2009). Toutefois, la présence même de roches métamorphiques à la surface du globe démontre que l'état d'équilibre n'est (heureusement) pas toujours atteint. Un paramètre crucial, outre la pression, la température et la disponibilité des fluides, est en effet la durée du métamorphisme qui doit être suffisante pour atteindre les conditions d'équilibre. Le temps est de plus un paramètre clef quant à la compréhension des événements géologiques menant à la construction et au démantèlement des chaînes de montagnes, tant pour déterminer leur séquence relative que leur durée absolue (Spear 1993 ; Johnson et Harley 2012).

La géochronologie, c'est à dire la datation des minéraux et par extension des roches, est donc d'une importance particulière puisqu'elle permet d'accéder aux durées et vitesses des processus orogéniques étudiés. Deux stratégies existent pour déterminer l'âge des roches métamorphiques. La première consiste à exploiter les méthodes isochrones (Nicolaysen 1961) en déterminant les rapports isotopiques père/fils de plusieurs minéraux supposés à l'équilibre. L'avantage d'une telle méthode est de dater directement les minéraux métamorphiques, permettant par là même de relier aisément l'âge obtenu à des conditions *P–T* (p. ex. Duchene et al. 1997). Le

succès de la datation par méthode isochrone requiert que la roche n'ait retenu qu'un seul épisode ou événement métamorphique. En effet, toute superposition mènerait à des mesures radiochronométriques dénuées de sens géologique que nous qualifierons de « dates » par opposition à « âges ». La seconde stratégie utilise des minéraux peu abondants dans les roches, dits accessoires (Tilton et al. 1955 ; Krogh 1973 ; Lancelot et al. 1976), qui incorporent des éléments radioactifs (p. ex U et Th) en quantité appréciable, de 100 partie par million (ppm) à 10 % massiques (Wt% pour *weight percent*). Dans un minéral donné et pour un couple isotopique connu, la mesure actuelle de la quantité d'élément fils produit par décroissance de l'élément père permet de déduire l'âge de fermeture du système isotopique ; à condition toutefois que le minéral en question incorpore une quantité négligeable d'élément fils lors de sa cristallisation ou que celle-ci soit connue par ailleurs. Parmi les minéraux accessoires remplissant les conditions présentées ci-dessus, on trouve le zircon ($ZrSiO_4$), la monazite ($CePO_4$), le xénotime (YPO_4), le rutile (TiO_2) ou encore la titanite ($CaTiSiO_5$). Le zircon et la monazite sont certainement les plus utilisés pour la datation des roches métamorphiques en raison de leur exceptionnelle résistance à haute température, notamment dans les roches partiellement fondues du faciès granulite (p. ex. Schaltegger et al.1999).

De manière analogue aux minéraux silicatés majeurs, la stabilité des minéraux accessoires dépend de variables intensives comme la pression et la température mais aussi extensives comme la concentration de la roche en éléments traces tels que le Zr, dans le cas du zircon (Watson et Harisson 1983), ou des Terres Rares (REE pour *Rare Earth Element*), pour la monazite (e.g. Montel 1993). Tout comme il est indispensable de connaître les propriétés des minéraux majeurs constituant la roche pour déduire des conditions *P–T* de leur formation, il est nécessaire d'étudier les paramètres qui contôlent la stabilité des minéraux accessoires pour espérer comprendre la signification d'un âge isotopique. En effet, dans le cas le plus simple, le système isotopique est clos au moment de la cristallisation du minéral étudié. On peut dès lors se demander ce qui a provoqué cette cristallisation (variations de pression *P*, de température *T*, de chimie *X*, de déformation du milieu *D*). D'autre part, les minéraux accessoires peuvent subir des altérations de leur réseau cristallin, ayant pour effet d'obscurcir le signal isotopique et donc de « fausser » l'âge mesuré (Silver et Deutsch 1963 ; Geisler et al. 2007). La compréhension du message isotopique demande, par conséquent, de mettre en évidence les mécanismes et processus minéralogiques opérant à l'échelle du cristal puis de relier ces processus à des variables d'intérêt *P–T–fluides*.

La compréhension de la dynamique des chaînes de montagnes est par conséquent dépendante au premier ordre de la qualité des données géochronologiques et de leur interprétation. Pour optimiser ces deux derniers points, une meilleure connaissance du comportement des minéraux accessoires utilisés en géochronologie, en particulier la monazite et le zircon, est

essentielle. Cette thèse s'inscrit ainsi dans une démarche naturaliste visant à collecter des échantillons sur le terrain pour ensuite replacer la cristallisation des minéraux accessoires dans le cadre de l'histoire thermodynamique de la roche et étudier la manière dont les systèmes isotopiques U–Th–Pb répondent à cette histoire. Nous nous concentrerons sur la caractérisation des conditions de formation (*P–T–X*) de la monazite et du zircon dans les roches ayant atteint des températures crustales extrêmes supérieures à 900 °C, dans l'objectif d'éclairer l'origine très débattue du métamorphisme de ultra-haute température (T > 900 °C) et d'une manière plus générale les interactions magmatisme–métamorphisme lors de la construction des chaînes de montagnes.

Définitions et causes du métamorphisme de UHT

Le métamorphisme de ultra-haute température (UHT) a été défini par Harley (1998) comme une subdivision du faciès granulite au-delà de 900°C. Ce type de métamorphisme matérialise les conditions les plus extrêmes auxquelles la croûte continentale est soumise. Le seuil des 900 °C ne correspond en fait qu'à une convention puisqu'il n'existe pas de discontinuité dans les températures enregistrées au sein du facies granulite (de 750 °C à plus de 1000 °C ; Brown 2007; Kelsey et Hand 2015). Le métamorphisme de UHT est reconnu sans interruption au cours des temps géologiques depuis l'Archéen (p. ex. Napier complex ; Kelly et Harley 2005) jusqu'au Cénozoïque (p. ex. Indonesia ; Pownall et al. 2014) et est suspecté dans la croûte profonde actuelle de nombreuses régions du monde grâce à la mesure des flux de chaleur en surface (Currie et Hyndman 2006). Avec plus de 60 occurrences reconnues (Kelsey et Hand 2015) il est donc clair que ce phénomène n'est pas marginal et que sa compréhension est cruciale pour contraindre les processus de grande échelle affectant la lithosphère (Brown 2009; Sizova et al. 2014).

Assemblages minéralogiques et relations de phase

Les assemblages minéralogiques typiques du métamorphisme de UHT dans les métapélites magnésiennes sont sapphirine + quartz, orthopyroxène + sillimanite + quartz ainsi que les assemblages à osumilite (Fig. 1a ; Harley 1998). Dans les roches basiques, l'apparition de la pigeonite souligne des températures proches ou supérieures à 900 °C (Fig. 1b ; Sandiford et Powell 1986).

↓ **Fig. I–1**: Photographies d'assemblages minéraux de UHT du Rogaland en lumière polarisée analysée **a–** Gneiss alumineux à osumilite (Osm) – grenat (Grt) – orthopyroxène (Opx) – hercynite (Hc). **b–** métabasite à pigeonite ; remarquez les exsolutions de clinopyroxène calcique (Cpx) dans les orthopyroxènes (Opx)

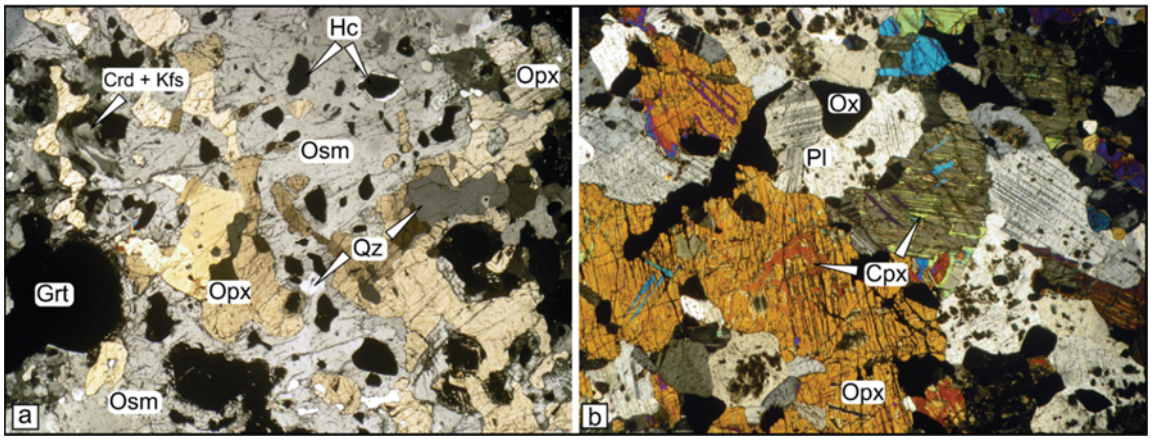

Les premières estimations quantitatives de pression (*P*) et température (*T*) ont été effectuées dans le système chimique simplifié FeO–MgO–Al_2O_3–SiO_2 (dit FMAS) sur la base des travaux de Schreyer et Seifert (1967) et Hensen et Green (Hensen 1971; Hensen et Green 1973; Hensen 1977). La grille FMAS historique (Hensen et Green 1973) a longtemps coexisté avec celles dérivées de systèmes chimiques plus complets qui prennent en compte la production de liquide silicaté comme K_2O–FMAS–H_2O (Fig. 2 ; voir aussi Carrington et Harley 1995). Simultanément, la quantification des conditions *P–T* a été affinée par des méthodes thermo-barométriques utilisant le partitionnement du Fe et du Mg entre orthopyroxène et grenat (Harley et Green 1982), la teneur en Al de l'orthopyroxène (Harley et Motoyoshi 2000), la composition des mésoperthites (Kroll et al. 1993), entre autres.

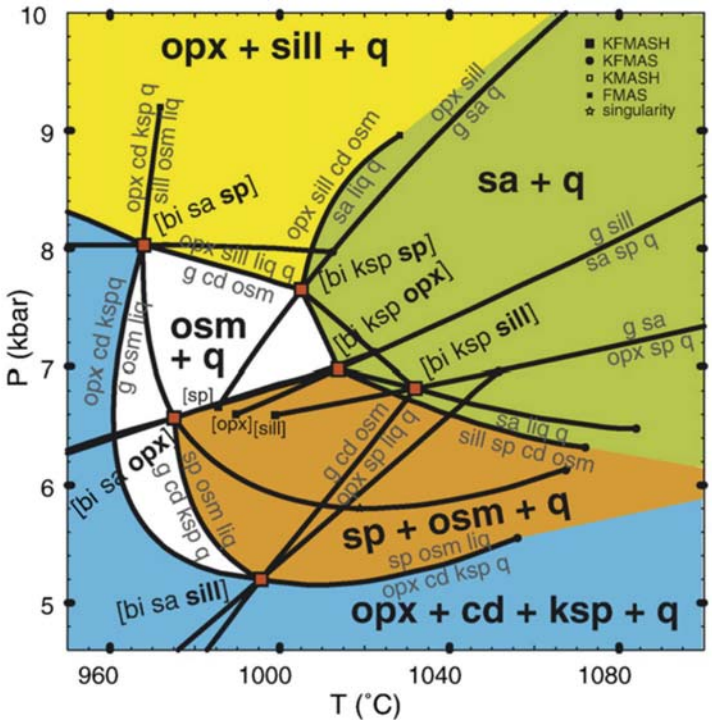

Fig. I–2: Grille pétrogénétique dans le système KFMAH montrant les champs de stabilité des assemblages à osumilite et sapphirine calculée avec la base de données de Kelsey et al. (2004) par Kelsey (2008)

Un point crucial dans la reconnaissance de la ultra-haute température doit cependant être souligné : les invariants du système FMAS et KFMASH sont très rapprochés dans l'espace *P–T*, ce qui implique une forte sensibilité des assemblages minéralogiques aux alentours de 6–10 kbar et 960–1040 °C (Kelsey 2008 ; Fig. 2). De plus, seules les roches ayant une composition suffisamment magnésienne développeront de tels assemblages, ce qui complique la reconnaissance de la ultra-haute température lorsqu'elles sont absentes des terrains étudiés (voir p. ex. la Fig. 10 de Harley 1998b).

Modélisation thermodynamique

Aujourd'hui, les conditions *P–T* dans les roches sont estimées grâce à l'approche des pseudosections (Hensen 1971), calculées dans des systèmes chimiques de plus en plus complets (MnO)–Na_2O–CaO–K_2O–FeO–MgO–Al_2O_3–SiO_2–H_2O–TiO_2–O_2 (Berman 1988; Powell et Holland 1988; Kelsey et al. 2004; White et al. 2007). Les pseudosections correspondent à la projection des champs de stabilité *P–T* prédits par les grilles pétrogénétiques dans l'espace *P–T–X* pour une composition (*X*) fixe. Il est de plus possible de compléter cette représentation en traçant le mode de minéraux index ou leurs compositions (p. ex. X_{Mg} dans le grenat). Dans ce travail de thèse, nous avons utilisé le code Perple_X (Connolly 1990; Connolly et Petrini 2002; Connolly 2009) qui est basé sur la minimisation de l'énergie libre de Gibbs (*G*) du système. Dans le cas de la pétrologie métamorphique, le système est composé de phases (minéraux) liés au nombre de composants (oxydes) par la règle des phases. Les minéraux sont eux-mêmes des mélanges entre pôles chimiques purs, c'est-à-dire qu'ils montrent des solutions solides (complètes ou non) qui imposent d'effectuer des minimisations prenant en compte l'enthalpie molaire partielle de chaque constituant (pôle pur). Le choix des solutions solides et de leur traitement est donc un critère de premier ordre quant à la fiabilité des résultats et à l'efficacité des calculs. Dans ce travail de thèse, nous avons commencé avec la base de données thermodynamiques autocohérente de Holland et Powell (1998) couplé aux modèles de solution solides de White et al. (2007) puis nous avons utilisé la base de données de Holland et Powell (2011) avec les modèles de solutions solides de White et al. (2014) qui intègrent le Fe^{2+}/Fe^{3+} dans la sapphirine, l'orthopyroxène et le spinelle.

Pour obtenir des résultats de qualité, il faut en outre apporter un soin particulier à (1) la composition chimique du système correspondant à la pseudosection, qui dans le cas d'assemblages de UHT sera celle du pic en température, (2) la teneur en H_2O qui contrôle notamment la température du solidus et la production de liquide silicaté (à T constante), (3) la spéciation du Fe (Fe^{3+}/Fe^{2+}) ainsi que (4) la présence de composants mineurs non intégrés aux bases de données (p. ex. Cr, Zn dans le spinelle). La composition chimique du système peut être estimée à partir de cartographies quantitatives (cartographie EDS au microscope électonique à balayage) à l'échelle

de l'assemblage minéral observé en lame mince (Fig. 3). Ces cartographies permettent d'avoir accès à une chimie très locale adaptée à l'échelle d'équilibre des réactions métamorphiques et de compter automatiquement la proportion des phases grâce au logiciel adapté. Par contre, la cartographie EDS ne permet pas de mesurer la spéciation du Fe ou de quantifier l'hydratation des phases (p. ex cordierite ou biotite). Une solution alternative est de faire varier la proportion d'H_2O et de Fe^{3+} dans des sections *P–X* ou *T–X* modélisées jusqu'à reproduire l'assemblage minéralogique observé. Procéder par ajustement de la composition chimique mesurée est cependant une pente glissante, puisqu'une estimation *P–T* ne vaut, par définition de la pseudosection, que pour une chimie donnée. Pour cette raison, les pseudosections présentées dans ce travail ont été réalisées à partir des analyses chimiques roche totale, avec mesure de la perte au feu et la titration du FeO, effectuées sur le sucre ayant servi à confectionner la lame mince.

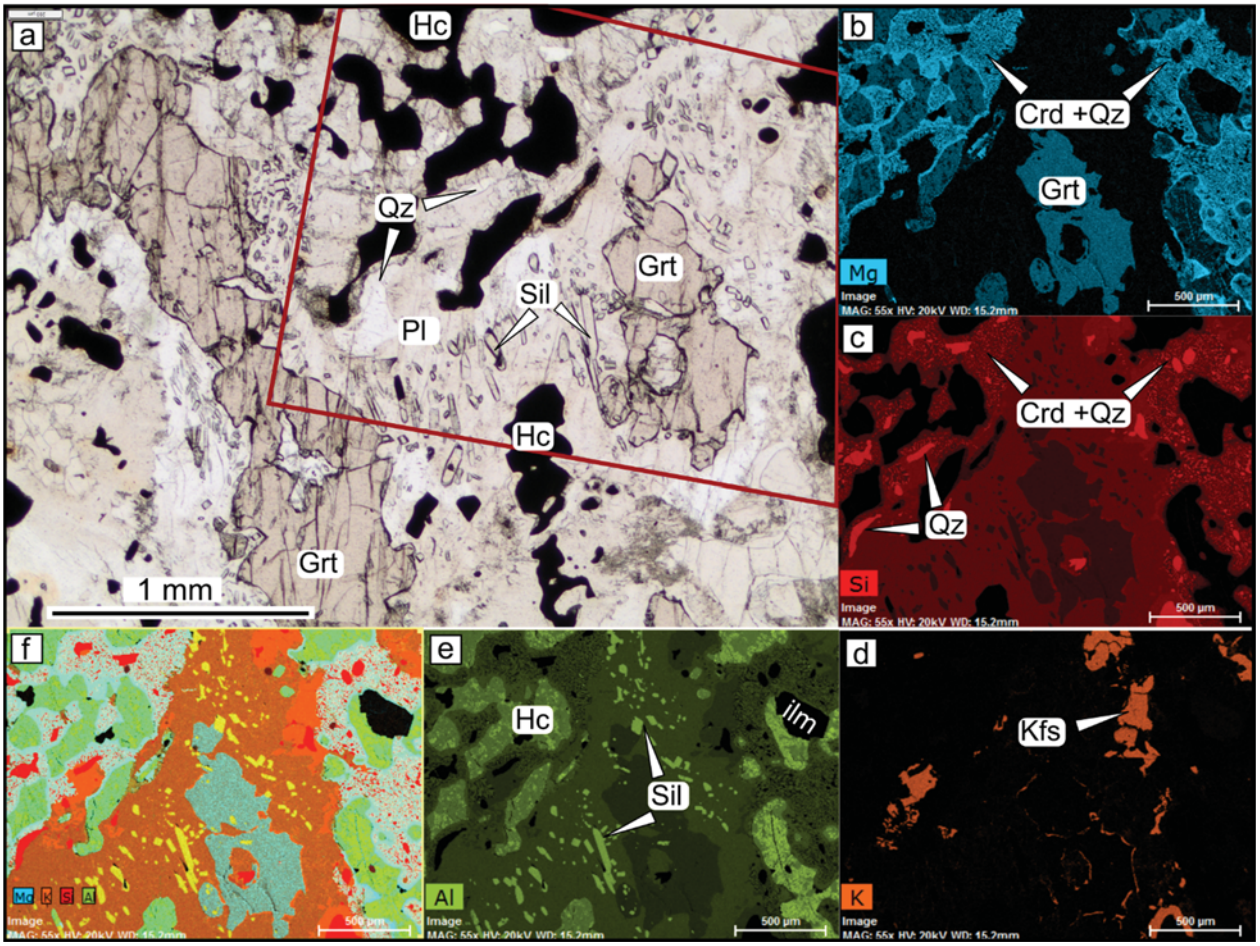

Fig. I–3: Exemple d'échelle pertinente pour l'acquisition d'une zone de micro-composition chimique par carte EDS (Energy Dispersive Spectrometry) au microscope électronique à balayage (MEB). **a**– photographie en lumière polarisée ; le grenat (Grt) se décompose en une couronne externe de hercynite entouré d'une symplectite de cordiérite (Crd) + quartz (Qz) et une couronne interne de sillimanite (Sil) + plagioclase (Pl). **b**– cartographie EDS du Mg. **c**– cartographie EDS du Si. **d**– cartographie EDS du K. **e**– cartographie EDS de l'Al. **f**– carte compilée de Mg, K, Si, Al permettant d'observer les microstructures chimiques.

Les chemins P–T et leur signification géodynamique

Les avancées considérables dans la modélisation thermodynamique ont permis de définir des chemins *P–T* toujours plus précis (Korhonen et al. 2014). Toutefois, les conditions de températures extrêmes subies par les roches favorisent la perte de la zonation prograde des minéraux (Spear 1991). Par conséquent, les deux grandes familles de chemin *P–T* dans les granulites UHT sont distinguées sur la base du trajet post-pic (Harley 2008). La plupart des granulites UHT sont caractérisées par une trajectoire de décompression isotherme (ITD pour *isothermal decompression* ; Fig. 4a) tandis qu'une partie moindre suit un chemin de refroidissement isobare (IBC pour i*sobaric cooling* ; Fig. 4b).

Les granulites suivant un chemin IBC se sont équilibrées à basse pression (3–6 kbar) au sein de vastes domaines granulitiques de basse-pression/haute-température (*BP*/*HT*) suivant des boucles *P–T* horaires ou anti-horaires. Ces domaines sont souvent associés à des orogènes d'accrétion dans lesquels la collision n'a jamais eu lieu (Collins 2002; Walsh et al. 2014) ou directement associés à un contexte d'arc ou d'arrière-arc (Bohlen 1991; Kemp et al. 2007). La chaleur, dans les exemples cités ci-dessus, est apportée par des magmas issus du manteau (Wells 1980; Brown 2009). D'autre part, dans certains cas, les domaines qui suivent des chemins IBC ont préalablement séjourné à plus haute pression (*c*. 6–10 kbar), le cas classique étant celui du Complexe de Napier (Antarctique ; Fig. 4b ; Harley 1998b). Ces roches de moyenne pression et UHT sont interprétées comme les niveaux profonds d'un orogène de collision qui restent enfouis en profondeur au cours de l'orogenèse et arrivent à la surface au gré d'évènements tectoniques postérieurs (Harley 2016).

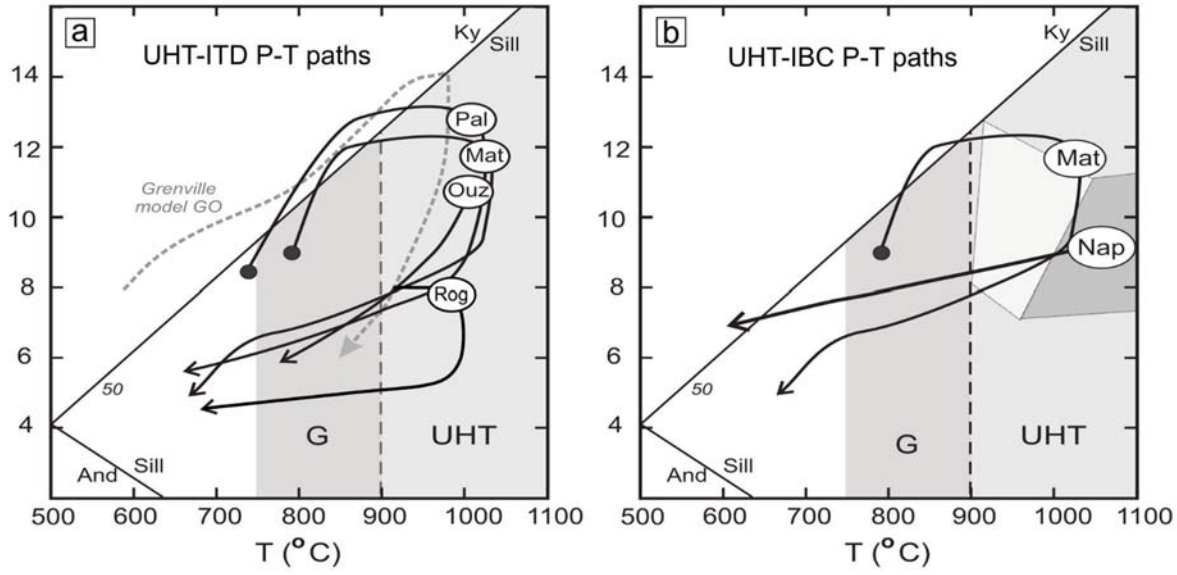

Fig. I–4: Diagrammes *P–T* montrant les chemins suivis par différentes localités de UHT. **a**– chemins *P–T* horaires avec une décompression isothermale dominante ; Pal – Palni Hills, S de l'Inde, Mat – Mather paragneiss, E de l'Antarctique, Ouz – Ouzzal, Algérie ; Rog – Rogaland, S de la Norvège. **b**– Chemin *P–T* montrant le refroidissement (quasi) isobare du complexe de Napier (Antarctique) comparativement au chemin ITD des paragneiss de Mather pour comparaison. Figure adaptée de Harley (2016)

Les granulites caractérisées par un chemin de décompression isotherme (ITD) passent pour la plupart dans la fenêtre *P–T* 12–8 kbar et 850–1050 °C suivant un chemin horaire (Fig. 4b). Dans un certain nombre de localités, il est possible de déterminer leur chemin prograde grâce aux reliques minérales dans les grenats montrant la succession biotite + sillimanite vers disthène dans les grenats puis dans la matrice (Harley 2008). La présence de disthène marque un épaississement crustal, typique des orogènes de collision, qui est suivi d'une exhumation des roches partiellement fondues à UHT. Suivant les modèles thermiques (Clark et al. 2011) qui sont capables de reproduire les chemins *P–T* observés dans la nature, il est désormais accepté que les granulites UHT–ITD puissent se former dans les orogènes de collision sous l'effet de l'enfouissement de matériel à forte production de chaleur radioactive en profondeur, associé à de faibles taux d'érosion (Harley 2016).

Durée du métamorphisme de UHT

Malgré les avancées dans la détermination des chemins *P–T*, le contexte géodynamique de la plupart des localités de UHT reste débattu car le chemin prograde, l'âge exact du pic de métamorphisme ainsi que la durée de l'épisode métamorphique sont imprécisément déterminés. Il est crucial pour comprendre les conditions géodynamiques du métamorphisme de UHT d'estimer la durée du métamorphisme de UHT au sens strict (Δt_{900}), celle du métamorphisme granulitique non-UHT associé (Δt_{800}) et enfin du taux de refroidissement suivant le pic en température (Fig. 5; Harley 2016).

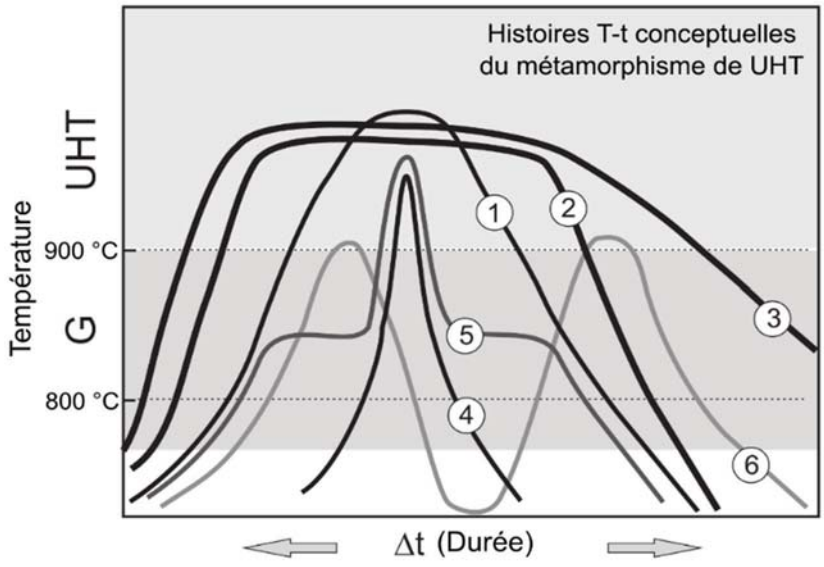

Fig. I–5: Diagramme illustrant schématiquement six types d'évolution température–temps (*T–t*) lors du métamorphisme de ultra-haute température. Notez que l'axe du temps ne possède pas de graduation absolue. Le cas (1) illustre le chemin le plus simple consistant en un réchauffement suivi d'un refroidissement symétrique. Le cas (2) est similaire à (1) hormis l'existence d'une longue phase plateau à UHT. Le cas (3) est similaire à (2) sauf que le métamorphisme de UHT est suivi d'un refroidissement lent et donc d'un séjour prolongé dans le faciès granulite (G). Le cas (4) est celui d'une incursion extrêmement rapide à UHT. Le cas (5) est caractérisé par un long épisode de métamorphisme dans le faciès granulite (~850 °C) avec une incursion rapide à UHT. Le cas (6) est celui d'un poly-métamorphisme avec deux épisodes de UHT séparés par un refroidissement important. La figure et la légende sont traduites de Harley (2016)

En effet, la durée du métamorphisme à l'échelle de la chaîne est intrinsèquement liée à la nature de la source de chaleur (advection de magmas mantelliques, réchauffement de la croûte par désintégration radioactive) et au contexte tectonique (épaisseur de croûte, taux d'érosion). Il faudra néanmoins distinguer la durée du métamorphisme dans la chaîne, de la durée « vue » par un échantillon qui est fonction de son trajet *P–T*, particulièrement pour les granulites ITD qui quittent rapidement le cœur chaud de l'orogène alors même que la source de chaleur n'est pas tarie. Enfin, la métastabilité des assemblages minéralogiques dans les roches anhydres demande une analyse fine des textures réactionnelles couplée à la géochronologie pour décider s'il s'agit d'un unique chemin *P–T* ou de la superposition de deux événements éloignés dans le temps (e.g. Vernon 1996; Goncalves 2004; Fig. 5 cas 6).

Même si la durée du métamorphisme de UHT est variable suivant les localités avec une dispersion de 1 Ma à plus de 100 Ma (Kelsey et Hand 2015), il est possible de distinguer deux régimes temporels principaux : les régimes rapides (<40 Ma) et les régimes lents (> 40 Ma). Kelsey et Hand (2015) notent en particulier que la plupart des localités ayant évolué à UHT plus de 40 Ma sont caractérisées par des chemins IBC, la seule exception semblant être le Rogaland (Sud de la Norvège ; Fig. 4). Cette occurrence est en effet caractérisée selon Drüppel et al. (2013) par une décompression isotherme à UHT entre 7.5 et 5 kbar s'étendant d'environ 1010 Ma à 930 Ma.

Lier le temps à la température dans les granulites

Lier température et temps dans les granulites est un des défis actuels de la géochronologie visant à mieux comprendre la dynamique profonde des orogènes (Korhonen et al. 2013). Au cours du temps plusieurs stratégies ont été explorées, parmi lesquelles nous en décrirons trois toujours en vigueur. La première stratégie est permise par l'avènement des techniques de micro-analyses et vise à lier l'âge d'un grain de monazite/zircon à sa position texturale dans la lame mince (p. ex. Möller et al. 2003; Goncalves 2005). Cette technique s'est révélée efficace en particulier pour dater les phases prograde via les minéraux accessoires encapsulés dans les grenats (Goncalves 2004) ou encore pour dater la déformation via les grains de monazites sigmoïdes (Dumond et al. 2013). De même, la caractérisation texturale permet de proposer des réactions impliquant des minéraux majeurs dans la formation du zircon (p. ex. Fraser et al. 1997; Bingen et al. 2001). La seconde stratégie vise à lier la signature chimique des minéraux accessoires à leur environnement de cristallisation. Cette méthode est largement utilisée aujourd'hui notamment pour lier stabilité relative du zircon par rapport au grenat grâce à la connaissance des coefficients de partitionnement des terres rares (Whitehouse et Platt 2003; Kelly et Harley 2005; Hacker et al. 2015). La monazite n'est pas en reste puisque sa teneur en Y est liée à la stabilité du xénotime et du grenat (Pyle et al.

2001). La stabilité du grenat peut donc qualitativement être suivie, au cours du temps, en étudiant différentes zones d'un même grain de monazite (Fig. 6 ; Williams et al. 2007). Enfin, la stratégie qui est développée à l'heure actuelle est celle de la mesure ponctuelle température–temps sur le même minéral accessoire. Cela est rendu possible par l'application de méthodes thermométriques couplées à la géochronologie. Dans le faciès granulite, le partage du Zr et du Ti entre zircon et rutile est de plus en plus utilisé (Baldwin et al. 2007; Fu et al. 2008; Ewing et al. 2013).

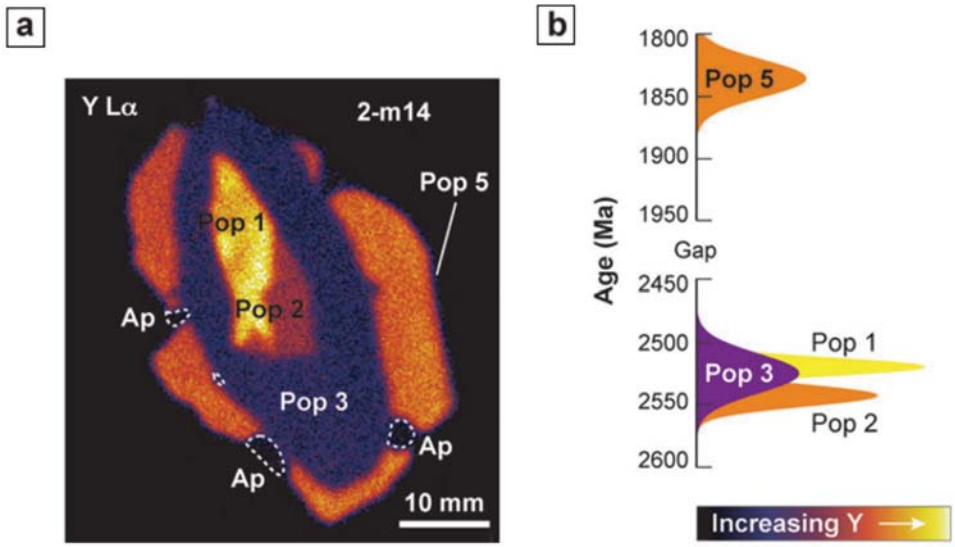

Fig. I–6: Carte de composition en Y et âge des différentes zones d'un grain de monazite extrait d'une granulite felsique (Snowbird tectonic zone Canada). Il est possible d'identifier plusieurs épisodes de croissances de la monazite à l'Archéen et au Paléoprotérozoïque grâce à la datation *in-situ* par microsonde électronique. Figure tirée de Williams et al. (2007)

Pour interpréter les données géochronologiques et thermométriques obtenues, il est critique de comprendre les processus gouvernant le comportement des zircons et monazites dans un environnement anhydre partiellement fondu. La diversité des processus à l'œuvre a été synthétisé pour les zircons par Harley et al. (2007 ; Fig. 7), tandis que le comportement de la monazite reste mal compris et est souvent relié à des phases tardives de rééquilibration (Hermann et Rubatto 2003; Bhowmik et al. 2014; Taylor et al. 2014). Par ailleurs, Kelsey et al. (2008) ont développé une approche alternative basée sur les équations de solubilité du zircon et de la monazite dans un liquide silicaté (Watson et Harrison 1983; Montel 1993). Ces auteurs concluent que monazite et zircon seront dissous durant le chemin prograde et une éventuelle décompression post-pic pour finalement cristalliser durant le refroidissement de la roche vers son solidus, impliquant une croissance tardive, et dans tous les cas, le non-enregistrement du passage au pic de température. A l'incertitude sur les mécanismes conduisant à la cristallisation des monazites et zircons s'ajoute la possibilité d'une perturbation post-cristallisation des systèmes chronométriques.

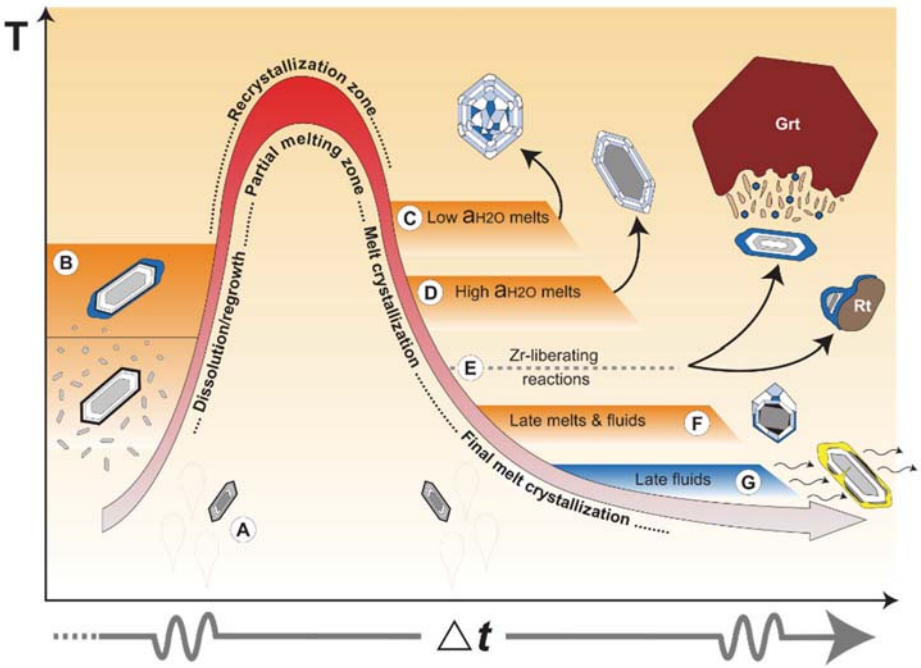

Fig. I–7: Schéma illustrant le comportement du zircon lors d'un épisode de métamorphisme granulitique, incluant la dissolution des zircons pré-existants (B), suivi de la cristallisation de différentes générations (C), (D), (F) en fonction de l'activité en H_2O du liquide silicaté et de sa composition. De nouveaux zircons peuvent aussi croitre (E) grâce au Zr libéré par la déstabilisation du grenat (Grt) ou du rutile (Rt). Enfin, la circulation de saumures tardives exsolvées des derniers magmas peut causer une recristallisation du zircon et la perturbation des systèmes chronométriques U–Th–Pb (G). Figure tirée de Harley et al. (2007)

La mesure du temps dans les granulites

Principe de la géochronologie

La mesure du temps dans les granulites est essentiellement menée via la datation des minéraux accessoires incorporant lors de leur cristallisation un ou des isotopes radioactifs à longue demi-vie tels que ^{238}U, ^{232}Th, ^{40}K. La désintégration radioactive d'un élément père en un élément fils est un phénomène spontané dépendant seulement du temps, qui peut être considéré comme direct si la chaîne de désintégration a atteint son équilibre séculaire. Il est donc possible d'exprimer pour tout temps t la quantité d'élément père restant $N(t)$ en fonction de la quantité d'élément père initiale N_0 et de la constante de désintégration radioactive λ du couple isotopique étudié :

$$N(t) = N_0 e^{-\lambda t}$$

La quantité initiale d'atomes pères N_0 est de plus égale au nombre d'atomes pères restants additionnés du nombre d'atomes fils produits par désintégration. Si le nombre actuel d'atomes père et fils peut être mesuré, alors il est possible d'évaluer depuis quand le système isotopique est clos, à la condition toutefois d'estimer la quantité initiale d'atomes fils.

Parmi les différents couples isotopiques, il est rapidement apparu que le système U–Pb présentait deux avantages intrinsèques pour la datation des roches anciennes et de haut degré

métamorphique. D'abord, l'U est intégré dans plusieurs minéraux capables de survivre à plusieurs cycles de Wilson et à des températures élevées (p. ex. la monazite et le zircon). Ensuite, le système U–Pb est composé de deux chaînes de désintégration indépendantes (demi-vies différentes) $^{238}U/^{206}Pb$ et $^{235}U/^{207}Pb$ avec des éléments père et fils chimiquement identiques. Pour ces deux couples isotopiques, il est donc possible d'écrire l'équation d'âge dérivée de (1) et normalisée à un isotope stable du Pb (^{204}Pb) :

$$\left(\frac{^{206}Pb}{^{204}Pb}\right) = \left(\frac{^{206}Pb}{^{204}Pb}\right)_0 + \left(\frac{^{238}U}{^{204}Pb}\right)\left(e^{\lambda_{238}t} - 1\right)$$

$$\left(\frac{^{207}Pb}{^{204}Pb}\right) = \left(\frac{^{207}Pb}{^{204}Pb}\right)_0 + \left(\frac{^{235}U}{^{204}Pb}\right)\left(e^{\lambda_{235}t} - 1\right)$$

L'identité chimique du père et du fils dans les deux chaînes permet de tester si les deux systèmes donnent la même information d'âge, auquel cas ils sont dits concordants, ou bien s'ils retournent des âges différents que l'on qualifiera de discordants. Enfin, monazite et zircon incorporent également du ^{232}Th qui se désintègre en ^{208}Pb.

Un des prérequis pour calculer un âge est de connaître la quantité d'élément fils au temps de fermeture du système. Par chance, la monazite et le zircon n'incorporent pas habituellement de Pb dans leurs réseaux cristallins. Ainsi, grâce à la mesure de seulement cinq isotopes ^{206}Pb, ^{238}U, ^{207}Pb, ^{208}Pb et ^{232}Th, par spectrométrie de masse à thermo-ionisation (TIMS), par spectrométrie de masse à ionisation secondaire (SIMS) ou par spectrométrie de masse avec plasma à couplage inductif (ICP-MS), il est possible de calculer trois âges en considérant le rapport $^{238}U/^{235}U$ constant et connu.

$$^{206}Pb = {}^{238}U\left(e^{\lambda_{238}t} - 1\right)$$

$$^{207}Pb = {}^{235}U\left(e^{\lambda_{235}t} - 1\right)$$

$$^{208}Pb = {}^{232}Th\left(e^{\lambda_{232}t} - 1\right)$$

Il est également possible d'obtenir un âge à partir des concentrations élémentaires en U, Th, Pb mesurées à la microsonde électronique (EPMA pour *Electron Probe Micro-Analyser*) où le Pb mesuré (Pb_{tot}) correspond au Pb radiogénique produit par les trois chaînes présentées ci-dessus et au Pb commun (^{204}Pb) :

$$Pb_{tot} = \left[{}^{232}Th\left(e^{\lambda_{232}t} - 1\right)\right] + \left[{}^{238}U\left(e^{\lambda_{238}t} - 1\right)\right] + \left[{}^{235}U\left(e^{\lambda_{235}t} - 1\right)\right] + {}^{204}Pb$$

En considérant une fois de plus une incorporation de Pb commun négligeable, l'âge est obtenu par itération de l'équation :

$$Pb_{tot} = \left[Th\left(e^{\lambda_{232}t} - 1\right)\right] + \left[U \times 0.9928\left(e^{\lambda_{238}t} - 1\right)\right] + \left[U \times 0.072\left(e^{\lambda_{235}t} - 1\right)\right]$$

Comportement du zircon et de la monazite

Le zircon ($ZrSiO_4$) et la monazite (phosphate de Terre Rares Légères : $(LREE)PO_4$) sont les deux minéraux les plus utilisés en géochronologie U–Pb (Parrish 1990; Corfu 2013). Dans le cas idéal, les deux systèmes isotopiques U–Pb délivrent des dates concordantes qui peuvent immédiatement être interprétées comme l'âge de cristallisation du minéral. Cependant, il est fréquent d'obtenir dans les échantillons naturels des rapports isotopiques discordants (Ahrens 1955) qui reflètent une mobilité différentielle de l'U et du Pb. Le développement de méthodes analytiques *in-situ* (SIMS, LA–ICP–MS, EPMA) permet d'échantillonner différentes parties d'un même minéral qui préserve des chimies et/ou des rapports isotopiques distincts. Le choix de la méthode analytique pour un problème donné requiert d'évaluer la précision analytique requise ainsi que le volume à analyser par rapport au volume minimal pour lequel les systèmes U–Pb sont clos. Ainsi, toute mobilité différentielle de l'U, du Th ou Pb à une échelle supérieure au volume analytique, ou l'analyse simultanée de deux parties du minéral ayant des rapports isotopiques distincts, mène invariablement à la perturbation de l'âge mesuré (Fig. 8).

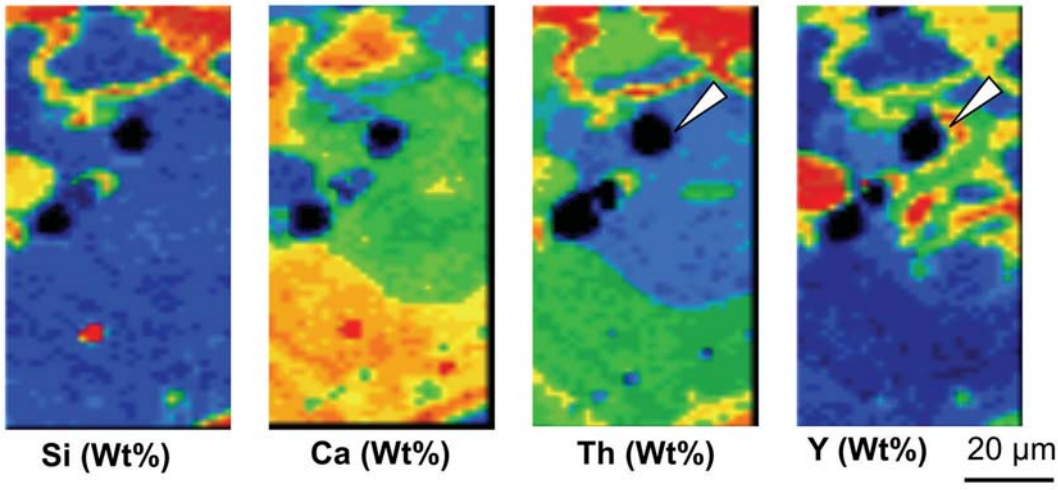

Fig. I–8: Cartographies WDS de la composition chimique (Si–Ca–Th–Y) d'un grain de monazite extrait de gneiss alumineux de UHT du Rogaland (Norvège). Les cercles noirs sont les traces d'ablation laser pour datation U–Th–Pb par LA–ICP–MS. Le volume échantillonné par le laser recoupe plusieurs zones chimiques qui ne sont visibles que sur la carte d'Y (flèche blanche). Notez la mobilité différentielle de l'Y et du Th par exemple.

Ces perturbations peuvent être appréciées dans le diagramme dit *Concordia* (Wetherill 1956), dans lequel sont reportés les rapports $^{206}Pb/^{238}U$ en fonction de $^{207}Pb/^{235}U$ (Fig. 9a–b). La courbe représentée dans un tel diagramme marque les lieux où les deux systèmes isotopiques sont concordants. Si le système a été ouvert, alors l'âge devient discordant. La reconnaissance de la discordance est directement proportionnelle à la précision de la méthode analytique choisie. Par exemple, Corfu (2013) discute d'un exemple tiré de Moser et al. (2009) où les données acquises à la sonde ionique montrent une dispersion des points analytiques le long de la courbe *Concordia*

suggérant plusieurs épisodes métamorphiques (Fig. 9b), alors qu'une étude par ID-TIMS révèle que les données s'alignent en fait sur une droite (*Discordia*) dont seuls les intercepts inférieur et supérieur ont une signification géologique (Fig. 9a).

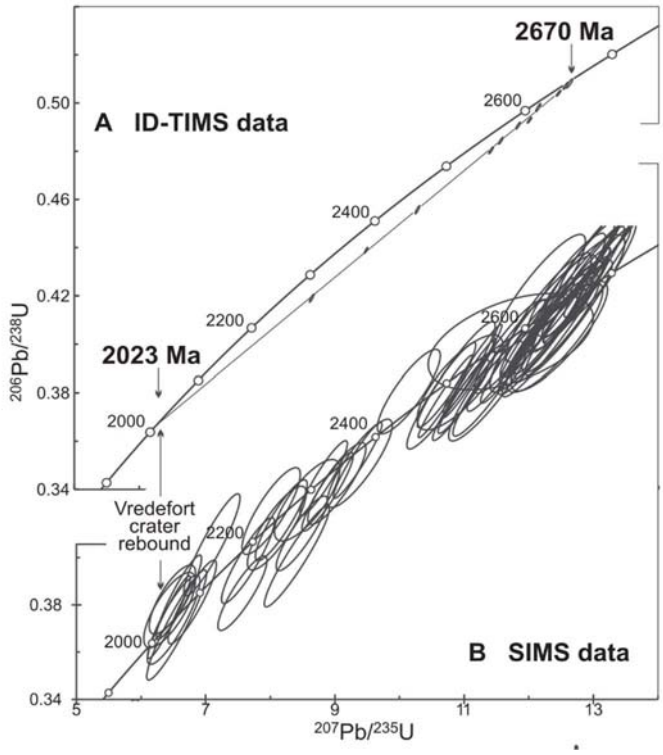

Fig. I–9: Diagrammes concordia de zircons magmatiques Archéens (2.67 Ga) ayant subi un métamorphisme d'impact à 2.02 Ga (Cratère de Vredefort). **a**– analyses ID-TIMS définissant une Discordia. **b**– analyses SIMS distribués entre l'âge magmatique de la roche et l'âge du métamorphisme. Exemple de Moser et al. 2009. (les ellipses représentent l'incertitude associée aux analyses). Tiré de Corfu (2013)

D'une manière générale, deux processus sont responsables de la mobilité U–Th–Pb et donc de la remise (partielle) à zéro des couples isotopiques. Il s'agit des réactions chimiques et de la diffusion volumique (Cole et Chakraborty 2001). L'efficacité relative et les interactions existantes entre ces deux processus au sein de mécanismes plus larges dépendent principalement de la température, du temps, de la taille du grain ou de sa surface, des défauts structuraux (lacunes, défauts d'irradiation) et de la présence de fluides. Les réponses de la monazite et du zircon à ces différents paramètres sont relativement différentes et brièvement exposées ci-dessous.

Tout d'abord il faut préciser que les études expérimentales ont démontré que la diffusion du Pb dans la monazite et le zircon sans défauts cristallins était négligeable aux températures crustales (Gardés et al. 2006; Cherniak 2010). Ces deux minéraux sont donc capables, en théorie, d'enregistrer des âges de cristallisation dans le faciès granulite sans être affectés par la diffusion du Pb durant le refroidissement. Toutefois, la diffusion volumique du Pb devient une réalité lorsque le réseau cristallin est affecté de défauts ponctuels ou planaires (McLaren et al. 1994). La plus grande faiblesse du zircon réside ainsi dans l'accumulation de défauts cristallins dus à l'irradiation qui sont liés principalement aux reculs alpha des chaînes de l'U (Ewing et al. 2003). Au-dessus d'une certaine dose, l'interaction minéral–fluide est facilitée menant à la perte de Pb et à la mobilisation de l'U, même à basse température (Nasdala et al. 2001; Geisler et al. 2007; Seydoux-Guillaume et al. 2015). La monazite, quant à elle, n'est que peu affectée par la

métamictisation malgré des concentrations en U (> 1 wt%) et en Th (> 30 wt%) extrêmement élevées (Seydoux-Guillaume et al. 2004). Par contre, la monazite est connue pour sa réactivité chimique en présence de fluides alcalins via le mécanisme de dissolution–précipitation (Harlov et al. 2011; Didier et al. 2013; Grand'Homme et al. 2016). Si le déséquilibre chimique est trop grand entre le fluide perturbateur et le minéral recristallisé, alors la réaction de dissolution–précipitation sera associée à de nouvelles phases comme la thorite/huttonite ($ThSiO_4$) ou l'uraninite (UO_2). La présence de ces phases, éventuellement d'échelle nanométrique, est une difficulté à prendre en compte lors de la datation isotopique puisque leur échantillonnage compromettrait irrémédiablement l'âge mesuré du fait de leur concentration élevée en U et Th (Seydoux-Guillaume et al. 2012; Seydoux-Guillaume et al. 2015).

L'utilisation simultanée des monazites est des zircons dans un même échantillon permet donc d'accéder à des informations complémentaires du fait des forces et faiblesses relatives de ces deux minéraux.

Enjeux pour les ressources naturelles stratégiques

Le comportement de la monazite et de ses systèmes U–Pb et Th–Pb dans les roches partiellement fondues comporte également des enjeux économiques et stratégiques. En effet, à l'échelle de la croûte, la monazite est la principale source de terres rares légères (LREE). Ce groupe d'éléments est indispensable dans les technologies de pointe aussi variées que les aimants permanents ou les émetteurs lasers tandis que les actinides contenus dans la monazite constituent des ressources énergétiques (p. ex. Birraux et Kert 2011).

Ces éléments nous sont accessibles en surface car un fluide, aqueux ou silicaté, a drainé les roches de la croûte profonde, dissout les minéraux qui les immobilisaient et les en a extraits. Dans la croûte moyenne et inférieure, la monazite est la principale phase porteuse de l'U et de Th (Bea 1996). Ainsi, la quantification de la redistribution de l'U, du Th et des terres rares au cours d'un cycle orogénique passe nécessairement par l'étude de la stabilité de la monazite dans la croûte profonde. Les études expérimentales montrent par ailleurs que la présence d'un liquide silicaté favorise la dissolution de la monazite en fonction de la température (*T*), de la pression (*P*), de la proportion de liquide et de sa composition (Na, K, Ca, Al; H_2O; LREE ; Montel 1993; Stepanov et al. 2012). Toutefois, l'influence des anions comme Cl^-, F^-, SO_4^{2-}, qui sont connus pour augmenter la solubilité de la monazite dans les phases aqueuses (hydrothermales ; Hetherington et al. 2010), est très peu connue dans les liquides silicatés où les interactions sont plus complexes. En attendant les études expérimentales, il est nécessaire, par une approche naturaliste, d'évaluer l'influence de ces éléments mineurs et de leur spéciation dans les roches partiellement fondues.

Problématique et plan de l'étude

Ce travail de thèse se positionne à l'interface entre pétrologie métamorphique, géochronologie et comportement minéralogique de la monazite et du zircon dans des conditions de ultra-haute température. Ce positionnement est justifié par l'interconnexion existant entre toutes ces problématiques à l'échelle du cristal comme à celle de la lithosphère. Ce manuscrit est focalisé sur deux questions centrales qui sont : (1) les modalités de l'enregistrement des âges U–Th–Pb dans la monazite et le zircon au cours du métamorphisme de ultra-haute température et (2) la quantification des conditions *P–T–fluides* subies par les roches de UHT. Les éléments de réponses à ces deux questions permettent enfin de discuter de l'origine du métamorphisme de UHT et des interactions magmatisme–métamorphisme dans la croûte du Rogaland (sud de la Norvège) qui constitue notre objet d'étude. Deux campagnes de terrain ont permis de collected environ 150 échantillons dans le socle granulitique du Rogaland et au-delà. Les principales caractéristiques de chaque échantillon sont reportées dans le tableau I-1.

Ce travail a permis d'aborder différentes facettes de la recherche en géosciences allant du travail de terrain à la modélisation, en passant par des mesures géochimiques, géochronologiques et des considérations minéralogiques. Ces différentes thématiques transparaissent dans chacun des cinq chapitres de cette thèse.

- Le premier chapitre constitue une introduction à la géologie du terrain d'étude, le Rogaland. Nous y présentons brièvement les éléments nécessaires à la compréhension globale de l'orogène Sveconorvégien avant de nous plonger au cœur du réseau cristallin de la monazite et du zircon.

- Le second chapitre s'intéresse aux modalités d'incorporation du S dans la monazite et ses implications en termes de traçage de fluides dans la croûte et de datation des minéralisations. Enfin, le cycle du S dans les roches de haut degré métamorphique est discuté. *Le cœur de ce chapitre est constitué par un manuscrit accepté pour publication à Contributions to Mineralogy and Petrology.*

- Le troisième chapitre s'attache à caractériser les assemblages minéralogiques et à quantifier les conditions *P–T* subies par les roches du Rogaland. Nous montrons qu'il existe en fait deux métamorphismes de (U)HT successifs en couplant modélisation thermodynamique des minéraux majeurs et équilibre de phases monazite–xénotime–huttonite. *Le cœur de ce chapitre est constitué par un manuscrit qui sera soumis à Journal of Metamorphic Geology*

- Le quatrième chapitre étudie la réponse des zircons au métamorphisme de UHT. En particulier les mécanismes menant à la remise à zéro partielle du chronomètre U–Pb ou à la préservation des âges sont discutés. Nous quantifions ensuite les échelles de temps de la fusion partielle dans la croûte du Rogaland. *Le cœur de ce chapitre est constitué par un manuscrit en cours de préparation*

- Le dernier chapitre se présente sous la forme d'une synthèse régionale des données géochronologiques présentées de manière thématique dans les quatre premiers chapitres, complémenté de nouvelles données structurales et géochronologiques. Nous discutons de manière plus générale des sources de chaleurs possibles et de leurs contributions relatives pour atteindre la UHT et maintenir des conditions thermiques élevées pendant 100 Ma, au Rogaland. *Le cœur de ce chapitre est constitué par un manuscrit en cours de préparation*

Références

Ahrens LH (1955) The convergent lead ages of the oldest monazite and uraninites (Rhodesia, Manitoba, Madagascar, and Transval). Geochim Cosmochim Acta 7:294–300.

Austrheim H. (1987) Eclogitization of lower crustal granulites by fluid migration through shear zones. Earth Planet Sci Lett 81:221–232.

Baldwin JA, Brown M, Schmitz MD (2007) First application of titanium-in-zircon thermometry to ultrahigh-temperature metamorphism. Geology 35:295–298.

Barrow G. (1912) On the geology of the lower Dee-side and the southern Highland border. Proceedings of the Geologists Association, 23:274–290

Bea F (1996) Residence of REE, Y, Th and U in granites and crustal protoliths; implications for the chemistry of crustal melts. J Petrol 37:521–552.

Berman RG (1988) Internally-consistent thermodynamic data for minerals in the system Na_2O-K_2O-CaO-MgO-FeO-Fe_2O_3-Al_2O_3-SiO_2-TiO_2-H_2O-CO_2. J Petrol 29:445–522.

Bhowmik SK, Wilde SA, Bhandari A, Basu Sarbadhikari A (2014) Zoned monazite and zircon as monitors for the thermal history of granulite terranes: an example from the Central Indian Tectonic Zone. J Petrol 55:585–621.

Bingen B, Austrheim H, Whitehouse MJ (2001) Ilmenite as a source for zirconium during high-grade metamorphism? textural evidence from the Caledonides of western Norway and implications for zircon geochronology. J Petrol 42:355–375.

Bohlen SR (1991) On the formation of granulites. J Metamorph Geol 9:223–229.

Brown M (2007) Metamorphic Conditions in Orogenic Belts: A Record of Secular Change. Int Geol Rev 49:193–234.

Brown M (2009) Metamorphic patterns in orogenic systems and the geological record. Geol Soc Lond Spec Publ 318:37–74.

Carrington DP, Harley SL (1995) Partial melting and phase relations in high-grade metapelites: an experimental petrogenetic grid in the KFMASH system. Contrib Mineral Petrol 120:270–291.

Cherniak DJ (2010) Diffusion in Accessory Minerals: Zircon, Titanite, Apatite, Monazite and Xenotime. Rev Mineral Geochem 72:827–869.

Clark C, Fitzsimons ICW, Healy D, Harley SL (2011) How Does the Continental Crust Get Really Hot? Elements 7:235–240.

Cole DR, Chakraborty S (2001) Rates and Mechanisms of Isotopic Exchange. Rev Mineral Geochem 43:83–223

Collins WJ (2002) Hot orogens, tectonic switching, and creation of continental crust. Geology 30:535–538.

Connolly JAD (1990) Multivariable phase diagrams: an algorithm based on generalized thermodynamics. Am J Sci 290:666–718.

Connolly JAD (2009) The geodynamic equation of state: What and how. Geochem Geophys Geosystems 10, Q10014. doi: 10.1029/2009GC002540

Connolly JAD, Petrini K (2002) An automated strategy for calculation of phase diagram sections and retrieval of rock properties as a function of physical conditions. J Metamorph Geol 20:697–708.

Corfu F (2013) A century of U-Pb geochronology: The long quest towards concordance. Geol Soc Am Bull 125:33–47.

Currie CA, Hyndman RD (2006) The thermal structure of subduction zone back arcs. J Geophys Res. 111, B08404, doi: 10.1029/2005JB004024

Daubrée A. (1857) Observations sur le métamorphisme et recherches expérimentales sur quelques uns des agents qui ont pu le produire. Annales des mines 5:155–218

Didier A, Bosse V, Boulvais P, Bouloton J, Paquette J-L, Montel J-M, Devidal J-L (2013) Disturbance versus preservation of U–Th–Pb ages in monazite during fluid–rock interaction: textural, chemical and isotopic in situ study in microgranites (Velay Dome, France). Contrib Mineral Petrol 165:1051–1072.

Drüppel K, Elsasser L, Brandt S, Gerdes A (2013) Sveconorwegian Mid-crustal Ultrahigh-temperature Metamorphism in Rogaland, Norway: U–Pb LA–ICP–MS Geochronology and Pseudosections of Sapphirine Granulites and Associated Paragneisses. J Petrol 54:305–350.

Duchene S., Blichert-Toft J., Luais B., Lardeaux J.M., Albarède F. (1997) The Lu–Hf dating of garnets and the ages of the Alpine high-pressure metamorphism. Nature 387:586–588.

Dumond G, Mahan KH, Williams ML, Jercinovic MJ (2013) Transpressive uplift and exhumation of continental lower crust revealed by synkinematic monazite reactions. Lithosphere 5:507–512.

England P. C. Thompson A. B. (1984) Pressure–temperature–time paths of regional metamorphism I. Heat transfer during the evolution of regions of thickened continental crust. J Petrol 25:894–928

Ernst W. G. (1975) Metamorphism and plate tectonic regimes. Dowden, Hutchinson and Ross, New York 410pp.

Eskola P. (1920) The mineral facies of rocks. Norsk Geologisk Tidsskrift 6:143–194

Ewing RC, Meldrum A, Wang L, Weber WJ, Corrales LR (2003) Radiation effects in zircon. Rev Mineral Geochem 53:387–425.

Ewing TA, Hermann J, Rubatto D (2013) The robustness of the Zr-in-rutile and Ti-in-zircon thermometers during high-temperature metamorphism (Ivrea-Verbano Zone, northern Italy). Contrib Mineral Petrol 165:757–779.

Fraser G, Ellis D, Eggins S (1997) Zirconium abundance in granulite-facies minerals, with implications for zircon geochronology in high-grade rocks. Geology 25:607–610.

Fu B, Page FZ, Cavosie AJ, Fournelle J, Kita NT, Lackey JS, Wilde SA, Valley JW (2008) Ti-in-zircon thermometry: applications and limitations. Contrib Mineral Petrol 156:197–215.

Gardés E, Jaoul O, Montel J-M, Seydoux-Guillaume A-M, Wirth R (2006) Pb diffusion in monazite: An experimental study of interdiffusion. Geochim Cosmochim Acta 70:2325–2336.

Geisler T, Schaltegger U, Tomaschek F (2007) Re-equilibration of zircon in acueous fluids and melts. Elements 3:43–50.

Goldschmidt V.M. (1912) Die Gesetze der Gesteinsmetamorphose. Norsk Videnskapsselskaps Skrifter I. Mathematisk-Naturvidenskapelig Klasse 22, 16pp

Goncalves P (2004) Petrology and in situ U-Th-Pb Monazite Geochronology of Ultrahigh-Temperature Metamorphism from the Andriamena Mafic Unit, North-Central Madagascar. Significance of a Petrographical P-T Path in a Polymetamorphic Context. J Petrol 45:1923–1957.

Goncalves P (2005) Electron-microprobe age mapping of monazite. Am Mineral 90:578–585.

Grand'Homme A, Janots E, Seydoux-Guillaume A-M, Guillaume D, Bosse V, Magnin V (2016) Partial resetting of the U-Th-Pb systems in experimentally altered monazite: Nanoscale evidence of incomplete replacement. Geology 44:431–434.

Hacker BR, Kylander-Clark ARC, Holder R, Andersen TB, Peterman EM, Walsh EO, Munnikhuis JK (2015) Monazite response to ultrahigh-pressure subduction from U–Pb dating by laser ablation split stream. Chem Geol 409:28–41.

Harley SL (2008) Refining the P–T records of UHT crustal metamorphism. J Metamorph Geol 26:125–154.

Harley SL (2016) A matter of time: The importance of the duration of UHT metamorphism. J Mineral Petrol Sci 111:50–72.

Harley SL (1998a) On the occurence and characterization of ultrahigh-temperature crustal metamorphism. In: Treloar P.J. & O'Brien P.J. (eds) What drives metamorphism and metamorphic reactions? Geol Soc Lond Spec Publ 138:81–107.

Harley SL (1998b) Ultrahigh temperature granulite metamorphism (1050 °C, 12 kbar) and decompression in garnet (Mg70)-orthopyroxene-sillimanite gneisses from the Rauer Group, East Antarctica. J Metamorph Geol 16:541–562.

Harley SL, Green DH (1982) Garnet-orthopyroxene barometry for granulites and peridotites. Nature 300:697–700.

Harley SL, Kelly NM, Möller A (2007) Zircon behaviour and the thermal histories of mountain chains. Elements 3:25–30.

Harley SL, Motoyoshi Y (2000) Al zoning in orthopyroxene in a sapphirine quartzite: evidence for > 1120°C UHT metamorphism in the Napier Complex, Antarctica, and implications for the entropy of sapphirine. Contrib Mineral Petrol 138:293–307.

Harlov DE, Wirth R, Hetherington CJ (2011) Fluid-mediated partial alteration in monazite: the role of coupled dissolution–reprecipitation in element redistribution and mass transfer. Contrib Mineral Petrol 162:329–348.

Haüy R.J. (1822) Traité de minéralogie, 2nd ed., vol. 4. Bachelier, Paris, 604pp.

Helgeson H.C., Delany J.M., Nesbitt H. W., Bird D.K. (1978) Summary and critique of the thermodynamic properties of rock-forming minerals. Am. J. Sci. 278-A:1-229

Hensen BJ (1971) Theoretical phase relations involving cordierite and garnet in the system MgO–FeO–Al_2O_3–SiO_2. Contrib Mineral Petrol 33:191–214.

Hensen BJ (1977) The stability of osumilite in high grade metamorphic rocks. Contrib Mineral Petrol 64:197–204.

Hensen BJ, Green DH (1973) Experimental study of the stability of cordierite and garnet in pelitic compositions at high pressures and temperatures. Contrib Mineral Petrol 38:151–166.

Hermann J, Rubatto D (2003) Relating zircon and monazite domains to garnet growth zones: age and duration of granulite facies metamorphism in the Val Malenco lower crust. J Metamorph Geol 21:833–852.

Hetherington CJ, Harlov DE, Budzyń B (2010) Experimental metasomatism of monazite and xenotime: mineral stability, REE mobility and fluid composition. Mineral Petrol 99:165–184.

Holland T.J.B., Powell R. (1990) An enlarged and updated internally consistent thermodynamic dataset with undertainties and correlations: the system K_2O–Na_2O–CaO–MgO–MnO–FeO–Fe_2O_3–Al_2O_3–TiO_2–SiO_2–C–H_2–O_2. J Metamorph Geol 8:89-124

Holland TJB, Powell R (1998) An internally consistent thermodynamic data set for phases of petrological interest. J Metamorph Geol 16:309–343.

Holland TJB, Powell R (2011) An improved and extended internally consistent thermodynamic dataset for phases of petrological interest, involving a new equation of state for solids. J Metamorph Geol 29:333–383.

Johnson M. R., Harley S. L. (2012) Orogenesis: the making of mountains. Cambridge university press, Cambridge, 338pp

Kelly NM, Harley SL (2005) An integrated microtextural and chemical approach to zircon geochronology: refining the Archaean history of the Napier Complex, east Antarctica. Contrib Mineral Petrol 149:57–84.

Kelsey DE (2008) On ultrahigh-temperature crustal metamorphism. Gondwana Res 13:1–29.

Kelsey DE, Clark C, Hand M (2008) Thermobarometric modelling of zircon and monazite growth in melt-bearing systems: examples using model metapelitic and metapsammitic granulites. J Metamorph Geol 26:199–212.

Kelsey DE, Hand M (2015) On ultrahigh temperature crustal metamorphism: Phase equilibria, trace element thermometry, bulk composition, heat sources, timescales and tectonic settings. Geosci Front 6:311–356.

Kelsey DE, White RW, Holland TJB, Powell R (2004) Calculated phase equilibria in K_2O–FeO–MgO–Al_2O_3–SiO_2–H_2O for sapphirine-quartz-bearing mineral assemblages. J Metamorph Geol 22:559–578.

Kemp AIS, Shimura T, Hawkesworth CJ, others (2007) Linking granulites, silicic magmatism, and crustal growth in arcs: Ion microprobe (zircon) U-Pb ages from the Hidaka metamorphic belt, Japan. Geology 35:807–810.

Korhonen FJ, Clark C, Brown M, Bhattacharya S, Taylor R (2013) How long-lived is ultrahigh temperature (UHT) metamorphism? Constraints from zircon and monazite geochronology in the Eastern Ghats orogenic belt, India. Precambrian Res 234:322–350.

Korhonen FJ, Clark C, Brown M, Taylor RJM (2014) Taking the temperature of Earth's hottest crust. Earth Planet Sci Lett 408:341–354.

Korzhinskii D.S. (1959) Physicochemical basis of the analysis of the paragenesis of minerals (translation). Consultat Bureau, New-York, p.143

Krogh T.E. (1973) A low contamination method for the hydrothermal decomposition of zircon and extraction of U and Pb for isotopic age determinations. Geochimica et Cosmochimica Acta 37:485–494

Kroll H, Evangelakakis C, Voll G (1993) Two-feldspar geothermometry: a review and revision for slowly cooled rocks. Contrib Mineral Petrol 114:510–518.

Lancelot J.R., Vitrac A., Allègre C.J. (1976) Uranium and lead isotopic dating with grain-by-grain analysis: A study of complex geological history with a single rock: Earth Planet Sci Lett 29:357–366.

McLaren AC, Fitz Gerald JD, Williams IS (1994) The microsctructure of zircon and its influence on the age determination from Pb/U isotopic ratios measured by ion microprobe. Geochim Cosmochim Acta 58:993–1005.

Miyashiro A. (1961) Evolution of metamorphic belts. J Petrol 2:277-311.

Möller A, O'Brien PJ, Kennedy A, Kröner A (2003) Linking growth episodes of zircon and metamorphic textures to zircon chemistry: an example from the ultrahigh-temperature granulites of Rogaland (SW Norway). Geol Soc Lond Spec Publ 220:65–81.

Montel JM (1993) A model for monazite/melt equilibrium and application to the generation of granitic magmas. Chem Geol 127–146.

Montel J-M, Foret S, Veschambre M, Nicollet C, Provost A (1996) Electron microprobe dating of monazite. Chem Geol 131:37–53.

Moser DE, Davis WJ, Reddy SM, Flemming RL, Hart RJ (2009) Zircon U–Pb strain chronometry reveals deep impact-triggered flow. Earth Planet Sci Lett 277:73–79.

Nasdala L, Wenzel M, Vavra G, Irmer G, Wenzel T, Kober B (2001) Metamictisation of natural zircon: accumulation versus thermal annealing of radioactivity-induced damage. Contrib Mineral Petrol 141:125–144.

Nicolaysen L.O. (1961) Graphic interpretation of discordant age measurements on metamorphic rocks. Annals of the New-York academy of Sciences 91:198-206.

Parrish RR (1990) U–Pb dating of monazite and its application to geological problems. Can J Earth Sci 27:1431–1450.

Passchier C.W., Trouw R.A. (1996) Microtectonics. Springer, Berlin, 289pp.

Powell R, Holland TJB (1988) An internally consistent dataset with uncertainties and correlations: 3. Applications to geobarometry, worked examples and a computer program. J Metamorph Geol 6:173–204.

Pownall JM, Hall R, Armstrong RA, Forster MA (2014) Earth's youngest known ultrahigh-temperature granulites discovered on Seram, eastern Indonesia. Geology 42:279–282.

Putnis, A. (1992) An introduction to mineral sciences. Cambridge University press, Cambridge, 487pp.

Pyle JM, Spear FS, Rudnick RL, McDonough WF (2001) Monazite-Xenotime-Garnet equilibrium in metapelites and a new monazite-garnet thermometer. J Petrol 42:2083–2107.

Sandiford M, Powell R (1986) Pyroxene exsolution in granulites from Fyfe Hills, Enderby Land, Antarctica: Evidence for 1000 °C metamorphic temperatures in Archean continental crust. Am Mineral 71:946–954.

Schaltegger U, Fanning CM, Günther D, Maurin JC, Schulmann K, Gebauer D (1999) Growth, annealing and recrystallization of zircon and preservation of monazite in high-grade metamorphism: conventional and in-situ U-Pb isotope, cathodoluminescence and microchemical evidence. Contrib Mineral Petrol 134:186–201.

Schreyer W, Seifert F (1967) Metastability of an osumilite end member in the system K_2O–MgO–Al_2O_3–SiO_2–H_2O and its possible bearing on the rarity of natural osumilites. Contrib Mineral Petrol 14:343–358.

Seydoux-Guillaume A-M, Bingen B, Paquette J-L, Bosse V (2015) Nanoscale evidence for uranium mobility in zircon and the discordance of U–Pb chronometers. Earth Planet Sci Lett 409:43–48.

Seydoux-Guillaume A-M, Montel J-M, Bingen B, Bosse V, de Parseval P, Paquette J-L, Janots E, Wirth R (2012) Low-temperature alteration of monazite: Fluid mediated coupled dissolution–precipitation, irradiation damage, and disturbance of the U–Pb and Th–Pb chronometers. Chem Geol 330–331:140–158.

Seydoux-Guillaume A-M, Wirth R, Deutsch A, Schärer U (2004) Microstructure of 24-1928 Ma concordant monazites; implications for geochronology and nuclear waste deposits. Geochim Cosmochim Acta 68:2517–2527.

Silver L.T., Deutsch S. (1963) Uranium-lead isotopic variations in zircons: a case study. J Geol 71:721–758.

Sizova E, Gerya T, Brown M (2014) Contrasting styles of Phanerozoic and Precambrian continental collision. Gondwana Res 25:522–545.

Spear FS (1991) On the interpretation of peak metamorphic temperatures in light of garnet diffusion during cooling. J Metamorph Geol 9:379–388.

Spear F.S. (1995) Metamorphic phase equilibria and pressure-temperature-time paths. Mineralogical society of America, Washington, 799pp.

Stepanov AS, Hermann J, Rubatto D, Rapp RP (2012) Experimental study of monazite/melt partitioning with implications for the REE, Th and U geochemistry of crustal rocks. Chem Geol 300–301:200–220.

Taylor RJM, Clark C, Fitzsimons ICW, Santosh M, Hand M, Evans N, McDonald B (2014) Post-peak, fluid-mediated modification of granulite facies zircon and monazite in the Trivandrum Block, southern India. Contrib Mineral Petrol. 168:1-17

Thompson J.B. (1957) The graphical analysis of mineral assemblage in pelitic schists. Am Mineral 42:842-858.

Tilton G.R., Patterson C., Brown H., Inghram M., Hayden R., Hess D., Larsen E. (1955) Isotopic composition and distribution of lead, uranium and thorium in a Precambrian granite: Geological Society of America Bulletin 66:1131–1148.

Turner F.J. (1948) Mineralogical and structural evolution of the metamorphic rocks. Geological Society of America Memoirs 30, 332pp.

Vernon RH (1996) Problems with inferring P–T–t paths in low-P granulite facies rocks. J Metamorph Geol 14:143–153.

Walsh AK, Kelsey DE, Kirkland CL, Hand M, Smithies RH, Clark C, Howard HM (2014) P–T–t evolution of a large, long-lived, ultrahigh-temperature Grenvillian belt in central Australia. Gondwana Res. 28:531-564

Watson EB, Harrison TM (1983) Zircon saturation revisited: temperature and composition effects in a variety of crustal magma types. Earth Planet Sci Lett 64:295–304.

Wells PRA (1980) Thermal models for the magmatic accretion and subsequent metamorphism of continental crust. Earth Planet Sci Lett 46:253–265.

Wetherill GW (1956) Discordant Uranium-Lead Ages, I. Trans Am Geophys Union 37:320–326.

White RW, Powell R, Holland TJB (2007) Progress relating to calculation of partial melting equilibria for metapelites. J Metamorph Geol 25:511–527.

White RW, Powell R, Holland TJB, Johnson TE, Green ECR (2014) New mineral activity-composition relations for thermodynamic calculations in metapelitic systems. J Metamorph Geol 32:261–286.

Whitehouse MJ, Platt JP (2003) Dating high-grade metamorphism—constraints from rare-earth elements in zircon and garnet. Contrib Mineral Petrol 145:61–74.

Williams ML, Jercinovic MJ, Hetherington CJ (2007) Microprobe Monazite Geochronology: Understanding Geologic Processes by Integrating Composition and Chronology. Annu Rev Earth Planet Sci 35:137–175.

Tableau

Tab. 1-1: Sample set sorted by sample name. The samples' (x,y) coordinates are given in UTM zone 32 (WGS84).

Outcrop	Locality	x	y	Sample	Description & mineralogy
ALR3	Gyadal	349712	6499705	13-01	Opx-Bt gneiss (Py, Po)
ALR4	Gyadal	349198	6500134	13-02	Opx migmatitic gneiss
ALR5	Gyadal	349028	6500074	13-03	Grt-Opx melanosome (+ Qtz, Hc)
ALR6	Gyadal	348746	6499700	13-04	cm-scale (Opx + Grt) layer (+ Hc)
ALR6	Gyadal	348746	6499700	13-05	Grt leucosome (Grt, Opx, Crd, Hc, Bt, Qz)
ALR7	Gyadal	348495	6499696	13-06	fine grained leucocratic Hc + Qtz rock (+ Crd, Sil)
ALR7	Gyadal	348495	6499696	13-07	fine grained leucocratic Opx + Bt rock
ALR7	Gyadal	348495	6499696	13-08	leucocratic Hc + Qtz rock (+ Sil)
ALR8	Gyadal	348447	6499594	13-09	homogenous fine grained Hc + Qtz rock (+ Crd, Sil)
ALR10	Gyadal	348434	6499583	13-10	deformed garnet leucosome (?) (Grt, Hc, Qtz, Sil, Crd)
ALR11	Gyadal	342906	6496411	13-11	banded gneiss – fine grained layer (Cpx, Opx, Bt)
ALR11	Gyadal	342906	6496411	13-12	banded gneiss – coarse grained layer (Cpx, Opx, Bt)
ALR12	Gyadal	342353	6495983	13-13	migmatitic charnockite (Opx)
ALR12	Gyadal	342353	6495983	13-14	migmatitic charnockite (Opx leucosome)
ALR13	Ivesdal	335841	6510379	13-15	Opx gneiss (wheathered)
ALR14	Ivesdal	335800	6510382	13-16	Opx-Hc gneiss (+Bt)
ALR17	Ivesdal	335797	6510397	13-17	melanocratic boudin (Spr, Opx, Spl, Crd)
ALR17	Ivesdal	335797	6510397	13-18	Spr gneiss (Spr, Opx, Spl, Crd, Bt, no Qtz)
ALR18	Ivesdal	335796	6510416	13-19	strongly deformed Spr-Opx gneiss (Spr, Opx, Spl, Bt, Crd)
ALR20	Ivesdal	335704	6510392	13-20	leucocratic rock (Opx, Spl)
ALR21	Ivesdal	335619	6510453	13-21	Opx, Spl migmatite with snowball garnet (no Crd)
ALR22	Ivesdal	335550	6510354	13-22	Spr gneiss schlieren (Spr, Opx, Spl, Crd, Bt, no Qtz)
ALR22	Ivesdal	335565	6510355	13-23	Opx, Spl migmatite (+ Bt)
ALR22	Ivesdal	335564	6510349	13-24	fine grained felsic granulite (Opx)
ALR22	Ivesdal	335548	6510362	13-25	Opx-Bt migmatite
ALR22	Ivesdal	335548	6510362	13-26	Opx-Hc migmatite with snowball garnet
ALR23	Ivesdal	335447	6510184	13-27	melanocratic Px granulite
ALR23	Ivesdal	335573	6510024	13-28	garnet-bearing migmatite
ALR23	Ivesdal	335523	6510074	13-29	Opx leucosome (Bt, Chl)
ALR25	Ivesdal	335664	6509976	13-30	aluminous gneiss (Grt, Sil, Crd)
ALR26	Ivesdal	335628	6509549	13-31	aluminous gneiss (Grt, Hc, Qtz)
ALR27	Frafjord	336541	6525418	13-32	garnet granite (+ altered Opx)
ALR28	Frafjord	334182	6525512	13-33	migmatitic gneiss (Bt, Grt, Sil, Hc, sulphides)
ALR28	Frafjord	334388	6522539	13-34	Grt- Opx-rich layer in migmatitic gneiss (Hc, Crd, Bt)
ALR29	Oltedal	327380	6523584	13-35	banded gneiss -leucocratic layer (Bt, Chl)
ALR29	Oltedal	327380	6523584	13-36	banded gneiss -melanocratic layer (Opx, Hbl)
ALR30	Oltedal	327823	6523951	13-37	felsic rock with folded garnet layers
ALR30	Oltedal	327821	6523960	13-38	Grt-Bt migmatite
ALR31	Oltedal	327761	6523970	13-39	Grt-Bt migmatite
ALR31	Oltedal	327761	6523970	13-40	Grt-Bt migmatite (– Sil in Grt)
ALR31	Oltedal	327754	6523979	13-41	Qtz-Grt vein (hydrothermal?)
ALR31	Oltedal	327754	6523979	13-42	Qtz-Grt vein (hydrothermal?)
ALR32	Oltedal	327846	6523925	13-43	fine grained leucocratic Hc + Qtz rock (+ Grt, Sil)
ALR33	Oltedal	327962	6523881	13-44	fine grained leucocratic Hc + Qtz rock (+ Grt, Sil)
ALR34	Oltedal	327720	6524288	13-45	Grt-Opx gneiss
ALR34	Oltedal	327720	6524288	13-46	fine grained mafic band

Tab. I-1: continued

ALR35	Oltedal	326754	6526314	13-47	mafic lens in Opx-gneiss (Opx-Bt)
ALR35	Oltedal	326754	6526314	13-48	Opx-gneiss (altered in Chl)
ALR1	Algard	321660	6516436	13-49	Grt-Bt migmatite (−Hc, Crd)
ALR1	Algard	321660	6516436	13-50	Grt-Bt migmatite (−Sil)
ALR36	Vikesa	331825	6503460	13-51	Grt-Opx gneiss (Hc, Bt, Qz)
ALR36	Vikesa	331836	6503456	13-52	Grt-Opx gneiss (leucosome ?)
ALR36	Vikesa	331838	6503424	13-53	Opx gneiss
ALR36	Vikesa	331777	6503471	13-54	Grt leucosome
ALR37	Vikesa	332535	6503984	13-55	Osm gneiss (Grt, Sil, Hc, Qtz, Opx)
ALR37	Vikesa	332535	6503984	13-56	Osm gneiss (Grt, Sil, Hc, Qtz, Opx)
ALR37	Vikesa	332496	6503977	13-57	Osm gneiss (Grt, Sil, Hc, Qtz, Opx + Crd)
ALR37	Vikesa	332468	6503977	13-58	Osm gneiss (Grt, Sil, Hc, Qtz, Opx + Crd)
ALR37	Vikesa	332444	6503988	13-59	Osm gneiss (Grt, Sil, Hc, Qtz, Opx)
ALR37	Vikesa	332482	6503981	13-60	Osm gneiss (Grt, Sil, Hc, Qtz, Opx)
ALR38	Vikesa	331068	6503797	13-61	Opx leucosome from 13-62
ALR38	Vikesa	331068	6503797	13-62	Pigeonite granulite
ALR1	Algard	321514	6516488	13-63	Grt leucosome
ALR1	Algard	321547	6516474	13-64	aluminous gneiss (Grt, Sil, Hc, Crd, Bt)
ALR1	Algard	321685	6516422	13-65	Grt granite
ALR39	Gyadal	342875	6496401	13-66	Grt-Opx gneiss
ALR39	Gyadal	342824	6496326	13-67	fine grained opx-rich layer
ALR40	Hunnendal	354638	6524591	13-68	Grt-Opx gneiss
ALR41	Hunnendal	355264	6524649	13-69	Grt-Bt gneiss (+Opx)
ALR42	Hunnendal	353139	6523676	13-70	charnockite
ALR43	Hunnendal	353185	6523710	13-71	Opx leucosome (altered)
ALR65	Ivesdal	346920	6499314	14-01	Opx-Grt gneiss (+Bt)
ALR66	Gyadal	347012	649930	14-02	cm-scale Grt migmatite (Sil, Bt, Crd)
ALR66	Gyadal	346950	6499284	14-03	Gt-Opx gneiss (Bt, Pl)
ALR 67	Gyadal	346914	6499444	14-04	Gt-Bt-Opx restite (Crd)
ALR68	Gyadal	346409	6500906	14-05	Opx-Pl boudin in aluminous gneiss
ALR69	Martseinsfjell	336763	6504582	14-06	Grt leucosome
ALR70	Martseinsfjell	336741	6504544	14-07	Opx-Grt gneiss (+Bt)
ALR71	Martseinsfjell	336826	6504244	14-08	Opx-Grt gneiss (altered)
ALR72	Martseinsfjell	336746	6503948	14-09	Grt leucosome
ALR73	Martseinsfjell	336662	6503786	14-10	fine grained Grt+Hc+Qtz rock
ALR75	Gjedal	369981	6532632	14-11	Opx leucosome (banded gneiss)
ALR75	Gjedal	369981	6532632	14-12	Opx-Bt melanosome (banded gneiss)
ALR76	Gjedal	355847	6525056	14-13	charnockite (Opx altered in Chl)
ALR77	Maudal	345887	6517284	14-14	Opx-Grt massive gneiss (+ Bt, Chl)
ALR77	Maudal	345845	6517324	14-15	Grt-Bt migmatite
ALR77	Maudal	345845	6517324	14-16	Opx-Bt restite
ALR77	Maudal	345809	6517358	14-17	Grt-Bt migmatite
ALR77	Maudal	345794	6517366	14-18	Grt-Bt-Hc migmatite rich in sulphhide (−Crd)
ALR77	Maudal	345793	6517377	14-19	aluminous gneiss (Grt, Sil, Bt, Crd, Hc, Kfs, Qtz)
ALR79	Faurefjell	330301	6508449	14-20	Grt-Opx-Hc gneiss
ALR80	Martseinsfjell	337819	6502488	14-21	Osm gneiss (Grt, Opx, Hc, Qtz, Crd, Sil)
ALR80	Martseinsfjell	337819	6502488	14-22	fine grained Hc+Qtz rock (+Crd altered)

Tab. I-1: continued

ALR81	Ivesdal	335830	6509705	14-23	Opx-Bt restite (altered)
ALR83	Faurefjell	330444	6508060	14-24	Di marble / quartzite contact
ALR83	Faurefjell	330444	6508060	14-25	Diospide-phlogopite quartzite
ALR83	Faurefjell	330444	6508060	14-26	Diospside-phlogopite gneiss
ALR83	Faurefjell	330444	6508060	14-27	Diospside gneiss
ALR83	Faurefjell	330432	6508053	14-28	iron-stone (Opx, Spl, Pl, oxides)
ALR84	Faurefjell	330334	6508341	14-29	Grt-Opx-Hc gneiss
ALR84	Faurefjell	330334	6508341	14-30	Grt-Opx-Hc gneiss
ALR84	Faurefjell	330334	6508341	14-31	Grt-Opx-Hc gneiss
ALR85	Orsdal	350273	6505422	14-32	Grt-Bt migmatite, rich in sulfides (+Crd-Qtz)
ALR86	Orsdal	351656	6506383	14-33	Grt-Opx gneiss
ALR86	Orsdal	351663	6506374	14-34	Grt leucosome rich in molybdenite (+Bt)
ALR87	Orsdal	351581	6506527	14-35	Opx-Bt undeformed leucosome
ALR37	Vikesa	332482	6503981	14-36	Osm gneiss (reserve!)
ALR88	Martseinsfjell	336568	6503699	14-37	Grt-Hc-Qtz gneiss
ALR89	Martseinsfjell	336612	6503721	14-38	Grt-Hc-Qtz gneiss (+ Crd)
ALR89	Martseinsfjell	336612	6503721	14-39	Grt-Hc-Qtz gneiss (+ Crd)
ALR89	Martseinsfjell	336612	6503721	14-40	Grt leucosome (Crd+Hc)
ALR90	Martseinsfjell	336644	6503725	14-41	Grt-Opx-Hc gneiss
ALR91	Martseinsfjell	336674	6503713	14-42	Grt leucosome (Hc)
ALR91	Martseinsfjell	336674	6503713	14-43	
ALR92	Martseinsfjell	336785	6503670	14-44	aluminous gneiss (Grt, Sil, Crd, Hc, Kfs, Qtz)
ALR93	Martseinsfjell	336841	6503607	14-45	Grt-Hc-Qtz gneiss (+ Crd)
ALR94	Gyadal	350580	6498603	14-46	Grt-Opx migmatite
ALR95	Gyadal	349922	6498625	14-47	aluminous gneiss (Grt, Sil, Crd, Hc, Bt, Kfs, Qtz)
ALR97	Gyadal	349912	6498757	14-48	Grt-Bt migmatite
ALR98	Gyadal	349812	6498756	14-49	Grt-Crd gneiss (+Sill)
ALR99	Gyadal	350098	6498949	14-50	aluminous gneiss (Grt, Sil, Crd, Hc, Kfs, Qtz)
ALR100	Bue	324036	6505826	14-51	Grt-Cpx marble
ALR100	Bue	324036	6505826	14-52	Kfs-Di gneiss (rich in titanite)
ALR100	Bue	324036	6505826	14-53	Diopside-phlogopite gneiss
ALR100	Bue	324051	6505845	14-54	Opx-Spl-Qtz gneiss (altered)
ALR100	Bue	324051	6505845	14-55	contact quartzite / Opx-Spl-Qtz gneiss
ALR100	Bue	324051	6505843	14-56	Opx quartzite
ALR100	Bue	324078	6505843	14-57	Osm gneiss (Grt, Opx, Hc, Qtz, Crd)
ALR100	Bue	310780	6496226	14-58	Px quartzite (rich in titanite)
ALR101	Hadland	321174	6516728	14-59	Grt-Opx gneiss (altered)
ALR1	Algard	321660	6516436	14-60	Grt-Bt migmatite
ALR103	Orsdal	343550	6510010	14-61	Grt-Bt migmatite + sulfides
ALR104	Orsdal	343585	6510014	14-62	Grt-Bt migmatite + sulfides (Hc, Crd, Po, Ru)
ALR105	Orsdal	340166	6508057	14-63	Grt-Opx leucosome (associated with 13-64)
ALR105	Orsdal	340166	6508057	14-64	Grt-Opx gneiss (+Bt)
ALR106	Martseinsfjell	337396	6504960	14-65	Grt-Crd gneiss (+Sill, Bt inclusions)
ALR107	Martseinsfjell	337661	6505281	14-66	Grt leucosome (associated with 14-65)
ALR108	Martseinsfjell	337473	6505040	14-67	aluminous gneiss (Grt, Sil, Crd, Hc, Kfs, Qtz)

Tab. I-1: continued

Samples collected by B. Bingen in 2001

similar to 13-58	332472	6503971	B01029	Grt-Osm-Opx granulite gneiss
	327706	6524341	B00155	Grt-Bt felsic gneiss
	327694	6524281	B00156	Grt-Opx-Bt granulite
	336494	6525437	B00157	Grt-Bt felsic gneiss
	354545	6524603	B00158	Grt-Opx-Bt granulite
	355253	6524677	B00159	Grt-Bt felsic gneiss, altered
	356069	6525164	B00160	Granitic gneiss

Chapitre 1

Overview of the Sveconorwegian orogeny and Mesoproterozoic evolution of Rogaland, S-Norway

Résumé

Dans ce chapitre, nous introduisons les éléments de contexte géologique nécessaires à la compréhension du manuscrit de thèse dans son ensemble. Le terrain d'étude choisi fait partie de la chaine Svéconorvégienne, localisée en Scandinavie, qui constitue la terminaison latérale de la chaîne Grenvillienne d'Amérique du Nord. Ces deux orogènes résultent de l'assemblage du supercontinent Rodinia au Néoprotérozoïque et sont caractérisés par une architecture lithotectonique similaire et des événements métamorphiques synchrones entre 1140 et 900 Ma. La chaîne Svéconorvégienne est interprétée classiquement comme étant le résultat de la collision entre Baltica et un autre ensemble continental majeur, peut-être Amazonia. La chaîne se divise de l'est vers l'ouest en un segment Paléoprotérozoïque autochtone (Eastern Segment), d'un domaine para-autochtone (Idefjorden) conservant des reliques de haute pression (HP) puis de cinq autres domaines allochtones (Kongsberg, Bamble, Telemark, Hardangervidda-Agder et Rogaland) caractérisés par un métamorphisme de moyenne à haute température (HT). Par ailleurs, des reliques de la chaîne Svéconorvégienne affleurent dans les nappes Calédoniennes de Lindås, Dalsfjord et Jotun.

Un passage en revue des données géologiques et géochronologiques existantes permettent d'isoler quatre phases orogéniques principales suivant Bingen et al. (2008c). (1) À 1150–1080 Ma, la phase dite d'Arendal représente la collision entre Idefjorden et Telemarkia (comprenant les domaines du Telemark, Hardangervidda-Agder et Rogaland) qui entraine la formation de prismes tectoniques que sont le Bamble et le Kongsberg. Cet événement est marqué par un pic de métamorphisme dans le faciès granulite (0.7 GPa ; 800 °C) à environ 1100 Ma dans le Bamble et le Kongsberg. (2) La phase orogénique principale (dite d'Agder) s'étendant de 1050 à 1000 Ma est interprétée comme une collision continentale (oblique ?) entre les deux macro-continents. Cette collision entraine l'enfouissement du domaine d'Idefjorden à HP (1.0–1.5 GPa ; T ~ 800 °C) à environ 1050 Ma, suivi de son exhumation dans l'intervalle 1030–1000 Ma. L'épaississement crustal affecte aussi Telemarkia et se traduit par la mise en place entre 1060 et 1025 Ma d'importants volumes de magmas à signature calco-alcaline. Simultanément, un événement granulitique de moyenne pression affecte tout le domaine du Rogaland avec l'enregistrement local de conditions de UHT (0.75 GPa ; 1000°C). (3) À 990–980 Ma, la phase orogénique de Falkenberg traduit la fin de la convergence avec la propagation du métamorphisme de HP vers l'est dans l'Eastern Segment qui enregistre des conditions éclogitiques (P > 1.5 GPa). Cet épisode de HP est rapidement suivi de l'exhumation des éclogites dans une nappe partiellement fondue à 976 ± 6 Ma. (4) Entre 970 et 920 Ma la phase Dalane correspond à l'effondrement gravitaire de la chaîne.

Elle est associée à un important magmatisme post-collisionel comprenant des séries à anorthosite–charnockite–mangérite et des granitoïdes à hornblende–biotite. Dans le domaine du Rogaland, l'intrusion d'un massif d'anorthosite extrêmement volumineux cause un métamorphisme de ultra-haute température à basse pression (0.5 GPa ; 900–1000°C).

Framework of Rodinia assembly

Plate tectonic reconstruction in the Proterozoic suggests that Laurentia, corresponding roughly to present-day North-America, and Baltica, comprising much of Northeastern Europe, share a geological history encompassing an entire Wilson cycle (e.g. Gower et al. 1990; Karlstrom et al. 2001). The final assembly of Baltica and Laurentia at the end of the Mesoproterozoic lead to the amalgamation of supercontinent Rodinia welded along Grenvillian–Sveconorwegian orogenic belts (Hoffman 1991). Although most authors agree on the involvement of Amazonia in Rodinia assembly, the exact position of this continental plate and its interactions with Baltica remains disputed (Li et al. 2008; Evans 2009; Johansson 2009). The classical Neoproterozoic Baltica–Laurentia–Amazonia reconstruction is presented on Fig. 1, following Cawood et al. (2007).

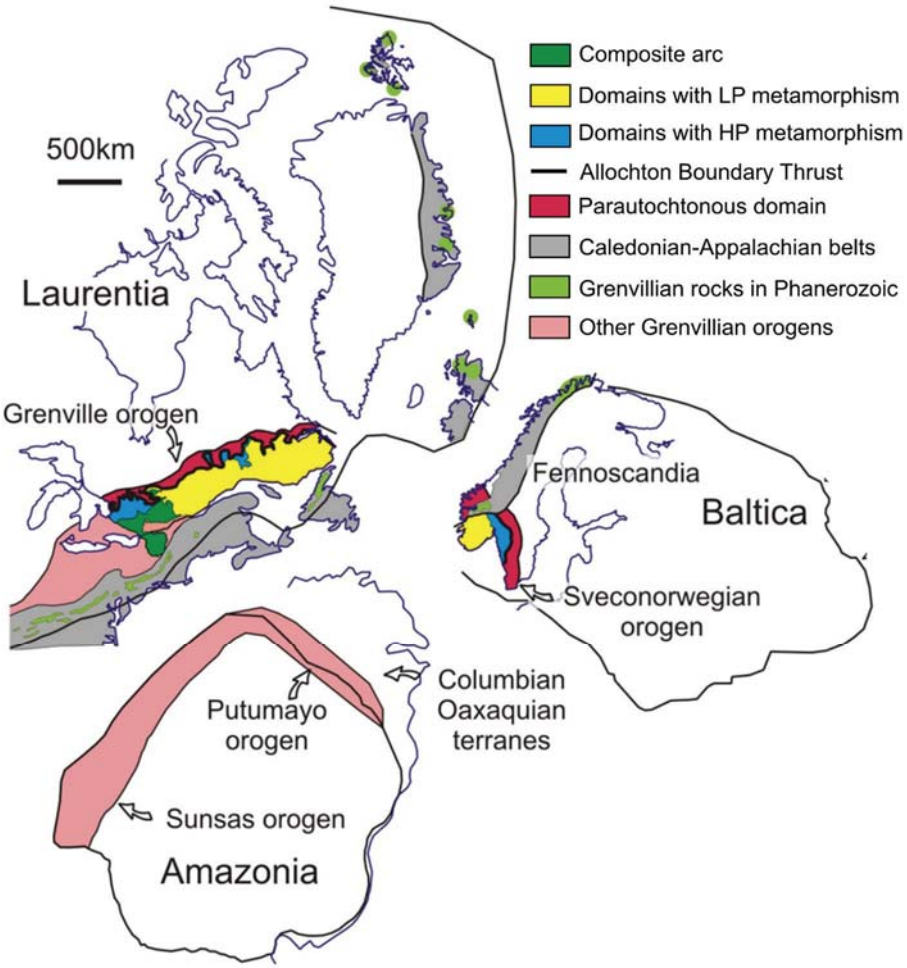

Fig. 1–1: Laurentia–Baltica–Amazonia reconstruction at around 600 Ma, modified from Cawood et al. (2007), showing the distribution of Grenvillian orogens, with their main tectono-metamorphic units.

The Grenville orogeny of Laurentia and the Sveconorwegian orogeny of Baltica share numerous features including their linear shape (Bingen et al. 2008a). The most important similarity however lies in their orogenic architecture, which reflects similar and partly coeval tectono-metamorphic evolutions. In fact, the same succession of three major lithotectonic units is

recognized in the Grenville and Sveconorwegian belts (Fig. 1). These are, from the cratonic foreland toward the hinterland i) a parautochton domain, locally affected by high-pressure (HP) metamorphism (Möller 1998), ii) immediately above a major thrust, which may have accommodated several 100's kilometres of displacement (Rivers 2009), an allochtonous domain also characterized by HP metamorphism (Fig.1) and iii) a wide domain characterized by medium- to low-P granulite facies metamorphism (Fig. 1). The age of the main Grenvillian–Sveconorwegian metamorphic events largely overlap with the 1.08–1.02 Ga Ottawan and 1.01–0.98 Ga Rigolet phases in Laurentia and the 1.05–0.98 Ga Arendal and 0.98–0.97 Falkenberg phases in Baltica (Rivers 1997; Bingen et al. 2008c). Both orogenic systems have been interpreted as hot, long-lived, collisional belts (e.g. Bingen et al. 2008c; Rivers 2009) although Slagstad et al. (2013) proposed an entirely accretionary setting for the Sveconorwegian part of the belt.

The Sveconorwegian orogeny

Along the western margin of Baltica, the crust reworked during the Sveconorwegian orogeny comprises the Sveconorwegian belt *sensu-stricto* (Fig. 2), exposed to the south-east of the Caledonian front, but also several lithotectonic units that were affected by the Caledonian orogenic cycle, including the Western Gneiss Region (WGR), as well as Lindås, Dalsfjord and Jotun nappes attributed to the Middle Allochton (Roffeis and Corfu 2014 and references therein).

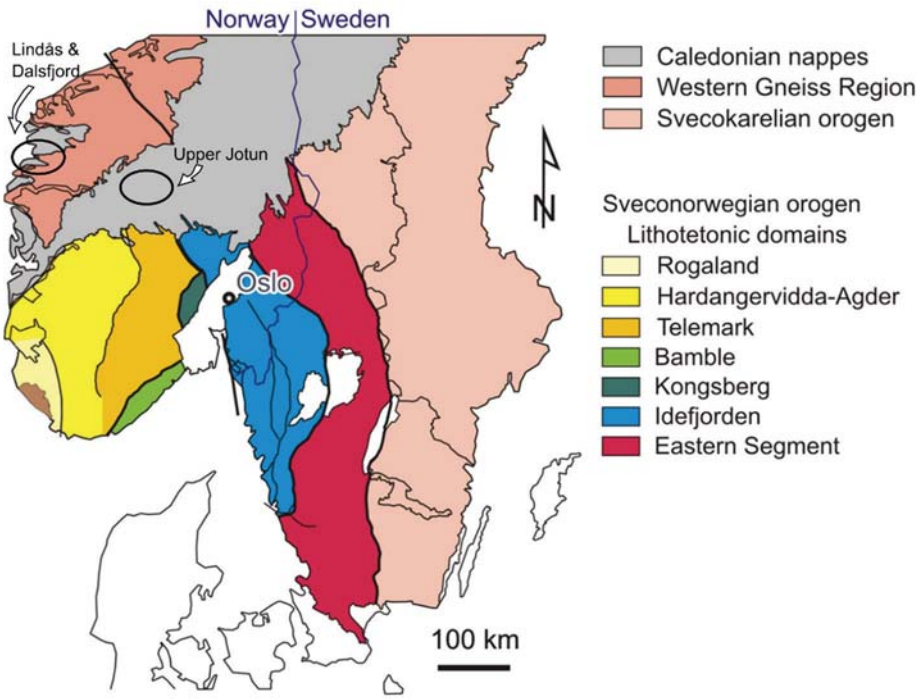

Fig. 1–2: Map of southern Norway and Sweden showing the different lithotectonic units of the Sveconorwegian orogen (Bingen et al. 2008c). The circles denotes the location of Sveconorwegian rocks in Caledonian nappes.

The Sveconorwegian orogen has been divided in seven lithotectonic units which are from east to west, the Eastern Segment, Idefjorden, Kongsberg, Bamble, Telemark, Hardangervidda-

Agder and Rogaland domains (Fig. 2; review by Bingen et al. 2008c). The three last domains are pulled together in several publications into a large unit called Telemarkia terrane (Bingen et al. 2005). These different domains record incremental Mesoproterozoic continental growth from (present-day) east to west at the margin of Baltica. The oldest parautochtonous Eastern segment is characterized by the presence of plutonism related to the 1900–1650 Ma Transcandinavian Igneous Belt (Fig. 3). The Idefjorden, Kongsberg and the Bamble lithotectonic domains record a magmatism of Gothian affinity (1650–1520; Fig. 3). The Telemarkia terrane was formed during a short-lived magmatic event at 1480–1520 Ma, called Telemarkian (Fig. 3). The Kongsberg and Bamble lithotectonic unit, lying between Telemarkia and Idefjorden, display magmatism of both Gothian and Telemakian affinity (Fig. 3).

The Sveconorwegian orogeny may be described with four-orogenic phases following Bingen et al. (2008c). We present the major geological events affecting the western margin of Baltica in the 1280–900 Ma time span in map-view (data compiled and maps drawn by B. Bingen).

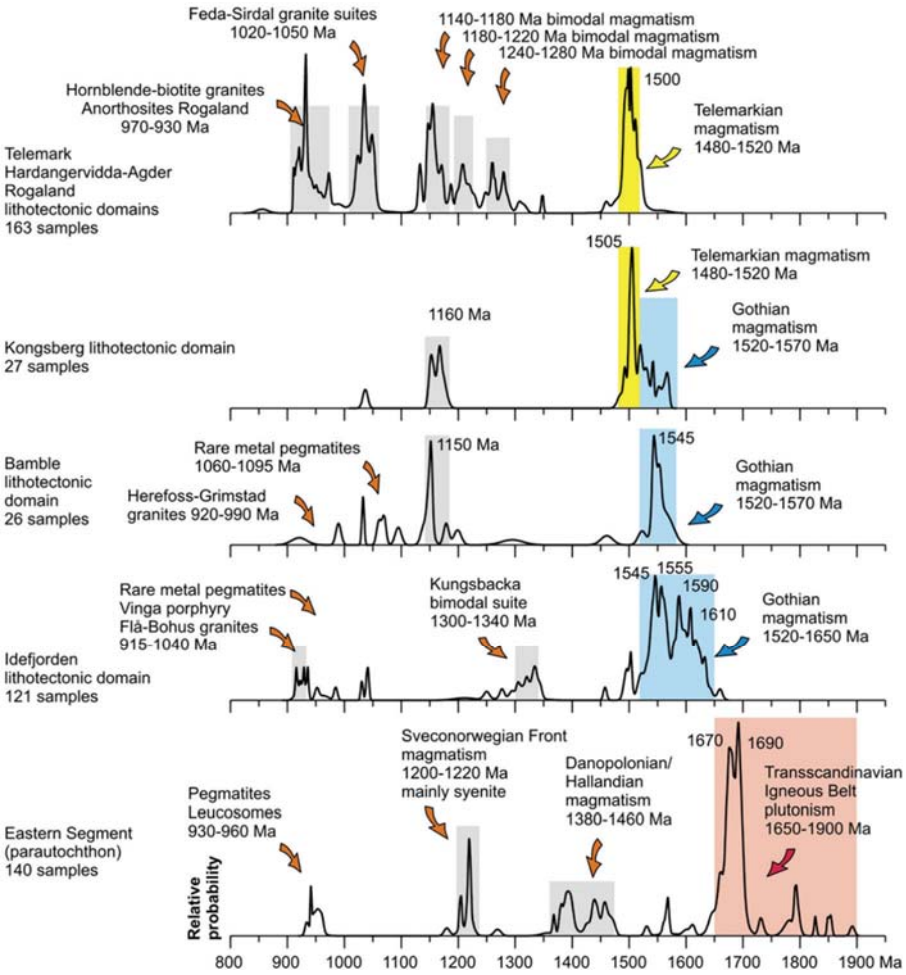

1280–1150 Ma time interval (pre-Sveconorwegian)

Fig. 1–3: Cumulative probability plot of geochronological data on magmatic events in the main lithotectonic units of the Sveconorwegian orogeny (Bingen et al.2008 ; Bingen et al. unpublished)

The pre- to early- Sveconorwegian time interval is dominated by repeated magmatic events affecting all lithotectonic units (Fig. 4). In particular, the Telemarkia basement was subject to repeated bimodal volcanism and deposition of sediments in intramontane basins at c. 1285–1250 Ma, 1220–1180 Ma and 1170–1145 Ma (Laajoki et al. 2002; Bingen et al. 2003; Brewer et al. 2004; Andersen et al. 2007; Roberts et al. 2011). The 1170–1145 event is moreover associated with A-type charnockitic plutonism (Zhou et al. 1995). The geotectonic interpretation of these volcano-sedimentary units and associated magmatic rocks in Telemarkia is controversial. Continental rifting (Laajoki et al. 2002; Andersen et al. 2007), continent back-arc (Andersen et al. 2007) or Basin and Range (Bingen et al. 2003) settings have been proposed.

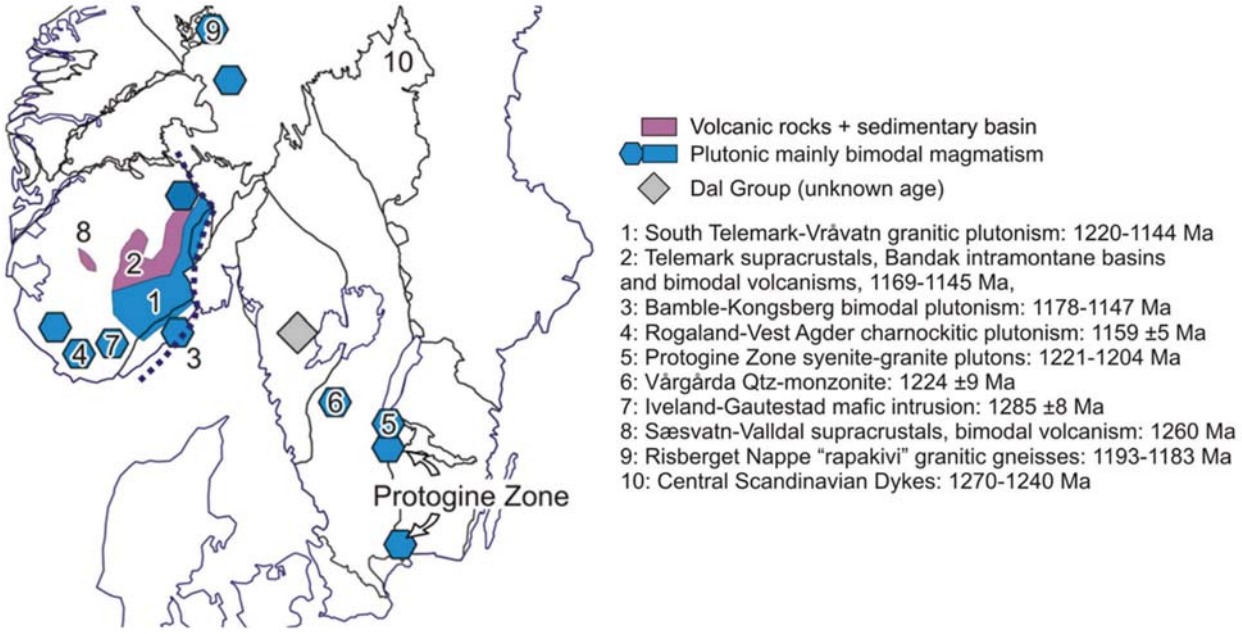

Fig. 1–4: Sketchmap showing the distribution of magmatic rocks and intramontane sedimentary basins between 1280–1150 Ma (Bingen, unpublished)

1150–1080 Ma time interval (Arendal phase)

The oldest recorded Sveconorwegian high-grade metamorphism occurred in the Bamble and Kongsberg lithotectonic units (Fig.5). This early metamorphic event reached intermediate-pressure granulite facies near Arendal (c. 0.7 GPa: 800 °C ; Harlov 2000; Engvik et al. 2016). The Bamble and Kongsberg lithotectonic units thus recorded crustal thickening associated with SW-directed shortening. By c. 1100 Ma, the high-grade metamorphism propagated through most of the Bamble and Kongsberg units that were thrusted onto the Telemark along the Kristiansand-Porsgrunn shear zone. Compression in the Bamble and Kongsberg was contemporaneous with extension in Telemarkia upper crust recorded by intramontane sedimentary basins younger than c.1120 Ma (e.g. Eidsborg Formation; Bingen et al. 2003). This early-Sveconorwegian metamorphic event is commonly interpreted as the collision between the Telemarkia and

Idefjorden Terranes resulting in the formation of the Bamble and Kongsberg tectonic wedges (Ebbing et al. 2005). The 1080–1050 Ma time span is a period of apparent tectonic quiescence in the Sveconorwegian belt.

1050–1030 Ma time interval (Agder phase)

The main Sveconorwegian orogenic event started at c. 1050 Ma. It involved crustal

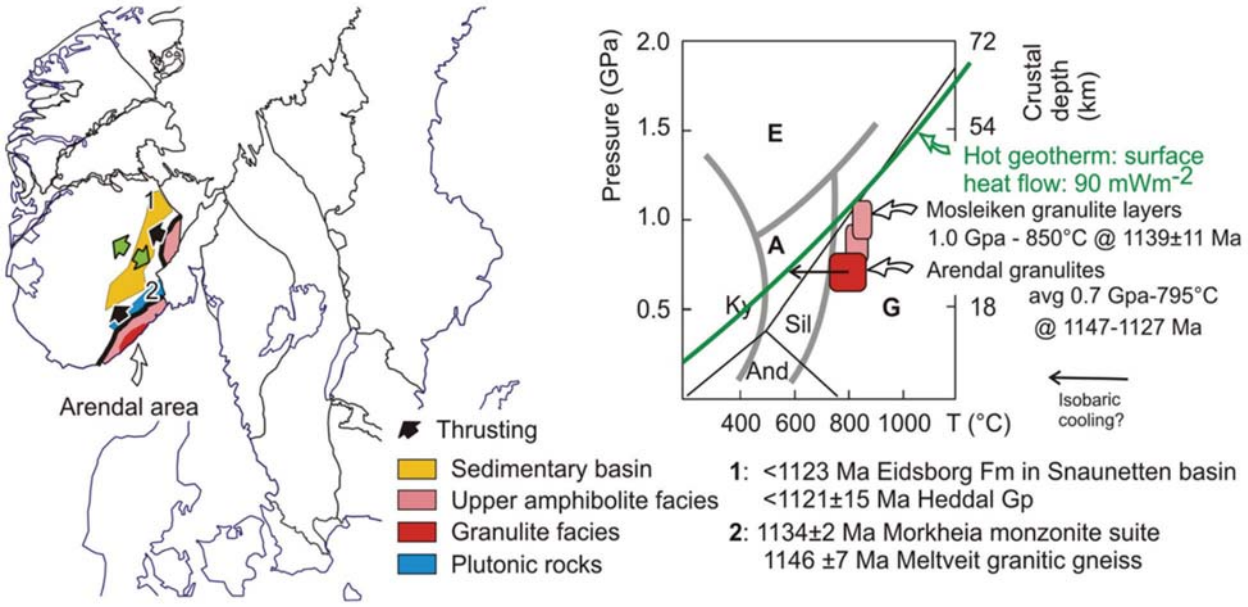

Fig. 1–5: Sketchmap showing the distribution of magmatic rocks, sedimentary basins and metamorphic rocks between 1150–1080 Ma (Bingen, unpublished) and P–T diagram showing quantitative estimates of metamorphism (see description in text).

thickening in the Idefjorden domain (Fig. 6) testified by high-pressure granulite facies metamorphism (c. 1.0–1.5 GPa and T ~ 800 °C) at 1052 ± 4 Ma (Söderlund et al. 2008). The preserved upper crust of northern Telemarkia was probably still in extension by that time with the deposition of Kalhvod formation (younger than 1065 ± 11 Ma; Bingen et al. 2003) whereas the southern part of Telemarkia (Rogaland domain) is intruded between c. 1060 and 1020 Ma by the voluminous high-K calc-alkaline, Feda and Sirdal suites (Bingen and Van Breemen 1998a; Slagstad et al. 2013) merged together as the Sirdal Magmatic Belt (Coint et al. 2015). Available geochronological data for the Telemark, Hardangervidda-Agder and Rogaland domains moreover shows that a widespread metamorphism in the amphibolite facies (Jansen et al. 1985) started at c. 1035–1030 Ma (Bingen et al. 2008b). This phase has been interpreted by Bingen et al. (2008c) to result from tectonic imbrication and crustal thickening in the central part of the orogen in response to (oblique ?) continent–continent collision between Fennoscandia and possibly Amazonia.

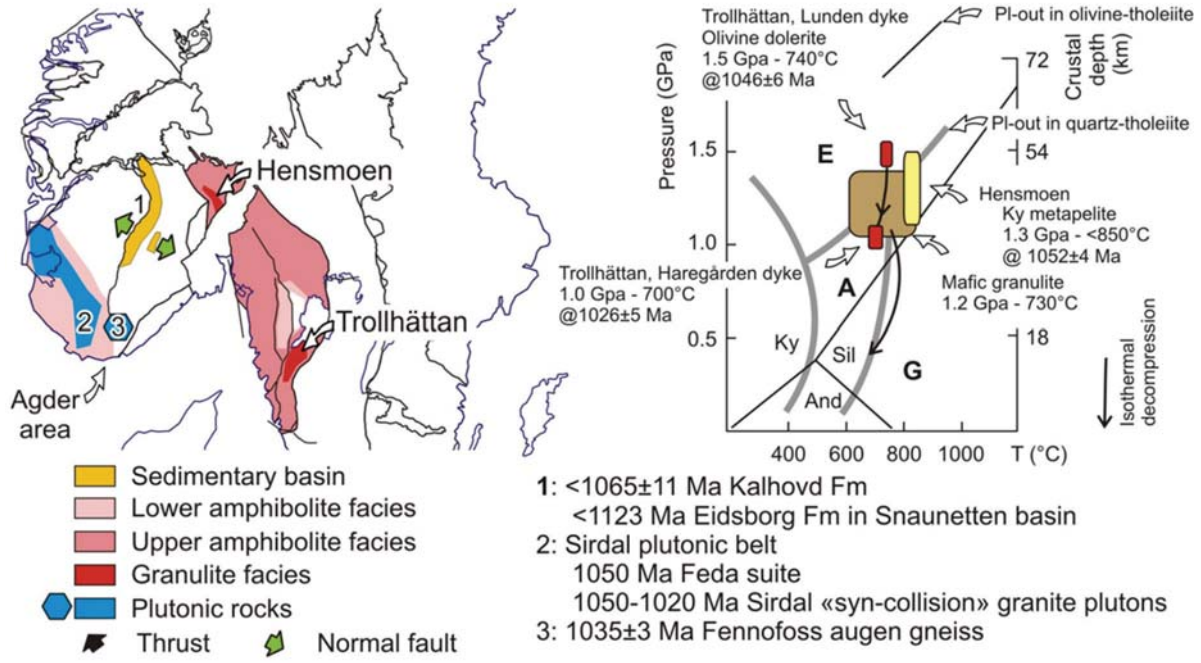

Fig. 1–6: Sketchmap showing the distribution of magmatic rocks, sedimentary basins and metamorphic rocks between 1050–1030 Ma (Bingen, unpublished) and P–T diagram showing quantitative estimates of metamorphism (see description in text).

1030–1000 Ma time interval (Agder phase)

Following crustal thickening in the first part of Agder phase, the Idefjorden domain is affected by syn-migmatitic west-verging exhumation (Fig. 7). In the Rogaland domain, granulite facies metamorphic conditions are established (Bingen and Van Breemen 1998b) with localized attainment of ultra-high-temperature (UHT) metamorphism reaching 0.75 GPa and 1000 °C at 1006 ± 6 Ma, following Drüppel et al. (2013). The amphibolite facies metamorphism propagates toward the north in the Hardangervidda-Agder domain, testified by monazite growth at 1005 ±7 Ma during partial melting in the Botsvatn Complex (Bingen et al. 2008b).

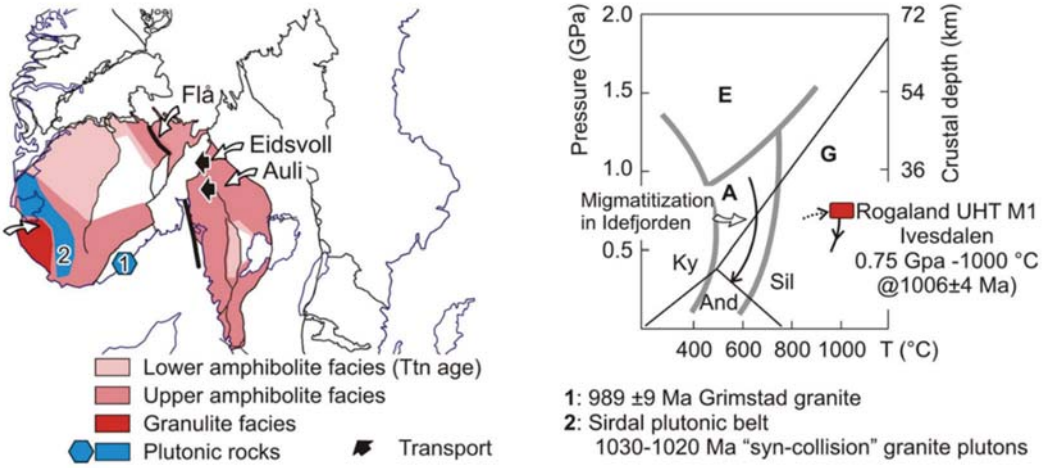

Fig. 1–7: Sketchmap showing the distribution of magmatic rocks, sedimentary basins and metamorphic rocks between 1030–1000 Ma (Bingen, unpublished) and P–T diagram showing quantitative estimates of metamorphism (see description in text).

990–970 Ma time interval (Falkenberg phase)

At c. 990 Ma the orogen is still globally in convergence with eclogite facies metamorphism (P > 1.5 GPa; Möller 1998) recorded in the Eastern segment at 988 ± 7 Ma and 978 ± 6 Ma (U–Pb zircon; Möller et al. 2015; Fig. 8) and east-verging thrusting along the allochtonous boundary thrust, called "Mylonite Zone" in the Sveconorwegian orogeny (Viola et al. 2011). Formation of the eclogites was shortly followed by their exhumation in a partially molten, low viscosity, east-verging fold nappe at 976 ± 6 Ma (Möller et al. 2015). Protracted granulite facies is recorded in Rogaland and in the Western Gneiss Region (Rohr et al. 2004) while titanite U–Pb ages record progressive cooling of the Northern part of Telemarkia.

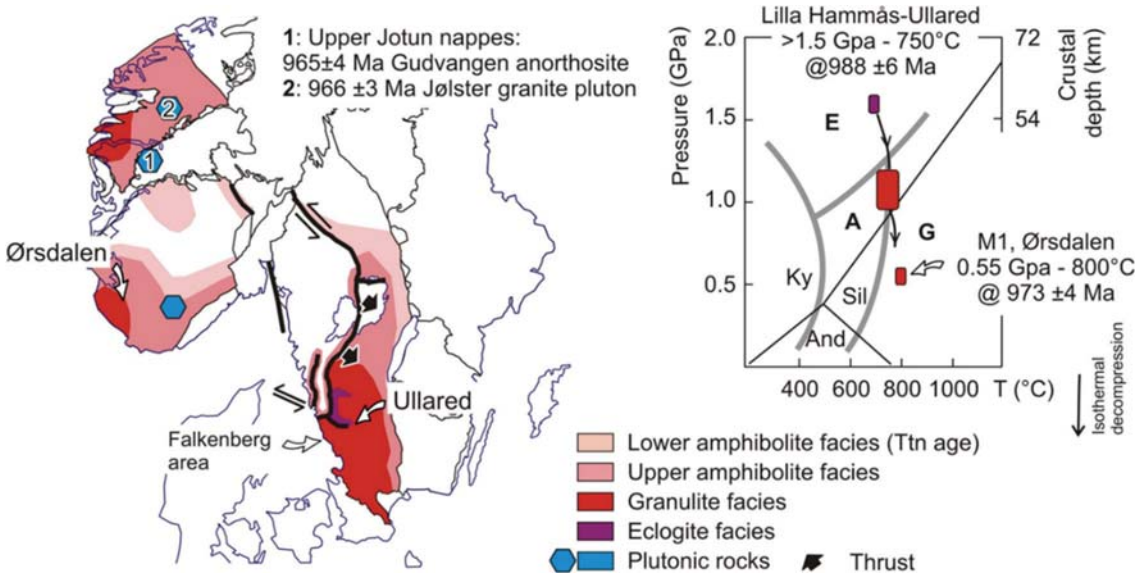

Fig. 1–8: Sketchmap showing the distribution of magmatic rock and metamorphic rocks at 990 Ma (Bingen, unpublished) and P–T diagram showing quantitative estimates of metamorphism (see description in text)

970–950 Ma time interval (Dalane phase)

This time interval is characterized by abundant "post-collisional" magmatism thorough the belt (Andersson et al. 1996; Andersen et al. 2001; Vander Auwera et al. 2011; Jensen and Corfu 2016) including the WGR (Skar and Pedersen 2003; Fig. 9). It also marks the onset of anorthosite–mangerite–charnockite (AMC) magmatism in the Upper Jotun Nappe (c. 965 Ma; Lundmark and Corfu 2008) and in the Lindås nappe (c. 980–950 Ma). The autochthonous foreland of the orogen is intruded by the orogen-parallel Blekinge-Dalarna dolerite dyke swarm at 978–946 Ma (Söderlund et al. 2005). The Eastern segment, Rogaland and Western Gneiss Region remained above titanite closure temperature (c. 600–650 °C).

↓ **Fig. 1–9**: Sketchmap showing the distribution of magmatic rock and metamorphic rocks between 970–950 Ma (Bingen, unpublished)

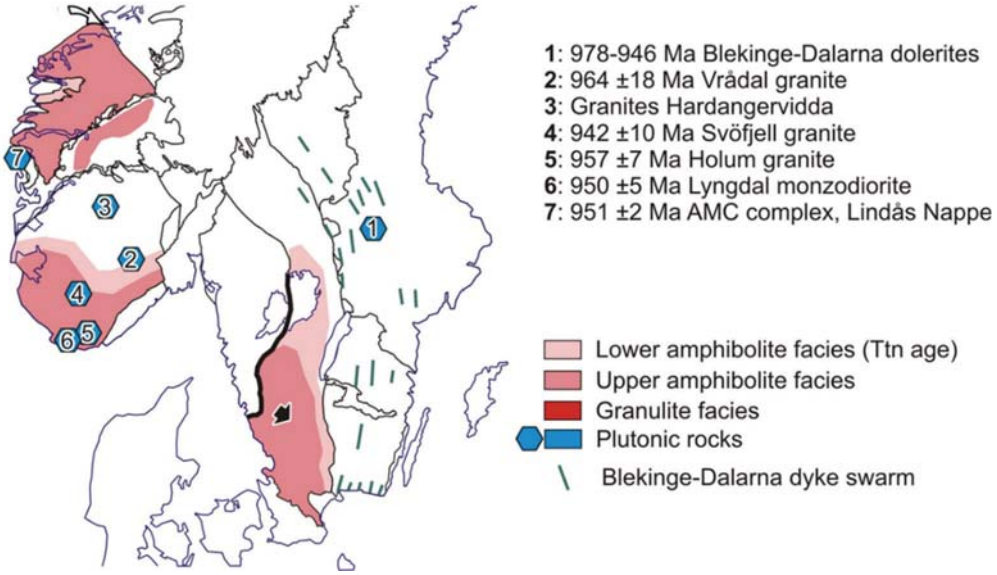

950–920 Ma time interval (Dalane phase)

This last phase of Sveconorwegian orogeny corresponds to widespread magmatism in all lithotectonic units and a globally extensional regime demonstrated by normal shear zones (Fig. 10). This magmatism may be related to the upwelling of hot asthenospheric mantle close to the Moho as the result of orogenic collapse (Bingen et al. 2006). All parts of the orogen are cooling down except the Upper Jotun and Lindås nappe, where high-pressure granulite facies overprints the AMC complex (Austrheim and Griffin 1985; Cohen et al. 1988) at 945–930 Ma (Boundy et al. 1997; Bingen et al. 2001) and in Rogaland, where the emplacement of voluminous AMC suite at 931 ± 2 Ma (Schärer et al. 1996) caused UHT contact metamorphism in the country rocks (c. 0.5 GPa at 950 °C; Westphal et al. 2003). Granulite facies metamorphism at 940–930 Ma seems therefore not restricted to a particular lithotectonic domain (Lindås and Jotun nappes have Gothian affinity) but is spatially related to AMC emplacement.

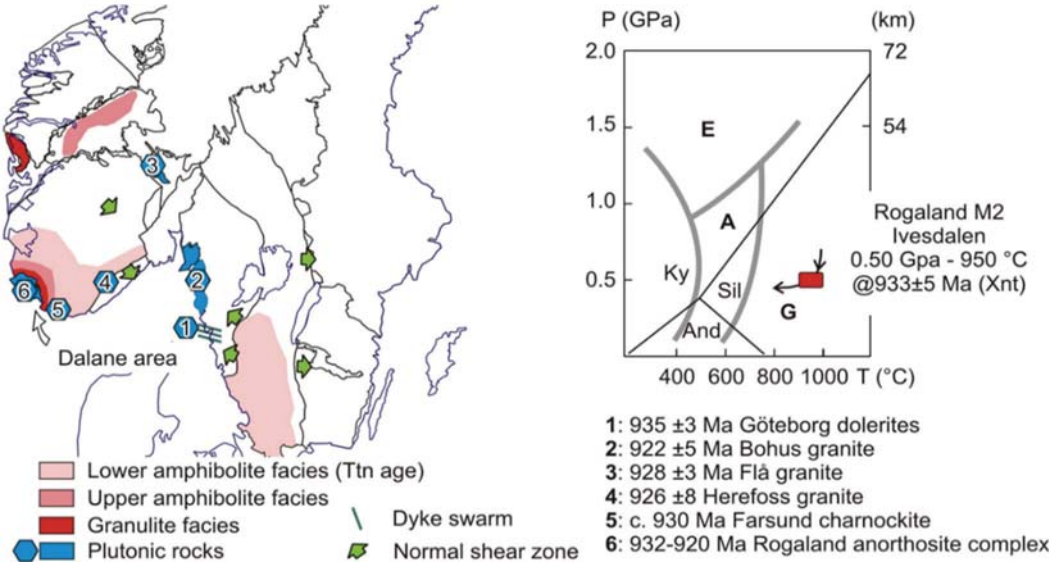

Fig. 1–10: Sketchmap showing the distribution of magmatic rocks and metamorphic rocks between 950–920 Ma (Bingen, unpublished) and P–T diagram showing quantitative estimates of metamorphism (see description in text).

Tectono-magmatic evolution of Rogaland

Magmatism

The Telemarkia terrane, to which the Rogaland domain belongs, is made up of *c*. 1520–1480 Ma magmatic rocks intruded by plutonic rocks and overlaid by thick (> 10 km) supracrustal sequence composed of sedimentary and bimodal volcanic rocks dated between *c*. 1500 and 920 Ma (Andersen et al. 2001; Laajoki et al. 2002; Bingen et al. 2003; Roberts et al. 2013; Spencer et al. 2014). The ε_{Nd} vs time plot of all magmatic rocks suggests repeated magma extraction from the depleted mantle array (Fig. 11; compiled data are from Bolle et al. 2003 and Vander Auwera et al. 2011). Two main cycles of syn-orogenic (1050–920 Ma) magmatism may be identified more specifically in Rogaland.

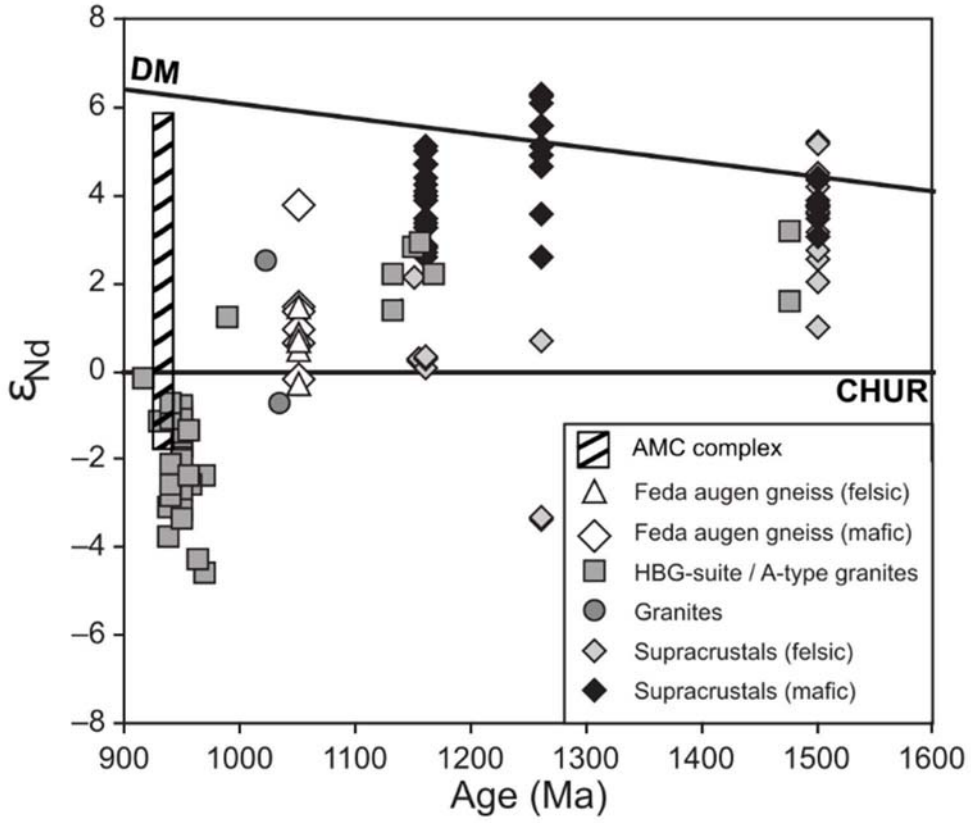

Fig. 1–11: ε_{Nd} vs time for Mesoproterozoic magmatism in the Telemarkia domain. CHUR = chondritic uniform reservoir; DM = Depleted Mantle calculated following the model of DePaolo et al. (1991). Figure modified after Slagstad et al. (2013) (see text)

The first cycle consists in the emplacement of the Sirdal Magmatic Belt (SMB) representing a *c*. 200 × 50 km multi-pluton batholith built up between *c*. 1060 and 1020 Ma (Fig.3–4; Fig. 12; Slagstad et al. 2013; Coint et al. 2015). The SMB includes the Feda suite intruded during a short period at *c*. 1051 $^{+2}/_{-8}$ Ma (Bingen and Van Breemen 1998a) and a variety of granitoids that possess a high-K calc-alkaline geochemical signature (Bingen 1989; Slagstad et al. 2013; Bingen et al. 2015). Rocks from the Feda suite display low Sri ratio and positive εNd demonstrating the involvement of a mantle-derived source in their genesis (Bingen et al. 1993; Vander Auwera et al. 2011; Fig. 11). The calc-alkaline geochemical signature of granitoids of the SMB leads to a controversy. It can be interpreted as evidence for active subduction at *c*. 1050 Ma (Bingen et al. 1993; Slagstadt et al. 2013; Coint et al. 2015) or alternatively, of re-melting, of continental crust previously formed in a subduction (accretionary) setting (Bingen et al. 2008c).

After a period of magmatic quiescence of *c.* 50 My, the high-grade basement was intruded by two ferroan plutonic suite, (i) the hydrous Hornblende–Biotite–Granite (HBG) suite spanning 970-932 Ma (Vander Auwera et al. 2011) and (ii) the anhydrous massif-type anorthosite-charnockite-mangerite complex (AMC) at 931 ± 2 Ma (Schärer et al. 1996; Fig. 12). Examination of major- and trace-element geochemistry along with Sr–Nd–Pb isotopic signature of both suites suggest that they are the result of re-melting of the same sources (Vander Auwera et al. 2011; Vander Auwera et al. 2014a).

It is generally accepted that Proterozoic anorthosite crystallized from high-Al basaltic magmas. These magmas are either mantle-derived (Morse 1982) or results from re-melting of gabbro-noritic lower crust (Duchesne et al. 1999; Vander Auwera et al. 2011). Both hypotheses assume that enrichement of anorthosite in plagioclase stems from fractional crystallisation of some 30–40 % of mafic minerals. The anorthosite plutons are characterized by sporadic large (up to metre size) Al-rich orthopyroxene and plagioclase megacrysts. These crystallized at a pressure of c. 1.3–1.1 GPa much higher than the final emplacement pressure of c. 0.5 GPa (Charlier et al. 2010; Vander Auwera et al. 2011). An internal Sm–Nd isochron for Al-rich orthopyroxene yields an age of 1041 ± 17 Ma (Bybee et al. 2014), that is some 100 My older than the age of the final emplacement of the plutons dated by U–Pb on zircon at 931 ± 2 Ma (Schärer et al. 1996). This age difference can imply the existence of a long-lived (80–100 My) magmatic system at the crust–mantle interface (Bybee et al. 2014). Alternatively, and in accordance with the Nd and Pb isotopic compositions, Vander Auwera et al. (2014b) suggest that Al-rich orthopyroxene megacryst belong to mafic underplates coeval or cogenetic with the Feda suite, that were re-melted some 100 My later to form the AMC complex.

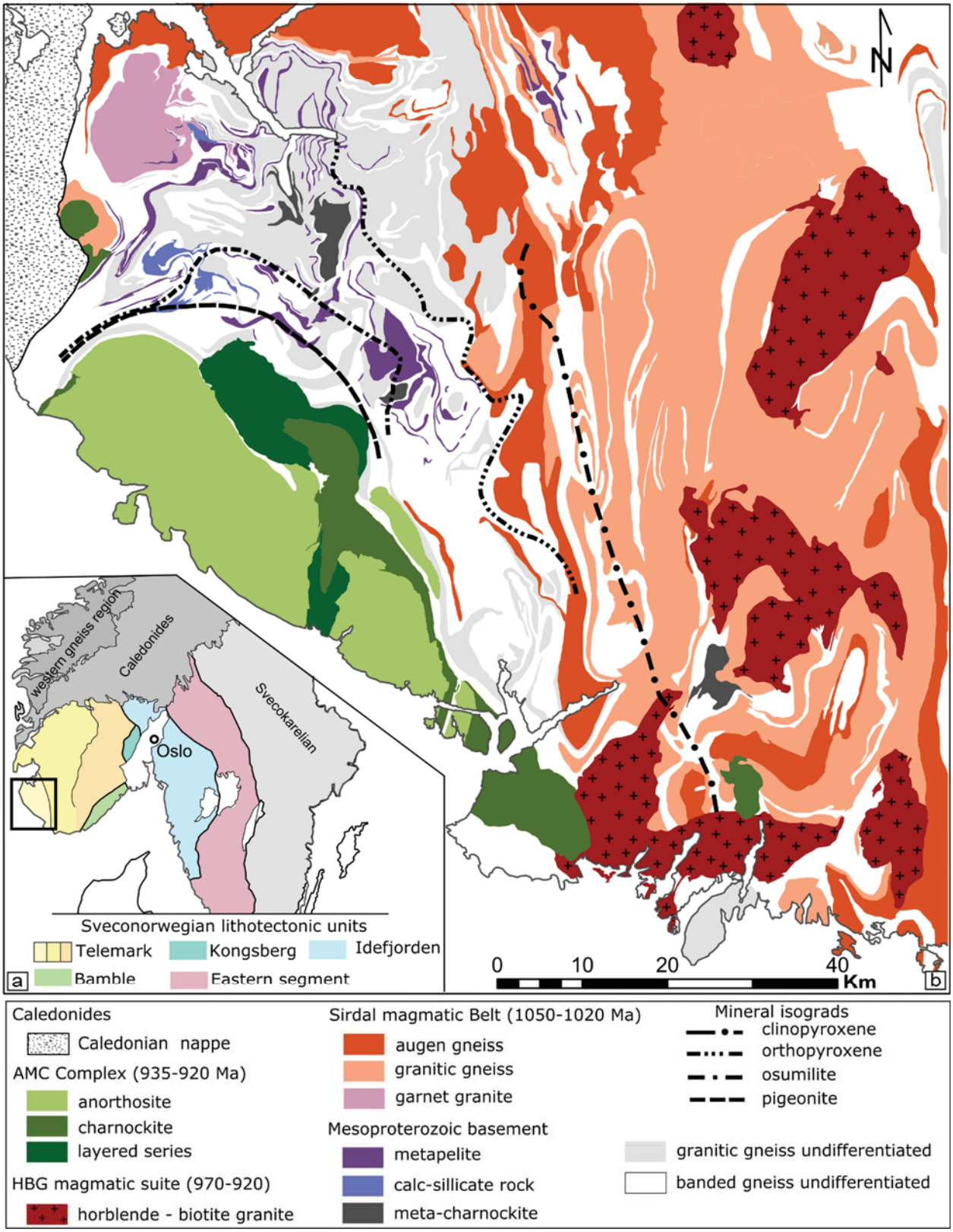

Fig. 1–12: Geological maps. **a**– Sketch map of the Sveconorwegian Province in SW Scandinavia from Bingen et al. (2008b), black rectangle depicts the studied area. **b**– Simplified geological map of Rogaland and Agder modified after (Falkum 1982; Coint et al. 2015) with mineral isograds drawn after (Tobi et al. 1985; Bingen et al. 1990).

Metamorphism

The Rogaland bedrock (Fig. 12) is composed of high-grade meta-igneous rocks of broadly granitic to tonalitic composition (granitic gneiss and meta-charnockite) interlayered with mafic rocks (amphibolites and banded gneisses) and metasedimentary rocks (Hermans et al. 1975). Metasedimentary rocks are further divided into the "garnetiferous migmatite" derived from Al-rich protolith and the "Faurefjell metasediments" comprising a succession of calc-silicate rocks, quartzite and minor marble. Most of the deformation is localized within metasedimentary layers compared to the adjacent granitic and banded gneisses. Structural analysis indicates four phases of folding (Hermans et al. 1975; Huijsmans et al. 1981; Falkum 1985). The oldest involved isoclinal folding resulting in a transposition foliation within the garnetiferous migmatite. The two latter phases, coeval with regional *(M1)* metamorphism, have structured much of the area and consist in tight kilometric folds with N- to NW-striking axial plane dipping *c*. 40° eastwards. The youngest phase of deformation produced large scale open folds with E–W trending axial planes that are not visible in the map view.

Four metamorphic mineral isograd were mapped in Rogaland (Fig. 12), reflecting a southwestward increase in metamorphic grade from upper-amphibolite to ultra-high temperature granulite facies. From north-east to south-west four isograds are traced: the clinopyroxene isograd in granodioritic gneiss, the orthopyroxene isograd in quartzo-feldspathic rocks, the osumilite isograd in paragneiss and the pigeonite isograd in leucocratic gneisses (Tobi et al. 1985). Recognizing that the rocks are polymetamorphic, Kars et al. (1980) distinguished three metamorphic events (M1, M2, M3) in metapelites which were later generalized to all lithologies by Maijer and Padget (1987). The oldest M1 metamorphism is a regional upper amphibolite facies event associated with extensive migmatization and is best recorded in metapelite preserving porphyroblastic garnet enclosing micro-folded needles of sillimanite, biotite flakes, sodic plagioclase, K-feldspar, quartz and ilmenite. Jansen et al. (1985) proposed estimates of 600–700 °C at 0.6–0.8 GPa for this event (Fig. 13). Absolute timing for this regional phase of metamorphism is bracketed between 1035 and 970 Ma by U–Pb data on zircon and monazite (Bingen and Van Breemen 1998b; Bingen et al. 2008b; Fig. 14; Tab. 1). In contrast, recent investigations of sapphirine-bearing restitic granulite located within the osumilite isograd suggest that this portion of the crust already reached UHT conditions of 1000 °C (Drüppel et al. 2013; Fig. 13) during M1 event at 1006 ± 4 Ma (U–Pb zircon; Fig. 14). Regional decompression to 0.55 GPa is recorded at 955 ± 8 Ma by zircon included in cordierite (Tomkins et al. 2005; Fig. 14).

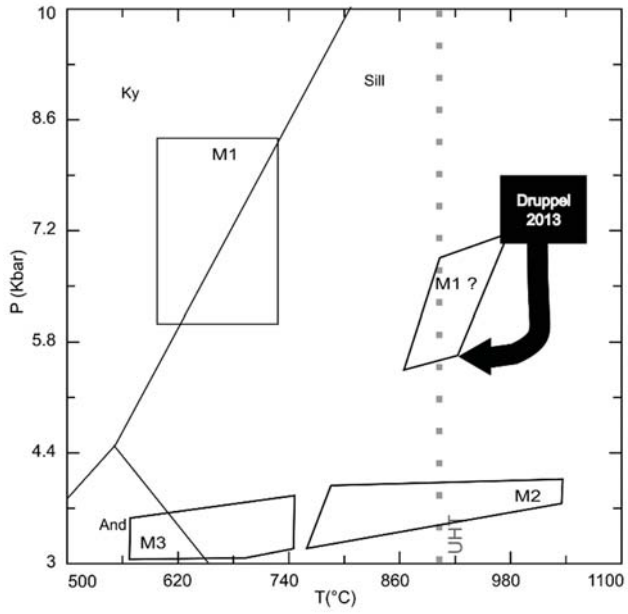

Fig. 1–13: Compilation of P–T estimates from Drüppel et al. (2013) in black and from Jansen et al. (1985) in white. *Note that M1 estimates of Jansen et al. (1985) are unclear since at that time, Bamble and Rogaland were thought to share the same metamorphic history; estimates for Rogaland (Ky absent) were thus influenced by the existing P–T estimates in Bamble (Sil + Ky present)*

A detailed in-situ U–Pb geochronological study on zircon, complemented by thermal modelling demonstrates that emplacement of the AMC complex is responsible for M2 UHT contact metamorphism at 927 ± 7 Ma (Möller et al. 2002; Möller et al. 2003; Westphal et al. 2003). Typical M2 mineral assemblages comprise green spinel, osumilite and Al-rich orthopyroxene in metapelite and pigeonite in granitic rocks. Temperature estimates for M2 metamorphism range from 850 to 1050 °C at 0.3–0.6 GPa within the osumilite isograd (Fig. 13; Jansen et al. 1985; Wilmart and Duchesne 1987; Holland et al. 1996; Drüppel et al. 2013) which is consistent with the low pressures of 0.4–0.55 GPa postulated for the emplacement of the AMC complex (Vander Auwera and Longhi 1994). Finally, slow isobaric cooling of intrusive bodies is dated at 908 ± 9 Ma by mean of U–Pb in zircon overgrown by M3 minerals such as late garnet, biotite, cordierite, low-Al orthopyroxene (Möller et al. 2003). A regional scale average titanite U–Pb age of 918 ± 2 Ma also record regional cooling after M2 metamorphism (Bingen and Van Breemen 1998).

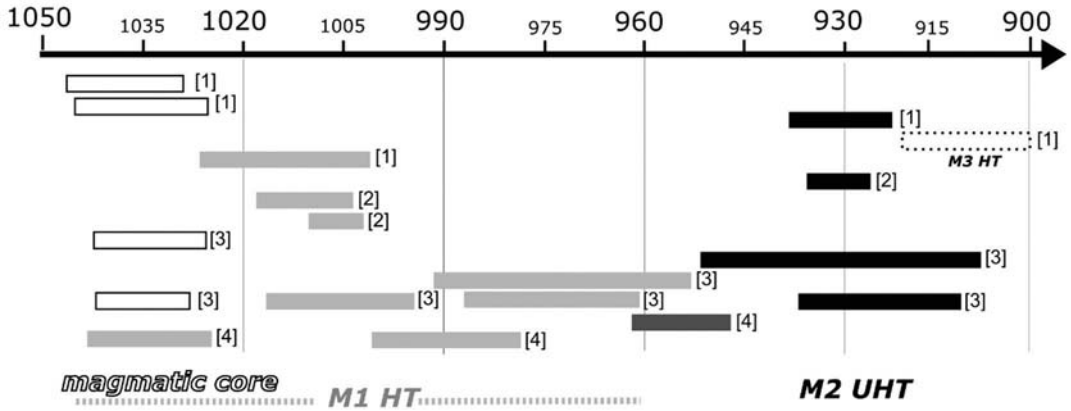

Fig. 1–14: Selected in-situ U–Pb zircon data recording metamorphism, from [1] Möller et al. (2003); [2] Drüppel et al. (2013); [3] Möller et al. (2002); [4] Tomkins et al. (2005) colour-coded with the interpretation provided by the authors.

References

Andersen T, Andresen A, Sylvester AH (2001) Nature and distribution of deep crustal reservoirs in the southwestern part of the Baltic shield: evidence from Nd, Sr and Pb isotope data on late Sveconorwegian granites. J Geol Soc 158:235–267.

Andersen T, Griffin WL, Sylvester AG (2007) Sveconorwegian crustal underplating in southwestern Fennoscandia: LAM-ICPMS U–Pb and Lu–Hf isotope evidence from granites and gneisses in Telemark, southern Norway. Lithos 93:273–287. doi: 10.1016/j.lithos.2006.03.068

Andersson M, Lie JE, Husebye ES (1996) Tectonic setting of post-orogenic granites within SW Fennoscandia based on deep seismic and gravity data. Terra Nova 8:558–566.

Austrheim H, Griffin WL (1985) Shear deformation and eclogite formation within granulite-facies anorthosites of the Bergen arcs, Western Norway. Chem Geol 50:267–281.

Bingen B (1989) Geochemistry of Sveconorwegian augen gneisses from SW Norway at the amphibolite-granulite facies transition. Nor Geol Tidsskr 69:177–189.

Bingen B, Andersson J, Soderlun U, Moller C (2008a) The Mesoproterozoic in the Nordic countries. Episodes 31:29.Bingen B, Austrheim H, Whitehouse MJ (2001) Ilmenite as a source for zirconium during high-grade metamorphism? textural evidence from the Caledonides of western Norway and implications for zircon geochronology. J Petrol 42:355–375.

Bingen B, Corfu F, Stein HJ, Whitehouse MJ (2015) U–Pb geochronology of the syn-orogenic Knaben molybdenum deposits, Sveconorwegian Orogen, Norway. Geol Mag 152:537–556.

Bingen B, Davis WJ, Hamilton MA, Engvik AK, Stein HJ, Skar O, Nordgulen O (2008b) Geochronology of high-grade metamorphism in the Sveconorwegian belt, S. Norway: U-Pb, Th-Pb and Re-Os data. Nor Geol Tidsskr 88:13.

Bingen B, Demaiffe D, Hertogen J, Weis D, Michot J (1993) K-rich calc-alkaline augen gneisses of Grenvillian age in SW Norway: mingling of mantle-derived and crustal components. J Geol 101:763–778.

Bingen B, Nordgulen Ø, Sigmond EMO, Tucker R, Mansfeld J, Högdahl K (2003) Relations between 1.19–1.13 Ga continental magmatism, sedimentation and metamorphism, Sveconorwegian province, S Norway. Precambrian Res 124:215–241. doi: 10.1016/S0301-9268(03)00087-1

Bingen B, Nordgulen O, Viola G (2008c) A four-phase model for the Sveconorwegian orogeny, SW Scandinavia. Nor Geol Tidsskr 88:43.

Bingen B, Skaar Ø, Marker M, Sigmond EM, Nordgulen Ø, Ragnhildstveit J, Mansfeld J, Tucker RD, Liégeois J-P (2005) Timing of continental building in the Sveconorwegian orogen, SW Scandinavia. Nor J Geol 85:87–116.

Bingen B, Stein HJ, Bogaerts M, Bolle O, Mansfeld J (2006) Molybdenite Re–Os dating constrains gravitational collapse of the Sveconorwegian orogen, SW Scandinavia. Lithos 87:328–346. doi: 10.1016/j.lithos.2005.06.017

Bingen B, Van Breemen O (1998a) Tectonic regimes and terrane boundaries in the high-grade Sveconorwegian belt of SW Norway, inferred from U–Pb zircon geochronology and geochemical signature of augen gneiss suites. J Geol Soc 155:143–154.

Bingen B, Van Breemen O (1998b) U-Pb monazite ages in amphibolite- to granulite-facies orthogneiss reflect hydrous mineral breakdown reactions: Sveconorwegian Province of SW Norway. Contrib Mineral Petrol 132:336–353.

Bolle O, Demaiffe D, Duchesne J-C (2003) Petrogenesis of jotunitic and acidic members of an AMC suite (Rogaland anorthosite province, SW Norway): a Sr and Nd isotopic assessment. Precambrian Res 124:185–214. doi: 10.1016/S0301-9268(03)00086-X

Boundy TM, Mezger K, Essene EJ (1997) Temporal and tectonic evolution of the granulite-eclogite association from the Bergen Arcs, Western Norway. Lithos 39:159–178.

Brewer TS, Åhäll K-I, Menuge JF, Storey CD, Parrish RR (2004) Mesoproterozoic bimodal volcanism in SW Norway, evidence for recurring pre-Sveconorwegian continental margin tectonism. Precambrian Res 134:249–273. doi: 10.1016/j.precamres.2004.06.003

Bybee GM, Ashwal LD, Shirey SB, Horan M, Mock T, Andersen TB (2014) Pyroxene megacrysts in Proterozoic anorthosites: Implications for tectonic setting, magma source and magmatic processes at the Moho. Earth Planet Sci Lett 389:74–85. doi: 10.1016/j.epsl.2013.12.015

Cawood PA, Nemchin AA, Strachan R, Prave T, Krabbendam M (2007) Sedimentary basin and detrital zircon record along East Laurentia and Baltica during assembly and breakup of Rodinia. J Geol Soc 164:257–275.

Charlier B, Duchesne J-C, Vander Auwera J, Storme J-Y, Maquil R, Longhi J (2010) Polybaric Fractional Crystallization of High-alumina Basalt Parental Magmas in the Egersund-Ogna Massif-type Anorthosite (Rogaland, SW Norway) Constrained by Plagioclase and High-alumina Orthopyroxene Megacrysts. J Petrol 51:2515–2546.

Cohen AS, O'nions RK, Siegenthaler R, Griffin WL (1988) Chronology of the pressure-temperature history recorded by a granulite terrain. Contrib Mineral Petrol 98:303–311.

Coint N, Slagstad T, Roberts NMW, Marker M, Røhr T, Sørensen BE (2015) The Late Mesoproterozoic Sirdal Magmatic Belt, SW Norway: Relationships between magmatism and metamorphism and implications for Sveconorwegian orogenesis. Precambrian Res 265:57–77. doi: 10.1016/j.precamres.2015.05.002

Drüppel K, Elsasser L, Brandt S, Gerdes A (2013) Sveconorwegian Mid-crustal Ultrahigh-temperature Metamorphism in Rogaland, Norway: U-Pb LA-ICP-MS Geochronology and Pseudosections of Sapphirine Granulites and Associated Paragneisses. J Petrol 54:305–350. doi: 10.1093/petrology/egs070

Duchesne J-C, Liégeois J-P, Vander Auwera J, Longhi J (1999) The crustal tongue melting model and the origin of massive anorthosites. Terra Nova 11:100–105.

Ebbing J, Afework Y, Olesen O, Nordgulen Ø (2005) Is there evidence for magmatic underplating beneath the Oslo Rift?: Magmatic underplating beneath the Oslo Rift? Terra Nova 17:129–134. doi: 10.1111/j.1365-3121.2004.00592.x

Engvik AK, Bingen B, Solli A (2016) Localized occurrences of granulite: P–T modeling, U–Pb geochronology and distribution of early-Sveconorwegian high-grade metamorphism in Bamble, South Norway. Lithos 240–243:84–103. doi: 10.1016/j.lithos.2015.11.005

Evans DAD (2009) The palaeomagnetically viable, long-lived and all-inclusive Rodinia supercontinent reconstruction. Geol Soc Lond Spec Publ 327:371–404. doi: 10.1144/SP327.16

Falkum T (1985) Geotectonic evolution of southern Scandinavia in light of a late-Proterozoic plate-collision. In: The Deep Proterozoic Crust in the North Atlantic Provinces. Springer, pp 309–322

Gower CF, Ryan AB, Rivers T (1990) Mid-Proterozoic Laurentia–Baltica: an overview of its geological evolution and a summary of the contributions made by this volume. -Proterozoic Laurentia-Balt 38:1–20.

Harlov DE (2000) Pressure-temperature estimation in orthopyroxene-garnet bearing granulite facies rocks, Bamble Sector, Norway. Mineral Petrol 69:11–33.

Hermans GAE., Tobi AC, Poorter RP, Maijer C (1975) The high-grade metamorphic Precambrian of the Sirdal-Ørsdal area, Rogaland/Vest-Agder, south-west Norway. Nor Geol Undersokelse 318:351–374.

Hoffman PF (1991) Did the breakout of Laurentia turn Gondwanaland inside-out? Science 252:1409–1412.

Holland TJB, Babu E, Waters DJ (1996) Phase relations of osumilite and dehydration melting in pelitic rocks: a simple thermodynamic model for the KFMASH system. Contrib Mineral Petrol 124:383–394.

Huijsmans J, Kabel A, Steenstra S (1981) On the structure of a high-grade metamorphic Precambrian terrain in Rogaland, South Norway. Nor Geol Tidsskr 61:183–192.

Jansen JBH, Blok RJ, Bos A, Scheelings M (1985) Geothermometry and geobarometry in Rogaland and preliminary results from the Bamble area, S Norway. In: The deep Proterozoic crust in the North Atlantic provinces. Springer, pp 499–516

Jensen E, Corfu F (2016) The U–Pb age of the Finse batholith, a composite bimodal Sveconorwegian intrusion. Nor J Geol. doi: 10.17850/njg96-3-01

Johansson Å (2009) Baltica, Amazonia and the SAMBA connection—1000 million years of neighbourhood during the Proterozoic? Precambrian Res 175:221–234. doi: 10.1016/j.precamres.2009.09.011

Karlstrom KE, \AAhäll K-I, Harlan SS, Williams ML, McLelland J, Geissman JW (2001) Long-lived (1.8–1.0 Ga) convergent orogen in southern Laurentia, its extensions to Australia and Baltica, and implications for refining Rodinia. Precambrian Res 111:5–30.

Kars H, Jansen JBH, Tobi AC, Poorter RP (1980) The metapelitic rocks of the polymetamorphic Precambrian of Rogaland, SW Norway. Contrib Mineral Petrol 74:235–244.

Laajoki K, Corfu F, Andersen T (2002) Lithostratigraphy and U-Pb geochronology of the Telemark supracrustals in the Bandak-Sauland area, Telemark, South Norway. Nor Geol Tidsskr 82:119–138.

Li ZX, Bogdanova SV, Collins AS, Davidson A, De Waele B, Ernst RE, Fitzsimons ICW, Fuck RA, Gladkochub DP, Jacobs J, Karlstrom KE, Lu S, Natapov LM, Pease V, Pisarevsky SA, Thrane K, Vernikovsky V (2008) Assembly, configuration, and break-up history of Rodinia: A synthesis. Precambrian Res 160:179–210. doi: 10.1016/j.precamres.2007.04.021

Lundmark AM, Corfu F (2008) Late-orogenic Sveconorwegian massif anorthosite in the Jotun Nappe Complex, SW Norway, and causes of repeated AMCG magmatism along the Baltoscandian margin. Contrib Mineral Petrol 155:147–163. doi: 10.1007/s00410-007-0233-5

Maijer C, P. (1987) The geology of southermost Norway : an excursion guide. In: Norges Geologiske undersokelse.

Möller A, O'brien PJ, Kennedy A, Kröner A (2002) Polyphase zircon in ultrahigh-temperature granulites (Rogaland, SW Norway): constraints for Pb diffusion in zircon. J Metamorph Geol 20:727–740.

Möller A, O'Brien PJ, Kennedy A, Kröner A (2003) Linking growth episodes of zircon and metamorphic textures to zircon chemistry: an example from the ultrahigh-temperature granulites of Rogaland (SW Norway). Geol Soc Lond Spec Publ 220:65–81.

Möller C (1998) Decompressed eclogites in the Sveconorwegian (–Grenvillian) orogen of SW Sweden: petrology and tectonic implications. J Metamorph Geol 16:641–656.

Möller C, Andersson J, Dyck B, Antal Lundin I (2015) Exhumation of an eclogite terrane as a hot migmatitic nappe, Sveconorwegian orogen. Lithos 226:147–168. doi: 10.1016/j.lithos.2014.12.013

Morse SA (1982) A partisan review of Proterzoic anorthosites. Am Mineral 67:1087–1100.

Rivers T (1997) Lithotectonic elements of the Grenville Province: review and tectonic implications. Precambrian Res 86:117–154.

Rivers T (2009) The Grenville Province as a large hot long-duration collisional orogen - insights from the spatial and thermal evolution of its orogenic fronts. Geol Soc Lond Spec Publ 327:405–444. doi: 10.1144/SP327.17

Roberts NM, Parrish RR, Horstwood MS, Brewer TS (2011) The 1.23 Ga Fjellhovdane rhyolite, Grøss\a e-Totak; a new age within the Telemark supracrustals, southern Norway. Nor J Geol 91:239–246.

Roberts NMW, Slagstad T, Parrish RR, Norry MJ, Marker M, Horstwood MSA (2013) Sedimentary recycling in arc magmas: geochemical and U–Pb–Hf–O constraints on the Mesoproterozoic Suldal Arc, SW Norway. Contrib Mineral Petrol 165:507–523. doi: 10.1007/s00410-012-0820-y

Roffeis C, Corfu F (2014) Caledonian nappes of southern Norway and their correlation with Sveconorwegian basement domains. Geol Soc Lond Spec Publ 390:193–221. doi: 10.1144/SP390.13

Rohr TS, Corfu F, Austrheim H akon, Andersen TB (2004) Sveconorwegian U-Pb zircon and monazite ages of granulite-facies rocks, Hisaroya, Gulen, Western Gneiss Region, Norway. Nor Geol Tidsskr 84:251–256.

Schärer U, Wilmart E, Duchesne J-C (1996) The short duration and anorogenic character of anorthosite magmatism: U-Pb dating of the Rogaland complex, Norway. Earth Planet Sci Lett 139:335–350.

Skar O, Pedersen RB (2003) Relations between granitoid magmatism and migmatization: U–Pb geochronological evidence from the Western Gneiss Complex, Norway. J Geol Soc 160:935–946.

Slagstad T, Roberts NMW, Marker M, Røhr TS, Schiellerup H (2013) A non-collisional, accretionary Sveconorwegian orogen: A non-collisional, accretionary Sveconorwegian orogen. Terra Nova 25:30–37. doi: 10.1111/ter.12001

Söderlund U, HellströM FA, Kamo SL (2008) Geochronology of high-pressure mafic granulite dykes in SW Sweden: tracking the P–T–t path of metamorphism using Hf isotopes in zircon and baddeleyite. J Metamorph Geol 26:539–560. doi: 10.1111/j.1525-1314.2008.00776.x

Söderlund U, Isachsen CE, Bylund G, Heaman LM, Jonathan Patchett P, Vervoort JD, Andersson UB (2005) U–Pb baddeleyite ages and Hf, Nd isotope chemistry constraining repeated mafic magmatism in the Fennoscandian Shield from 1.6 to 0.9 Ga. Contrib Mineral Petrol 150:174–194. doi: 10.1007/s00410-005-0011-1

Spencer CJ, Roberts NMW, Cawood PA, Hawkesworth CJ, Prave AR, Antonini ASM, Horstwood MSA (2014) Intermontane basins and bimodal volcanism at the onset of the Sveconorwegian Orogeny, southern Norway. Precambrian Res 252:107–118. doi: 10.1016/j.precamres.2014.07.008

Tobi AC, Hermans GAE., Maijer C, Jansen JBH (1985) Metamorphic zoning in the high-grade proterozoic of Rogaland-Vest Agder SW Norway. In: The deep Proterozoic crust in the North Atlantic provinces, D. Reidel publishing compagny. A.C. Tobi & J.L.R. Touret, pp 477–497

Tomkins HS, Williams IS, Ellis DJ (2005) In situ U-Pb dating of zircon formed from retrograde garnet breakdown during decompression in Rogaland, SW Norway. J Metamorph Geol 23:201–215. doi: 10.1111/j.1525-1314.2005.00572.x

Vander Auwera J, Bolle O, Bingen B, Liégeois J-P, Bogaerts M, Duchesne JC, De Waele B, Longhi J (2011) Sveconorwegian massif-type anorthosites and related granitoids result from post-collisional melting of a continental arc root. Earth-Sci Rev 107:375–397. doi: 10.1016/j.earscirev.2011.04.005

Vander Auwera J, Bolle O, Dupont A, Pin C, Paquette J-L, Charlier B, Duchesne JC, Mattielli N, Bogaerts M (2014a) Source-derived heterogeneities in the composite (charnockite-granite) ferroan Farsund intrusion (SW Norway). Precambrian Res 251:141–163. doi: 10.1016/j.precamres.2014.06.003

Vander Auwera J, Charlier B, Duchesne J-C, Bingen B, Longhi J, Bolle O (2014b) Comment on Bydee et al. (2014): Pyroxene megacrysts in Proterozoic anorthosites: Implications for tectonic settings, magma source and magmatic processes at the Moho.

Vander Auwera J, Longhi J (1994) Experimental study of a jotunite (hypersthene monzodiorite): constraints on the parent magma composition and crystallization conditions (P, T, f O 2) of the Bjerkreim-Sokndal layered intrusion (Norway). Contrib Mineral Petrol 118:60–78.

Viola G, Henderson IHC, Bingen B, Hendriks BWH (2011) The Grenvillian–Sveconorwegian orogeny in Fennoscandia: Back-thrusting and extensional shearing along the "Mylonite Zone." Precambrian Res 189:368–388.

Westphal M, Schumacher JC, Boschert S (2003) High-temperature metamorphism and the role of magmatic heat sources at the Rogaland anorthosite complex in southwestern Norway. J Petrol 44:1145–1162.

Wilmart E, Duchesne J-C (1987) Geothermobarometry of igneous and metamorphic rocks around the Ana-Sira anorthosite massif: Implications for the depth of emplacement of the South Norwegian anorthosites. Nor Geol Tidsskr 67:185–196.

Zhou X, Bingen B, Demaiffe D, Liégeois J-P, Hertogen J, Weis D, Michot J (1995) The 1160 Ma Hidderskog meta-charnockite: implications of this A-type pluton for the Sveconorwegian belt in Vest Agder (SW Norway). Lithos 51–66.

Tables

Tab. 1: Compilation of published geochronogical data on igneous and metamorphic events in the Rogaland area

Igneous/metamorphic stage	Reference	Lithology	Mineral and method	Age (Ma)
Igneous (prc- to syn- M_1)	Pasteels & Michot (1975)	Granitic gneiss	U-Pb zircon	*c.* 1486
	Zhou *et al.* (1992)	Charnockitic gneiss	U-Pb zircon	1159 ± 5
	Bingen & Van Bremen (1998)	Augen gneiss	U-Pb zircon	1049 +2/-8, 1051 +2/-8, 1051 +2/-4
	Anderson *et al.* (2002)	Granite	U-Pb zircon	1036 +23/-22
	Möller *et al.* (2002)	Pigeonite charnockite	U-Pb zircon	1588 ⊥ 10 (inherited), 1033 ⊥20, 1056 ⊥10
		Pigeonite charnockite	U-Pb zircon	1520 ±7 (inherited), 1035 ⊥6
		Augen gneiss	U-Pb zircon	1034 ±7
	Möller *et al.* (2003)	Pegmatitic leucosome	U-Pb zircon	1039 ±11
		Migmatitic garnet gneiss	U-Pb zircon	1046 +12
	Tomkins *et al.* (2005)	Metapelitic migmatite	U-Pb zircon	1233 ⊥69 to 3053 ⊥67
Metamorphic (syn- M_1)	Pasteels & Michot (1975)	Garnet gneiss	U-Pb zircon	*c.* 1018-951
		Augen gneiss	U-Pb zircon	1001-1041
	Bingen & Van Bremen (1998)	Augen gneiss	U-Pb monazite	1006 +3, 975 +2, 1010 +2, 1000 +1, 1012 +1, 1008⊥1, 990 ⊥1, 974 ⊥2
		Charnockitic gneiss	U-Pb monazite	1019 ±1, 1005 ±1, 1004 ±1, 1001 ±1
		Augen gneiss	U-Pb monazite	1024 ±1, 1009 ±1, 987 ±2, 986 ±2, 970 ±5, 971 ±2, 951 ±6
		Charnockitic gneiss	U-Pb monazite	997 +1, 986 +2, 985 +1, 972 +1, 1004 +1, 950 +1, 943 ⊥1
		Augen gneiss	U-Pb monazite	1007 ±2, 979 ±1
	Möller *et al.* (2002)	Augen gneiss	U-Pb zircon	1020 ±7 to 980 ±7
		Pigeonite charnockite	U-Pb zircon	1013 ±8, 1014 ±11, 1017 ±12 to 992 ±14, 972 ±20
	Tomkins *et al.* (2005)	Metapelitic migmatite (peak)	U-Pb zircon	1035 +9, 989 +11
		Metapelitic migmatite (decompression)	U-Pb zircon	955 ⊥8
	Bingen *et al.* (2008b)	Granitic gneiss	U-Pb monazite	1002 ±7
		Augen gneiss	Th-Pb monazite	999 ±5, 997 ±5
		Charnockitic gneiss	Th-Pb monazite	1013 ±5, 980 ±5
		Felsic granulite	U-Pb monazite	1032 +5, 990 +8
Metamorphic (post- M_1 decompression)	Bingen & Stein (2003)	Qtz-Pl-Kfs-Leucosome in Grt-Opx-gneiss	Re-Os molybdenite	974 ⊥3 to 969 ⊥3
	Tomkins *et al.* (2005)	Metapelitic migmatite (decompression)	U-Pb zircon	955 ⊥8
	Bingen *et al.* (2008b)	Granitic gneiss	Re-Os molybdenite	982 ±4 to 974 ⊥3 ; 959 ±3, 956 ±3 to 947 ±3, 946 ±3 to 939 ±3
		Augen gneiss	Re-Os molybdenite	953 ⊥3 to 931 ⊥3
Igneous (syn- M_2)	Pasteels *et al.* (1979)	Pegmatite	U-Pb zircon	914 ⊥6
		Charnockite	U-Pb zircon	931 ⊥10
	Shärer *et al.* (1996)	Anorthosite	U-Pb baddeleyite	915 ±4, 929 ±2, 939 ±3, 939 ±3
		Norite	U-Pb zircon	920 +3
		Quartz mangerite	U-Pb zircon	931 ⊥5
Metamorphic (M_2 to M_3)	Pasteels & Michot (1975)	Garnet gneiss	U-Pb zircon	910 ⊥30
	Bingen & Van Bremen (1998)	Augen gneiss	U-Pb monazite	928 ±3, 927 ±1, 925 ±2, 912 ±3, 907 ±5, 930 ±1, 928 ±1, 904 ±5, 904 ±8
		Charnockitic gneiss	U-Pb monazite	932 +1
	Möller *et al.* (2002)	Pigeonite charnockite	U-Pb zircon	931 ⊥22, 920 ⊥5, 911 ⊥6
	Bingen *et al.* (2008b)	Augen gneiss	Th-Pb monazite	927 ±5, 924 ±5, 922 ±5, 914 ±4, 910 ±9
	Bingen *et al.* (2006)	Qtz vein	Re-Os molybdenite	918 ⊥3 to 917 ⊥3

Chapitre 2

Sulphate incorporation in monazite lattice and dating the cycle of sulphur in metamorphic belts

ANTONIN T. LAURENT[1]*, ANNE-MAGALI SEYDOUX-GUILLAUME[2], STEPHANIE DUCHENE[1], BERNARD BINGEN[3], VALERIE BOSSE[4], LUCIEN DATAS[5]

[1]GET, UMR 5563 CNRS–UPS–IRD, Université de Toulouse III, 14 av. E. Belin, 31400 Toulouse, France (*correspondence: antonin.laurent@get.obs-mip.fr)

[2]LMV, UMR 6524 CNRS–UBP–IRD Faculté des Sciences et Techniques, Saint-Etienne, France

[3]Geological Survey of Norway, 7491 Trondheim, Norway

[4]LMV, UMR 6524 CNRS–UBP–IRD, Université Blaise Pascal, Clermont-Ferrand, France

[5]Centre de micro-caractérisation Raimond Castaing, UMS 3623 CNRS–UPS, Université de Toulouse, France

Keywords: monazite – sulphate – U–Pb geochronology – metamorphism – S cycle

Accepted for publication in **Contributions to Mineralogy and Petrology** (15/09/2016)

Résumé

L'étude géochimique associée à la caractérisation nano-structurale *in-situ* de cristaux de monazite riche en S montre que le S y est incorporé en tant que sulfate (SO_4^{2-}) via la substitution clino-anhydrite ($Ca^{2+} + S^{6+} = REE^{3+} + P^{5+}$). Les cristaux de monazite riches en S montrent des exsolutions (5–10 nm) de $CaSO_4$ qui suggèrent une immiscibilité à basse température. L'échantillon étudié est un gneiss à osumilite du domaine de ultra-haute température du Rogaland (Norvège) qui préserve des cristaux de monazites à la zonation complexe. Trois domaines chimiques et texturaux peuvent être distingués : (1) un cœur riche en sulfate (0.45–0.72 wt% SO_2) où le Th est incorporé suivant la substitution chéralite ($Th^{4+} + Ca^{2+} = 2REE^{3+}$), (2) des domaines secondaires contenant du S ($SO_2 > 0.05$ wt%) et criblés d'inclusions minérales et fluides et enfin (3) des domaines tardifs dépourvus de S mais riches en Y (0.8–2.5 wt% Y_2O_3) où le Th est incorporé suivant la substitution huttonite ($Th^{4+} + Si^{4+} = REE^{3+} + P^{5+}$). Ces trois domaines chimiques possèdent des âges isotopiques U–Pb distincts de 1034 ± 6, 1005 ± 7 et 935 ± 7 Ma, respectivement. La datation U–Th/Pb par microsonde électronique, suivant un protocole développé durant cette étude, confirme les âges obtenus par LA-ICP-MS cités précédemment qui démontrent qu'il est possible de discriminer différentes générations de monazites sur la base de leur teneur en S. A partir du contexte pétrologique de l'échantillon, contraint par ailleurs, nous proposons que les monazites riches en S aient cristallisé à 1034 ± 6 Ma à partir d'un liquide silicaté oxydé où le S était présent sous forme de sulfate (S^{6+}). L'enrichissement du liquide silicaté en S est relié à la déstabilisation de la pyrite en pyrrhotite lors du métamorphisme prograde et à la fusion incongruente des sulfures de Fe–Cu–As qui est globalement simultanée de la réaction de fusion–déshydratation de la biotite. Les inclusions minérales et fluides présentes dans les domaines secondaires datés à 1005 ± 7 Ma résultent d'une réaction de dissolution–cristallisation des domaines primaires riches en S. Enfin, les domaines tardifs ayant cristallisés à 935 ± 7 Ma sont dépourvus de S. Ce changement de chimie reflète un changement dans les conditions d'oxydo-réduction régionales marquées par ailleurs par la précipitation de molybdenite. Nous concluons que la concentration en S de la monazite peut être utilisée pour dater la mobilisation du S dans les roches métamorphiques et explorer le potentiel minéralisateur d'un événement géologique particulier au cours d'une orogenèse prolongée. Cette propriété peut également permettre de dater le dépôt de gîtes minéraux oxydés, en distinguant le domaine du cristal de monazite co-génétique à la minéralisation des domaines résultant de recristallisations tardives.

Abstract

Microgeochemical data and transmission electron microscope (TEM) imaging of S-rich monazite crystals demonstrate that S has been incorporated in the lattice of monazite as a clino-anhydrite component via the following exchange $Ca^{2+} + S^{6+} = REE^{3+} + P^{5+}$, and that it is now partly exsolved in nanoclusters (5–10 nm) of $CaSO_4$. The sample, an osumilite-bearing ultra-high temperature granulite from Rogaland, Norway, is characterized by complexly patchy zoned monazite crystals. Three chemical domains are distinguished (1) a sulphate-rich core (0.45–0.72 wt% SO_2, Th incorporated as cheralite component), (2) secondary sulphate-bearing domains (SO_2 > 0.05 wt%, partly clouded with solid inclusions), and (3) late S-free, Y-rich, domains (0.8–2.5 wt% Y_2O_3, Th accommodated as the huttonite component). These three domains yield distinct isotopic U–Pb ages of 1034 ± 6, 1005 ± 7 and 935 ± 7 Ma, respectively. Uranium–Th–Pb EPMA dating independently confirms these ages. This study illustrates that it is possible to discriminate different generations of monazite based on their S-contents. From the petrological context, we propose that sulphate-rich monazite reflects high temperature Fe-sulphide breakdown under oxidizing conditions, coeval with biotite dehydration melting. Monazite may therefore reveal the presence of S in anatectic melts from high-grade terrains at a specific point in time and date S mobilisation from a reduced to an oxidized state. This property can be used to investigate the mineralization potential of a given geological event within a larger orogenic framework.

Introduction

Most metamorphic rocks contain S both as mineral constituent and in the fluid phase, as sulphide (S2-), sulphate (S6+) (e.g. Tracy and Robinson 1988; Harlov and Hansen 2005; Métrich and Mandeville 2010; Simon and Ripley 2011) and possibly trisulfur ion (S3- ; Jacquemet et al. 2014). The stability of sulphide, sulphate and other S-bearing minerals depends on pressure (P), temperature (T) and S speciation in the fluid phase which is controlled by the oxidation state of the bulk rock (Whitney 1984; Fleet 2006; Parat et al. 2011). Under favourable redox conditions, S stored in Fe–Cu sulphides is liberated during upper greenschist to amphibolite facies metamorphism in response to hydrous mineral breakdown (Connolly and Cesare 1993). This *P–T* window of sulphur liberation is extensively discussed as it bears important implications for the transport and deposition of Au and other strategic resources (Tomkins 2010; Evans et al. 2010). A somewhat less constrained episode of sulphur release occurs in the granulite facies, usually in the presence of a silicate melt (Tomkins et al. 2007).

Addressing the S cycle and related mineralization potential in metamorphic belts thus require to unravel the redox state of past and transient metamorphic C–O–H±S±Cl±F fluids and silicate melts. Indeed, the abundance and speciation of minor elements like S, Cl or F have strong effects on the stability of accessory minerals (e.g. zircon, uraninite, and monazite) that control the whole-rock budget of REE, U and Th (Hetherington et al. 2010; Budzyn et al. 2011; Aseri et al. 2015; Migdisov et al. 2016). Mobilization of U and Th, moreover give the opportunity to date hydrothermal events occurring in different structural levels of an orogen if suitable geochronometers are found (e.g. Rasmussen et al. 2006; Muhling et al. 2012; Villa and Williams 2013).

It is possible to trace S and other volatiles in the deep crust by direct observation and characterisation of primary fluid inclusions in minerals that are part of a specific metamorphic assemblage (Touret 2001; Seo et al. 2009). Alternatively, indirect evidence of mineral–fluid equilibria are recorded by sulphide, apatite or scapolite that incorporate S in their lattice as major or minor component (Parat and Holtz 2004; Satish-Kumar et al. 2006; Parat et al. 2011). Some of these S-bearing minerals may be dated directly thanks to radiometric methods such as Rb–Sr in scapolite–biotite pairs (Engvik et al. 2011) or Re–Os in molybdenite (Stein et al. 2001). This approach is however mostly restricted to ore deposits and other geochemical anomalies concentrating S. In contrast, the report of sulphur-bearing monazite (Chakhmouradian and Mitchell 1999; Ondrejka et al. 2007; Krenn et al. 2011) open the perspective of tracing S content and oxidation state through time in a large number of rocks thanks to the U–Pb and Th–Pb isotopic

systems. The petrogenesis of S-bearing monazite should be, however, understood in detail before isotopic ages can be correctly interpreted (e.g. Villa and Williams 2013).

In this study, we address the significance of S-rich monazite in high-grade metamorphic conditions, using a granulite facies example from the Sveconorwegian province in Rogaland, Norway. This study elucidates the mechanism of sulphur incorporation in monazite. It demonstrates correlations between the S content of monazite zones, their petrological context of crystallization and their age using two different analytical methods. These correlations underscore the importance of anatectic melts as a vector of S and lead to a discussion on dating the sulphur cycle, i.e. the processes by which sulphur moves from minerals to fluids or melts as a function of its oxidation state, in metamorphic environment.

Monazite crystal chemistry

Monazite is a rare earth element (REE) phosphate that crystallizes in a monoclinic lattice with space group $P2_{1/n}$. The structure consists of chains parallel to the c-axis with alternating PO_4 tetrahedra and an $REEO_9$ polyhedron, accommodating light REE (Ni et al. 1995). The nine-fold site may also host large cations such as Th, U, Ca, which are incorporated by two well documented substitution schemes (Montel et al. 2002). The cheralite substitution $M^{2+} + An^{4+} = 2REE^{3+}$ with M^{2+} = (Ca, Sr, Pb, Ba) and An^{4+} = (Th, U) involves the nine-fold site alone while the huttonite substitution involves a coupled replacement on both the tetrahedral and the nine-fold site: $Si^{4+} + An^{4+} = REE^{3+} + P^{5+}$. Additionally, heavy rare earth elements (HREE) and Y enter the monazite structure through the xenotime substitution $Y^{3+} = REE^{3+}$. Monazite can also incorporate several exotic cations into its structure, including S (Chakhmouradian and Mitchell 1999) but also V and As in the tetrahedral site (Ondrejka et al. 2007; Prsek et al. 2010). In particular, Gnos et al. (2015) suggested a direct relationship between the oxidation state of the host rock and the As content of hydrothermal monazite. The large number of cations substituting in its lattice makes monazite particularly responsive to changes in the bulk rock and fluid composition (e.g. Heinrich et al. 1997; Finger and Krenn 2007; Didier et al. 2013). Indeed, monazite has the ability to record geological events over a large range of P–T–fluid conditions ranging from low grade greenschist facies (Rasmussen and Muhling 2007; Janots et al. 2008) to granulite facies or a magmatic environment (Kelly et al. 2012; Dumond et al. 2015; Kirkland et al. 2016).

Geological background

The Sveconorwegian province (Fig. 1) is made up of Mesoproterozoic crust accreted at the margin of Fennoscandia and reworked during the 1140–900 Ma Sveconorwegian orogeny (Bingen et al. 2008b). Rogaland is located at the southwesternmost end of the province. The bedrock is composed of high-grade meta-igneous rocks of broadly granitic to tonalitic composition (granitic gneiss and meta-charnockite) interlayered with mafic rocks (amphibolites and banded gneiss) and metasedimentary rocks of either pelitic or calc-silicate composition (Hermans et al. 1975). Three metamorphic isograds (the orthopyroxene-, osumilite-, and pigeonite-in isograds) reflect a south-westward increase in metamorphic grade from upper-amphibolite to ultra-high temperature (UHT) granulite facies (Tobi et al. 1985). This apparent thermal gradient results from the superposition of three metamorphic events (Kars et al. 1980; Maijer 1987). The oldest M1 metamorphism is an upper amphibolite to granulite facies event associated with extensive migmatization, characterized by *P–T* estimates of 650–750 °C at 0.6–0.8 GPa (Jansen et al. 1985). Timing for this regional phase of metamorphism is bracketed between 1035 and 970 Ma by U–Pb data on zircon and monazite (Bingen and Van Breemen 1998; Bingen et al. 2008a). Recent investigations of sapphirine-bearing granulites suggest that UHT conditions of 1000 °C and 0.75 GPa were locally achieved at 1006 ± 4 Ma (U–Pb zircon; Drüppel et al. 2013) followed by decompression to 0.5 GPa recorded by zircon included in cordierite (Tomkins et al. 2005). The high-grade basement was subsequently intruded by a massif-type anorthosite–mangerite–charnockite plutonic complex (AMC) at 931 ± 2 Ma (Schärer et al. 1996), causing a M2 UHT metamorphic aureole marked by the osumilite and pigeonite isograds (Möller et al. 2002; Möller et al. 2003; Westphal et al. 2003). Estimates for M2 conditions range from 850 to 1050 °C at 0.4–0.55 GPa (Jansen et al. 1985; Drüppel et al. 2013). Finally, slow isobaric cooling is dated at 908 ± 9 Ma (Möller et al. 2003).

Analytical methods

Monazite zoning and micro-chemistry

Monazite crystals were studied both in thin section, which preserves their textural context, and in mineral separates recovered by standard procedures, including crushing, heavy liquids, and magnetic separation. They were examined using transmitted and reflected light microscopy, followed by Scanning Electron Microscopy (SEM) using a Jeol 6360LV equipped with a Bruker XFlash 5010 SDD detector (EDS), which allowed for quantitative phase mapping. Back Scattered

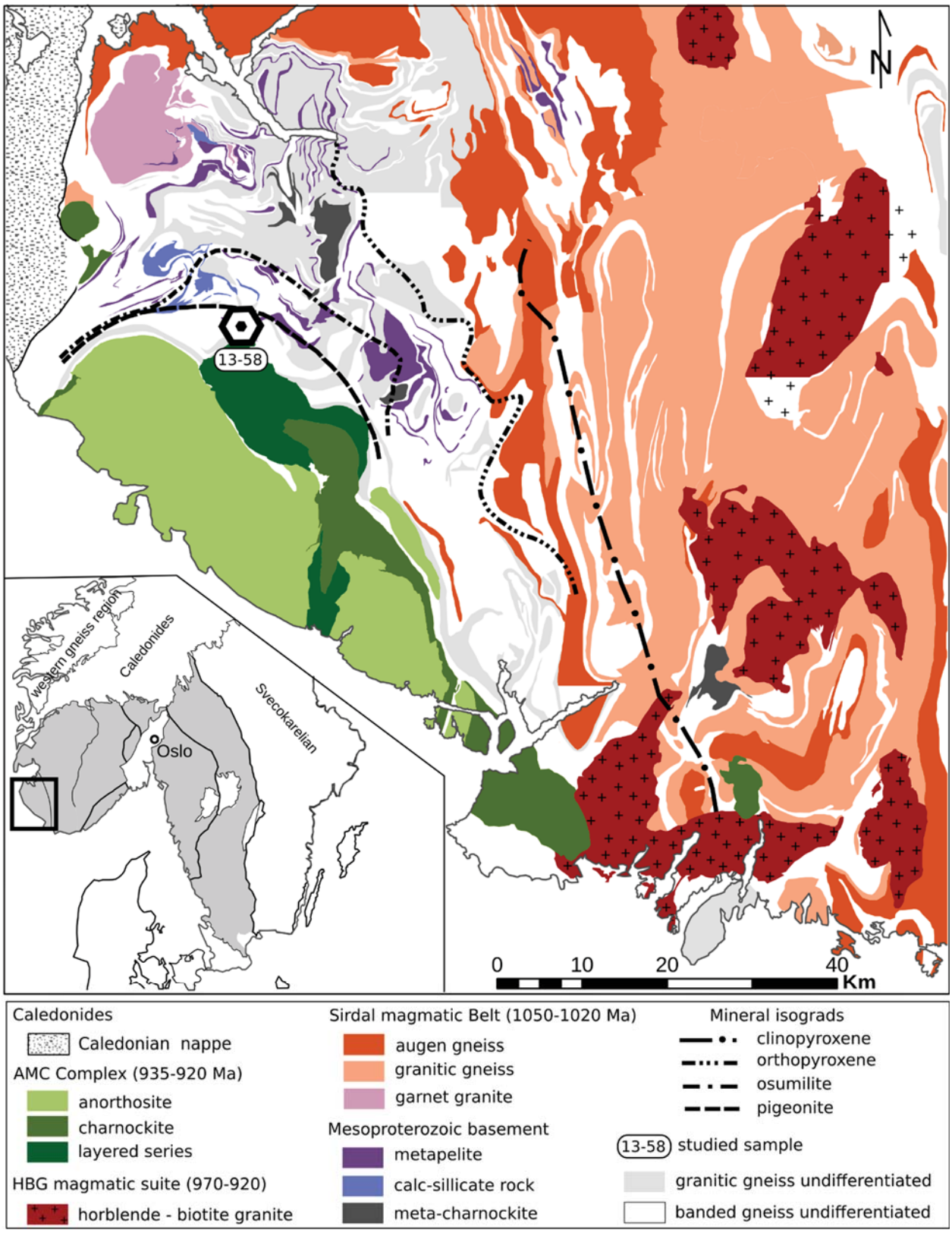

Fig. 2–1: Simplified geological map of Rogaland-Vest Agder modified after Falkum (1982) and Coint et al. (2015) with mineral isograds after Tobi et al. (1985) and Bingen et al. (1990). Inset – Sketch map of the Sveconorwegian Province in SW Scandinavia, grey rectangle depicts the studied area

Electron (BSE) images were taken at 20 kV with the Jeol 6360LV SEM to guide *in-situ* chemical analysis acquired using a Cameca SX-FIVE electron probe micro-analyser (EPMA) hosted at the Raimond Castaing micro-characterization centre (Toulouse). The EPMA was operated with a focused beam at standard operating conditions of 15 kV and 20 nA using a TAP–LLIF–PET–LPET configuration for point analyses. Selected grains were subsequently mapped for their minor elements, including Si–Th–Ca–S and Y–U–Th–Pb using a TAP–LPET–PET–LPET configuration. Element maps were generated at 15 kV and 200 nA with a step–size of 1 μm, and a dwell time of 1 s. ZAF matrix corrections were calculated using fixed REE and P content, which were chosen from point analysis. The following X–rays and mineral standards were used: Y Lα on YPO_4, Th Mα on synthetic ThO_2, S Kα on $BaSO_4$, Si Kα and Ca Kα on Wollastonite, P Kα and REE (Ce Lα, La Lα, Pr Lβ, Nd Lβ, Sm Lβ, Gd Lβ, Dy Lα) on Pb-free $(REE)PO_4$, Pb Mβ on an in-house $Pb_2P_2O_7$ and U Mβ on synthetic UO_2.

Background positions were carefully selected after acquiring a Wavelength Dispersive Spectrometer (WDS) intensity spectrum on the area of interest. In particular, the S Kα background was carefully chosen at (-1800; +500) in order to avoid any interference (Fig. 2). A selected 95% confidence level in analytical errors for point analyses, calculated following the formula of Ancey et al. (1977), are as follows: 0.08 wt% for SO_2, 0.06 wt% for CaO, 0.7 wt% for ThO_2, and 0.25 wt% for both SiO_2 and Y_2O_3. Monazite formula were calculated in the system $2(REE)PO_4$ – $CaTh(PO_4)_2$ –$2ThSiO_4$, utilizing the following sequence: (1) Ca + Th + U are assigned to the cheralite $[CaTh(PO_4)_2]$ component, (2) any remaining Th is combined with Si are assigned to the huttonite $[ThSiO_4]$ component, (3) Y and HREE (Gd–Lu) are assigned to the xenotime $[(HREE,Y)PO_4]$ component, and (4) the light rare earth elements (La–Eu) are assigned to the monazite $[(LREE)PO_4]$ component.

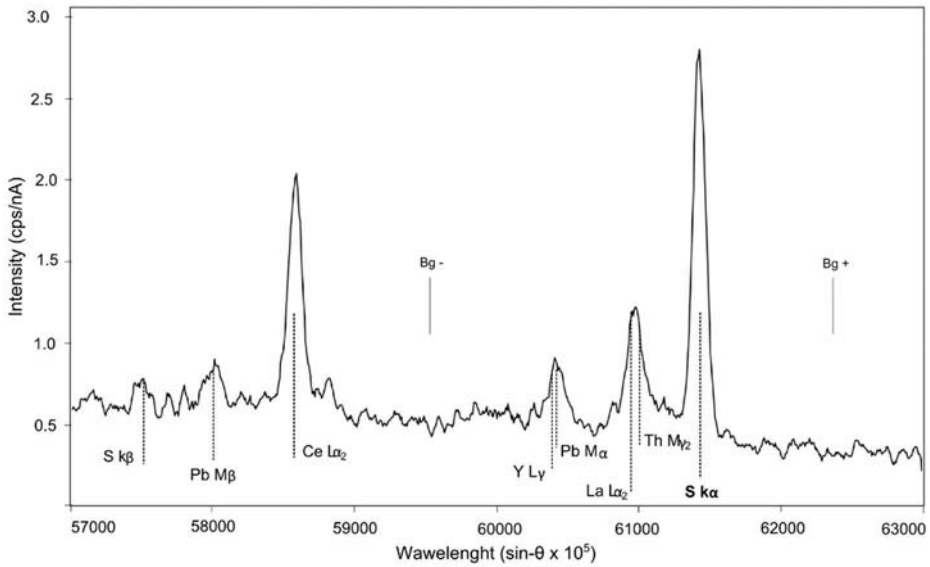

Fig. 2–2: Scans of the S Kα region performed with WDS using a LPET crystal within S-rich monazite core (D1)

Additional microanalyses of monazite were collected by laser ablation inductively coupled plasma mass spectrometry (LA–ICP–MS), including the full suite of REE (^{139}La, ^{140}Ce, ^{141}Pr, ^{146}Nd, ^{147}Sm, ^{153}Eu, ^{157}Gd, ^{159}Tb, ^{163}Dy, ^{165}Ho, ^{166}Er, ^{169}Tm, ^{172}Yb, ^{175}Lu) along with ^{29}Si, ^{31}P, $^{(43+44)}$Ca, ^{89}Y, ^{238}U, ^{232}Th, ^{208}Pb, and ^{88}Sr. The Moacyr monazite (Seydoux-Guillaume et al. 2002) was used for calibration as an external standard in order to avoid the chemical fractionation observed with NIST610 for U and Pb. Lanthanum was used as an internal standard and NIST 610 used for external calibration following the procedure outlined in Didier et al. (2015). The spot size was 12 µm with a repetition rate of 1 Hz.

Monazite U–Th–Pb geochronology

Laser ablation ion coupled mass spectrometry (LA–ICP–MS)

Uranium–Th–Pb isotopic analyses were performed by LA–ICP–MS on 23 grains at the laboratoire Magmas et Volcans (Clermont-Ferrand, France). Laser ablation spots were guided by BSE images and chemical compositions, previously acquired by EPMA, together with reflected and transmitted light microphotography. The laser ablation systems consists of a Resonetics Resolution M-50E system equipped with an ultra-short pulse (< 4 ns) ATL excimer 193 nm laser coupled to an Agilent 7500 cs ICP–MS. Detailed analytical procedures are reported in Paquette and Tiepolo (2007) and Didier et al. (2015). A spot diameter of 9 µm was used with 1 Hz repetition rate and a fluence of 6 J/cm². The ^{204}(Hg+Pb) signal was monitored but no common Pb correction was applied. Raw data were corrected for U–Pb and Th–Pb fractionation during laser ablation and instrumental mass discrimination by standard bracketing with the C83-32 monazite (2681 ± 2 Ma; Corfu 1988). Repeated analysis of the Manangotry (555 ± 2 Ma; Paquette and Tiepolo 2007) and Moacyr monazite (Seydoux-Guillaume et al. 2002; Gasquet et al. 2010; Fletcher et al. 2010) during the run were used to monitor accuracy and reproducibility of the applied correction. The data were acquired during a single session. Six analyses of the Manangotry monazite yielded a weighted ^{206}Pb/^{238}U age of 560 ± 8 Ma (MSWD = 1.1) and 12 analyses of the Moacyr monazite yielded a weighted ^{208}Pb/^{232}Th age of 504 ± 6 Ma (MSWD = 0.8). Data reduction was carried out using the Glitter software package (Van Achterbergh et al. 2001).

Electron probe micro analysis (EPMA)

The U–Th–Pb EPMA dating was carried out on a Cameca SX-FIVE EPMA with an accelerating voltage of 15 kV and 200 nA probe current. Thorium was measured on a PET crystal using the Th Mα line with synthetic ThO_2 as a standard (background: -1200; +1000). Uranium was

measured on a LPET crystal using U Mβ with synthetic UO_2 as a standard (background: -1200; +950). Lead was measured on a LPET crystal using the Pb Mα on an in-house $Pb_2P_2O_7$ standard (background: -3500; +2240). Additionally, Y and Si were measured simultaneously on two TAP crystals using Y Lα and Si Kα lines. Counting time for each element was 240 s on peak and 120 s on background. The pulse height analyser was set in automatic mode (Spear 2009). A linear background fit was chosen for U, Th, Si, Y and an exponential fit for Pb because of the large offset in Pb background positions (Jercinovic 2005; Williams et al. 2007; Spear et al. 2009). To monitor any drift in the measured peak and background intensities during analysis, the counting time was divided into 6 cycles of peak/background acquisition (sub-counting method described in Spear et al. 2009). The Chi^2 test was then applied to each analysis point (6 cycles), so that inconsistent counting cycles were not taken into account when summing the total counts for each element. Interference of Th $M\gamma_1$ on U Mβ and Y $L\gamma_{2,3}$, + Th $M\zeta_{1,2}$ on Pb Mα were quantified using Pb-free (REE)PO_4 crystals and pure ThO_2 reference material, following the approach of Spear et al. (2009). Consequently, the measured values were corrected as follows: $U_{corr} = U_{meas.}$ - 96.6 ppm/wt.% Th and $Pb_{corr.} = Pb_{meas.}$ - 83.55 ppm/wt.% Y - 16.5 ppm/wt.% Th. Typical uncertainties arising from counting statistics, which were calculated following Ancey et al. (1977) for monazite crystals with Th in the range 4–8 wt%, are 110 ppm for Pb, 150 ppm for U, 135 ppm for Y, and 650 ppm for Th. Uncertainties for Pb, U, and Th are estimated for each analysis, and then the age is calculated with the 95% confidence interval estimated by propagation of errors using Monte-Carlo simulation (Montel et al. 1996). The age and associated confidence interval were calculated with the R-package NileDam[1] (Montel et al. 1996; Seydoux-Guillaume et al. 2012). Repeated analysis of the

Manangotry reference monazite (555 ± 2 Ma; MSWD = 1.6; Paquette and Tiepolo 2007) during the session was used to control the reproducibility and accuracy of the correction applied. Twenty-six analyses gave a pooled age of 558 ± 12 Ma (MSWD = 1.4), in good agreement with the published ID-TIMS age of 555 ± 2 Ma (Paquette and Tiepolo 2007).

Transmission electron microscopic (TEM) imaging

Three Focused Ion Beam (FIB) foils were prepared by the *in-situ* lift-out technique, on a FEI dual-beam microscope (Hélios600i) at the LAAS laboratory in Toulouse. The foils were first examined with a JEOL 2100F Transmission Electron Microscope (TEM) operated at 200 KeV, equipped with a field emission gun (FEG) as an electron source, an Energy Dispersive Spectrometer (EDS SDD Brücker), a CCD Camera from Gatan (1Kx1K), and a High-Angle Annular Dark Field (HAADF). The foils were then investigated in high-resolution (HR) mode

[1] Villa-Vialaneix N., Montel J-M and Seydoux-Guillaume A-M (2013) *NiLeDAM: Monazite Datation for the NiLeDAM team*. R package version 0.1

using a JEOL cold FEG ARM200F TEM operated at 200 keV, equipped with a CS corrector, EDS, STEM HAADF detector and a GIF QUANTUM. Both TEM are located in the Raimond Castaing micro-characterization center (Toulouse).

Results

Sample petrology

The sample in this study is an osumilite-bearing granulite facies gneiss from the Vikeså locality situated within the pigeonite isograd (UTM WGS84 coordinates zone 32: x = 322482; y = 6503981). The heterogeneous outcrop consists of coarse quartz–mesoperthite layers alternating with discontinuous osumilite-rich pinkish layers containing scarce relicts of garnet porphyroblasts (garnet $_{I}$). On the microscopic scale the sample contains porphyroblastic garnet enclosing needles of sillimanite together with biotite, quartz, K-feldspar, ilmenite, and magnetite that are typical of an M1 metamorphic event (Maijer et al. 1981). Porphyroblastic garnet is isolated from atoll-like Al-rich orthopyroxene by a broad osumilite + hercynite rim enclosing numerous quartz blebs as well as orthopyroxene blades (Fig. 3a-b). The osumilite-bearing assemblage is interpreted to reflect M2 UHT contact metamorphism although phase equilibria modelling points to conditions of 850 °C - 0.55 GPa (i.e. nominally slightly below 900°C; Holland et al. 1996). Overall, the osumilite–spinel assemblage formed at low water activity and high oxygen fugacity, well above the quartz–fayalite–magnetite (QFM) oxygen buffer (Das et al. 2001). Retrograde garnet $_{II}$ rims develop around hercynite, magnetite and garnet $_{I}$. Spinel group minerals formed an extensive solid solution at high temperature, but were subsequently exsolved into hercynite, magnetite, and ilmenite (Kars et al. 1980). Sulphide minerals are present in the matrix as scarce corroded pyrite grains (up to 700 μm). Exsolution textures of isocubanite and minor chalcopyrite are interpreted to represent a former intermediate solid solution in the Fe–Cu–S system. Pyrite grains are surrounded by a double corona of magnetite (inner rim) and garnet $_{II}$ (outer rim; Fig. 3c).

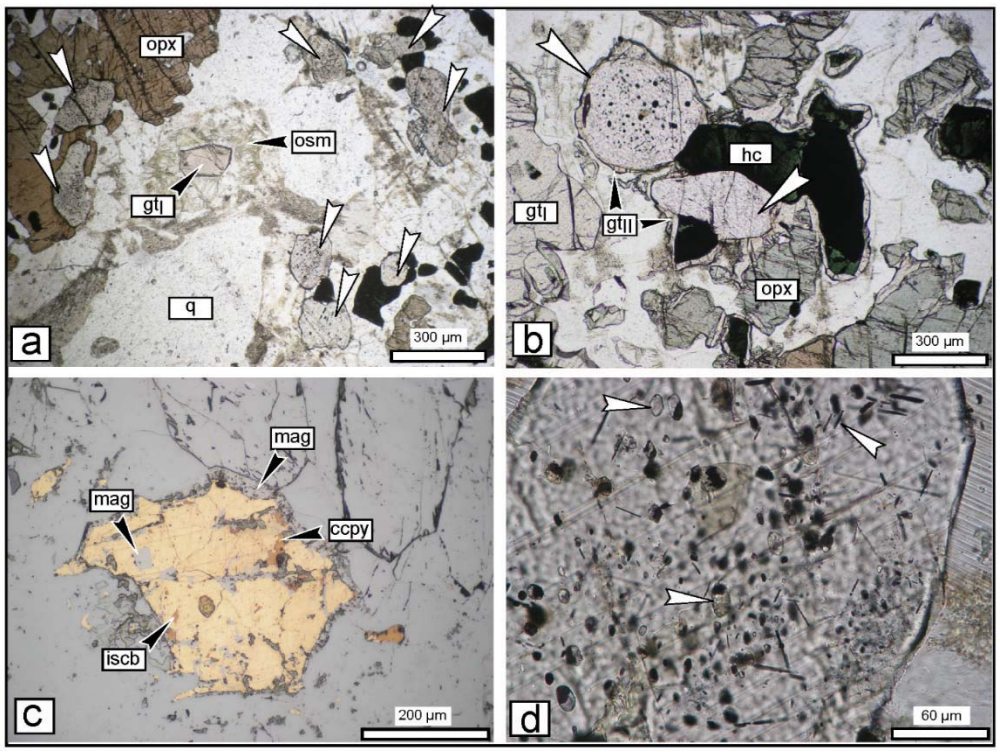

Fig. 2–3: Petrography of the osumilite-bearing granulite sample. **a**– Osumilite corona around garnet with several monazite crystals (white arrows). **b**– Retrograde garnet II rims around spinel and monazite. **c**– Corroded pyrite crystal with exsolutions of isocubanite (iscb) and chalcopyrite (ccpy) and a rim of magnetite (Mag). **d**– Monazite crystal with monomineralic inclusions showing preferred orientation on the top right (pyrrhotite lath), polymineralic inclusion (centre), and transparent fluid inclusion (top left); note the twinning in monazite

Monazite texture, composition and inclusions

Garnet-rich layers in sample ALR 13-58 contain large (up to 900 µm) monazite grains clouded with solid inclusions. The monazite grains make up to ~ 1 % of the volume of the mineral assemblage (Fig. 3b,d). These grains are anhedral and usually found in the matrix or partly included within peak metamorphic minerals such as orthopyroxene or green spinel and are eventually overgrown by retrograde garnet II rims (Fig. 3b). In addition, BSE mapping of thin sections reveals small monazite grains (< 15 µm) hosted in garnet I. These inclusions were too small to be analysed by LA–ICP–MS and are not discussed further.

Zoning and micro-chemistry

High contrast BSE imaging of over 140 monazite grains reveals almost systematic patchy zoning. Rare crystals preserve an apparently unzoned dark core surrounded by a thick patchy rim (Fig. 4a). The limits between different chemical zones are sharp (< 1 µm) with several lobate fronts reflecting inward propagation, as well as worm-like zones (Fig. 4b-c). Compositional WDS maps and transects demonstrate that core domains and restricted areas of the patchy rim contain an appreciable SO_2 content up to 0.72 wt% (Fig. 4d). The spatial distribution of SO_2 within the grains is positively correlated with CaO but shows no correlation with SiO_2 or ThO_2 (Fig. 4d–g, Fig. 5).

Monazite formula were calculated to quantify the amount of Ca + Si that cannot be incorporated in the cheralite and huttonite components (Tab. 1). In a binary plot of S + excess (Ca + Si) versus total REE + P + Th + U + Ca + Si (Fig.6), the negative correlation demonstrates that S-bearing crystals follow the exchange vector between anhydrite and monazite expressed as $Ca^{2+} + S^{6+} = REE^{3+} + P^{5+}$ (Chakhmouradian and Mitchell 1999). The maximum anhydrite ($CaSO_4$) mole fraction detected in the dataset is 2.7 mol. %.

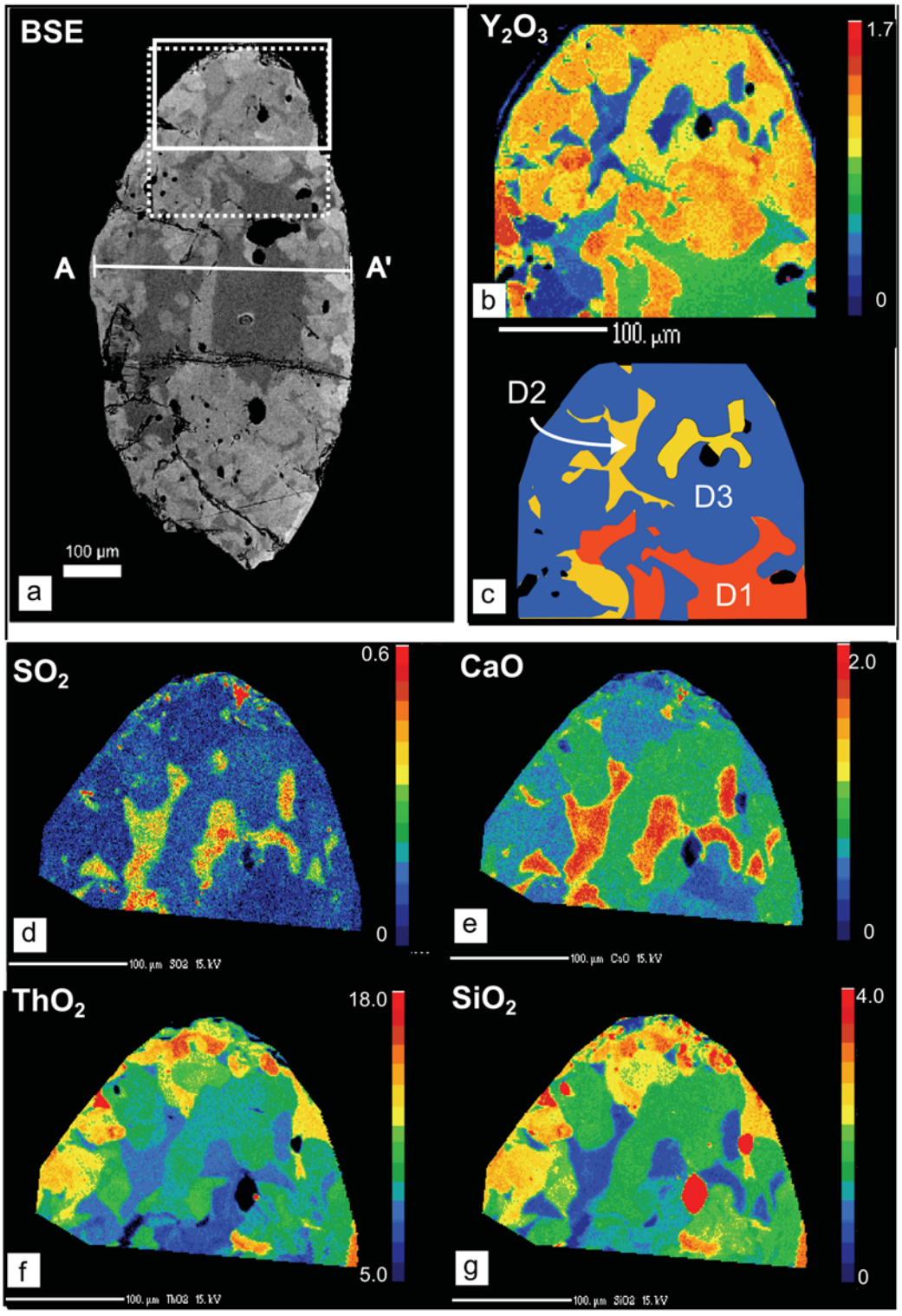

↑ **Fig. 2–4**: Chemical zoning of monazite crystal 1029-17. **a**– BSE image collected with SEM. Dotted rectangle depicts the area in panels b–c. The solid-line rectangle depicts the area in panels d–g. The A–A' line corresponds to the profile of Fig. 5. **b**– Quantified EPMA chemical map of Y2O3. **c**– Sketch of the grain showing the different chemical domains, i.e., S-rich core D1 in red, S-bearing D2 in orange, and S-free D3 in blue. **d–g** Quantified EPMA chemical map of SO2, CaO, ThO2, SiO2

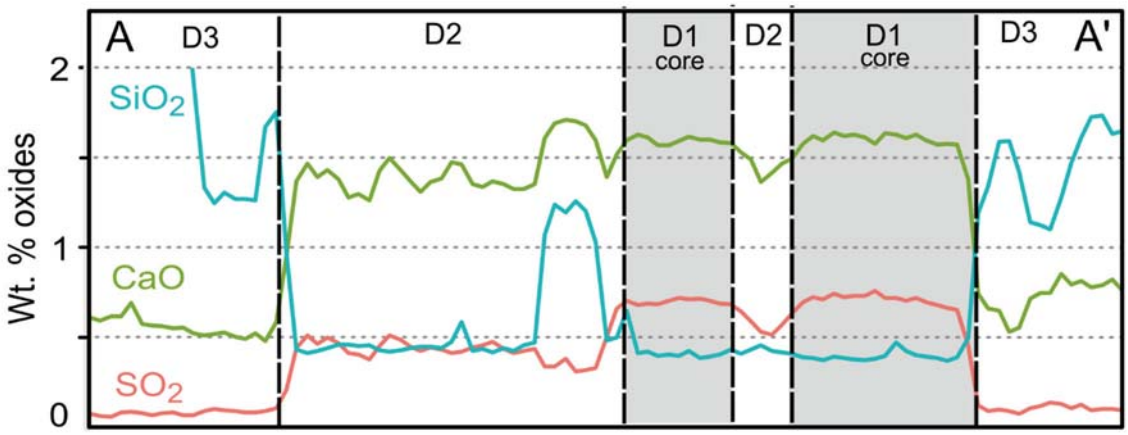

Fig. 2–5: Chemical profile in SO2, CaO, SiO2 across monazite crystal 1029-17. The profile (A-A') is located on Fig. 4a

Based on the SO_2 content and BSE zoning, it is possible to distinguish three distinct compositional domains (Fig. 4c). Domain 1 (D1) consists of unzoned, inclusion-free cores that have a high SO_2 content (0.45–0.72 wt%; Tab. 1), moderate Th (3–5 wt% ThO_2), and Y (0.9–1.4 wt% Y_2O_3). The dominant vector for Th substitution is cheralite (X_{crl} =7–10 %; Fig. 7). Domain 2 (D2) shows a patchy zoning. It contains a significant amount of SO_2 (> 0.05 wt%), together with variable Y (0.5-1.6 wt% Y_2O_3) and Th (4.5–8.5 wt% ThO_2) which is accommodated by the cheralite substitution (X_{crl} = 7–17 %). Domain 3 (D3) defines either patchy zones or bright embayments near the grain boundary in the BSE images (Fig. 4). It is lacking SO_2, and instead is characterized by high Y (0.8-2.5 wt% Y_2O_3) and Th (5–11 w% ThO_2) accommodated dominantly along the huttonite substitution vector (X_{htn} = 3–8 %; X_{crl} = 2.5–5 %). Chondrite-normalized REE patterns of monazite, collected in individual micro-domains by LA–ICP–MS, are characterized by a strong enrichment in LREE (LaN ~ 3.105) relative to HREE (LuN = 1–5.102), and a negative Eu anomaly (Fig. 8; Tab. 2). In detail, the three compositional domains, D1 to D3, display significantly distinct REE signatures. The negative Eu anomaly deepens from D1 (Eu/Eu* = 0.18–0.09) to D2 (Eu/Eu* = 0.09–0.05) to D3 (Eu/Eu* = 0.04–0.02). The LREE slope decreases from D1 (LaN/NdN = 1.9–1.6) to D2 (LaN/NdN = 1.8–1.0), to D3 (LaN/NdN = 1.4–0.9). Although the three domains display parallel HREE slope, the average HREE content is higher for D3 (Tb–Lu = 8078 ppm) than for D2 (Tb–Lu = 5254 ppm) confirming the Y signature. In D1, the variable HREE content correlates with the variable Y content. The Sr concentration (Tab. 2) is always lower than 20 ppm.

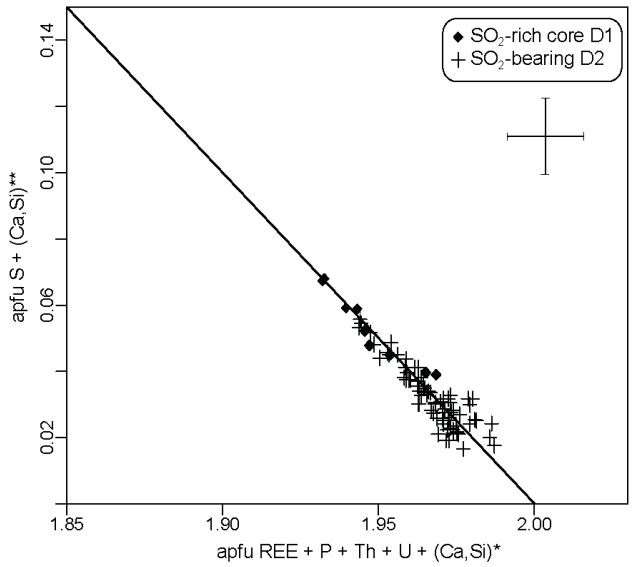

Fig. 2–6: Binary compositional diagram for monazite analysed by EPMA, representing the amount of S + (Ca + Si)* that cannot be incorporated in cheralite and huttonite as a function of total REE + P + Th + U + (Ca + Si)** incorporated in cheralite and huttonite in atom per formula unit (apfu). Only the S-rich core D1 and S-bearing D2 monazites are plotted. Error cross of 95% confidence of EPMA analyses is shown on the top right

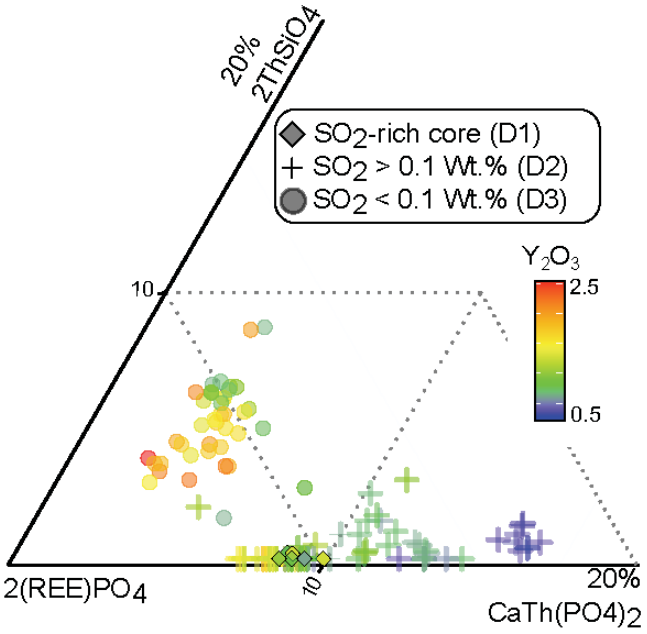

Fig. 2–7: Ternary compositional diagram (mol. %) for monazite D1, D2 and D3 in the system 2(REE)PO4 (monazite + xenotime) – CaTh(PO4)2 (cheralite) – 2ThSiO4 (huttonite). The analyses are collected by EPMA and colour coded following their Y content.

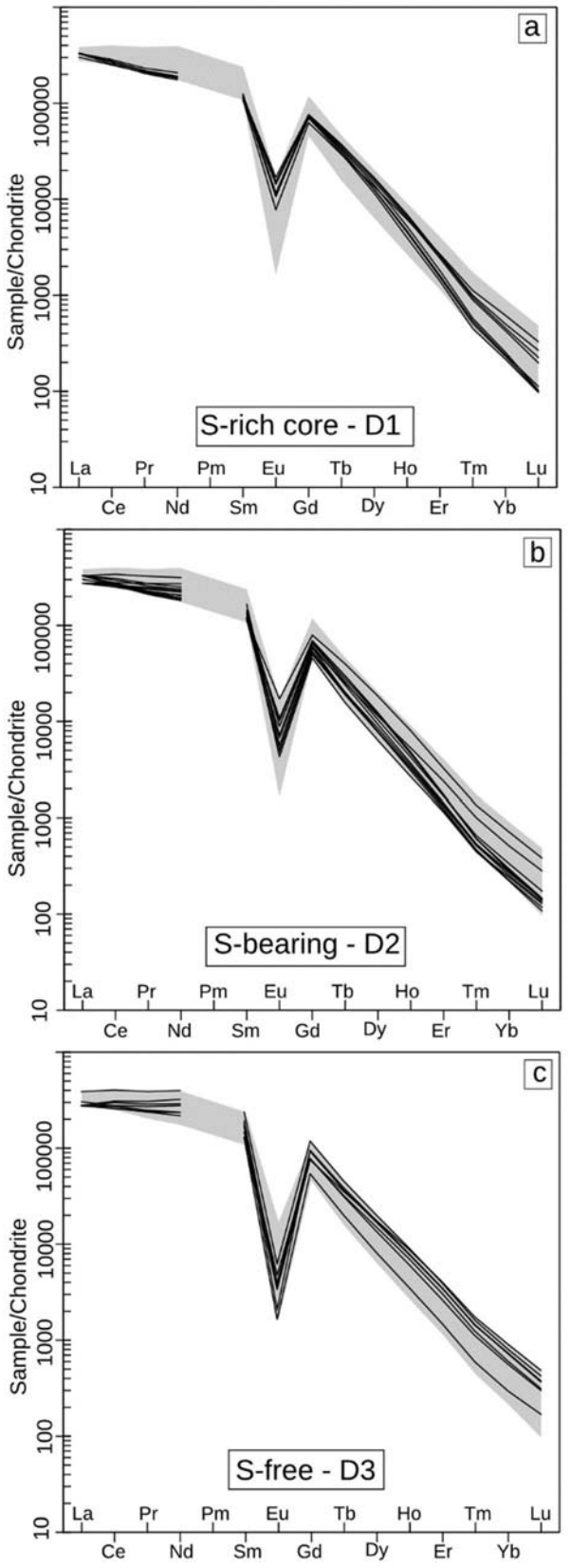

Fig. 2–8: Chondrite normalized REE pattern (Boynton 1984) for monazite D1, D2, and D3, collected by LA–ICP–MS. The grey-shaded area represents the overall variability of the dataset.

Inclusions

Sulphur-bearing domain D2 and S-free domain D3 are variably clouded with solid inclusions ranging in size from a few nanometres up to 50 µm. Inclusions in D2 and D3 are apparently similar in size and nature. Using optical and SEM + EDS characterization, the inclusions can be subdivided into monomineralic- and polymineralic-type. Monomineralic inclusions are by order of decreasing abundance: pyrrhotite, quartz, zircon, hematite and magnetite. Pyrrhotite may occur as euhedral lath-shaped crystals with preferred orientation that may correspond to the crystallographic planes of the host monazite (Fig. 3d). Polymineralic inclusions typically have an external anhedral rounded shape, with some preserving a hexagonal euhedral shape. A sub-type of polymineralic inclusions consists of Fe–(Cu) sulphides set in a Al–Si–Fe–Mg–K matrix that may contain small crystals of apatite, Th-rich phosphate, as well as Fe and Ti oxides (supplementary material 2–1). Optically clear trails of fluid inclusions (1–10 µm) crosscutting the crystal, occur along well defined planes whereas larger fluid inclusions along healed cracks enclose euhedral cubic pyrite crystals with hematite lamellae (Fig. 9a–b)

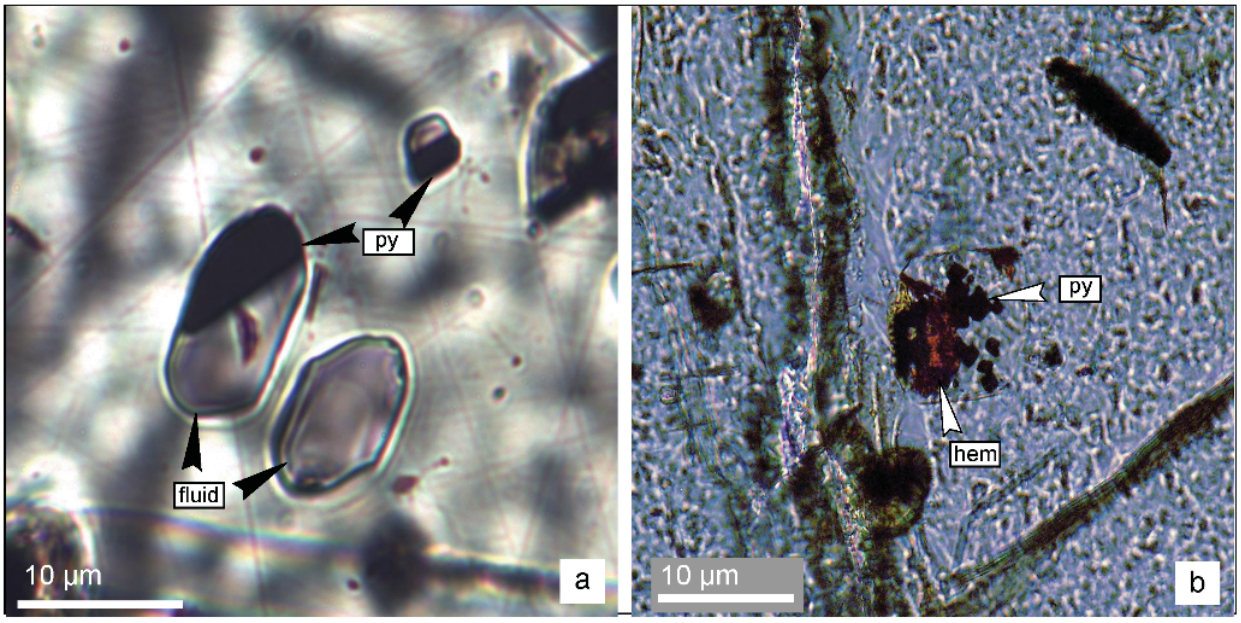

Fig. 2–9: **a–b** Transmitted light microphotograph of inclusions containing a fluid phase, pyrite (py), and hematite (hem)

Nano-characterization of monazite by TEM

Three FIB foils were cut in one large monazite crystal (1029-48) in the three compositional domains (D1, D2, D3) for detailed inspection. The foil in D1 was cut in the S-rich core that is free of inclusions. Imaging in STEM mode and dark-field (with the HAADF detector) were used to reveal density contrasts. Low magnification images (Fig. 10a) show black dots, representing a negative density contrast, homogenously distributed all over the foil, that represent a negative density contrast in monazite. These dots are 5–10 nm large with an equant shape (Fig.10b-c) and distributed in a short period modulation of ~15–25 nm. Energy dispersive spectroscopy (EDS) point or line scans acquisitions across the black dots reveal that they are enriched in Ca + S and depleted in Ce + P compared with the host monazite (Fig. 10b). Bright-field imaging (Fig. 10d) qualitatively show little or no lattice misorientation between the (Ca + S)-rich nanoclusters and the host monazite. Inspection of the foil cut in SO_2-bearing D2 (Fig. 10e) did not reveals (Ca + S)-rich nanoclusters but contains a polymineralic inclusion. Examination of this inclusion by TEM coupled with EDS mapping shows that euhedral pyrite is associated with iron oxide (hematite), apatite, and a phyllosilicate tentatively identified as celadonite (Fig. 10f). The boundary between the monazite and the phyllosilicate is irregular. The foil from the SO_2-free D3 is homogenous, i.e. devoid of (Ca + S)-rich nanoclusters and other inclusions. Only some porosity is observable (not shown).

U–Th–Pb geochronology

U–Pb isotopic dating

Uranium–Pb LA–ICP–MS isotopic data for the three compositional domains (D1–D3) are presented in Tera-Wasserburg concordia diagrams and are color-coded with their SO_2 content, measured by EPMA prior to laser ablation (Fig. 11; Tab. 3). Additionally, analyses in the inclusion-rich parts of the grains are plotted separately, with D2a and D3a corresponding to the inclusion-rich part of D2 and D3, respectively. All together, analyses of monazite plot along the concordia curve quasi continuously from *c*. 1040 Ma down to 920 Ma (Fig. 11a). The three compositional domains (D1–D3), nevertheless yields consistent pooled ages in line with their contrasting SO_2 content. Domain 1, representing S-rich cores, yields a concordia age of 1034 ± 6 Ma (2σ; 10 analyses; Fig. 11b). The inclusion-free D2 yields a significantly younger concordia age of 1005 ± 7 Ma (2σ; 17 analyses; Fig. 11c), excluding one discordant analysis, which has an equivalent $^{207}Pb/^{206}Pb$ age of 995 ± 27 Ma ($^{206}Pb/^{238}U$ age = 931 ± 30 Ma). The S-free D3 defines a concordia age of 935 ± 7 Ma (2σ; 11 analyses; Fig. 11d). Inclusion-bearing D2a and D3a show

scattered age distributions that partly overlap with each other, although they are easily distinguished by their contrasting SO_2 content. The age scattering and the Pb excess of some analyses in each group are interpreted to originate from the sulphide inclusions that have inevitably been sampled. For D2a, a regression, anchored towards a common Pb composition following the model of Stacey and Kramers (1975) at 1 Ga, yields a lower intercept age of 1000 ± 15 Ma (MSWD = 2.1; Fig. 11e). The D3a analyses, regressed in the same way, result in a lower intercept at 937 ± 10 Ma (Fig. 11f). These lower intercept ages for D2a and D3a are equivalent, within the error, with the concordia age calculated for inclusion-free D2 and D3 domains, respectively. Monazite from D1 and D2 displays a $^{208}Pb/^{232}Th$ age scattering between *c*. 1035 and 930 Ma and reverse discordance.

U–Th–Pb EPMA dating

Uranium–Th–Pb EPMA data are presented in a weighted histogram (Fig. 12; Tab. 4; Montel 1996), respecting the three chemical groups, D1, D2, and D3. Domain 1 analyses (S-rich cores) yield a statistical age of 1028 ± 8 Ma (48 analyses) in excellent agreement with the U–Pb isotopic age. Domain 2 analyses (S-bearing domains) define a statistical age of 998 ± 6 Ma (31 analyses) that is equivalent within the error range to the U–Pb isotopic age. The S-free D3 domain shows a more scattered age distribution, but yields a single population with an age of 952 ± 7 Ma (41 analyses). If all the analyses are considered together, i.e. without chemical grouping, the statistical treatment of Montel et al. (1996) demonstrates that the data are likely to come from three populations with ages of 1035 ± 8 Ma, 991 ± 6 Ma, and 945 ± 6 Ma that are in good agreement with the ages of D1, D2 and D3 as described above. When comparing the U–Pb isotopic data and the EPMA data, the two assumptions made when utilizing EPMA dating method should be kept in mind: (1) insignificant common Pb is incorporated at the time of crystallization and (2) no isotopic disturbance occurred since the formation of the monazite, i.e. concordance cannot be evaluated. In addition, the spatial resolution of the EPMA (interaction volume of c. 1.8 μm^3) is nearly three orders of magnitude better than that of the LA–ICP–MS method (c. 1350 μm^3), which is critical in dating replacement process that may result in micro-domains < 10 μm (Fig. 4; Grand'homme et al., 2016).

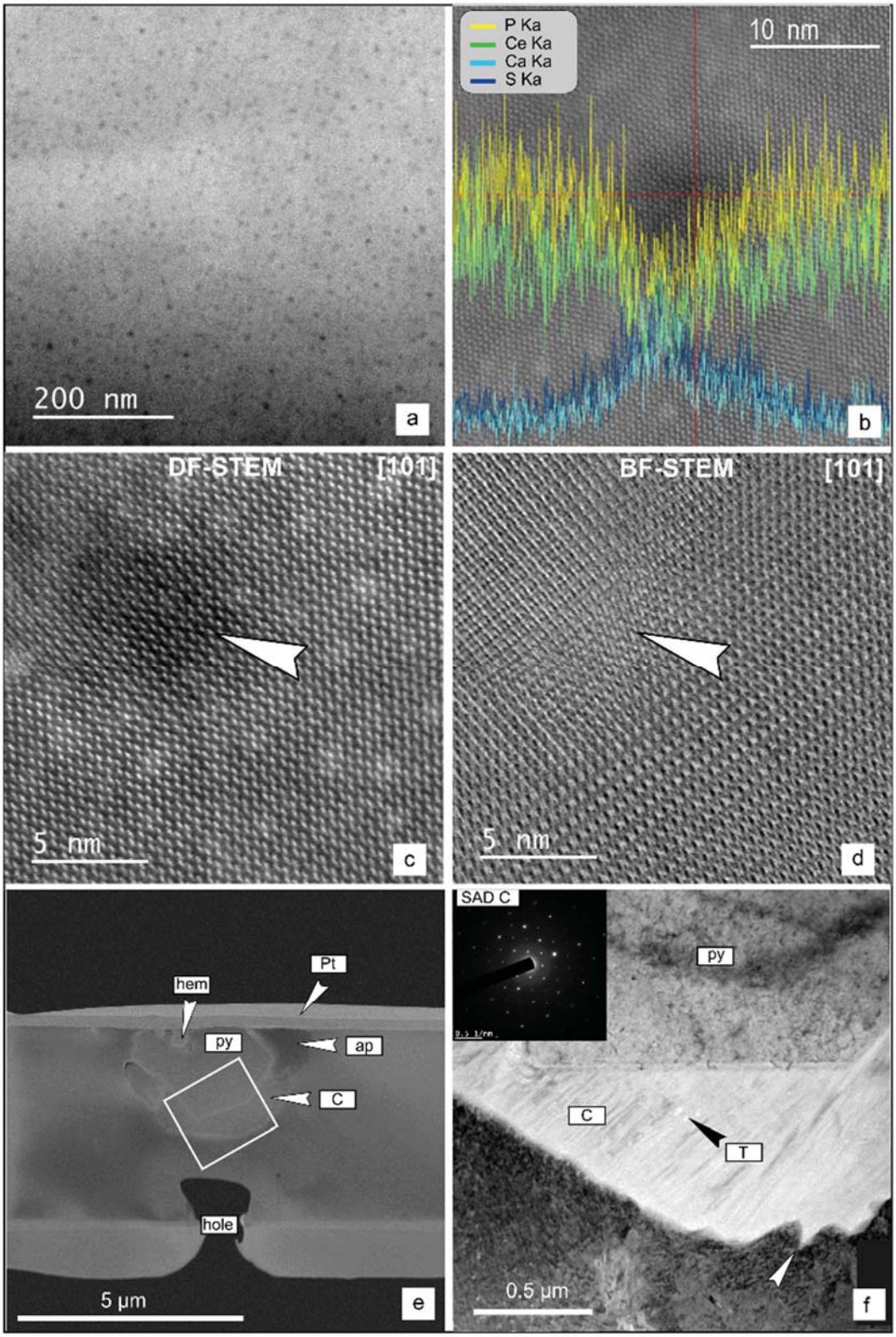

Fig. 2–10: Images and chemical profile of the FIB foil cut in S-rich monazite core D1 (a–d) and in the S-bearing D2 monazite (e–f). **a**– STEM dark field (DF) image (HAADF) at low magnification. Note the black dots corresponding to negative density contrasts. **b**– EDS profile across a CaSO4-rich nanocluster. **c–d** High-resolution STEM-DF (c) and bright field (d) in an image along the [101] axis. The white arrows point to a CaSO4 nanocluster. Bright spots on panel (c) correspond to Ga implantation during sample preparation. **e**– SEM image of the FIB foil from D2 containing a polymineralic inclusion. The white rectangle shows the area of panel (f). **f**– TEM bright field image of a part of the inclusion containing euhedral pyrite (py), iron oxide (hem), apatite (ap), phyllosilicate (C), and Th-silicate (T). The inset corresponds to Selective Area Electron Diffraction (SAED) in phyllosilicate (C)

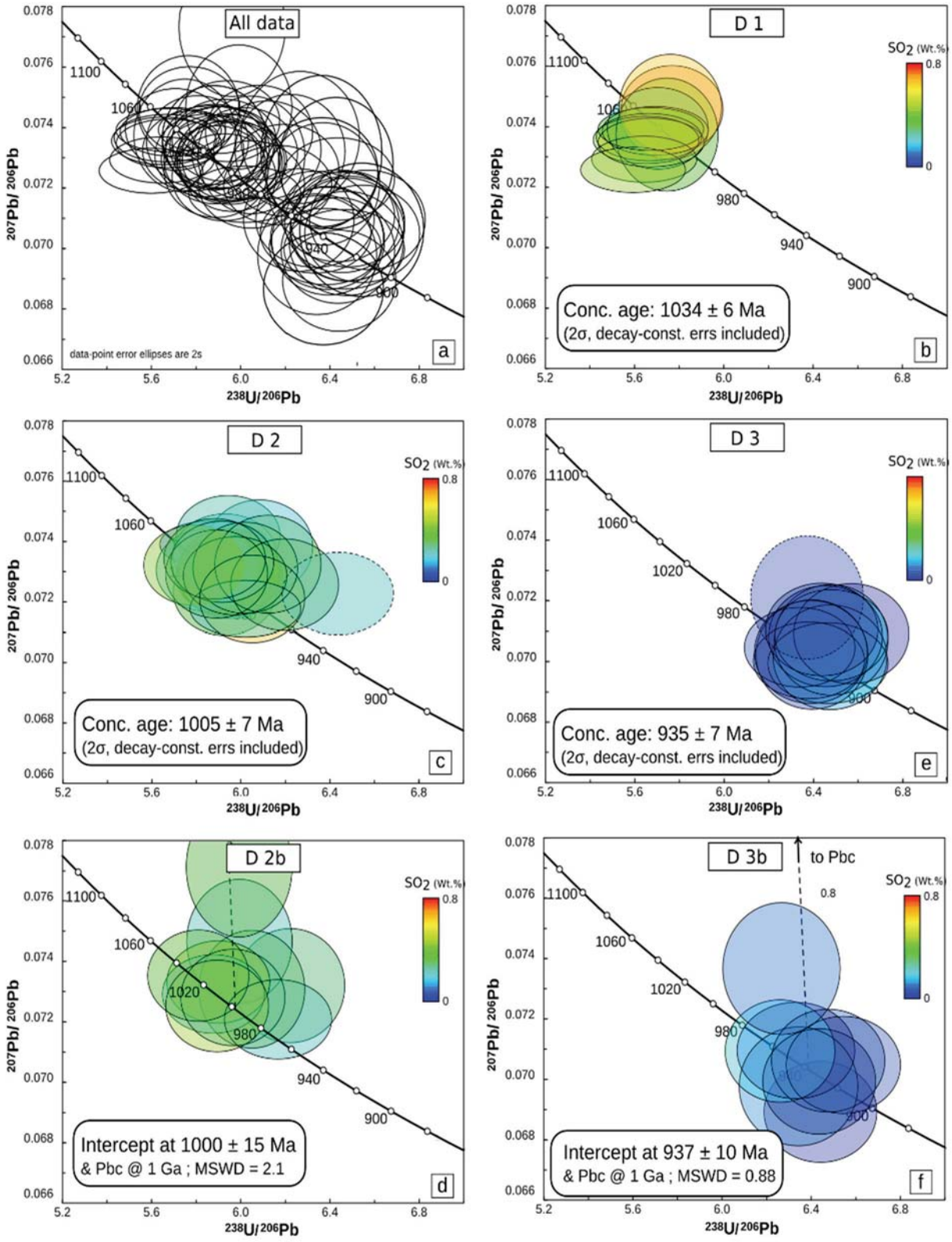

Fig. 2–11: U–Pb data of monazite D1, D2 and D3 collected by LA–ICP–MS in Tera-Wasserburg concordia diagrams. **a**– All analyses. **b–f** Analyses are plotted separately for domains D1, D2, and D3, with colour coding corresponding to the S concentration measured by EPMA prior to laser ablation. **b**– S-rich monazite core (D1). **c**– S-bearing domain without inclusions (D2). **d**– S-free domain free of inclusions (D3). **e**– S-bearing domain with inclusions (D2a). **f**– S-free domain with inclusions (D3a). All error ellipses are 2σ. Decay constant errors are included in the pooled ages.

Discussion

Mechanism of S incorporation in monazite

Investigation of spatial distribution of S and Ca in monazite (Fig. 4) complemented by EPMA point analyses in S-bearing domains D1 and D2 (Fig. 6) indicate that S is accommodated as sulphate through the anhydrite substitution mechanism $Ca^{2+} + S^{6+} = REE^{3+} + P^{5+}$. This substitution vector has been already proposed by Kukharenko et al. (1961) and later confirmed by several workers on the basis of EPMA analyses (Chakhmouradian and Mitchell 1999; Ondrejka et al. 2007; Krenn et al. 2011). Because Sr is only present at the trace level, the Sr–Ca substitution in the anhydrite component is negligible. High-resolution TEM investigations reveal 5–10 nm nanoclusters composed of $CaSO_4$ with a coherent interface relative to the host monazite (in D1; Fig. 10c-d). In a theoretical perspective, the presence of clino-anhydrite in monazite is not surprising as $CaSO_4$ crystallizes in the monazite-type structure ($P2_{1/n}$) at high pressure (> 2 GPa ; Crichton 2005; Ma et al. 2007; Bradbury and Williams 2009). Moreover, size wise, $[SO_4]^{2-}$ and $[ClO_4]^-$ closely resemble $[PO_4]^{3-}$, and Ca^{2+} is the cation closest to Ce^{3+} (Shannon 1976). Two contrasting interpretations of such nanoclusters may be proposed. The first one involves the presence of primary heterogeneities incorporated during the crystallization of monazite. Such nanoclusters heterogeneities (*c.* 5–50 nm) are frequently observed during mineral synthesis when annealing duration is too short (e.g. in Ca–Pb fluoro-vanadinite apatites, Dong and White 2004), and reflect disequilibrium conditions and/or heterogeneous crystalizing medium. The second possibility is the presence of exsolution of nanophases (here $CaSO_4$) due to homogeneous nucleation. Indeed, the regularity in shape, the short period modulation (~ 15–25 nm; Fig. 10a) of the $CaSO_4$ nanoclusters, together with a coherent interface, rather point to exsolution by homogeneous nucleation. Such phase separation is documented for instance in apatite where nanoclusters (5–10 nm) of ellestadite (S-rich apatite) developed in short period modulation (Ferraris et al. 2005). The second mechanism is the preferred one for our monazite sample and implies the possible existence of a miscibility gap. Experimental data could bring useful geothermometric tools to unravel any temperature or pressure dependence on the incorporation of clino-anhydrite in monazite. With this respect, the absence of clino-anhydrite nanoclusters in the S-bearing D2 monazite investigated by TEM (SO_2 ~ 1500 ppm) may be interpreted as a solubility limit.

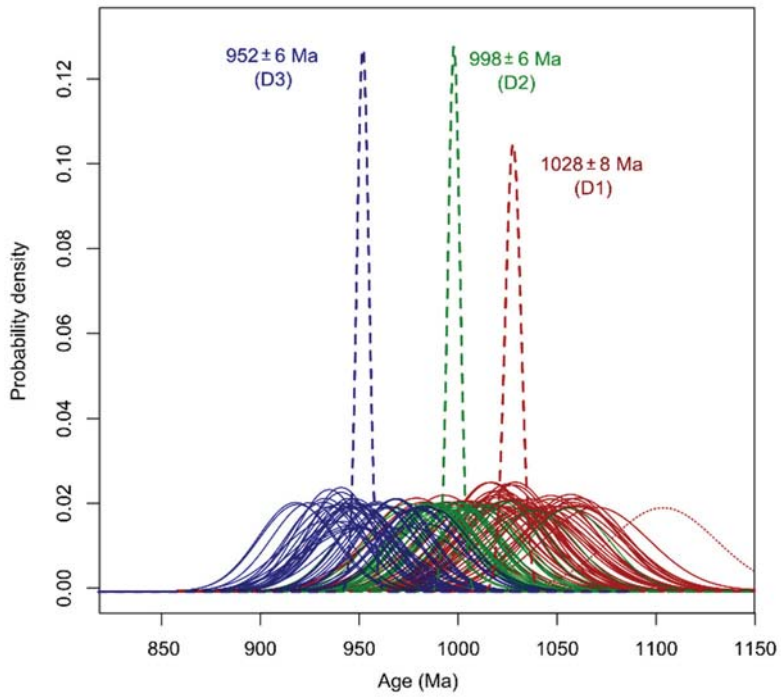

Fig. 2–12: Weighted-histogram representation of monazite EPMA U–Th–Pb data generated with the NiLeDam R-package (see text). The small bell-shaped curve represents the probability density function of one measurement. The tick dotted curve represents the ages calculated for the three domains: D1 in red, D2 in green, and D3 in blue

Significance of S-rich monazite

Within the S-rich monazite core (D1), U and Th are mainly accommodated through the cheralite substitution, while radiogenic lead (Pb*) is considered to be in an interstitial position. The phase separation of clino-anhydrite from monazite did not lead to obvious U, Th, or Pb mobility as no U–Th–Pb-rich nanoclusters were detected in STEM-DF (e.g. Seydoux-Guillaume et al. 2003). This is consistent with the concordant behaviour of the $^{235}U/^{207}Pb$ and $^{238}U/^{206}Pb$ isotopic systems as well as with the perfect match of U–Th–Pb EPMA ages and U–Pb isotopic ages. The U–Pb concordia age of 1034 ± 6 Ma (Fig. 11b) is thus interpreted to record the crystallization of S-rich core D1. On the regional scale, monazite crystallization is coeval with migmatization recorded in metapelite by oscillatory zoned zircon (Möller et al. 2002; Tomkins et al. 2005). On the sample scale, this event is responsible for the formation of garnet relicts (garnet I) enclosing sillimanite, biotite, K-feldspar, quartz, ilmenite, and magnetite, in line with a variable Y and HREE content relating to the frequent occurrence of S-rich D1 monazite within garnet porphyroblasts (Tab. 1). The latter silicate–oxide metamorphic assemblage points to fluid-absent biotite dehydration melting (Clemens and Vielzeuf 1987).

The enrichment of the metamorphic medium in S may be explained by two sulphide breakdown mechanisms operating in the range 650-800 °C: (1) the conversion of pyrite to pyrrhotite in order to maintain the pyrite + pyrrhotite + magnetite equilibrium with increasing temperature (Fig. 13), and/or (2) the partial melting of sulphide minerals in the presence of galena

or arsenopyrite (Tomkins et al. 2007). Dissolution of sulphides in the silicate melt is limited by sulphide/sulphate or Fe–O–S liquid saturation (Métrich and Mandeville 2010). Estimates of S solubility in a rhyolitic melt at pyrrhotite saturation (H_2O = 0.5 to 5 wt%) is rather low, i.e. in the range 10–250 ppm S at 800 °C and 0.5 GPa (Clemente et al. 2004; Liu et al. 2007; Baker and Moretti 2011). However, there is a marked increase (× 2–10) in S solubility from a sulphide (S^{2-})-dominated to a sulphate (S^{6+})-dominated silicate melt between QFM and QFM +2 (Wilke et al. 2011).

Because monazite incorporates S as sulphate, it can only incorporate S when it crystallizes from a silicate melt in which S is present as S^{6+}. These oxidation conditions are met when considering a pyrite-rich rock evolving along the pyrite–pyrrhotite–magnetite buffer, i.e. according to mechanism (1) above (Fig. 13). Moreover, monazite is also expected to partly dissolve in (i.e. saturate) the melt fraction of a metapelitic migmatite at 800 °C and 0.5 GPa (Kelsey et al. 2008; Stepanov et al. 2012). We conclude that S-rich monazite cores D1 in our sample likely crystalized from an oxidized, sulphate dominated granitic melt during fluid-absent partial melting at granulite facies. The enrichment of the silicate melt in S reflects the conversion of pyrite to pyrrhotite, and eventually Fe–Cu–As–(Pb) sulphide melting, collectively referred to as high-T sulphide breakdown.

Metasomatic replacement of S-rich monazite

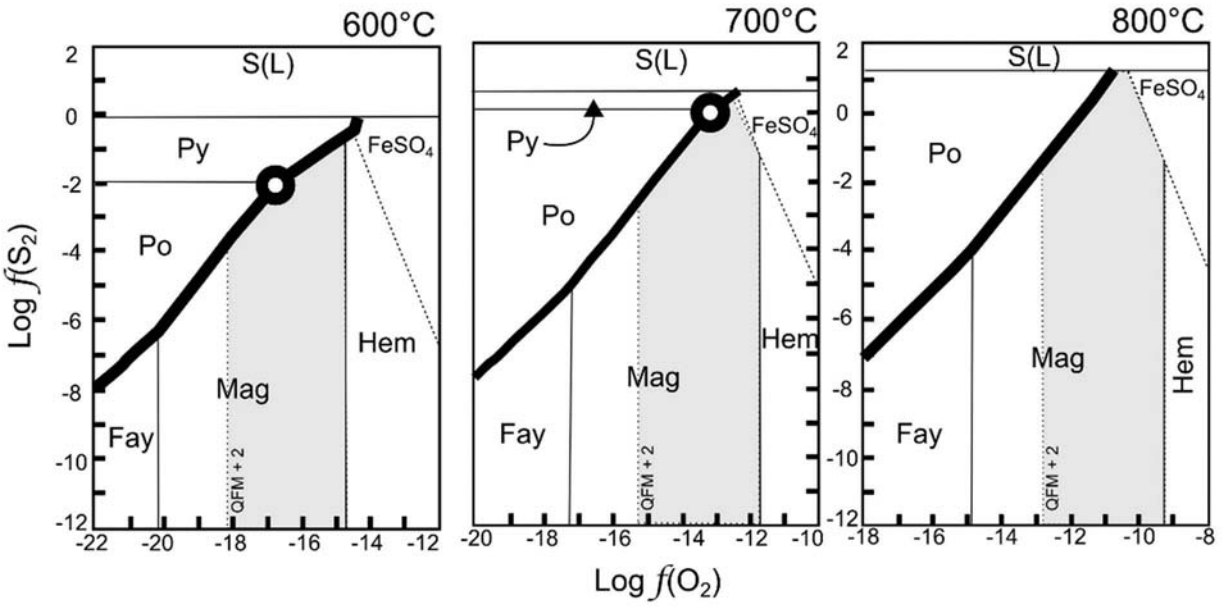

Fig. 2–13: Isothermal phase diagrams (600, 700, and 800 °C) in the Fe–O–S–Si chemical system modified after Whitney (1984). The grey shaded area between QFM + 2 and the hematite–magnetite oxygen buffer highlights the area where sulphate is dominant in the silicate melt (see text)

The S-bearing D2 preserves textural evidence for fluid assisted dissolution–precipitation including (1) sharp interfaces, (2) the presence of porosity and (3) numerous mineral inclusions filling in the pores (Putnis 2009). Domain 2 is thus interpreted as a replacement product of D1. Preservation of variable S concentrations in D2 reflects variable removal of the anhydrite component during replacement. This may be explained by fluid saturation along the dissolution–precipitation interface and/or by a continuum in redox conditions between c. 1035 and 1005 Ma. A single age of replacement may be proposed for D2 at 1005 ± 7 Ma (Fig. 11c; Fig. 12). The replacement process is associated with a variable signature in Y and REE, and therefore cannot be linked conclusively with reactions involving garnet in the metamorphic assemblage.

Both monomineralic and polymineralic inclusions are interpreted to be the result of *in-situ* precipitation, because they are not found in any other co-existing major mineral. The S necessary for sulphide precipitation may be directly derived from the $CaSO_4$ component removed from D1 domains. The composition of the inclusions additionally suggests that the metasomatic fluid was enriched in Si, Fe, Zr, and K as these elements are absent in monazite. The presence of pyrite + hematite and a phyllosilicate points (Fig. 10f) to equilibration temperatures below 500 °C, hydrous conditions, and a high oxygen fugacity. It is unlikely that these assemblages reflect the *P–T* conditions of their entrapment, as phyllosilicates would not have been stable during UHT metamorphism at *c*. 930 Ma. We propose that low-T phases are the result of a late recrystallization after total amorphisation of the initial ferromagnesian minerals (orthopyroxene or biotite for instance) caused by radiation damage related to decay of ^{235}U, ^{238}U, and ^{232}Th in the monazite (Seydoux-Guillaume et al. 2009).

The S-free D3 replaces D2, and in places D1, with subordinate Th-rich (> 7 wt% ThO_2) overgrowth. The composition of D3 differs drastically from D1 and D2 with enrichment in Si + HREE, increase of the Nd/La ratio, and a very pronounced negative Eu anomaly. These compositional changes are accommodated by switching from a dominant cheralite to a huttonite substitution (Fig. 7). The latter substitution mechanism affects both the tetrahedral and octahedral sites resulting in an efficient recrystallization of the P–O–(Si)–(S) framework, leading to complete redistribution of Th and U, and the removal of interstitial Pb.

The isotopic age of 935 ± 5 Ma (Fig. 11d) is interpreted to reflect garnet breakdown in the presence of a (Si-rich) silicate melt in response to the intrusion of the AMC complex at 931 ± 2 Ma. The deepening of the Eu anomaly together with the decrease of the cheralite mole fraction in monazite through time may be interpreted to reflect plagioclase co-crystallization (Dumond et al. 2015), but it is worth noting that Eu^{2+}/Eu^{3+} is also sensitive to $f(O_2)$ (Wilke and Behrens 1999). The U–Th–Pb EPMA ages for the S-free D3 yield a pooled age of 952 ± 6 Ma, slightly older that

the isotopic age. This difference may be tentatively explained by differential mobility of Y, U, Pb and Th resulting in "discordant" ages that cannot be resolved.

Lobate reaction fronts and worm-like zoning (Fig. 4) testify that the dissolution–reprecipitation mechanism is efficient even in the most anhydrous osumilite-bearing samples. This study confirms experimental evidence that dissolution–precipitation is not restricted to H_2O saturated rocks and may operate at even very low H_2O activities (Milke et al. 2013).

Dating S mobility in metamorphic belts

Occurrences of S-bearing monazite reported in the literature are commonly associated with carbonatite (Kukharenko et al. 1961; Chakhmouradian and Mitchell 1999; Cressey et al. 1999; Bulakh et al. 2000) or with mineral deposits in low-grade metamorphic rocks typically containing sulphide + magnetite ± sulphate (Prsek et al. 2010; Krenn et al. 2011). Alternatively, S-bearing monazite with a SO_2 content ranging from a few ppm up to ~ 1.8 wt% SO_2 is also known in some high-temperature metamorphic rocks (e.g. Jercinovic & Williams 2005; Suzuki and Kato 2008; this study). Sulphur-bearing monazite therefore occurs in a variety of rocks with contrasting *P–T*

conditions of equilibration. The common feature between these occurrences is the oxidizing conditions at the time of monazite formation. Indeed, S-bearing monazite is expected to crystallize only from geological fluids in which S is present as S^{6+}.

During prograde metamorphism, hydrous minerals (e.g. chlorite) break down and release H_2O that will tend to dilute S-bearing component (SO_2 and H_2S) in the fluid. To maintain S activity pyrite breaks down to pyrrhotite, liberating one mole of S for each mole of Fe through the ideal reaction $FeS_2 = FeS + ½\ S_2$. Nevertheless, S is only liberated in significant proportion as H_2S when the fluid is at equilibrium with low $f(O_2)$ graphite-bearing rocks (Tomkins 2010). It is thus unlikely that S-bearing monazite records desulphidation of graphite-bearing rocks since sulphate species are absent in this case. Rather, monazite will record the circulation of externally-derived oxidized hydrothermal fluids that are responsible for the deposition or remobilization of ore-minerals (e. g. Schandl and Gorton 2004; Mcfarlane 2006; Rasmussen et al. 2007; Muhling et al. 2012). Indeed, it has been experimentally shown that fluid with high concentration of "strong" acid anions like $(SO_4)^{2-}$ will promote monazite dissolution (Hetherington et al. 2010). Measuring the S content in monazite, associated with ore-deposits, may help to fingerprint specific chemical domains or generations that grew during deposition and thus, constrain the age of ore deposition.

During fluid-absent melting in high-grade rocks, most of the volatile components (O–H–Cl–F–S) would be expected to dissolve into the silicate melt (review by Baker and Alletti 2012). Sulphur dissolves in silicate melt as two main species, S^{2-} and S^{6+}, with the sulphate species being dominant in rhyolite/andesitic melt two log units above the QFM buffer (Wilke et al. 2011). These

redox conditions are typically in the range of those recorded by high-grade metamorphic rocks (Harlov 1992, 2000; Harlov et al. 1997, 2005; Diener and Powell 2010; Boger et al. 2012), providing a favourable medium for S-rich monazite crystallization. However, the presence of even a minor CO_2 content (> 1 wt%) in equilibrium with a granitic melt at 800 °C and 0.8 GPa will favour the existence of a separate fluid phase (C–O–H–S–Cl–F) into which the most volatile component would partition (Webster and Botcharnikov 2011; Baker and Alletti 2012). Experimental data on fluid-saturated haplogranitic melts indicate solubility of up to 0.12 wt% S in the silicate melt along with a concentration of ~ 6 wt% S in the coexisting C–O–H–S fluid at 900°C and 0.2 GPa (Keppler 1999; Keppler 2010; Webster et al. 2011). The mechanism behind S enrichment in a fluid-saturated rock should not be different from those in a rock experiencing biotite dehydration melting, but the consequences in term of mineralization potential is important (Simon and Ripley 2011). As a consequence, S-rich monazite (D1) records the mobilization of S from a solid to a dissolved state and from a reduced (S^{2-}) to an oxidized (S^{6+}) state. As exemplified in this study, caution is however necessary because a second generation of monazite (D2) may partially inherit the S from the first generation of monazite (D1). At least in the example presented here, the presence of sulphide inclusions may be taken as evidence of fluid-assisted replacement of an initially S-rich monazite.

Finally, it is worth noting that the transition from S-bearing monazite with a U-Pb age in the range of 1035-980 Ma to S-free monazite with concordant U-Pb ages younger than c. 960 Ma coincides with molybdenite precipitation in the granulite domain dated by the Re-Os method at 973 ± 4 Ma (Bingen and Stein 2003). Consequently, we suggest that dating of S-rich monazite may also provide direct insight into the oxidation state, the mineral assemblages, and the fluids present in ancient metamorphic belts.

Conclusion

The S content of monazite can be used to record the timing of the mobilization of S from a solid to dissolved and from a reduced (S^{2-}) to an oxidized (S^{6+}) state in high-grade metamorphic rocks. Indeed, chemical and nanostructural data on monazite crystals document that S is accommodated as sulphate through the clino-anhydrite substitution mechanism $Ca^{2+} + S^{6+} = REE^{3+} + P^{5+}$. Sulphate-bearing monazite is thus expected to crystallize only from geological fluids or melts in which S is present as S^{6+}. In this sample, monazite U–Th–Pb ages measured both by LA–ICP–MS (isotopic dating) and EPMA (total-Pb dating) show a remarkable correlation with the sulfate content of the monazite domain, implying that it is possible to precisely date S (re-)incorporation in monazite. From the petrological context we propose that S-rich monazite cores

(D1) crystallized at 1034 ± 6 Ma from an oxidized, sulphate dominated granitic melt during fluid-absent partial melting. The enrichment of the silicate melt in S is interpreted to reflect pyrite conversion to pyrrhotite and eventually Fe–Cu–As–(Pb) sulphide melting. The occurrence of secondary S-bearing domains (D2) clouded with solid inclusions results from a dissolution–precipitation event dated at 1005 ± 7 Ma. Finally, D3 monazite domains that crystalized after *c*. 950 Ma and give a pooled age of 935 ± 6 Ma are sulphate-free. This implies a change in fluid redox conditions that may be interpreted as a distinct metamorphic event. This property can be further used to investigate the mineralization potential of a given geological event within a larger orogenic framework.

Acknowledgement

We thank Ph. De Parseval and S. Gouy for their technical assistance with the microprobe and J.M. Montel for synthesizing the Pb-free (REE)PO_4 crystals used in this study. This work was supported by the CNRS NEEDS program and a PHC Aurora grant (Ministry of Foreign Affairs, Norway and France). The access to the FIB facility was possible thanks to the French RENATECH network. D. Harlov and M. Williams are thanked for constructive review.

References

Ancey M, Bastenaire F, Tixier R (1977) Statistical control and optimization of X-ray intensity measurements. J Phys Appl Phys 10:817.

Aseri AA, Linnen RL, Dong Che X, Thibault Y, Holtz F (2015) Effects of fluorine on the solubilities of Nb, Ta, Zr and Hf minerals in highly fluxed water-saturated haplogranitic melts. Ore Geol Rev 64:736–746.

Baker DR, Alletti M (2012) Fluid saturation and volatile partitioning between melts and hydrous fluids in crustal magmatic systems: The contribution of experimental measurements and solubility models. Earth-Sci Rev 114:298–324.

Baker DR, Moretti R (2011) Modeling the Solubility of Sulfur in Magmas: A 50-Year Old Geochemical Challenge. Rev Mineral Geochem 73:167–213.

Bingen B, Davis WJ, Hamilton MA, Engvik AK, Stein HJ, Skar O, Nordgulen O (2008a) Geochronology of high-grade metamorphism in the Sveconorwegian belt, S. Norway: U–Pb, Th–Pb and Re–Os data. Norw J Geol 88:13–42.

Bingen B, Demaiffe D, Hertogen J (1990) Evolution of feldspars at the amphibolite-granulite-facies transition in augen gneisses (SW Norway): geochemistry and Sr isotopes. Contrib Mineral Petrol 105:275–288.

Bingen B, Nordgulen O, Viola G (2008b) A four-phase model for the Sveconorwegian orogeny, SW Scandinavia. Norw J Geol 88:43–72.

Bingen B, Stein H (2003) Molybdenite Re–Os dating of biotite dehydration melting in the Rogaland high-temperature granulites, S Norway. Earth Planet Sci Lett 208:181–195.

Bingen B, Van Breemen O (1998) U-Pb monazite ages in amphibolite- to granulite-facies orthogneiss reflect hydrous mineral breakdown reactions: Sveconorwegian Province of SW Norway. Contrib Mineral Petrol 132:336–353.

Boger SD, White RW, Schulte B (2012) The importance of iron speciation (Fe^{2+} /Fe^{3+}) in determining mineral assemblages: an example from the high-grade aluminous metapelites of southeastern Madagascar. J Metamorph Geol 30:997–1018.

Boynton W (1984) Cosmochemistry of the rare earth elements: meteorite studies. In: Henderson P (ed) Rare Earth Element Geochemistry. Elsevier, Amsterdam, pp 63–114

Bradbury SE, Williams Q (2009) X-ray diffraction and infrared spectroscopy of monazite-structured $CaSO_4$ at high pressures: Implications for shocked anhydrite. J Phys Chem Solids 70:134–141.

Budzyn B, Harlov DE, Williams ML, Jercinovic MJ (2011) Experimental determination of stability relations between monazite, fluorapatite, allanite, and REE-epidote as a function of pressure, temperature, and fluid composition. Am Mineral 96:1547–1567.

Bulakh AG, Nesterov AR, Zaitsev AN, Pilipiuk AN, Wall F, Kirillov AS (2000) Monazite-(Ce) from late-stage mineral assemblage at the Kandaguba and Vuoriyarvi carbonatite complexes, Kola peninsula, Russia. Neues Jahrb Mineral Monathefte 217–233.

Chakhmouradian AR, Mitchell RH (1999) Niobian ilmenite, hydroxylapatite and sulfatian monazite: alternative hosts for incompatible elements in calcite kimberlite from Internatsional'naya, Yakutia. Can Mineral 37:1177–1189.

Clemens JD, Vielzeuf D (1987) Constraints on melting and magma production in the crust. Earth Planet Sci Lett 86:287–306.

Clemente B, Scaillet B, Pichavant M (2004) The Solubility of Sulphur in Hydrous Rhyolitic Melts. J Petrol 45:2171–2196.

Coint N, Slagstad T, Roberts NMW, Marker M, Røhr T, Sørensen BE (2015) The Late Mesoproterozoic Sirdal Magmatic Belt, SW Norway: Relationships between magmatism and metamorphism and implications for Sveconorwegian orogenesis. Precambrian Res 265:57–77.

Connolly JAD, Cesare B (1993) C-O-H-S fluid composition and oxygen fugacity in graphictic metapelites. J Metamorph Geol 11:379–388.

Corfu F (1988) Differential response of U–Pb systems in coexisting accessory minerals, Winnipeg River Subprovince, Canadian Shield: implications for Archean crustal growth and stabilization. Contrib Mineral Petrol 98:312–325.

Cressey G, Wall F, Cressey BA (1999) Differential REE uptake by sector growth of monazite. Mineral Mag 63:813–813.

Crichton WA (2005) Evidence for monazite-, barite-, and AgMnO4 (distorted barite)-type structures of $CaSO_4$ at high pressure and temperature. Am Mineral 90:22–27.

Das K, Dasgupta S, Miura H (2001) Stability of osumilite coexisting with spinel solid solution in metapelitic granulites at high oxygen fugacity. Am Mineral 86:1423–1434.

Didier A, Bosse V, Bouloton J, Mostefaoui S, Viala M, Paquette JL, Devidal JL, Duhamel R (2015) NanoSIMS mapping and LA–ICP–MS chemical and U–Th–Pb data in monazite from a xenolith enclosed in andesite (Central Slovakia Volcanic Field). Contrib Mineral Petrol. doi: 10.1007/s00410-015-1200-1

Didier A, Bosse V, Boulvais P, Bouloton J, Paquette J-L, Montel J-M, Devidal J-L (2013) Disturbance versus preservation of U–Th–Pb ages in monazite during fluid–rock interaction: textural, chemical and isotopic in situ study in microgranites (Velay Dome, France). Contrib Mineral Petrol 165:1051–1072.

Diener JFA, Powell R (2010) Influence of ferric iron on the stability of mineral assemblages. J Metamorph Geol 28:599–613.

Dong Z, White TJ (2004) Calcium–lead fluoro-vanadinite apatites. I. Disequilibrium structures. Acta Crystallogr B 60:138–145.

Drüppel K, Elsasser L, Brandt S, Gerdes A (2013) Sveconorwegian Mid-crustal Ultrahigh-temperature Metamorphism in Rogaland, Norway: U–Pb LA–ICP–MS Geochronology and Pseudosections of Sapphirine Granulites and Associated Paragneisses. J Petrol 54:305–350.

Dumond G, Goncalves P, Williams ML, Jercinovic MJ (2015) Monazite as a monitor of melting, garnet growth, and feldspar recrystallization in continental lower crust. J Metamorph Geol. doi: 10.1111/jmg.12150

Engvik AK, Mezger K, Wortelkamp S, Bast R, Corfu F, Korneliussen A, Ihlen P, Bingen B, Austrheim H (2011) Metasomatism of gabbro - mineral replacement and element mobilization during the Sveconorwegian metamorphic event J Metamorph Geol 29:399–423.

Evans KA, Powell R, Holland TJB (2010) Internally consistent data for sulphur-bearing phases and application to the construction of pseudosections for mafic greenschist facies rocks in Na_2O–CaO–K_2O–FeO–MgO–Al_2O_3–SiO_2–CO_2–O–S–H_2O. J Metamorph Geol 28:667–687.

Falkum T (1982) Geologisk kart over Norge, berggrunnskart Mandal, 1:250000, Norges Geologiske Undersøkelse, Trondheim.

Ferraris C, White TJ, Plévert J, Wegner R (2005) Nanometric modulation in apatite. Phys Chem Miner 32:485–492.

Finger F, Krenn E (2007) Three metamorphic monazite generations in a high-pressure rock from the Bohemian Massif and the potentially important role of apatite in stimulating polyphase monazite growth along a PT loop. Lithos 95:103–115.

Fleet ME (2006) Phase Equilibria at High Temperatures. Rev Mineral Geochem 61:365–419.

Fletcher IR, McNaughton NJ, Davis WJ, Rasmussen B (2010) Matrix effects and calibration limitations in ion probe U–Pb and Th–Pb dating of monazite. Chem Geol 270:31–44.

Gasquet D, Bertrand J-M, Paquette J-L, Lehmann J, Ratzov G, De Ascenção Guedes R, Tiepolo M, Boullier A-M, Scaillet S, Nomade S (2010) Miocene to Messinian deformation and hydrothermal activity in a pre-Alpine basement massif of the French western Alps: new U-Th-Pb and argon ages from the Lauzière massif. Bull Soc Geol Fr 181:227–241.

Gnos E, Janots E, Berger A, Whitehouse M, Walter F, Pettke T, Bergemann C (2015) Age of cleft monazites in the eastern Tauern Window: constraints on crystallization conditions of hydrothermal monazite. Swiss J Geosci 108:55–74.

Grand'homme A, Janots E, Seydoux-Guillaume A-M, Guillaume D, Bosse V, and Magnin V (2016) Partial resetting of the U–Th–Pb systems in experimentally altered monazite: nano-scale evidence of incomplete replacement. Geology 44:431–434.

Harlov DE (1992) Comparative oxygen barometry in granulites, Bamble Sector, SE Norway. J Geology 100:447–464.

Harlov DE, Newton RC, Hansen EC, Janardhan AS (1997) Oxide and sulfide minerals in highly oxidized, Rb-depleted, Archean granulites of the Shevaroy Hills Massif, South India: oxidation states and the role of metamorphic fluids. J Metamorph Geol 15:701–717.

Harlov DE (2000) Titaniferous magnetite–ilmenite thermometry and titaniferous magnetite–ilmenite–orthopyroxene–quartz oxygen barometry in granulite facies gneisses, Bamble Sector, SE Norway: implications for the role of high-grade CO_2-rich fluids during granulite genesis. Contrib Mineral Petrol 139:180–197.

Harlov DE, Hansen EC (2005) Oxide and sulphide isograds along a Late Archean, deep-crustal profile in Tamil Nadu, south India. J Metamorph Geol 23:241–259.

Heinrich W, Andrehs G, Franz G (1997) Monazite–xenotime miscibility gap thermometry. I. An empirical calibration. J Metamorph Geol 15:3–16.

Hermans GAE., Tobi AC, Poorter RP, Maijer C (1975) The high-grade metamorphic Precambrian of the Sirdal-Ørsdal area, Rogaland/Vest-Agder, south-west Norway. Norg Geol Unders B 318:51–74.

Hetherington CJ, Harlov DE, Budzyń B (2010) Experimental metasomatism of monazite and xenotime: mineral stability, REE mobility and fluid composition. Mineral Petrol 99:165–184.

Holland TJB, Babu E, Waters DJ (1996) Phase relations of osumilite and dehydration melting in pelitic rocks: a simple thermodynamic model for the KFMASH system. Contrib Mineral Petrol 124:383–394.

Jacquemet N, Guillaume D, Zwick A, Pokrovski GS (2014) In situ Raman spectroscopy identification of the S3- ion in S-rich hydrothermal fluids from synthetic fluid inclusions. Am Mineral 99:1109–1118.

Janots E, Engi M, Berger A, Allaz J, Schwarz J-O, Spandler C (2008) Prograde metamorphic sequence of REE minerals in pelitic rocks of the Central Alps: implications for allanite–monazite–xenotime phase relations from 250 to 610 °C. J Metamorph Geol 26:509–526.

Jansen JBH, Blok RJ, Bos A, Scheelings M (1985) Geothermometry and geobarometry in Rogaland and preliminary results from the Bamble area, S Norway. In: Tobi AC &Touret JLR (eds) The deep Proterozoic crust in the North Atlantic provinces. D. Reidel, Dordrecht, pp 477–497

Jercinovic MJ (2005) Analytical perils (and progress) in electron microprobe trace element analysis applied to geochronology: Background acquisition, interferences, and beam irradiation effects. Am Mineral 90:526–546.

Kars H, Jansen JBH, Tobi AC, Poorter RP (1980) The metapelitic rocks of the polymetamorphic Precambrian of Rogaland, SW Norway. Contrib Mineral Petrol 74:235–244.

Kelly NM, Harley SL, Möller A (2012) Complexity in the behavior and recrystallization of monazite during high-T metamorphism and fluid infiltration. Chem Geol 322-323:192–208.

Kelsey DE, Clark C, Hand M (2008) Thermobarometric modelling of zircon and monazite growth in melt-bearing systems: examples using model metapelitic and metapsammitic granulites. J Metamorph Geol 26:199–212.

Keppler H (1999) Experimental evidence for the source of excess sulfur in explosive volcanic eruptions. Science 284:1652–1654.

Keppler H (2010) The distribution of sulfur between haplogranitic melts and aqueous fluids. Geochim Cosmochim Acta 74:645–660.

Kirkland CL, Erickson TM, Johnson TE, Danišík M, Evans NJ, Bourdet J, McDonald BJ (2016) Discriminating prolonged, episodic or disturbed monazite age spectra: An example from the Kalak Nappe Complex, Arctic Norway. Chem Geol 424:96–110.

Krenn E, Putz H, Finger F, Paar WH (2011) Sulfur-rich monazite with high common Pb in ore-bearing schists from the Schellgaden mining district (Tauern Window, Eastern Alps). Mineral Petrol 102:51–62.

Kukharenko AA, Bulakh AG, Balanova KA (1961) Sulfate-monazite from the Kola Peninsula carbonatites. Zap Vses Miner Obshchest 90:373–381.

Liu Y, Samaha N-T, Baker DR (2007) Sulfur concentration at sulfide saturation (SCSS) in magmatic silicate melts. Geochim Cosmochim Acta 71:1783–1799.

Ma YM, Zhou Q, He Z, Li FF, Yang KF, Cui QL, Zou GT (2007) High-pressure and high-temperature study of the phase transition in anhydrite. J Phys Condens Matter 19:425221.

Maijer C, Andriessen PAM, Hebeda EH, Jansen JBH, Verschure RH (1981) Osumilite, an approximately 970 Ma old high-temperature index mineral of the granulite-facies metamorphism in Rogaland, SW Norway. Geol Mijnbouw 60:267–272.

Maijer C, (1987) The metamorphic envelope of the Rogaland intrusive complex. In: Maijer C & Padget P (eds) The geology of southermost Norway: an excursion guide. Norges Geologiske undersokelse special publication 1, Trondheim, pp 68–72.

Mcfarlane CRM (2006) Palaeoproterozoic evolution of the Challenger Au deposit, South Australia, from monazite geochronology. J Metamorph Geol 24:75–87.

Métrich N, Mandeville CW (2010) Sulfur in Magmas. Elements 6:81–86

Migdisov A, Williams-Jones AE, Brugger J, Caporuscio FA (2016) Hydrothermal transport, deposition, and fractionation of the REE: Experimental data and thermodynamic calculations. Chem Geol 439:13–42.

Milke R, Neusser G, Kolzer K, Wunder B (2013) Very little water is necessary to make a dry solid silicate system wet. Geology 41:247–250.

Möller A, O'brien PJ, Kennedy A, Kröner A (2002) Polyphase zircon in ultrahigh-temperature granulites (Rogaland, SW Norway): constraints for Pb diffusion in zircon. J Metamorph Geol 20:727–740.

Möller A, O'Brien PJ, Kennedy A, Kröner A (2003) Linking growth episodes of zircon and metamorphic textures to zircon chemistry: an example from the ultrahigh-temperature granulites of Rogaland (SW Norway). Geol Soc Lond Spec Publ 220:65–81.

Montel J-M, Devidal J-L, Avignant D (2002) X-ray diffraction study of brabantite-monazite solid solution. Chem Geol 191:89–104.

Montel J-M, Foret S, Veschambre M, Nicollet C, Provost A (1996) Electron microprobe dating of monazite. Chem Geol 131:37–53.

Muhling JR, Fletcher IR, Rasmussen B (2012) Dating fluid flow and Mississippi Valley type base-metal mineralization in the Paleoproterozoic Earaheedy Basin, Western Australia. Precambrian Res 212-213:75–90.

Ni Y, Hughes JM, Mariano AN (1995) Crystal chemistry of the monazite and xenotime structures. Am Mineral 80:21–26.

Ondrejka M, Uher P, Pršek J, Ozdín D (2007) Arsenian monazite-(Ce) and xenotime-(Y), REE arsenates and carbonates from the Tisovec-Rejkovo rhyolite, Western Carpathians, Slovakia: Composition and substitutions in the (REE,Y)XO4 system (X = P, As, Si, Nb, S). Lithos 95:116–129.

Paquette JL, Tiepolo M (2007) High resolution (5 μm) U–Th–Pb isotope dating of monazite with excimer laser ablation (ELA)-ICPMS. Chem Geol 240:222–237.

Parat F, Holtz F (2004) Sulfur partitioning between apatite and melt and effect of sulfur on apatite solubility at oxidizing conditions. Contrib Mineral Petrol 147:201–212.

Parat F, Holtz F, Streck MJ (2011) Sulfur-bearing Magmatic Accessory Minerals. Rev Mineral Geochem 73:285–314.

Prsek J, Ondrejka M, Bacik P, Budzyn B, Uher P (2010) Metamorphic-hydrothermal REE minerals in the Bacuch magnetite deposit, Western Carpathians, Slovakia: (S,Sr)-rich monazite-(Ce) and Nd-dominant hingganite. Can Mineral 48:81–94.

Putnis A (2009) Mineral Replacement Reactions. Rev Mineral Geochem 70:87–124.

Rasmussen B, Fletcher IR, Muhling JR, Thorne WS, Broadbent GC (2007) Prolonged history of episodic fluid flow in giant hematite ore bodies: Evidence from in situ U–Pb geochronology of hydrothermal xenotime. Earth Planet Sci Lett 258:249–259.

Rasmussen B, Muhling JR (2007) Monazite begets monazite: evidence for dissolution of detrital monazite and reprecipitation of syntectonic monazite during low-grade regional metamorphism. Contrib Mineral Petrol 154:675–689.

Rasmussen B, Sheppard S, Fletcher IR (2006) Testing ore deposit models using in situ U-Pb geochronology of hydrothermal monazite: Paleoproterozoic gold mineralization in northern Australia. Geology 34:77–80.

Satish-Kumar M, Hermann J, Tsunogae T, Osanai Y (2006) Carbonation of Cl-rich scapolite boudins in Skallen, East Antarctica: evidence for changing fluid condition in the continental crust. J Metamorph Geol 24:241–261.

Schandl ES, Gorton MP (2004) A textural and geochemical guide to the identification of hydrothermal monazite: criteria for selection of samples for dating epigenetic hydrothermal ore deposits. Econ Geol 99:1027–1035.

Schärer U, Wilmart E, Duchesne J-C (1996) The short duration and anorogenic character of anorthosite magmatism: U-Pb dating of the Rogaland complex, Norway. Earth Planet Sci Lett 139:335–350.

Seo JH, Guillong M, Heinrich CA (2009) The role of sulfur in the formation of magmatic–hydrothermal copper–gold deposits. Earth Planet Sci Lett 282:323–328.

Seydoux-Guillaume A-M, Goncalves P, Wirth R, Deutsch A (2003) Transmission electron microscope study of polyphase and discordant monazites: Site-specific specimen preparation using the focused ion beam technique. Geology 31:973–976.

Seydoux-Guillaume A-M, Montel J-M, Bingen B, Bosse V, de Parseval P, Paquette J-L, Janots E, Wirth R (2012) Low-temperature alteration of monazite: Fluid mediated coupled dissolution–precipitation, irradiation damage, and disturbance of the U–Pb and Th–Pb chronometers. Chem Geol 330-331:140–158.

Seydoux-Guillaume A-M, Montel J-M, Wirth R, Moine B (2009) Radiation damage in diopside and calcite crystals from uranothorianite inclusions. Chem Geol 261:318–332.

Seydoux-Guillaume A-M, Paquette J-L, Wiedenbeck M, Montel J-M, Heinrich W (2002) Experimental resetting of the U–Th–Pb systems in monazite. Chem Geol 191:165–181.

Shannon R (1976) Revised effective ionic radii and systematic studies of interatomic distances in halides and chalcogenides. Acta Crystallogr A 32:751–767.

Simon AC, Ripley EM (2011) The Role of Magmatic Sulfur in the Formation of Ore Deposits. Rev Mineral Geochem 73:513–578.

Spear FS, Pyle JM, Cherniak D (2009) Limitations of chemical dating of monazite. Chem Geol 266:218–230.

Stacey J, Kramers J (1975) Approximation of terrestrial lead isotope evolution by a two-stage model. Earth Planet Sci Lett 26:207–221.

Stein HJ, Markey RJ, Morgan JW, et al (2001) The remarkable Re–Os chronometer in molybdenite: how and why it works. Terra Nova 13:479–486.

Stepanov AS, Hermann J, Rubatto D, Rapp RP (2012) Experimental study of monazite/melt partitioning with implications for the REE, Th and U geochemistry of crustal rocks. Chem Geol 300-301:200–220.

Suzuki K, Kato T (2008) CHIME dating of monazite, xenotime, zircon and polycrase: Protocol, pitfalls and chemical criterion of possibly discordant age data. Gondwana Res 14:569–586.

Tobi AC, Hermans GAE., Maijer C, Jansen JBH (1985) Metamorphic zoning in the high-grade proterozoic of Rogaland-Vest Agder SW Norway. In: Tobi AC &Touret JLR (eds) The deep Proterozoic crust in the North Atlantic provinces. D. Reidel, Dordrecht, pp 477–497

Tomkins AG (2010) Windows of metamorphic sulfur liberation in the crust: Implications for gold deposit genesis. Geochim Cosmochim Acta 74:3246–3259.

Tomkins AG, Pattison DRM, Frost BR (2007) On the Initiation of Metamorphic Sulfide Anatexis. J Petrol 48:511–535.

Tomkins HS, Williams IS, Ellis DJ (2005) In situ U-Pb dating of zircon formed from retrograde garnet breakdown during decompression in Rogaland, SW Norway. J Metamorph Geol 23:201–215.

Touret J (2001) Fluids in metamorphic rocks. Lithos 55:1–25.

Tracy RJ, Robinson P (1988) Silicate-sulfide-oxide fluid reactions in granulitic-grade pelitic rocks, Central Massachusetts. Am J Sci 288:45–74.

Van Achterbergh E, Ryan C, Jackson S, Griffin W (2001) Data reduction software for LA–ICP–MS. In: Sylvester P (ed) Laser ablation-ICP-MS in the Earth sciences. Mineral Assoc Can 29:239–243.

Villa IM, Williams ML (2013) Geochronology of metasomatic events. In: Harlov D & Austrheim H (eds) Metasomatism and the Chemical Transformation of Rock: the role of fluids in terrestrial and extraterrestrial processes. Springer, Berlin, pp 171–202

Webster JD, Botcharnikov RE (2011) Distribution of sulfur between melt and fluid in S–O–H–C–Cl-bearing magmatic systems at shallow crustal pressures and temperatures. Rev Mineral Geochem 73:247–283.

Webster JD, Goldoff B, Shimizu N (2011) C–O–H–S fluids and granitic magma: how S partitions and modifies CO_2 concentrations of fluid-saturated felsic melt at 200 MPa. Contrib Mineral Petrol 162:849–865.

Westphal M, Schumacher JC, Boschert S (2003) High-temperature metamorphism and the role of magmatic heat sources at the Rogaland anorthosite complex in southwestern Norway. J Petrol 44:1145–1162.

Whitney J (1984) Fugacities of sulfurous gases in pyrrhotite-bearing silicic magmas. Am Mineral 69:69–78.

Wilke M, Behrens H (1999) The dependence of the partitioning of iron and europium between plagioclase and hydrous tonalitic melt on oxygen fugacity. Contrib Mineral Petrol 137:102–114.

Wilke M, Klimm K, Kohn SC (2011) Spectroscopic Studies on Sulfur Speciation in Synthetic and Natural Glasses. Rev Mineral Geochem 73:41–78.

Williams ML, Jercinovic MJ, Hetherington CJ (2007) Microprobe Monazite Geochronology: Understanding Geologic Processes by Integrating Composition and Chronology. Annu Rev Earth Planet Sci 35:137–175.

Tables

Tab. 1: EPMA chemical analyses of monazite crystals in % wt. Monazite formula is recalculated on the basis of 4 O

Grain	1029-00	1029-01	1029-01b	1029-01c	1029-01d	1029-01e	1029-03a	1029-03b	1029-03c	1029-04a	1029-04b	1029-04c	1029-04d	1029-05	1029-05b	1029-05c
Group	D2	D2	D2	D3	D2	D2	D3	D2	D2	D3	D2	D2	D2	D2	D2	D3
P_2O_5	30.24	29.97	29.08	28.82	28.41	28.71	30.28	29.10	30.00	28.19	29.58	29.90	30.16	30.21	30.05	28.67
SiO_2	0.32	0.31	0.93	0.90	1.14	1.09	0.32	1.08	0.30	1.46	0.39	0.40	0.25	0.34	0.26	1.31
ThO_2	4.38	4.79	9.49	5.41	6.40	6.36	5.05	5.23	4.64	7.58	5.51	4.71	4.28	4.39	4.59	7.01
UO_2	0.30	0.26	0.14	0.15	0.17	0.27	0.30	0.19	0.29	0.21	0.11	0.39	0.40	0.24	0.40	0.08
Ce_2O_3	27.12	27.80	25.08	26.85	27.01	26.45	26.90	26.74	26.67	25.11	27.35	27.03	27.43	27.07	27.48	25.15
Y_2O_3	1.50	1.57	0.40	2.28	1.96	2.25	1.64	2.24	1.91	1.57	0.65	2.12	1.70	2.14	1.35	2.08
La_2O_3	11.82	11.97	8.48	10.54	10.06	9.98	11.94	11.36	11.86	9.35	11.92	11.87	12.40	12.09	11.93	9.89
Pr_2O_3	3.10	3.24	3.48	3.30	3.24	3.32	3.35	3.13	2.76	3.76	2.87	2.82	2.97	3.31	3.25	3.25
Nd_2O_3	13.14	12.87	16.54	15.09	15.43	15.85	12.64	13.94	12.70	15.97	14.31	12.67	13.04	13.11	13.24	15.14
Sm_2O_3	2.71	2.17	2.10	2.82	2.62	2.82	2.49	2.84	2.32	2.91	2.49	2.44	2.33	2.21	2.55	3.01
Gd_2O_3	2.19	1.91	0.63	2.29	1.32	2.20	2.00	2.50	1.79	1.96	1.51	2.37	1.93	2.32	1.81	1.92
Dy_2O_3	0.45	0.33	0.00	0.77	0.46	0.73	0.50	0.74	0.49	0.53	0.32	0.69	0.41	0.60	0.39	0.65
SO_2	0.22	0.22	0.36	0.02	0.03	0.04	0.25	0.01	0.20	0.04	0.24	0.20	0.21	0.11	0.28	0.01
CaO	1.12	1.28	1.80	0.39	0.47	0.46	1.29	0.32	1.21	0.44	1.34	1.08	1.12	0.98	1.28	0.43
PbO	0.38	0.38	0.44	0.46	0.57	0.59	0.36	0.28	0.38	0.35	0.29	0.15	0.25	0.26	0.30	0.28
Total	**99.00**	**99.06**	**98.93**	**100.08**	**99.27**	**101.10**	**99.32**	**99.69**	**97.52**	**99.42**	**98.37**	**98.82**	**98.87**	**99.38**	**99.14**	**98.88**
P	0.996	0.990	0.968	0.965	0.959	0.955	0.994	0.969	0.999	0.951	0.985	0.989	0.996	0.995	0.991	0.964
Si	0.012	0.012	0.036	0.036	0.045	0.043	0.012	0.042	0.012	0.058	0.015	0.016	0.010	0.013	0.010	0.052
Th	0.039	0.043	0.085	0.049	0.058	0.057	0.045	0.047	0.042	0.069	0.049	0.042	0.038	0.039	0.041	0.063
U	0.003	0.002	0.001	0.001	0.001	0.002	0.003	0.002	0.003	0.002	0.001	0.003	0.003	0.002	0.003	0.001
Ce	0.386	0.397	0.361	0.389	0.394	0.381	0.382	0.385	0.384	0.366	0.394	0.387	0.392	0.386	0.392	0.366
Y	0.031	0.033	0.008	0.048	0.042	0.047	0.034	0.047	0.040	0.033	0.014	0.044	0.035	0.044	0.028	0.044
La	0.170	0.172	0.123	0.154	0.148	0.145	0.171	0.165	0.172	0.138	0.173	0.171	0.178	0.173	0.171	0.145
Pr	0.044	0.046	0.050	0.048	0.047	0.048	0.047	0.045	0.040	0.055	0.041	0.040	0.042	0.047	0.046	0.047
Nd	0.183	0.179	0.232	0.213	0.220	0.223	0.175	0.196	0.178	0.227	0.201	0.177	0.182	0.182	0.184	0.215
Sm	0.036	0.029	0.028	0.038	0.036	0.038	0.033	0.039	0.031	0.040	0.034	0.033	0.031	0.030	0.034	0.041
Gd	0.028	0.025	0.008	0.030	0.017	0.029	0.026	0.033	0.023	0.026	0.020	0.031	0.025	0.030	0.023	0.025
Dy	0.006	0.004	0.000	0.010	0.006	0.009	0.006	0.009	0.006	0.007	0.004	0.009	0.005	0.008	0.005	0.008
S^{6+}	0.008	0.008	0.013	0.001	0.001	0.001	0.009	0.000	0.007	0.001	0.009	0.007	0.008	0.004	0.010	0.000
Ca	0.047	0.053	0.076	0.016	0.020	0.019	0.054	0.013	0.051	0.019	0.057	0.045	0.047	0.041	0.053	0.018
Pb	0.004	0.004	0.005	0.005	0.006	0.006	0.004	0.003	0.004	0.004	0.003	0.002	0.003	0.003	0.003	0.003
Total	1.985	1.990	1.981	2.001	1.999	2.001	1.985	1.995	1.986	1.995	1.990	1.988	1.987	1.992	1.986	1.992
Σ(P)	0.984	0.996	0.991	1.001	0.996	1.005	0.988	0.983	0.982	0.987	0.999	0.990	0.989	0.988	0.995	0.977
Σ(T)	1.009	1.002	1.004	1.000	1.004	0.998	1.006	1.012	1.011	1.009	1.001	1.005	1.005	1.008	1.001	1.016
Σ(P-T)	0.02	0.01	0.01	0.00	0.01	0.01	0.02	0.03	0.03	0.02	0.00	0.01	0.02	0.02	0.01	0.04
(Ca + Si) excess	0.030	0.033	0.044	0.008	0.013	0.011	0.032	0.011	0.030	0.012	0.034	0.024	0.026	0.020	0.033	0.010
Crl	**8.3**	**9.1**	**16.6**	**4.3**	**5.3**	**5.2**	**9.5**	**3.2**	**8.8**	**4.5**	**10.2**	**9.2**	**8.3**	**8.2**	**8.9**	**4.3**
Hfn	**0.0**	**0.0**	**0.6**	**2.9**	**3.4**	**3.4**	**0.0**	**3.2**	**0.0**	**4.8**	**0.0**	**0.0**	**0.0**	**0.0**	**0.0**	**4.2**
Mnz	**91.7**	**90.9**	**82.9**	**92.8**	**91.4**	**91.4**	**90.5**	**93.5**	**91.2**	**90.7**	**89.8**	**90.8**	**91.7**	**91.8**	**91.1**	**91.5**

Tab. 1: continued

Grain	1029-05d	1029-05c	1029-06	1029-06b	1029-06c	1029-07b	1029-07c	1029-08c	1029-107	1029-17a	1029-17b	1029-17c	1029-17d	1029-17e	1029-17f	1029-17g
Group	D2	D3	D3	D2	D2	D2	D2	D3	D2	D1	D1	D1	D1	D3	D1	D3
P_2O_5	29.78	30.06	28.33	30.19	30.04	28.66	29.29	27.55	29.27	29.36	29.15	29.56	28.65	28.18	28.83	26.80
SiO_2	0.32	0.46	1.47	0.30	0.34	0.76	0.36	1.46	0.30	0.39	0.39	0.39	0.37	1.64	0.38	1.69
ThO_2	5.08	4.25	7.75	4.29	4.53	8.94	4.30	8.49	4.23	4.79	4.73	4.70	5.09	8.54	4.60	7.80
UO_2	0.16	0.30	0.13	0.26	0.24	0.18	0.16	0.06	0.29	0.30	0.12	0.25	0.25	0.06	0.23	0.10
Ce_2O_3	27.54	27.88	25.25	27.53	27.69	26.76	28.75	26.99	27.81	26.70	26.60	27.00	26.46	22.73	26.90	24.37
Y_2O_3	0.79	1.50	1.76	1.43	1.17	0.51	1.43	1.09	1.15	0.86	0.87	0.87	1.29	1.59	0.79	1.31
La_2O_3	11.51	11.75	9.11	11.93	11.68	8.72	12.54	9.59	12.90	11.77	11.91	12.07	11.86	7.74	11.94	8.92
Pr_2O_3	3.49	3.10	3.56	3.31	3.28	3.48	3.25	3.52	3.11	3.34	3.51	3.14	3.67	3.66	3.43	3.33
Nd_2O_3	14.96	13.57	15.81	14.06	14.32	16.82	13.80	17.02	12.63	12.94	13.19	13.12	12.85	17.04	13.37	15.84
Sm_2O_3	2.84	2.97	3.24	2.10	2.62	2.41	2.99	2.28	2.43	2.24	2.11	2.44	2.60	3.50	2.08	2.92
Gd_2O_3	1.60	2.01	2.26	2.22	1.78	0.72	1.99	1.54	2.09	1.65	1.74	2.03	2.06	1.95	1.58	1.78
Dy_2O_3	0.18	0.34	0.30	0.49	0.41	0.00	0.58	0.62	0.49	0.32	0.65	0.37	0.55	0.31	0.39	0.50
SO_2	0.17	0.08	0.00	0.15	0.13	0.15	0.21	0.04	0.34	0.42	0.45	0.44	0.36	0.09	0.58	0.03
CaO	1.34	0.80	0.42	1.01	1.04	1.75	1.08	0.48	1.17	1.41	1.43	1.40	1.34	0.50	1.48	0.28
PbO	0.24	0.30	0.27	0.24	0.18	0.18	0.40	0.32	0.39	0.60	0.30	0.15	0.25	0.23	0.26	0.36
Total	**99.99**	**99.36**	**99.66**	**99.01**	**98.94**	**100.04**	**101.13**	**101.04**	**98.10**	**95.73**	**97.14**	**97.92**	**97.66**	**97.76**	**96.82**	**96.03**
P	0.985	0.994	0.953	0.995	0.993	0.960	0.968	0.932	0.979	1.000	0.980	0.984	0.970	0.956	0.973	0.941
Si	0.012	0.018	0.058	0.012	0.013	0.030	0.014	0.058	0.012	0.016	0.015	0.015	0.015	0.066	0.015	0.070
Th	0.045	0.038	0.070	0.038	0.040	0.080	0.038	0.077	0.038	0.044	0.043	0.042	0.046	0.078	0.042	0.074
U	0.001	0.003	0.001	0.002	0.002	0.002	0.001	0.001	0.003	0.003	0.001	0.002	0.002	0.001	0.002	0.001
Ce	0.394	0.399	0.367	0.392	0.396	0.388	0.411	0.395	0.402	0.393	0.387	0.389	0.388	0.334	0.393	0.370
Y	0.016	0.031	0.037	0.030	0.024	0.011	0.030	0.023	0.024	0.018	0.018	0.018	0.028	0.034	0.017	0.029
La	0.166	0.169	0.134	0.171	0.168	0.127	0.181	0.141	0.188	0.175	0.174	0.175	0.175	0.114	0.176	0.136
Pr	0.050	0.044	0.052	0.047	0.047	0.050	0.046	0.051	0.045	0.049	0.051	0.045	0.054	0.054	0.050	0.050
Nd	0.209	0.189	0.224	0.195	0.200	0.238	0.192	0.243	0.178	0.186	0.187	0.184	0.184	0.244	0.190	0.235
Sm	0.038	0.040	0.044	0.028	0.035	0.033	0.040	0.031	0.033	0.031	0.029	0.033	0.036	0.048	0.029	0.042
Gd	0.021	0.026	0.030	0.029	0.023	0.009	0.026	0.020	0.027	0.022	0.023	0.026	0.027	0.026	0.021	0.024
Dy	0.002	0.004	0.004	0.006	0.005	0.000	0.007	0.008	0.006	0.004	0.008	0.005	0.007	0.004	0.005	0.007
S^{6-}	0.006	0.003	0.000	0.005	0.005	0.006	0.008	0.001	0.013	0.016	0.017	0.016	0.014	0.003	0.022	0.001
Ca	0.056	0.033	0.018	0.042	0.044	0.074	0.045	0.021	0.050	0.002	0.061	0.059	0.057	0.022	0.063	0.012
Pb	0.003	0.003	0.003	0.003	0.002	0.002	0.004	0.003	0.004	0.007	0.003	0.002	0.003	0.002	0.003	0.004
Total	1.998	1.991	1.995	1.990	1.992	2.004	2.004	2.005	1.989	1.950	1.981	1.979	1.991	1.982	1.977	1.995
Σ(P)	1.007	0.982	0.984	0.989	0.990	1.020	1.030	1.016	1.011	0.950	1.002	0.996	1.020	0.964	1.011	0.985
Σ(T)	0.997	1.012	1.011	1.007	1.006	0.990	0.982	0.990	0.991	1.016	0.996	0.999	0.985	1.022	0.988	1.011
Σ(P-T)	0.01	0.03	0.03	0.02	0.02	0.03	0.05	0.03	0.02	0.07	0.01	0.00	0.03	0.06	0.02	0.03
(Ca + Si) excess	0.031	0.017	0.008	0.021	0.021	0.030	0.032	0.006	0.038	-0.006	0.052	0.048	0.040	0.015	0.059	0.013
Crl	**9.5**	**7.3**	**4.1**	**8.1**	**8.5**	**15.8**	**8.2**	**4.9**	**8.3**	**1.7**	**8.9**	**9.0**	**10.0**	**4.8**	**9.0**	**3.3**
Htn	**0.0**	**0.4**	**5.0**	**0.0**	**0.0**	**0.6**	**0.0**	**5.5**	**0.0**	**3.6**	**0.0**	**0.0**	**0.0**	**5.4**	**0.0**	**5.8**
Mnz	**90.5**	**92.3**	**90.8**	**91.9**	**91.5**	**83.6**	**91.8**	**89.7**	**91.7**	**94.7**	**91.1**	**91.0**	**90.0**	**89.9**	**91.0**	**90.9**

Tab. 1: continued

Grain	1029-17h	1029-17i	1029-17j	1029-17k	1029-17l	1029-17m	1029-17o	1029-17q	1029-17q	1029-19	1029-21	1029-26a	1029-26b	1029-26c	1029-26d	1029-26e
Group	D2	D2	D3	D2	D2	D3	D2	D2	D2	D2	D2	D2	D3	D1	D3	D3
P_2O_5	27.31	27.92	27.43	27.96	28.77	27.90	29.06	29.36	28.77	30.01	30.02	29.75	28.46	30.05	29.17	29.94
SiO_2	1.17	0.66	1.35	1.29	0.40	1.48	0.52	0.39	0.40	0.36	0.31	0.44	1.26	0.36	1.10	0.54
ThO_2	8.89	8.49	6.79	6.62	4.97	7.51	5.17	4.79	4.97	4.67	4.72	6.03	6.55	4.60	5.39	4.56
UO_2	0.03	0.23	0.06	0.11	0.15	0.21	0.07	0.15	0.15	0.31	0.33	0.15	0.02	0.25	0.27	0.08
Ce_2O_3	24.55	24.47	23.84	24.77	27.14	24.05	26.82	26.70	27.14	27.96	26.42	27.15	26.67	27.08	26.24	27.34
Y_2O_3	0.98	0.42	1.74	1.77	0.65	1.60	0.54	0.86	0.65	1.28	2.05	0.77	2.01	1.51	2.56	1.43
La_2O_3	8.34	8.72	8.87	9.35	11.73	8.35	11.13	12.27	12.23	11.59	11.97	10.59	10.54	12.38	10.86	12.00
Pr_2O_3	3.88	3.39	3.05	3.51	3.43	3.61	3.58	3.34	3.43	3.28	3.12	3.56	3.76	3.29	3.24	3.40
Nd_2O_3	15.97	15.47	15.48	15.95	13.24	16.43	13.62	13.44	13.74	13.55	12.73	15.09	14.67	13.12	15.08	13.51
Sm_2O_3	2.35	2.66	3.10	3.44	2.09	3.16	2.59	2.24	2.09	2.54	2.29	2.39	2.21	2.26	2.35	2.49
Gd_2O_3	1.30	1.00	2.20	2.21	1.41	1.94	2.07	1.65	1.41	2.00	2.22	1.51	2.28	1.82	2.15	1.86
Dy_2O_3	0.30	0.15	0.51	0.67	0.19	0.57	0.59	0.32	0.19	0.24	0.69	0.01	0.49	0.36	0.66	0.41
SO_2	0.12	0.19	0.05	0.10	0.32	0.04	0.35	0.42	0.32	0.18	0.21	0.15	0.03	0.18	0.02	0.09
CaO	1.17	1.65	0.43	0.43	1.25	0.51	1.31	1.39	1.25	1.04	1.18	1.22	0.30	1.11	0.27	0.75
PbO	0.32	0.55	0.38	0.33	0.16	0.28	0.33	0.22	0.16	0.21	0.37	0.38	0.32	0.27	0.19	0.44
Total	**96.68**	**95.97**	**95.28**	**98.49**	**95.90**	**97.64**	**97.76**	**96.54**	**95.90**	**99.22**	**98.62**	**99.20**	**99.56**	**98.13**	**99.53**	**98.82**
P	0.949	0.970	0.959	0.952	0.984	0.954	0.978	0.982	0.978	0.992	0.994	0.989	0.957	0.995	0.970	0.994
Si	0.048	0.027	0.056	0.052	0.016	0.060	0.021	0.015	0.016	0.014	0.012	0.017	0.050	0.014	0.043	0.021
Th	0.083	0.079	0.064	0.061	0.046	0.069	0.047	0.043	0.045	0.042	0.042	0.054	0.059	0.041	0.048	0.041
U	0.000	0.002	0.001	0.001	0.001	0.002	0.001	0.001	0.001	0.003	0.003	0.001	0.000	0.002	0.002	0.001
Ce	0.369	0.367	0.360	0.365	0.401	0.356	0.390	0.386	0.399	0.400	0.378	0.390	0.388	0.388	0.377	0.393
Y	0.021	0.009	0.038	0.038	0.014	0.034	0.011	0.018	0.014	0.027	0.043	0.016	0.043	0.031	0.054	0.030
La	0.126	0.132	0.135	0.139	0.175	0.124	0.163	0.179	0.181	0.167	0.173	0.153	0.154	0.179	0.157	0.174
Pr	0.058	0.051	0.046	0.051	0.050	0.053	0.052	0.048	0.050	0.047	0.044	0.051	0.054	0.047	0.046	0.049
Nd	0.234	0.227	0.228	0.229	0.191	0.237	0.193	0.190	0.197	0.189	0.178	0.212	0.208	0.183	0.212	0.189
Sm	0.033	0.038	0.044	0.048	0.029	0.044	0.035	0.030	0.029	0.034	0.031	0.032	0.030	0.030	0.032	0.034
Gd	0.018	0.014	0.030	0.029	0.019	0.026	0.027	0.022	0.019	0.026	0.029	0.020	0.030	0.024	0.028	0.024
Dy	0.004	0.002	0.007	0.009	0.002	0.007	0.008	0.004	0.002	0.003	0.009	0.000	0.006	0.005	0.008	0.005
S^{6-}	0.005	0.007	0.002	0.004	0.012	0.002	0.013	0.016	0.012	0.007	0.008	0.006	0.001	0.006	0.001	0.003
Ca	0.051	0.072	0.019	0.018	0.054	0.022	0.056	0.059	0.054	0.044	0.049	0.051	0.013	0.047	0.011	0.031
Pb	0.004	0.006	0.004	0.004	0.002	0.003	0.003	0.002	0.002	0.002	0.004	0.004	0.003	0.003	0.002	0.005
Total	1.999	1.996	1.991	1.994	1.984	1.992	1.986	1.981	1.988	1.988	1.988	1.991	1.996	1.988	1.992	1.989
Σ(P)	1.006	1.006	0.979	0.994	0.997	0.980	1.000	0.999	1.006	0.988	0.990	0.990	0.990	0.986	0.979	0.977
Σ(T)	0.997	0.997	1.015	1.003	1.000	1.014	0.998	0.998	0.994	1.006	1.006	1.006	1.007	1.009	1.014	1.015
Σ(P-T)	0.01	0.01	0.04	0.01	0.00	0.03	0.00	0.00	0.01	0.02	0.02	0.02	0.02	0.02	0.04	0.04
(Ca + Si) excess	0.024	0.032	0.016	0.016	0.037	0.015	0.046	0.048	0.037	0.022	0.028	0.023	0.008	0.027	0.006	0.019
Crl	**11.2**	**16.1**	**4.7**	**4.4**	**9.5**	**5.0**	**9.7**	**9.0**	**9.5**	**8.9**	**9.0**	**11.1**	**3.2**	**8.7**	**2.6**	**7.2**
Htn	**2.9**	**0.3**	**4.1**	**4.0**	**0.0**	**4.6**	**0.0**	**0.0**	**0.0**	**0.0**	**0.0**	**0.0**	**4.3**	**0.0**	**3.7**	**0.5**
Mnz	**85.9**	**83.6**	**91.2**	**91.6**	**90.5**	**90.4**	**90.3**	**91.0**	**90.5**	**91.1**	**91.0**	**88.8**	**92.5**	**91.3**	**93.7**	**92.2**

Tab. 1: continued

Grain	**1029-36a**	**1029-36b**	**1029-36c**	**1029-36d**	**1029-37**	**1029-37b**	**1029-37c**	**1029-37d**	**1029-37e**	**1029-37f**	**1029-40**	**1029-40b**	**1029-40c**	**1029-40d**	**1029-40e**	**1029-40f**
Group	D2	D3	D2	D2	D3	D2	D3	D3	D2	D2	D3	D2	D2	D2	D2	D3
P_2O_5	29.34	28.62	29.18	29.55	27.90	29.60	27.92	27.92	29.46	29.07	27.43	29.67	29.46	28.99	29.10	27.96
SiO_2	0.40	1.39	0.55	0.37	1.55	0.49	1.76	1.76	0.58	0.66	1.91	0.43	0.34	0.74	0.86	1.71
ThO_2	5.02	6.40	7.10	3.76	7.67	5.22	8.63	8.63	7.40	7.40	8.83	4.37	4.45	8.86	9.15	8.19
UO_2	0.18	0.21	0.08	0.26	0.14	0.22	0.08	0.08	0.20	0.15	0.19	0.29	0.19	0.11	0.09	0.10
Ce_2O_3	28.19	27.17	26.49	28.03	26.42	28.37	26.31	26.31	26.46	26.53	26.13	27.78	28.24	25.75	25.36	26.50
Y_2O_3	0.69	1.72	0.56	1.52	1.46	0.89	1.39	1.39	0.66	0.65	1.03	1.21	1.11	0.39	0.30	0.79
La_2O_3	11.85	10.89	10.37	13.18	9.87	11.89	9.56	9.56	9.85	10.17	9.22	12.09	12.42	9.07	8.72	9.57
Pr_2O_3	2.92	3.08	3.36	3.26	3.21	3.54	3.29	3.29	3.42	3.77	3.51	3.13	3.17	3.71	3.75	3.84
Nd_2O_3	13.90	14.64	15.28	12.22	15.12	13.78	14.74	14.74	15.46	15.12	15.86	13.33	13.17	16.51	16.14	15.72
Sm_2O_3	2.19	2.44	2.41	2.45	2.19	2.39	2.59	2.59	2.55	2.44	2.46	2.49	2.49	2.26	2.51	2.53
Gd_2O_3	1.73	1.96	0.97	1.94	1.73	1.24	1.64	1.64	1.10	1.27	1.03	2.25	1.67	0.72	0.96	0.88
Dy_2O_3	0.24	0.54	0.00	0.37	0.50	0.38	0.21	0.21	0.02	0.15	0.32	0.36	0.38	0.15	0.00	0.36
SO_2	0.36	0.06	0.41	0.43	0.05	0.18	0.03	0.03	0.25	0.23	0.02	0.33	0.33	0.22	0.25	0.03
CaO	1.31	0.32	1.66	1.16	0.38	0.99	0.36	0.36	1.42	1.34	0.38	1.14	1.20	1.66	1.75	0.55
PbO	0.33	0.33	0.26	0.18	0.34	0.29	0.37	0.37	0.30	0.47	0.27	0.23	0.12	0.37	0.50	0.43
Total	**98.63**	**99.77**	**98.17**	**98.17**	**98.51**	**99.46**	**98.87**	**98.87**	**99.10**	**99.41**	**98.61**	**99.08**	**98.73**	**99.50**	**99.43**	**99.15**
P	0.979	0.957	0.973	0.979	0.949	0.983	0.946	0.946	0.980	0.972	0.937	0.982	0.981	0.969	0.969	0.946
Si	0.016	0.055	0.022	0.014	0.062	0.019	0.071	0.071	0.023	0.026	0.077	0.017	0.013	0.029	0.034	0.068
Th	0.045	0.058	0.064	0.033	0.070	0.047	0.079	0.079	0.066	0.066	0.081	0.039	0.040	0.080	0.082	0.074
U	0.002	0.002	0.001	0.002	0.001	0.002	0.001	0.001	0.002	0.001	0.002	0.003	0.002	0.001	0.001	0.001
Ce	0.407	0.393	0.382	0.401	0.389	0.407	0.386	0.386	0.381	0.384	0.386	0.398	0.407	0.372	0.365	0.388
Y	0.014	0.036	0.012	0.032	0.031	0.019	0.030	0.030	0.014	0.014	0.022	0.025	0.023	0.008	0.006	0.017
La	0.172	0.159	0.151	0.190	0.146	0.172	0.141	0.141	0.143	0.148	0.137	0.174	0.180	0.132	0.127	0.141
Pr	0.042	0.044	0.048	0.047	0.047	0.051	0.048	0.048	0.049	0.054	0.052	0.045	0.045	0.053	0.054	0.056
Nd	0.196	0.206	0.215	0.171	0.217	0.193	0.211	0.211	0.217	0.213	0.229	0.186	0.185	0.233	0.227	0.224
Sm	0.030	0.033	0.033	0.033	0.030	0.032	0.036	0.036	0.035	0.033	0.034	0.034	0.034	0.031	0.034	0.035
Gd	0.023	0.026	0.013	0.025	0.023	0.016	0.022	0.022	0.014	0.017	0.014	0.029	0.022	0.009	0.012	0.012
Dy	0.003	0.007	0.000	0.005	0.006	0.005	0.003	0.003	0.000	0.002	0.004	0.005	0.005	0.002	0.000	0.005
S^{6-}	0.013	0.002	0.015	0.016	0.002	0.007	0.001	0.001	0.009	0.008	0.001	0.012	0.012	0.008	0.009	0.001
Ca	0.055	0.013	0.070	0.049	0.016	0.041	0.015	0.015	0.060	0.057	0.016	0.048	0.050	0.070	0.074	0.024
Pb	0.003	0.004	0.003	0.002	0.004	0.003	0.004	0.004	0.003	0.005	0.003	0.002	0.001	0.004	0.005	0.005
Total	1.987	1.992	1.984	1.983	1.992	1.990	1.990	1.990	1.986	1.992	1.994	1.985	1.988	1.993	1.990	1.995
Σ(P)	1.005	0.983	1.005	1.005	0.983	0.995	0.975	0.975	0.992	1.002	0.980	0.999	1.006	1.003	0.996	0.982
Σ(T)	0.995	1.012	0.994	0.993	1.011	1.002	1.016	1.016	1.003	0.998	1.014	0.999	0.994	0.998	1.003	1.015
Σ(P-T)	0.01	0.03	0.01	0.01	0.03	0.01	0.04	0.04	0.01	0.00	0.03	0.00	0.01	0.01	0.01	0.03
(Ca + Si) excess	0.041	0.015	0.045	0.045	0.012	0.022	0.012	0.012	0.027	0.029	0.015	0.037	0.035	0.031	0.040	0.022
Crl	**9.5**	**3.4**	**13.2**	**7.3**	**4.0**	**9.0**	**3.9**	**3.9**	**12.8**	**12.6**	**3.9**	**8.4**	**8.5**	**15.2**	**16.3**	**5.7**
Htn	**0.0**	**4.2**	**0.0**	**0.0**	**5.1**	**0.4**	**5.9**	**5.9**	**0.5**	**0.6**	**6.3**	**0.0**	**0.0**	**0.7**	**0.4**	**4.8**
Mnz	**90.5**	**92.4**	**86.8**	**92.7**	**90.9**	**90.6**	**90.2**	**90.2**	**86.7**	**86.7**	**89.8**	**91.6**	**91.5**	**84.1**	**83.4**	**89.6**

Tab. 1: continued

Grain	1029-40g	1029-41a	1029-41b	1029-41c	1029-41d	1029-41e	1029-41f	1029-41g	1029-41h	1029-41i	1029-41j	1029-41k	1029-44	1029-44a	1029-44b	1029-44c
Group	D2	D3	D3	D2	D3	D2	D2	D2	D2	D3	D2	D3	D2	D2	D3	D3
P_2O_5	29.51	26.35	28.62	28.93	27.66	29.15	29.25	29.04	28.66	27.74	29.07	27.34	30.46	29.71	29.10	29.52
SiO_2	0.56	2.35	0.91	0.58	1.72	0.38	0.55	0.77	0.82	1.73	0.45	1.85	0.30	0.24	0.94	0.59
ThO_2	7.31	10.61	7.03	7.32	7.91	4.74	7.62	7.40	9.60	8.21	4.84	9.02	4.30	4.33	4.63	4.93
UO_2	0.19	0.23	0.29	0.18	0.15	0.12	0.20	0.20	0.14	0.14	0.21	0.00	0.31	0.36	0.19	0.15
Ce_2O_3	26.69	24.79	27.07	26.24	26.38	28.21	26.16	26.44	25.40	25.74	27.89	25.92	26.94	27.68	26.88	28.37
Y_2O_3	0.61	2.06	0.86	0.56	1.83	0.91	0.72	0.60	0.36	2.21	0.87	0.98	1.94	1.35	1.54	0.66
La_2O_3	10.06	9.59	10.33	10.32	10.42	12.70	9.62	9.96	8.79	9.83	12.47	9.33	12.59	12.79	11.22	12.19
Pr_2O_3	3.46	3.24	3.38	3.39	2.97	2.76	3.41	3.82	3.55	3.55	3.54	3.75	3.08	3.06	3.09	3.29
Nd_2O_3	15.53	13.74	15.10	14.61	14.32	13.18	14.98	14.78	16.51	14.48	13.65	15.12	12.48	12.62	13.99	14.24
Sm_2O_3	2.27	2.77	2.56	2.52	2.35	2.23	2.54	2.61	2.37	2.77	2.11	3.10	2.31	2.61	3.76	2.44
Gd_2O_3	1.39	1.75	1.34	1.08	1.69	2.07	1.14	1.02	0.61	1.65	1.47	1.53	1.98	1.86	2.78	1.74
Dy_2O_3	0.24	0.53	0.31	0.18	0.59	0.13	0.05	0.36	0.22	0.56	0.36	0.10	0.71	0.60	0.74	0.20
SO_2	0.21	0.05	0.07	0.54	0.04	0.38	0.31	0.14	0.20	0.03	0.45	0.04	0.16	0.20	0.05	0.04
CaO	1.45	0.27	0.89	1.82	0.42	1.30	1.69	1.19	1.68	0.25	1.30	0.35	0.99	1.11	0.30	0.68
PbO	0.33	0.50	0.21	0.30	0.27	0.31	0.29	0.41	0.47	0.40	0.46	0.47	0.28	0.17	0.28	0.16
Total	**99.82**	**98.83**	**98.95**	**98.05**	**98.70**	**98.05**	**98.52**	**98.72**	**99.38**	**99.28**	**98.63**	**98.90**	**98.33**	**98.19**	**99.47**	**99.21**
P	0.978	0.908	0.967	0.965	0.940	0.975	0.977	0.976	0.964	0.940	0.968	0.935	1.002	0.990	0.973	0.986
Si	0.022	0.096	0.036	0.023	0.069	0.015	0.022	0.031	0.032	0.069	0.018	0.075	0.012	0.009	0.037	0.023
Th	0.065	0.098	0.064	0.066	0.072	0.043	0.068	0.067	0.087	0.075	0.043	0.083	0.038	0.039	0.042	0.044
U	0.002	0.002	0.003	0.002	0.001	0.001	0.002	0.002	0.001	0.001	0.002	0.000	0.003	0.003	0.002	0.001
Ce	0.383	0.370	0.395	0.379	0.388	0.408	0.378	0.384	0.369	0.377	0.402	0.383	0.383	0.399	0.389	0.410
Y	0.013	0.045	0.018	0.012	0.039	0.019	0.015	0.013	0.008	0.047	0.018	0.021	0.040	0.028	0.032	0.014
La	0.145	0.144	0.152	0.150	0.154	0.185	0.140	0.146	0.129	0.145	0.181	0.139	0.180	0.186	0.164	0.177
Pr	0.049	0.048	0.049	0.049	0.043	0.040	0.049	0.055	0.051	0.052	0.051	0.055	0.044	0.044	0.044	0.047
Nd	0.217	0.200	0.215	0.206	0.205	0.186	0.211	0.209	0.234	0.207	0.192	0.218	0.173	0.177	0.197	0.201
Sm	0.031	0.039	0.035	0.034	0.032	0.030	0.035	0.036	0.032	0.038	0.029	0.043	0.031	0.035	0.051	0.033
Gd	0.018	0.024	0.018	0.014	0.023	0.027	0.015	0.013	0.008	0.022	0.019	0.020	0.026	0.024	0.036	0.023
Dy	0.003	0.007	0.004	0.002	0.008	0.002	0.001	0.005	0.003	0.007	0.005	0.001	0.009	0.008	0.009	0.003
S^{6-}	0.008	0.002	0.002	0.020	0.002	0.014	0.011	0.005	0.007	0.001	0.017	0.002	0.006	0.007	0.002	0.001
Ca	0.061	0.012	0.038	0.077	0.018	0.055	0.072	0.051	0.071	0.011	0.055	0.015	0.041	0.047	0.013	0.029
Pb	0.004	0.005	0.002	0.003	0.003	0.003	0.003	0.004	0.005	0.004	0.005	0.005	0.003	0.002	0.003	0.002
Total	1.991	1.998	1.997	1.980	1.996	1.989	1.987	1.991	1.995	1.995	1.986	1.994	1.984	1.991	1.993	1.993
Σ(P)	0.998	0.996	0.996	1.012	0.989	1.013	0.999	0.990	1.006	0.987	1.017	0.986	0.976	0.999	0.984	0.985
Σ(T)	1.000	1.004	1.003	0.988	1.009	0.990	0.999	1.006	0.996	1.009	0.986	1.010	1.014	0.999	1.011	1.010
Σ(P-T)	0.00	0.01	0.01	0.02	0.02	0.02	0.00	0.02	0.01	0.02	0.03	0.02	0.04	0.00	0.03	0.02
(Ca + Si) excess	0.028	0.014	0.013	0.056	0.018	0.044	0.037	0.022	0.028	0.009	0.049	0.014	0.021	0.023	0.011	0.010
Crl	**13.2**	**3.5**	**8.1**	**13.9**	**4.2**	**9.0**	**14.4**	**11.1**	**15.7**	**2.9**	**9.3**	**4.1**	**8.1**	**8.5**	**3.1**	**6.1**
Htn	**0.2**	**8.4**	**2.6**	**0.0**	**5.3**	**0.0**	**0.0**	**1.4**	**1.2**	**6.1**	**0.0**	**6.3**	**0.0**	**0.0**	**2.8**	**1.5**
Mnz	**86.6**	**88.1**	**89.2**	**86.1**	**90.5**	**91.0**	**85.6**	**87.5**	**83.1**	**90.9**	**90.7**	**89.6**	**91.9**	**91.5**	**94.1**	**92.4**

Tab. 1: continued

Grain	1029-48a	1029-48b	1029-48c	1029-48d	1029-48e	1029-48f	1029-48g	1029-51	1029-56a	1029-56b	1029-56c	1029-56d	1029-56e	1029-56f	1029-56g	1029-56h
Group	D2	D1	D2	D1	D3	D2	D3	D2	D2	D2	D3	D2	D2	D2	D2	D2
P_2O_5	29.14	29.20	28.22	29.07	27.17	28.42	26.22	29.36	29.38	28.58	27.06	29.46	29.19	29.94	29.73	29.42
SiO_2	0.44	0.47	0.75	0.27	1.78	1.07	2.28	0.54	0.39	1.00	1.98	0.36	0.86	0.37	0.65	0.58
ThO_2	4.62	4.52	9.08	4.99	8.65	8.05	10.88	6.60	4.77	9.71	8.75	3.91	7.18	4.90	4.85	6.98
UO_2	0.17	0.14	0.15	0.10	0.20	0.12	0.21	0.16	0.08	0.09	0.10	0.22	0.28	0.23	0.22	0.25
Ce_2O_3	27.59	27.85	25.29	27.92	26.13	26.22	25.77	26.09	28.31	25.11	26.39	28.23	26.92	27.84	26.92	26.26
Y_2O_3	0.97	1.03	0.45	0.64	0.74	0.70	0.68	0.42	0.79	0.34	0.71	1.22	0.73	0.71	1.46	0.70
La_2O_3	12.04	12.08	8.64	12.26	9.45	9.68	9.02	10.36	12.61	8.63	10.10	13.08	10.37	11.79	12.63	10.10
Pr_2O_3	3.36	3.52	3.66	3.45	3.40	3.28	3.13	3.62	3.19	3.74	3.45	3.52	3.50	3.13	3.24	3.54
Nd_2O_3	13.27	13.78	16.30	13.48	16.02	15.56	15.93	15.10	14.05	16.31	15.59	12.79	14.97	14.59	12.75	15.33
Sm_2O_3	2.35	2.04	2.38	2.13	2.16	2.34	1.78	2.48	2.02	1.95	2.42	2.72	2.36	2.80	2.35	1.99
Gd_2O_3	1.80	1.68	1.12	1.60	1.27	0.89	0.94	1.50	1.47	0.82	1.35	1.29	1.20	1.36	2.12	1.28
Dy_2O_3	0.39	0.42	0.05	0.34	0.00	0.10	0.28	0.21	0.10	0.00	0.17	0.36	0.18	0.05	0.44	0.12
SO_2	0.72	0.72	0.27	0.66	0.05	0.16	0.04	0.46	0.28	0.19	0.04	0.40	0.16	0.34	0.14	0.42
CaO	1.51	1.48	1.63	1.55	0.36	1.11	0.31	1.75	1.14	1.64	0.29	1.23	1.20	1.30	1.08	1.78
PbO	0.31	0.31	0.53	0.39	0.37	0.29	0.50	0.29	0.30	0.62	0.41	0.14	0.18	0.24	0.29	0.28
Total	**98.65**	**99.23**	**98.52**	**98.34**	**97.74**	**97.98**	**97.96**	**98.95**	**98.12**	**98.74**	**98.82**	**98.41**	**99.28**	**99.57**	**98.37**	**99.04**
P	0.965	0.963	0.959	0.967	0.938	0.964	0.914	0.973	0.980	0.964	0.929	0.977	0.973	0.985	0.985	0.974
Si	0.017	0.018	0.030	0.011	0.073	0.043	0.094	0.021	0.016	0.040	0.080	0.014	0.034	0.014	0.025	0.023
Th	0.041	0.040	0.083	0.045	0.080	0.073	0.102	0.059	0.043	0.088	0.081	0.035	0.064	0.043	0.043	0.062
U	0.001	0.001	0.001	0.001	0.002	0.001	0.002	0.001	0.001	0.001	0.001	0.002	0.002	0.002	0.002	0.002
Ce	0.395	0.397	0.372	0.402	0.390	0.385	0.389	0.374	0.408	0.366	0.392	0.405	0.388	0.396	0.386	0.376
Y	0.020	0.021	0.010	0.013	0.016	0.015	0.015	0.009	0.016	0.007	0.015	0.025	0.015	0.015	0.030	0.015
La	0.174	0.174	0.128	0.178	0.142	0.143	0.137	0.150	0.183	0.127	0.151	0.189	0.151	0.169	0.182	0.146
Pr	0.048	0.050	0.054	0.049	0.051	0.048	0.047	0.052	0.046	0.054	0.051	0.050	0.050	0.044	0.046	0.050
Nd	0.185	0.192	0.234	0.189	0.233	0.223	0.234	0.211	0.198	0.232	0.226	0.179	0.210	0.203	0.178	0.214
Sm	0.032	0.027	0.033	0.029	0.030	0.032	0.025	0.033	0.027	0.027	0.034	0.037	0.032	0.037	0.032	0.027
Gd	0.023	0.022	0.015	0.021	0.017	0.012	0.013	0.019	0.019	0.011	0.018	0.017	0.016	0.018	0.027	0.017
Dy	0.005	0.005	0.001	0.004	0.000	0.001	0.004	0.003	0.001	0.000	0.002	0.004	0.002	0.001	0.006	0.001
S^{6-}	0.026	0.026	0.010	0.024	0.002	0.006	0.002	0.017	0.010	0.007	0.002	0.015	0.006	0.012	0.005	0.016
Ca	0.063	0.062	0.070	0.065	0.016	0.047	0.014	0.073	0.048	0.070	0.013	0.051	0.051	0.054	0.045	0.075
Pb	0.003	0.003	0.006	0.004	0.004	0.003	0.006	0.003	0.003	0.007	0.005	0.002	0.002	0.003	0.003	0.003
Total	1.973	1.974	1.995	1.978	1.992	1.990	1.995	1.982	1.990	1.993	1.996	1.987	1.990	1.984	1.992	1.983
Σ(P)	1.017	1.020	1.015	1.024	0.983	0.989	0.988	1.005	1.004	0.996	0.989	1.010	0.990	0.997	0.986	1.003
Σ(T)	0.982	0.981	0.989	0.978	1.011	1.007	1.008	0.994	0.996	1.003	1.009	0.991	1.006	1.000	1.011	0.996
Σ(P-T)	0.04	0.04	0.03	0.05	0.03	0.02	0.02	0.01	0.01	0.01	0.02	0.02	0.02	0.00	0.02	0.01
(Ca + Si) excess	0.067	0.068	0.032	0.059	0.012	0.025	0.011	0.055	0.034	0.035	0.018	0.045	0.026	0.038	0.034	0.052
Crl	**8.8**	**8.6**	**15.7**	**9.4**	**3.9**	**10.3**	**3.9**	**12.4**	**8.9**	**15.7**	**3.5**	**7.5**	**10.7**	**9.2**	**9.2**	**13.2**
Htn	**0.0**	**0.0**	**0.9**	**0.0**	**6.2**	**2.4**	**8.5**	**0.0**	**0.0**	**1.3**	**6.5**	**0.0**	**1.4**	**0.0**	**0.0**	**0.0**
Mnz	**91.2**	**91.4**	**83.4**	**90.6**	**89.8**	**87.3**	**87.7**	**87.6**	**91.1**	**83.1**	**90.0**	**92.5**	**87.9**	**90.8**	**90.8**	**86.8**

Tab. 1: continued

Grain	1029-56i	1029-56j	1029-56k	1029-57	1029-57b	1029-57c	1029-57d	1029-57e	1029-57f	1029-57g	1029-57h	1029-57i	1029-57j	1029-57k	1029-57l	1029-57m
Group	D3	D3	D2	D3	D3	D2	D2	D2	D2	D3	D2	D2	D2	D3	D3	D2
P_2O_5	27.78	27.47	29.67	27.74	28.32	29.81	28.96	29.37	29.24	28.68	29.55	29.98	30.01	29.18	28.40	29.75
SiO_2	1.83	1.90	0.38	1.50	1.23	0.32	0.61	0.50	0.55	1.15	0.64	0.52	0.30	1.12	1.52	0.32
ThO_2	8.29	8.65	4.83	7.89	6.13	4.15	6.98	6.36	6.18	5.48	6.41	5.88	3.93	5.58	7.32	3.88
UO_2	0.16	0.11	0.02	0.15	0.15	0.23	0.11	0.12	0.15	0.10	0.19	0.03	0.27	0.00	0.15	0.21
Ce_2O_3	26.55	26.05	27.19	25.46	27.13	28.21	26.09	27.09	26.94	27.25	26.73	26.91	27.48	26.48	25.62	28.10
Y_2O_3	0.78	0.67	0.66	1.66	1.40	1.39	0.68	0.91	0.97	1.86	0.65	1.12	1.43	1.88	1.38	1.43
La_2O_3	9.87	9.54	11.54	9.62	10.43	13.07	10.27	10.82	10.76	10.86	10.79	11.24	13.20	10.48	9.81	13.54
Pr_2O_3	3.43	3.86	3.70	3.11	3.59	3.22	3.34	3.65	3.33	3.56	3.77	3.31	3.23	3.54	3.61	3.27
Nd_2O_3	15.59	15.85	14.27	15.66	15.51	12.74	14.82	14.40	14.81	14.45	15.19	14.02	13.20	14.97	16.13	12.57
Sm_2O_3	2.43	2.56	2.15	2.89	2.66	2.12	2.89	2.41	2.44	2.83	2.89	2.41	2.10	2.69	2.84	2.10
Gd_2O_3	1.76	0.99	1.52	2.05	1.54	1.78	1.57	1.57	1.31	1.70	1.21	1.53	1.88	2.14	1.81	1.68
Dy_2O_3	0.15	0.15	0.13	0.55	0.43	0.33	0.23	0.21	0.24	0.49	0.17	0.36	0.44	0.43	0.28	0.51
SO_2	0.03	0.04	0.43	0.03	0.03	0.22	0.25	0.24	0.17	0.03	0.12	0.12	0.26	0.06	0.02	0.23
CaO	0.32	0.28	1.50	0.41	0.37	1.09	1.42	1.25	1.19	0.31	1.10	1.05	1.14	0.28	0.35	1.05
PbO	0.54	0.41	0.29	0.27	0.35	0.26	0.35	0.19	0.41	0.24	0.40	0.32	0.36	0.30	0.35	0.16
Total	**99.52**	**98.50**	**98.28**	**98.96**	**99.27**	**98.44**	**98.54**	**99.08**	**98.68**	**98.97**	**99.80**	**98.77**	**99.23**	**99.12**	**99.59**	**98.04**
P	0.941	0.939	0.984	0.945	0.957	0.988	0.974	0.979	0.980	0.964	0.981	0.994	0.990	0.973	0.954	0.987
Si	0.073	0.077	0.015	0.060	0.049	0.013	0.024	0.019	0.022	0.046	0.025	0.020	0.012	0.044	0.060	0.013
Th	0.075	0.079	0.043	0.072	0.056	0.037	0.063	0.057	0.056	0.050	0.057	0.052	0.035	0.050	0.066	0.035
U	0.001	0.001	0.000	0.001	0.001	0.002	0.001	0.001	0.001	0.001	0.002	0.000	0.002	0.000	0.001	0.002
Ce	0.389	0.385	0.390	0.375	0.396	0.404	0.379	0.390	0.390	0.396	0.384	0.386	0.392	0.382	0.372	0.403
Y	0.017	0.014	0.014	0.035	0.030	0.029	0.014	0.019	0.020	0.039	0.013	0.023	0.030	0.039	0.029	0.030
La	0.146	0.142	0.167	0.143	0.154	0.189	0.150	0.157	0.157	0.159	0.156	0.162	0.190	0.152	0.144	0.196
Pr	0.050	0.057	0.053	0.046	0.052	0.046	0.048	0.052	0.048	0.051	0.054	0.047	0.046	0.051	0.052	0.047
Nd	0.223	0.229	0.200	0.225	0.221	0.178	0.210	0.202	0.209	0.205	0.213	0.196	0.184	0.211	0.229	0.176
Sm	0.033	0.036	0.029	0.040	0.037	0.029	0.039	0.033	0.033	0.039	0.039	0.033	0.028	0.037	0.039	0.028
Gd	0.023	0.013	0.020	0.027	0.020	0.023	0.021	0.021	0.017	0.022	0.016	0.020	0.024	0.028	0.024	0.022
Dy	0.002	0.002	0.002	0.007	0.006	0.004	0.003	0.003	0.003	0.006	0.002	0.004	0.005	0.005	0.004	0.006
S^{6-}	0.001	0.001	0.016	0.001	0.001	0.008	0.009	0.009	0.006	0.001	0.005	0.004	0.010	0.002	0.001	0.009
Ca	0.014	0.012	0.063	0.017	0.016	0.046	0.060	0.053	0.050	0.013	0.046	0.044	0.048	0.012	0.015	0.044
Pb	0.006	0.004	0.003	0.003	0.004	0.003	0.004	0.002	0.004	0.003	0.004	0.003	0.004	0.003	0.004	0.002
Total	1.993	1.991	1.982	1.997	1.998	1.991	1.991	1.989	1.993	1.995	1.992	1.987	1.988	1.987	1.992	1.990
Σ(P)	0.981	0.976	0.998	0.993	0.993	0.998	1.003	0.999	0.997	0.986	0.991	0.976	0.997	0.972	0.979	0.999
Σ(T)	1.014	1.016	0.999	1.005	1.006	1.001	0.998	0.999	1.002	1.010	1.006	1.015	1.001	1.017	1.015	1.000
Σ(P-T)	0.03	0.04	0.001	0.01	0.01	0.00	0.01	0.00	0.00	0.02	0.02	0.04	0.00	0.05	0.04	0.00
(Ca + Si) excess	0.017	0.014	0.053	0.008	0.013	0.030	0.033	0.025	0.026	0.012	0.021	0.019	0.035	0.011	0.012	0.030
Crl	**3.9**	**3.3**	**8.8**	**4.1**	**3.9**	**7.9**	**13.2**	**11.2**	**11.2**	**3.1**	**10.1**	**9.5**	**7.5**	**2.9**	**3.7**	**7.4**
Htn	**5.7**	**6.4**	**0.0**	**5.3**	**3.8**	**0.0**	**0.0**	**0.3**	**0.2**	**3.5**	**0.9**	**0.5**	**0.0**	**3.5**	**4.9**	**0.0**
Mnz	**90.3**	**90.4**	**91.2**	**90.6**	**92.3**	**92.1**	**86.8**	**88.5**	**88.6**	**93.4**	**89.0**	**90.0**	**92.5**	**93.6**	**91.4**	**92.6**

Tab. 2: LA-ICP-MS chemical analysis of the full suite of REE and selected trace elements in ppm

Name	Gp	^{238}U	^{208}Pb	^{232}Th	^{31}P	^{44}Ca	^{88}Sr	^{89}Y	^{139}La	^{140}Ce	^{141}Pr	^{146}Nd	^{147}Sm	^{153}Eu	^{157}Gd	^{159}Tb	^{163}Dy	^{165}Ho	^{166}Er	^{169}Tm	^{172}Yb	^{175}Lu
17-6	*D1*	2809	2262	40679	627627	13094	14.1	7610	102322	216793	26557	113172	22273	786	18176	1415	3725	285	296	15	45	3.1
17-7	*D1*	2894	2733	50024	670109	12619	14.3	8709	102322	229829	28258	124655	24302	789	18876	1496	4075	335	338	17	50	3.6
17-8	*D1*	3006	2301	41641	638928	12933	16.6	8469	102322	221001	26722	114277	22933	818	19147	1518	4034	324	324	16	48	3.2
17-9	*D1*	3097	2264	40984	638690	12611	14.6	9706	102322	219861	26392	110694	22291	853	18881	1594	4538	373	378	19	53	3.3
57-7	*D2*	878	2269	48546	629773	9142	7.4	9504	93795	212699	27837	122663	22635	495	15046	1191	3662	380	503	33	107	9.1
57-10	*D2*	1526	2741	57511	604293	9773	5.8	5514	85268	202648	27084	124306	23643	364	13962	954	2506	220	252	14	46	3.5
56-12	*D2*	1396	2917	58761	699505	13759	13.5	6650	102322	239313	31559	141673	25673	527	15955	1134	3001	264	301	17	56	4.6
56-13	*D2*	2410	3616	72642	728489	16272	16.7	7865	102322	248958	33296	151044	28168	650	17003	1224	3358	304	351	21	70	5.6
48-4	*D2*	2105	2107	39885	655513	20947	13.9	7988	102322	218875	27052	116115	22331	745	17163	1312	3810	329	360	20	61	4.7
48-5	*D2*	2165	2124	39722	670360	19912	16.4	8214	102322	222557	27595	115345	23116	776	18039	1411	3975	344	365	20	62	4.7
48-6	*D2*	2245	2045	37863	653616	17827	14.8	8131	102322	214363	26404	112452	21944	791	17706	1408	3896	339	363	20	59	4.5
48-7	*D2*	1439	3530	70319	650696	14054	6.2	5959	85268	212120	29548	137152	23264	359	13137	947	2730	250	287	17	53	4.3
48-8	*D2*	1262	3831	74620	664121	15607	8.3	5588	85268	214137	30233	143875	23728	362	12900	916	2528	235	267	15	47	3.8
107-10	*D2*	4064	2266	41302	661719	13882	15.9	14574	102322	211488	25765	109185	22785	1261	20535	1884	5911	574	682	44	149	12.3
37-11	*D2*	1457	3262	62787	662425	14524	10.0	5585	85268	211740	29093	132952	23427	361	13211	899	2484	235	284	17	57	4.7
37-12	*D2*	720	4819	89835	729329	17814	15.0	4599	85268	225043	33435	163084	26554	316	11871	743	2045	191	241	14	50	4.1
37-13	*D2*	1231	5199	97583	872656	23688	19.8	5575	102322	275200	39636	189383	32443	412	15145	944	2525	234	282	17	57	4.6
57-8	*D2*	1689	1822	38019	580954	6416	7.6	11531	93795	202040	25550	109244	21085	572	16263	1384	4351	441	563	36	129	10.6
44-14	*D2*	3519	1924	38987	635904	7915	8.4	12015	102322	219191	26527	113004	23130	1120	19774	1765	5199	481	537	31	95	7.3
44-16	*D2*	3632	1898	38057	630447	7628	8.8	11269	102322	218455	26316	112735	22921	1245	19412	1661	4890	457	510	29	89	6.4
107-9	*D2*	3463	1955	35492	634979	12832	14.0	12869	102322	206546	24930	105028	21007	1051	19069	1741	5393	499	550	32	105	8.6
57-9	*D3*	964	2328	49212	635557	3053	1.8	16043	93795	220434	28834	129393	25319	247	19582	1702	5716	632	852	56	189	15.6
56-11	*D3*	845	3590	74824	606855	2962	1.6	6119	85268	218225	30090	140447	25172	121	14033	967	2656	254	313	19	62	5.4
17-10	*D3*	588	3833	76586	708211	5568	3.8	14084	85268	222447	32893	165432	35152	151	24642	1860	5686	571	738	46	154	12.1
17-11	*D3*	978	4934	96829	745844	9029	11.1	12299	85268	239221	34793	172625	32467	271	20088	1546	4890	506	646	40	126	10.1
17-12	*D3*	917	3351	65984	622720	2943	3.0	10839	85268	207037	28914	140078	28682	347	20223	1512	4422	440	556	36	117	9.6
17-13	*D3*	799	5643	111328	773999	7927	5.9	13982	85268	248127	37129	191521	37431	287	24035	1766	5491	560	730	47	151	11.8
17-14	*D3*	1517	6309	124154	988363	8649	7.6	16113	119376	323362	47152	237030	46347	454	30676	2189	6518	654	831	52	168	13.6

Tab. 3: U–Th–Pb isotopic ratio and date measured by LA-ICP-MS

			Isotope ratio[a]									Dates								
Grain n°	Textural position	Gp	$^{207}Pb/^{206}Pb$	2s %	$^{207}Pb/^{235}U$	2s %	$^{206}Pb/^{238}U$	2s %	Rho	$^{208}Pb/^{232}Th$	2s %	$^{207}Pb/^{206}Pb$	2s abs	$^{207}Pb/^{235}U$	2s abs	$^{206}Pb/^{238}U$	2s abs	$^{208}Pb/^{232}Th$	2s abs	% conc.[b]
1029-26d	in Grt I	*D3*	0.0710	3.0	1.489	3.7	0.1523	3.2	0.86	0.0440	2.7	956	29	926	35	914	29	871	23	95.6
1029-17i	mineral separate	*D3*	0.0700	2.9	1.493	3.7	0.1547	3.4	0.91	0.0476	3.1	928	27	927	35	927	32	941	29	99.9
1029-03b	in opx II	*D3*	0.0709	3.0	1.514	3.8	0.1550	3.2	0.86	0.0441	2.7	954	29	936	35	929	30	873	23	97.4
1029-44b	n garnet I (fracture	*D3*	0.0701	2.7	1.515	3.5	0.1568	3.2	0.91	0.0445	2.6	931	25	936	33	939	30	879	23	100.9
1029-44c	n garnet I (fracture	*D3*	0.0705	2.7	1.534	3.5	0.1578	3.2	0.90	0.0452	2.6	943	26	944	33	945	30	893	23	100.2
1029-48e	in opx	*D3*	0.0711	2.9	1.523	3.7	0.1554	3.2	0.88	0.0467	2.6	960	28	940	34	931	30	922	24	97.0
1029-04a	partly in opx	*D3*	0.0704	3.0	1.519	3.8	0.1566	3.2	0.86	0.0456	2.7	939	28	938	35	938	30	902	24	99.9
1029-56i**	in osm	*D3*	0.0721	3.3	1.561	4.0	0.1570	3.2	0.82	0.0475	2.6	990	33	955	38	940	30	938	24	94.9
1029-56j	in osm	*D3*	0.0703	3.1	1.516	3.8	0.1564	3.2	0.84	0.0475	2.6	936	29	937	36	937	30	938	24	100.1
1029-57e	partly in Hc	*D3*	0.0708	3.1	1.506	3.8	0.1544	3.2	0.84	0.0442	2.6	950	30	933	36	925	30	873	23	97.4
1029-57h	partly in Hc	*D3*	0.0709	2.9	1.508	3.7	0.1543	3.2	0.88	0.0441	2.6	955	27	934	34	925	30	872	23	96.9
1029-57i	partly in Hc	*D3*	0.0702	3.1	1.495	3.8	0.1545	3.2	0.85	0.0436	2.6	934	29	928	35	926	30	862	22	99.2
1029-37	partly in Hc	*D3a*	0.0710	3.0	1.562	3.8	0.1597	3.2	0.86	0.0451	2.6	956	29	955	36	955	31	891	24	99.9
1029-17e	mineral separate	*D3a*	0.0698	3.5	1.517	4.1	0.1577	3.4	0.83	0.0478	3.1	922	32	937	39	944	32	943	29	102.4
1029-17g	mineral separate	*D3a*	0.0710	3.1	1.545	3.9	0.1579	3.4	0.88	0.0469	3.1	957	30	949	37	945	32	926	29	98.8
1029-17h	mineral separate	*D3a*	0.0737	3.6	1.621	4.2	0.1596	3.5	0.82	0.0474	3.1	1033	37	978	41	954	33	936	29	92.4
1029-26b	gt-II corrona	*D3a*	0.0699	3.1	1.498	3.8	0.1554	3.2	0.85	0.0443	2.6	927	29	930	36	931	30	876	23	100.5
1029-48f	in opx	*D3a*	0.0705	3.0	1.485	3.7	0.1528	3.2	0.87	0.0454	2.6	943	28	924	34	917	29	897	24	97.2
1029-57k	partly in Hc	*D3a*	0.0706	3.0	1.504	3.8	0.1544	3.2	0.85	0.0443	2.6	947	29	932	35	926	30	875	23	97.8
1029-57l	partly in Hc	*D3a*	0.0690	3.0	1.475	3.8	0.1552	3.2	0.85	0.0445	2.6	897	27	920	35	930	30	880	23	103.7
1029-00	in opx	*D2*	0.0729	2.8	1.688	3.6	0.1680	3.2	0.90	0.0471	2.7	1010	28	1004	36	1001	32	931	25	99.1
1029-19	in opx	*D2*	0.0738	2.9	1.674	3.7	0.1644	3.2	0.88	0.0468	2.6	1037	30	999	36	981	32	924	24	94.6
1029-21**	partly in opx	*D2*	0.0723	2.7	1.549	3.6	0.1554	3.2	0.90	0.0473	2.7	995	27	950	34	931	30	934	25	93.6
1029-48	in opx	*D2*	0.0732	2.8	1.676	3.6	0.1662	3.2	0.89	0.0471	2.6	1018	29	999	36	991	32	930	24	97.3
1029-107	in garnet I	*D2*	0.0729	2.7	1.692	3.5	0.1684	3.2	0.91	0.0488	2.6	1011	27	1006	35	1003	32	964	25	99.2
1029-107	in garnet I	*D2*	0.0729	2.7	1.683	3.7	0.1674	3.2	0.91	0.0491	2.6	1011	27	1002	35	998	32	968	26	98.7
1029-107	in garnet I	*D2*	0.0735	2.7	1.722	3.5	0.1701	3.2	0.91	0.0494	2.6	1026	28	1017	36	1013	32	974	26	98.7
1029-26e	in garnet I	*D2*	0.0736	2.7	1.712	3.5	0.1688	3.2	0.91	0.0486	2.6	1030	28	1013	36	1005	32	959	25	97.6
1029-01a	partly in Hc	*D2*	0.0731	2.7	1.724	3.6	0.1711	3.2	0.90	0.0483	2.6	1016	28	1017	36	1018	33	954	25	100.2
1029-36a	in feldspar	*D2*	0.0724	2.8	1.684	3.6	0.1688	3.2	0.89	0.0470	2.6	996	28	1002	36	1005	32	928	24	100.9
1029-03a	in opx II	*D2*	0.0742	2.7	1.722	3.5	0.1683	3.2	0.91	0.0498	2.7	1047	28	1017	36	1003	32	981	26	95.8
1029-03c	in opx II	*D2*	0.0734	2.7	1.710	3.5	0.1691	3.2	0.91	0.0495	2.7	1024	28	1012	36	1007	32	977	26	98.4
1029-40c	in opx	*D2*	0.0730	2.8	1.708	3.6	0.1698	3.2	0.89	0.0482	2.6	1013	28	1012	37	1011	33	951	25	99.9
1029-41f	in opx	*D2*	0.0726	2.8	1.615	3.6	0.1614	3.2	0.88	0.0475	2.6	1003	29	976	36	965	31	938	25	96.2
1029-48a	in opx	*D2*	0.0730	2.8	1.693	3.6	0.1682	3.2	0.89	0.0482	2.6	1014	28	1006	36	1002	32	951	25	98.8
1029-48a	in opx	*D2*	0.0721	2.8	1.644	3.6	0.1653	3.2	0.89	0.0474	2.6	990	28	987	36	986	32	936	24	99.7
1029-56f	in osm	*D2*	0.0733	2.9	1.651	3.7	0.1634	3.2	0.87	0.0466	2.6	1022	30	990	36	976	31	920	24	95.5
1029-56k	in osm	*D2*	0.0732	2.7	1.745	3.5	0.1728	3.2	0.91	0.0496	2.6	1021	28	1025	36	1028	33	979	25	100.7
1029-01b	partly in Hc	*D2a*	0.0774	3.4	1.789	4.1	0.1677	3.3	0.80	0.0516	2.6	1130	39	1041	42	1000	33	1016	27	88.5
1029-36d	in feldspar	*D2a*	0.0733	2.7	1.715	3.5	0.1696	3.2	0.91	0.0486	2.6	1023	28	1014	36	1010	32	959	25	98.7
1029-37e	partly in Hc	*D2a*	0.0747	3.2	1.719	3.9	0.1669	3.2	0.82	0.0502	2.6	1060	34	1016	40	995	32	991	26	93.9
1029-40e	in opx	*D2a*	0.0728	2.9	1.684	3.7	0.1677	3.2	0.87	0.0475	2.6	1009	29	1003	37	1000	32	937	25	99.0
1029-41e	in opx	*D2a*	0.0736	2.8	1.746	3.6	0.1722	3.2	0.89	0.0490	2.6	1029	29	1026	37	1024	33	968	25	99.5
1029-41e	in opx	*D2a*	0.0737	3.1	1.768	3.8	0.1739	3.2	0.84	0.0483	2.6	1035	32	1034	40	1034	33	953	25	99.9

Tab. 3: continued

			Isotope ratio[a]									Dates								
Grain n°	**Textural position**	**Gp**	**$^{207}Pb/^{206}Pb$**	**2s %**	**$^{207}Pb/^{235}U$**	**2s %**	**$^{206}Pb/^{238}U$**	**2s %**	**Rho**	**$^{208}Pb/^{232}Th$**	**2s %**	**$^{207}Pb/^{206}Pb$**	**2s abs**	**$^{207}Pb/^{235}U$**	**2s abs**	**$^{206}Pb/^{238}U$**	**2s abs**	**$^{208}Pb/^{232}Th$**	**2s abs**	**% conc.[b]**
1029-41j	in opx	*D2a*	0.0726	2.8	1.698	3.6	0.1698	3.2	0.88	0.0482	2.6	1001	29	1008	37	1011	33	951	25	100.9
1029-48d	in opx	*D2a*	0.0732	3.1	1.622	3.9	0.1607	3.2	0.84	0.0465	2.6	1020	32	979	38	961	31	918	24	94.2
1029-48	in opx	*D2a*	0.0731	3.2	1.666	3.9	0.1654	3.2	0.83	0.0501	2.6	1017	32	996	39	987	32	989	26	97.0
1029-04d	partly in opx	*D2a*	0.0721	2.7	1.612	3.5	0.1622	3.2	0.91	0.0478	2.7	989	27	975	34	969	31	944	25	98.0
1029-57j	partly in IIc	*D2a*	0.0730	2.7	1.712	3.5	0.1702	3.2	0.91	0.0483	2.6	1013	27	1013	36	1013	32	953	25	100.1
1029-26c	in garnet I	*D1*	0.0739	2.7	1.786	3.5	0.1752	3.2	0.91	0.0498	2.7	1040	28	1040	37	1041	33	982	26	100.1
1029-17a	mineral separate	*D1*	0.0736	2.6	1.793	3.5	0.1768	3.4	0.97	0.0518	3.1	1030	27	1043	36	1050	36	1020	32	101.9
1029-17a	mineral separate	*D1*	0.0737	2.6	1.792	3.5	0.1764	3.4	0.97	0.0523	3.1	1032	27	1042	37	1047	36	1030	32	101.5
1029-17b	mineral separate	*D1*	0.0739	2.6	1.788	3.5	0.1756	3.4	0.97	0.0519	3.1	1038	27	1041	36	1043	35	1024	32	100.5
1029-17b	mineral separate	*D1*	0.0729	2.6	1.781	3.5	0.1771	3.4	0.97	0.0520	3.1	1012	26	1038	36	1051	36	1025	32	103.8
1029-17c	mineral separate	*D1*	0.0726	2.6	1.787	3.5	0.1786	3.4	0.97	0.0517	3.1	1002	26	1041	36	1060	36	1018	31	105.7
1029-17d	mineral separate	*D1*	0.0739	2.6	1.795	3.5	0.1761	3.4	0.97	0.0518	3.1	1039	27	1044	36	1046	35	1020	32	100.6
1029-17f	mineral separate	*D1*	0.0735	2.6	1.784	3.5	0.1761	3.4	0.97	0.0517	3.1	1027	27	1040	36	1046	35	1020	32	101.8
1029-48b	in opx	*D1*	0.0746	2.8	1.782	3.6	0.1733	3.2	0.90	0.0488	2.6	1057	29	1039	37	1030	33	963	25	97.5
1029-48d	in opx	*D1*	0.0747	3.0	1.785	3.7	0.1735	3.2	0.86	0.0482	2.6	1059	31	1040	39	1031	33	952	25	97.4

[a] *No common Pb correction was applied*

[**] *Grains not used for age calculation*

Tab. 3: continued

			(ppm)			Chemical composition*								
Grain n°	**Textural position**	**Gp**	**^{232}Th**	**^{238}U**	**Th/U**	**Y_2O_3**	**ThO_2**	**SiO_2**	**UO_2**	**Nd_2O_3**	**Gd_2O_3**	**Dy_2O_3**	**CaO**	**SO_2**
1029-26d	in Grt I	*D3*	45182	1739	26	2.56	5.39	1.10	0.74	15.08	2.15	0.66	0.27	0.02
1029-17i	mineral separate	*D3*	94171	1740	54	0.42	8.49	0.66	0.23	15.47	1.00	0.15	1.65	0.19
1029-03b	in opx II	*D3*	45931	1559	29	2.24	5.23	1.08	0.19	13.94	2.50	0.74	0.32	0.01
1029-44b	in garnet I (fracture)	*D3*	39960	4366	9	1.54	4.63	0.94	0.19	13.99	2.78	0.74	0.30	0.05
1029-44c	in garnet I (fracture)	*D3*	40552	4090	10	0.66	4.93	0.59	0.15	14.24	1.74	0.20	0.68	0.04
1029-48e	in opx	*D3*	71712	2031	35	0.74	8.65	1.78	0.20	16.02	1.27	0.00	0.36	0.05
1029-04a	partly in opx	*D3*	64707	1259	51	1.57	7.58	1.46	0.21	15.97	1.96	0.53	0.44	0.04
1029-56i**	in osm	*D3*	77451	875	89	0.78	8.29	1.83	0.16	15.54	1.75	0.15	0.32	0.03
1029-56j	in osm	*D3*	79466	1011	79	0.67	8.65	1.90	0.11	15.54	0.99	0.15	0.28	0.04
1029-57e	partly in Hc	*D3*	55342	1104	50	0.91	6.36	0.50	0.12	14.69	1.57	0.21	1.25	0.12
1029-57h	partly in Hc	*D3*	56553	2048	28	0.64	6.41	0.64	0.19	15.19	1.21	0.17	1.10	0.12
1029-57i	partly in Hc	*D3*	49413	1232	40	1.12	5.88	0.52	0.03	14.16	1.53	0.36	1.05	0.12
1029-37	partly in Hc	*D3a*	59712	1790	33	0.89	5.22	0.49	0.22	13.78	1.24	0.38	0.99	0.18
1029-17e	mineral separate	*D3a*	77428	595	130	1.59	8.54	1.64	0.06	17.04	1.95	0.31	0.50	0.09
1029-17g	mineral separate	*D3a*	74605	1103	68	1.31	7.80	1.69	0.10	15.84	1.78	0.50	0.28	0.03
1029-17h	mineral separate	*D3a*	86220	692	125	1.39	8.43	1.66	0.08	16.53	1.91	0.39	0.48	0.07
1029-26b	gt-II corrona	*D3a*	50069	1317	38	2.01	6.55	1.26	0.02	14.67	2.27	0.49	0.30	0.03
1029-48f	in opx	*D3a*	75004	2073	36	0.70	8.05	1.07	0.12	15.56	0.59	0.10	1.11	0.04
1029-57k	partly in Hc	*D3a*	46529	1161	40	1.88	5.58	1.12	0.01	14.38	2.14	0.43	0.28	0.06
1029-57l	partly in Hc	*D3a*	57747	1128	51	1.38	7.32	1.52	0.15	16.13	1.81	0.28	0.35	0.02
1029-00	in opx	*D2*	40490	3896	10	1.50	4.38	0.32	0.30	13.14	2.19	0.45	1.12	0.22
1029-19	in opx	*D2*	44787	2552	18	1.28	4.67	0.60	0.31	13.55	2.00	0.24	1.04	0.18
1029-21**	partly in opx	*D2*	43447	6265	7	2.05	4.72	0.31	0.33	12.73	2.22	0.69	1.18	0.21
1029-48	in opx	*D2*	44053	2943	15	0.84	4.58	0.43	n.a	n.a	n.a	n.a	1.49	0.55
1029-107	in garnet I	*D2*	38375	5055	8	1.15	4.23	0.30	0.29	12.63	2.09	0.49	1.17	0.34
1029-107	in garnet I	*D2*	38322	5219	7	1.15	4.23	0.30	0.29	12.63	2.09	0.49	1.17	0.34
1029-107	in garnet I	*D2*	38643	4919	8	1.15	4.23	0.30	0.29	12.63	2.09	0.49	1.17	0.34
1029-26e	in garnet I	*D2*	36888	4892	8	1.43	4.56	0.54	0.09	13.51	1.86	0.41	0.75	0.19
1029-01a	partly in Hc	*D2*	41939	3850	11	1.57	4.79	0.31	0.26	12.868	1.91	0.33	1.28	0.22
1029-36a	in feldspar	*D2*	41071	2689	15	0.69	5.02	0.40	0.18	13.90	1.73	0.24	1.31	0.36
1029-03a	in opx II	*D2*	38884	5119	8	1.64	5.05	0.32	0.30	12.64	2.00	0.50	1.29	0.25
1029-03c	in opx II	*D2*	36339	4983	7	1.91	4.64	0.30	0.29	12.80	1.79	0.49	1.21	0.20
1029-40c	in opx	*D2*	41364	2439	17	1.11	4.45	0.34	0.19	13.17	1.67	0.38	1.20	0.33
1029-41f	in opx	*D2*	66026	2087	32	0.72	7.62	0.55	0.20	14.96	1.14	0.05	1.69	0.31
1029-48a	in opx	*D2*	45821	2666	17	0.97	4.62	0.44	0.17	13.27	1.80	0.39	1.51	0.71
1029-48a	in opx	*D2*	46606	2516	19	0.97	4.62	0.44	0.17	13.27	1.80	0.39	1.51	0.66
1029-56f	in osm	*D2*	40733	1573	26	0.71	4.90	0.37	0.23	14.05	1.35	0.05	1.30	0.34
1029-56k	in osm	*D2*	35477	4097	9	0.66	4.83	0.38	0.02	12.79	1.52	0.13	1.50	0.43
1029-01b	partly in Hc	*D2a*	83790	671	125	0.40	9.49	0.93	0.14	16.54	0.63	0.00	1.80	0.36
1029-36d	in feldspar	*D2a*	32921	4041	8	1.52	3.76	0.37	0.26	12.22	1.94	0.37	1.16	0.43
1029-37e	partly in Hc	*D2a*	72569	753	96	0.65	7.40	0.66	0.15	15.12	1.27	0.15	1.34	0.23
1029-40e	in opx	*D2a*	52632	1697	31	0.30	9.15	0.86	0.09	16.14	0.96	0.00	1.75	0.25
1029-41e	in opx	*D2a*	45323	1907	24	0.91	4.74	0.38	0.12	13.18	2.07	0.13	1.30	0.38
1029-41e	in opx	*D2a*	48376	1008	48	0.91	4.74	0.38	0.12	13.18	2.07	0.13	1.30	0.38

Tab. 3: continued

			(ppm)			Chemical composition*								
Grain n°	**Textural position**	**Gp**	**^{232}Th**	**^{238}U**	**Th/U**	**Y_2O_3**	**ThO_2**	**SiO_2**	**UO_2**	**Nd_2O_3**	**Gd_2O_3**	**Dy_2O_3**	**CaO**	**SO_2**
1029-41j	in opx	*D2a*	43598	1976	22	0.87	4.84	0.45	0.21	13.65	1.47	0.36	1.30	0.45
1029-48d	in opx	*D2a*	54230	1024	53	0.64	4.99	0.28	0.10	13.48	1.61	0.34	1.55	0.30
1029-48	in opx	*D2a*	71664	823	87	0.79	6.05	0.72	n.a	n.a	n.a	n.a	1.32	0.31
1029-04d	partly in opx	*D2a*	35393	5285	7	1.70	4.28	0.25	0.40	13.04	1.93	0.41	1.12	0.21
1029-57j	partly in IIc	*D2a*	31895	4512	7	1.43	3.93	0.30	0.27	14.16	1.88	0.44	1.14	0.26
1029-26c	in garnet I	*D1*	35562	4377	8	1.51	4.60	0.36	0.25	13.12	1.82	0.36	1.10	0.18
1029-17a	mineral separate	*D1*	41061	3668	11	0.86	4.79	0.39	0.30	12.94	1.65	0.32	1.55	0.42
1029-17a	mineral separate	*D1*	40455	3535	11	0.86	4.79	0.39	0.30	12.94	1.65	0.32	1.55	0.42
1029-17b	mineral separate	*D1*	41536	3704	11	0.87	4.73	0.39	0.12	13.19	1.74	0.65	1.43	0.45
1029-17b	mineral separate	*D1*	41736	3856	11	0.87	4.73	0.39	0.12	13.19	1.74	0.65	1.43	0.45
1029-17c	mineral separate	*D1*	40681	4104	10	0.87	4.70	0.39	0.25	13.12	2.03	0.37	1.40	0.44
1029-17d	mineral separate	*D1*	45395	4483	10	1.29	5.09	0.37	0.25	12.85	2.06	0.55	1.34	0.36
1029-17f	mineral separate	*D1*	41556	3691	11	0.79	4.60	0.38	0.23	13.37	1.58	0.39	1.48	0.58
1029-48b	in opx	*D1*	41469	2838	15	1.03	4.52	0.47	0.14	13.78	1.68	0.42	1.48	0.72
1029-48d	in opx	*D1*	47268	1217	39	0.64	4.99	0.28	0.10	13.48	1.61	0.34	1.55	0.66

**Chemical composition acquired by EPMA prior to laser ablation - full chemical analyses are available in Supplementary material and Tab. 1*

*** Grains not used for age calculation*

Tab. 4: U-Th-Pb abundance and date measured by EPMA

D1											Mole fraction		
Name	Y	inc. (95%)	U	inc. (95%)	Th	inc. (95%)	Pb	inc. (95%)	Age	inc. (95%)	Htn	Crl	Xtm
48_scan1	0.755	0.010	0.114	0.014	4.091	0.095	0.215	0.010	1059	53	1.6	5.6	2.1
48_scan1	0.780	0.010	0.117	0.014	4.066	0.095	0.206	0.010	1019	52	1.7	5.5	2.1
48_scan1	0.750	0.010	0.143	0.014	4.023	0.094	0.226	0.010	1105	54	1.7	5.3	2.1
48_scan1	0.834	0.010	0.149	0.014	3.738	0.088	0.200	0.010	1040	54	1.7	4.8	2.3
48_scan1	0.832	0.010	0.147	0.014	3.842	0.090	0.204	0.010	1036	55	1.7	5.0	2.3
48_scan1	0.820	0.010	0.143	0.014	3.754	0.088	0.199	0.010	1036	55	1.5	5.1	2.3
48_scan1	0.676	0.009	0.125	0.014	4.479	0.103	0.228	0.010	1028	52	1.7	6.2	1.9
48_scan1	0.585	0.009	0.126	0.014	4.552	0.105	0.232	0.010	1028	49	1.6	6.7	1.6
48_scan1	0.588	0.009	0.126	0.014	4.423	0.102	0.225	0.010	1024	51	1.6	6.4	1.6
48_scan1	0.600	0.009	0.117	0.014	4.482	0.103	0.221	0.010	1000	49	1.8	6.2	1.6
48_scan1	0.638	0.009	0.110	0.014	4.627	0.106	0.237	0.010	1047	50	1.8	6.4	1.8
48_scan1	0.785	0.010	0.118	0.014	4.325	0.100	0.210	0.010	985	48	1.8	5.8	2.2
48_scan1	0.667	0.009	0.106	0.014	4.142	0.096	0.205	0.010	1005	53	1.7	5.5	1.8
56_scan1	0.495	0.008	0.062	0.013	4.579	0.105	0.215	0.010	995	50	1.8	6.1	1.4
56_scan1	0.520	0.008	0.065	0.013	4.615	0.106	0.221	0.010	1011	50	2.3	5.4	1.4
56_scan1	0.499	0.008	0.070	0.013	4.736	0.108	0.220	0.010	979	49	2.0	6.2	1.4
56_scan1	0.362	0.007	0.067	0.013	5.855	0.131	0.282	0.010	1026	42	2.1	8.3	1.0
56_scan1	0.352	0.007	0.067	0.013	5.962	0.134	0.288	0.010	1030	42	2.1	8.5	1.0
56_scan1	0.364	0.007	0.061	0.013	5.327	0.120	0.255	0.010	1020	43	3.5	4.4	1.0
56_scan1	0.405	0.008	0.061	0.013	5.313	0.120	0.255	0.010	1021	46	2.1	7.0	1.1
56_scan1	0.342	0.007	0.063	0.013	5.747	0.129	0.277	0.010	1026	41	2.0	8.2	0.9
56_scan1	0.378	0.007	0.070	0.013	5.987	0.134	0.286	0.010	1016	41	2.3	8.3	1.0
56_scan1	0.367	0.007	0.060	0.013	6.018	0.135	0.286	0.010	1017	40	2.2	8.4	1.0
56_scan1	0.396	0.007	0.069	0.013	5.028	0.114	0.243	0.010	1023	48	1.9	6.9	1.1
56_scan2	0.500	0.008	0.068	0.013	4.275	0.099	0.207	0.010	1015	54	1.6	5.9	1.4
56_scan2	0.482	0.008	0.056	0.013	4.280	0.099	0.211	0.010	1043	54	1.6	6.0	1.3
56_scan2	0.460	0.008	0.065	0.013	4.301	0.100	0.217	0.010	1060	54	1.5	6.2	1.3
56_scan2	0.472	0.008	0.067	0.013	4.334	0.100	0.216	0.010	1046	53	1.6	6.0	1.3
56_scan2	0.512	0.008	0.063	0.013	4.321	0.100	0.216	0.010	1050	54	1.6	6.0	1.4
56_scan2	0.462	0.008	0.069	0.013	4.616	0.106	0.225	0.010	1023	51	1.8	6.2	1.3
56_scan2	0.466	0.008	0.057	0.013	4.632	0.106	0.231	0.010	1060	51	1.9	6.2	1.3
56_scan2	1.154	0.013	0.229	0.014	4.112	0.096	0.230	0.010	1036	49	1.9	5.3	3.2
56_scan2	1.233	0.013	0.225	0.014	3.965	0.093	0.221	0.010	1032	49	1.8	5.2	3.4
56_scan2	1.205	0.013	0.234	0.014	4.421	0.102	0.250	0.010	1055	46	2.4	5.0	3.3
56_scan2	1.170	0.013	0.220	0.014	4.177	0.097	0.237	0.010	1063	49	2.1	5.1	3.2
57_scan1	0.528	0.008	0.057	0.013	4.628	0.106	0.219	0.010	1005	52	1.4	7.0	1.4
57_scan1	0.479	0.008	0.049	0.013	4.537	0.104	0.216	0.010	1014	51	1.3	7.0	1.3
57_scan1	0.611	0.009	0.077	0.013	4.173	0.097	0.212	0.010	1056	54	1.4	6.2	1.7
57_scan1	0.633	0.009	0.103	0.014	4.107	0.096	0.216	0.010	1069	54	1.2	6.4	1.7
57_scan1	0.571	0.009	0.073	0.013	4.219	0.098	0.209	0.010	1035	55	1.5	6.1	1.6
57_scan1	0.579	0.009	0.094	0.013	4.103	0.096	0.205	0.010	1026	56	1.9	5.0	1.6
57_scan1	0.574	0.009	0.073	0.013	4.235	0.098	0.199	0.010	984	53	1.6	5.9	1.6
57_scan1	0.753	0.010	0.079	0.013	4.309	0.100	0.209	0.010	1008	53	1.9	5.5	2.1
57_scan1	1.008	0.012	0.098	0.013	4.103	0.096	0.208	0.010	1035	53	1.8	5.2	2.8
57_scan1	1.303	0.014	0.249	0.014	4.163	0.097	0.225	0.010	994	45	1.5	6.2	3.6
57_scan1	1.322	0.014	0.241	0.014	4.162	0.097	0.230	0.010	1020	48	1.6	6.0	3.6
57_scan1	1.350	0.014	0.255	0.014	4.147	0.096	0.238	0.010	1046	48	1.4	6.4	3.7
57_scan1	1.294	0.014	0.239	0.014	4.166	0.097	0.230	0.010	1022	48	1.5	6.3	3.6
57_scan1	1.256	0.014	0.232	0.014	4.093	0.095	0.234	0.010	1055	48	1.7	5.6	3.4

All concentrations are in Wt. %

The concentration of U and Pb have been corrected for intereference following U = U-96.6 ppm/wt%Th: Pb= Pb-83.55ppm/wt%Y - 16.5ppm/wt%Th

Tab. 4: continued

D2											Mole fraction		
Name	**Y**	**inc. (95%)**	**U**	**inc. (95%)**	**Th**	**inc. (95%)**	**Pb**	**inc. (95%)**	**Age**	**inc. (95%)**	**Htn**	**Crl**	**Xtm**
48_scan1	0.422	0.008	0.093	0.014	7.333	0.162	0.344	0.011	996	39	3.1	9.4	1.2
48_scan1	0.405	0.008	0.091	0.014	7.322	0.162	0.345	0.011	999	38	3.2	9.3	1.1
48_scan1	0.395	0.007	0.093	0.014	7.033	0.156	0.329	0.011	991	39	3.1	8.8	1.1
48_scan1	0.417	0.008	0.095	0.014	7.101	0.157	0.331	0.011	986	39	2.8	9.6	1.1
48_scan1	0.391	0.007	0.096	0.014	6.982	0.155	0.325	0.011	985	37	2.6	9.8	1.1
48_scan1	0.436	0.008	0.103	0.014	6.669	0.148	0.317	0.011	1001	41	2.6	9.2	1.2
48_scan1	0.385	0.007	0.107	0.014	6.583	0.146	0.315	0.011	1003	41	2.2	9.6	1.1
48_scan1	0.490	0.008	0.124	0.014	6.427	0.143	0.310	0.011	1003	41	2.6	8.7	1.3
48_scan1	0.330	0.007	0.053	0.014	6.530	0.145	0.295	0.011	975	41	2.8	8.3	0.9
48_scan1	0.391	0.007	0.083	0.014	7.207	0.159	0.342	0.011	1010	37	2.8	9.7	1.1
48_scan1	0.397	0.007	0.087	0.014	7.195	0.159	0.338	0.011	998	38	2.9	9.6	1.1
48_scan1	0.358	0.007	0.043	0.013	6.990	0.155	0.326	0.011	1017	41	2.7	9.4	1.0
56_scan1	0.345	0.007	0.056	0.013	5.929	0.133	0.279	0.010	1010	42	2.5	7.6	0.9
56_scan1	0.383	0.007	0.057	0.013	5.972	0.134	0.277	0.010	994	40	2.7	7.3	1.1
56_scan1	0.485	0.008	0.134	0.014	6.811	0.151	0.320	0.011	974	38	2.9	8.9	1.3
56_scan1	0.460	0.008	0.111	0.014	7.079	0.157	0.337	0.011	1002	38	2.8	9.5	1.3
56_scan2	0.279	0.007	0.054	0.014	7.697	0.169	0.364	0.011	1022	38	3.1	10.1	0.8
56_scan2	0.515	0.008	0.089	0.014	7.515	0.166	0.363	0.011	1028	38	3.3	9.4	1.4
56_scan2	0.465	0.008	0.102	0.014	6.597	0.147	0.332	0.011	1057	40	2.7	8.8	1.3
56_scan2	0.484	0.008	0.104	0.014	6.581	0.146	0.310	0.011	990	39	2.7	8.6	1.3
56_scan2	0.454	0.008	0.099	0.014	6.430	0.143	0.303	0.011	990	42	2.7	8.4	1.2
56_scan2	0.454	0.008	0.098	0.014	6.404	0.143	0.305	0.011	1001	41	2.6	8.5	1.2
56_scan2	0.477	0.008	0.121	0.014	6.839	0.152	0.314	0.011	959	38	3.0	8.7	1.3
56_scan2	0.465	0.008	0.130	0.014	6.916	0.153	0.329	0.011	989	40	2.8	9.3	1.3
56_scan2	0.508	0.008	0.124	0.014	6.912	0.153	0.326	0.011	985	40	2.8	9.2	1.4
56_scan2	0.471	0.008	0.112	0.014	6.860	0.152	0.332	0.011	1014	40	2.8	9.1	1.3
56_scan2	0.514	0.008	0.070	0.013	5.236	0.119	0.245	0.010	991	46	2.3	6.6	1.4
57_scan1	0.397	0.007	0.053	0.013	6.929	0.154	0.318	0.011	991	40	2.2	10.3	1.1
57_scan1	0.404	0.008	0.085	0.014	6.281	0.140	0.293	0.010	988	40	1.8	9.9	1.1
57_scan1	0.425	0.008	0.091	0.014	6.275	0.140	0.294	0.010	989	40	1.9	9.5	1.2
57_scan1	0.474	0.008	0.071	0.014	6.365	0.142	0.310	0.011	1036	43	2.0	9.6	1.3
57_scan1	0.397	0.007	0.087	0.014	6.330	0.141	0.295	0.010	987	39	1.9	9.7	1.1

All concentrations are in Wt. %

The concentration of U and Pb have been corrected for intereference following U U-96.6 ppm/wt%Th; Pb Pb-83.55ppm/wt%Y - 16.5ppm/wt%Th

Tab. 4: continued

D3											Mole fraction		
Name	Y	inc. (95%)	U	inc. (95%)	Th	inc. (95%)	Pb	inc. (95%)	Age	inc. (95%)	Htn	Crl	Xtm
48_scan1	0.692	0.009	0.080	0.014	7.103	0.157	0.305	0.011	919	37	4.9	5.3	1.9
48_scan1	0.590	0.009	0.096	0.014	6.607	0.147	0.296	0.011	947	40	4.0	6.1	1.6
48_scan1	0.584	0.009	0.091	0.014	6.999	0.155	0.307	0.011	930	38	4.2	6.5	1.6
48_scan1	0.576	0.009	0.100	0.014	6.982	0.155	0.317	0.011	959	39	4.1	6.8	1.6
48_scan1	0.612	0.009	0.110	0.014	6.940	0.154	0.305	0.011	926	37	3.7	7.4	1.7
48_scan1	0.626	0.009	0.104	0.014	6.898	0.153	0.314	0.011	960	38	3.9	6.9	1.7
48_scan1	0.677	0.009	0.109	0.014	6.783	0.151	0.306	0.011	948	40	4.0	6.6	1.9
48_scan1	0.562	0.009	0.053	0.014	9.104	0.199	0.394	0.011	942	34	8.8	1.7	1.5
48_scan1	0.592	0.009	0.059	0.014	7.732	0.170	0.338	0.011	945	36	7.5	1.3	1.6
48_scan1	0.640	0.009	0.075	0.014	8.620	0.189	0.374	0.011	936	35	9.0	0.3	1.8
48_scan1	0.664	0.009	0.074	0.014	8.305	0.182	0.363	0.011	940	35	8.8	0.1	1.8
56_scan1	0.657	0.009	0.082	0.014	6.461	0.144	0.298	0.011	979	41	6.5	0.8	1.8
56_scan1	0.621	0.009	0.079	0.014	6.801	0.151	0.293	0.011	918	39	6.8	0.9	1.7
56_scan1	0.596	0.009	0.074	0.014	6.695	0.149	0.293	0.011	935	39	6.7	0.8	1.6
56_scan1	0.575	0.009	0.076	0.014	7.496	0.165	0.339	0.011	968	36	7.7	0.7	1.6
56_scan1	0.559	0.008	0.068	0.014	7.623	0.168	0.343	0.011	967	38	7.8	0.5	1.5
56_scan1	0.672	0.009	0.052	0.014	6.723	0.149	0.300	0.011	964	40	6.1	2.1	1.8
56_scan1	0.655	0.009	0.055	0.014	6.945	0.154	0.306	0.011	951	38	6.4	2.0	1.8
56_scan1	0.601	0.009	0.050	0.014	6.776	0.150	0.307	0.011	979	40	6.2	2.0	1.7
56_scan1	0.670	0.009	0.034	0.013	6.443	0.144	0.284	0.010	959	40	5.5	2.6	1.8
56_scan1	0.621	0.009	0.050	0.013	6.362	0.142	0.285	0.010	968	38	4.6	4.2	1.7
56_scan1	0.605	0.009	0.056	0.014	6.364	0.142	0.281	0.010	952	40	4.1	5.2	1.7
56_scan1	0.490	0.008	0.101	0.014	6.394	0.143	0.300	0.011	987	42	6.5	0.8	1.3
56_scan2	0.948	0.011	0.073	0.014	7.198	0.159	0.318	0.011	947	39	7.6	0.1	2.6
56_scan2	0.589	0.009	0.077	0.014	7.249	0.160	0.319	0.011	942	38	7.4	0.6	1.6
56_scan2	0.572	0.009	0.078	0.014	7.605	0.168	0.331	0.011	932	35	7.9	0.4	1.6
56_scan2	0.557	0.008	0.070	0.014	7.790	0.171	0.351	0.011	970	36	8.0	0.6	1.5
56_scan2	0.555	0.008	0.059	0.014	7.752	0.171	0.340	0.011	947	37	8.0	0.5	1.5
56_scan2	0.679	0.009	0.054	0.014	6.678	0.148	0.292	0.011	944	41	6.3	1.7	1.9
56_scan2	0.646	0.009	0.053	0.014	6.997	0.155	0.304	0.011	939	41	6.5	1.8	1.8
56_scan2	0.708	0.010	0.038	0.013	6.407	0.143	0.290	0.010	981	39	5.6	2.4	1.9
56_scan2	0.681	0.009	0.052	0.013	6.230	0.139	0.275	0.010	952	39	5.3	2.6	1.9
56_scan2	0.667	0.009	0.045	0.013	6.269	0.140	0.284	0.010	980	40	5.2	2.8	1.8
56_scan2	0.607	0.009	0.049	0.014	6.285	0.140	0.281	0.010	963	40	4.9	3.5	1.7
57_scan1	2.057	0.020	0.071	0.013	4.234	0.098	0.197	0.010	974	54	4.2	0.7	5.6
57_scan1	2.022	0.019	0.072	0.013	4.219	0.098	0.191	0.010	949	53	4.2	0.6	5.6
57_scan1	1.998	0.019	0.073	0.013	4.207	0.098	0.191	0.010	952	54	4.6	-0.1	5.5
57_scan1	1.250	0.014	0.063	0.013	4.677	0.107	0.217	0.010	982	49	3.8	2.5	3.4
57_scan1	2.095	0.020	0.072	0.014	4.809	0.110	0.213	0.010	933	49	4.8	0.6	5.8
57_scan1	2.086	0.020	0.069	0.013	4.799	0.110	0.214	0.010	941	46	4.8	0.6	5.7
57_scan1	2.055	0.020	0.067	0.013	4.651	0.107	0.211	0.010	959	47	4.7	0.5	5.6
57_scan1	2.024	0.020	0.073	0.013	4.477	0.103	0.202	0.010	946	53	4.5	0.5	5.6

All concentrations are in Wt. %

The concentration of U and Pb have been corrected for interefference following U – U-96.6 ppm/wt%Th; Pb– Pb-83.55ppm/wt%Y - 16.5ppm/wt%Th

Supplementary material

supplementary material - Laurent et al. 2016

EDS maps of polymineralic inclusions

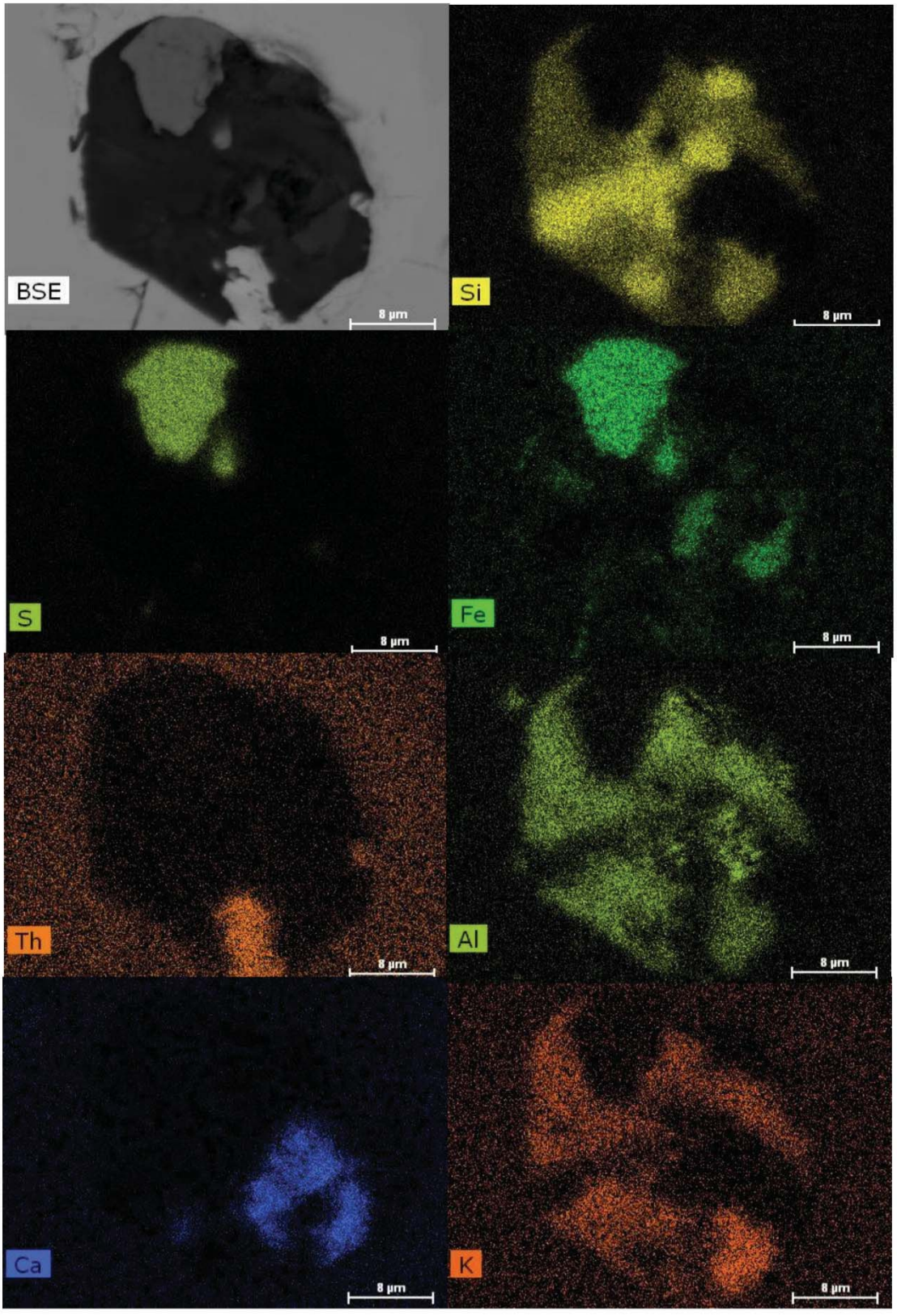

EDS maps of polymineralic inclusions

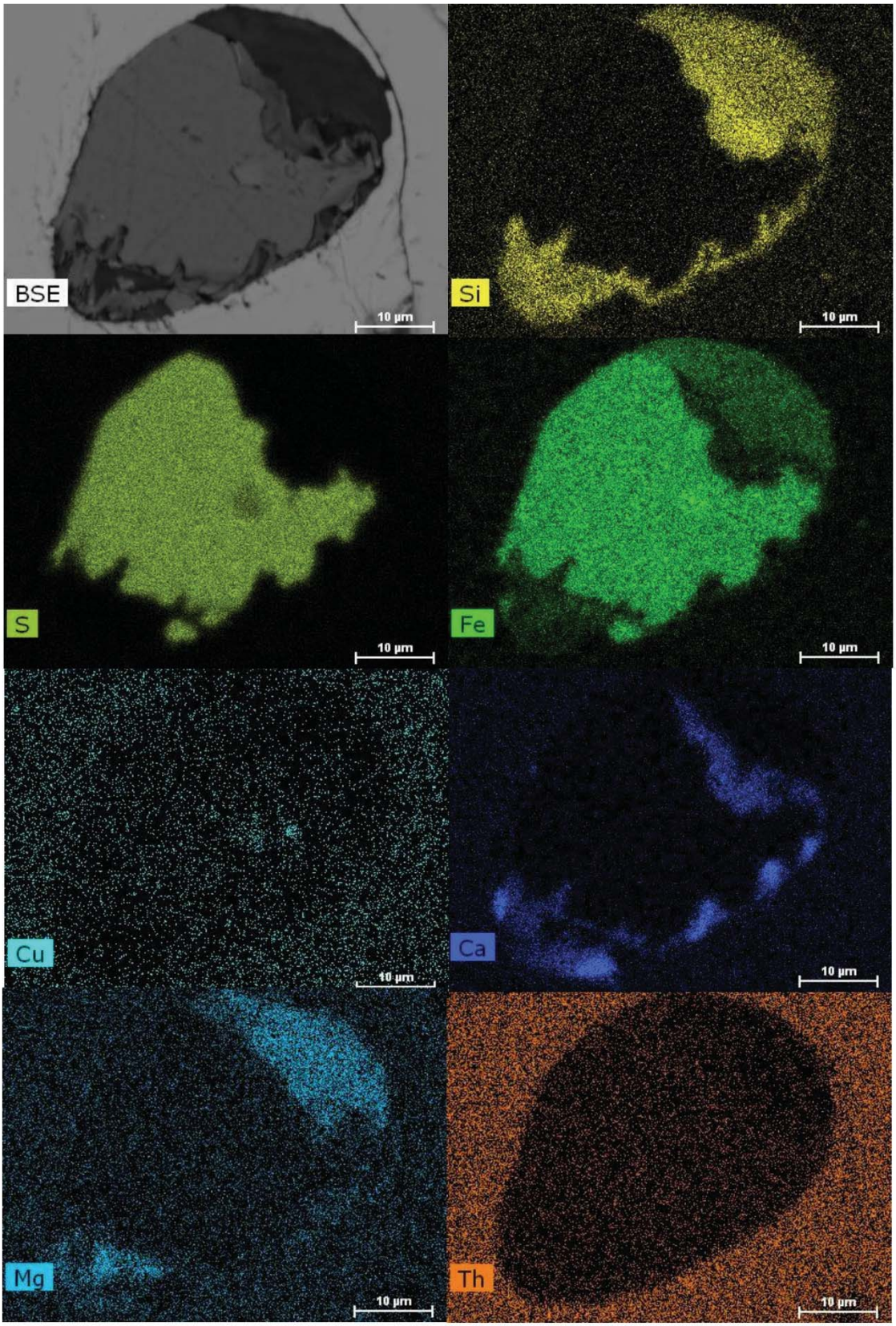

supplementary material - Laurent et al. 2016

EDS maps of polymineralic inclusions

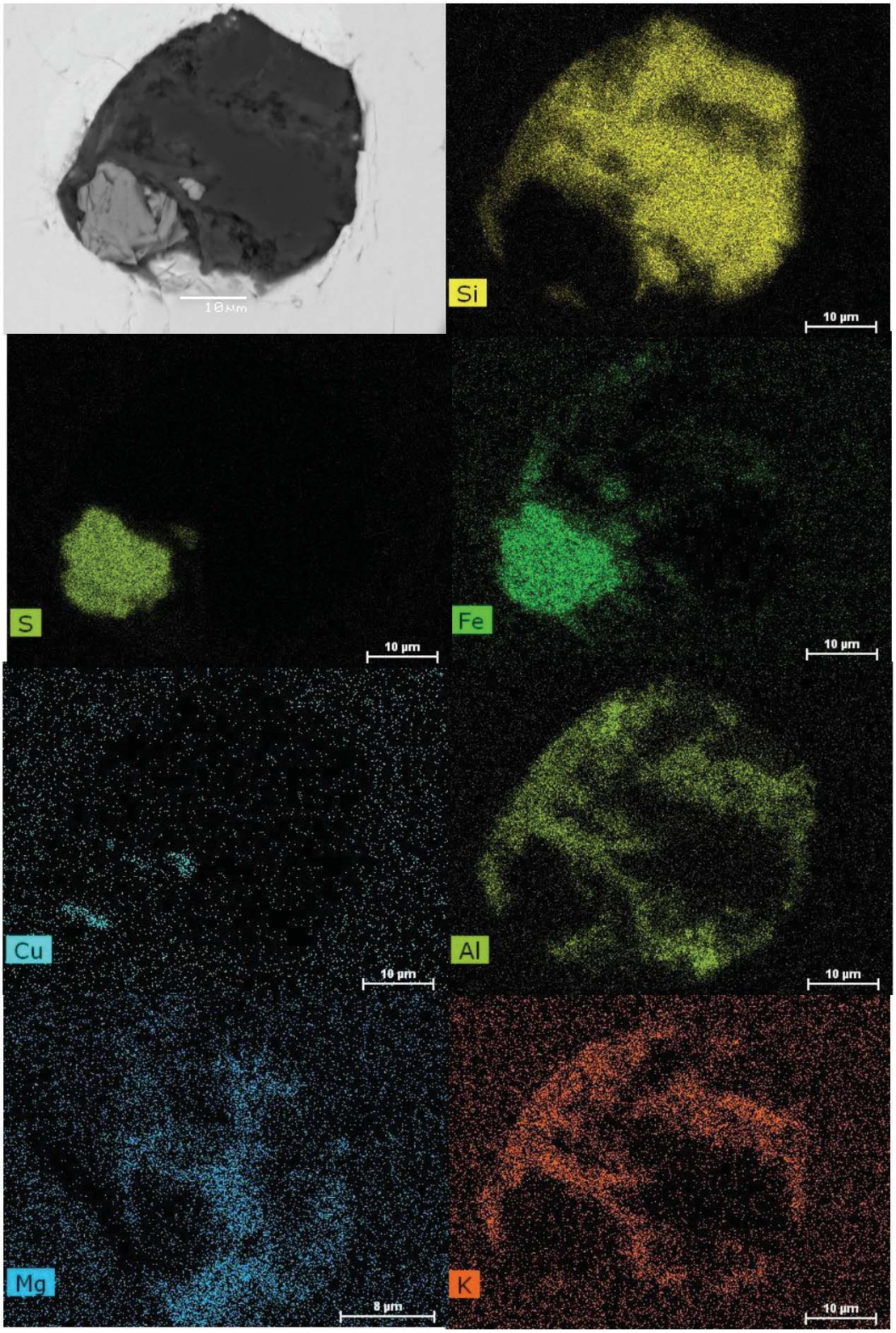

supplementary material - Laurent et al. 2016

EDS maps of polymineralic inclusions

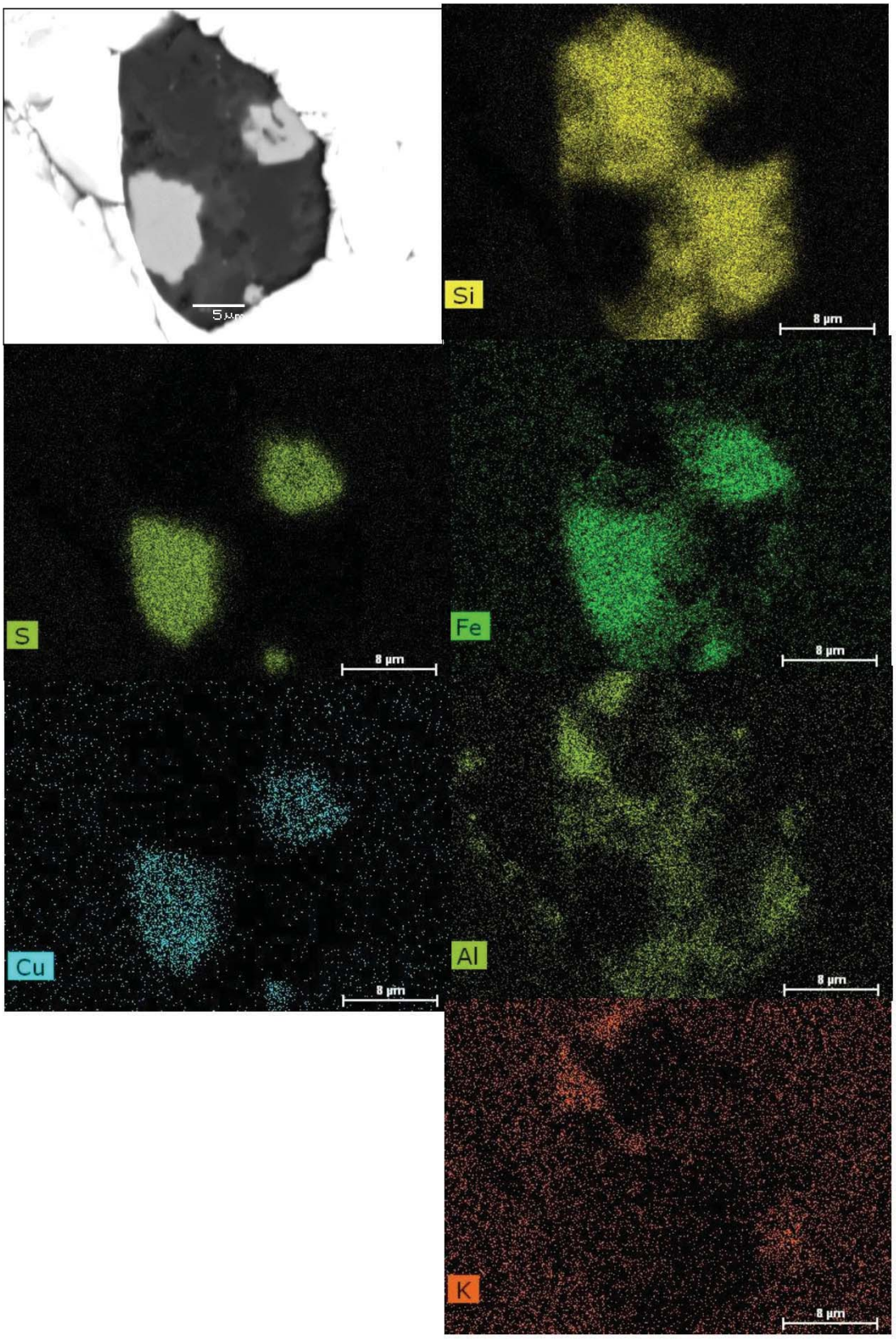

Chapitre 3

Two cycles of ultra-high temperature metamorphism in Rogaland, S. Norway: critical evidence from monazite Y-thermometry & U–Pb geochronology

ANTONIN T. LAURENT[1]*, STEPHANIE DUCHENE[1], BERNARD BINGEN[2], VALERIE BOSSE[3], ANNE-MAGALI SEYDOUX-GUILLAUME[4]

[1]GET, UMR 5563 CNRS-UPS-IRD, Université de Toulouse III, 14 av. E. Belin, 31400 Toulouse, France (*correspondence : antonin.laurent@get.obs-mip.fr)

[2]Geological Survey of Norway, 7491 Trondheim, Norway

[3]LMV, UMR 6524 CNRS-UBP-IRD, Université Blaise Pascal, Clermont-Ferrand, France

[4]LMV, UMR 6524 CNRS-UBP-IRD Faculté des Sciences et Techniques, Saint-Etienne, France

Keywords: monazite – UHT granulite – U–Pb geochronology – phase equilibria modelling – Y-in-monazite thermometry

Résumé

Le domaine de ultra-haute température du Rogaland est caractérisé par la présence de deux isogrades métamorphiques, osumilite et pigeonite, qui s'incurvent autour d'un complexe d'anorthosite–mangerite–charnockite (AMC) tardi-Svéconorvégien. Dans ce chapitre, nous reconstituons le chemin pression–température (*P–T*) des granulites de ultra-haute température (UHT) grâce à une étude pétrologique détaillée couplée à la modélisation thermodynamique de l'équilibre des phases. Nous étudions, de plus, la réponse géochimique et isotopique de la monazite dans six échantillons pour lier les réactions minéralogiques identifiées dans les silicates à l'âge isotopique U–Pb des grains de monazite. Cette approche nous permet de discuter la controverse persistante existant au Rogaland autour de l'âge du métamorphisme de UHT et de sa durée. Nos nouvelles données apportent un éclairage décisif en faveur d'un modèle à deux cycles métamorphiques superposés. Un premier cycle de métamorphisme granulitique atteignant 920 °C à 6 kbar est enregistré dans tous les échantillons étudiés entre 1040 ± 9 Ma et 990 ± 9 Ma par des monazites. L'étude des relations de phase entre monazite–xénotime et huttonite dans un gneiss à sapphirine, en particulier, permet d'estimer la température de cristallisation de différentes générations de monazites grâce à la thermométrie Y. Dans cet échantillon, les monazites enregistrent des températures de cristallisation d'environ 895 et 880 °C entre 1029 ± 9 et 1006 ± 8 Ma. Un second cycle métamorphique relativement court, atteignant également la UHT (environ 900–950 °C à 3.5–5 kbar) est ensuite identifié grâce à des monazites riches en Y conservant des âges U–Pb de 929 ± 12 Ma dans un gneiss à osumilite et de 931 ± 6 Ma dans un leucosome à grenat se décomposant en orthopyroxène–cordiérite–hercynite. Ces deux échantillons montrent des textures de décomposition du grenat à UHT qui permettent de lier les âges U–Pb obtenus sur les monazites riches en Y à cet épisode métamorphique. Ce second cycle métamorphique est lié temporellement et spatialement à la mise en place de massifs d'anorthosites à 931 ± 2 Ma. La superposition de deux cycles métamorphiques permet la déshydratation complète de la croûte lors du premier avec des assemblages de UHT locaux, tandis que lors du second cycle l'osumilite se forme de manière généralisée dans les protolithes anhydres alumineux. La superposition de deux cycles métamorphiques permet donc d'expliquer l'extrême rareté de l'osumilite en contexte métamorphique (moins de 10 occurrences mondiales) mais aussi la taille exceptionnelle (~10 km) de l'auréole métamorphique autour du massif d'anorthosite du Rogaland.

Abstract

In Rogaland, S Norway, an ultra-high temperature (UHT) granulite facies metamorphic domain, characterized by osumilite-in and pigeonite-in isograds, surrounds the late-Sveconorwegian anorthosite–mangerite–charnockite (AMC) plutonic complex. Phase equilibrium modelling and monazite microchemistry coupled with U–Th–Pb geochronology in six samples, distributed across the metamorphic gradient, address the controversy on single vs polyphase UHT metamorphism. The new data provide robust evidence for two cycles of metamorphism with clockwise path and post-peak near isobaric cooling. A first long-lived metamorphic cycle is recorded in all samples between 1040 ± 9 and 990 ± 9 Ma by monazite with variable composition. It is interpreted to represent prograde melt production in fertile protoliths, reaching peak UHT conditions of *c*. 5–6 kbar and 900–940 °C. Monazite–xenotime Y-thermometry in a residual sapphirine granulite provides critical evidence for average temperature of 895 and 880 °C between 1029 ± 9 and 1006 ± 8 Ma. A second short-lived metamorphic cycle peaking also in UHT conditions, estimated at *c*. 3.5–5 kbar and 900–950°C, is recorded by Y-rich monazite at 929 ± 12 Ma in an osumilite gneiss or 931 ± 6 Ma in an orthopyroxene–cordierite–hercynite gneiss. Both samples show evidence for garnet-breakdown textures. This metamorphism is related to intrusion of the AMC plutonic complex at 931 ± 2 Ma. Osumilite is forming in the second of the two metamorphic cycles. Superposition of two metamorphic cycles separated by partial cooling may explain the rarity of osumilite-bearing assemblages, but also the exceptional width of the aureole of contact metamorphism in Rogaland, at temperature conditions beyond usual dehydration melting reactions.

Introduction

The occurrence of ultra-high temperature (UHT; > 900 °C) granulite facies crustal metamorphism is being increasingly recognized worldwide (Harley 2008; Kelsey and Hand 2015). Independently of the clockwise or anticlockwise shape of the pressure–temperature (*P–T*) path, both short-lived (≤ 15 My; e.g. Baldwin and Brown 2008) and long-lived (*c*. 100 My; e.g. Korhonen et al. 2013; Walsh et al. 2014) UHT events have been reported (review by Kelsey and Hand 2015). Based on the petrological, structural and geochronological record of UHT samples, it is however challenging to decide whether UHT is reached episodically in specific part of the orogen or whether significant part of the lower-crust reside at T > 900 °C for timescales approaching 50–100 My (Harley 2016). This complication arises from the propensity of metamorphic assemblages to remain metastable after melt extraction, resulting in an intrinsically fragmentary mineral record for metamorphism, that may lead to fictive portion of *P–T* paths in polymetamorphic samples (Vernon 1996; Goncalves 2004). As a consequence, unravelling the precise timing of UHT requires close linking between estimates of metamorphic *P–T* conditions and geochronology of accessory minerals that should ideally be able to crystalize near peak condition but also to record subtle physico-chemical changes associated with post-melt-loss retrograde evolution. Three avenue are explored for the moment (Kohn 2016): (1) textural correlation between silicate–oxide assemblage and accessory minerals (Möller et al. 2003; Kelly et al. 2012); (2) chemical correlation, especially using REE patterns in zircon and monazite to tie accessory mineral growth with garnet stability or demise (Whitehouse and Platt 2003; Kelly and Harley 2005; Dumond et al. 2015); (3) combined chronometric and thermometric analyses like Ti-in-zircon or Zr-in-rutile (Baldwin et al. 2007; Ewing et al. 2013) that allow to decipher temperature–time path for individual crystals. Systematic chemical variation as a function of temperature is also demonstrated quantitatively for Y in monazite in equilibrium with xenotime (Heinrich et al. 1997; Pyle et al. 2001; Krenn and Finger 2010).

In Rogaland, S Norway, a UHT metamorphic domain is known for decades surrounding the Sveconorwegian (Grenvillian) Rogaland anorthosite–mangerite–charnockite (AMC) plutonic complex (Maijer et al. 1981; Tobi et al. 1985). *In-situ* geochronological studies in the UHT zone have shown that zircon intergrown with or included within UHT metamorphic minerals crystalized at 927 ± 7 Ma (Moller 2002; Moller 2003). In contrast, Drüppel et al. (2013) interpreted a single zircon population at 1010 ± 7 Ma and 1006 ± 4 Ma in two sapphirine-bearing samples to reflect the peak-metamorphic UHT conditions, leading to controversial interpretations (e.g. Slagstad et al. 2013). In this contribution, we re-examine the *P–T* path of the UHT metamorphism in Rogaland

and perform *in-situ* monazite U–Th–Pb dating coupled to micro-chemistry. We address the chemical behaviour of monazite in contrasted rock-types and discuss the use of Y thermometry in high-Th monazite. Finally, we propose a new *P–T–*t evolution for the Sveconorwegian metamorphism emphasizing that apparent continuous UHT metamorphism may be the result of two superposed events distant in time.

Geological setting

The Sveconorwegian province (Fig. 1a), located at the margin of Fennoscandia, is made up of Mesoproterozoic crust reworked during the Sveconorwegian orogeny. The orogen is divided in four lithotectonic units which are from east to west, the parautochtonous Eastern Segment, the Idefjorden terrane, the Bamble-Kongsberg terrane and Telemarkia terrane (Bingen et al. 2008b). The Telemarkia terrane is made up of *c*. 1520–1480 Ma magmatic rocks intruded by plutonic rocks and overlaid by sedimentary and bimodal volcanic rocks dated between *c*. 1500 and 920 Ma (Andersen et al. 2001; Laajoki et al. 2002; Roberts et al. 2013; Spencer et al. 2014). The Rogaland sector, under scrutiny in this study, is located at the southwestern end of the Telemarkia terrane. In detail, the Rogaland bedrock (Fig. 1b) is composed of high-grade meta-igneous rocks of broadly granitic to tonalitic composition (granitic gneiss and meta-charnockite) interlayered with mafic rocks (amphibolites and banded gneisses) and metasedimentary rocks (Hermans et al. 1975). Metasedimentary rocks are further divided into the "garnetiferous migmatite" derived from Al-rich protolith and the "Faurefjell metasediments" comprising a succession of calc-silicate rocks, quartzite and minor marble. Most of the deformation is localized within metasedimentary layers compared to the adjacent granitic and banded gneisses. Structural analysis indicates four phases of folding (Hermans et al. 1975; Huijsmans et al. 1981; Falkum 1985). The oldest involved isoclinal folding resulting in a transposition foliation within the garnetiferous migmatite. The two latter phases, coeval with regional *(M1)* metamorphism, have structured much of the area and consist in tight kilometric folds with N- to NW-striking axial plane dipping *c*. 40° eastwards. The youngest phase of deformation produced large scale open folds with E–W trending axial planes that are not visible in the map view.

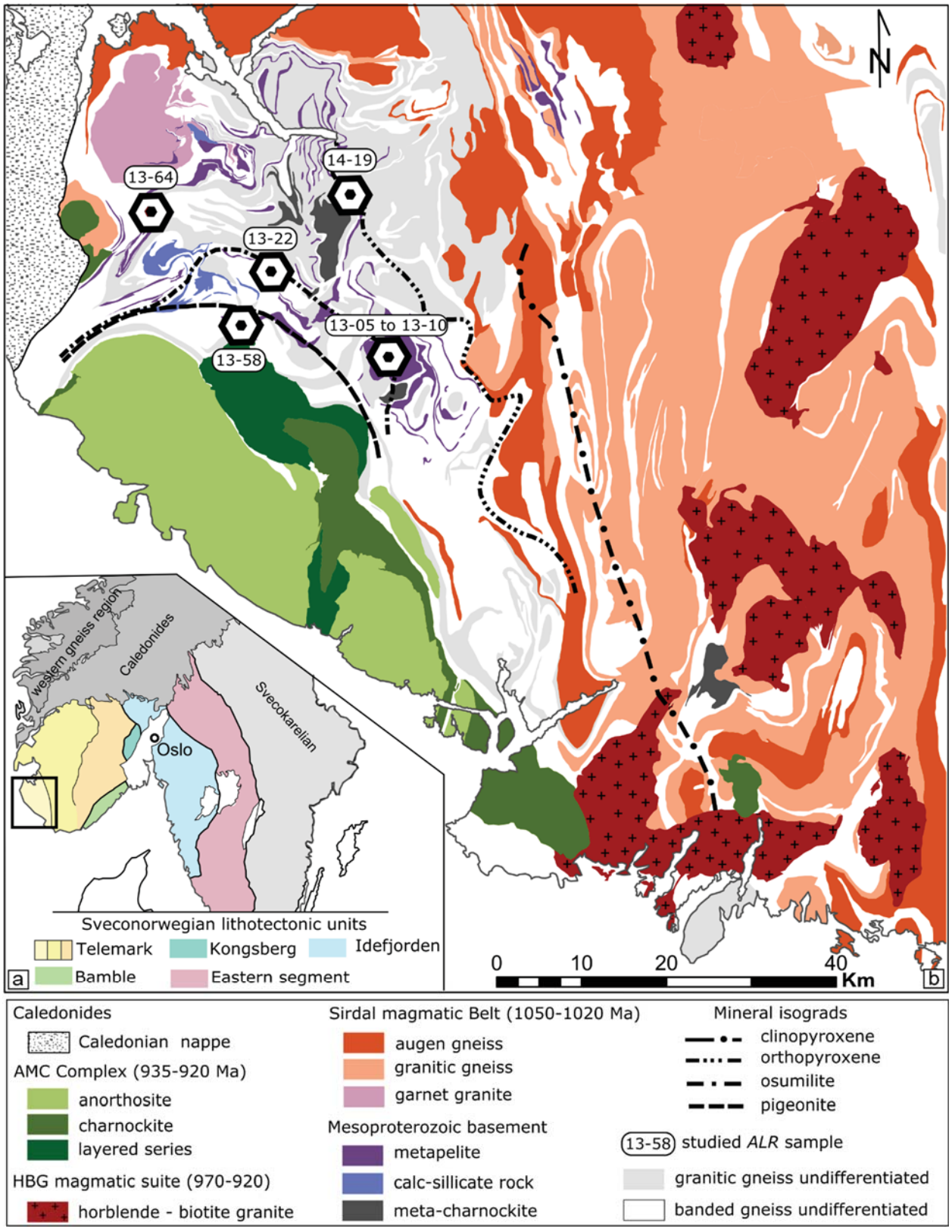

Fig. 3–1: Geological maps. **a**– Sketch map of the Sveconorwegian Province in SW Scandinavia from Bingen et al. (2008b), black rectangle depicts the studied area. **b**– Simplified geological map of Rogaland-Vest Agder modified after (Falkum 1982; Coint et al. 2015) with mineral isograds drawn after (Tobi et al. 1985; Bingen et al. 1990) and localization of the studied localities.

The metamorphic evolution of the area resulted in the development of four mineral isograd reflecting a southwestward increase in metamorphic grade from upper-amphibolite facies to ultra-high temperature granulite facies. From north-east to south-west, these are the clinopyroxene isograd in granodioritic gneisses, the orthopyroxene isograd in quartzo-feldspathic rocks, the osumilite isograd in metasedimentary rocks and the pigeonite isograd in leucocratic gneisses (Tobi et al. 1985). On the basis of petrographic analysis, Kars et al. (1980) distinguished three metamorphic events –M1, M2, M3– in "garnetiferous migmatites" which were later generalized to all lithologies by Maijer (1987). The oldest M1 metamorphism is a regional upper amphibolite facies event associated with extensive migmatization, deformation and emplacement of voluminous granitoids in the amphibolite to granulite transition zone (Feda suite of Bingen and Van Breement 1998 and Sirdal Magmatic Belt of Coint et al. 2015). Jansen et al. (1985) proposed quantitative estimates of 600–700 °C and 6–8 kbar for this event. Absolute timing for this regional phase of metamorphism is bracketed between 1035 and 970 Ma by U–Pb data on zircon and monazite (Bingen and Van Breemen 1998; Bingen et al. 2008a). In contrast, recent investigations of sapphirine-bearing restite located within the osumilite isograd suggest that this portion of the crust already reached UHT conditions of 1000 °C (Drüppel et al. 2013) [*or 900–950 °C (Blereau et al.)*] and 7–8 kbar at 1006 ± 4 Ma (U–Pb zircon). Regional decompression to 5.5 kbar is recorded at 955 ± 8 Ma by zircon included in cordierite (Tomkins et al. 2005). The high-grade basement was subsequently intruded by two plutonic suite, (i) the hydrous Hornblende–Biotite Granite (HBG) suite between 970 and 932 Ma (Vander Auwera et al. 2011) and (ii) the anhydrous massif-type anorthosite–mangerite–charnockite (AMC) suite at 931 ± 2 Ma (Schärer et al. 1996; Fig. 1b). A detailed *in-situ* U–Pb geochronological study on zircon, complemented by thermal modelling, suggests that emplacement of the AMC plutonic complex is responsible for M2 UHT contact metamorphism at 927 ± 7 Ma (Möller et al. 2002; Möller et al. 2003; Westphal et al. 2003). Typical M2 mineral assemblage comprises green spinel, osumilite and Al-rich orthopyroxene in metapelite and pigeonite in granitic rocks. M2 temperature estimates ranges from 850 to 1050 °C at 3–6 kbar within the osumilite isograd (Jansen et al. 1985; Wilmart and Duchesne 1987; Holland et al. 1996; Drüppel et al. 2013). Finally a M3 retrograde event in lower granulite facies is attributed to slow isobaric cooling of intrusive bodies dated at 908 ± 9 Ma by mean of U–Pb in zircon overgrown by M3 minerals such as late garnet, biotite, cordierite, low-Al orthopyroxene (Möller et al. 2003). A regional scale average titanite U–Pb age of 918 ± 2 Ma also record regional fast cooling after M2 metamorphism (Bingen and van Breemen, 1998).

Methods

Micro-chemistry

Monazite crystals were studied both in thin section to preserve their textural context and in mineral separates recovered by standard procedures, including crushing, heavy liquors and magnetic separation. Back Scattered Electron (BSE) images were taken at 20 kV with a SEM to guide *in-situ* chemical analysis acquired with a Cameca SX-FIVE electron probe micro-analyser (EPMA) hosted at the Raimond Castaing micro-characterization centre (Toulouse). The EPMA was operated with a focused beam at standard conditions of 15 kV and 20 nA. The following X–rays and reference material have been used: Y Lα on YPO_4, Th Mα on synthetic ThO_2, S Kα on $BaSO_4$, Si Kα and Ca Kα on Wollastonite, P Kα and REE (Ce Lα, La Lα, Pr Lβ, Nd Lβ, Sm Lβ, Gd Lβ, Dy Lα, Er Lα, Yb Lα) on Pb-free $(REE)PO_4$, Pb Mβ on an in-house $Pb_2P_2O_7$, U Mβ on synthetic UO_2. Monazite and xenotime formula were calculated in the system $2(REE)PO_4 – CaTh(PO_4)_2 –2ThSiO_4$, by incorporating sequentially (1) Ca + Th + U in cheralite $[CaTh(PO_4)_2]$, (2) any remaining Th is combined with Si in huttonite $[ThSiO_4]$, (3) Y and HREE (Gd–Lu) are combined in xenotime $[(HREE,Y)PO_4]$ and (4) Light Rare Earth Elements (La–Eu) are combined in monazite $[(LREE)PO_4]$.

U–Th–Pb geochronology

LA–ICP–MS

Uranium–thorium–lead isotopic analyses were performed by LA–ICP–MS in at the Laboratoire Magmas et Volcans (Clermont-Ferrand, France). Laser ablation spots were guided with BSE images, chemical composition previously acquired by EPMA together with reflected and transmitted light microphotograph. The laser ablation systems consists of a Resonetics Resolution M-50E system equipped with an ultra-short pulse (< 4 ns) ATL excimer 193 nm laser coupled to an Agilent 7500 cs ICP–MS. Detailed analytical procedures are reported in Paquette and Tiepolo (2007) and Didier et al. (2015). A spot diameter of 9 µm was used with 1 Hz repetition rate and a fluence of 6 J/cm². The ^{204}(Hg+Pb) signal was monitored but no common-Pb correction was applied. Raw data are corrected for U–Pb and Th–Pb fractionation during laser ablation and instrumental mass discrimination by standard bracketing with the C83-32 monazite (2681 ± 2 Ma; Corfu 1988). Repeated analysis during the run of Moacyr monazite (Seydoux-Guillaume et al. 2002a; Gasquet et al. 2010; Fletcher et al. 2010) and either Trebilcock monazite (272 ± 2 Ma; Tomascak et al. 1996) or Manangotry monazite (555 ± 2 Ma; Paquette and Tiepolo 2007) was

used to monitor accuracy and reproducibility of the correction applied. The data were acquired during 2 different sessions. During the first session (sample *ALR 13-22*) 4 analyses of Manangotry yielded a weighted $^{206}Pb/^{238}U$ age of 562 ± 7 Ma (MSWD = 1) and 20 analyses of Moacyr yielded a weighted $^{208}Pb/^{232}Th$ age of 503 ± 6 Ma (MSWD = 0.3). During the second session (samples *ALR 13-05*; *ALR 13-06*; *ALR 13-64*) 49 analyses of Trebilcock yielded a weighted $^{206}Pb/^{238}U$ age of 268 ± 3 Ma (MSWD = 1.3) and 8 analyses of Moacyr yielded a weighted $^{208}Pb/^{232}Th$ age of 502 ± 5 Ma (MSWD = 0.4). Data reduction was carried out using the Glitter software package (Van Achterbergh et al. 2001).

EPMA

The U–Th–Pb chemical dating was carried out on a Cameca SX-FIVE EPMA with an accelerating voltage of 15 kV and 200 nA probe current. Thorium was measured on a PET crystal using the Th Mα line with synthetic ThO_2 as standard (background: -1200; +1000). Uranium was measured on a LPET crystal using the U Mβ with synthetic UO_2 as standard (background: -1200; +950). Lead was measured on a LPET crystal using the Pb Mα on an in-house $Pb_2P_2O_7$ as standard (background: -3500; +2240). Additionally, Y and Si were measured simultaneously on two TAP crystals using Y Lα and Si Kα lines. Counting time for each element was 240 s on peak and 120 s on background. The pulse height analyser was set in automatic mode (Spear 2009). A linear background fit was chosen for U, Th, Si and Y and an exponential fit for Pb because of the large offset in Pb background positions (Jercinovic 2005; Williams et al. 2007; Spear et al. 2009). To monitor any drift of the measured peak–background intensities during analysis, the counting time was divided in 6 cycles of peak/background acquisition (sub-counting method described in Spear et al. 2009). The Chi² test was then applied to each analysis point (6 cycles), so that inconsistent counting cycles were not taken into account when summing the total counts for each element. Interference of Th $M\gamma_1$ on U Mβ and Y $L\gamma_{2,3}$, + Th $M\zeta_{1,2}$ on Pb Mα were quantified using Pb-free $(REE)PO_4$ crystals and pure ThO_2 reference material, following the approach of Spear et al. (2009). Consequently, the measured values were corrected as follows: $U_{corr} = U_{meas.}$ - 96.6 ppm/Wt. % Th and $Pb_{corr.} = Pb_{meas.}$ - 83.55 ppm/Wt.% Y - 16.5 ppm/Wt.% Th. Typical uncertainties arising from counting statistics calculated following Ancey et al. (1977) for monazite crystals with Th in the range 4–8 Wt. % are 110 ppm for Pb, 150 ppm for U, 135 ppm for Y and 650 ppm for Th. Uncertainties on Pb, U and Th are estimated for each analysis, then the age are calculated and the 95% confidence interval estimated by propagation of errors using Monte-Carlo simulation (Montel et al. 1996). The age and associated confidence interval were calculated with the R-package

NileDam[2] (Montel et al. 1996; Seydoux-Guillaume et al. 2012). Repeated analysis of the Manangotry reference monazite (555 ± 2 Ma; Paquette and Tiepolo 2007) during the session was used to control the reproducibility and accuracy of the correction applied; 26 analyses yields a pooled age of 561 ± 12 Ma, in good agreement with the published ID-TIMS age of 555 ± 2 Ma (Paquette and Tiepolo 2007).

Mineral composition and phase equilibria modelling

Phase equilibria of metamorphic assemblages were modelled using *P–T* and *T–X* pseudosections in the Na_2O–CaO–K_2O–FeO–MgO–Al_2O_3–SiO_2–H_2O–TiO_2–O_2 chemical system using Perple_X (version 6.7.2; Connolly 2009). All samples were modelled using the internally consistent thermodynamic database of Holland and Powell (2011) together with activity–composition models of White et al. (2014) except for the osumilite gneiss (*ALR 13-58*). For this sample we used the Kelsey et al. (2004) database for UHT rocks in conjunction with updated models of spinel from White et al. (2007) and osumilite from Holland et al. (1996). The phases under consideration are garnet, silicate melt, plagioclase, K-feldspar, sillimanite, spinel, magnetite, ilmenite–hematite, rutile, orthopyroxene, sapphirine, cordierite, biotite, muscovite, quartz with additional osumilite in the Kelsey et al. (2004) database.

The bulk rock composition have been determined by ICP–OES on the rock chips left over after thin section preparation at the CRPG (Nancy), following standard procedure described in Carignan et al. (2001). FeO has been measured by titration to estimate the oxidation state of the whole rock. Oxidation ratio measured from the bulk rock was tested with *T–X* sections and found suitable to model the observed paragenesis for all samples. Modelled H_2O content were constrained using *T–X* sections considering all loss on ignition (LOI) as H_2O and H_2O = 0.1 mol %. Because our aim is to model the evolution of the rock at the peak *T* conditions, we chose H_2O value so-that the solidus is the closer to the interpreted peak field. A value of 1 mol. % H_2O was found suitable for all samples. Chemical composition used for modelling are reported as oxides weight percentage along with measured compositions in Tab. 1.

Quantitative analysis of silicate and oxides were collected with the Cameca SX-Five microprobe with standard operating conditions of 15 kV and 20 nA. Representative mineral analyses are reported for sample *ALR 13-64*, *13-05*, *13-06*, *13-22*, *13-58; 14-19* in supplementary material S3-1, S3-2, S3-3, S3-4, S3-5 and S3-6 respectively The mineral formula of orthopyroxene (Opx) was recalculated on the basis of 4 cations with Fe^{3+} estimated by normalizing the analyses

[2] Villa-Vialaneix N., Montel Jean-Marc and Seydoux-Guillaume Anne-Magali (2013) *NiLeDAM: Monazite Datation for the NiLeDAM team*. R package version 0.1

to 6 O. Garnet (Grt) and feldspar formula were calculated on the basis of 8 cations. Minerals belonging to the magnetite–ulvospinel–spinel–hercynite solid solution were calculated on the basis of 3 cations and 4 oxygens. Biotite (Bt) analyses were recalculated on the basis of 11 O. Cordierite (Crd) formula was calculated on the basis of 18 O. Osumilite (Osm) was calculated on the basis of 30 cations following Das et al. (2001). Sapphirine (Spr) formula was calculated on the basis of 7 cations and normalized to 10 O to evaluate Fe^{3+} substitution. All mineral abbreviations follow Whitney and Evans (2010).

Monazite–xenotime Y and REE thermometry

Thermometry based on the partitioning of Y and REE between monazite and xenotime was applied in one monazite–xenotime bearing sample (*ALR 13-22*). Because the original experimental calibration of the thermometer, performed in the simple $CePO_4$–YPO_4 system revealed only small pressure dependence (Gratz and Heinrich 1997), it has been neglected in the present case study. However, Seydoux-Guillaume et al. (2002b) showed that incorporation of Th through the huttonite ($ThSiO_4$) substitution enhances Y solubility in $CePO_4$ and proposed an improved calibration curve together with a phase diagram in the $CePO_4$–YPO_4–$ThSiO_4$ system. For that reason, the temperature calculated with the Gratz and Heinrich (1997) calibrations should be treated as maximum temperature. Conversely, the empirical calibrations of Pyle et al. (2001) and Heinrich et al. (1997) have the advantage to integrate the full range of REE distribution for typical monazite in metapelitic rocks and a moderate content of ThO_2 (< 10 Wt. %) but are restricted to T < 750 °C and garnet-present samples. We performed temperature calculation on the basis of monazite EPMA analyses (Tab. 2), which were acquired prior to laser ablation U–Th–Pb analyses. The four calibrations of Gratz and Heinrich (1997), Heinrich et al. (1997), Pyle et al. (2001) and Seydoux-Guillaume et al. (2002b) are presented in Tab. 2. The calibration of Seydoux-Guillaume et al. (2002b) is preferred for comparison purpose and geological interpretation since the associated phase diagrams explicitly take into account the Th-component in monazite and because the experiments were performed up to 1000°C, i.e. at UHT conditions.

Microstructures, petrography and mineral compositions

Six samples distributed in the metamorphic basement of Rogaland were selected for this study (Fig. 1b). In order to constrain the *P–T* conditions outside of the mapped UHT zone, two sample within the Opx-zone (*ALR 13-64* & *ALR 14-19*) were chosen at the Ålgård and Maudal

localities. Five samples from the UHT-zone were investigated including four samples from two localities within the osumilite isograd at localities Gyadalen and Ivesdal and one sample within the pigeonite isograd at the Vikeså locality. Field relationships are illustrated on Fig. 2a–e.

Orthopyroxene zone

Sample ALR 13-64 (UTM zone 32 coordinates: x = 321547; y = 6516474) is a garnet–hercynite–cordierite migmatite from Ålgård. The overall structure of the outcrop, defined by alternating melanosome and leucosome, is shallowly dipping to the NE (Fig. 2a). The rock fabric is underlined by dark seams composed of cordierite + hercynite wrapping around garnet. The dominant minerals are garnet (25 %), cordierite (15 %), hercynite (5 %), perthite (20 %), plagioclase (10 %) quartz (15 %) and sillimanite (> 5 %) with minor ilmenite, biotite, pinite and accessory monazite, zircon, pyrite and pyrrhotite. Porphyroblastic garnets are strongly deformed (sigma shape) and contain numerous inclusions. Garnet cores (X_{Mg} core = 0.30; X_{grs} core = 0.027; Tab. S3-1a) contain abundant needles of sillimanite, rounded biotite blades (X_{Mg} = 0.70−0.76; Ti = 0.28−0.30 apfu; Tab. S3-1c), K-feldspar and quartz while garnet rims (X_{Mg} rim = 0.28; X_{grs} rim = 0.03) contain sillimanite, hercynite (X_{Mg} = 0.41−0.42; ZnO = 3.2−3.3 Wt. %; Tab. S3-1b), biotite (X_{Mg} = 0.67−0.68; Ti = 0.40−0.45 apfu; Tab. S3-1c) and ilmenite. In *c*. 5 mm thick high strain zones, garnet is replaced by a cordierite (X_{Mg} = 0.68−0.72; Tab. S3-1d) plus hercynite (X_{Mg} = 0.23−0.24; ZnO = 2.0−2.2 Wt. %; Tab. S3-1b) layer that is further isolated from the (quartz saturated) matrix by a continuous ribbon of K-feldspar (Fig. 3a). In low strain zones, hercynite is absent and cordierite follows quartz and feldspar grain boundaries.

Fig. 3–2: Outcrop photographs and field relationships. **a–** Outcrop of Grt–Hc–Crd migmatite from Ålgård with syn-migmatitic penetrative deformation **b–** Undeformed garnet leucosome from Gyadalen. **c–** Fine grained Hc–Qz rock with folded garnet layer from Gyadalen **d–** Close-up view of a Spr–bearing boudin (centre) enclosed in the foliation of Opx–Hc–Grt gneiss at Ivesdal **e–** Detail of garnet-rich layers of the osumilite gneiss at Vikeså

The sample ALR 14-19 (x = 345793; y = 6517377) is a garnet–hercynite–cordierite migmatite from the Maudal locality. The outcrop consists of garnet-bearing migmatite with biotite-orthopyroxene rich horizons and orthopyroxene-bearing leucocratic gneiss. The sample is macroscopically identical to *ALR 13-64* with dark seams composed of cordierite + hercynite wrapping around porphyroblastic garnet. The dominant minerals are garnet (25 %), cordierite (20 %), spinel (5 %), perthite (20 %), plagioclase (10 %) quartz (15 %) with minor ilmenite, biotite, sillimanite, corundum, diaspore, pinite and accessory monazite, zircon, pyrite and pyrrhotite.

The porphyroblastic garnets are slightly zoned (X_{Mg} core = 0.27, X_{Mg} rim = 0.24; S3-6a) and contain numerous inclusions of oriented sillimanite needles together with rounded biotite blades (X_{Mg} = 0.64−0.67; Ti =0.22−0.29 apfu; S3-6c), K-feldspar, plagioclase and quartz. Spinel hercynite (X_{Mg} = 0.22) with low Cr and Zn content (Cr_2O_3 < 0.2 Wt. %; ZnO < 0.5 Wt. %; S3-6b) is intergrown with cordierite (X_{Mg} = 0.67−0.70; S3-6d) and ilmenite, forming *c*. 250−500 µm thick layers isolated from the (quartz-saturated) matrix by a continuous rim of K-feldspar. Within the hercynite-cordierite bands rare corundum occurs on spinel and small relicts of almandine-rich garnets (X_{Mg} core = 0.24, X_{Mg} rim = 0.21; S3-6a) may be found. Secondary cordierite, sometimes with quartz blebs, is present around garnet and in garnet cracks, leading to partial replacement. In the matrix, biotite is only found as anhedral flakes (X_{Mg} = 0.37−0.42; Ti =0.21−0.24 apfu; S3-6c) in interstitial position. Finally, spinel is retrogressed to diaspore, cordierite II is fully replaced by pinite and ilmenite adjacent to spinel show decomposition into rutile + quartz.

Osumilite zone

Sample ALR 13-05 (x = 348746; y = 6499700) is taken from a garnet-rich leucosome interlayered with quartz-free orthopyroxene–hercynite–garnet–rich melanosome from Gyadalen (Fig. 1b). The sample lacks any mineral fabric but displays well developed reaction textures (Fig. 2b). The main constituent are garnet (35 %), micro- to mesoperthite (20 %), antiperthite (10 %), cordierite (10 %), orthopyroxene (10 %), quartz (5 %), hercynite (3 %), and biotite (10 %) with accessory monazite and zircon. Porphyroblastic garnet (X_{Mg} = 0.36–0.38; Tab. S3-2c) preserves inclusion of rounded biotite (X_{Mg} = 0.82; Ti = 0.21–0.29 apfu; Tab. S3-2c) and quartz. Around garnet, a spatially organized corona is present. This corona consists of an inner cordierite (X_{Mg} = 0.78–0.82; Tab. S3-2d) plus orthopyroxene (X_{Mg} = 0.54–0.56; Al_2O_3 = 8.4–9.2 Wt. %; Tab. S3-2a) plus hercynite (X_{Mg} = 0.35–0.37) symplectite rimmed by a continuous blocky orthopyroxene layer (Al_2O_3 = 8.3–8.8 Wt. %; Tab. S3-2a) that occasionally contains rounded inclusions of biotite (Fig. 3b).

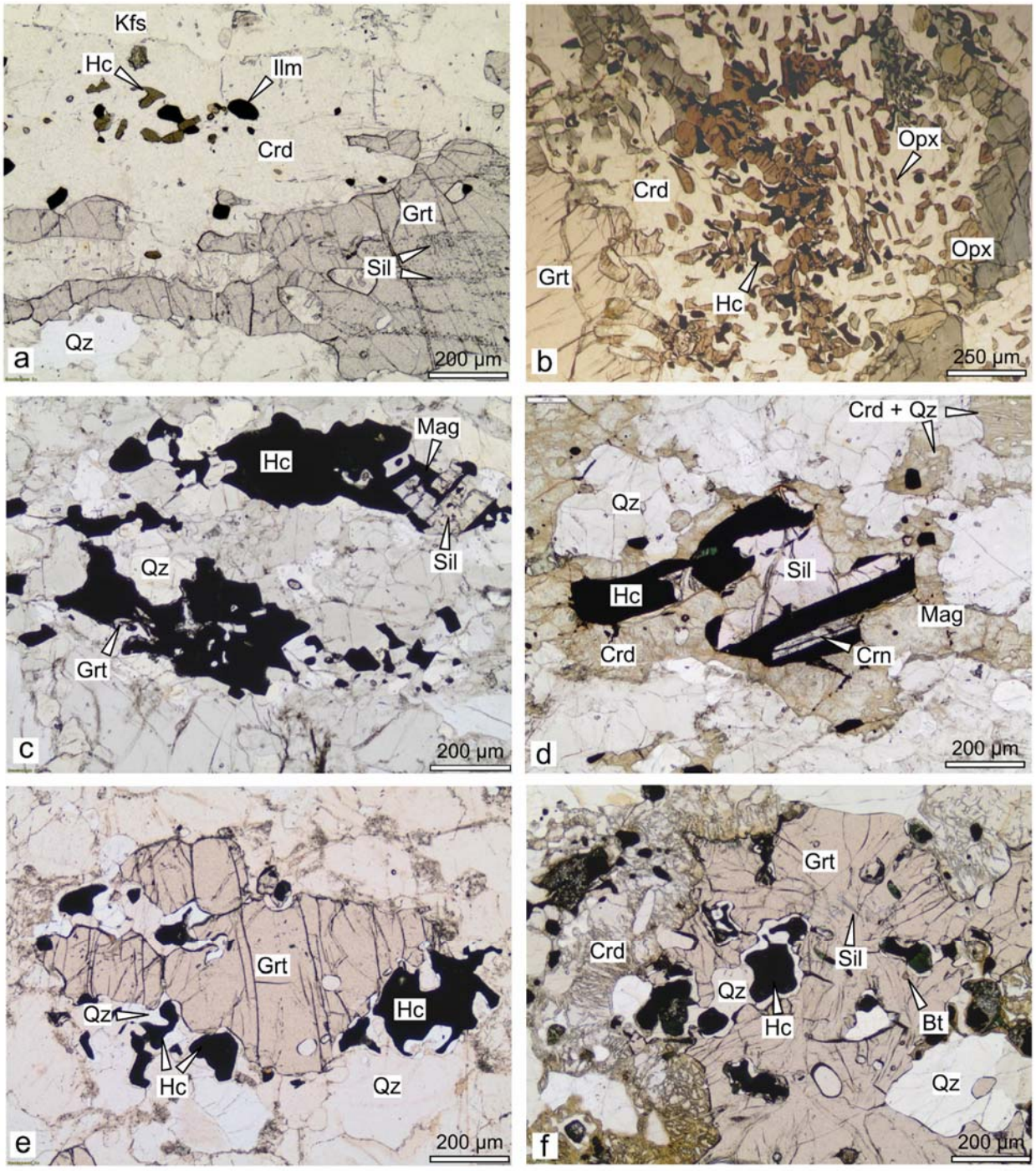

Fig. 3–3: Microstructure and parageneses **a–** Sample *ALR 13-64*; elongate garnet with sillimanite inclusions, underlining the foliation, reacts in Crd + Hc ± Ilm **b–** *ALR 13-05*; symplectite of Crd + Hc + Opx around garnet rimmed by a blocky Opx rim toward the quartzo-feldspathic matrix **c–** *ALR 13-06*; hercynite + quartz paragenesis reacts into Mag + Sil aggregate or display a thin garnet corona around hercynite **d–** *ALR 13-06*; close-up view of Sil + Mag aggregate after hercynite that is further rimmed by altered cordierite (pinite) or Crd + Qz intergrowth. **e–** *ALR 13-08*; Reaction texture of Grt decomposing in Hc + Qz **f–** *ALR 13-08*; Porhyroblastic garnet with inclusions of sillimanite and biotite breaks down into Hc + Qz and is further rimmed by cordierite.

Sample ALR 13-06 (x = 348495; y = 6499696) is a fine-grained rock showing a weak foliation defined by dark streaks of hercynite–magnetite enclosing folded garnet-bearing layers (see sample *ALR 13-08*; Fig. 2c). At the microscopic scale the foliation is defined by the preferred orientation of sillimanite blade and elongated hercynite–magnetite aggregates alternating with quartz ribbons. The main constituents are quartz (40 %), green spinel (15 %), sillimanite (10 %), magnetite (5%), cordierite (5 %), mesoperthite (15 %) and anti-perthite (5 %) with minor garnet. Spinel is mainly preserved as hercynite grains with exsolutions of magnetite and ilmenite platelets or forms composite grains associating blocky hercynite, magnetite and ilmenite. Hercynite grains (ZnO < 0.3 Wt. %; X_{Mg} = 0.32–0.37; S3-3b) mainly preserve a direct contact with quartz although, in place, they have reacted to form large sillimanite (up to 1.51 Wt. % Fe_2O_3; S3-3d) plus magnetite intergrowth (Fig. 3c). Alternatively, rare hercynite grains have thin (<20 μm) garnet corona (X_{Mg} = 0.3; S3-3a). Localized millimetre-scale layers bands containing both hercynite and sillimanite–magnetite intergrowth have further reacted to develop a symplectite of cordierite + quartz while other levels are preserved from retrogression (Fig. 3d). Finally, hercynite may be decomposed into diaspore and ilmenite into rutile + quartz at the contact with magnetite grains.

Sample ALR 13-08 (x = 348495; y = 6499696) comes from a folded garnet-bearing layer enclosed in fine-grained hercynite–quartz rock (Fig. 2c). The main constituent are garnet (35 %), quartz (20 %), hercynite (10 %), sillimanite (2 %), cordierite (5 %), perthite (20 %), antiperthite (5 %) with accessory monazite and zircon. Porphyroblastic garnets encloses micro-folded needles of sillimanite together with biotite, quartz and ilmenite. Garnet breaks down to a hercynite plus quartz assemblage. The outer part of garnet is further replaced by pure cordierite or occasionally cordierite plus quartz symplectite (Fig. 3e–f). In the matrix, sillimanite and hercynite coexist with coarse grained quartz, perthite and antiperthite.

The sample ALR 13-22 (x = 335550; y = 6510354) is a sapphirine–orthopyroxene gneiss taken from the same locality as Hermans et al. (1975) and Drüppel et al. (2013).The gneiss occurs as an E–W striking, tightly folded layer, enclosed in felsic garnet–orthopyroxene–spinel–cordierite migmatite (Fig. 2d). The sample is Foliation within the sapphirine layer is well-defined by the preferred orientation of biotite and the rather weak alignment of sapphirine crystals (up to 2 cm). The dominant minerals are orthopyroxene (20%), sapphirine (15%), cordierite (15%), spinel (5%), biotite (20%), antiperthitic plagioclase (15 %), mesoperthite (10%) with accessory ilmenite, monazite, xenotime and zircon; quartz is absent. Sapphirine crystals (X_{Mg} = 0.78−0.82; Tab. S3-4b) are prismatic and rarely in direct contact with a mantle of aluminous orthopyroxene (Al_2O_3 =

7.9–8.8 Wt. %; Tab. S3-4a). More frequent is the occurrence of a cordierite (X_{Mg} = 0.87−0.89; Tab. S3-4d) plus spinel (X_{Mg} = 0.51−0.52; Tab. S3-4c) reaction rim surrounded by pure cordierite (X_{Mg} = 0.88) toward orthopyroxene (Fig. 4a). Occasionally, biotite (X_{Mg} = 0.81−0.83; Ti = 0.21−0.23 apfu; Tab. S3-4e) replaces cordierite in the cordierite + spinel symplectite. Both biotite (X_{Mg} = 0.80) and cordierite (X_{Mg} = 0.86−0.88) also occur as isolated grains in the matrix.

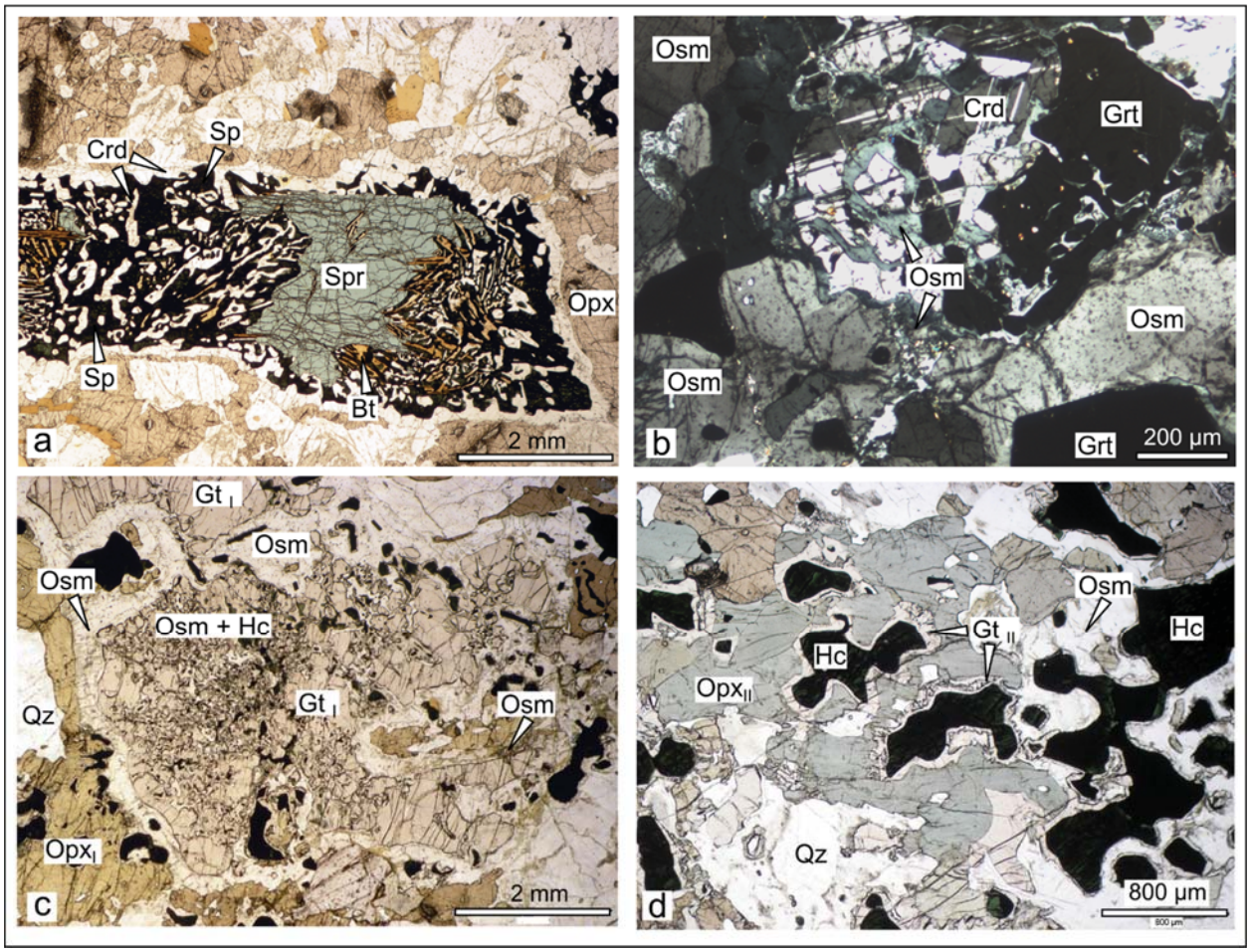

Fig. 3–4: Microstructure and paragenesis of sample ALR 13-22 (a), ALR 13-58 (b–d) **a–** Sapphirine mantled by orthopyroxene decomposes into Sp + Crd ± Bt **b–** Equant garnet crystal is pseudomorphosed by twinned cordierite that is in turn replaced by osumilite **c–** Garnet I porphyroblast breaks down into Osm + Hc with orthopyroxene in apparent equilibrium **d–** Hercynite crystals are rimmed by garnet II that are both enclosed in large Opx II

Pigeonite zone

The sample ALR 13-58 (x = 332482; y = 6503981) is an osumilite gneiss from the Vikeså locality reported by Maijer et al. (1981; Fig. 1b), within the Pig-in isograd. The highly heterogeneous structure of the outcrop consists of coarse quartz–mesopertite layers alternating with discontinuous pinkish layers rich in osumilite (up to 40 % in volume). Scarce garnet porphyroblast are unevenly distributed within the osumilite-rich layers (Fig. 2e). The dominant minerals are garnet (20 %), orthopyroxene (15 %), hercynite (10 %), osumilite (15 %),

mesoperthite (10 %), antiperthite (5 %), plagioclase (5 %) quartz (15%) with minor cordierite, sillimanite and accessory monazite, zircon and pyrrhotite.

At the microscopic scale no clear foliation is visible, except for unzoned sigmoid garnet (X_{Mg} = 0.36–0.38; Tab. S3-5b) enclosing oriented, and occasionally folded, needles of sillimanite together with F–Ti-rich biotite (X_{Mg} = 0.85–0.86; Ti = 0.22–0.28 apfu; F = 0.46–1.48 apfu; Tab. S3-5f), quartz, K-feldspar, ilmenite and magnetite. On the outcrop scale, preserved sigmoid garnet display two breakdown reactions that are texturally anterior to the osumilite-bearing paragenesis. The first one consists of a rim of plagioclase ($An_{27–28}$; Tab S3-5g) surrounded by a blocky high-Al orthopyroxene corona (X_{Mg} = 0.55–0.57; Al_2O_3 = 9.3–9.6 Wt. %; Tab. S3-5a). The second consists in isomorphic replacement of garnet by twinned cordierite (X_{Mg} = 0.78–0.81) that is further rimmed and partially replaced by osumilite (Fig. 4b). Most garnet crystal however are surrounded by a broad osumilite + hercynite domain enclosing numerous quartz blebs (Ti = 540–420 ± 40 ppm) as well as orthopyroxene blades (X_{Mg} = 0.57–0.60; Al_2O_3 = 9.3–9.6 Wt. %; Fig. 4c; Tab S3-5a). Overall, osumilite forms large grains (up to 1 mm) with composition ranging from X_{Mg} = 0.75–0.77 and Na = 0.15–0.18 apfu to X_{Mg} = 0.79–0.81 and Na = 0.14–0.16 apfu (Tab S3-5d). Spinel is mostly hercynite (X_{Mg} = 0.32–0.36; Tab S3-5c) with low ZnO + Cr_2O_3 content (< 0.3 Wt. %) along with minor magnetite. Secondary garnet rims (X_{Mg} = 0.29–0.32) occur alone or as a symplectite intergrowth with quartz on hercynite and garnet I crystals. Some of the hercynite grains with garnet II corona are themselves enclosed in secondary orthopyroxene (X_{Mg} = 0.57–0.59; Al_2O_3 = 7.2–8.8 Wt. %; Fig. 4d; Tab S3-5a). In localized areas of the thin section, osumilite breaks down to a fine symplectite of cordierite and K-feldspar ± quartz.

Phase equilibria modelling and textural interpretation

Orthopyroxene zone

Sample ALR 13-64 & 14-19

Given the similarities between samples *ALR 13-64* and *14-19*, we present only the pseudosection calculated for sample *ALR 13-64* (Fig. 5a). The pseudosection shows fields of mineral assemblages stable at low pressure granulite facies conditions and is contoured with the calculated X_{Mg} of cordierite and hercynite. The main features of the pseudosection includes solidus at *c*. 780 °C with disappearance of Ti-rich biotite at slightly higher temperature. Cordierite is consistently stable over the section for P < 6 kbar and coexists with hercynite ± magnetite above 850 °C in the pressure range of 3.5–6.5 kbar. Orthopyroxene is predicted on the low-P, high-T part

of the modelled section while garnet is stable on the low-T and high-P part. The interpreted peak assemblage of garnet, hercynite, cordierite, melt, plagioclase, K-feldspar, quartz and ilmenite defines a stability field between 860–970 °C and 4.5–6 kbar. Compositional isopleths of X_{Mg} in cordierite and hercynite intersect in the inferred peak temperature field at 875–910 °C and 5.2–4.5 kbar. Hercynite however contains significant amount of Cr and Zn in sample *ALR 13-64* in contrast

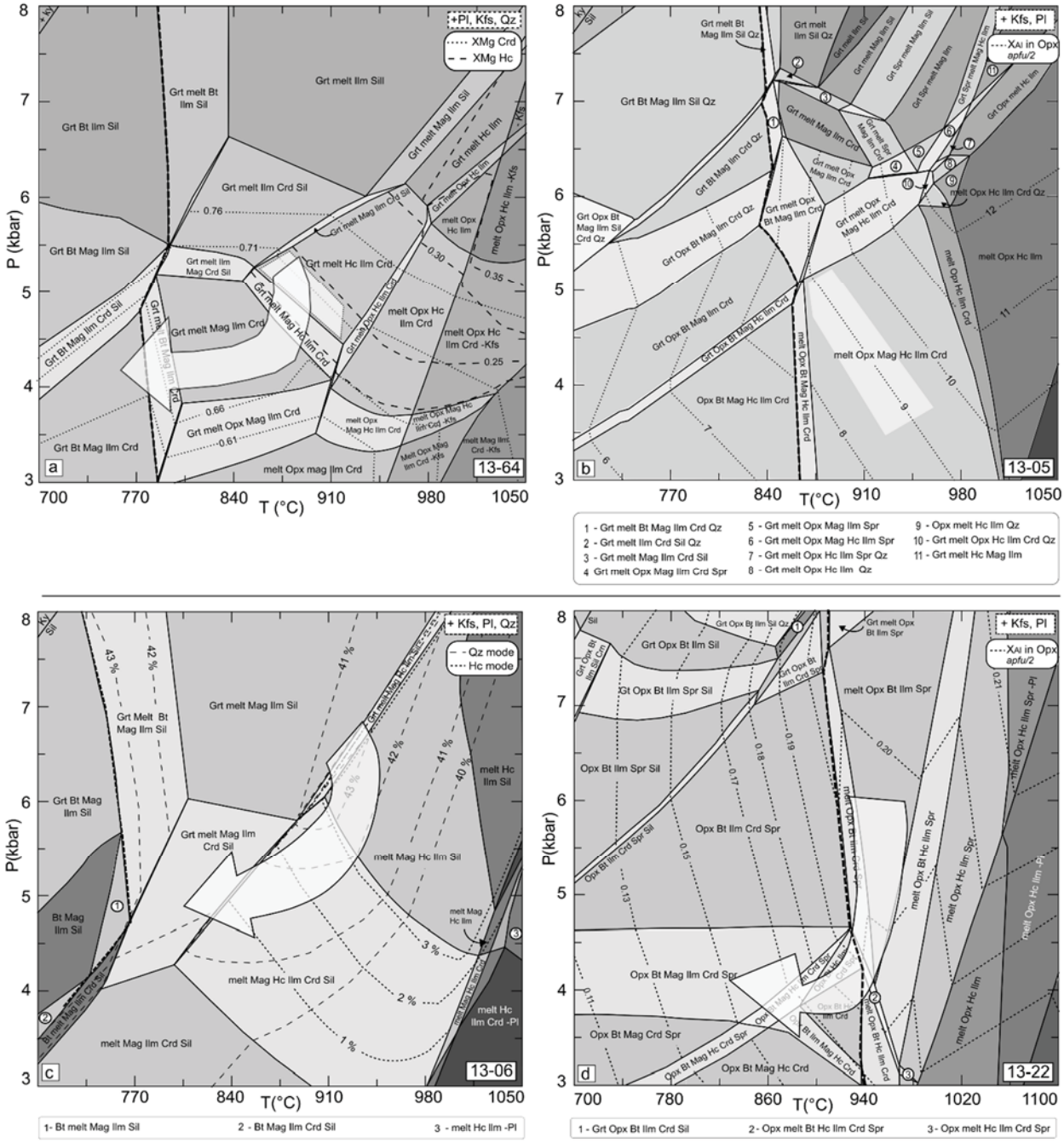

Fig. 3–5: *P–T* pseudosection generated with Perple_X 6.7.2 using the bulk composition reported in Tab. 1; the solidus is highlighted by bold dashes; the light grey arrow corresponds to the interpreted petrographical *P–T* path (see text) **a–** *P–T* pseudosection for sample *ALR 13-64* with superimposed isopleth of X_{Mg} in hercynite and cordierite **b–** P–T pseudosection for sample *ALR 13-05* with superimposed isopleth of Al_2O_3 in orthopyroxene **c–** *P–T* pseudosection for sample *ALR 13-06* with superimposed mode of quartz and hercynite **d–** *P–T* pseudosection for sample *ALR 13-22* with superimposed of isopleth of Al_2O_3 in orthopyroxene.

to sample *ALR 14-19*. These elements are yet not incorporated in thermodynamic models and should qualitatively expand hercynite stability field down temperature (Waters 1991).

Additionally, to account for the fact that quartz is largely present in the rock matrix but isolated from hercynite–cordierite layers by K-feldspar, we investigated the micro-chemistry of the hercynite–cordierite–K-feldspar microdomain by quantitative EDS mapping and *T–X* sections for sample *ALR 14-19* (supplementary material S3-7). The pseudosection calculated with the local chemistry retrieved from EDS mapping, indicates that, for quartz-undersaturated conditions, the hercynite phase may be stabilized at slightly lower temperature, in accordance with White (2003). However, the minimum stability temperature of the assemblage is controlled by the biotite-out and cordierite-in reactions which are only realized some 25 °C below the quartz-saturated estimates at constant pressure. As a consequence, a conservative peak temperature can be estimated as 850–900 °C at 5 kbar. The absence of orthopyroxene in the rock constrains the post-peak path to P > 4 kbar. Crystallization of cordierite at quartz and feldspar boundaries in the matrix is consistent with the cordierite-present, hercynite-absent field just above the solidus. A clockwise prograde path within the sillimanite stability field may be qualitatively deduced from the biotite + sillimanite inclusions in low-Ca garnet.

Osumilite zone

Sample ALR 13-05

On the pseudosection calculated for the garnet leucosome (Fig. 5b), the solidus is situated at *c*. 860°C. Garnet is predicted to be modally abundant above 5 kbar and to break down into a hercynite-bearing assemblage above the solidus at conditions ranging from 5 kbar and 850 °C to 7 kbar and 1050 °C. Sapphirine is stable at high-temperature and *P* > 6 kbar while cordierite has a wide stability field below 7 kbar. The peak mineral assemblage orthopyroxene, cordierite, hercynite, melt, K-feldspar, plagioclase, magnetite and ilmenite defines a wide stability field below 5.5 kbar and between 880 and 1000 °C. The isopleths of Al in orthopyroxene are superimposed on the calculated section and indicate temperature ranging from 900 °C at 5 kbar to 950°C at 3.5 kbar.

Sample ALR 13-06

The calculated pseudosection for sample *ALR 13-06* (Fig. 5c) shows a low solidus of *c*. 760 °C due to its essentially quartzo-feldspathic nature. Garnet is stable above a line crossing the section at 3 kbar, 700 °C to 8 kbar 980 °C while cordierite is stable at supra-solidus conditions below *c*. 6 kbar. The interpreted peak metamorphic assemblage hercynite + quartz is stable in a

wide field above *c*. 910 °C. Although remnants of garnet are scarce in the rock, the FMAS reaction Grt + Sil → Hc + Qz observed in the adjacent folded garnet layer (Fig. 2c; 3e–f), is favoured to explain the occurrence of hercynite + quartz assemblage. The pseudosection is contoured with quartz and hercynite mode (in vol. %). Above the solidus at 6 kbar, quartz mode decreases because of biotite melting reaction and increases when crossing the Grt + Sil → Hc + Qz reaction to reach a maximum of *c*. 43 vol% at *c*. 6 kbar and 920 °C. Further reaction involves Hc decomposing into Mag + Sil aggregates sometimes surrounded by cordierite that essentially reflects cooling outside the hercynite stability field.

Incursion in the UHT field for the rock package containing *ALR 13-05* and *13-06* in Gyadalen is recorded at two contrasting pressures: *c*. 6 kbar for sample *ALR 13-06* and between 5 and 3.5 kbar for sample *ALR 13-05* suggesting either decompression at UHT conditions or superposition of two thermal cycles.

Sample ALR 13-22

Important features of the pseudosection for the sapphirine–orthopyroxene gneiss (Fig. 5d) include a very high solidus temperature (*c*. 940 °C) and high-Ti biotite stability until 975 °C reflecting the refractory nature of this high-Al–Mg quartz-free granulite. Garnet is predicted stable at $P > 7$ kbar while orthopyroxene and sapphirine share a large stability field. Hercynite and cordierite are stable together only between 780 and 940 °C at low pressure. The interpreted quartz-absent peak assemblage consisting of orthopyroxene, sapphirine, melt, ilmenite, biotite, K-feldspar, plagioclase define a stability field between 950 and 1000°C and 4–8 kbar. The isopleths of Al in orthopyroxene indicate rather low pressure around 5 kbar and 950 °C. Replacement of peak mineral sapphirine by spinel + cordierite ± biotite intergrowth which reflects decompression to *c*. 3.5 kbar and 900 °C. The abundances and compositions of phases are in overall good agreement between the model and thin section estimates. However, the modelled composition of sapphirine lies between 7:9:3 and 3:5:1 endmember while the measured composition is a mixture between the 7:9:3 and 2:2:1 endmember. This discrepancy in sapphirine composition urges caution in the interpretation of the pressure difference between this sample and the other from the osumilite zone.

Pigeonite zone

Sample ALR 13-58

The pseudosection for the osumilite gneiss (Fig. 6) was calculated with the database of Kelsey et al. (2004) and the osumilite model of Holland et al. (1996). The section is designed to constrain the peak temperature and is thus calculated metastable with respect to cordierite in order to stabilize osumilite at $T > 900$°C in accordance with experimental and field studies (Carrington and Harley 1995; Mitchell et al. 2014). The solidus temperature of approximately 850 °C coincides with the disappearance of biotite. The bulk X_{Mg} composition of the rock is not high enough to stabilize sapphirine at the investigated pressure whereas hercynite is stable in a large portion of the section from 5 to 8 kbar and 850 to 1050 °C. Orthopyroxene is stable throughout the section while garnet stability limit evolves from *c*. 4.7 kbar at 800°C to 6.8 bar at 950 °C. The interpreted peak assemblage minerals osumilite, orthopyroxene, hercynite, magnetite, ilmenite, melt, K-feldspar and plagioclase coexist in a field extending from 6 kbar and 875 °C to 4.8 kbar and 1020 °C. Isopleths of Al in orthopyroxene superimposed on the pseudosection indicate a temperature of 910 ± 30 °C. The modelled X_{Mg} composition of osumilite (calculated: 0.78–0.81; measured: 0.75–0.81), orthopyroxene (calculated: 0.55–0.56; measured: 0.55–0.57) and hercynite (calculated: 0.34–0.36; measured: 0.32–0.36) are in excellent agreement. The peak temperature assemblage osumilite–hercynite–orthopyroxene has been reproduced experimentally at high-f(O_2) and low-X_{Mg} (X_{Mg} = 0.53) bulk composition by Das et al. (2001). These authors have shown that the assemblage is restricted to pressure below 7–8 kbar, which is slightly higher than the modelled one, and temperature in the range of 850–950 °C.

↓ **Fig. 3–6**: P–T pseudosection generated with Perple_X 6.7.2 using the bulk composition reported in Tab. 1 for sample ALR 13-58 with superimposed isopleth of Al2O3 in orthopyroxene; the solidus is highlighted by bold dashes; the light grey field corresponds to the interpreted P–T peak (see text)

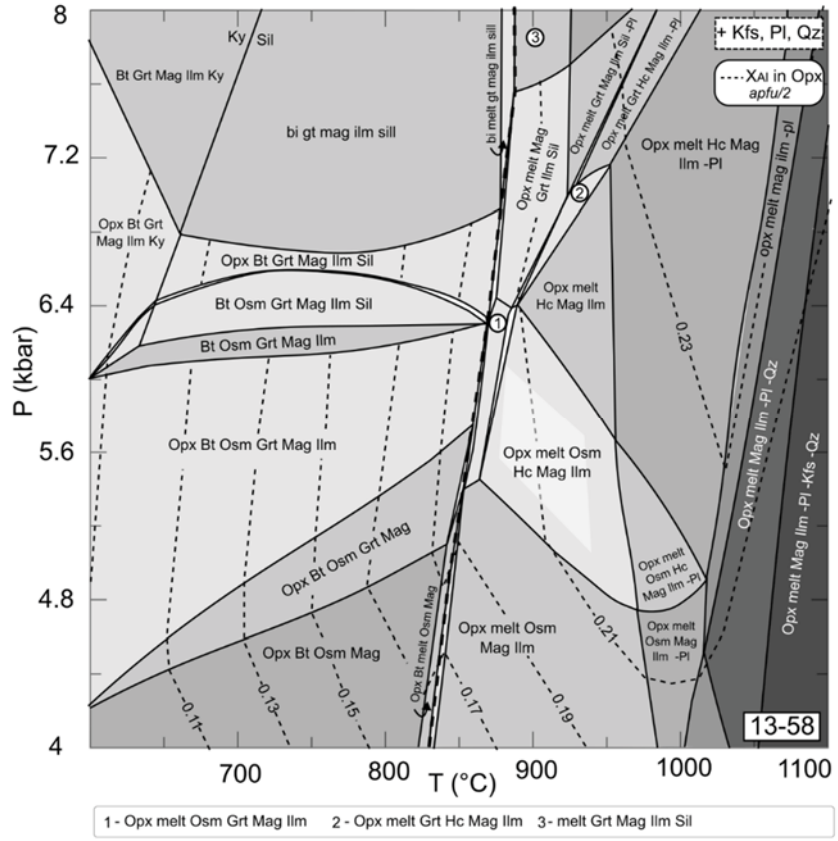

Monazite–xenotime chemistry and monazite U–Th–Pb geochronology

Orthopyroxene zone

Monazite crystals from the *cordierite–hercynite gneiss ALR 13-64* generally preserve distinct core–rim zoning. In a ternary compositional plot of molar monazite–huttonite–cheralite (Fig. 7a; Tab. 3), the core domains are distinguished by overall higher cheralite + huttonite than the rims. All grains and domains are low in Y_2O_3. The rim of zoned crystals gives a U–Th–Pb age consistently younger than the core, although the data overlap within the 2σ uncertainty of 2.5–3 % (Tab. 4). At the population scale core and rim domains have also overlapping ages within error. Core domains define a weighted $^{206}Pb/^{238}U$ age of 1020 ± 7 Ma (Fig. 7b; 2σ; MSWD = 0.30; *n* = 17) while rim domains yield 1011 ± 7 Ma (Fig.7b; 2σ; MSWD = 0.38; *n* = 20). The $^{208}Pb/^{232}Th$ isotopic system define consistent but significantly older weighted mean values of 1048 ± 8 Ma for the core group (MSWD = 0.6) and 1035 ± 7 Ma (MSWD = 0.6) for the rim group.

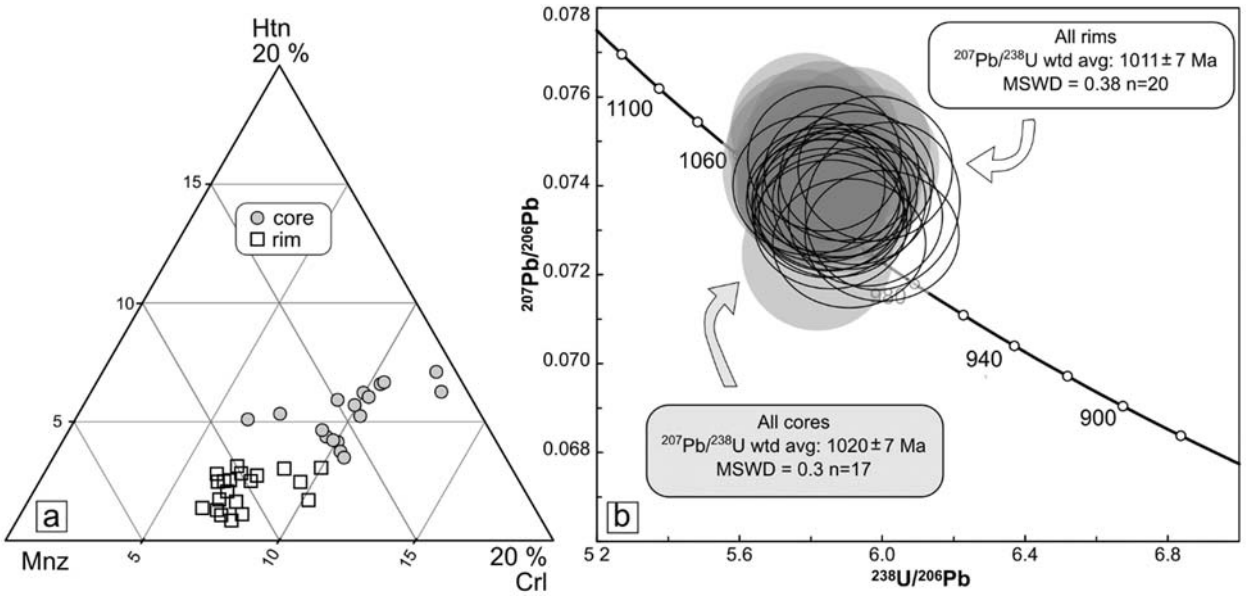

Fig. 3–7: Monazite micro-chemistry and geochronology for sample *ALR 13-64*. **a–** Ternary compositional diagram (mol. %) in the system monazite (Mnz: REEPO4) – cheralite (Crl: (Ca,Th)(PO4)2) – huttonite (Htn: ThSiO4) **b–** U–Pb data in Tera-Wasserburg diagrams by group (see text). All error ellipses are 2σ, decay constant errors are included in the pooled ages.

Sample *ALR 14-19* contains monazite crystals of light yellow colour, hosting numerous solid and fluid inclusions. High contrast BSE imaging reveals complex patchy zoning rather than core–rim concentric zoning. Overall the chemical composition (Tab. 5) of the different zones are mostly rich in U (UO_2 > 0.5 Wt. %) but poor in Y (Y_2O_3 < 1 Wt. %) with variable Th content (ThO2 = 2.2–11.7 Wt. %). Forty-four U–Th–Pb isotopic analyses were performed in 26 grains (Tab. 5). They divide in two broad age groups with some analyses scattering between them. The oldest age groups consists of 27 analyses in 20 grains defining a weighted $^{206}Pb/^{238}U$ age of 1035 ± 7 Ma (Fig. 8; 2σ; MSWD = 0.4), equivalent within the error to the $^{206}Pb/^{207}Pb$ weighted average of 1039 ± 6 Ma (Fig. 8; 2σ; MSWD = 0.7). Individual $^{206}Pb/^{238}U$ ages in this group ranges from 1060 ± 35 to 1018 ± 34 Ma. The youngest age group show excess scattering but may nevertheless be estimated by the weighted $^{206}Pb/^{238}U$ age of 955 ± 22 Ma retrieved from the two concordant spot located in the centre of the cluster (Fig. 8; 2σ). We have not been able to find any correlation between age and chemistry. However patchy zoning with the presence of fluid inclusions hints to several dissolution–precipitation episodes.

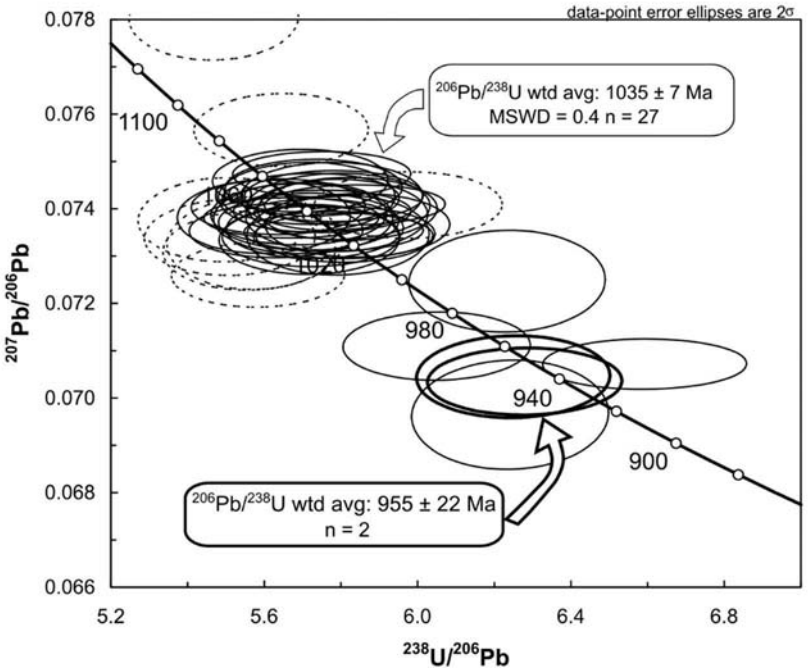

Fig. 3–8: Monazite U–Pb geochronology for sample *ALR 14-19* presented in Tera-Waserburg diagram. All error ellipses are 2σ, decay constant errors are included in the pooled ages.

Osumilite zone

Within the *undeformed garnet leucosome ALR 13-05*, BSE imaging of large monazite grains reveal a bright high-Th core rimmed by dark-grey medium-Th rims. Chemical analyses document that both core and rims have similar cheralite content but huttonite content decreases from core to rim (Fig. 9a; Tab. 6). Among medium Th rims it is further possible to distinguish a high-Y population incorporating up to 17 mol. % of xenotime component. The high-Y population is moreover lacking S and has low La/Gd ratio normalized to chondrite ($La_N/Gd_N < 2$) compared to the high-Th core and low-Y rims (Tab. 6). Isotopic U–Th–Pb analyses were performed on a total of 41 spots in 29 grains (Tab. 7). All analyses are presented in a Tera-Wasserburg concordia diagram and are colour-coded with their Th/Y ratio measured by EPMA prior to laser ablation (Fig. 9b). Thorium-rich monazite cores define a U–Pb concordia age of 1032 ± 5 Ma (2σ; $n = 24$). Medium Th-rims, poor in Y display some scatter in individual $^{206}Pb/^{238}U$ ages ranging from 1017 ± 28 Ma down to 968 ± 28 Ma. If pooled together, medium-Th, low-Y rims yield a $^{206}Pb/^{238}U$ weighted average of 992 ± 13 Ma (2σ; MSWD = 1.4; $n = 8$). Finally, high-Y rims define a concordia age of 931 ± 6 Ma (2σ; $n = 9$). The $^{208}Pb/^{232}Th$ isotopic system define weighted mean ages of 1027 ± 6 Ma for high Th core (MSWD = 0.56), 986 ± 9 Ma (MSWD = 0.73) for medium-Th, low-Y rims and 933 ± 14 (MSWD = 2.4) for high-Y rims, in good agreement with U–Pb ages.

The *hercynite–quartz sample ALR 13-06* contains zoned monazite grains consisting of a BSE-dark, high Y core (up to 5.36 Wt. % Y_2O_3) surrounded or cross-cut by a BSE-bright rim with overall lower Y content (Tab. 8). When considering all grains together, the chemistry of the different zones largely overlap (Fig. 9c) and are characterized by high S content (up to 6400 ppm SO_2; Tab. 8). Geochronological data were collected on a total of 33 spots in 23 grains (Tab. 9).

All U–Pb analyses are presented in Tera-Wasserburg concordia diagram (Fig. 9d); two considerably older spots yielding $^{206}Pb/^{207}Pb$ ages older than 1100 Ma point to unresolved inheritance and are not taken into account in the following pooled ages. Core and rim domains yield equivalent $^{206}Pb/^{207}Pb$ ages of 1042 ± 11 Ma (MSWD = 0.33; n = 14) and 1037 ± 12 (MSWD = 0.27; n = 16) respectively. Taken together, core and rim groups define a pooled $^{206}Pb/^{207}Pb$ age of 1040 ± 9 (MSWD = 0.23; n = 29). One analysis has a significantly younger $^{206}Pb/^{207}Pb$ age of 984 ± 31 Ma.

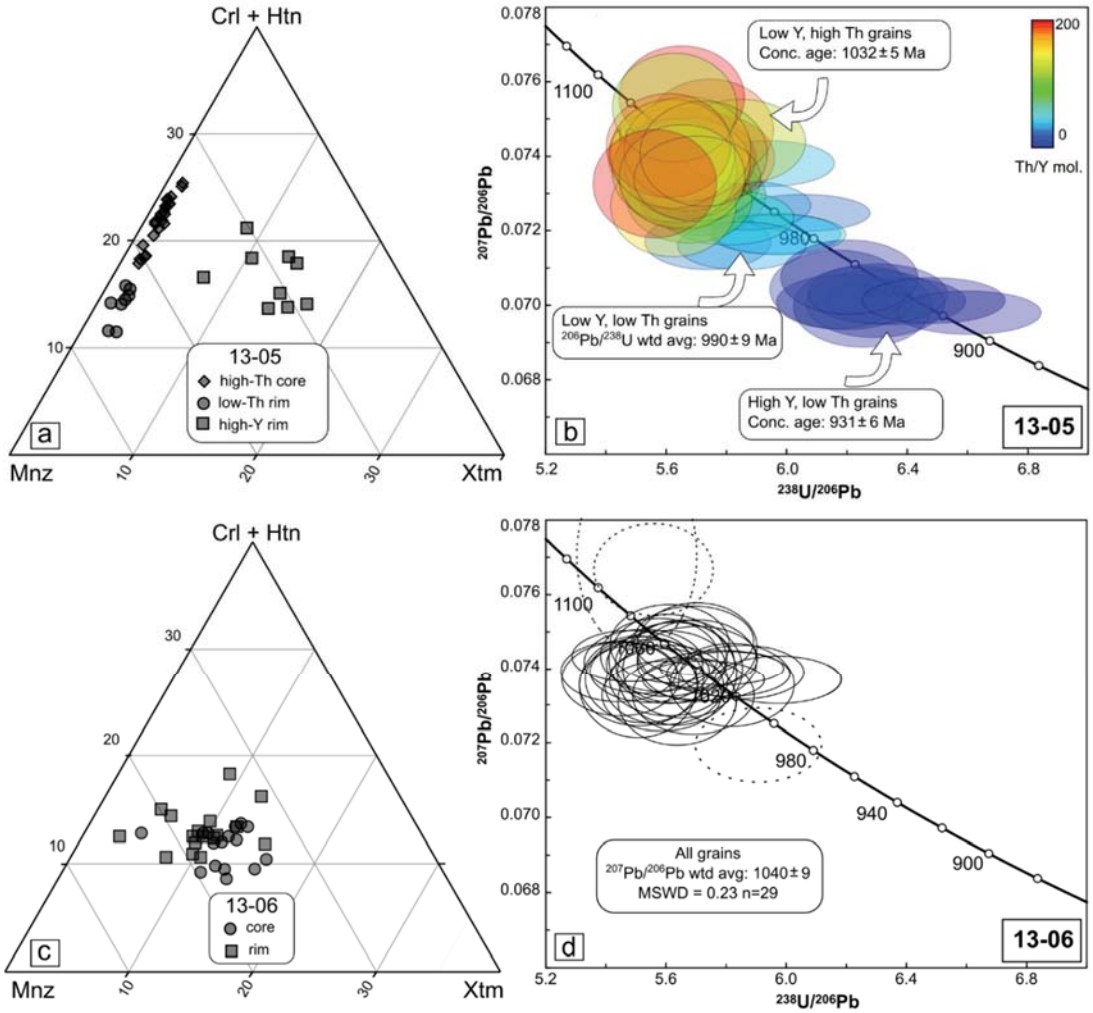

Fig. 3–9: Monazite micro-chemistry and geochronology for sample *ALR 13-05* (a–b) and ALR 13-06 (c–d). **a**– Ternary compositional diagram (mol. %) in the system monazite (Mnz) –cheralite (Crl) – huttonite (Htn) for sample *ALR 13-05* **b**– U–Pb data for sample *ALR 13-05*. Analyses are colour-coded with their molar Y/Th ratio (see text) **c**– Ternary compositional diagram (mol. %) for monazite in sample *ALR 13-06* **d**– U–Pb data for sample *ALR 13-06*; dotted ellipses are not integrated in the pooled age (see text). All error ellipses are 2σ, decay constant errors are included in the pooled ages.

The *sapphirine gneiss (ALR 13-22)* contains monazite, xenotime and zircon (Fig. 10a–d), and is therefore amenable to monazite–xenotime geothermometry. Monazite crystals may be split into two chemical populations that correlates well with crystal size (Tab. 2). The first population (S1) consists of small crystals (< 100 μm) that are very rich in ThO_2 (up to 33.0 Wt. %) and Y_2O_3 (up to 7.15 Wt. %) and show either oscillatory (S1a) or patchy (S1b) zoning in BSE images (Fig. 10a–b). Thorium is incorporated dominantly through the cheralite substitution (X_{Crl} up to 31 mol. %) and to a lesser extent through the huttonite substitution. Mole fraction of xenotime component in high-Th crystals ranges from 13 % to 21 % (Fig. 10e). Additionally, high-Y patchy zoned monazite preserves large intra-grain variation of Th while Y remains almost constant (e.g. grain 44; ThO_2 = 33.02–16.99 and Y_2O_3 = 6.10–6.47 Wt. %; Tab. 2). The second population (S2) is composed of large crystals (100–350 μm) that have low-Y content (Y_2O_3 = 0.3–2.4Wt. %), moderate concentration of ThO_2 (2.9–5.2 Wt. %) and typically show numerous inclusions (< 5μm) of $ThSiO_4$ and xenotime with minor apatite and K-feldspar (Fig. 10c). Mole fraction of xenotime in low-Y crystals ranges from 3 % to 10 %. In the matrix, xenotime is found either as large (up to 400 μm) zoned grains or as small crystals grown in epitaxy on zircon (Fig. 10d). The latter show lower huttonite–coffinite substitution (up to 6 mol. %) than xenotime from the matrix (Tab. 2).

Monazite grains from each population were selected for U–Th–Pb geochronology by LA–ICP–MS (Tab. 10). All U–Pb analyses are presented in a Tera-Wasserburg concordia diagram and are colour-coded with their Y_2O_3 content (Fig. 10f). Monazite analyses plot along the concordia curve quasi continuously from *c*. 1040 Ma down to 920 Ma. They show a strong correlation between Y_2O_3 content and U–Pb age. Twelve analyses in 9 oscillatory zoned grains rich in Y and Th define a $^{206}Pb/^{238}U$ weighted average age of 1029 ± 9 Ma (2σ; *n* = 12; MSWD = 0.3). Patchy zoned grains rich in Y and Th define a $^{206}Pb/^{238}U$ weighted average age of 1006 ± 8 Ma (2σ; *n* = 18; MSWD = 0.5). Eighteen analyses achieved in 13 low Y grains spread along the concordia curve between *c*. 980 and 920 Ma with no significant clustering. The $^{208}Pb/^{232}Th$ isotopic system defines significantly older mean values of 1086 ± 17 Ma for the high-Y oscillatory group (MSWD = 3.4) and 1062 ± 14 Ma (MSWD = 3) for the high-Y patchy group. Low-Y monazite with xenotime and $ThSiO_4$ inclusions display individual $^{208}Pb/^{232}Th$ ages ranging from 965 ± 23 to 892 ± 24 Ma.

Previous geochronological studies from the same locality by Drüppel et al. (2013) has established that xenotime was stable during the whole duration of Sveconorwegian metamorphism, since large xenotime grains in the matrix preserve detrital cores *($^{206}Pb/^{238}U$ age between 1490 and 1300 Ma)* and record both M1 and M2 metamorphic events (*$^{206}Pb/^{238}U$ ages ranging from c. 1011*

to 925 Ma). Therefore we can confidently assume monazite–xenotime coexistence in the sample at different stage of evolution and apply monazite–xenotime thermometry. Analyses of oscillatory and patchy-zoned high-Y monazite crystals yield equivalent and well clustered mean temperature of 895 °C and 883 °C, respectively. With high-Y but variable Th, these analyses are well distributed along a long segment of a single isotherm in the ternary $CePO_4$–YPO_4–$ThSiO_4$ system, as calibrated by Seydoux-Guillaume et al. (2002b). Analyses of the low-Y monazite population S2 yields lower temperatures scattering from 245 to 877 °C, with an average value of 500 °C (Fig. 10e).

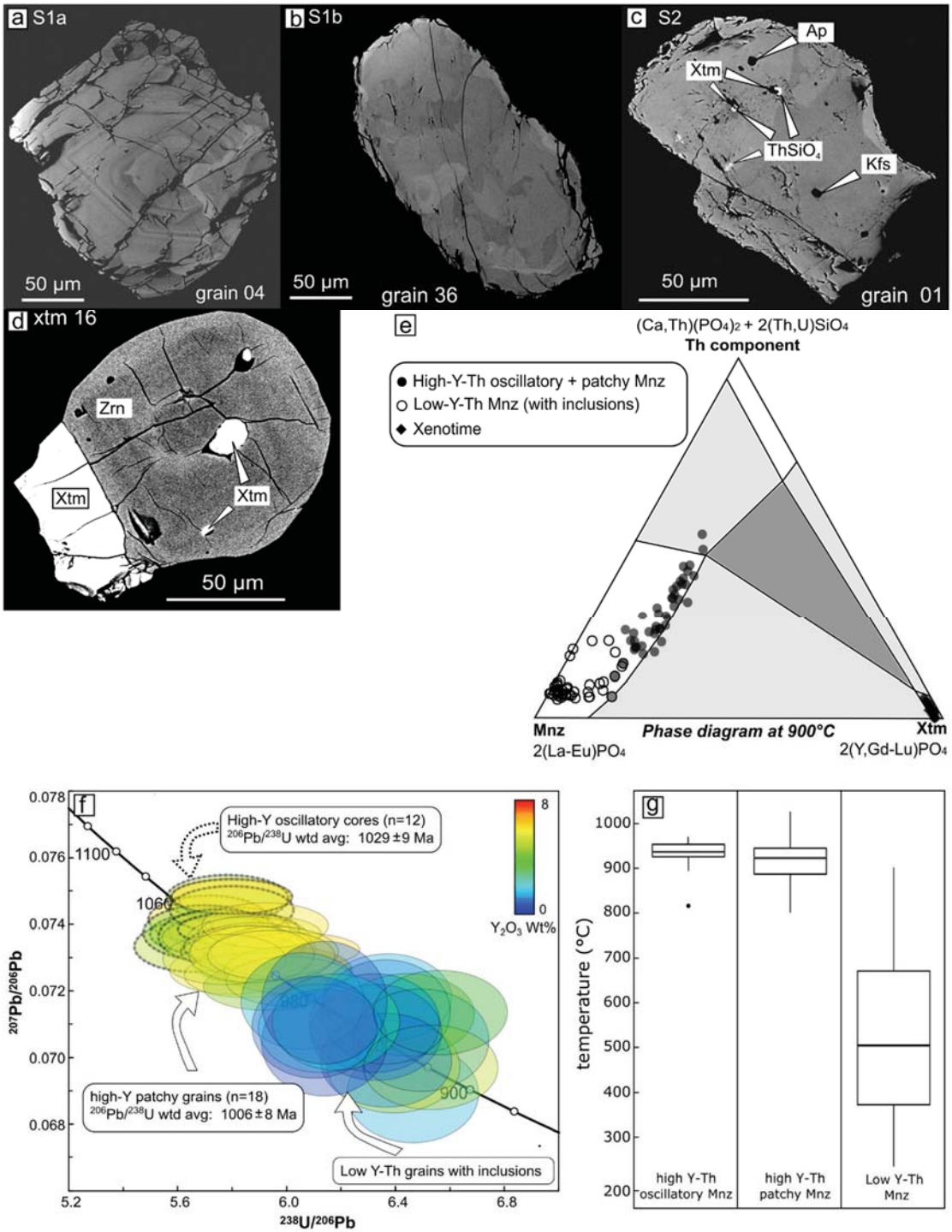

↑ **Fig. 3–10**: Monazite–xenotime–zircon textural relationships (a–d), geochronology (e) and phase diagram for sample *ALR 13-22*. **a–** BSE image of high-Y oscillatory zoned monazite crystal (S1a). **b–** BSE image of high-Y patchy zoned monazite crystal (S1b) **c–** BSE image of low-Y monazite crystal (S2) with inclusions of xenotime (Xtm), apatite (Ap), K-feldspar (Kfs) and unidentified ThSiO4 polymorph **d–** BSE image of xenotime (Xtm) grown in epitaxy on oscillatory zoned zircon (Zrn). **e–** U–Pb data for sample ALR 13-22. Analyses are colour-coded with their molar Y_2O_3 content (see text). All error ellipses are 2σ, decay constant errors are included in the pooled ages. **f–** Monazite and xenotime micro-chemistry reported in ternary compositional diagram (mol. %) in the system monazite (Mnz) – xenotime (Xtm) – Th-component (Crl + Htn) with superimposed phase diagram in the system CePO4–YPO4–ThSiO4 (Seydoux-Guillaume et al. 2002b) at 900°C; greyscale colour correspond to variance

Pigeonite zone

In the *osumilite gneiss (ALR 13-58),* large monazite grains (> 100 μm) from the matrix have been investigated in detail in Chp. 2. Overall, they show three chemical domains, (1) a sulphate-rich core D1 (0.45–0.72 Wt. % SO_2, Th incorporated as cheralite component), (2) secondary sulphate-bearing domains D2 (SO_2> 0.05 Wt. %), and (3) late sulphur-free, Y-rich domains D3 (0.8–2.5 Wt. % Y_2O_3, Th accommodated as huttonite component). Here, we focus on the occurrence of small crystals (< 15 μm) of monazite that are texturally linked to garnet breakdown reaction into osumilite (Fig. 11a). These small grains have been divided in two textural groups that correlates with their chemistry (Tab. 11). The first group D5 is present in small "pockets" (< 50 μm) filled with osumilite and K-feldspar within porphyroblastic garnets (Fig. 11b–c) while grains from the second group D4 are located within the broader reaction rim of osumilite + hercynite ± orthopyroxene in the exterior of garnet porphyroblasts. The D5 group has low to very low ThO_2 (1.5–4.1 Wt. %) and high but variable Y_2O_3 (3.4–7.2 Wt. %) and HREE contents together with low La_N/Gd_N ratio (0.3–1.6). The group D4 has chemical composition intermediate between D5 and D3 (Fig. 11d) with Y_2O_3 ranging from 0.7 to 5.7 Wt. %. The investigated grains of D4 and D5 monazite are too small for isotopic analyses by LA–ICP–MS, but were dated using the EPMA U–Th–Pb total chemical method (Tab. 12). The results are presented in a probability plot (Fig. 12). The statistical treatment of Montel et al. (1996) demonstrates that all analyses represent a single age population at 95 % confidence level. The pooled age of all (D4 + D5) grains is 929 ± 12 Ma with individual ages ranging from 892 ± 71 Ma to 967 ± 57 Ma.

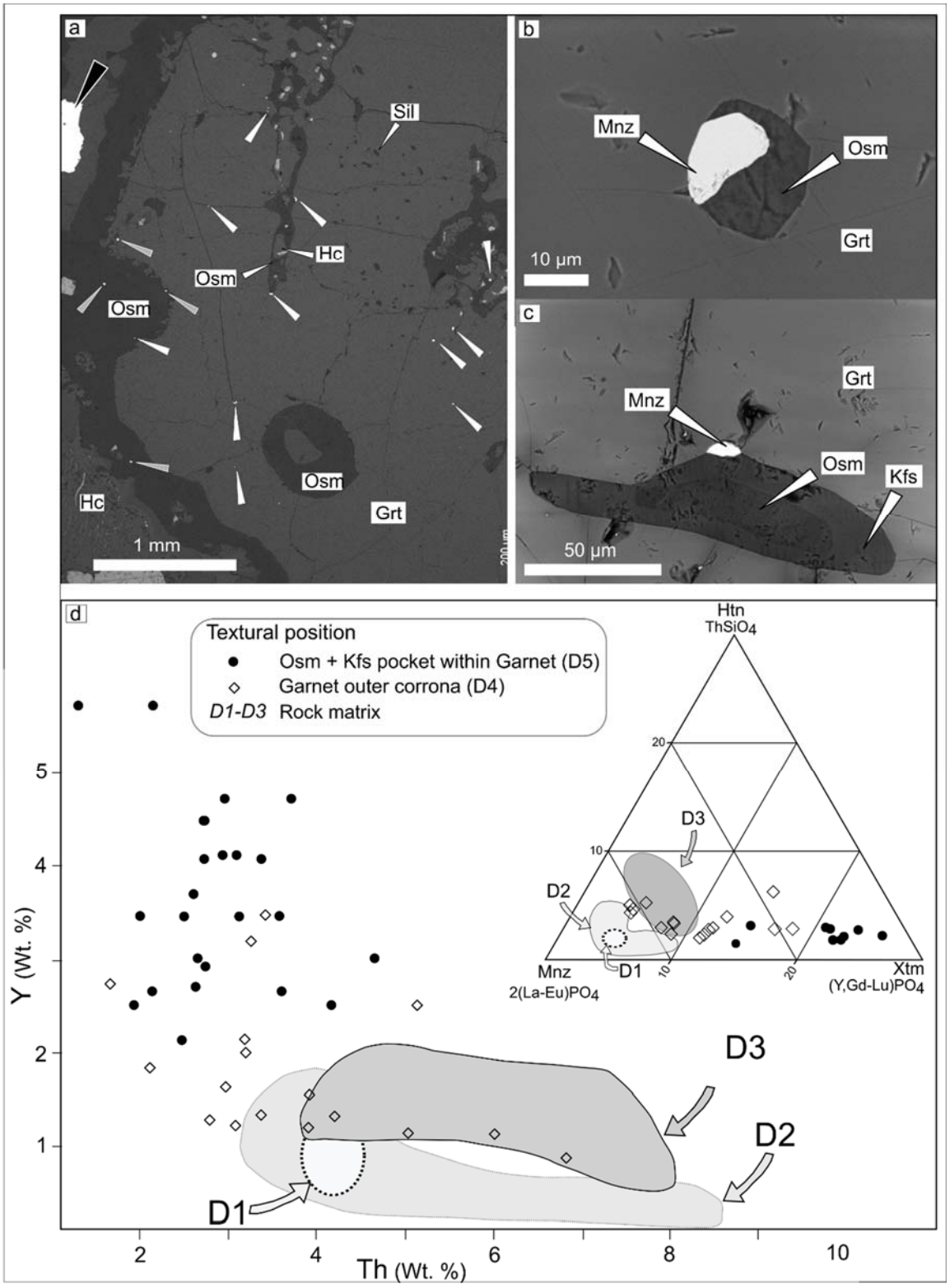

Fig. 3–11: Monazite texture (a–c) and micro-chemistry (d) for sample ALR 13-58. **a–** BSE image showing monazite location (arrows) within the reaction texture Grt + Sil → Osm + Hc (see also Fig. 4c) **b–c** BSE images of small monazite crystals (D5) enclosed in osumilite-bearing pockets inside garnet porphyroblasts **d–** Composition of monazite crystals occurring within the garnet-breakdown products (D4 & D5) compared to matrix monazite (D1–3) studied in Chp. 3; top-right inset shows monazite composition in ternary diagram (mol. %) monazite (Mnz) – cheralite (Crl) – huttonite (Htn).

Discussion

A monazite based temperature–time path

The garnet-absent sapphirine gneiss (*ALR 13-22)* contains monazite and xenotime, and therefore provides critical linking between temperature and time, via Y thermometry in monazite. Phase relationships between monazite and xenotime show that despite variable and high-Th content, the oscillatory and patchy high-Y monazite populations are distributed along a single isotherm of c. 900 °C in the ternary $CePO_4$–YPO_4–$ThSiO_4$ system (Fig. 10d). It is hence possible to infer with confidence that oscillatory and patchy high-Y monazite crystalized near or at UHT conditions between 1029 ± 9 Ma and 1006 ± 8 Ma from a stable physico-chemical environment. The oscillatory zoning further indicates melt-present conditions at 1029 ± 9 Ma suggesting crystallization in the orthopyroxene–sapphirine stability field (T > 900 °C; Fig. 5d). This conclusion is in line with Ti-in-zircon thermometry performed by Druppel et al. (2013) indicating zircon crystallization at 1010 ± 7 Ma and 1006 ± 4 Ma at a minimum temperature of 850 °C.

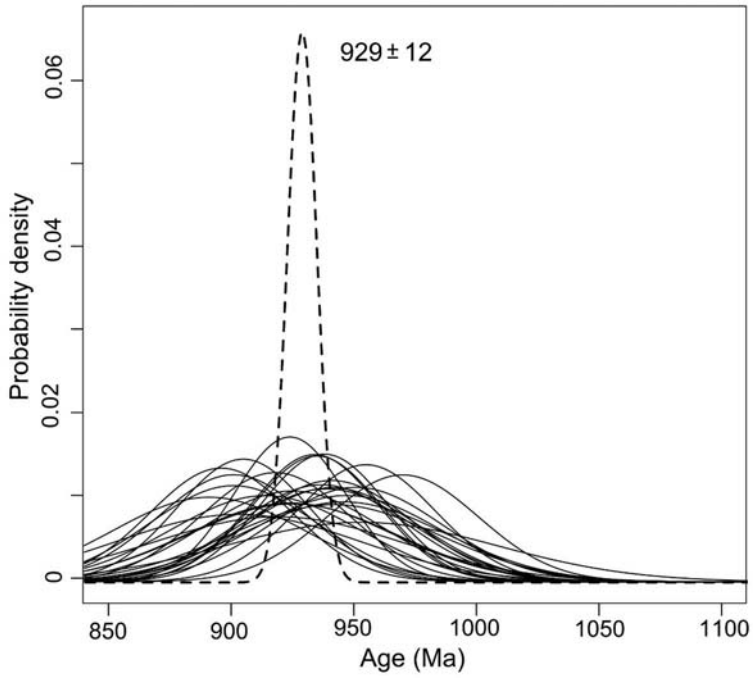

Fig. 3–12: Weighted-histogram representation of monazite EPMA U–Th–Pb data for sample ALR 13-58 generated with the NiLeDam R-package (see text). The small bell-shaped curve represents the probability density function of one measurement; the tick dotted curve represents the calculated age.

Following the peak temperature, granulite facies rocks that kept record of their peak mineral assemblage generally undergo melt loss (Brown 2002). Although this event cannot be specifically dated in sample *ALR 13-22*, the low-Y monazite population record significantly lower apparent temperatures in the 990–950 Ma time interval (Fig. 10f). The disequilibrium reaction

texture, with $ThSiO_4$, xenotime and apatite inclusions, observed in these grains suggest that they result from the breakdown of primary high-Y-Th monazite as described by Seydoux-Guillaume et al. (2012). The huttonite and xenotime component in monazite are redistributed isochemically as thorite and xenotime, respectively. In contrast, the cheralite component of monazite is redistributed between apatite ($CaPO_4$) and thorite ($ThSiO_4$) or thorianite (ThO_2) (Popa et al. 2008; Harlov et al. 2011). In our sample, only a $ThSiO_4$ polymorph was observed indicating that Si was probably in excess in the fluid thereby favouring $ThSiO_4$ precipitation over ThO_2. Complete resetting of the U–Th–Pb system in monazite at T > 600 °C has been demonstrated experimentally by Williams et al. (2011) and Seydoux-Guillaume et al. (2002a) supporting the interpretation of U–Pb ratio from re-equilibrated grains as meaningful geological ages. The large spread in measured temperature is however equivocal and the mean temperature may well be meaningless, since it is hard to find which part (if any) of recrystallized monazite is in equilibrium with xenotime (Fig. 10c; Fig. 13). The occurrence of low-Y monazite nevertheless demonstrates that high-Y monazite were no longer stable in the 980–950 Ma time interval and suggests repeated fluid infiltration events perhaps in response to volatile exsolution upon crystallization of surrounding mobile partial melt.

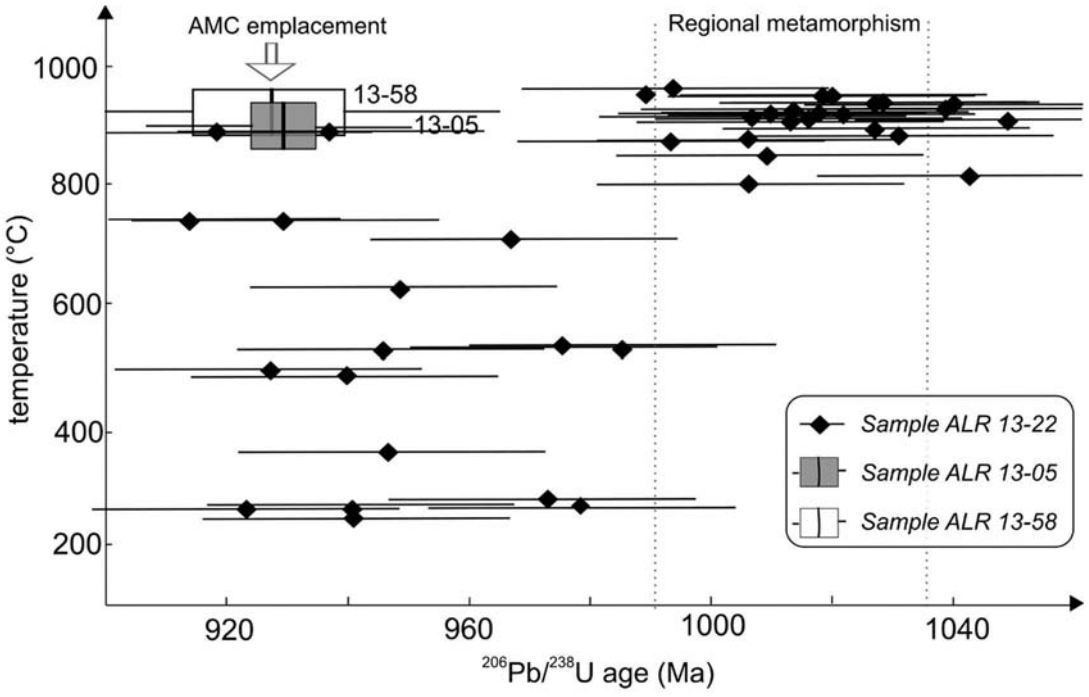

Fig. 3–13: Temperature–time evolution of the samples in the osumilite-zone constrained by Y-in-monazite thermometry for sample *ALR 13-22* (see discussion in text) and *P–T–t* estimates of UHT conditions for sample *ALR 13-58* and *ALR 13-05* (see discussion in text). Horizontal size of the boxes for samples *ALR 13-05* and *ALR 13-58* represent 2σ uncertainty on pooled age determination, while horizontal lines correspond to minimum and maximum age for single spot data. Emplacement of the AMC complex is dated at 931 ± Ma by Schärer et al. (1996).

In garnet-present samples, textural correlation and microchemical analyses link monazite U–Th–Pb ages with silicate stability. In a typical metapelite, a major part of HREE and Y are hosted in garnet that will control the budget of these elements and hence Y incorporation in monazite in the absence of xenotime (Spear and Pyle 2002; Berger et al. 2005; Didier et al. 2015). In the osumilite gneiss (*ALR 13-58*), small, unzoned, monazite crystals located within garnet breakdown products display high, although variable, Y enrichment compared to matrix monazite (Fig. 11d). In detail, small monazite crystals in Kfs ± Osm pockets within the garnet interior (D5) define a high-Y, low-Th endmember while grains located in the outer corona (D4) have intermediate composition between the high-Y endmember (D5) and matrix monazite (D3). This trend strongly suggests that the control of Y budget by garnet in this sample is limited to short distances implying a lack of garnet–monazite equilibrium in the reacting volume. Under these conditions, the YAG thermometer certainly cannot be applied (Pyle et al. 2001). Taken together, all Y-rich crystals analysed in this study (D4 in Osm + Hc ± Opx rim, D5 in inclusion in garnet) define a single chemical age of 929 ± 12 Ma that is interpreted to reflect garnet breakdown into osumilite + hercynite and hence the timing of M2 UHT conditions. Although the concordance of EPMA dates cannot be assessed, this interpretation is supported by LA–ICP–MS isotopic dating of monazite D3 domains which yields a concordia age of 935 ± 7 Ma (Chp. 3). Similar conclusions can be reached from the high-Y monazite rim in the garnet leucosome (*ALR 13-05*) which is interpreted to record the garnet breakdown into the low-*P* UHT mineral assemblage cordierite–hercynite–orthopyroxene at 931 ± 6 Ma (Fig. 9b).

Two phases of UHT metamorphism

The *P–T* evolution of the investigated samples are characterized by a rather tight clockwise loop with minor (1.5–2 kbar) decompression (Fig. 13). The sample from the Opx zone (*ALR 13-64*) yields peak conditions of 850–900°C and *c.* 5 kbar (Fig. 5a). Monazite geochronology indicates a protracted regional metamorphic event that resulted in crystallization of zoned crystals defining a continuous chemical and geochronological trend clustering at 1020 ± 7 Ma and 1011 ± 7 Ma (Fig. 7b), in broad accordance with previous age determinations on monazite (Bingen and Van Breemen 1998; Bingen et al. 2008a) and zircon (Möller et al. 2002; Tomkins et al. 2005; Coint et al. 2015).

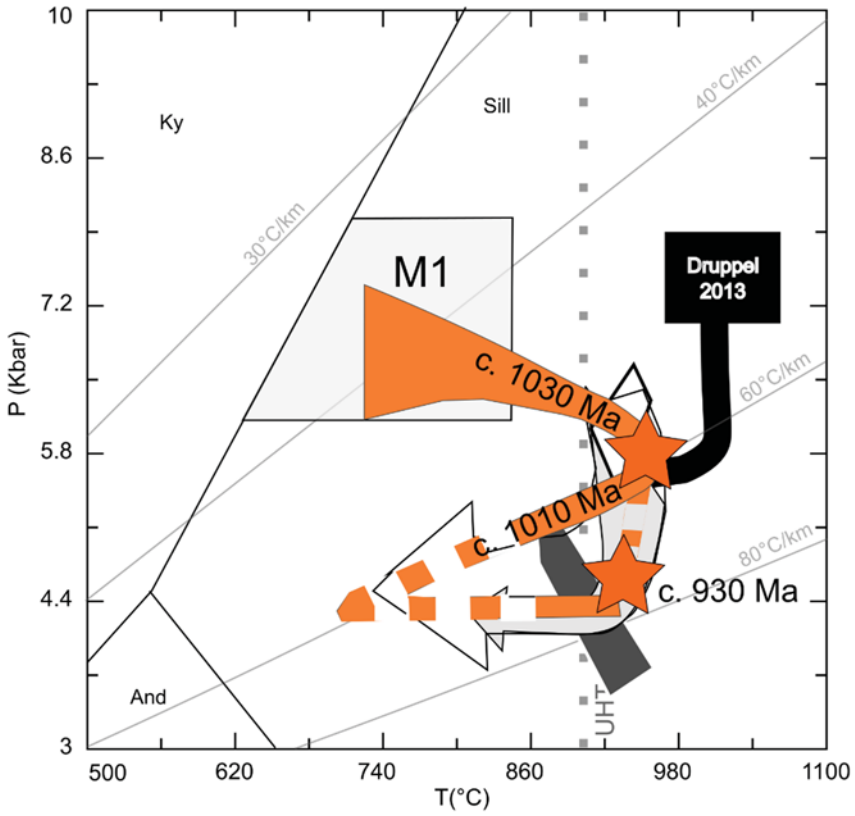

Fig. 3–14: Synthetic *P–T* diagram for osumilite- and pigeonite-zone samples. P–T conditions deduced from petrography only are in grey shades while the proposed new two phase P–T–t path is coloured.

Considering the three samples from the osumilite and pigeonite zones (*ALR 13-22, 13-05, 13-58*), two distinct UHT events emerge at *c*. 1030–1005 Ma and at *c*. 930 Ma (Fig. 12). Evidence of the early prograde path in UHT samples is tenuous and mainly represented by sillimanite + biotite inclusions in porphyroblastic garnet. These inclusions suggest a shared prograde evolution between the Opx, osumilite and pigeonite zone samples showing the same mineral assemblage. The three samples belonging to the UHT zone display overall the same age distribution during the regional metamorphic event M1. The oldest dates are recorded by S-rich monazite crystals from both the hercynite + quartz sample (*ALR 13-06*) at 1040 ± 9 Ma (Fig. 9d) and the osumilite-bearing sample (*ALR 13-58*) at 1035 ± 7 Ma (Chp. 3). This age is in broad agreement with the crystallization of high-Th monazite cores in the garnet leucosome at 1032 ± 5 Ma (*ALR 13-05;* Fig. 9b) and simultaneous crystallization of oscillatory zoned high-Y monazite crystals in the sapphirine-bearing gneiss 1029 ± 9 Ma (Fig. 9g). We interpret this age to reflect the main melt producing event linked with prograde evolution of fertile protoliths close to peak temperature conditions, prior to significant melt extraction. Peak temperature in the UHT field is constrained for the deformed hercynite–quartz gneiss adjacent to the garnet leucosome at *c*. 920°C and pressure of 6 kbar that is consistent with the inferred 940 °C and 6–5 kbar conditions for the sapphirine–orthopyroxene gneiss. This *P–T* peak is followed by a second episode (M1b) of diffuse monazite

re-crystallization that yields pooled ages of *c*. 1006 ± 8 Ma (*ALR 13-22*), 1005 ± 7 Ma (*ALR 13-58*; Chp. 2) and 992 ± 13 Ma (*ALR* 13-05). These ages are linked with a melt-rich post-peak environment, as illustrated by the income of cordierite in the sapphirine gneiss and hercynite–quartz sample (Fig. 3d and f). This interpretation relies on the analogy with the evolution of the Opx-zone sample that is situated on the same apparent geothermal gradient of *c*. 60 °C/km, but remains uncertain in the absence of clear chemical correlation between monazite and silicate phases. Within the osumilite gneiss sample *ALR 13-58*, petrographic evidence of granulite facies conditions prior to osumilite crystallization is suggested by plagioclase + orthopyroxene or cordierite + orthopyroxene corona around garnet (Fig. 4b) but cannot be modelled in conjunction with the osumilite-bearing assemblage due to the lack of appropriate thermodynamic models.

Two samples of the osumilite and pigeonite zones record a second thermal maxima constrained by high-Y monazite in sample *ALR 13-05* at 931 ± 6 Ma (Fig. 9b) and at 929 ± 12 Ma in sample *ALR 13-58* (Fig. 12), associated with *P–T* estimates of 900–5 kbar to 950°C– 3.5 kbar and *c.* 910 °C at 4.8–6 kbar, respectively. This results confirms previous study of Möller et al. (2003) that established a metamorphic age of 927 ± 7 Ma for zircon intergrown with M2 hercynite and orthopyroxene in a sample close to the AMC plutons contact. Rocks within the osumilite isograd (up to 8 km from the AMC contact) experienced UHT contact metamorphism in response to anorthosite emplacement at 931 ± 2 Ma (Schärer et al. 1996) as postulated by numerous authors (Maijer 1987; Möller et al. 2002; Möller et al. 2003; Westphal et al. 2003) relying on the facts that (1) osumilite and pigeonite isograds wrap around the Bjerkreim-Sokndal lopolith and (2) no preferred orientation or deformation is associated with M2 event, consistent with static contact metamorphism, (except in a *c.* 500m thick belt at the contact of the AMC plutons carrying a late foliation Bolle et al., 2010). The pressure calculated for M2 metamorphism with the Holland and Powell (2011) database (< 5 kbar; Fig. 5b) is consistent with the low pressures of 4–5 kbar inferred from experimental petrology for the emplacement of the Bjerkreim-Sokndal lopolith (Vander Auwera and Longhi 1994).

The superposition of two metamorphic events yielding locally nearly the same *P* and *T* blurs the petrological and geochronological signal of individual samples. Only the comparison of different rock types allows to draw the thermal evolution of the area because meta-stability of minerals during the retrograde M1 path is widespread. A striking example that support this view is the occurrence of unreacted metric garnet leucosome outside the osumilite zone which contrasts with garnet crystals systematically surrounded by a cordierite + orthopyroxene + hercynite corona in leucosome veins within the osumilite zone (Maijer 1987). Such pattern of "two-step" metamorphism has been proposed as a prerequisite in terrain reaching UHT conditions by Vielzeuf

and Vidal (1990). These authors argue that with progressive crustal maturation, i.e. melt-depletion, a significant part of the heat budget of the orogen that would have been otherwise spent in chemical work of metamorphic reaction and melting is available for temperature increase (at constant *P*). The so-called melt-buffering effect has been modelled by Clark et al. (2011) and found to be responsible for a temperature difference of up to 40 °C at 950 °C.

Conclusion

New data do not support the idea that Rogaland was the theatre of extremely long-lived isothermal decompression at UHT (>900 °C) lasting for more than 100 Myr. Rather, they provide good evidence for two distinct thermal maxima of UHT metamorphism between 1029 ± 9 Ma and 1006 ± 8 Ma and at *c*. 931 ± 6 Ma, followed by near-isobaric cooling. The first event (M1) is characterized by a clockwise *P–T* path reaching 920 °C at moderate pressure of *c*. 6 kbar. This metamorphic event is associated with penetrative deformation while the second M2 event consists essentially in static crystallization at somewhat lower pressure (*c*. 3.5–5 kbar) but still in UHT conditions (> 900 °C). Careful study of textures and chemical signature of monazite crystals in both garnet-present and garnet-absent samples suggests that regional metamorphism (M1) lasted at least 25 Ma (from *c.* 1030 to *c.* 1005 Ma), followed by a relative cooling period deduced from xenotime–monazite disequilibrium textures in the 990–950 Ma time span. The second UHT metamorphic event (M2) at *c*. 930 Ma is spatially and temporally related to voluminous anorthosite massif emplacement. Thermal preconditioning of the crust was a condition necessary to develop such a wide (~ 10 km) UHT metamorphic aureole around the AMC. Finally, we emphasize that the propensity of monazite to re-equilibrate during fluid infiltration through time may provide valuable tool to monitor temperature–time path of low-pressure granulite terrains when associated with Y-in-monazite thermometry applicable to xenotime present samples.

References

Ancey M, Bastenaire F, Tixier R (1977) Statistical control and optimization of X-ray intensity measurements. J Phys Appl Phys 10:817.

Baldwin JA, Brown M (2008) Age and duration of ultrahigh-temperature metamorphism in the Anápolis–Itauçu Complex, Southern Brasília Belt, central Brazil – constraints from U–Pb geochronology, mineral rare earth element chemistry and trace-element thermometry. J Metamorph Geol 26:213–233.

Baldwin JA, Brown M, Schmitz MD (2007) First application of titanium-in-zircon thermometry to ultrahigh-temperature metamorphism. Geology 35:295–298.

Berger A, Scherrer NC, Bussy F (2005) Equilibration and disequilibration between monazite and garnet: indication from phase-composition and quantitative texture analysis. J Metamorph Geol doi: 10.1111/j.1525-1314.2005.00614.x

Bingen B, Davis WJ, Hamilton MA, et al (2008a) Geochronology of high-grade metamorphism in the Sveconorwegian belt, S. Norway: U-Pb, Th-Pb and Re-Os data. Nor Geol Tidsskr 88:13.

Bingen B, Demaiffe D, Hertogen J (1990) Evolution of feldspars at the amphibolite-granulite-facies transition in augen gneisses (SW Norway): geochemistry and Sr isotopes. Contrib Mineral Petrol 105:275–288.

Bingen B, Nordgulen O, Viola G (2008b) A four-phase model for the Sveconorwegian orogeny, SW Scandinavia. Nor Geol Tidsskr 88:43.

Bingen B, Van Breemen O (1998) U-Pb monazite ages in amphibolite- to granulite-facies orthogneiss reflect hydrous mineral breakdown reactions: Sveconorwegian Province of SW Norway. Contrib Mineral Petrol 132:336–353.

Carignan J, Hild P, Mevelle G, et al (2001) Routine analyses of trace elements in geological samples using flow injection and low pressure on-line liquid chromatography coupled to ICP-MS: a study of geochemical reference materials BR, DR-N, UB-N, AN-G and GH. Geostand Newsl 25:187–198.

Carrington DP, Harley SL (1995) The stability of osumilite in metapelitic granulites. J Metamorph Geol 13:613–625.

Clark C, Fitzsimons ICW, Healy D, Harley SL (2011) How Does the Continental Crust Get Really Hot? Elements 7:235–240.

Coint N, Slagstad T, Roberts NMW, et al (2015) The Late Mesoproterozoic Sirdal Magmatic Belt, SW Norway: Relationships between magmatism and metamorphism and implications for Sveconorwegian orogenesis. Precambrian Res 265:57–77.

Connolly JAD (2009) The geodynamic equation of state: What and how. Geochem Geophys Geosystems 10:n/a–n/a. doi: 10.1029/2009GC002540

Corfu F (1988) Differential response of U-Pb systems in coexisting accessory minerals, Winnipeg River Subprovince, Canadian Shield: implications for Archean crustal growth and stabilization. Contrib Mineral Petrol 98:312–325.

Corfu F (2013) A century of U-Pb geochronology: The long quest towards concordance. Geol Soc Am Bull 125:33–47.

Das K, Dasgupta S, Miura H (2001) Stability of osumilite coexisting with spinel solid solution in metapelitic granulites at high oxygen fugacity. Am Mineral 86:1423–1434.

Didier A, Bosse V, Bouloton J, et al (2015) NanoSIMS mapping and LA-ICP-MS chemical and U–Th–Pb data in monazite from a xenolith enclosed in andesite (Central Slovakia Volcanic Field). Contrib Mineral Petrol. doi: 10.1007/s00410-015-1200-1

Drüppel K, Elsasser L, Brandt S, Gerdes A (2013) Sveconorwegian Mid-crustal Ultrahigh-temperature Metamorphism in Rogaland, Norway: U-Pb LA-ICP-MS Geochronology and Pseudosections of Sapphirine Granulites and Associated Paragneisses. J Petrol 54:305–350.

Dumond G, Goncalves P, Williams ML, Jercinovic MJ (2015) Monazite as a monitor of melting, garnet growth, and feldspar recrystallization in continental lower crust. J Metamorph Geol in press. doi: 10.1111/jmg.12150

Ewing TA, Hermann J, Rubatto D (2013) The robustness of the Zr-in-rutile and Ti-in-zircon thermometers during high-temperature metamorphism (Ivrea-Verbano Zone, northern Italy). Contrib Mineral Petrol 165:757–779.

Falkum T (1985) Geotectonic evolution of southern Scandinavia in light of a late-Proterozoic plate-collision. In: The Deep Proterozoic Crust in the North Atlantic Provinces. Springer, pp 309–322

Falkum T (1982) Geologisk kart over Norge, berggrunnskart Mandal, 1:250000, Norges Geologiske Undersøkelse.

Fletcher IR, McNaughton NJ, Davis WJ, Rasmussen B (2010) Matrix effects and calibration limitations in ion probe U–Pb and Th–Pb dating of monazite. Chem Geol 270:31–44. doi: 10.1016/j.chemgeo.2009.11.003

Gapais D, Cagnard F, Gueydan F, et al (2009) Mountain building and exhumation processes through time: inferences from nature and models. Terra Nova 21:188–194.

Gasquet D, Bertrand J-M, Paquette J-L, et al (2010) Miocene to Messinian deformation and hydrothermal activity in a pre-Alpine basement massif of the French western Alps: new U-Th-Pb and argon ages from the Lauzière massif. Bull Soc Geol Fr 181:227–241.

Goncalves P (2004) Petrology and in situ U-Th-Pb Monazite Geochronology of Ultrahigh-Temperature Metamorphism from the Andriamena Mafic Unit, North-Central Madagascar. Significance of a Petrographical P-T Path in a Polymetamorphic Context. J Petrol 45:1923–1957.

Gratz R, Heinrich W (1997) Monazite-xenotime thermobarometry: Experimental calibration of the miscibility gap in the binary system $CePO_4$–YPO_4. Am Mineral 82:772–780.

Harley SL (2008) Refining the P–T records of UHT crustal metamorphism. J Metamorph Geol 26:125–154.

Harlov DE, Wirth R, Hetherington CJ (2011) Fluid-mediated partial alteration in monazite: the role of coupled dissolution–reprecipitation in element redistribution and mass transfer. Contrib Mineral Petrol 162:329–348.

Heinrich W, Andrehs G, Franz G (1997) Monazite–xenotime miscibility gap thermometry. I. An empirical calibration. J Metamorph Geol 15:3–16.

Hermans GAE, Tobi AC, Poorter RP, Maijer C (1975) The high-grade metamorphic Precambrian of the Sirdal-Ørsdal area, Rogaland/Vest-Agder, south-west Norway. Nor Geol Undersokelse 318:351–374.

Holland TJB, Babu E, Waters DJ (1996) Phase relations of osumilite and dehydration melting in pelitic rocks: a simple thermodynamic model for the KFMASH system. Contrib Mineral Petrol 124:383–394.

Holland TJB, Powell R (2011) An improved and extended internally consistent thermodynamic dataset for phases of petrological interest, involving a new equation of state for solids. J Metamorph Geol 29:333–383.

Huijsmans J, Kabel A, Steenstra S (1981) On the structure of a high-grade metamorphic Precambrian terrain in Rogaland, South Norway. Nor Geol Tidsskr 61:183–192.

Jansen JBH, Blok RJ, Bos A, Scheelings M (1985) Geothermometry and geobarometry in Rogaland and preliminary results from the Bamble area, S Norway. In: The deep Proterozoic crust in the North Atlantic provinces. Springer, pp 499–516

Jercinovic MJ (2005) Analytical perils (and progress) in electron microprobe trace element analysis applied to geochronology: Background acquisition, interferences, and beam irradiation effects. Am Mineral 90:526–546.

Kars H, Jansen JBH, Tobi AC, Poorter RP (1980) The metapelitic rocks of the polymetamorphic Precambrian of Rogaland, SW Norway. Contrib Mineral Petrol 74:235–244.

Kelly NM, Harley SL (2005) An integrated microtextural and chemical approach to zircon geochronology: refining the Archaean history of the Napier Complex, east Antarctica. Contrib Mineral Petrol 149:57–84.

Kelly NM, Harley SL, Möller A (2012) Complexity in the behavior and recrystallization of monazite during high-T metamorphism and fluid infiltration. Chem Geol 322-323:192–208.

Kelsey DE, Hand M (2015) On ultrahigh temperature crustal metamorphism: Phase equilibria, trace element thermometry, bulk composition, heat sources, timescales and tectonic settings. Geosci Front 6:311–356.

Kelsey DE, White RW, Holland TJB, Powell R (2004) Calculated phase equilibria in K_2O–FeO–MgO–Al_2O_3–SiO_2–H_2O for sapphirine-quartz-bearing mineral assemblages. J Metamorph Geol 22:559–578.

Kohn MJ (2016) Metamorphic chronology—a tool for all ages: Past achievements and future prospects. Am Mineral 101:25–42.

Korhonen FJ, Clark C, Brown M, et al (2013) How long-lived is ultrahigh temperature (UHT) metamorphism? Constraints from zircon and monazite geochronology in the Eastern Ghats orogenic belt, India. Precambrian Res 234:322–350.

Krenn E, Finger F (2010) Unusually Y-rich monazite-(Ce) with 6–14 wt.% Y_2O_3 in a granulite from the Bohemian Massif: implications for high temperature monazite growth from the monazite-xenotime miscibility gap thermometry. Mineral Mag 74:217–225.

Laajoki K, Corfu F, Andersen T (2002) Lithostratigraphy and U-Pb geochronology of the Telemark supracrustals in the Bandak-Sauland area, Telemark, South Norway. Nor Geol Tidsskr 82:119–138.

Maijer C, Andriessen PAM, Hebeda EH, et al (1981) Osumilite, an approximately 970 Ma old high-temperature index mineral of the granulite-facies metamorphism in Rogaland, SW Norway. Geol En Mijnb 60:267–272.

Maijer C, (1987) The metamorphic envelope of the Rogaland intrusive complex. In: Maijer C & Padget P (eds) The geology of southermost Norway: an excursion guide. Norges Geologiske undersokelse special publication 1, Trondheim, pp 68–72.

Mitchell RK, Indares A, Ryan B (2014) High to ultrahigh temperature contact metamorphism and dry partial melting of the Tasiuyak paragneiss, Northern Labrador. J Metamorph Geol 32:535–555.

Möller A, O'brien PJ, Kennedy A, Kröner A (2002) Polyphase zircon in ultrahigh-temperature granulites (Rogaland, SW Norway): constraints for Pb diffusion in zircon. J Metamorph Geol 20:727–740.

Möller A, O'Brien PJ, Kennedy A, Kröner A (2003) Linking growth episodes of zircon and metamorphic textures to zircon chemistry: an example from the ultrahigh-temperature granulites of Rogaland (SW Norway). Geol Soc Lond Spec Publ 220:65–81.

Montel J-M, Foret S, Veschambre M, et al (1996) Electron microprobe dating of monazite. Chem Geol 131:37–53.

Paquette JL, Tiepolo M (2007) High resolution (5 μm) U–Th–Pb isotope dating of monazite with excimer laser ablation (ELA)-ICPMS. Chem Geol 240:222–237.

Popa K, Shvareva T, Mazeina L, et al (2008) Thermodynamic properties of $CaTh(PO_4)_2$ synthetic cheralite. Am Mineral 93:1356–1362.

Pyle JM, Spear FS, Rudnick RL, McDonough WF (2001) Monazite-Xenotime-Garnet equilibrium in metapelites and a new monazite-garnet thermometer. J Petrol 42:2083–2107.

Roberts NMW, Slagstad T, Parrish RR, et al (2013) Sedimentary recycling in arc magmas: geochemical and U–Pb–Hf–O constraints on the Mesoproterozoic Suldal Arc, SW Norway. Contrib Mineral Petrol 165:507–523.

Schärer U, Wilmart E, Duchesne J-C (1996) The short duration and anorogenic character of anorthosite magmatism: U-Pb dating of the Rogaland complex, Norway. Earth Planet Sci Lett 139:335–350.

Seydoux-Guillaume A-M, Montel J-M, Bingen B, et al (2012) Low-temperature alteration of monazite: Fluid mediated coupled dissolution–precipitation, irradiation damage, and disturbance of the U–Pb and Th–Pb chronometers. Chem Geol 330-331:140–158.

Seydoux-Guillaume A-M, Paquette J-L, Wiedenbeck M, et al (2002a) Experimental resetting of the U–Th–Pb systems in monazite. Chem Geol 191:165–181.

Seydoux-Guillaume A-M, Wirth R, Heinrich W, Montel J-M (2002b) Experimental determination of Thorium partitioning between monazite and xenotime using analytical electron microscopy and X-ray diffraction Rietveld analysis. Eur J Mineral 14:869–878.

Slagstad T, Roberts NMW, Marker M, et al (2013) A non-collisional, accretionary Sveconorwegian orogen: A non-collisional, accretionary Sveconorwegian orogen. Terra Nova 25:30–37.

Spear FS, Pyle JM (2002) Apatite, monazite, and xenotime in metamorphic rocks. Rev Mineral Geochem 48:293–335.

Spear FS, Pyle JM, Cherniak D (2009) Limitations of chemical dating of monazite. Chem Geol 266:218–230.

Spencer CJ, Roberts NMW, Cawood PA, et al (2014) Intermontane basins and bimodal volcanism at the onset of the Sveconorwegian Orogeny, southern Norway. Precambrian Res 252:107–118.

Tobi AC, Hermans GAE., Maijer C, Jansen JBH (1985) Metamorphic zoning in the high-grade proterozoic of Rogaland-Vest Agder SW Norway. In: AC Tobi & JLR Touret (eds) The deep Proterozoic crust in the North Atlantic provinces, D. Reidel publishing compagny. pp 477–497

Tomascak PB, Krogstad EJ, Walker RJ (1996) U-Pb Monazite Geochronology of Granitic Rocks from Maine: Implications for Late Paleozoic Tectonics in the Northern Appalachians. J Geol 104:185–195.

Tomkins HS, Williams IS, Ellis DJ (2005) In situ U-Pb dating of zircon formed from retrograde garnet breakdown during decompression in Rogaland, SW Norway. J Metamorph Geol 23:201–215.

Van Achterbergh E, Ryan C, Jackson S, Griffin W (2001) Data reduction software for LA–ICP–MS. In: Sylvester P (ed) Laser ablation-ICP-MS in the Earth sciences. Mineral Assoc Can 29:239–243.

Vander Auwera J, Bolle O, Bingen B, et al (2011) Sveconorwegian massif-type anorthosites and related granitoids result from post-collisional melting of a continental arc root. Earth-Sci Rev 107:375–397.

Vander Auwera J, Longhi J (1994) Experimental study of a jotunite (hypersthene monzodiorite): constraints on the parent magma composition and crystallization conditions (*P*, *T*, $f(O_2)$ of the Bjerkreim-Sokndal layered intrusion (Norway). Contrib Mineral Petrol 118:60–78.

Vernon RH (1996) Problems with inferring P–T–t paths in low-P granulite facies rocks. J Metamorph Geol 14:143–153.

Vielzeuf D, Vidal P (eds) (1990) Granulites and Crustal Evolution. Springer Netherlands, Dordrecht

Walsh AK, Kelsey DE, Kirkland CL, et al (2014) P–T–t evolution of a large, long-lived, ultrahigh-temperature Grenvillian belt in central Australia. Gondwana Res. doi: 10.1016/j.gr.2014.05.012

Waters DJ (1991) Hercynite-quartz granulite phase relationships, and implications for crustal processes. Eur J Mineral 3:367–386.

Westphal M, Schumacher JC, Boschert S (2003) High-temperature metamorphism and the role of magmatic heat sources at the Rogaland anorthosite complex in southwestern Norway. J Petrol 44:1145–1162.

White RW (2003) Prograde Metamorphic Assemblage Evolution during Partial Melting of Metasedimentary Rocks at Low Pressures: Migmatites from Mt Stafford, Central Australia. J Petrol 44:1937–1960.

White RW, Powell R, Holland TJB, et al (2014) New mineral activity-composition relations for thermodynamic calculations in metapelitic systems. J Metamorph Geol 32:261–286.

White RW, Powell R, Holland TJB (2007) Progress relating to calculation of partial melting equilibria for metapelites. J Metamorph Geol 25:511–527.

Whitehouse MJ, Platt JP (2003) Dating high-grade metamorphism—constraints from rare-earth elements in zircon and garnet. Contrib Mineral Petrol 145:61–74.

Whitney DL, Evans BW (2010) Abbreviations for names of rock-forming minerals. Am Mineral 95:185–187.

Williams ML, Jercinovic MJ, Harlov DE, et al (2011) Resetting monazite ages during fluid-related alteration. Chem Geol 283:218–225.

Williams ML, Jercinovic MJ, Hetherington CJ (2007) Microprobe Monazite Geochronology: Understanding Geologic Processes by Integrating Composition and Chronology. Annu Rev Earth Planet Sci 35:137–175.

Wilmart E, Duchesne J-C (1987) Geothermobarometry of igneous and metamorphic rocks around the Ana-Sira anorthosite massif: Implications for the depth of emplacement of the South Norwegian anorthosites. Nor Geol Tidsskr 67:185–196.

Yakymchuk C, Brown M (2014) Behaviour of zircon and monazite during crustal melting. J Geol Soc 171:465–479.

Tables

Tab. 1: Composition used for modelling and measured composition (in % wt)

Composition used for modelling

Sample	SiO_2	TiO_2	Al_2O_3	FeO	Fe_2O_3	MgO	CaO	Na_2O	K_2O	H_2O	XMg
13-08	73.58	0.44	13.73	2.34	2.21	0.39	0.84	2.10	4.10	0.27	0.14
13-05	54.35	0.65	20.49	7.40	2.85	4.66	1.62	3.72	3.85	0.40	0.39
13-22	52.64	0.69	20.29	5.00	1.65	10.20	0.89	1.77	6.47	0.41	0.67
13-58	62.62	0.53	15.75	6.25	3.48	3.86	0.68	2.37	4.18	0.27	0.38
13-64	66.62	0.92	16.85	4.92	1.12	1.84	1.75	2.19	3.43	0.35	0.27

Measured composition

Sample	SiO_2	TiO_2	Al_2O_3	FeO	Fe_2O_3	MgO	CaO	Na_2O	K_2O	LOI	Total
13-08	72.47	0.43	13.52	2.3	2.18	0.38	0.83	2.07	4.04	0.84	99.07
13-05	54.58	0.65	20.58	7.43	2.03	4.68	1.63	3.74	3.87	0.61	99.78
13-22	52.1	0.67	20.1	4.98	1.6	9.82	0.86	1.72	6.28	1.27	99.40
13-58	62.5	0.53	15.8	6.27	3.48	3.87	0.68	2.38	4.18	0.16	99.85
13-64	65.71	0.91	16.62	5.02	1.02	1.82	1.73	2.16	3.38	1.46	99.83

Tab. 2: EPMA monazite microchemistry for sample *ALR 13-22* (in wt %)

Name	1322-02	1322-04a	1322-04b	1322-07b	1322-07a	1322-14a	1322-17a	1322-17b	1322-18
Group*	S1b	S1a	S1a	S2	S2	S2	S2	S2	S2
P_2O_5	26.363	27.601	28.267	29.789	29.757	29.354	29.142	29.718	28.683
SiO_2	2.581	2.189	1.362	0.434	0.506	0.545	0.948	0.751	0.957
ThO_2	25.012	16.45	12.104	4.29	4.583	4.499	5.269	4.899	4.461
UO_2	1.016	0.844	0.505	0.154	0.24	0.096	0.164	0.045	0.152
Ce_2O_3	14.418	18.318	20.676	28.764	27.964	30.667	25.446	24.55	30.123
Y_2O_3	5.556	6.928	6.649	1.443	1.747	0.353	1.411	2.446	0.606
La_2O_3	5.839	6.729	8.228	11.98	12.11	12.593	8.102	7.374	12.687
Pr_2O_3	1.895	2.073	2.725	3.446	3.007	3.463	3.621	3.29	3.476
Nd_2O_3	7.267	10.558	10.719	15.116	14.594	14.806	18.436	19.361	15.335
Sm_2O_3	1.128	2.427	2.49	2.345	2.746	1.481	4.97	4.258	2.949
Gd_2O_3	2.381	1.29	1.81	1.619	1.748	0.38	1.593	3.285	0.901
Dy_2O_3	1.229	1.048	1.286	0.154	0.118	0	0.218	0.822	0.456
SO_2	0	0.003	0.032	0.098	0.089	0.354	0.018	0.027	0.329
CaO	3.279	1.714	1.498	0.725	0.754	0.977	0.362	0.425	0.521
PbO	0.265	0.54	0.366	0.11	0.235	0.301	0.141	0.178	0.095
Total	**98.229**	**98.712**	**98.717**	**100.467**	**100.198**	**99.869**	**99.841**	**101.429**	**101.731**
P	0.892	0.919	0.939	0.983	0.982	0.971	0.972	0.976	0.950
Si	0.103	0.086	0.053	0.017	0.020	0.021	0.037	0.029	0.037
Th	0.228	0.147	0.108	0.038	0.041	0.040	0.047	0.043	0.040
U	0.009	0.007	0.004	0.001	0.002	0.001	0.001	0.000	0.001
Ce	0.211	0.264	0.297	0.411	0.399	0.439	0.367	0.349	0.431
Y	0.118	0.145	0.139	0.030	0.036	0.007	0.030	0.050	0.013
La	0.086	0.098	0.119	0.172	0.174	0.182	0.118	0.106	0.183
Pr	0.028	0.030	0.039	0.049	0.043	0.049	0.052	0.047	0.050
Nd	0.104	0.148	0.150	0.211	0.203	0.207	0.259	0.268	0.214
Sm	0.016	0.033	0.034	0.032	0.037	0.020	0.067	0.057	0.040
Gd	0.032	0.017	0.024	0.021	0.023	0.005	0.021	0.042	0.012
Dy	0.016	0.013	0.016	0.002	0.001	0.000	0.003	0.010	0.006
Yb	0.022	0.015	0.015	0.000	0.000	0.002	0.002	0.000	0.000
S^{6+}	0.000	0.000	0.001	0.004	0.003	0.013	0.001	0.001	0.012
Ca	0.140	0.072	0.063	0.030	0.032	0.041	0.015	0.018	0.022
Pb	0.003	0.006	0.004	0.001	0.002	0.003	0.001	0.002	0.001
Total	2.006	2.000	2.005	1.998	1.996	1.987	1.994	1.997	1.999
Σ(A)	1.01	1.00	1.01	1.00	1.00	1.01	0.99	0.99	1.02
Σ(T)	1.00	1.00	0.99	1.00	1.00	0.99	1.01	1.01	0.99
Σ(A-T)	0.02	0.01	0.02	0.00	0.01	0.02	0.02	-0.01	0.04
Crl	28.3	14.8	12.6	5.3	5.7	5.6	3.0	3.4	1.9
Xtm	16.7	17.9	17.9	5.3	6.1	1.2	5.4	10.4	3.0
Htn	10.4	8.8	5.4	1.7	2.0	2.1	3.8	2.9	3.7
Mnz	44.7	58.5	64.1	87.3	86.0	89.7	87.8	83.2	90.3
An	0.0	0.0	0.0	0.4	0.3	1.3	0.1	0.1	1.2
T°C (G&H)**	1022	1054	1054	517	577		527	814	262
T°C (S)	927	957	957	455	512		465	733	217
T°C (H)	840	859	860	528	565		534	711	370
T°C (P)	778	800	800	434	475		441	636	260
T°C (mean)	892	918	918	483	532		492	724	277

* *S1a refers to the oscillatory high-Y monazite crystals*
S1b refers to the patchy high-Y monazite crystals
S2 refers to low-Y monazite crystals

** ***T°C G&H*** *refers to calibration of Gratz R, Heinrich W (1997) Monazite-xenotime thermobarometry: Experimental calibration of the miscibility gap in the binary system CePO4-YPO4. Am Mineral 82:772–780.*

T°C S *refers to calibration of Seydoux-Guillaume A-M, Wirth R, Heinrich W, Montel J-M (2002) Experimental determination of Thorium partitioning between monazite and xenotime using analytical electron microscopy and X-ray diffraction Rietveld analysis.*

T°C P *refers to calibration of Pyle JM, Spear FS, Rudnick RL, McDonough WF (2001) Monazite-Xenotime-Garnet equilibrium in metapelites and a new monazite-garnet thermometer. J Petrol 42:2083–2107*

T°C H *refers to calibration of Heinrich W, Andrehs G, Franz G (1997) Monazite–xenotime miscibility gap thermometry. I. An empirical calibration. J Metamorph Geol 15:3–16*

Tab. 2: continued

Name	1322-22a	1322-22b	1322-22c	1322-23a	1322-24a	1322-27a	1322-26	1322-29a	1322-29b
Group*	S1a	S1a	S1a	S1b	S1a	S1b	S2	S1b	S1b
P_2O_5	26.773	27.016	26	24.111	27.15	27.511	29.477	28.786	28.854
SiO_2	1.95	2.004	2.433	3.704	2.054	1.873	0.441	0.874	1.407
ThO_2	22.384	17.83	22.474	27.102	24.568	14.959	4.724	11.075	18.58
UO_2	1.102	0.725	1.089	1.413	1.072	1.133	0.025	1.121	1.007
Ce_2O_3	15.352	18.245	16.14	13.908	14.256	21.11	28.631	22.424	18.334
Y_2O_3	6.234	6.417	5.747	5.18	6.144	3.89	1.477	5.464	5.818
La_2O_3	6.338	6.16	6.418	4.923	5.343	8.286	12.582	9.234	7.746
Pr_2O_3	1.887	2.301	1.969	2.07	1.68	3.008	3.86	2.698	1.855
Nd_2O_3	7.632	10.313	8.105	8.367	6.938	11.937	13.666	10.252	8.816
Sm_2O_3	1.482	2.615	0.965	2.31	1.642	1.699	2.515	2.363	2.133
Gd_2O_3	1.605	2.268	2.634	2.874	1.855	3.105	1.876	2.156	1.818
Dy_2O_3	1.224	1.736	0.886	1.126	1.13	0.684	0.466	1.003	1.279
SO_2	0.007	0.053	0.033	0	0.007	0.002	0.378	0.06	0
CaO	3.158	2.029	2.841	2.58	3.645	1.724	1.181	1.917	2.928
PbO	1.199	0.904	1.163	1.489	1.354	0.948	0.169	0.654	1.032
Total	**98.327**	**100.616**	**98.897**	**101.157**	**98.838**	**101.869**	**101.468**	**100.081**	**101.607**
P	0.907	0.907	0.888	0.834	0.913	0.918	0.967	0.955	0.943
Si	0.078	0.079	0.098	0.151	0.082	0.074	0.017	0.034	0.054
Th	0.204	0.161	0.206	0.252	0.222	0.134	0.042	0.099	0.163
U	0.010	0.006	0.010	0.013	0.009	0.010	0.000	0.010	0.009
Ce	0.225	0.265	0.238	0.208	0.207	0.305	0.406	0.322	0.259
Y	0.133	0.135	0.123	0.113	0.130	0.082	0.030	0.114	0.120
La	0.094	0.090	0.095	0.074	0.078	0.120	0.180	0.133	0.110
Pr	0.028	0.033	0.029	0.031	0.024	0.043	0.055	0.039	0.026
Nd	0.109	0.146	0.117	0.122	0.098	0.168	0.189	0.143	0.122
Sm	0.020	0.036	0.013	0.033	0.022	0.023	0.034	0.032	0.028
Gd	0.021	0.030	0.035	0.039	0.024	0.041	0.024	0.028	0.023
Dy	0.016	0.022	0.012	0.015	0.014	0.009	0.006	0.013	0.016
Yb	0.020	0.000	0.014	0.000	0.014	0.000	0.000	0.000	0.000
S^{6+}	0.000	0.002	0.001	0.000	0.000	0.000	0.014	0.002	0.000
Ca	0.135	0.086	0.123	0.113	0.155	0.073	0.049	0.080	0.121
Pb	0.013	0.010	0.013	0.016	0.014	0.010	0.002	0.007	0.011
Total	2.014	2.008	2.014	2.015	2.010	2.009	2.001	2.009	2.006
Σ(A)	1.03	1.02	1.03	1.03	1.02	1.02	1.03	1.02	1.01
Σ(T)	0.99	0.99	0.99	0.99	0.99	0.99	0.98	0.99	1.00
Σ(A-T)	0.04	0.04	0.04	0.04	0.02	0.03	0.05	0.03	0.01
Crl	27.2	17.1	24.4	22.3	31.3	14.4	5.9	15.8	24.2
Xtm	17.1	18.6	16.9	16.5	17.0	13.0	6.0	15.2	15.9
Htn	7.8	7.9	9.7	15.0	8.2	7.3	1.7	3.4	5.4
Mnz	47.8	56.5	49.0	46.2	43.5	65.3	85.1	65.7	54.5
An	0.0	0.0	0.0	0.0	0.0	0.0	1.4	0.0	0.0
T°C (G&H)**	1033	1070	1028	1017	1032	912	570	981	1001
T°C (S)	938	972	933	922	936	824	505	889	907
T°C (H)	847	869	844	836	846	772	560	815	827
T°C (P)	786	811	782	774	785	703	470	750	763
T°C (mean)	901	930	897	887	900	803	526	859	874

Tab. 2: continued

Name	1322-36a	1322-37	1322-38c	1322-39a	1322-39b	1322-101a	1322-40	1322-41	1322-44a
Group*	S1b	S1a	S1a	S1b	S1a	S2	S2	S1b	S1a
P_2O_5	25.906	29.323	28.718	23.048	27.831	28.701	28.786	28.701	23.218
SiO_2	2.849	1.21	1.095	4.076	1.905	0.969	0.835	1.354	4.813
ThO_2	22.099	17.223	11.971	29.438	23.663	4.766	5.055	17.46	32.671
UO_2	1.567	1.366	1.08	1.23	1.549	0.21	0.318	1.08	1.414
Ce_2O_3	13.774	16.395	20.734	12.759	14.391	30.65	29.773	16.888	13.024
Y_2O_3	7.151	6.64	5.954	5.756	6.32	0.654	0.62	6.27	5.151
La_2O_3	4.147	6.807	8.969	4.142	5.353	12.655	12.082	6.977	4.048
Pr_2O_3	1.833	2.168	2.512	1.491	1.872	3.428	3.737	2.412	1.58
Nd_2O_3	9.437	9.581	9.486	7.232	7.6	14.658	15.228	9.312	7.834
Sm_2O_3	2.237	2.021	1.924	1.953	1.832	1.809	2.494	2.346	1.379
Gd_2O_3	3.514	1.924	1.771	1.947	2.017	0.861	1.062	3.388	1.546
Dy_2O_3	1.109	1.224	1.195	1.321	1.196	0.238	0.209	1.248	1.467
SO_2	0.017	0.049	0.048	0	0	0.484	0.293	0.016	0
CaO	2.481	2.865	1.854	2.762	3.583	0.976	0.859	2.796	2.577
PbO	1.225	0.831	0.784	1.526	1.226	0.314	0.191	0.951	0.526
Total	**99.346**	**99.627**	**98.095**	**98.681**	**100.338**	**101.373**	**101.542**	**101.199**	**101.248**
P	0.880	0.960	0.953	0.813	0.925	0.948	0.951	0.942	0.803
Si	0.114	0.047	0.043	0.170	0.075	0.038	0.033	0.053	0.197
Th	0.202	0.152	0.107	0.279	0.211	0.042	0.045	0.154	0.304
U	0.014	0.012	0.009	0.011	0.014	0.002	0.003	0.009	0.013
Ce	0.202	0.232	0.297	0.195	0.207	0.438	0.425	0.240	0.195
Y	0.153	0.137	0.124	0.128	0.132	0.014	0.013	0.129	0.112
La	0.061	0.097	0.130	0.064	0.078	0.182	0.174	0.100	0.061
Pr	0.027	0.031	0.036	0.023	0.027	0.049	0.053	0.034	0.024
Nd	0.135	0.132	0.133	0.108	0.107	0.204	0.212	0.129	0.114
Sm	0.031	0.027	0.026	0.028	0.025	0.024	0.034	0.031	0.019
Gd	0.047	0.025	0.023	0.027	0.026	0.011	0.014	0.044	0.021
Dy	0.014	0.015	0.015	0.018	0.015	0.003	0.003	0.016	0.019
Yb	0.008	0.004	0.023	0.017	0.000	0.000	0.000	0.000	0.000
S^{6+}	0.001	0.002	0.002	0.000	0.000	0.018	0.011	0.001	0.000
Ca	0.107	0.119	0.078	0.123	0.151	0.041	0.036	0.116	0.113
Pb	0.013	0.009	0.008	0.017	0.013	0.003	0.002	0.010	0.006
Total	2.009	1.997	2.005	2.018	2.005	1.999	1.997	2.007	2.000
Σ(A)	1.01	0.99	1.01	1.04	1.00	1.03	1.02	1.01	1.00
Σ(T)	0.99	1.01	1.00	0.98	1.00	0.99	0.98	0.99	1.00
Σ(A-T)	0.02	-0.01	0.02	0.05	0.00	0.05	0.04	0.02	0.00
Crl	21.4	24.2	15.8	24.5	30.4	4.5	4.9	23.1	22.8
Xtm	21.4	18.0	16.5	17.1	17.5	2.7	2.9	18.7	15.4
Htn	11.5	4.8	4.4	16.9	7.5	3.7	3.2	5.2	19.9
Mnz	45.8	53.0	63.3	41.4	44.6	87.4	88.0	53.0	41.8
An	0.0	0.0	0.0	0.0	0.0	1.7	1.1	0.0	0.0
T°C (G&H)**	1133	1057	1018	1035	1043	222	248	1073	988
T°C (S)	1031	960	924	939	947	180	204	975	896
T°C (H)	908	861	837	848	853	346	362	871	819
T°C (P)	853	802	776	787	793	233	251	813	755
T°C (mean)	981	920	889	902	909	245	266	933	864

Tab. 2: continued

Name	1322-44b	1322-44c	1322-45	13-22-46	1322-47a	1322-47b	1322-51a	1322-52	1322-53a
Group*	S1b	S1b	S2	S1b	S1b	S1a	S2	S2	S2
P_2O_5	24.814	26.808	30.305	26.92	29.31	27.517	24.468	29.433	28.976
SiO_2	3.863	2.045	0.393	2.161	1.023	2.107	3.626	0.843	0.728
ThO_2	33.022	17.615	2.874	19.198	11.658	16.592	19.537	5.168	4.448
UO_2	1.284	0.743	0.734	0.951	1.357	0.966	0.322	0.226	0.286
Ce_2O_3	10.939	17.798	27.667	19.104	21.963	20.327	20.453	24.287	28.662
Y_2O_3	6.103	5.835	3.469	4.448	5.523	4.414	1.512	5.135	1.434
La_2O_3	3.908	6.432	13.017	7.538	9.241	7.831	6.331	10.503	12.386
Pr_2O_3	1.499	2.261	3.145	2.737	2.446	2.752	2.833	2.36	3.462
Nd_2O_3	5.929	10.301	12.484	9.823	10.301	11.662	14.598	13.187	14.23
Sm_2O_3	1.225	2.465	2.365	1.42	1.87	1.869	3.266	2.788	2.693
Gd_2O_3	2.232	2.496	1.966	0.764	1.573	1.853	2.884	2.368	2.091
Dy_2O_3	1.297	1.223	0.681	1.439	1.154	0.851	0.291	1.423	0.22
SO_2	0.016	0.021	0.198	0.018	0.036	0	0.011	0.019	0.245
CaO	3.641	2.022	0.747	2.372	1.887	1.831	0.784	0.369	0.667
PbO	0.441	0.356	0.261	0.229	0.341	0.215	0.823	0.274	0.312
Total	**100.213**	**98.421**	**100.306**	**99.122**	**99.683**	**100.787**	**101.739**	**98.383**	**100.84**
P	0.846	0.907	0.988	0.909	0.963	0.918	0.848	0.971	0.962
Si	0.156	0.082	0.015	0.086	0.040	0.083	0.148	0.033	0.029
Th	0.303	0.160	0.025	0.174	0.103	0.149	0.182	0.046	0.040
U	0.012	0.007	0.006	0.008	0.012	0.008	0.003	0.002	0.002
Ce	0.161	0.261	0.390	0.279	0.312	0.293	0.306	0.347	0.412
Y	0.131	0.124	0.071	0.094	0.114	0.093	0.033	0.107	0.030
La	0.058	0.095	0.185	0.111	0.132	0.114	0.096	0.151	0.179
Pr	0.022	0.033	0.044	0.040	0.035	0.040	0.042	0.034	0.049
Nd	0.085	0.147	0.172	0.140	0.143	0.164	0.213	0.184	0.199
Sm	0.017	0.034	0.031	0.020	0.025	0.025	0.046	0.037	0.036
Gd	0.030	0.033	0.025	0.010	0.020	0.024	0.039	0.031	0.027
Dy	0.017	0.016	0.008	0.018	0.014	0.011	0.004	0.018	0.003
Yb	0.000	0.019	0.000	0.011	0.004	0.000	0.000	0.019	0.000
S^{6+}	0.001	0.001	0.007	0.001	0.001	0.000	0.000	0.001	0.009
Ca	0.157	0.087	0.031	0.101	0.078	0.077	0.034	0.015	0.028
Pb	0.005	0.004	0.003	0.002	0.004	0.002	0.009	0.003	0.003
Total	1.999	2.008	1.994	2.004	1.998	2.001	2.004	1.997	2.000
Σ(A)	1.00	1.02	1.00	1.01	1.00	1.00	1.01	0.99	1.02
Σ(T)	1.00	0.99	1.00	1.00	1.00	1.00	1.00	1.00	0.99
Σ(A-T)	0.00	0.03	0.00	0.01	0.01	0.00	0.01	0.01	0.03
Crl	31.7	17.4	4.8	20.3	15.8	15.4	6.8	3.0	3.8
Xtm	17.9	17.3	10.5	12.3	15.0	12.7	7.6	16.0	5.9
Htn	15.7	8.2	1.5	8.6	4.0	8.3	14.9	3.4	2.8
Mnz	34.7	57.1	82.5	58.8	65.2	63.5	70.6	77.5	86.6
An	0.0	0.0	0.7	0.0	0.0	0.0	0.0	0.1	0.9
T°C (G&H)**	1054	1040	819	888	976	904	678	1004	567
T°C (S)	957	944	738	802	884	817	606	910	503
T°C (H)	859	851	715	757	811	767	627	829	559
T°C (P)	800	790	640	687	747	698	544	766	468
T°C (mean)	918	906	728	784	854	797	614	877	524

Tab. 2: continued

Name	1322-53b	1322-54a	1322-54b	3122-58
Group*	S2	S2	S2	S2
P_2O_5	28.807	29.207	28.544	30.038
SiO_2	0.695	0.804	0.94	0.532
ThO_2	4.297	4.246	4.162	3.826
UO_2	0.192	0.203	0.355	0.764
Ce_2O_3	29.537	30.163	29.115	27.386
Y_2O_3	0.78	0.724	1.358	2.916
La_2O_3	12.259	13.236	12.561	13.094
Pr_2O_3	3.234	3.43	3.357	3.22
Nd_2O_3	14.282	14.798	13.828	11.911
Sm_2O_3	2.147	2.137	2.415	2.233
Gd_2O_3	1.039	1.045	0.895	2.173
Dy_2O_3	0.524	0	0.233	0.475
SO_2	0.226	0.373	0.283	0.201
CaO	0.676	0.744	0.661	0.828
PbO	0.159	0.175	0.154	0.287
Total	**98.854**	**101.285**	**98.861**	**99.884**
P	0.963	0.961	0.952	0.983
Si	0.027	0.031	0.037	0.021
Th	0.039	0.038	0.037	0.034
U	0.002	0.002	0.003	0.007
Ce	0.427	0.429	0.420	0.387
Y	0.016	0.015	0.028	0.060
La	0.179	0.190	0.183	0.187
Pr	0.047	0.049	0.048	0.045
Nd	0.202	0.205	0.195	0.164
Sm	0.029	0.029	0.033	0.030
Gd	0.014	0.013	0.012	0.028
Dy	0.007	0.000	0.003	0.006
Yb	0.014	0.000	0.014	0.001
S^{6+}	0.008	0.014	0.010	0.007
Ca	0.029	0.031	0.028	0.034
Pb	0.002	0.002	0.002	0.003
Total	1.995	1.995	1.995	1.989
Σ(A)	1.01	1.02	1.02	0.99
Σ(T)	0.99	0.99	0.99	1.00
Σ(A-T)	0.02	0.02	0.03	0.01
Crl	4.1	3.4	3.5	5.5
Xtm	3.7	2.8	4.3	9.5
Htn	2.8	3.1	3.7	2.1
Mnz	88.7	89.3	87.5	82.3
An	0.8	1.3	1.0	0.7
T°C (G&H)**	358	241	426	774
T°C (S)	308	198	371	696
T°C (H)	430	357	472	687
T°C (P)	326	246	372	609
T°C (mean)	355	260	410	691

Tab. 3: EPMA monazite microchemistry for sample *ALR 13-64* (in wt %)

Name	1364-01	1364-03	1364-03b	1364-06	1364-09	1364-09b	1364-14	1364-14b	1364-20	1364-20b	1364-19	1364-21	1364-21b
Group	Homogeneous	Homogeneous	Homogeneous	Homogeneous	Homogeneous	Homogeneous	Homogeneous	Homogeneous	Homogeneous	Homogeneous	Homogeneous	Homogeneous	Homogeneous
P_2O_5	28.49	28.17	28.15	30.01	30.00	29.86	28.66	28.70	29.47	29.06	29.68	29.19	29.16
SiO_2	0.76	1.30	1.24	0.34	0.20	0.28	1.06	1.01	0.68	0.62	0.27	0.69	0.60
ThO_2	6.33	8.93	7.63	3.92	2.45	2.83	8.84	8.87	5.57	5.75	3.40	6.02	5.83
UO_2	0.20	0.23	0.08	0.44	1.91	1.81	0.26	0.24	0.34	0.29	1.01	0.19	0.23
Ce_2O_3	29.08	28.21	28.60	29.42	29.54	29.04	27.10	27.26	29.46	29.75	29.56	29.38	29.93
Y_2O_3	0.11	0.07	0.08	0.14	0.35	0.37	0.06	0.05	0.19	0.10	0.31	0.12	0.14
La_2O_3	11.46	10.33	10.78	11.43	12.42	12.31	11.27	11.34	12.00	11.78	12.49	11.65	11.64
Pr_2O_3	3.76	3.77	3.58	3.72	3.55	3.65	3.55	3.46	3.61	3.70	3.88	3.84	3.86
Nd_2O_3	14.59	14.95	15.44	15.42	13.58	14.13	13.97	14.05	14.98	14.59	14.21	14.12	14.98
Sm_2O_3	2.02	1.55	1.47	2.17	2.68	2.65	2.08	1.84	2.01	2.03	2.29	2.31	1.85
Gd_2O_3	0.30	0.52	0.45	0.73	0.79	1.33	0.75	0.84	0.84	0.09	1.12	0.46	0.77
Dy_2O_3	0.16	0.00	0.03	0.11	0.00	0.21	0.00	0.10	0.15	0.10	0.10	0.00	0.11
SO_2	0.00	0.00	0.00	0.02	0.03	0.02	0.01	0.02	0.00	0.04	0.00	0.01	0.01
CaO	0.79	0.83	0.72	0.74	0.89	0.93	1.08	1.14	0.73	0.79	0.85	0.83	0.76
PbO	0.34	0.57	0.43	0.11	0.47	0.45	0.51	0.59	0.37	0.42	0.25	0.21	0.38
Total	**98.40**	**99.41**	**98.67**	**98.73**	**98.84**	**99.86**	**99.18**	**99.51**	**100.41**	**99.12**	**99.41**	**99.01**	**100.24**
P	0.974	0.958	0.962	1.004	1.004	0.997	0.970	0.970	0.973	0.982	0.987	0.984	0.979
Si	0.031	0.052	0.050	0.013	0.008	0.011	0.043	0.040	0.027	0.025	0.011	0.027	0.024
Th	0.058	0.082	0.070	0.035	0.022	0.025	0.080	0.081	0.051	0.052	0.031	0.055	0.053
U	0.002	0.002	0.001	0.004	0.017	0.016	0.002	0.002	0.003	0.003	0.009	0.002	0.002
Ce	0.430	0.415	0.422	0.426	0.428	0.418	0.397	0.398	0.432	0.435	0.434	0.428	0.434
Y	0.002	0.001	0.002	0.003	0.007	0.008	0.001	0.001	0.004	0.002	0.007	0.003	0.003
La	0.171	0.153	0.160	0.167	0.181	0.178	0.166	0.167	0.177	0.173	0.185	0.171	0.170
Pr	0.055	0.055	0.053	0.054	0.051	0.052	0.052	0.050	0.053	0.054	0.057	0.056	0.056
Nd	0.029	0.022	0.021	0.031	0.038	0.037	0.030	0.026	0.029	0.029	0.033	0.033	0.026
Sm	0.203	0.207	0.215	0.210	0.185	0.191	0.192	0.193	0.207	0.201	0.196	0.194	0.205
Gd	0.004	0.007	0.006	0.010	0.010	0.017	0.010	0.011	0.011	0.001	0.015	0.006	0.010
Dy	0.002	0.000	0.000	0.001	0.000	0.003	0.000	0.001	0.002	0.001	0.001	0.000	0.001
S^{6+}	0.000	0.000	0.000	0.001	0.001	0.001	0.000	0.001	0.000	0.002	0.000	0.000	0.000
Ca	0.034	0.036	0.031	0.031	0.038	0.039	0.046	0.049	0.031	0.034	0.036	0.035	0.032
Pb	0.004	0.006	0.005	0.001	0.005	0.005	0.005	0.006	0.004	0.004	0.003	0.002	0.004
Total	2.00	2.00	2.00	1.99	1.99	2.00	1.99	2.00	2.00	2.00	2.00	2.00	2.00
Σ(A)	0.99	0.99	0.99	0.97	0.98	0.99	0.98	0.99	1.00	0.99	1.01	0.98	1.00
Σ(T)	1.01	1.01	1.01	1.02	1.01	1.01	1.01	1.01	1.00	1.01	1.00	1.01	1.00
Σ(A-T)	0.01	0.02	0.03	0.04	0.03	0.02	0.03	0.02	0.00	0.02	0.01	0.03	0.01
Crl	6.9	7.3	6.2	6.4	7.7	7.8	9.4	9.9	6.2	6.9	7.2	7.1	6.5
Ilm	3.1	5.3	5.1	1.4	0.8	1.1	4.3	4.1	2.7	2.5	1.1	2.8	2.4
xtm	0.9	0.8	0.8	1.4	1.8	2.8	1.1	1.4	1.7	0.5	2.2	0.9	1.5
Mnz	89.2	86.6	87.9	90.8	89.7	88.3	85.1	84.6	89.3	90.2	89.5	89.2	89.7

Tab. 3: continued

Name	1364-52	1364-52b	1364-53	1364-200	1364-200b	1364-73	1364-102	1364-102b	1364-149	1364-150	1364-150b	1364-153	1364-153b
Group	Homogeneous	Homogeneous	Homogeneous	Core	Rim	Homogeneous	Homogeneous	Homogeneous	Homogeneous	Core	Core	Core	Rim
P_2O_5	28.67	28.75	29.16	27.51	29.36	27.45	29.21	29.28	27.52	28.79	28.30	27.75	29.40
SiO_2	0.90	0.84	0.41	1.59	0.66	1.61	0.73	0.61	1.50	1.03	1.27	1.68	0.60
ThO_2	8.72	8.42	6.24	11.64	6.05	12.43	6.31	5.49	10.87	8.66	10.05	13.14	6.99
UO_2	0.41	0.40	0.35	0.25	0.33	0.25	0.54	0.57	0.00	0.32	0.24	0.30	0.44
Ce_2O_3	26.76	27.27	27.64	25.67	28.58	25.23	27.80	29.16	26.01	27.22	26.68	24.79	27.47
Y_2O_3	0.22	0.21	0.16	0.09	0.12	0.07	0.36	0.27	0.08	0.18	0.15	0.15	0.25
La_2O_3	10.78	10.75	11.58	9.66	10.29	9.41	10.29	11.24	9.89	10.33	10.90	9.62	11.00
Pr_2O_3	3.25	3.49	3.20	3.64	4.03	3.55	3.68	3.70	3.91	3.54	3.30	3.19	3.87
Nd_2O_3	14.24	13.86	14.28	14.93	15.21	15.40	15.13	14.92	14.36	15.24	14.46	13.52	14.45
Sm_2O_3	2.11	1.85	2.08	1.58	1.94	1.96	2.36	1.72	1.85	2.05	1.52	1.94	2.13
Gd_2O_3	0.80	1.32	0.99	0.47	0.83	0.44	1.07	0.71	0.62	0.55	0.25	0.66	0.76
Dy_2O_3	0.00	0.00	0.10	0.18	0.01	0.00	0.12	0.00	0.10	0.11	0.10	0.00	0.17
SO_2	0.00	0.05	0.00	0.00	0.01	0.02	0.02	0.04	0.00	0.03	0.01	0.02	0.00
CaO	1.16	1.19	1.15	1.17	0.88	1.18	0.97	0.75	1.12	1.13	1.17	1.35	1.08
PbO	0.61	0.37	0.29	0.70	0.27	0.57	0.45	0.25	0.67	0.41	0.53	0.66	0.49
Total	**98.63**	**98.76**	**97.64**	**99.09**	**98.60**	**99.57**	**99.04**	**98.72**	**98.50**	**99.57**	**98.92**	**98.75**	**99.10**
P	0.982	0.975	0.989	0.944	0.990	0.966	0.984	0.987	0.948	0.970	0.969	0.949	0.967
Si	0.036	0.034	0.017	0.064	0.026	0.063	0.029	0.024	0.061	0.041	0.051	0.068	0.025
Th	0.079	0.077	0.058	0.107	0.055	0.110	0.057	0.050	0.101	0.078	0.091	0.121	0.065
U	0.004	0.004	0.003	0.002	0.003	0.002	0.005	0.005	0.000	0.003	0.002	0.003	0.004
Ce	0.390	0.400	0.411	0.381	0.417	0.359	0.405	0.426	0.388	0.397	0.388	0.367	0.414
Y	0.005	0.004	0.004	0.002	0.003	0.002	0.008	0.006	0.002	0.004	0.003	0.003	0.006
La	0.158	0.159	0.173	0.144	0.151	0.135	0.151	0.166	0.148	0.152	0.160	0.143	0.167
Pr	0.047	0.051	0.047	0.054	0.059	0.050	0.053	0.054	0.058	0.051	0.048	0.047	0.058
Nd	0.030	0.026	0.030	0.023	0.028	0.027	0.034	0.025	0.027	0.029	0.022	0.028	0.031
Sm	0.195	0.191	0.200	0.209	0.209	0.206	0.207	0.205	0.201	0.209	0.198	0.188	0.205
Gd	0.011	0.018	0.013	0.006	0.011	0.006	0.014	0.009	0.008	0.007	0.003	0.009	0.010
Dy	0.000	0.000	0.001	0.002	0.000	0.000	0.002	0.000	0.001	0.001	0.001	0.000	0.002
S^{6+}	0.000	0.002	0.000	0.000	0.000	0.001	0.001	0.001	0.000	0.001	0.000	0.001	0.000
Ca	0.049	0.051	0.050	0.051	0.038	0.049	0.042	0.032	0.049	0.048	0.050	0.058	0.047
Pb	0.007	0.004	0.003	0.008	0.003	0.006	0.005	0.003	0.007	0.004	0.006	0.007	0.005
Total	1.99	1.99	2.00	2.00	1.99	1.98	1.99	1.99	2.00	1.99	1.99	1.99	2.01
Σ(A)	0.97	0.99	0.99	0.99	0.98	0.95	0.98	0.98	0.99	0.98	0.97	0.97	1.02
Σ(T)	1.02	1.01	1.01	1.01	1.02	1.03	1.01	1.01	1.01	1.01	1.02	1.02	0.99
Σ(A-T)	0.04	0.02	0.01	0.02	0.04	0.08	0.03	0.03	0.02	0.03	0.05	0.04	0.02
Crl	10.2	10.4	10.1	10.3	7.7	10.4	8.4	6.6	9.8	9.7	10.2	12.0	9.4
Ilm	3.7	3.4	1.7	6.5	2.7	6.6	2.9	2.5	6.2	4.2	5.2	7.0	2.4
xtm	1.6	2.2	1.8	1.1	1.4	0.8	2.4	1.5	1.1	1.3	0.8	1.2	1.8
Mnz	84.5	84.0	86.5	82.1	88.2	82.2	86.3	89.4	82.9	84.8	83.8	79.7	86.4

Tab. 3: continued

Name	1364-131	1364-131b	1364-113	1364-113b	1364-89	1364-89b	1364-76	1364-76b	1364-57	1364-57b	1364-57c	1364-23	1364-23b	1364-59
Group	Rim	Core	Rim	Rim	Rim	Core	Core	Core	Rim	Core	Rim	Core	Rim	Rim
P_2O_5	29.84	29.15	29.59	28.73	29.94	27.92	28.43	28.01	29.15	27.84	29.50	27.64	30.14	29.40
SiO_2	0.32	0.63	0.42	0.74	0.40	1.47	1.14	1.43	0.51	1.38	0.61	1.51	0.26	0.60
ThO_2	3.59	5.84	4.73	7.49	4.53	11.13	8.88	10.76	4.67	10.32	5.84	12.35	2.76	5.47
UO_2	0.85	0.24	0.27	0.32	0.69	0.18	0.18	0.18	0.30	0.26	0.27	0.28	1.48	0.28
Ce_2O_3	29.37	28.70	28.84	27.99	29.41	26.08	27.57	26.41	29.37	26.13	28.42	25.42	29.64	29.11
Y_2O_3	0.25	0.16	0.17	0.12	0.23	0.11	0.16	0.10	0.15	0.06	0.11	0.18	0.32	0.13
La_2O_3	12.24	11.00	11.32	10.48	11.38	9.68	10.98	9.47	11.10	9.81	10.68	9.58	12.44	11.89
Pr_2O_3	3.40	3.74	4.04	3.38	4.08	3.73	3.82	3.80	3.99	3.60	3.74	3.55	3.79	3.74
Nd_2O_3	14.32	15.67	15.66	14.38	14.46	14.81	14.26	15.39	15.97	15.32	15.48	13.73	13.50	14.21
Sm_2O_3	2.87	2.20	2.18	1.86	2.17	1.99	1.87	1.81	2.17	1.68	2.00	1.87	2.39	1.85
Gd_2O_3	1.04	0.65	1.02	0.82	1.02	0.00	0.73	0.38	0.76	0.31	0.29	0.90	1.25	0.63
Dy_2O_3	0.15	0.00	0.00	0.11	0.10	0.08	0.00	0.02	0.00	0.00	0.00	0.07	0.06	97.30
SO_2	0.00	0.00	0.01	0.00	0.04	0.00	0.01	0.00	0.00	0.01	0.00	0.02	0.00	0.00
CaO	0.81	0.84	0.79	1.12	0.87	1.16	1.06	1.03	0.82	1.12	0.87	1.44	0.84	0.79
PbO	0.37	0.34	0.33	0.42	0.35	0.63	0.60	0.48	0.30	0.48	0.30	0.72	0.37	0.33
Total	**99.42**	**99.16**	**99.37**	**97.94**	**99.65**	**98.96**	**99.69**	**99.26**	**99.26**	**98.33**	**98.11**	**99.26**	**99.24**	**98.42**
P	0.998	0.984	0.987	0.981	0.981	0.954	0.962	0.960	0.984	0.974	0.996	0.946	0.972	0.992
Si	0.012	0.025	0.017	0.030	0.016	0.059	0.046	0.057	0.020	0.054	0.024	0.061	0.011	0.024
Th	0.032	0.053	0.043	0.069	0.042	0.102	0.081	0.098	0.042	0.093	0.053	0.114	0.026	0.050
U	0.007	0.002	0.002	0.003	0.006	0.002	0.002	0.002	0.003	0.002	0.002	0.003	0.014	0.002
Ce	0.425	0.419	0.422	0.413	0.434	0.385	0.403	0.386	0.429	0.377	0.415	0.376	0.450	0.425
Y	0.005	0.003	0.004	0.003	0.005	0.002	0.003	0.002	0.003	0.001	0.002	0.004	0.007	0.003
La	0.178	0.162	0.167	0.156	0.169	0.144	0.162	0.139	0.163	0.143	0.157	0.143	0.191	0.175
Pr	0.049	0.054	0.059	0.050	0.060	0.055	0.056	0.055	0.058	0.052	0.054	0.052	0.057	0.054
Nd	0.040	0.031	0.031	0.027	0.031	0.029	0.027	0.026	0.031	0.024	0.029	0.027	0.035	0.026
Sm	0.195	0.215	0.216	0.200	0.201	0.206	0.196	0.212	0.220	0.208	0.213	0.191	0.193	0.195
Gd	0.014	0.009	0.013	0.011	0.014	0.000	0.010	0.005	0.010	0.004	0.004	0.012	0.017	0.008
Dy	0.002	0.000	0.000	0.001	0.001	0.001	0.000	0.000	0.000	0.000	0.000	0.001	0.001	0.000
S^{6+}	0.000	0.000	0.000	0.000	0.002	0.000	0.000	0.000	0.000	0.000	0.000	0.001	0.000	0.000
Ca	0.034	0.036	0.034	0.049	0.038	0.050	0.045	0.044	0.035	0.047	0.037	0.062	0.037	0.034
Pb	0.004	0.004	0.004	0.005	0.004	0.007	0.006	0.005	0.003	0.005	0.003	0.008	0.004	0.003
Total	2.00	2.00	2.00	2.00	2.00	2.00	2.00	1.99	2.00	1.98	1.99	2.00	2.02	1.99
Σ(A)	0.99	0.99	1.00	0.99	1.01	0.98	0.99	0.97	1.00	0.96	0.97	0.99	1.03	0.98
Σ(T)	1.01	1.01	1.00	1.01	1.00	1.01	1.01	1.02	1.00	1.03	1.02	1.01	0.98	1.02
Σ(A-T)	0.02	0.02	0.01	0.03	0.01	0.03	0.02	0.04	0.01	0.07	0.05	0.01	0.05	0.04
Crl	6.9	7.3	6.8	9.8	7.5	10.2	9.1	9.1	7.0	9.8	7.7	12.6	7.2	6.93
Ilm	1.3	2.5	1.7	3.0	1.6	6.0	4.6	5.9	2.0	5.7	2.5	6.2	1.0	2.43
xtm	2.1	1.2	1.7	1.5	2.0	0.3	1.3	0.8	1.3	0.6	0.6	1.7	2.4	1.14
Mnz	89.7	89.0	89.8	85.6	89.0	83.4	85.0	84.3	89.7	83.9	89.2	79.6	89.4	89.51

Tab. 4: LA-ICP-MS monazite U-Th-Pb data for sample *ALR 13-64*

		Isotope ratio								
Grain n°	**Texture**	$^{207}Pb/^{206}Pb$	**2s %**	$^{207}Pb/^{235}U$	**2s %**	$^{206}Pb/^{238}U$	**2s %**	**Rho**	$^{208}Pb/^{232}Th$	**2s %**
1364-01	core	0.074	2.7	1.751	3.5	0.172	3.031	0.86	0.053	3.0
1364-03	core	0.074	2.9	1.768	3.7	0.172	3.039	0.83	0.054	2.9
1364-03b	core	0.074	3.0	1.778	3.7	0.173	3.045	0.82	0.054	2.9
1364-06	rim	0.074	2.5	1.732	3.4	0.170	3.017	0.88	0.053	2.9
1364-09	rim	0.074	2.5	1.741	3.4	0.171	3.009	0.89	0.053	3.0
1364-14b	core	0.075	2.7	1.787	3.5	0.173	3.019	0.86	0.054	3.0
1364-19	rim	0.074	2.5	1.746	3.4	0.171	3.010	0.89	0.053	3.0
1364-20	rim	0.074	2.6	1.741	3.5	0.170	3.009	0.87	0.052	2.9
1364-21	rim	0.074	2.6	1.761	3.5	0.173	3.003	0.87	0.053	3.0
1364-21b	rim	0.075	2.7	1.762	3.5	0.171	3.010	0.86	0.053	2.9
1364-52	core	0.074	2.6	1.766	3.4	0.173	3.002	0.87	0.053	2.9
1364-52b	core	0.074	2.6	1.759	3.4	0.172	2.996	0.87	0.053	2.9
1364-53	rim	0.074	2.6	1.738	3.4	0.171	3.000	0.87	0.053	3.0
1364-09b	rim	0.073	2.5	1.723	3.4	0.170	2.981	0.89	0.053	2.9
1364-102b	rim	0.073	2.6	1.722	3.4	0.171	2.986	0.88	0.053	2.9
1364-102	rim	0.074	2.6	1.732	3.4	0.171	2.987	0.88	0.053	2.9
1364-149	core	0.075	2.8	1.772	3.6	0.171	3.001	0.84	0.053	2.9
1364-153	core	0.074	2.7	1.764	3.5	0.172	2.989	0.86	0.053	2.9
1364-153b	rim	0.074	2.6	1.726	3.4	0.169	2.973	0.88	0.053	2.9
1364-150	core	0.074	2.7	1.752	3.5	0.172	2.978	0.86	0.053	2.9
1364-150b	core	0.075	2.7	1.793	3.5	0.173	2.981	0.85	0.053	2.9
1364-131	rim	0.073	2.6	1.730	3.4	0.171	2.973	0.88	0.052	2.9
1364-131b	core	0.073	2.7	1.730	3.5	0.171	2.978	0.86	0.053	2.9
1364-113	rim	0.074	2.6	1.720	3.4	0.169	2.965	0.87	0.052	2.9
1364-113b	rim	0.074	2.6	1.736	3.4	0.171	2.973	0.87	0.053	2.9
1364-89b	core	0.072	2.8	1.716	3.6	0.172	2.983	0.84	0.053	2.9
1364-89	rim	0.073	2.6	1.697	3.4	0.169	2.965	0.88	0.052	2.9
1364-76	core	0.075	2.8	1.727	3.5	0.168	2.971	0.84	0.053	2.9
1364-76b	core	0.074	2.8	1.726	3.5	0.170	2.969	0.85	0.053	2.9
1364-57	rim	0.073	2.7	1.698	3.4	0.168	2.962	0.86	0.052	2.9
1364-57b	core	0.074	2.8	1.731	3.6	0.170	2.962	0.83	0.053	2.9
1364-57c	rim	0.074	2.7	1.715	3.4	0.167	2.952	0.86	0.052	2.9
1364-200	rim	0.074	2.7	1.718	3.4	0.169	2.950	0.86	0.052	2.9
1364-200b	core	0.075	2.8	1.743	3.5	0.169	2.962	0.84	0.053	2.9
1364-23	core	0.075	2.7	1.759	3.5	0.171	2.954	0.85	0.053	2.9
1364-23b	rim	0.073	2.6	1.675	3.4	0.167	2.938	0.87	0.052	2.9
1364-59	rim	0.074	2.7	1.690	3.5	0.167	2.949	0.80	0.052	2.9

No common Pb correction was applied

Tab. 4 : continued

		Dates									(ppm)		
Grain n°	**Texture**	**$^{207}Pb/^{206}Pb$**	**2s abs**	**$^{207}Pb/^{235}U$**	**2s abs**	**$^{206}Pb/^{238}U$**	**2s abs**	**$^{208}Pb/^{232}Th$**	**2s abs**	**% disc.**	**$^{232}Th^{a}$**	**$^{238}U^{a}$**	**Th/U**
1364-01	core	1037	27.6	1028	36.2	1023	31.0	1048	31.0	-0.4	47163	1351	35
1364-03	core	1053	29.7	1034	38.0	1025	31.1	1072	31.5	-0.9	63399	710	89
1364-03b	core	1053	30.6	1037	38.7	1030	31.4	1071	31.5	-0.7	54956	571	96
1364-06	rim	1037	25.7	1020	34.8	1013	30.6	1037	30.6	-0.8	31727	4554	7
1364-09	rim	1033	25.5	1024	34.5	1020	30.7	1049	31.0	-0.4	17875	17780	1
1364-14b	core	1068	27.7	1041	36.6	1028	31.0	1062	31.4	-1.2	62946	1320	48
1364-19	rim	1039	25.6	1026	34.7	1019	30.7	1048	31.0	-0.6	23919	8804	3
1364-20	rim	1050	26.5	1024	35.3	1012	30.4	1029	30.2	-1.2	40450	1970	21
1364-21	rim	1042	27.0	1031	35.7	1026	30.8	1049	31.0	-0.5	44866	1769	25
1364-21b	rim	1058	27.3	1032	36.1	1019	30.7	1051	31.0	-1.2	42203	1344	31
1364-52	core	1046	26.9	1033	35.6	1027	30.8	1044	30.6	-0.6	62134	2161	29
1364-52b	core	1042	26.7	1030	35.4	1025	30.7	1052	31.0	-0.5	62188	2287	27
1364-53	rim	1039	26.5	1023	35.1	1015	30.5	1051	31.0	-0.7	47815	2352	20
1364-09b	rim	1024	25.4	1017	34.2	1015	30.2	1038	30.6	-0.3	20668	17275	1
1364-102b	rim	1018	26.0	1017	34.5	1017	30.4	1050	30.7	0.0	33908	3697	9
1364-102	rim	1030	26.1	1021	34.8	1016	30.4	1039	30.6	-0.4	39205	3103	13
1364-149	core	1070	28.4	1035	36.8	1019	30.6	1050	30.7	-1.6	67263	857	79
1364-153	core	1051	27.3	1032	35.8	1024	30.6	1053	30.7	-0.9	83820	1562	54
1364-153b	rim	1047	25.7	1018	34.5	1005	29.9	1043	30.6	-1.3	39307	4339	9
1364-150	core	1037	27.2	1028	35.6	1024	30.5	1053	30.7	-0.4	58439	1731	34
1364-150b	core	1076	28.1	1043	36.6	1027	30.6	1050	30.7	-1.5	59526	1113	53
1364-131	rim	1025	26.2	1020	34.5	1018	30.3	1022	29.8	-0.2	32955	4551	7
1364-131b	core	1021	27.2	1020	35.3	1020	30.4	1037	30.2	0.0	40442	1584	26
1364-113	rim	1033	26.6	1016	34.8	1008	29.9	1027	29.8	-0.8	33468	2305	15
1364-113b	rim	1032	26.8	1022	35.1	1018	30.3	1038	30.2	-0.4	70699	2117	33
1364-89b	core	999	29.0	1015	36.2	1022	30.5	1044	30.3	0.7	70687	893	79
1364-89	rim	1006	26.1	1008	34.1	1008	29.9	1022	29.8	0.1	35718	4857	7
1364-76	core	1055	27.8	1019	35.9	1002	29.8	1034	30.2	-1.7	55661	1031	54
1364-76b	core	1034	27.8	1018	35.7	1011	30.0	1034	30.2	-0.7	57518	1141	50
1364-57	rim	1023	26.7	1008	34.6	1001	29.7	1027	29.8	-0.7	35273	2115	17
1364-57b	core	1044	28.6	1020	36.3	1009	29.9	1036	30.2	-1.1	69271	910	76
1364-57c	rim	1052	26.8	1014	35.0	997	29.4	1022	29.8	-1.7	41005	1773	23
1364-200	rim	1036	26.7	1015	34.8	1006	29.7	1028	29.8	-1.0	54530	2357	23
1364-200b	core	1066	28.3	1025	36.3	1005	29.8	1034	29.9	-1.9	81863	976	84
1364-23	core	1059	27.7	1031	35.7	1017	30.0	1042	30.3	-1.3	79568	1625	49
1364-23b	rim	1011	25.7	999	33.6	994	29.2	1024	29.8	-0.5	21500	11058	2
1364-59	rim	1029	27.2	1005	34.9	994	29.3	1015	29.4	-1.1	36892	1535	24

Tab. 5: LA-ICP-MS monazite U-Th-Pb data for sample *ALR 14-19*

		Isotope ratio							
Grain n°	**Group**	**$^{207}Pb/^{206}Pb$**	**2s %**	**$^{207}Pb/^{235}U$**	**2s %**	**$^{206}Pb/^{238}U$**	**2s %**	**Rho**	**$^{208}Pb/^{232}Th$**
1419-127	A	0.074	2.1	1.750	3.3	0.171	3.3	0.99	0.0526
1419-13a**	A	0.073	2.4	1.837	3.4	0.181	3.3	0.96	0.0547
1419-13b**	A	0.073	2.4	1.813	3.4	0.180	3.3	0.96	0.0548
1419-13c**	A	0.089	2.1	2.159	3.3	0.177	3.3	0.99	0.0543
1419-140	A	0.074	2.4	1.779	3.4	0.175	3.4	0.98	0.0533
1419-152a**	A	0.073	2.4	1.793	3.4	0.179	3.3	0.97	0.0545
1419-152b	A	0.073	2.2	1.744	3.3	0.172	3.3	0.99	0.0525
1419-172	A	0.074	2.4	1.785	3.4	0.175	3.4	0.97	0.0538
1419-18**	A	0.074	2.5	1.850	3.5	0.182	3.4	0.96	0.0536
1419-26**	A	0.074	2.4	1.709	3.4	0.167	3.4	0.97	0.0523
1419-2a	A	0.074	2.4	1.789	3.3	0.175	3.3	0.98	0.0555
1419-2b	A	0.074	2.3	1.811	3.3	0.177	3.3	0.98	0.0555
1419-30	A	0.074	2.4	1.762	3.4	0.173	3.4	0.97	0.0528
1419-35	A	0.074	2.2	1.790	3.4	0.176	3.3	0.98	0.0550
1419-37a	A	0.074	2.4	1.771	3.3	0.173	3.3	0.98	0.0541
1419-37b	A	0.074	2.4	1.818	3.4	0.179	3.3	0.97	0.0543
1419-38	A	0.074	2.4	1.759	3.4	0.173	3.4	0.97	0.0537
1419-3a	A	0.074	2.3	1.795	3.3	0.176	3.3	0.99	0.0548
1419-3b	A	0.074	2.3	1.801	3.3	0.178	3.3	0.98	0.0557
1419-40*	A	0.076	2.2	1.849	3.4	0.177	3.3	0.97	0.0549
1419-46a	A	0.073	2.4	1.769	3.4	0.175	3.4	0.97	0.0530
1419-46b	A	0.074	2.4	1.773	3.4	0.173	3.4	0.97	0.0535
1419-49	A	0.073	2.3	1.743	3.3	0.172	3.3	0.98	0.0544
1419-5	A	0.074	2.4	1.738	3.4	0.171	3.4	0.98	0.0524
1419-52	A	0.075	2.4	1.806	3.4	0.176	3.3	0.98	0.0545
1419-55a	A	0.074	2.1	1.773	3.3	0.174	3.3	0.99	0.0540
1419-55b	A	0.074	2.2	1.770	3.4	0.174	3.3	0.98	0.0541
1419-55c	A	0.074	2.2	1.792	3.3	0.175	3.3	0.98	0.0542
1419-56a**	A	0.073	2.5	1.812	3.5	0.179	3.4	0.95	0.0530
1419-56b	A	0.073	2.5	1.748	3.5	0.173	3.4	0.96	0.0549
1419-59	A	0.074	2.4	1.793	3.4	0.175	3.3	0.97	0.0547
1419-77b	A	0.075	2.2	1.792	3.3	0.174	3.3	0.99	0.0534
1419-77d**	A	0.078	2.3	1.968	3.4	0.183	3.3	0.96	0.0567
1419-90b	A	0.074	2.4	1.754	3.4	0.172	3.3	0.98	0.0541
1419-97a	A	0.074	2.1	1.754	3.3	0.173	3.3	0.99	0.0530
1419-97b	A	0.073	2.2	1.769	3.4	0.175	3.3	0.98	0.0528
1419-151	B	0.071	2.3	1.479	3.3	0.152	3.3	0.98	0.0476
1419-34a	B	0.072	2.6	1.603	3.5	0.160	3.4	0.94	0.0499
1419-34b	B	0.070	2.6	1.539	3.6	0.160	3.4	0.93	0.0475
1419-77a	B	0.071	2.4	1.620	3.4	0.165	3.3	0.97	0.0522
1419-77c	B	0.070	2.4	1.545	3.4	0.159	3.3	0.97	0.0499
1419-90a	B	0.070	2.5	1.554	3.4	0.160	3.3	0.96	0.0484

*** Grains not used for age calculation*

Tab. 5: continued

		Dates										Chemical composition		
Grain n°	**Group**	**2s %**	**$^{207}Pb/^{206}Pb$**	**2s abs**	**$^{207}Pb/^{235}U$**	**2s abs**	**$^{206}Pb/^{238}U$**	**2s abs**	**$^{208}Pb/^{232}Th$**	**2s abs**	**% disc.**	**ThO2**	**UO2**	**Y2O3***
1419-127	A	2.8	1044	22	1027	34	1020	34	1035	29	-2.4	5.26	0.77	1.08
1419-13a**	A	2.8	1025	25	1059	36	1075	36	1079	30	4.7	16.28	0.40	0.06
1419-13b**	A	2.8	1017	25	1050	38	1066	35	1114	31	4.6	11.05	0.56	1.00
1419-13c**	A	2.8	1397	30	1168	35	1048	35	1073	30	-33.3	17.84	0.31	0.08
1419-140	A	2.8	1034	25	1038	35	1039	35	1050	30	0.5	3.76	1.18	1.10
1419-152a**	A	2.8	1003	24	1043	36	1062	35	1076	30	5.5	7.30	0.27	0.02
1419-152b	A	2.8	1026	22	1025	34	1025	34	1034	29	-0.1	5.88	0.35	0.14
1419-172	A	2.9	1036	25	1040	36	1042	35	1059	30	0.5	2.19	0.88	0.37
1419-18**	A	2.8	1035	26	1064	35	1077	36	1031	29	3.9	4.60	0.71	0.48
1419-26**	A	2.9	1044	25	1012	37	998	33	1043	29	-4.6	5.53	0.23	0.18
1419-2a	A	2.8	1047	25	1041	35	1039	34	1091	30	-0.9	3.89	0.69	1.26
1419-2b	A	2.8	1043	24	1050	35	1053	35	1092	30	1.0	4.50	0.75	0.76
1419-30	A	2.8	1043	25	1032	35	1026	35	1039	29	-1.6	5.17	0.73	1.01
1419-35	A	2.8	1038	23	1042	35	1044	34	1083	30	0.5	4.51	0.37	0.57
1419-37a	A	2.8	1049	25	1035	35	1028	34	1065	30	-2.0	4.47	0.83	0.89
1419-37b	A	2.8	1037	25	1052	36	1059	35	1069	30	2.1	6.22	0.51	0.10
1419-38	A	2.8	1038	25	1031	35	1027	34	1058	30	-1.0	9.86	0.67	0.96
1419-3a	A	2.8	1036	24	1044	35	1047	35	1079	30	1.0	5.13	1.19	2.80
1419-3b	A	2.8	1029	24	1046	35	1054	35	1095	31	2.4	5.31	0.86	1.20
1419-40**	A	2.8	1086	24	1063	37	1052	35	1055	30	-3.3	4.38	0.71	1.29
1419-46a	A	2.9	1024	25	1034	36	1039	35	1044	30	1.5	3.95	0.66	0.85
1419-46b	A	2.8	1049	25	1036	36	1030	35	1054	30	-1.9	5.09	0.72	0.86
1419-49	A	2.8	1027	24	1025	34	1024	34	1071	30	-0.3	n.a	n.a	n.a
1419-5	A	2.9	1032	25	1023	35	1018	34	1033	29	-1.4	3.26	0.99	0.40
1419-52	A	2.8	1057	25	1048	35	1043	34	1073	30	-1.4	5.94	0.50	0.34
1419-55a	A	2.8	1040	22	1036	34	1034	34	1064	30	-0.6	4.12	0.74	0.78
1419-55b	A	2.8	1030	23	1035	35	1037	34	1065	30	0.6	6.42	0.45	0.17
1419-55c	A	2.8	1053	23	1042	35	1037	34	1066	30	-1.6	7.20	0.52	0.13
1419-56a**	A	2.8	1022	26	1050	39	1064	36	1069	30	4.0	n.a	n.a	n.a
1419-56b	A	2.8	1026	25	1027	36	1027	34	1080	31	0.0	10.99	0.42	0.55
1419-59	A	2.8	1048	25	1043	35	1040	34	1077	30	-0.8	6.12	0.58	1.96
1419-77b	A	2.8	1061	23	1043	35	1034	34	1051	29	-2.7	4.71	0.71	1.47
1419-77d**	A	2.8	1148	26	1105	36	1083	36	1079	30	-6.0	4.13	0.75	0.27
1419-90b	A	2.8	1041	25	1029	35	1023	34	1066	30	-1.8	3.48	0.62	0.83
1419-97a	A	2.8	1029	22	1029	34	1029	34	1044	29	0.0	5.10	0.74	1.33
1419-97b	A	2.8	1026	23	1034	35	1038	34	1041	29	1.2	6.29	0.38	0.11
1419-151	B	2.8	949	22	922	31	910	30	941	26	-4.3	11.77	0.47	0.57
1419-34a	B	2.8	999	26	971	34	959	32	984	28	-4.2	9.25	0.34	0.59
1419-34b	B	2.8	918	24	946	34	958	32	938	27	4.2	4.89	0.38	0.28
1419-77a	B	2.8	960	23	978	33	986	33	1028	29	2.6	11.64	0.51	0.66
1419-77c	B	2.8	939	23	948	32	953	31	984	27	1.5	n.a	n.a	n.a
1419-90a	B	2.8	942	23	952	33	957	32	955	27	1.6	6.38	0.49	0.28

Tab. 6: EPMA monazite microchemistry for sample *ALR 13-05* (in wt. %)

Name	1305-4	1305-25	1305-103	1305-106	1305-164	1305-200	1305-111	1305-25b	1305-8	1305-21	1305-41	1305-41b	1305-61
Group	G1	G1	G1	G1	G1	G1	G1	G1	G2	G2	G2	G2	G2
P_2O_5	29.506	29.473	29.24	28.87	29.506	29.53	28.843	28.931	30.194	28.433	29.397	28.949	29.501
SiO_2	0.473	0.455	0.768	0.64	0.612	0.595	1.051	0.727	0.178	1.127	0.612	0.945	0.705
ThO_2	4.962	5.887	8.874	7.483	7.014	7.731	8.846	7.608	6.606	12.839	10.25	10.651	10.495
UO_2	0.977	0.429	0.528	0.226	0.535	0.446	0.359	0.45	0.748	0.373	0.424	0.303	0.331
Ce_2O_3	23.83	25.214	23.838	24.079	24.311	23.717	23.855	24.507	20.874	20.395	19.672	19.404	20.555
Y_2O_3	0.281	0.209	0.219	0.222	0.275	0.225	0.12	0.143	3.298	2.747	3.894	3.916	3.023
La_2O_3	7.708	7.718	7.761	7.706	8.368	7.689	7.323	7.706	7.982	6.896	6.435	6.538	6.707
Pr_2O_3	3.856	3.886	3.428	3.864	3.443	3.92	4.066	3.816	2.927	3.088	3.231	3.05	3.117
Nd_2O_3	19.614	19.306	17.339	18.39	17.078	18.083	18.436	18.363	14.213	15.293	14.903	14.875	16.089
Sm_2O_3	4.798	3.313	3.427	3.905	3.278	3.726	2.962	3.345	4.17	2.346	2.806	3.174	3.219
Gd_2O_3	1.642	1.272	0.983	0.984	1.112	1.164	0.907	0.607	4.088	1.258	2.346	2.895	2.058
Dy_2O_3	0.125	0.066	0.1	0.125	0	0.097	0	0	1.247	0.734	1.412	1.601	0.955
SO_2	0.102	0.142	0.076	0.062	0.064	0.115	0.064	0.117	0.013	0	0.026	0.011	0.024
CaO	1.118	1.122	1.402	1.327	1.359	1.446	1.324	1.285	1.509	1.903	1.86	1.641	1.823
PbO	0.47	0.38	0.558	0.421	0.29	0.471	0.394	0.51	0.398	0.623	0.465	0.492	0.514
Total	**99.462**	**98.872**	**98.541**	**98.304**	**97.245**	**98.955**	**98.55**	**98.115**	**98.445**	**98.055**	**97.733**	**98.445**	**99.116**
P	0.990	0.960	0.931	0.982	0.948	0.990	0.945	0.983	0.997	0.966	0.988	0.979	0.984
Si	0.019	0.019	0.033	0.026	0.027	0.024	0.044	0.029	0.007	0.045	0.024	0.037	0.028
Th	0.045	0.056	0.088	0.068	0.069	0.070	0.084	0.069	0.060	0.117	0.093	0.095	0.094
U	0.009	0.004	0.005	0.002	0.005	0.004	0.003	0.004	0.007	0.003	0.004	0.003	0.003
Ce	0.346	0.385	0.380	0.354	0.386	0.344	0.367	0.360	0.305	0.300	0.286	0.279	0.296
Y	0.006	0.005	0.005	0.005	0.006	0.005	0.003	0.003	0.070	0.059	0.082	0.082	0.063
La	0.113	0.119	0.124	0.114	0.134	0.112	0.113	0.114	0.117	0.102	0.094	0.095	0.097
Pr	0.056	0.059	0.054	0.057	0.054	0.057	0.062	0.056	0.043	0.045	0.047	0.044	0.045
Nd	0.068	0.049	0.053	0.056	0.051	0.053	0.044	0.048	0.059	0.034	0.040	0.045	0.045
Sm	0.268	0.278	0.260	0.255	0.255	0.247	0.267	0.254	0.195	0.211	0.204	0.202	0.218
Gd	0.022	0.018	0.014	0.013	0.016	0.015	0.013	0.008	0.054	0.017	0.031	0.038	0.027
Dy	0.002	0.001	0.001	0.002	0.000	0.001	0.000	0.000	0.016	0.009	0.018	0.020	0.012
S^{6+}	0.004	0.0056	0.0031	0.002	0.0026	0.004	0.0025	0.004	0.0005	0.000	0.001	0.0004	0.001
Ca	0.047	0.050	0.065	0.057	0.063	0.061	0.060	0.055	0.065	0.082	0.079	0.069	0.077
Pb	0.005	0.004	0.007	0.005	0.003	0.005	0.004	0.006	0.004	0.007	0.005	0.005	0.005
Total	1.993	2.007	2.021	1.996	2.018	1.988	2.009	1.989	1.999	1.997	1.994	1.993	1.995
Σ(A)	0.988	1.034	1.060	0.990	1.047	0.978	1.023	0.981	0.996	0.986	0.983	0.977	0.985
Σ(T)	1.008	0.979	0.965	1.008	0.974	1.014	0.989	1.012	1.004	1.011	1.012	1.016	1.011
Σ(A-T)	0.02	0.05	0.10	0.02	0.07	0.04	0.03	0.03	0.01	0.03	0.03	0.04	0.03
Crl	9.6	9.7	12.4	11.5	12.0	12.5	11.5	11.2	13.0	16.6	16.1	14.1	15.6
Hfn	1.9	1.8	3.2	2.6	2.5	2.4	4.3	3.0	0.7	4.6	2.5	3.8	2.8
xtm	2.9	2.2	2.0	2.0	2.1	2.2	1.5	1.1	14.1	8.6	13.3	14.3	10.4
Mnz	85.6	86.2	82.5	84.0	83.4	82.9	82.7	84.7	72.3	70.2	68.1	67.8	71.2
LaN/GdN	0.03	0.03	0.02	0.02	0.03	0.03	0.02	0.01	0.19	0.12	0.20	0.21	0.15

Tab. 6: continued

Name	1305-65	1305-76	1305-88b	1305-11	1305-18	1305-18b	1305-47	1305-88	1305-103	1305-106	1305-136	1305-164	1305-172
Group	G2	G2	G2	G3	G3	G3	G3	G3	G3	G3	G3	G3	G3
P_2O_5	30.393	29.048	30.702	27.284	27.082	25.896	27.168	26.311	25.295	25.536	26.577	25.793	25.769
SiO_2	0.29	0.801	0.166	1.722	1.652	2.574	2.048	2.399	2.909	2.726	2.172	2.634	2.434
ThO_2	6.864	8.69	6.977	13.884	12.427	16.237	14.633	16.956	18.309	16.903	14.994	16.776	15.953
UO_2	0.538	0.361	0.601	0.25	0.186	0.247	0.284	0.227	0.288	0.266	0.26	0.125	0.222
Ce_2O_3	21.106	19.899	20.489	21.616	23.215	21.481	21.776	20.769	20.301	21.095	21.304	20.989	20.778
Y_2O_3	4.757	3.649	5.323	0.122	0.181	0.068	0.153	0.109	0.102	0.066	0.117	0.064	0.073
La_2O_3	6.982	7.055	7.02	6.264	8.472	6.721	6.652	6.151	6.115	6.687	6.627	6.44	6.32
Pr_2O_3	3.201	2.783	3.415	3.962	3.701	3.193	3.571	3.562	3.607	3.505	3.74	3.676	3.567
Nd_2O_3	15.3	14.716	14.249	17.357	16.528	16.787	17.426	17.64	16.947	16.926	17.143	17.045	17.004
Sm_2O_3	2.911	3.805	3.609	3.229	2.363	2.429	2.982	3.192	2.353	2.378	2.815	2.673	2.539
Gd_2O_3	2.649	3.652	3.035	0.748	0.8	0.577	0.826	0.696	0.563	0.602	0.954	0.508	0.545
Dy_2O_3	1.607	1.141	1.498	0.081	0.187	0.103	0.063	0	0.019	0.036	0.072	0.083	0.156
SO_2	0.025	0.01	0.006	0.087	0.124	0.08	0.083	0.089	0.055	0.038	0.113	0.052	0.063
CaO	1.485	1.362	1.594	1.702	1.345	1.382	1.445	1.553	1.304	1.328	1.425	1.471	1.372
PbO	0.348	0.509	0.388	0.665	0.53	0.79	0.722	0.731	0.908	0.782	0.826	0.783	0.672
Total	**98.456**	**97.481**	**99.072**	**98.973**	**98.793**	**98.565**	**99.832**	**100.385**	**99.075**	**98.874**	**99.139**	**99.112**	**97.467**
P	0.992	0.969	1.006	0.937	0.937	0.904	0.963	0.905	0.888	0.895	0.951	0.899	0.909
Si	0.012	0.033	0.006	0.070	0.067	0.106	0.078	0.097	0.121	0.113	0.084	0.108	0.101
Th	0.062	0.081	0.061	0.128	0.115	0.152	0.127	0.157	0.173	0.159	0.133	0.157	0.151
U	0.005	0.003	0.005	0.002	0.002	0.002	0.002	0.002	0.003	0.002	0.002	0.001	0.002
Ce	0.307	0.298	0.290	0.321	0.345	0.324	0.305	0.309	0.308	0.320	0.303	0.316	0.317
Y	0.101	0.079	0.110	0.003	0.004	0.001	0.003	0.002	0.002	0.001	0.002	0.001	0.002
La	0.102	0.106	0.100	0.094	0.127	0.102	0.094	0.092	0.093	0.102	0.095	0.098	0.097
Pr	0.046	0.041	0.048	0.059	0.055	0.048	0.050	0.053	0.054	0.053	0.053	0.055	0.054
Nd	0.041	0.056	0.050	0.047	0.034	0.036	0.041	0.046	0.035	0.035	0.039	0.039	0.038
Sm	0.209	0.207	0.190	0.243	0.231	0.239	0.230	0.247	0.242	0.241	0.230	0.242	0.244
Gd	0.035	0.049	0.039	0.010	0.011	0.008	0.010	0.009	0.008	0.008	0.012	0.007	0.008
Dy	0.021	0.015	0.019	0.001	0.002	0.001	0.001	0.000	0.000	0.000	0.001	0.001	0.002
S^{6+}	0.0009	0.0004	0.000	0.003	0.0047	0.003	0.0030	0.003	0.002	0.001	0.0041	0.002	0.002
Ca	0.063	0.060	0.066	0.074	0.058	0.061	0.059	0.068	0.058	0.059	0.059	0.065	0.061
Pb	0.004	0.006	0.004	0.007	0.006	0.009	0.007	0.008	0.010	0.009	0.009	0.009	0.008
Total	2.000	2.003	1.995	1.996	1.993	1.994	1.972	1.996	1.995	1.998	1.974	1.999	1.994
Σ(A)	0.997	1.001	0.983	0.992	0.994	0.987	0.934	0.997	0.989	0.992	0.943	0.994	0.986
Σ(T)	1.004	1.002	1.012	1.007	1.004	1.010	1.041	1.003	1.008	1.008	1.035	1.007	1.010
Σ(A-T)	0.01	0.00	0.03	0.02	0.01	0.02	0.11	0.01	0.02	0.02	0.09	0.01	0.02
Crl	12.6	11.9	13.4	14.9	11.8	12.4	12.7	13.6	11.8	11.9	12.6	13.0	12.4
Htn	1.2	3.3	0.7	7.0	6.8	10.7	8.4	9.8	12.3	11.4	9.0	10.9	10.3
xtm	15.6	14.3	17.0	1.4	1.7	1.1	1.5	1.2	1.0	1.0	1.7	0.9	1.1
Mnz	70.6	70.5	68.9	76.7	79.7	75.8	77.3	75.4	74.8	75.7	76.7	75.2	76.1
LaN/GdN	0.22	0.20	0.25	0.02	0.02	0.01	0.02	0.02	0.01	0.01	0.02	0.01	0.01

Tab. 6: continued

Name	1305-172b	1305-135	1305-135b	1305-115b	1305-92	1305-73	1305-74	1305-76	1305-76b	1305-107	1305-108	1305-151	1305-158	1305-171
Group	G3	G3	G3	G3	G3	G3	G3	G3	G3	G3	G3	G3	G3	G3
P_2O_5	28.03	26.077	25.502	26.587	26.387	27.12	28.025	26.594	27.095	24.98	27.662	25.929	25.864	26.355
SiO_2	1.479	2.543	2.982	2.355	2.327	1.898	1.15	2.188	1.867	3.093	1.455	2.506	2.612	2.25
ThO_2	11.204	15.699	17.942	15.247	15.225	12.395	9.838	14.599	12.907	18.013	11.208	15.336	16.218	15.211
UO_2	0.143	0.255	0.224	0.16	0.156	0.129	0.203	0.231	0.171	0.233	0.331	0.183	0.211	0.246
Ce_2O_3	22.938	21.241	20.124	21.117	21.235	22.6	23.252	21.415	22.372	20.607	23.064	20.992	20.831	21.519
Y_2O_3	0.077	0.038	0.098	0.091	0.114	0.114	0.096	0.099	0.067	0.074	0.119	0.115	0.074	0.103
La_2O_3	7.187	6.714	5.848	6.928	6.374	7.155	7.453	6.676	6.93	6.009	7.169	6.542	6.344	6.284
Pr_2O_3	3.547	3.193	3.379	3.743	3.593	3.763	3.736	3.689	3.436	3.372	3.472	3.624	3.255	3.273
Nd_2O_3	18.417	17.367	17.42	17.891	17.07	17.861	18.448	17.283	16.454	16.585	17.578	17.702	17.199	17.141
Sm_2O_3	2.706	2.39	2.542	2.644	2.978	2.47	2.69	2.815	2.761	2.384	3.114	2.916	2.46	2.789
Gd_2O_3	0.945	0.773	0.734	0.569	0.592	0.517	0.951	0.519	0.802	0.82	0.575	0.573	0.416	0.588
Dy_2O_3	0.235	0.059	0.117	0	0	0	0	0	0.098	0	0.264	0.165	0.017	0
SO_2	0.099	0.102	0.07	0.046	0.063	0.05	0.12	0.084	0.091	0.056	0.096	0.097	0.07	0.073
CaO	1.458	1.463	1.42	1.338	1.379	1.339	1.528	1.431	1.415	1.4	1.404	1.387	1.436	1.457
PbO	0.453	0.736	0.529	0.793	0.845	0.545	0.316	0.727	0.522	0.925	0.537	0.696	0.748	0.658
Total	**98.918**	**98.65**	**98.931**	**99.509**	**98.338**	**97.956**	**97.806**	**98.35**	**96.988**	**98.551**	**98.048**	**98.763**	**97.755**	**97.947**
P	0.968	0.955	0.890	0.916	0.918	0.938	0.961	0.930	0.942	0.881	0.912	0.903	0.908	0.919
Si	0.058	0.097	0.123	0.096	0.096	0.078	0.047	0.089	0.077	0.129	0.063	0.103	0.108	0.093
Th	0.100	0.136	0.168	0.141	0.142	0.115	0.091	0.135	0.121	0.171	0.110	0.144	0.153	0.143
U	0.001	0.002	0.002	0.001	0.001	0.001	0.002	0.002	0.002	0.002	0.003	0.002	0.002	0.002
Ce	0.330	0.297	0.304	0.315	0.319	0.338	0.345	0.318	0.336	0.314	0.364	0.316	0.315	0.325
Y	0.002	0.001	0.002	0.002	0.002	0.002	0.002	0.002	0.001	0.002	0.003	0.003	0.002	0.002
La	0.104	0.095	0.089	0.104	0.097	0.108	0.111	0.100	0.105	0.092	0.114	0.099	0.097	0.096
Pr	0.051	0.044	0.051	0.056	0.054	0.056	0.055	0.054	0.051	0.051	0.055	0.054	0.049	0.049
Nd	0.038	0.033	0.037	0.038	0.044	0.036	0.039	0.041	0.040	0.035	0.048	0.043	0.036	0.041
Sm	0.249	0.229	0.247	0.251	0.242	0.251	0.258	0.241	0.233	0.238	0.261	0.251	0.245	0.243
Gd	0.012	0.010	0.010	0.008	0.008	0.007	0.013	0.007	0.011	0.011	0.008	0.008	0.006	0.008
Dy	0.003	0.001	0.002	0.000	0.000	0.000	0.000	0.000	0.001	0.000	0.004	0.002	0.000	0.000
S^{6+}	0.0036	0.0037	0.003	0.002	0.002	0.002	0.005	0.0032	0.004	0.002	0.0039	0.004	0.0027	0.003
Ca	0.061	0.060	0.063	0.058	0.061	0.059	0.066	0.062	0.062	0.062	0.065	0.061	0.064	0.064
Pb	0.005	0.008	0.006	0.009	0.009	0.006	0.003	0.008	0.006	0.010	0.006	0.008	0.008	0.007
Total	1.983	1.967	1.993	1.995	1.993	1.995	1.993	1.989	1.988	1.999	2.016	1.997	1.993	1.993
Σ(A)	0.960	0.918	0.983	0.985	0.982	0.981	0.990	0.973	0.973	0.992	1.045	0.994	0.979	0.983
Σ(T)	1.027	1.052	1.013	1.012	1.014	1.015	1.008	1.018	1.018	1.009	0.975	1.007	1.016	1.012
Σ(A-T)	0.07	0.13	0.03	0.03	0.03	0.03	0.02	0.05	0.05	0.02	0.07	0.01	0.04	0.03
Crl	12.7	12.9	12.7	11.8	12.4	11.8	13.2	12.7	12.7	12.5	12.4	12.2	12.9	13.1
Hfn	6.0	10.5	12.4	9.7	9.7	7.8	4.6	9.1	7.8	12.9	6.0	10.3	11.0	9.4
xtm	1.7	1.2	1.4	1.0	1.1	1.0	1.5	0.9	1.4	1.3	1.4	1.3	0.8	1.0
Mnz	79.6	75.3	73.5	77.5	76.8	79.4	80.6	77.3	78.1	73.3	80.3	76.2	75.4	76.5
LaN/GdN	0.02	0.02	0.02	0.01	0.01	0.01	0.02	0.01	0.02	0.02	0.02	0.02	0.01	0.01

Tab. 7: LA-ICP-MS monazite U-Th-Pb data for sample ALR 13-05

			Isotope ratio								
Grain n°	**Texture**	**Group**	$^{207}Pb/^{206}Pb$	**2s %**	$^{207}Pb/^{235}U$	**2s %**	$^{206}Pb/^{238}U$	**2s %**	**Rho**	$^{208}Pb/^{232}Th$	**2s %**
1305-4		*1*	0.0725	2.35	1.620	3.36	0.1621	3.31	0.99	0.049	2.79
1305-25		*1*	0.0719	2.36	1.632	3.36	0.1646	3.30	0.98	0.050	2.77
1305-25b		*1*	0.0719	2.36	1.627	3.37	0.1642	3.31	0.98	0.051	2.79
1305-103		*1*	0.0738	2.39	1.681	3.37	0.1651	3.30	0.98	0.051	2.80
1305-106		*1*	0.0727	2.39	1.676	3.39	0.1673	3.30	0.98	0.050	2.80
1305-164		*1*	0.0717	2.45	1.690	3.42	0.1710	3.31	0.97	0.049	2.79
1305-115		*1*	0.0724	2.45	1.685	3.41	0.1689	3.31	0.97	0.050	2.80
1305-200		*1*	0.0716	2.42	1.655	3.39	0.1677	3.31	0.98	0.050	2.78
1305-8		*2*	0.0701	2.41	1.492	3.39	0.1544	3.31	0.98	0.046	2.79
1305-88		*2*	0.0704	2.64	1.545	3.55	0.1591	3.32	0.94	0.048	2.78
1305-21		*2*	0.0700	2.55	1.506	3.48	0.1560	3.31	0.95	0.048	2.78
1305-41		*2*	0.0701	2.47	1.532	3.42	0.1586	3.31	0.97	0.048	2.80
1305-41b		*2*	0.0699	2.66	1.515	3.55	0.1571	3.31	0.93	0.048	2.79
1305-61		*2*	0.0703	2.49	1.510	3.44	0.1558	3.31	0.96	0.047	2.78
1305-65		*2*	0.0698	2.40	1.431	3.37	0.1488	3.30	0.98	0.046	2.77
1305-76		*2*	0.0707	2.60	1.543	3.52	0.1582	3.32	0.94	0.048	2.78
1305-88b		*2*	0.0701	2.41	1.464	3.38	0.1514	3.31	0.98	0.047	2.80
1305-11		*3*	0.0729	2.67	1.735	3.58	0.1728	3.32	0.93	0.051	2.79
1305-18		*3*	0.0740	2.61	1.758	3.52	0.1724	3.32	0.94	0.052	2.81
1305-18b		*3*	0.0739	2.81	1.759	3.67	0.1726	3.34	0.91	0.052	2.78
1305-47		*3*	0.0739	2.68	1.771	3.59	0.1738	3.33	0.93	0.052	2.79
1305-88		*3*	0.0740	2.73	1.783	3.61	0.1747	3.32	0.92	0.052	2.78
1305-103b		*3*	0.0727	2.80	1.747	3.67	0.1744	3.33	0.91	0.052	2.79
1305-106b		*3*	0.0740	2.68	1.740	3.57	0.1707	3.32	0.93	0.053	2.78
1305-136		*3*	0.0734	2.75	1.756	3.62	0.1736	3.33	0.92	0.052	2.79
1305-164b		*3*	0.0737	2.79	1.757	3.66	0.1730	3.33	0.91	0.052	2.77
1305-172		*3*	0.0747	2.78	1.760	3.65	0.1708	3.33	0.91	0.052	2.78
1305-172b		*3*	0.0744	2.64	1.721	3.54	0.1678	3.32	0.94	0.051	2.77
1305-135		*3*	0.0756	2.80	1.809	3.65	0.1736	3.33	0.91	0.053	2.77
1305-135b		*3*	0.0741	2.88	1.782	3.72	0.1745	3.34	0.90	0.052	2.80
1305-115b		*3*	0.0738	2.74	1.760	3.61	0.1730	3.33	0.92	0.052	2.80
1305-92		*3*	0.0736	2.82	1.769	3.67	0.1743	3.33	0.91	0.053	2.78
1305-73		*3*	0.0741	2.83	1.750	3.68	0.1714	3.33	0.90	0.051	2.79
1305-74		*3*	0.0729	2.61	1.725	3.53	0.1715	3.32	0.94	0.052	2.77
1305-76		*3*	0.0741	2.85	1.782	3.70	0.1745	3.33	0.90	0.053	2.77
1305-76b		*3*	0.0742	2.82	1.770	3.68	0.1730	3.33	0.91	0.052	2.77
1305-107		*3*	0.0733	2.88	1.781	3.71	0.1763	3.33	0.90	0.053	2.79
1305-108		*3*	0.0734	2.67	1.741	3.56	0.1720	3.32	0.93	0.052	2.80
1305-151		*3*	0.0753	2.86	1.810	3.69	0.1743	3.33	0.90	0.052	2.79
1305-158		*3*	0.0743	2.82	1.791	3.67	0.1749	3.33	0.91	0.052	2.78
1305-166		*3*	0.0735	2.85	1.757	3.69	0.1735	3.33	0.90	0.052	2.80

Tab. 7: continued

		Dates							Chemical composition			
Grain n°	Group	$^{207}Pb/^{206}Pb$	2s abs	$^{207}Pb/^{235}U$	2s abs	$^{206}Pb/^{238}U$	2s abs	$^{208}Pb/^{232}Th$	2s abs	% disc.	ThO_2	UO_2	Y_2O_3*
1305-4	1	1000	23	978	33	968	32	972	27	1.0	4.96	0.98	0.28
1305-25	1	983	23	983	33	982	32	991	27	0.0	5.89	0.43	0.21
1305-25b	1	983	23	981	33	980	32	998	28	0.1	7.61	0.45	0.14
1305-103	1	1037	25	1001	34	985	33	997	28	1.6	8.87	0.53	0.22
1305-106	1	1005	24	1000	34	997	33	981	27	0.3	7.48	0.23	0.22
1305-164	1	977	24	1005	34	1017	34	972	27	-1.2	7.01	0.54	0.28
1305-115	1	996	24	1003	34	1006	33	994	28	-0.3	8.85	0.36	0.12
1305-200	1	974	24	992	34	1000	33	987	27	-0.8	7.73	0.45	0.23
1305-8	2	931	22	927	31	926	31	911	25	0.2	6.61	0.75	3.30
1305-88	2	940	25	948	34	952	32	942	26	-0.4	10.13	0.21	1.66
1305-21	2	929	24	933	32	935	31	945	26	-0.2	12.84	0.37	2.75
1305-41	2	930	23	943	32	949	31	950	27	-0.6	10.25	0.42	3.89
1305-41b	2	926	25	936	33	941	31	956	27	-0.4	10.65	0.30	3.92
1305-61	2	937	23	934	32	933	31	928	26	0.1	10.50	0.33	3.02
1305-65	2	922	22	902	30	894	30	903	25	0.9	6.86	0.54	4.76
1305-76	2	950	25	948	33	947	31	943	26	0.1	8.69	0.36	3.65
1305-88b	2	932	22	916	31	909	30	923	26	0.7	6.98	0.60	5.32
1305-11	3	1010	27	1022	37	1027	34	1015	28	-0.6	13.88	0.25	0.12
1305-18	3	1041	27	1030	36	1025	34	1022	29	0.5	12.43	0.19	0.18
1305-18b	3	1040	29	1031	38	1026	34	1033	29	0.4	16.24	0.25	0.07
1305-47	3	1040	28	1035	37	1033	34	1030	29	0.2	14.63	0.28	0.15
1305-88	3	1042	28	1039	38	1038	34	1033	29	0.1	16.96	0.23	0.11
1305-103b	3	1005	28	1026	38	1036	34	1029	29	-1.0	18.31	0.29	0.10
1305-106b	3	1041	28	1024	37	1016	34	1035	29	0.8	16.90	0.27	0.07
1305-136	3	1024	28	1029	37	1032	34	1030	29	-0.3	14.99	0.26	0.12
1305-164b	3	1033	29	1030	38	1029	34	1022	28	0.1	16.78	0.13	0.06
1305-172	3	1062	30	1031	38	1016	34	1016	28	1.4	15.95	0.22	0.07
1305-172b	3	1053	28	1016	36	1000	33	1006	28	1.7	11.20	0.14	0.08
1305-135	3	1085	30	1049	38	1032	34	1036	29	1.7	15.70	0.26	0.04
1305-135b	3	1044	30	1039	39	1037	35	1024	29	0.2	17.94	0.22	0.10
1305-115b	3	1036	28	1031	37	1029	34	1023	29	0.2	15.25	0.16	0.09
1305-92	3	1031	29	1034	38	1036	34	1048	29	-0.2	15.23	0.16	0.11
1305-73	3	1044	30	1027	38	1020	34	1014	28	0.7	12.40	0.13	0.11
1305-74	3	1012	26	1018	36	1020	32	1023	28	-0.3	9.84	0.20	0.10
1305-76	3	1044	30	1039	38	1037	34	1038	29	0.2	14.60	0.23	0.10
1305-76b	3	1047	30	1034	38	1029	34	1021	28	0.6	12.91	0.17	0.07
1305-107	3	1022	29	1039	39	1047	35	1045	29	-0.8	18.01	0.23	0.07
1305-108	3	1025	27	1024	36	1023	34	1026	29	0.1	11.21	0.33	0.12
1305-151	3	1077	31	1049	39	1036	34	1027	29	1.3	15.34	0.18	0.12
1305-158	3	1050	30	1042	38	1039	35	1019	28	0.3	16.22	0.21	0.07
1305-166	3	1026	29	1030	38	1031	34	1024	29	-0.2	15.21	0.25	0.10

Tab. 8: EPMA monazite microchemistry for sample *ALR 13-06* (in wt. %)

Name	1306-1	1306-1b	1306-6	1306-39	1306-39b	1306-48	1306-48b*	1306-91	1306-91b*	1306-101
P_2O_5	30.456	27.703	30.214	29.31	29.201	29.288	30.072	29.492	27.673	28.541
SiO_2	0.247	1.52	0.403	0.573	0.672	0.894	0.312	0.179	1.465	0.893
ThO_2	4.402	10.908	4.916	4.62	4.862	6.502	5.709	4.808	9.166	6.534
UO_2	0.273	0.251	0.258	0.364	0.198	0.253	0.521	0.455	0.236	0.136
Ce_2O_3	24.104	20.85	22.786	24.078	24.32	20.83	23.073	23.921	20.516	24.855
Y_2O_3	4.324	2.254	5.235	3.042	2.806	4.597	4.043	3.76	3.035	0.969
La_2O_3	12.096	8.134	11.005	11.387	11.243	8.083	11.254	11.706	8.168	10.844
Pr_2O_3	3.089	3.295	3.121	3.397	3.046	3.212	3.204	3.289	3.059	3.47
Nd_2O_3	2.177	2.949	2.505	2.437	2.717	3.187	2.38	1.847	2.816	2.631
Sm_2O_3	12.205	13.672	12.103	13.433	13.805	14.324	12.154	11.893	14.123	13.948
Gd_2O_3	2.253	2.445	2.218	2.42	2.234	2.869	2.159	2.129	2.897	1.507
Dy_2O_3	1.424	0.845	1.417	0.958	0.912	1.473	1.104	0.814	1.056	0.425
SO_2	0.143	0.232	0.098	0.372	0.388	0.305	0.445	0.464	0.166	0.358
CaO	0.917	1.452	0.959	1.019	1.009	0.998	1.585	1.366	1.132	1.08
PbO	0.175	0.332	0.178	0.372	0.255	0.221	0.348	0.242	0.408	0.29
Total	**98.285**	**96.842**	**97.416**	**97.782**	**97.668**	**97.036**	**98.363**	**96.365**	**95.916**	**96.481**
P	1.003	0.985	1.000	0.990	0.976	0.988	0.987	0.989	0.979	0.973
Si	0.010	0.058	0.016	0.022	0.027	0.035	0.012	0.007	0.057	0.036
Th	0.039	0.095	0.044	0.041	0.044	0.057	0.050	0.043	0.082	0.060
U	0.002	0.002	0.002	0.003	0.002	0.002	0.004	0.004	0.002	0.001
Ce	0.343	0.292	0.326	0.341	0.352	0.296	0.327	0.347	0.294	0.366
Y	0.089	0.046	0.109	0.063	0.059	0.095	0.083	0.079	0.063	0.021
La	0.173	0.115	0.159	0.163	0.164	0.116	0.161	0.171	0.118	0.161
Pr	0.044	0.046	0.044	0.048	0.044	0.045	0.045	0.047	0.044	0.051
Nd	0.030	0.040	0.035	0.034	0.038	0.044	0.033	0.026	0.039	0.038
Sm	0.164	0.180	0.163	0.179	0.188	0.192	0.162	0.162	0.191	0.193
Gd	0.029	0.031	0.029	0.031	0.029	0.037	0.028	0.028	0.038	0.020
Dy	0.018	0.010	0.018	0.012	0.012	0.018	0.014	0.010	0.013	0.006
S^{6+}	0.005	0.0083	0.004	0.0135	0.014	0.0111	0.016	0.017	0.0061	0.014
Ca	0.038	0.059	0.040	0.042	0.043	0.041	0.066	0.058	0.048	0.047
Pb	0.002	0.003	0.002	0.004	0.003	0.002	0.004	0.003	0.004	0.003
Total	1.984	1.963	1.986	1.973	1.978	1.969	1.977	1.975	1.972	1.975
Σ(A)	0.977	0.928	0.974	0.974	0.990	0.958	0.994	0.996	0.942	0.980
Σ(T)	1.012	1.043	1.016	1.012	1.003	1.023	0.999	0.996	1.036	1.009
Σ(A-T)	0.04	0.12	0.04	0.04	0.01	0.07	0.00	0.00	0.09	0.03
Crl	6.8	11.0	7.5	6.0	5.8	10.1	6.4	8.3	8.8	6.8
An	0.5	0.9	0.4	1.4	1.5	1.6	1.2	1.8	0.6	1.4
Htn	1.0	6.3	1.6	2.3	2.7	1.2	3.7	0.7	6.1	3.7
Xtm	14.0	9.4	15.9	11.0	10.2	12.7	15.8	12.0	12.1	4.8
Mnz	77.6	72.4	74.6	79.4	79.9	74.3	73.0	77.1	72.5	83.3

** No geochro*

Tab. 8: continued

Name	1306-117	1306-137	1306-137b	1306-142	1306-142b	1306-145	1306-192	1306-192b	1306-189	1306-212*
P_2O_5	29.169	27.962	28.138	29.726	28.742	30.348	30.071	29.216	28.945	28.572
SiO_2	0.408	1.267	0.873	0.405	1.028	0.176	0.01	0.643	0.861	0.827
ThO_2	4.739	8.545	5.761	5.539	7.192	4.468	4.794	5.692	6.415	6.413
UO_2	0.528	0.186	0.297	0.27	0.173	0.701	0.059	0.178	0.253	0.145
Ce_2O_3	23.353	22.916	24.133	23.724	22.73	22.408	23.704	24.334	23.245	24.842
Y_2O_3	3.915	0.979	2.262	3.871	2.316	4.277	3.261	1.908	2.611	1.086
La_2O_3	11.349	8.782	9.354	11.629	8.961	11.817	12.727	10.699	8.954	10.915
Pr_2O_3	3.144	3.759	3.463	2.736	3.531	2.797	3.189	3.69	3.646	3.355
Nd_2O_3	2.205	3.4	2.718	2.06	2.634	2.373	2.261	2.803	3.094	2.449
Sm_2O_3	11.729	15.594	14.905	11.277	15.15	11.779	11.245	14.724	15.001	13.903
Gd_2O_3	1.994	1.836	2.886	2.288	2.242	2.259	1.615	2.146	2.521	2.055
Dy_2O_3	1.069	0.515	0.947	1.158	1.043	1.059	0.928	0.746	0.961	0.445
SO_2	0.642	0.27	0.463	0.517	0.132	0.499	0.542	0.26	0.354	0.362
CaO	1.432	1.184	1.054	1.475	1.069	1.554	1.525	0.972	1.117	1.046
PbO	0.42	0.41	0.282	0.337	0.278	0.335	0.253	0.209	0.252	0.246
Total	**96.096**	**97.605**	**97.536**	**97.012**	**97.221**	**96.85**	**96.184**	**98.22**	**98.23**	**96.661**
P	0.977	0.971	0.955	0.964	0.974	0.999	1.004	0.980	0.972	0.973
Si	0.016	0.050	0.035	0.016	0.041	0.007	0.000	0.025	0.034	0.033
Th	0.043	0.076	0.053	0.051	0.066	0.040	0.043	0.051	0.057	0.059
U	0.005	0.002	0.003	0.002	0.002	0.006	0.001	0.002	0.002	0.001
Ce	0.338	0.330	0.354	0.352	0.333	0.319	0.339	0.353	0.334	0.366
Y	0.082	0.020	0.048	0.083	0.049	0.089	0.068	0.040	0.055	0.023
La	0.166	0.127	0.138	0.174	0.132	0.169	0.183	0.156	0.130	0.162
Pr	0.045	0.054	0.051	0.040	0.052	0.040	0.045	0.053	0.052	0.049
Nd	0.031	0.048	0.039	0.030	0.038	0.033	0.032	0.040	0.043	0.035
Sm	0.160	0.211	0.206	0.157	0.209	0.158	0.151	0.201	0.203	0.193
Gd	0.026	0.024	0.038	0.031	0.030	0.029	0.021	0.028	0.033	0.027
Dy	0.014	0.007	0.012	0.015	0.013	0.013	0.012	0.010	0.012	0.006
S^{6+}	0.024	0.0100	0.017	0.0196	0.005	0.018	0.0199	0.010	0.0130	0.014
Ca	0.061	0.050	0.045	0.064	0.046	0.065	0.064	0.041	0.047	0.045
Pb	0.004	0.004	0.003	0.004	0.003	0.004	0.003	0.002	0.003	0.003
Total	1.968	1.975	1.981	1.984	1.988	1.970	1.965	1.983	1.978	1.975
Σ(A)	0.999	0.964	1.008	1.023	0.977	0.982	0.981	0.987	0.985	0.983
Σ(T)	0.993	1.021	0.990	0.981	1.015	1.006	1.004	1.005	1.006	1.006
Σ(A-T)	0.01	0.06	0.02	0.04	0.04	0.02	0.02	0.02	0.02	0.02
Crl	7.6	8.3	5.6	8.8	8.3	9.6	9.2	6.5	7.0	6.5
An	2.4	1.0	1.7	1.9	0.5	1.9	2.1	1.0	1.3	1.4
Htn	1.7	5.2	3.5	1.6	4.2	0.7	0.0	2.6	3.5	3.4
Xtm	12.5	5.3	9.9	12.8	9.4	13.5	10.5	8.0	10.2	5.8
Mnz	75.8	80.2	79.2	74.8	77.6	74.3	78.3	82.0	78.1	82.9

Tab. 8: continued

Name	1306-248	1306-248b	1306-233	1306-233b*	1306-126	1306-66	1306-66b*	1306-64	1306-62*	1306-62b*
P_2O_5	29.72	28.66	29.969	28.847	28.74	29.84	29.746	30.234	28.857	28.873
SiO_2	0.424	0.824	0.255	1.159	1.024	0.117	0.355	0.393	0.962	0.914
ThO_2	5.097	6.018	3.721	7.44	7.362	2.868	5.535	4.44	7.561	6.758
UO_2	0.343	0.246	0.229	0.196	0.314	0.258	0.36	0.167	0.197	0.308
Ce_2O_3	23.646	22.754	24.543	21.609	22.491	24.623	24.165	22.594	22.503	23.359
Y_2O_3	4.07	3.06	3.91	4.345	2.58	3.66	4.081	5.36	2.814	2.258
La_2O_3	11.55	9.427	12.223	9.421	7.964	13.631	11.124	10.481	7.914	9.037
Pr_2O_3	2.999	3.34	2.957	3.194	3.438	3.499	2.933	2.957	3.517	3.434
Nd_2O_3	2.43	2.82	2.131	2.539	3.215	1.909	2.087	2.832	3.111	3.009
Sm_2O_3	12.13	14.072	12.069	13.275	15.065	12.513	11.085	12.339	15.297	14.55
Gd_2O_3	1.534	2.48	2.195	2.607	2.535	2.153	2.128	2.753	2.87	1.962
Dy_2O_3	1.159	0.979	0.971	1.072	0.799	0.917	1.252	1.317	0.845	0.803
SO_2	0.412	0.38	0.388	0.204	0.32	0.565	0.394	0.299	0.327	0.343
CaO	1.312	1.13	1.058	1.038	1.188	1.08	1.389	1.09	1.191	1.143
PbO	0.264	0.189	0.331	0.369	0.324	0.1	0.436	0.348	0.389	0.248
Total	**97.09**	**96.379**	**96.95**	**97.315**	**97.359**	**97.733**	**97.07**	**97.604**	**98.355**	**96.999**
P	0.987	0.985	0.995	0.982	0.969	0.986	0.990	0.994	0.984	0.974
Si	0.017	0.032	0.010	0.045	0.041	0.005	0.014	0.015	0.037	0.036
Th	0.045	0.054	0.033	0.066	0.067	0.025	0.049	0.039	0.066	0.061
U	0.003	0.002	0.002	0.002	0.003	0.002	0.003	0.001	0.002	0.003
Ce	0.339	0.326	0.352	0.306	0.328	0.352	0.347	0.321	0.317	0.341
Y	0.085	0.064	0.082	0.090	0.055	0.076	0.085	0.111	0.058	0.048
La	0.167	0.136	0.177	0.135	0.117	0.196	0.161	0.150	0.112	0.133
Pr	0.043	0.048	0.042	0.045	0.050	0.050	0.042	0.042	0.049	0.050
Nd	0.034	0.039	0.030	0.035	0.046	0.027	0.029	0.039	0.043	0.043
Sm	0.164	0.190	0.163	0.177	0.207	0.168	0.150	0.165	0.203	0.200
Gd	0.020	0.032	0.029	0.033	0.033	0.028	0.028	0.035	0.037	0.026
Dy	0.015	0.012	0.012	0.013	0.010	0.012	0.016	0.016	0.010	0.010
S^{6+}	0.015	0.0139	0.014	0.0074	0.012	0.021	0.0145	0.011	0.0118	0.013
Ca	0.055	0.047	0.044	0.043	0.051	0.045	0.058	0.045	0.049	0.049
Pb	0.003	0.002	0.003	0.004	0.003	0.001	0.005	0.004	0.004	0.003
Total	1.976	1.969	1.976	1.975	1.978	1.973	1.976	1.980	1.970	1.976
Σ(A)	0.988	0.966	0.985	0.956	0.981	1.003	0.987	0.981	0.961	0.978
Σ(T)	1.003	1.017	1.005	1.027	1.009	0.991	1.004	1.010	1.021	1.010
Σ(A-T)	0.01	0.05	0.02	0.07	0.03	0.01	0.02	0.03	0.06	0.03
Crl	8.2	7.0	6.2	7.4	7.9	5.0	9.0	7.1	7.8	7.4
An	1.5	1.5	1.5	0.8	1.2	2.1	1.5	1.1	1.2	1.3
Htn	1.7	3.4	1.0	4.7	4.2	0.5	1.4	1.6	3.9	3.7
Xtm	12.2	11.3	12.6	14.2	10.1	11.7	13.2	16.7	11.0	8.7
Mnz	76.4	77.0	78.7	72.9	76.6	80.7	74.9	73.6	76.0	78.9

Tab. 8: continued

Name	1306-55	1306-43	1306-24	1306-13*	1306-14b	1306-14c	1306-14	1306-7	1306-7b	1306-34	1306-34b
P_2O_5	29.971	29.733	28.965	28.42	28.624	28.434	29.357	28.206	27.404	29.169	28.037
SiO_2	0.243	0.183	0.762	1.096	0.858	0.998	0.523	0.844	1.316	0.742	1.299
ThO_2	3.697	4.762	4.93	7.022	6.876	6.406	5.133	5.466	8.103	6.062	9.211
UO_2	0.268	0.419	0.238	0.04	0.267	0.154	0.393	0.217	0.252	0.244	0.166
Ce_2O_3	24.225	24.427	24.117	23.731	23.703	22.72	24.68	26.403	22.77	21.991	19.928
Y_2O_3	4.263	4.304	3.298	2.165	2.238	2.786	2.92	0.47	1.165	3.605	3.618
La_2O_3	11.897	11.642	9.803	9.369	9.256	8.023	11.906	11.705	8.813	9.686	7.588
Pr_2O_3	2.706	2.566	3.59	3.288	3.237	3.389	2.921	3.437	3.313	3	3.18
Nd_2O_3	2.113	1.85	2.576	2.971	3.085	3.036	2.717	2.271	3.045	2.978	2.968
Sm_2O_3	12.191	11.558	13.832	14.107	14.663	15.279	12.113	13.723	15.059	13.534	13.725
Gd_2O_3	2.092	1.856	2.34	2.697	2.44	2.884	2.061	1.343	2.21	2.641	2.727
Dy_2O_3	1.151	1.109	0.986	1.045	0.917	0.956	0.862	0.196	0.643	0.988	1.103
SO_2	0.226	0.448	0.509	0.361	0.373	0.346	0.494	0.427	0.343	0.43	0.318
CaO	1.018	1.384	1.103	1.064	1.108	1.018	1.325	1.078	1.067	1.271	1.296
PbO	0.407	0.302	0.281	0.343	0.307	0.354	0.324	0.205	0.382	0.283	0.527
Total	**96.468**	**96.543**	**97.33**	**97.719**	**97.952**	**96.783**	**97.729**	**95.991**	**95.885**	**96.624**	**95.691**
P	1.001	0.994	0.968	0.967	0.965	0.965	0.964	0.968	0.962	0.977	0.959
Si	0.010	0.007	0.030	0.043	0.034	0.040	0.021	0.034	0.053	0.029	0.053
Th	0.033	0.042	0.044	0.063	0.062	0.058	0.047	0.050	0.074	0.055	0.085
U	0.002	0.004	0.002	0.000	0.002	0.001	0.004	0.002	0.002	0.002	0.001
Ce	0.350	0.350	0.349	0.343	0.346	0.334	0.362	0.392	0.336	0.319	0.295
Y	0.090	0.090	0.069	0.045	0.047	0.059	0.062	0.010	0.025	0.076	0.078
La	0.173	0.168	0.143	0.136	0.136	0.119	0.176	0.175	0.131	0.141	0.113
Pr	0.039	0.037	0.052	0.047	0.047	0.050	0.043	0.051	0.049	0.043	0.047
Nd	0.030	0.026	0.036	0.042	0.044	0.043	0.039	0.033	0.044	0.042	0.043
Sm	0.166	0.156	0.188	0.192	0.201	0.211	0.167	0.192	0.209	0.185	0.191
Gd	0.027	0.024	0.031	0.035	0.032	0.038	0.027	0.018	0.030	0.035	0.037
Dy	0.015	0.014	0.013	0.013	0.012	0.012	0.011	0.003	0.008	0.013	0.014
S^{6+}	0.008	0.0165	0.019	0.0134	0.014	0.013	0.0186	0.016	0.0130	0.016	0.012
Ca	0.043	0.058	0.047	0.045	0.047	0.044	0.057	0.047	0.046	0.054	0.056
Pb	0.004	0.003	0.003	0.004	0.003	0.004	0.003	0.002	0.004	0.003	0.006
Total	1.983	1.974	1.975	1.976	1.979	1.980	1.983	1.976	1.973	1.973	1.977
Σ(A)	0.981	0.989	0.995	0.979	0.994	0.987	1.016	0.991	0.971	0.983	0.978
Σ(T)	1.011	1.001	0.998	1.010	0.999	1.005	0.985	1.002	1.015	1.007	1.012
Σ(A-T)	0.03	0.01	0.00	0.03	0.01	0.02	0.03	0.01	0.04	0.02	0.03
Crl	7.1	8.6	5.6	6.5	6.8	6.3	7.6	6.2	6.9	7.8	9.1
An	0.9	1.7	1.9	1.4	1.4	1.3	1.8	1.6	1.3	1.6	1.2
Htn	1.0	0.7	3.1	4.4	3.5	4.1	2.1	3.5	5.5	3.0	5.4
Xtm	13.5	13.2	11.4	9.7	9.3	11.2	10.0	3.1	6.5	12.6	13.3
Mnz	77.6	75.8	78.0	78.0	79.0	77.1	78.4	85.5	79.8	74.9	71.0

Tab. 9: LA-ICP-MS monazite U-Th-Pb data for sample *ALR 13-06*

			Isotope ratio								
Grain n°	**Texture**	**Group**	$^{207}Pb/^{206}Pb$	**2s %**	$^{207}Pb/^{235}U$	**2s %**	$^{206}Pb/^{238}U$	**2s %**	**Rho**	$^{208}Pb/^{232}Th$	**2s %**
1306-1			0.0739	2.35	1.838	3.42	0.180	3.28	0.96	0.05406	2.81
1306-1b			0.0737	2.41	1.865	3.47	0.184	3.28	0.95	0.05648	2.80
1306-6			0.0742	2.35	1.851	3.42	0.181	3.28	0.96	0.05365	2.79
1306-39			0.0740	2.19	1.764	3.31	0.173	3.27	0.99	0.05463	2.79
1306-39b			0.0736	2.50	1.841	3.51	0.182	3.28	0.94	0.05388	2.78
1306-48			0.0733	2.40	1.808	3.44	0.179	3.27	0.95	0.05387	2.78
1306-91			0.0743	2.26	1.870	3.35	0.182	3.26	0.97	0.05433	2.80
1306-101			0.0767	2.53	1.902	3.53	0.180	3.28	0.93	0.05456	2.79
1306-117			0.0739	2.22	1.754	3.33	0.172	3.26	0.98	0.05431	2.80
1306-137			0.0737	2.52	1.838	3.52	0.181	3.27	0.93	0.05459	2.79
1306-137b			0.0733	2.45	1.775	3.47	0.176	3.27	0.94	0.05225	2.79
1306-142			0.0739	2.33	1.873	3.38	0.184	3.25	0.96	0.05437	2.80
1306-142b			0.0736	2.50	1.743	3.50	0.172	3.26	0.93	0.05112	2.77
1306-145			0.0737	2.20	1.775	3.31	0.175	3.25	0.98	0.05437	2.80
1306-192			0.0771	3.56	1.931	4.27	0.182	3.32	0.78	0.05438	2.80
1306-192b			0.0735	2.66	1.840	3.60	0.182	3.26	0.91	0.05461	2.79
1306-233			0.0741	2.35	1.826	3.39	0.179	3.25	0.96	0.053	2.79
1306-248			0.0737	2.25	1.701	3.32	0.167	3.24	0.98	0.05282	2.80
1306-248b			0.0720	2.44	1.679	3.44	0.169	3.25	0.94	0.05074	2.79
1306-189			0.0747	2.46	1.834	3.46	0.178	3.25	0.94	0.05434	2.80
1306-126			0.0742	2.48	1.816	3.46	0.178	3.24	0.94	0.05368	2.79
1306-66			0.0739	2.30	1.741	3.34	0.171	3.24	0.97	0.05411	2.77
1306-64			0.0735	2.45	1.812	3.44	0.179	3.24	0.94	0.05422	2.77
1306-55			0.0737	2.41	1.811	3.40	0.178	3.23	0.95	0.05342	2.77
1306-43			0.0743	2.34	1.796	3.35	0.175	3.22	0.96	0.05409	2.77
1306-24			0.0744	2.42	1.838	3.41	0.179	3.23	0.95	0.05438	2.76
1306-7			0.0739	2.70	1.807	3.60	0.177	3.24	0.90	0.05308	2.79
1306-7b			0.0740	2.64	1.804	3.56	0.177	3.24	0.91	0.0533	2.78
1306-14			0.0748	2.41	1.811	3.38	0.176	3.23	0.95	0.05288	2.76
1306-14b			0.0746	2.54	1.803	3.49	0.175	3.23	0.93	0.05309	2.79
1306-14c			0.0742	2.50	1.794	3.45	0.175	3.22	0.93	0.05367	2.76
1306-34			0.0743	2.55	1.826	3.50	0.178	3.23	0.92	0.05334	2.77
1306-34b			0.0731	2.57	1.789	3.48	0.177	3.22	0.92	0.05551	2.78

No common Pb correction was applied

Tab. 9: continued

			Dates								(ppm)		
Grain n°	Texture	Group	$^{207}Pb/^{206}Pb$	2s abs	$^{207}Pb/^{235}U$	2s abs	$^{206}Pb/^{238}U$	2s abs	$^{208}Pb/^{232}Th$	2s abs	% disc.	$^{232}Th^a$	$^{238}U^a$	Th/U
1306-1			1040	24	1059	36	1069	35	1064	30	0.9	34173	1883	18
1306-1b			1034	25	1069	37	1086	36	1111	31	1.6	93887	1342	70
1306-6			1047	25	1064	36	1072	35	1056	30	0.8	37572	1783	21
1306-39			1042	23	1032	34	1028	34	1075	30	-0.4	30740	7121	4
1306-39b			1030	26	1060	37	1075	35	1061	30	1.4	38363	1121	34
1306-48			1021	25	1049	36	1062	35	1061	30	1.2	56042	1595	35
1306-91			1051	24	1071	36	1080	35	1069	30	0.9	38217	3177	12
1306-101			1113	28	1082	38	1067	35	1074	30	-1.4	47041	964	49
1306-117			1038	23	1029	34	1024	33	1069	30	-0.4	42093	4445	9
1306-137			1033	26	1059	37	1072	35	1074	30	1.2	61600	1027	60
1306-137b			1021	25	1036	36	1044	34	1030	29	0.7	49152	1375	36
1306-142			1039	24	1071	36	1087	35	1070	30	1.5	43281	2286	19
1306-142b			1030	26	1025	36	1022	33	1008	28	-0.2	49073	1193	41
1306-145			1033	23	1036	34	1038	34	1070	30	0.2	34143	6410	5
1306-192			1123	40	1092	47	1076	36	1070	30	-1.4	32619	264	123
1306-192b			1028	27	1060	38	1076	35	1075	30	1.4	41846	785	53
1306-233			1045	25	1055	36	1059	34	1044	29	0.4	29608	2052	14
1306-248			1033	23	1009	33	998	32	1040	29	-1.1			
1306-248b			985	24	1001	34	1008	33	1000	28	0.7	49738	1619	31
1306-189			1060	26	1058	37	1057	34	1070	30	-0.1	44172	1374	32
1306-126			1046	26	1051	36	1054	34	1057	30	0.3	60463	1381	44
1306-66			1039	24	1024	34	1017	33	1065	30	-0.7	20446	4077	5
1306-64			1028	25	1050	36	1060	34	1067	30	1.0	34712	1522	23
1306-55			1033	25	1050	36	1058	34	1052	29	0.8	30711	2016	15
1306-43			1050	25	1044	35	1041	34	1065	30	-0.3	33366	3356	10
1306-24			1052	25	1059	36	1063	34	1070	30	0.4	42093	1986	21
1306-7			1038	28	1048	38	1053	34	1045	29	0.5	46912	831	56
1306-7b			1041	28	1047	37	1050	34	1050	29	0.3	63887	935	68
1306-14			1062	26	1050	36	1043	34	1042	29	-0.6	41674	2632	16
1306-14b			1058	27	1047	36	1042	34	1046	29	-0.5	53150	1293	41
1306-14c			1047	26	1043	36	1042	34	1057	29	-0.2	46307	1604	29
1306-34			1049	27	1055	37	1058	34	1050	29	0.3	47498	1249	38
1306-34b			1018	26	1041	36	1053	34	1092	30	1.1	68850	1355	51

No common Pb correction was applied

Tab. 10: LA-ICP-MS monazite U-Th-Pb data for sample *ALR 13-22*

		Isotope ratio								
Grain n°	**Gp**	**$^{207}Pb/^{206}Pb$**	**2s %**	**$^{207}Pb/^{235}U$**	**2s %**	**$^{206}Pb/^{238}U$**	**2s %**	**Rho**	**$^{208}Pb/^{232}Th$**	**2s %**
1322-58	*S2*	0.0712	2.82	1.587	3.54	0.162	3.13	0.88	0.0460	2.52
1322-57	*S1b*	0.0731	2.60	1.697	3.33	0.168	3.23	0.97	0.0559	3.02
1322-54	*S1b*	0.0731	2.64	1.719	3.36	0.170	3.23	0.96	0.0548	3.03
1322-54a	*S2*	0.0706	2.90	1.499	3.61	0.154	3.14	0.87	0.0452	2.52
1322-54b	*S2*	0.0700	2.80	1.516	3.53	0.157	3.12	0.89	0.0456	2.53
1322-53b	*S2*	0.0711	2.84	1.551	3.55	0.158	3.12	0.88	0.0455	2.54
1322-53a	*S2*	0.0708	2.83	1.543	3.54	0.158	3.12	0.88	0.0461	2.51
1322-52	*S2*	0.0698	2.78	1.505	3.52	0.156	3.13	0.89	0.0451	2.52
1322-52	*S2*	0.0698	2.69	1.473	3.44	0.153	3.11	0.90	0.0454	2.50
1322-51a	*S2*	0.0726	3.29	1.586	3.89	0.159	3.13	0.81	0.0480	2.50
1322-49	*S1a*	0.0737	2.63	1.766	3.35	0.174	3.23	0.96	0.0562	3.01
1322-49	*S1a*	0.0745	2.58	1.771	3.32	0.173	3.23	0.97	0.0562	3.01
1322-49	*S1a*	0.0730	2.60	1.745	3.33	0.173	3.22	0.97	0.0560	3.01
1322-49	*S1b*	0.0723	2.59	1.659	3.32	0.166	3.21	0.97	0.0549	3.03
1322-47b	*S1a*	0.0738	2.62	1.786	3.34	0.176	3.21	0.96	0.0537	3.01
1322-47a	*S1b*	0.0727	2.58	1.669	3.31	0.167	3.21	0.97	0.0524	3.00
1322-46	*S1b*	0.0722	2.60	1.681	3.31	0.169	3.21	0.97	0.0541	3.00
1322-45	*S2*	0.0714	2.68	1.500	3.41	0.152	3.08	0.91	0.0470	2.51
1322-45	*S2*	0.0714	2.63	1.526	3.38	0.155	3.07	0.91	0.0481	2.50
1322-44b	*S1b*	0.0740	2.57	1.724	3.29	0.169	3.21	0.97	0.0557	3.00
1322-44c	*S1b*	0.0733	2.62	1.720	3.33	0.170	3.21	0.96	0.0536	2.98
1322-44a	*S1a*	0.0737	2.56	1.761	3.28	0.173	3.20	0.98	0.0569	2.98
1322-41	*S1b*	0.0733	2.52	1.676	3.24	0.166	3.19	0.98	0.0546	2.98
1322-40	*S2*	0.0710	2.87	1.604	3.55	0.164	3.08	0.87	0.0470	2.51
1322-39b	*S1a*	0.0738	2.56	1.778	3.26	0.175	3.19	0.98	0.0569	2.98
1322-39a	*S1b*	0.0725	2.56	1.710	3.27	0.171	3.19	0.97	0.0552	2.98
1322-101a	*S2*	0.0715	2.90	1.548	3.57	0.157	3.09	0.87	0.0463	2.50
1322-38c	*S1a*	0.0734	2.59	1.788	3.30	0.177	3.18	0.97	0.0569	2.98
1322-38d	*S1b*	0.0726	2.54	1.667	3.26	0.167	3.18	0.98	0.0523	2.97
1322-37	*S1a*	0.0748	2.55	1.784	3.26	0.173	3.17	0.97	0.0530	2.97
1322-36a	*S1b*	0.0727	2.54	1.670	3.25	0.167	3.18	0.98	0.0552	2.98
1322-29b	*S1b*	0.0732	2.59	1.696	3.33	0.168	3.22	0.97	0.0541	3.03
1322-29b	*S1b*	0.0727	2.58	1.730	3.28	0.173	3.17	0.97	0.0526	2.96
1322-29a	*S1b*	0.0730	2.53	1.701	3.23	0.169	3.16	0.98	0.0506	2.94
1322-26	*S2*	0.0718	2.80	1.634	3.48	0.165	3.07	0.88	0.0489	2.50
1322-27a	*S1b*	0.0727	2.51	1.699	3.21	0.169	3.16	0.98	0.0529	2.95
1322-24a	*S1a*	0.0739	2.51	1.750	3.18	0.172	3.13	0.99	0.0546	2.92
1322-23a	*S1b*	0.0728	2.49	1.708	3.18	0.170	3.12	0.98	0.0542	2.93
1322-22c	*S1b*	0.0738	2.51	1.724	3.19	0.170	3.13	0.98	0.0552	2.92
1322-22b	*S1a*	0.0734	2.52	1.732	3.21	0.171	3.13	0.98	0.0555	2.94
1322-22b	*S1a*	0.0732	2.50	1.731	3.19	0.171	3.14	0.98	0.0559	2.93
1322-22a	*S1a*	0.0749	2.50	1.781	3.18	0.173	3.13	0.98	0.0563	2.92
1322-18	*S2*	0.0717	3.13	1.611	3.73	0.163	3.09	0.83	0.0473	2.49
1322-17a	*S2*	0.0690	2.88	1.471	3.54	0.155	3.07	0.87	0.0455	2.50
1322-14a	*S2*	0.0725	3.30	1.640	3.87	0.164	3.09	0.80	0.0489	2.50
1322-07a	*S2*	0.0710	2.71	1.598	3.41	0.163	3.05	0.89	0.0479	2.51
1322-07b	*S2*	0.0719	2.71	1.555	3.40	0.157	3.04	0.90	0.0464	2.50
1322-04a	*S1a*	0.0742	2.57	1.791	3.25	0.175	3.16	0.97	0.0529	2.95
1322-04b	*S1a*	0.0739	2.58	1.759	3.25	0.173	3.15	0.97	0.0528	2.95
1322-02	*S1b*	0.0736	2.54	1.733	3.22	0.171	3.15	0.98	0.0540	2.94

Tab. 10: continued

		Dates									(ppm)				
Grain n°	Gp	$^{207}Pb/^{206}Pb$	2s abs	$^{207}Pb/^{235}U$	2s abs	$^{206}Pb/^{238}U$	2s abs	$^{208}Pb/^{232}Th$	2s abs	% disc.	$^{232}Th^a$	$^{238}U^a$	Th/U	Y_2O_3	T°C mean
1322-58	*S2*	962	27	965	34	967	30	909	23	0.2	42137	2335	18	2.92	691
1322-57	*S1b*	1017	26	1007	34	1003	32	1100	33	-0.4	154389	13532	11	n.a	n.a
1322-54	*S1b*	1018	27	1016	34	1015	33	1077	33	-0.1	161518	9678	17	n.a	n.a
1322-54a	*S2*	946	27	930	34	923	29	893	22	-0.7	35869	2058	17	0.72	260
1322-54b	*S2*	928	26	937	33	941	29	902	23	0.4	35886	2668	13	1.358	260
1322-53b	*S2*	961	27	951	34	947	29	900	23	-0.5	32239	2096	15	0.78	524
1322-53a	*S2*	953	27	948	34	946	29	911	23	-0.2	30962	2066	15	1.434	355
1322-52	*S2*	923	26	933	33	937	29	892	22	0.5	36372	3104	12	5.14	877
1322-52	*S2*	922	25	919	32	918	29	897	22	-0.1	32558	5780	6	5.14	877
1322-51a	*S2*	1001	33	965	37	949	30	948	24	-1.7	152200	587	259	1.51	613
1322-49	*S1a*	1033	27	1033	35	1033	33	1105	33	0.0	218469	10929	20	n.a	n.a
1322-49	*S1a*	1054	27	1035	34	1026	33	1106	33	-0.9	204340	11182	18	n.a	n.a
1322-49	*S1a*	1014	26	1025	34	1031	33	1102	33	0.5	211379	11328	19	n.a	n.a
1322-49	*S1b*	995	26	993	33	992	32	1081	33	-0.1	213862	13264	16	n.a	n.a
1322-47b	*S1a*	1036	27	1041	35	1043	33	1058	32	0.2	114701	8434	14	4.41	797
1322-47a	*S1b*	1005	26	997	33	993	32	1032	31	-0.3	119324	11848	10	5.52	854
1322-46	*S1b*	991	26	1001	33	1006	32	1064	32	0.5	129754	12590	10	4.45	784
1322-45	*S2*	970	26	930	32	914	28	928	23	-1.8	20999	10207	2	3.47	728
1322-45	*S2*	968	25	941	32	929	29	950	24	-1.2	19912	11907	2	3.47	728
1322-44b	*S1b*	1042	27	1018	33	1007	32	1096	33	-1.1	235747	13485	17	6.1	895
1322-44c	*S1b*	1022	27	1016	34	1014	33	1056	31	-0.2	148234	8287	18	5.84	906
1322-44a	*S1a*	1032	26	1031	34	1031	33	1118	33	0.0	210280	14086	15	5.15	864
1322-41	*S1b*	1022	26	999	32	989	32	1075	32	-1.0	136518	18479	7	6.27	933
1322-40	*S2*	957	27	972	34	978	30	929	23	0.7	46906	1509	31	0.62	266
1322-39b	*S1a*	1035	26	1038	34	1039	33	1118	33	0.1	169630	11207	15	6.32	909
1322-39a	*S1b*	1000	26	1012	33	1018	32	1087	32	0.6	190080	12505	15	5.75	902
1322-101a	*S2*	970	28	950	34	941	29	915	23	-0.9	37871	1621	23	0.65	245
1322-38c	*S1a*	1025	27	1041	34	1049	33	1118	33	0.8	148803	9822	15	6.02	889
1322-38d	*S1b*	1002	25	996	32	994	32	1031	31	-0.2	84751	13661	6	n.a	n.a
1322-37	*S1a*	1064	27	1040	34	1028	33	1045	31	-1.1	78001	9359	8	6.64	920
1322-36a	*S1b*	1005	25	997	32	994	32	1086	32	-0.4	189239	13784	14	7.15	944
1322-29b	*S1b*	1020	26	1007	33	1001	32	1065	32	-0.6	134888	11887	11	5.81	874
1322-29b	*S1b*	1005	26	1020	33	1027	33	1035	31	0.7	127667	9574	13	5.81	874
1322-29a	*S1b*	1015	26	1009	33	1006	32	998	29	-0.8	106013	9574	11	5.46	859
1322-26	*S2*	980	27	983	34	985	30	964	24	0.2	35201	1876	19	1.48	526
1322-27a	*S1b*	1006	25	1008	32	1009	32	1042	31	0.1	110034	14114	8	3.89	831
1322-24a	*S1a*	1039	26	1027	33	1022	32	1074	31	-0.5	214384	14626	15	6.14	900
1322-23a	*S1b*	1008	25	1012	32	1013	32	1066	31	0.2	225622	17238	13	5.18	887
1322-22c	*S1b*	1035	26	1018	32	1010	32	1087	32	-0.8	177784	12558	14	5.74	901
1322-22b	*S1a*	1025	26	1020	33	1018	32	1093	32	-0.2	204752	13055	16	6.42	930
1322-22b	*S1a*	1021	26	1020	33	1020	32	1099	32	0.0	192660	13911	14	6.42	930
1322-22a	*S1a*	1065	27	1039	33	1026	32	1107	32	-1.2	184561	13688	13	6.23	897
1322-18	*S2*	978	31	975	36	973	30	935	23	-0.2	37027	779	48	0.61	277
1322-17a	*S2*	899	26	919	33	927	28	899	22	0.9	37082	1615	23	1.41	492
1322-14a	*S2*	1000	33	986	38	979	30	965	24	-0.7	50616	511	99	0.35	386
1322-07a	*S2*	956	26	969	33	975	30	946	24	0.6	31649	3516	9	1.75	483
1322-07b	*S2*	982	27	953	32	940	29	916	23	-1.4	31751	3549	9	1.44	532
1322-04a	*S1a*	1047	27	1042	34	1040	33	1042	31	-0.2	121680	7403	16	6.29	918
1322-04b	*S1a*	1038	27	1030	33	1027	32	1041	31	-0.3	75297	7632	10	6.69	918
1322-02	*S1b*	1031	26	1021	33	1016	32	1064	31	-0.5	258831	13244	20	5.56	892

Tab. 11: EPMA monazite microchemistry for sample *ALR 13-58* (in wt %)

Name	1029-202	1029-210	1029-213	1029-52	1029-71	1029-34	1029-35	1029-206
Position	osm pocket D5	osm pocket D5	grt fracture with osm D5	os pocket D5	garnet fracture D5	garnet fracture D5	garnet fracture D5	garnet fracture D5
P_2O_5	29.687	29.753	29.726	29.872	28.986	29.654	30.37	30.022
SiO_2	0.463	0.7	0.414	0.576	0.771	0.531	0.716	0.586
ThO_2	2.835	2.268	2.19	3.36	4.094	3.513	3.832	1.471
UO_2	0.175	0.085	0.137	0.155	0.183	0.145	0.199	0.102
Ce_2O_3	20.137	19.994	24.884	19.74	24.024	20.131	20.778	16.376
Y_2O_3	4.403	4.408	3.196	6.008	3.382	5.239	5.184	7.286
La_2O_3	6.771	6.788	9.012	7.057	8.589	6.374	7.477	5.411
Pr_2O_3	2.7	3.042	3.231	2.569	3.059	2.598	2.705	2.491
Nd_2O_3	14.781	15.042	16.198	14.753	15.794	15.127	14.265	12.002
Sm_2O_3	7.46	7.071	4.575	6.363	4.07	5.773	5.482	8.736
Gd_2O_3	8.054	9	4.883	8.224	4.302	5.964	5.21	12.383
Dy2O3	1.801	2.021	0.828	1.807	1.188	2.124	1.598	2.76
SO2	0.045	0.036	0	0.008	0.013	0.008	0.019	0.019
CaO	0.424	0.32	0.198	0.264	0.287	0.392	0.404	0.419
PbO	0.307	0.11	0.251	0.202	0.823	0.451	0.399	0.377
Total	**100.043**	**100.638**	**99.723**	**100.958**	**99.565**	**98.024**	**98.638**	**100.441**
P	0.983	0.978	0.988	0.978	0.972	0.991	0.997	0.981
Si	0.018	0.027	0.016	0.022	0.031	0.021	0.028	0.023
Th	0.025	0.020	0.020	0.030	0.037	0.032	0.034	0.013
U	0.002	0.001	0.001	0.001	0.002	0.001	0.002	0.001
Ce	0.288	0.284	0.358	0.279	0.348	0.291	0.295	0.231
Y	0.092	0.091	0.067	0.124	0.071	0.110	0.107	0.150
La	0.098	0.097	0.130	0.101	0.125	0.093	0.107	0.077
Pr	0.038	0.043	0.046	0.036	0.044	0.037	0.038	0.035
Nd	0.207	0.209	0.227	0.204	0.223	0.213	0.198	0.165
Sm	0.101	0.095	0.062	0.085	0.056	0.079	0.073	0.116
Gd	0.104	0.116	0.064	0.105	0.056	0.078	0.067	0.158
Dy	0.023	0.025	0.010	0.023	0.015	0.027	0.020	0.034
S^{6+}	0.002	0.001	0.000	0.000	0.000	0.000	0.001	0.001
Ca	0.018	0.013	0.008	0.011	0.012	0.017	0.017	0.017
Pb	0.003	0.001	0.003	0.002	0.009	0.005	0.004	0.004
Total	2.000	2.001	2.000	2.001	2.002	1.995	1.986	2.006
Σ(A)	1.000	0.997	0.996	1.001	1.000	0.983	0.962	1.003
Σ(T)	1.001	1.005	1.004	1.000	1.002	1.012	1.025	1.004
Σ(A-T)	0.00	0.01	0.01	0.00	0.00	-0.03	0.06	0.00
Crl	3.5	2.6	1.7	2.2	2.4	3.4	3.5	3.4
Htn	1.8	2.7	1.6	2.2	3.1	2.1	2.9	2.2
Xtm	21.8	22.9	14.1	25.1	14.4	21.9	20.1	33.4
Mnz	72.9	71.8	82.6	70.4	80.1	72.6	73.6	61.0
LaN/GdN	0.69	0.62	1.52	0.70	1.64	0.88	1.18	0.36
Th	2.49	1.99	1.92	2.95	3.60	3.09	3.37	1.29
Y	3.47	3.47	2.52	4.73	2.66	4.13	4.08	5.74

Tab. 11: continued

Name	1029-209	1029-63	1029-62	1029-61	1029-203	1029-72	1029-47	1029-36	1029-64
Position	osm pocket D5	in garnet D4	garnet corrona D4	corrona D4	corrona D4	garnet rim D4	corrona D4	corrona D4	in garnet D4
P_2O_5	29.549	29.024	28.613	29.167	29.42	29.027	27.574	28.727	28.548
SiO_2	0.709	0.691	0.903	0.693	0.57	0.735	1.153	0.974	0.842
ThO_2	3.011	3.631	3.193	3.7	3.372	3.884	5.727	5.842	4.452
UO_2	0	0.215	0.082	0.081	0.065	0.115	0.104	0.095	0.127
Ce_2O_3	19.912	26.927	28.533	23.724	24.55	21.452	28.553	24.037	26.716
Y_2O_3	3.832	2.535	0.695	4.064	2.068	4.422	1.132	3.192	1.966
La_2O_3	7.364	9.821	11.837	9.293	8.25	7.33	10.885	8.762	10.545
Pr_2O_3	2.701	3.503	3.418	3.051	3.396	3.451	3.747	3.409	3.586
Nd_2O_3	14.489	15.642	16.065	15.321	16.627	15	15.807	15.711	16.49
Sm_2O_3	7.856	3.557	3.315	4.301	5.603	5.769	2.682	4.573	3.343
Gd_2O_3	8.014	4.38	1.228	4.992	5.008	4.942	1.449	2.9	2.645
$Dy2O3$	1.799	0.503	0	1.262	0.133	1.402	0.245	1.19	0.647
$SO2$	0.021	0.014	0	0.042	0.043	0.031	0.035	0.014	0.016
CaO	0.305	0.259	0.262	0.19	0.588	0.26	0.289	0.547	0.232
PbO	0.348	0.192	0.317	0.498	0.318	0.246	0.171	0.354	0.25
Total	**99.91**	**100.894**	**98.461**	**100.379**	**100.011**	**98.066**	**99.553**	**100.327**	**100.405**
P	0.981	0.966	0.971	0.969	0.979	0.977	0.942	0.959	0.959
Si	0.028	0.027	0.036	0.027	0.022	0.029	0.047	0.038	0.033
Th	0.027	0.032	0.029	0.033	0.030	0.035	0.053	0.052	0.040
U	0.000	0.002	0.001	0.001	0.001	0.001	0.001	0.001	0.001
Ce	0.286	0.388	0.419	0.341	0.353	0.312	0.422	0.347	0.388
Y	0.080	0.053	0.015	0.085	0.043	0.094	0.024	0.067	0.042
La	0.106	0.142	0.175	0.135	0.120	0.108	0.162	0.127	0.154
Pr	0.039	0.050	0.050	0.044	0.049	0.050	0.055	0.049	0.052
Nd	0.203	0.220	0.230	0.215	0.234	0.213	0.228	0.221	0.234
Sm	0.106	0.048	0.046	0.058	0.076	0.079	0.037	0.062	0.046
Gd	0.104	0.057	0.016	0.065	0.065	0.065	0.019	0.038	0.035
Dy	0.023	0.006	0.000	0.016	0.002	0.018	0.003	0.015	0.008
S^{6+}	0.001	0.001	0.000	0.002	0.002	0.001	0.001	0.001	0.001
Ca	0.013	0.011	0.011	0.008	0.025	0.011	0.012	0.023	0.010
Pb	0.004	0.002	0.003	0.005	0.003	0.003	0.002	0.004	0.003
Total	1.999	2.005	2.002	2.001	2.002	1.995	2.007	2.005	2.005
Σ(A)	0.991	1.012	0.995	1.007	1.002	0.990	1.020	1.008	1.013
Σ(T)	1.009	0.993	1.007	0.997	1.002	1.007	0.989	0.998	0.993
Σ(A-T)	0.02	0.02	0.01	0.01	0.00	0.02	0.03	0.01	0.02
Crl	2.6	2.2	2.2	1.6	4.9	2.2	2.4	4.6	2.0
Hfn	2.8	2.7	3.6	2.7	2.2	3.0	4.6	3.8	3.3
Xtm	20.7	11.5	3.1	16.6	10.9	17.8	4.6	11.9	8.4
Mnz	74.0	83.7	91.1	79.1	82.0	77.0	88.4	79.8	86.4
LaN/GdN	0.75	0.96	1.84	7.91	1.53	1.35	1.22	6.17	2.48
Th	2.65	2.72	3.19	2.81	3.25	2.96	3.41	5.03	5.13
Y	3.02	4.49	2.00	0.55	3.20	1.63	3.48	0.89	2.51

Tab. 11: continued

Name / Position	1029-207 in garnet D4	1029-208 in garnet	1029-205a corrona D4	1029-205b corrona D4	1029-68 corrona D4	1029-65 corrona D4	1029-69b corrona D4	1029-100 corrona D4	1029-75 corrona D4	1029-31 corrona D4	1029-33 corrona D4
P_2O_5	28.799	29.483	27.497	28.611	29.06	28.669	29.351	27.871	28.198	30.596	30.067
SiO_2	1.58	0.519	0.757	0.828	0.73	0.245	0.307	1.274	1.071	0.579	0.459
ThO_2	1.881	2.396	3.831	3.167	3.619	4.374	4.778	7.766	6.843	3.499	3.1
UO_2	0.147	0.064	0.092	0.121	0.096	0.283	0.283	0.1	0.192	0.249	0.245
Ce_2O_3	23.245	25.361	26.897	26.322	25.725	28.76	28.294	26.224	28.019	26.162	20.221
Y_2O_3	3.482	2.328	1.588	1.623	2.718	1.45	1.675	1.108	0.876	1.549	5.708
La_2O_3	7.242	8.831	9.895	9.334	9.57	12.476	12.756	8.38	10.668	10.46	6.498
Pr_2O_3	3.069	3.48	3.92	3.292	3.529	3.112	3.146	3.896	3.658	3.126	3.434
Nd_2O_3	15.687	16.95	17.448	15.691	15.032	13.198	13.227	18.677	16.249	13.569	15.395
Sm_2O_3	5.858	5.546	3.487	3.246	3.946	2.456	2.374	2.832	2.047	4.676	6.834
Gd_2O_3	4.815	4.056	2.723	3.017	3.545	1.045	2.193	1.864	0.86	3.378	5.554
Dy2O3	1.105	0.767	0.568	0.433	0.909	0.25	0.794	0.285	0.531	0.436	1.725
SO2	0.026	0.014	0.059	0.069	0.032	0.209	0.163	0.045	0.06	0.16	0.023
CaO	0.321	0.271	0.344	0.339	0.257	1.12	1.179	0.629	0.596	0.976	0.361
PbO	0.229	0.22	0.374	0.276	0.159	0.175	0.154	0.337	0.373	0.357	0.182
Total	**97.486**	**100.286**	**99.48**	**96.369**	**98.927**	**97.822**	**100.674**	**101.288**	**100.241**	**99.772**	**99.806**
P	0.965	0.980	0.945	0.980	0.976	0.974	0.972	0.938	0.952	0.999	0.988
Si	0.063	0.020	0.031	0.034	0.029	0.010	0.012	0.051	0.043	0.022	0.018
Th	0.017	0.021	0.035	0.029	0.033	0.040	0.043	0.070	0.062	0.031	0.027
U	0.001	0.001	0.001	0.001	0.001	0.003	0.002	0.001	0.002	0.002	0.002
Ce	0.337	0.365	0.400	0.390	0.373	0.423	0.405	0.382	0.409	0.369	0.287
Y	0.073	0.049	0.034	0.035	0.057	0.031	0.035	0.023	0.019	0.032	0.118
La	0.106	0.128	0.148	0.139	0.140	0.185	0.184	0.123	0.157	0.149	0.093
Pr	0.044	0.050	0.058	0.049	0.051	0.046	0.045	0.056	0.053	0.044	0.049
Nd	0.222	0.238	0.253	0.227	0.213	0.189	0.185	0.265	0.231	0.187	0.213
Sm	0.080	0.075	0.049	0.045	0.054	0.034	0.032	0.039	0.028	0.062	0.091
Gd	0.063	0.053	0.037	0.040	0.047	0.014	0.028	0.025	0.011	0.043	0.071
Dy	0.014	0.010	0.007	0.006	0.012	0.003	0.010	0.004	0.007	0.005	0.022
S^{6+}	0.001	0.001	0.002	0.003	0.001	0.008	0.006	0.002	0.002	0.006	0.001
Ca	0.014	0.011	0.015	0.015	0.011	0.048	0.049	0.027	0.025	0.040	0.015
Pb	0.002	0.002	0.004	0.003	0.002	0.002	0.002	0.004	0.004	0.004	0.002
Total	2.000	2.003	2.016	1.993	1.997	2.001	2.005	2.007	2.003	1.989	1.996
Σ(A)	0.974	1.003	1.043	0.982	0.994	1.025	1.026	1.020	1.011	0.974	0.992
Σ(T)	1.027	1.001	0.975	1.014	1.004	0.984	0.984	0.989	0.995	1.021	1.006
Σ(A-T)	0.05	0.00	0.07	0.03	0.01	0.04	0.04	0.03	0.02	-0.05	0.01
Crl	2.6	2.3	2.9	3.0	2.2	9.4	9.5	5.2	5.0	8.1	3.0
Htn	6.1	2.0	2.9	3.4	2.9	1.0	1.2	5.0	4.2	2.2	1.8
Xtm	14.6	11.0	7.5	8.2	11.6	4.7	7.1	5.1	3.6	8.1	21.3
Mnz	76.6	84.7	86.7	85.5	83.3	85.0	82.2	84.7	87.1	81.6	73.9
LaN/GdN	3.27	1.24	1.79	2.98	2.54	2.22	9.80	4.78	3.69	10.19	2.54
Th	3.91	1.65	2.11	3.37	2.78	3.18	3.84	4.20	6.82	6.01	3.07
Y	1.55	2.74	1.83	1.25	1.28	2.14	1.14	1.32	0.87	0.69	1.22

Tab. 12: EPMA monazite U-Th-Pb dating for *sample ALR 13-58*

Grains	Position	Y	inc. (95%)	U	inc. (95%)	Th	inc. (95%)	Pb	inc. (95%)	Ages	Sd	Mole fraction*		
												Htn	Crl	YPO_4
1029-46	corrona D4	1.011	0.012	0.092	0.014	4.739	0.118	0.213	0.011	934	52	**4.8**	**0.5**	**2.8**
1029-47	corrona D4	1.110	0.013	0.088	0.013	4.660	0.113	0.209	0.011	935	51	**4.8**	**0.4**	**3.0**
1029-39	corrona D4	1.192	0.013	0.072	0.013	3.999	0.100	0.173	0.010	907	53	**3.6**	**1.4**	**3.3**
1029-59	corrona D4	2.055	0.020	0.078	0.014	4.818	0.118	0.215	0.011	937	52	**4.7**	**0.8**	**5.6**
1029-61	corrona D4	2.428	0.023	0.093	0.013	3.035	0.078	0.136	0.010	899	63	**3.1**	**0.3**	**6.6**
1029-76	corrona D4	1.729	0.017	0.073	0.013	2.563	0.068	0.120	0.010	948	76	**2.8**	**-0.1**	**4.7**
1029-62	corrona D4	1.213	0.013	0.086	0.013	3.098	0.080	0.144	0.010	940	65	**3.1**	**0.4**	**3.3**
1029-53	corrona D4	1.217	0.013	0.083	0.013	2.377	0.064	0.113	0.010	941	77	**2.1**	**1.0**	**3.3**
1029-203	corrona D4	0.721	0.010	0.116	0.014	5.344	0.129	0.239	0.011	924	45	**3.3**	**4.7**	**2.0**
1029-72	corrona D4	2.337	0.022	0.085	0.013	3.616	0.091	0.171	0.010	967	57	**3.4**	**0.9**	**6.4**
1029-15c	edge garnet D4	1.932	0.019	0.086	0.013	4.117	0.102	0.178	0.011	896	57	**3.6**	**1.6**	**5.3**
1029-15b	edge garnet D4	2.265	0.021	0.085	0.013	3.915	0.097	0.174	0.011	916	55	**3.6**	**1.1**	**6.2**
1029-71	garnet fracture D5	2.130	0.020	0.066	0.013	3.083	0.079	0.142	0.010	952	66	**3.1**	**0.3**	**5.8**
1029-202	osm pocket D5	2.623	0.024	0.104	0.013	2.358	0.064	0.113	0.010	925	79	**2.3**	**0.5**	**7.2**
1029-15e	garnet interior	1.861	0.018	0.092	0.013	2.938	0.076	0.138	0.010	938	71	**2.4**	**1.6**	**5.1**
1029-38	garnet fracture D5	2.140	0.021	0.085	0.014	2.390	0.066	0.109	0.011	904	85	**2.0**	**1.2**	**5.8**
1029-213	garnet fracture D5	2.468	0.023	0.069	0.013	1.856	0.054	0.090	0.010	957	99	**1.8**	**0.4**	**6.7**
1029-15f	garnet fracture D5	2.599	0.024	0.087	0.013	4.114	0.102	0.190	0.011	957	54	**3.4**	**2.0**	**7.1**
1029-50b	garnet fracture D5	2.712	0.025	0.085	0.013	2.752	0.073	0.130	0.010	945	70	**2.5**	**0.9**	**7.4**
1029-15a	garnet fracture D5	2.733	0.025	0.086	0.013	3.525	0.089	0.155	0.010	903	56	**2.6**	**2.3**	**7.5**
1029-50c	osm pocket D5	2.929	0.027	0.107	0.013	2.649	0.070	0.121	0.010	892	71	**2.6**	**0.6**	**8.0**
1029-51	osm pocket D5	2.721	0.025	0.068	0.013	2.884	0.075	0.132	0.010	936	71	**2.4**	**1.4**	**7.4**
1029-210	osm pocket D5	3.116	0.028	0.081	0.013	2.018	0.057	0.095	0.010	916	93	**2.8**	**-1.3**	**8.5**
1029-52	osm pocket D5	4.653	0.041	0.102	0.013	2.613	0.070	0.122	0.010	913	73	**2.5**	**0.8**	**12.7**
1029-34	garnet fracture D5	3.571	0.033	0.093	0.014	3.040	0.080	0.140	0.011	926	71	**2.4**	**1.7**	**9.7**
1029-50	garnet fracture D5	3.706	0.033	0.074	0.013	2.457	0.066	0.113	0.010	925	82	**2.7**	**-0.1**	**10.1**
1029-35	garnet fracture D5	4.163	0.037	0.079	0.013	3.209	0.082	0.147	0.010	937	60	**2.3**	**2.3**	**11.4**

Correction U = U-96.6 ppm/wt%Th; Pb= Pb-83.55ppm/wt%Y - 16.5ppm/wt%Th

Supplementary material

Tab. S3-1a: Representative analyses of garnet for sample ALR 13-64

Analysis	13-64_grt1	13-64_grt2	13-64_grt3	13-64_grt4	13-64_grt5	13-64_grt6	13-64_grt7	13-64_grt8
Texture		*rim*	*rim*	*rim*	*core p2*	*core p2*	*core p2*	*core p2*
Oxides (Wt%)								
SiO_2	38.43	38.34	38.51	38.66	38.65	38.56	38.31	38.41
TiO_2	0.07	0.05	0.07	0.03	0.02	0.04	0.04	0.02
Al_2O_3	21.55	21.61	21.82	21.52	21.77	21.79	21.95	21.59
Cr_2O_3	0.01	0.04	0.04	0.03	0.02	0.02	0.02	0.03
FeO	31.28	31.38	31.81	31.45	31.10	31.00	31.24	31.15
MnO	0.43	0.44	0.42	0.43	0.46	0.40	0.46	0.33
MgO	7.42	6.97	7.00	7.03	7.42	7.46	7.46	7.27
CaO	1.03	1.08	1.03	0.99	0.95	0.95	0.96	1.01
Total	**100.23**	**99.91**	**100.69**	**100.15**	**100.38**	**100.22**	**100.44**	**99.81**
Formula (O=12)								
Si	2.997	3.006	2.997	3.024	3.007	3.004	2.979	3.008
Ti	0.004	0.003	0.004	0.002	0.001	0.003	0.002	0.001
Al	1.981	1.997	2.001	1.984	1.997	2.000	2.012	1.993
Cr	0.001	0.002	0.003	0.002	0.001	0.001	0.001	0.002
Fe^{3+}	0.016	0.000	0.000	0.000	0.000	0.000	0.025	0.000
tot. cubic	2.002	2.002	2.007	1.988	1.999	2.004	2.040	1.996
Fe^{2+}	2.023	2.057	2.070	2.057	2.024	2.020	2.006	2.041
Mn	0.029	0.029	0.028	0.029	0.030	0.026	0.030	0.022
Mg	0.863	0.815	0.813	0.820	0.860	0.866	0.865	0.848
Ca	0.086	0.091	0.086	0.083	0.079	0.079	0.080	0.085
tot. oct	3.001	2.992	2.996	2.989	2.993	2.991	2.981	2.995
XMg	0.30	0.28	0.28	0.28	0.30	0.30	0.30	0.29
Xalm	67.07	68.75	69.09	68.83	67.61	67.52	66.75	68.12
Xpyr	28.59	27.22	27.12	27.43	28.74	28.95	28.77	28.32
Xgr	2.86	3.04	2.86	2.77	2.64	2.65	2.66	2.82
Xsps	0.95	0.99	0.93	0.96	1.00	0.88	1.00	0.74
Xand	0.54	0.00	0.00	0.00	0.00	0.00	0.82	0.00

Tab. S3-1b: Representative analyses of spinel for sample ALR 13-64

Analysis	**13-64_Sp1**	**13-64_Sp2**	**13-64_Sp3**	**13-64_Sp4**	**13-64_Sp5**	**13-64_Sp8**	**13-64_sp9**	**13-64_sp10**
Texture							*incl. in grt*	
Oxides (Wt%)								
SiO_2	0.04	0.04	0.00	0.01	0.03	0.02	0.00	0.00
TiO_2	0.01	0.03	0.03	0.03	0.04	0.06	0.02	0.04
Al_2O_3	56.65	57.00	56.50	56.68	56.21	56.12	59.80	59.97
Cr_2O_3	0.56	0.61	0.45	0.58	0.53	0.52	0.37	0.33
FeO	34.36	33.55	34.12	33.50	34.41	34.43	26.93	27.19
MnO	0.00	0.03	0.03	0.11	0.02	0.08	0.04	0.03
MgO	5.05	5.18	5.05	5.03	4.93	5.02	8.65	8.95
ZnO	2.11	2.23	2.02	2.21	1.98	1.97	3.17	3.31
Total	**98.77**	**98.66**	**98.21**	**98.15**	**98.15**	**98.23**	**98.98**	**99.81**
Formula (O=4)								
Si	0.00	0.00	0.00	0.00	0.00	0.00	0.00	0.00
Ti	0.00	0.00	0.00	0.00	0.00	0.00	0.00	0.00
Al(vi)	1.91	1.92	1.91	1.92	1.90	1.90	1.95	1.94
Cr	0.01	0.01	0.01	0.01	0.01	0.01	0.01	0.01
Fe^{3+}	0.12	0.11	0.12	0.11	0.12	0.13	0.11	0.12
Fe^{2+}	0.70	0.69	0.70	0.69	0.71	0.70	0.51	0.50
Mn	0.00	0.00	0.00	0.00	0.00	0.00	0.00	0.00
Mg	0.21	0.22	0.22	0.22	0.21	0.21	0.36	0.37
Zn	0.04	0.05	0.04	0.05	0.04	0.04	0.06	0.07
XMg	0.24	0.24	0.24	0.24	0.23	0.23	0.41	0.42

Tab. S3-1c: Representative analyses of biotite for sample ALR 13-64

Analysis	**13-64_bt1**	**13-64_bt2**	**13-64_bt3**	**13-64_bt4**	**13-64_bt5**	**13-64_bt6**	**13-64_bt7**	**13-64_bt8**	**13-64_bt9**	**13-64_bt10**
Texture	*incl. Gt rim*	*incl. Gt rim*	*incl. Grt core*	*incl. Grt core*	*incl. Grt core*	*matrix*	*matrix*	*matrix*	*matrix*	*matrix*
Oxides (Wt%)										
SiO_2	36.77	36.74	37.94	38.17	37.99	37.19	37.37	36.67	36.90	37.95
TiO_2	8.03	8.06	5.49	5.33	5.09	4.42	4.19	7.16	7.14	5.36
Al_2O_3	15.70	15.75	15.25	15.17	16.15	15.93	16.18	16.37	16.30	16.09
Cr_2O_3	0.00	0.00	0.06	0.06	0.00	0.07	0.07	0.06	0.07	0.10
FeO	11.51	11.04	11.58	11.26	9.22	10.28	10.24	11.23	11.43	10.36
MnO	0.00	0.03	0.00	0.02	0.04	0.01	0.00	0.02	0.00	0.00
MgO	13.33	13.26	15.32	15.44	16.36	16.27	16.32	13.13	13.47	14.90
CaO	0.00	0.00	0.00	0.00	0.00	0.01	0.02	0.00	0.00	0.00
Na_2O	0.40	0.37	0.23	0.18	0.24	0.25	0.23	0.32	0.29	0.21
K_2O	9.45	9.60	9.48	9.87	9.65	9.71	9.68	9.54	9.56	9.55
BaO	0.28	0.25	0.00	0.00	0.19	0.00	0.00	0.00	0.00	0.00
F	1.69	1.85	2.27	2.27	2.27	0.00	0.00	0.00	0.00	0.00
Cl	0.04	0.03	0.05	0.05	0.05	0.00	0.00	0.00	0.00	0.00
Total	**97.20**	**96.97**	**97.66**	**97.82**	**97.24**	**94.13**	**94.30**	**94.49**	**95.15**	**94.51**
Formula (O=11)										
Si	2.71	2.71	2.78	2.80	2.77	2.75	2.76	2.72	2.72	2.79
Al(iv)	1.29	1.29	1.22	1.20	1.23	1.25	1.24	1.28	1.28	1.21
Al	0.07	0.08	0.10	0.11	0.16	0.14	0.17	0.15	0.13	0.18
Mg	1.46	1.46	1.68	1.69	1.78	1.80	1.80	1.45	1.48	1.63
Fe^{2+}	0.71	0.68	0.71	0.69	0.56	0.64	0.63	0.70	0.70	0.64
Ti	0.44	0.45	0.30	0.29	0.28	0.25	0.23	0.40	0.40	0.30
Mn	0.00	0.00	0.00	0.00	0.00	0.00	0.00	0.00	0.00	0.00
Cr	0.00	0.00	0.00	0.00	0.00	0.00	0.00	0.00	0.00	0.01
Ca	0.00	0.00	0.00	0.00	0.00	0.00	0.00	0.00	0.00	0.00
Na	0.06	0.05	0.03	0.03	0.03	0.04	0.03	0.05	0.04	0.03
K	0.89	0.90	0.89	0.92	0.90	0.92	0.91	0.90	0.90	0.90
Ba	0.01	0.01	0.00	0.00	0.01	0.00	0.00	0.00	0.00	0.00
F	0.39	0.43	0.53	0.53	0.52	0.00	0.00	0.00	0.00	0.00
Cl	0.01	0.00	0.01	0.01	0.01	0.00	0.00	0.00	0.00	0.00
OH*	1.60	1.56	1.47	1.47	1.47	2.00	2.00	2.00	2.00	2.00
XMg	0.67	0.68	0.70	0.71	0.76	0.74	0.74	0.68	0.68	0.72

Tab. S3-1d: Representative analyses of cordierite for sample ALR 13-64

Analysis	**13-64_crd1**	**13-64_crd2**	**13-64_crd3**	**13-64_crd4**	**13-64_crd5**	**13-64_crd6**	**13-64_crd7**
Texture	*Crd+Hc*	*Crd+Hc*	*Crd−Hc*	*Crd−Hc*	*Crd+Hc*	*Crd+Hc*	*Crd+Hc*
Oxides (Wt%)							
SiO_2	48.76	49.27	48.93	49.33	49.19	49.34	49.06
TiO_2	0.00	0.00	0.00	0.02	0.02	0.04	0.02
Al_2O_3	31.77	31.93	32.00	32.06	31.88	32.04	32.14
FeO	7.01	6.58	6.65	7.15	7.41	7.43	7.37
MnO	0.05	0.07	0.06	0.00	0.04	0.02	0.03
MgO	9.02	9.34	9.04	9.21	8.95	8.70	8.84
CaO	0.03	0.02	0.00	0.00	0.02	0.00	0.04
Na_2O	0.06	0.07	0.01	0.02	0.03	0.05	0.06
K_2O	0.02	0.01	0.00	0.00	0.00	0.00	0.03
Total	**96.71**	**97.29**	**96.69**	**97.78**	**97.54**	**97.61**	**97.59**
Formula (O=18)							
Si	5.07	5.08	5.08	5.07	5.08	5.09	5.06
Al	3.89	3.88	3.91	3.89	3.88	3.89	3.91
Mg	1.40	1.44	1.40	1.41	1.38	1.34	1.36
Fe^{2+}	0.61	0.57	0.58	0.61	0.64	0.64	0.64
Ti	0.00	0.00	0.00	0.00	0.00	0.00	0.00
Mn	0.00	0.01	0.01	0.00	0.00	0.00	0.00
Cr	0.00	0.00	0.00	0.00	0.00	0.00	0.00
Ca	0.00	0.00	0.00	0.00	0.00	0.00	0.00
Na	0.01	0.01	0.00	0.00	0.01	0.01	0.01
K	0.00	0.00	0.00	0.00	0.00	0.00	0.00
XMg	0.70	0.72	0.71	0.70	0.68	0.68	0.68

Tab. S3-1c: Representative analyses of feldspar for sample ALR 13-64

Analysis	**13-64_fld1**	**13-64_fld2**	**13-64_fld3**	**13-64_fld4**	**13-64_fld5**
Texture	*matrix*	*matrix*	*matrix*	*matrix*	*matrix*
Oxides (Wt%)					
SiO_2	60.47	59.94	60.09	60.60	60.21
TiO_2	0.02	0.02	0.01	0.02	0.01
Al_2O_3	24.94	24.49	24.37	24.37	24.59
FeO	0.00	0.38	0.07	0.00	0.12
MnO	0.00	0.02	0.01	0.01	0.02
MgO	0.00	0.08	0.00	0.00	0.00
CaO	6.98	6.91	6.89	6.87	6.86
Na_2O	7.78	7.69	7.50	7.56	7.77
K_2O	0.29	0.30	0.15	0.20	0.18
BaO	0.00	0.00	0.00	0.00	0.00
Total	**100.47**	**99.83**	**99.09**	**99.61**	**99.75**
Formula(O=8)					
Si	2.68	2.68	2.71	2.71	2.69
Ti	0.00	0.00	0.00	0.00	0.00
Al	1.30	1.29	1.29	1.29	1.29
Cr	0.00	0.00	0.00	0.00	0.00
Fe^{2+}	0.00	0.01	0.00	0.00	0.00
Mn	0.00	0.00	0.00	0.00	0.00
Mg	0.00	0.01	0.00	0.00	0.00
Ca	0.33	0.33	0.33	0.33	0.33
Na	0.67	0.67	0.66	0.66	0.67
K	0.02	0.02	0.01	0.01	0.01
Ba	0.00	0.00	0.00	0.00	0.00
An (mol%)	32.6	32.6	33.4	33.0	32.5
Ab (mol%)	65.8	65.7	65.8	65.8	66.5
Or (mol%)	1.6	1.7	0.9	1.1	1.0

Tab. S3-2a: Representative analyses of orthopyroxene for sample ALR 13-05

Analysis	13-05_opx-1	13-05_opx-2	13-05_opx-3	13-05_opx-24	13-05_opx-36	13-05_opx-21	13-05_opx-23	13-05_opx-10	13-05_opx-15	13-05_opx-17	13-05_opx-8	13-05_opx-9	13-05_opx-37
Texture	*blocky rim*	*blocky rim*	*blocky rim*	*sympl*	*sympl*	*sympl*	*sympl*	*sympl*	*sympl*	*sympl*			
Oxides (Wt. %)													
SiO_2	47.32	47.16	47.25	47.43	47.17	46.97	47.90	47.11	46.49	46.57	47.26	47.52	47.16
TiO_2	0.10	0.14	0.14	0.11	0.16	0.15	0.09	0.11	0.12	0.11	0.17	0.15	0.16
Al_2O_3	8.36	8.75	8.38	9.15	8.68	8.43	7.61	8.68	8.65	9.17	8.63	8.24	8.59
Cr_2O_3	0.00	0.01	0.00	0.01	0.02	0.00	0.00	0.01	0.00	0.02	0.02	0.02	0.00
FeO	25.17	25.26	25.72	25.91	25.88	25.84	25.41	25.06	25.81	25.25	25.25	25.33	25.75
MnO	0.22	0.17	0.18	0.18	0.17	0.16	0.19	0.16	0.20	0.16	0.17	0.13	0.19
MgO	17.68	17.57	17.08	16.91	16.97	16.96	17.72	17.45	17.25	17.08	17.55	17.69	16.91
CaO	0.01	0.03	0.03	0.04	0.06	0.06	0.04	0.01	0.03	0.03	0.02	0.04	0.05
Na_2O	0.00	0.00	0.00	0.01	0.00	0.02	0.00	0.00	0.02	0.01	0.03	0.02	0.00
Total	**98.85**	**99.10**	**98.78**	**99.73**	**99.10**	**98.58**	**98.94**	**98.59**	**98.55**	**98.41**	**99.10**	**98.54**	**98.81**
Formula(O=6)													
Si	1.805	1.795	1.811	1.800	1.802	1.804	1.828	1.803	1.783	1.787	1.799	1.824	1.808
Ti	0.003	0.004	0.004	0.003	0.005	0.004	0.003	0.003	0.003	0.003	0.005	0.004	0.005
Al(iv)	0.195	0.205	0.189	0.200	0.198	0.196	0.172	0.197	0.217	0.213	0.201	0.176	0.192
Al(vi)	0.181	0.188	0.189	0.210	0.193	0.185	0.171	0.194	0.174	0.202	0.186	0.197	0.196
Cr	0.000	0.000	0.000	0.000	0.001	0.000	0.000	0.000	0.000	0.000	0.001	0.000	0.000
Fe^{3+}	0.008	0.009	0.000	0.000	0.000	0.003	0.000	0.000	0.038	0.005	0.006	0.000	0.000
Fe^{2+}	0.795	0.795	0.824	0.822	0.827	0.827	0.811	0.802	0.790	0.805	0.798	0.813	0.825
Mn	0.007	0.006	0.006	0.006	0.005	0.005	0.006	0.005	0.006	0.005	0.005	0.004	0.006
Mg	1.006	0.997	0.976	0.957	0.967	0.971	1.008	0.995	0.986	0.977	0.996	0.978	0.966
Ca	0.000	0.001	0.001	0.002	0.003	0.003	0.001	0.000	0.001	0.001	0.001	0.002	0.002
Na	0.000	0.000	0.000	0.001	0.000	0.001	0.000	0.000	0.001	0.001	0.002	0.002	0.000
XMg	0.56	0.56	0.54	0.54	0.54	0.54	0.55	0.55	0.56	0.55	0.56	0.55	0.54
Xen	0.56	0.55	0.54	0.54	0.54	0.54	0.55	0.55	0.54	0.55	0.55	0.55	0.54
Xfs	0.44	0.45	0.46	0.46	0.46	0.46	0.45	0.45	0.46	0.45	0.45	0.45	0.46
tot. Oxygen	6.000	6.000	6.004	6.008	6.003	6.000	6.002	6.001	6.000	6.000	6.000	6.014	6.007
tot. Cation	4.000	4.000	4.000	4.000	4.000	4.000	4.000	4.000	4.000	4.000	4.000	4.000	4.000

Tab. S3-2b: Representative analyses of garnet for sample ALR 13-05

Analysis	13-05_grt1	13-05_grt2	13-05_grt3	13-05_grt4	13-05_grt5	13-05_grt6	13-05_grt7
Texture	*Grt porphyroblast*	*Grt porphyroblast*	*Grt porphyroblast*		*Grt porphyroblast*	*Grt porphyroblast*	*Grt porphyroblast*
Oxides (Wt. %)							
SiO_2	39.29	39.09	39.13	39.08	39.38	39.24	39.40
TiO_2	0.03	0.01	0.03	0.01	0.01	0.03	0.02
Al_2O_3	21.97	22.28	22.02	22.02	21.96	21.95	22.08
Cr_2O_3	0.00	0.00	0.02	0.01	0.00	0.00	0.01
FeO	28.81	27.95	27.76	28.56	27.61	28.42	28.21
MnO	0.52	0.52	0.43	0.56	0.50	0.56	0.63
MgO	8.67	9.44	9.35	9.04	9.28	8.80	8.83
CaO	0.72	0.73	0.77	0.74	0.81	0.82	0.71
Total	**100.00**	**100.02**	**99.51**	**100.01**	**99.53**	**99.82**	**99.88**
Formula (O=12)							
Si	3.04	3.01	3.03	3.02	3.04	3.04	3.05
Ti	0.00	0.00	0.00	0.00	0.00	0.00	0.00
Al	2.00	2.02	2.01	2.00	2.00	2.00	2.01
Cr	0.00	0.00	0.00	0.00	0.00	0.00	0.00
Fe^{3+}	0.00	0.00	0.00	0.00	0.00	0.00	0.00
tot. cubic	2.00	2.02	2.01	2.00	2.00	2.00	2.01
Fe^{2+}	1.86	1.80	1.80	1.84	1.78	1.84	1.82
Mn	0.03	0.03	0.03	0.04	0.03	0.04	0.04
Mg	1.00	1.08	1.08	1.04	1.07	1.01	1.02
Ca	0.06	0.06	0.06	0.06	0.07	0.07	0.06
tot. oct	2.96	2.97	2.97	2.98	2.95	2.96	2.94
XMg	0.35	0.38	0.38	0.36	0.37	0.36	0.36
Xalm	63.02	60.45	60.54	61.83	60.42	62.16	62.01
Xpyr	33.80	36.39	36.36	34.89	36.21	34.29	34.60
Xgr	2.01	2.02	2.14	2.06	2.26	2.30	1.99
Xsps	1.16	1.14	0.96	1.22	1.11	1.25	1.40

Tab. S3-2c: Representative analyses of biotite for sample ALR 13-05

Analysis	13-05_bt-46	13-05_bt-47	13-05_bt-48	13-05_bt-49	13-05_bt-50	13-05_bt-55	13-05_bt-52	13-05bt-51	13-05bt-56	13-05_bt-54	13-05bt-53b	13-05bt-55
Texture	*garnet rim*	*garnet rim*	*garnet rim*	*garnet rim*	*incl. Grenat*	*incl. Grenat*	*incl. Grenat*	*incl. Grenat*	*incl. Grenat*	*incl. Grenat*	*incl. Grenat*	*incl. Grenat*
Oxides (Wt. %)												
SiO_2	36.00	33.97	37.97	37.71	39.10	38.11	38.44	39.07	38.01	38.37	38.36	37.76
TiO_2	5.34	5.28	5.08	5.20	4.64	3.88	4.77	4.69	3.72	3.96	5.29	5.01
Al_2O_3	13.24	12.51	13.96	14.00	14.02	13.91	14.35	14.11	14.18	13.71	14.43	13.72
Cr_2O_3	0.06	0.00	0.00	0.00	0.00	0.05	0.06	0.00	0.00	0.00	0.01	0.05
FeO	12.47	12.39	12.36	12.62	7.45	11.08	7.57	7.42	9.92	10.88	7.76	10.79
MnO	0.01	0.10	0.03	0.02	0.00	0.04	0.00	0.03	0.00	0.00	0.00	0.02
MgO	15.25	15.15	15.22	15.23	19.04	16.74	18.88	18.92	17.81	16.98	18.21	16.60
CaO	0.01	0.00	0.00	0.00	0.03	0.00	0.00	0.03	0.00	0.05	0.00	0.00
Na_2O	0.16	0.11	0.06	0.09	0.21	0.11	0.46	0.19	0.19	0.12	0.52	0.15
K_2O	9.83	9.92	9.52	9.51	9.83	9.67	9.46	9.60	9.95	9.65	9.13	9.58
BaO	0.21	0.21	0.14	0.13	0.16	0.07	0.15	0.06	0.13	0.04	0.11	0.15
F	3.10	2.61	3.06	4.19	3.95	3.20	4.34	4.67	2.37	3.90	3.42	2.34
Cl	0.02	0.03	0.02	0.02	0.02	0.03	0.04	0.03	0.03	0.01	0.05	0.01
Total	**95.70**	**92.27**	**97.43**	**98.71**	**98.44**	**96.87**	**98.53**	**98.82**	**96.31**	**97.68**	**97.28**	**96.18**
Formula (O=11)												
Si	2.77	2.72	2.83	2.81	2.85	2.85	2.81	2.85	2.82	2.86	2.81	2.82
Al(iv)	1.20	1.18	1.17	1.19	1.15	1.15	1.19	1.15	1.18	1.14	1.19	1.18
Al	0.00	0.00	0.06	0.04	0.05	0.07	0.05	0.06	0.06	0.06	0.05	0.02
Mg	1.75	1.81	1.69	1.69	2.07	1.86	2.06	2.06	1.97	1.89	1.99	1.85
Fe^{2+}	0.80	0.83	0.77	0.79	0.45	0.69	0.46	0.45	0.62	0.68	0.48	0.67
Ti	0.31	0.32	0.28	0.29	0.25	0.22	0.26	0.26	0.21	0.22	0.29	0.28
Mn	0.00	0.01	0.00	0.00	0.00	0.00	0.00	0.00	0.00	0.00	0.00	0.00
Cr	0.00	0.00	0.00	0.00	0.00	0.00	0.00	0.00	0.00	0.00	0.00	0.00
Ca	0.00	0.00	0.00	0.00	0.00	0.00	0.00	0.00	0.00	0.00	0.00	0.00
Na	0.02	0.02	0.01	0.01	0.03	0.02	0.07	0.03	0.03	0.02	0.07	0.02
K	0.96	1.01	0.91	0.90	0.91	0.92	0.88	0.89	0.94	0.92	0.85	0.91
Ba	0.01	0.01	0.00	0.00	0.00	0.00	0.00	0.00	0.00	0.00	0.00	0.00
Sr	0.00	0.00	0.00	0.00	0.00	0.00	0.00	0.00	0.00	0.00	0.00	0.00
Rb	0.00	0.00	0.00	0.00	0.00	0.00	0.00	0.00	0.00	0.00	0.00	0.00
F	0.75	0.66	0.72	0.99	0.91	0.76	1.00	1.08	0.56	0.92	0.79	0.55
Cl	0.00	0.00	0.00	0.00	0.00	0.00	0.00	0.00	0.00	0.00	0.01	0.00
OH*	1.24	1.33	1.27	1.01	1.09	1.24	0.99	0.92	1.44	1.08	1.20	1.45
XMg	0.69	0.69	0.69	0.68	0.82	0.73	0.82	0.82	0.76	0.74	0.81	0.73

Tab. S3-2d: Representative analyses of cordierite for sample ALR 13-05

Analysis	13-05_crd-4	13-05_crd-5	13-05_crd-6	13-05_crd-13	13-05_crd-16	13-05_crd-16l	13-05_crd-18	13-05_crd-19	13-05_crd-19l	13-05_crd-22	13-05_crd-25	13-05_crd35
Oxides (Wt. %)												
SiO_2	50.20	50.24	50.08	50.18	49.73	49.48	50.04	49.72	49.99	49.18	49.99	49.73
TiO_2	0.00	0.00	0.00	0.00	0.00	0.00	0.00	0.00	0.00	0.01	0.00	0.00
Al_2O_3	32.75	33.20	33.05	33.03	32.54	32.64	33.23	32.95	32.74	32.27	32.89	33.31
Cr_2O_3	0.02	0.00	0.01	0.00	0.00	0.00	0.00	0.00	0.00	0.03	0.00	0.00
FeO	4.36	4.31	4.89	4.83	4.94	4.87	5.01	4.70	4.98	5.23	5.11	5.34
MnO	0.03	0.03	0.07	0.04	0.05	0.04	0.02	0.01	0.05	0.04	0.02	0.03
MgO	10.76	10.72	10.47	10.17	9.73	10.00	10.38	10.15	10.37	9.92	10.13	10.01
Na_2O	0.22	0.08	0.05	0.04	0.45	0.06	0.20	0.11	0.02	0.01	0.03	0.04
CaO	0.03	0.00	0.00	0.00	0.02	0.00	0.00	0.00	0.00	0.00	0.00	0.00
K_2O	0.01	0.00	0.00	0.00	0.01	0.01	0.00	0.01	0.00	0.00	0.01	0.00
Total	**98.37**	**98.58**	**98.61**	**98.28**	**97.47**	**97.11**	**98.87**	**97.65**	**98.15**	**96.68**	**98.19**	**98.46**
Formula (O=18)												
Si	5.07	5.06	5.05	5.07	5.08	5.07	5.04	5.06	5.07	5.07	5.07	5.03
Al	3.90	3.94	3.93	3.94	3.92	3.94	3.94	3.95	3.91	3.92	3.93	3.97
Mg	1.62	1.61	1.57	1.53	1.48	1.53	1.56	1.54	1.57	1.52	1.53	1.51
Fe^{2+}	0.37	0.36	0.41	0.41	0.42	0.42	0.42	0.40	0.42	0.45	0.43	0.45
Ti	0.00	0.00	0.00	0.00	0.00	0.00	0.00	0.00	0.00	0.00	0.00	0.00
Mn	0.00	0.00	0.01	0.00	0.00	0.00	0.00	0.00	0.00	0.00	0.00	0.00
Cr	0.00	0.00	0.00	0.00	0.00	0.00	0.00	0.00	0.00	0.00	0.00	0.00
Ca	0.00	0.00	0.00	0.00	0.00	0.00	0.00	0.00	0.00	0.00	0.00	0.00
Na	0.04	0.01	0.01	0.01	0.09	0.01	0.04	0.02	0.00	0.00	0.01	0.01
K	0.00	0.00	0.00	0.00	0.00	0.00	0.00	0.00	0.00	0.00	0.00	0.00
XMg	0.81	0.82	0.79	0.79	0.78	0.79	0.79	0.79	0.79	0.77	0.78	0.77

Tab. S3-3a: Representative analyses of garnet for sample ALR 13-06

Analysis	**13-06_grt1**	**13-06_grt2**	**13-06_grt3**	**13-06_grt4**	**13-06_grt5**	**13-06_grt6**	**13-06_grt7**	**13-06_grt8**
Texture	*Grt rim*	*Grt rim*	*Grt rim*	*Grt rim*	*Grt core*	*Grt core*	*Grt core*	*Grt core*
Oxides (Wt. %)								
SiO_2	38.24	38.31	38.14	38.56	38.53	38.57	38.65	38.59
TiO_2	0.00	0.00	0.00	0.00	0.00	0.00	0.00	0.00
Al_2O_3	21.82	21.82	21.76	21.66	21.95	21.79	21.94	21.81
Cr_2O_3	0.00	0.00	0.01	0.00	0.02	0.00	0.01	0.01
FeO	29.51	29.80	29.52	29.78	29.31	29.56	29.72	29.89
MnO	2.26	2.24	2.27	2.29	1.94	1.94	1.99	2.02
MgO	6.92	6.89	6.80	6.81	7.43	7.33	7.06	6.84
CaO	0.94	0.94	0.90	0.93	0.70	0.78	0.72	0.73
Total	**99.69**	**100.00**	**99.39**	**100.03**	**99.87**	**99.97**	**100.09**	**99.89**
Formula (O=12)								
Si	3.003	3.001	3.006	3.022	3.011	3.014	3.021	3.027
Ti	0.000	0.000	0.000	0.000	0.000	0.000	0.000	0.000
Al	2.020	2.015	2.022	2.001	2.021	2.007	2.021	2.016
Cr	0.000	0.000	0.001	0.000	0.001	0.000	0.001	0.000
Fe^{+}	0.000	0.000	0.000	0.000	0.000	0.000	0.000	0.000
tot. cubic	2.020	2.015	2.023	2.001	2.023	2.007	2.021	2.016
Fe^{2+}	1.938	1.952	1.946	1.952	1.915	1.932	1.942	1.961
Mn	0.150	0.149	0.151	0.152	0.128	0.129	0.132	0.134
Mg	0.810	0.804	0.799	0.796	0.865	0.853	0.823	0.800
Ca	0.079	0.079	0.076	0.078	0.058	0.065	0.060	0.061
tot. oct	2.977	2.984	2.971	2.978	2.966	2.979	2.958	2.957
XMg	0.29	0.29	0.29	0.29	0.31	0.31	0.30	0.29
Xalm	65.1	65.4	65.5	65.5	64.6	64.8	65.7	66.3
Xpyr	27.2	26.9	26.9	26.7	29.2	28.6	27.8	27.1
Xgr	2.7	2.7	2.5	2.6	2.0	2.2	2.0	2.1
Xsps	5.0	5.0	5.1	5.1	4.3	4.3	4.5	4.5
Xand	0.0	0.0	0.0	0.0	0.0	0.0	0.0	0.0

Tab. S3-3d: Representative analyses of sillimanite for sample ALR 13-06

Analysis	13-06_sill-25	13-06_sill-26	13-06_sill-1	13-06_sill-2	13-06_sill-3	13-06_sill-4	13-05_sill-5
Oxides (Wt. %)							
SiO_2	37.42	37.31	37.16	37.38	37.64	37.33	37.17
TiO_2	0.00	0.02	0.01	0.02	0.01	0.00	0.00
Al_2O_3	62.32	62.15	62.31	62.32	62.56	62.45	62.20
Cr_2O_3	0.04	0.03	0.00	0.01	0.00	0.00	0.01
FeO	1.20	1.05	1.36	1.21	1.18	1.25	1.21
MnO	0.00	0.00	0.04	0.04	0.00	0.00	0.00
MgO	0.00	0.02	0.01	0.01	0.00	0.00	0.02
CaO	0.05	0.00	0.00	0.00	0.00	0.00	0.00
Na_2O	0.00	0.02	0.00	0.04	0.02	0.00	0.00
K_2O	0.01	0.00	0.00	0.00	0.00	0.00	0.00
Total	101.04	100.59	100.89	101.02	101.41	101.03	100.61

Tab. S3-4a: Representative analyses of orthopyroxene for sample ALR 13-22

Analysis	13-022-c1-2	13-022-c1-4	13-022-c1-15	13-022-c1-16	13-022-c1-18	13-22_opx-12	13-22_opx-10
Oxides (Wt. %)							
SiO_2	50.22	49.81	49.90	50.24	49.88	50.50	50.05
TiO_2	0.08	0.13	0.11	0.10	0.10	0.07	0.08
Al_2O_3	7.90	8.60	8.83	8.18	8.54	8.27	8.70
Cr_2O_3	0.03	0.01	0.00	0.04	0.00	0.01	0.00
FeO	17.28	16.06	16.43	16.63	16.83	16.52	16.41
MnO	0.25	0.21	0.25	0.26	0.24	0.30	0.29
MgO	23.85	24.20	23.91	23.65	23.79	24.22	23.71
CaO	0.10	0.10	0.11	0.10	0.08	0.11	0.05
Na_2O	0.00	0.03	0.02	0.01	0.02	0.00	0.00
Total	**99.70**	**99.15**	**99.56**	**99.20**	**99.47**	**99.991**	**99.286**
Formula(O=6)							
Si	1.827	1.813	1.812	1.836	1.816	1.826	1.825
Ti	0.002	0.003	0.003	0.003	0.003	0.002	0.002
Al(iv)	0.173	0.187	0.188	0.164	0.184	0.174	0.175
Al(vi)	0.166	0.182	0.190	0.188	0.182	0.179	0.198
Cr	0.001	0.000	0.000	0.001	0.000	0.000	0.000
Fe^{3+}	0.001	0.000	0.000	0.000	0.000	0.000	0.000
Fe^{2+}	0.525	0.488	0.499	0.508	0.512	0.500	0.500
Mn	0.008	0.007	0.008	0.008	0.007	0.009	0.009
Mg	1.294	1.313	1.294	1.288	1.291	1.306	1.288
Ca	0.004	0.004	0.004	0.004	0.003	0.004	0.002
Na	0.000	0.002	0.002	0.000	0.002	0.000	0.000
XMg	0.71	0.73	0.72	0.72	0.72	0.72	0.72
Al(tot)	0.34	0.37	0.38	0.35	0.37	0.35	0.37

Tab. S3-4b: Representative analyses of sapphirine for sample ALR 13-22

Analysis	13-022-c1-1	13-022-c1-17	13-22_spr-1	13-22_spr-2	13-22_spr-4	13-22_spr-5	13-22_spr-6	13-22_spr-7	13-22_spr-13
Oxides (Wt. %)									
SiO_2	14.00	14.13	14.16	14.35	14.11	13.79	13.77	14.19	14.61
TiO_2	0.06	0.11	0.02	0.04	0.10	0.08	0.07	0.06	0.03
Al_2O_3	59.05	58.14	56.98	58.16	57.95	56.25	56.95	58.32	57.92
Cr_2O_3	0.07	0.05	0.05	0.02	0.04	0.04	0.04	0.04	0.01
FeO	9.81	10.18	10.27	10.17	10.37	10.38	10.40	10.39	10.40
MnO	0.06	0.13	0.15	0.09	0.09	0.10	0.13	0.13	0.15
MgO	16.02	16.28	16.15	16.17	16.43	16.43	16.23	16.04	16.21
CaO	0.01	0.00	0.00	0.01	0.00	0.03	0.00	0.01	0.01
Total	**99.07**	**99.03**	**97.77**	**99.00**	**99.08**	**97.09**	**97.59**	**99.17**	**99.33**
Formula(O=10)									
Si	0.846	0.855	0.868	0.869	0.853	0.851	0.845	0.858	0.883
Ti	0.003	0.005	0.001	0.002	0.005	0.004	0.003	0.003	0.001
Al(iv)	2.154	2.145	2.132	2.131	2.147	2.149	2.155	2.142	2.117
Al(vi)	2.052	2.002	1.986	2.018	1.983	1.941	1.967	2.016	2.006
Cr	0.003	0.002	0.002	0.001	0.002	0.002	0.002	0.002	0.000
Fe^{3+}	0.094	0.131	0.142	0.109	0.153	0.199	0.178	0.119	0.109
Fe^{2+}	0.402	0.385	0.385	0.406	0.372	0.337	0.356	0.407	0.417
Mn	0.003	0.007	0.008	0.005	0.005	0.005	0.007	0.006	0.008
Mg	1.443	1.469	1.476	1.459	1.481	1.511	1.486	1.447	1.459
Ca	0.001	0.000	0.000	0.001	0.000	0.002	0.000	0.000	0.000
Na	0.000	0.000	0.000	0.000	0.000	0.000	0.000	0.000	0.000
XMg	0.78	0.79	0.79	0.78	0.80	0.82	0.81	0.78	0.78
tot. Oxygen	10.000	10.000	10.000	10.000	10.000	10.000	10.000	10.000	10.000
tot. Cation	7.000	7.000	7.000	7.000	7.000	7.000	7.000	7.000	7.000
Mg + Fe + si	2.69	2.71	2.73	2.73	2.71	2.70	2.69	2.71	2.76
2x(Al + Fe3 + Cr	8.61	8.56	8.52	8.52	8.57	8.58	8.60	8.56	8.46
Al(tot)	4.205	4.146	4.118	4.150	4.130	4.090	4.122	4.158	4.123
tot	11.30	11.27	11.25	11.25	11.28	11.28	11.29	11.27	11.22

Tab. S3-4d: Representative analyses of cordierite for sample ALR 13-22

Analysis	**13-022-c1-9**	**13-022-c1-10**	**13-022-c1-14**	**13-22_crd-14**	**13-22_crd-15**	**13-22_crd-16**	**13-22_crd-8**	**13-22_crd-9**	**13-22_crd-11**
Texture	*sympl crd/sp*	*sympl crd/sp*							
Oxides (Wt%)									
SiO_2	49.76	49.88	49.47	50.13	50.45	50.04	50.19	50.45	50.09
TiO_2	0.00	0.00	0.02	0.00	0.00	0.00	0.00	0.00	0.00
Al_2O_3	32.92	33.37	33.49	33.38	33.39	33.11	33.25	33.10	33.35
Cr_2O_3	0.01	0.02	0.01	0.00	0.01	0.01	0.01	0.00	0.02
FeO	2.71	2.67	2.81	3.10	3.04	2.87	2.76	2.82	2.91
MnO	0.04	0.04	0.02	0.03	0.08	0.05	0.09	0.06	0.10
MgO	11.71	11.52	11.59	11.51	11.55	11.69	11.83	11.60	11.81
CaO	0.01	0.01	0.06	0.01	0.05	0.02	0.00	0.02	0.02
Na_2O	0.13	0.10	0.05	0.07	0.10	0.12	0.10	0.12	0.07
K_2O	0.04	0.05	0.04	0.04	0.02	0.05	0.02	0.02	0.07
Total	**97.33**	**97.65**	**97.55**	**98.27**	**98.68**	**97.95**	**98.24**	**98.19**	**98.42**
Formula(O=10)									
Si	5.04	5.03	5.00	5.04	5.05	5.04	5.04	5.07	5.03
Al	3.93	3.97	3.99	3.95	3.94	3.93	3.93	3.92	3.94
Mg	1.77	1.73	1.75	1.72	1.72	1.76	1.77	1.74	1.77
Fe^{2+}	0.23	0.23	0.24	0.26	0.25	0.24	0.23	0.24	0.24
Ti	0.00	0.00	0.00	0.00	0.00	0.00	0.00	0.00	0.00
Mn	0.00	0.00	0.00	0.00	0.01	0.00	0.01	0.00	0.01
Cr	0.00	0.00	0.00	0.00	0.00	0.00	0.00	0.00	0.00
Ca	0.00	0.00	0.01	0.00	0.01	0.00	0.00	0.00	0.00
Na	0.02	0.02	0.01	0.01	0.02	0.02	0.02	0.02	0.01
K	0.00	0.01	0.00	0.01	0.00	0.01	0.00	0.00	0.01
XMg	0.89	0.88	0.88	0.87	0.87	0.88	0.88	0.88	0.88
tot. Oxygen	18.000	18.000	18.000	18.000	18.000	18.000	18.000	18.000	18.000
tot. Cation	11.007	10.993	11.006	10.996	10.995	11.007	11.005	10.989	11.013

Tab. S3-4e: Representative analyses of biotite for sample ALR 13-22

Analysis	13-022-c1-11	13-022-c1-12	13-022-c1-13	13-22_bt17	13-22_bt18	13-22_bt19	13-22_bt20	13-22_bt21
Oxides (Wt%)								
SiO_2	37.99	38.59	38.27	38.13	38.45	37.80	38.26	38.32
TiO_2	3.72	4.14	3.79	3.97	3.87	3.88	4.56	4.61
Al_2O_3	15.03	15.13	15.26	15.24	15.64	15.51	15.12	14.99
Cr_2O_3	0.01	0.02	0.00	0.00	0.00	0.08	0.04	0.00
FeO	7.51	7.33	8.37	7.91	8.06	7.76	7.63	7.70
MnO	0.00	0.00	0.09	0.00	0.01	0.10	0.00	0.03
MgO	19.32	19.42	18.79	18.45	18.58	18.76	19.06	18.87
CaO	0.00	0.00	0.00	0.00	0.00	0.02	0.00	0.00
Na_2O	0.17	0.18	0.15	0.18	0.19	0.33	0.16	0.08
K_2O	9.91	9.86	9.94	9.93	9.99	9.94	10.05	10.15
BaO	0.04	0.05	0.00	0.02	0.03	0.08	0.02	0.00
F	1.49	1.53	1.34	3.27	2.64	2.18	3.29	2.57
Cl	0.01	0.02	0.02	0.00	0.00	0.02	0.01	0.00
Total	**95.19**	**96.28**	**96.02**	**97.10**	**97.45**	**96.46**	**98.20**	**97.32**
Formula(O=11)								
Si	2.79	2.80	2.79	2.80	2.79	2.77	2.78	2.79
Al(iv)	1.21	1.20	1.21	1.20	1.21	1.23	1.22	1.21
Al	0.09	0.09	0.10	0.12	0.13	0.11	0.07	0.07
Mg	2.12	2.10	2.04	2.02	2.01	2.05	2.06	2.05
Fe^{2+}	0.46	0.44	0.51	0.49	0.49	0.48	0.46	0.47
Ti	0.21	0.23	0.21	0.22	0.21	0.21	0.25	0.25
Mn	0.00	0.00	0.01	0.00	0.00	0.01	0.00	0.00
Cr	0.00	0.00	0.00	0.00	0.00	0.00	0.00	0.00
Ca	0.00	0.00	0.00	0.00	0.00	0.00	0.00	0.00
Na	0.02	0.03	0.02	0.03	0.03	0.05	0.02	0.01
K	0.93	0.91	0.92	0.93	0.93	0.93	0.93	0.94
Ba	0.00	0.00	0.00	0.00	0.00	0.00	0.00	0.00
Sr	0.00	0.00	0.00	0.00	0.00	0.00	0.00	0.00
Rb	0.00	0.00	0.00	0.00	0.00	0.00	0.00	0.00
F	0.35	0.35	0.31	0.76	0.61	0.51	0.76	0.59
Cl	0.00	0.00	0.00	0.00	0.00	0.00	0.00	0.00
OH*	1.65	1.65	1.69	1.24	1.39	1.49	1.24	1.41
XMg	0.82	0.83	0.80	0.81	0.80	0.81	0.82	0.81

Tab. S3-5a: Representative analyses of orthopyroxene for sample ALR 13-58

Analysis	13-58_opx1	13-58_opx2	13-58_opx3	13-58_opx4	13-58_opx5	13-58_opx6	13-58_opx7	13-58_opx8	13-58_opx9	13-58_opx10
Texture	*Opx I*	*Opx I*	*Opx I*	*Opx I*	*Opx I*	*Opx I*	*Opx I*	*Opx I*	*Opx I*	*Opx I*
Oxides (Wt. %)										
SiO_2	46.80	46.48	46.84	46.83	46.41	46.45	46.58	46.61	46.54	46.62
TiO_2	0.19	0.26	0.27	0.24	0.24	0.25	0.21	0.21	0.28	0.22
Al_2O_3	9.27	9.49	9.30	9.66	9.30	9.50	9.44	9.67	9.28	9.49
Cr_2O_3	0.02	0.01	0.00	0.03	0.00	0.04	0.00	0.01	0.01	0.02
FeO	25.17	25.83	24.69	25.08	24.85	25.29	25.10	25.52	25.06	24.78
MnO	0.48	0.48	0.44	0.45	0.48	0.40	0.42	0.46	0.41	0.47
MgO	17.83	17.08	17.62	17.26	17.66	17.73	17.54	17.45	17.82	17.83
CaO	0.03	0.10	0.04	0.07	0.06	0.06	0.03	0.05	0.04	0.07
Na_2O	0.00	0.02	0.01	0.01	0.01	0.03	0.00	0.00	0.01	0.00
Total	**99.79**	**99.74**	**99.21**	**99.62**	**99.01**	**99.75**	**99.35**	**100.04**	**99.45**	**99.51**
Formula(O=6)										
Si	1.77	1.76	1.78	1.77	1.77	1.75	1.77	1.76	1.76	1.76
Ti	0.01	0.01	0.01	0.01	0.01	0.01	0.01	0.01	0.01	0.01
Al(iv)	0.23	0.24	0.22	0.23	0.23	0.25	0.23	0.24	0.24	0.24
Al(vi)	0.18	0.19	0.19	0.21	0.18	0.18	0.19	0.19	0.18	0.19
Cr	0.00	0.00	0.00	0.00	0.00	0.00	0.00	0.00	0.00	0.00
Fe^{3+}	0.04	0.04	0.01	0.01	0.04	0.05	0.03	0.04	0.05	0.04
Fe^{2+}	0.75	0.78	0.77	0.79	0.75	0.74	0.77	0.77	0.75	0.75
Mn	0.02	0.02	0.01	0.01	0.02	0.01	0.01	0.01	0.01	0.01
Mg	1.00	0.97	1.00	0.97	1.00	1.00	0.99	0.98	1.01	1.01
Ca	0.00	0.00	0.00	0.00	0.00	0.00	0.00	0.00	0.00	0.00
Na	0.00	0.00	0.00	0.00	0.00	0.00	0.00	0.00	0.00	0.00
XMg	0.57	0.55	0.56	0.55	0.57	0.57	0.56	0.56	0.57	0.57
Xwo	0.00	0.00	0.00	0.00	0.00	0.00	0.00	0.00	0.00	0.00
Xen	0.56	0.54	0.56	0.55	0.56	0.55	0.55	0.55	0.56	0.56
Xfs	0.44	0.46	0.44	0.45	0.44	0.44	0.45	0.45	0.44	0.44

Tab. S3-5a: continued

Analysis	13-58_opx11	13-058_c2-31	13-058_c2-10	13-058_c2-13	13-058_c2-20	13-058_c2-17	opx2-24	opx2-25	13-058_c1-7	13-058_c2-22
Texture	*Opx I*	*Opx I*	*incl. in osm*	*incl. in osm*	*incl. in osm*	*incl. in Hc*	*Opx II*	*Opx II*	*Opx II*	*sympl opx-grt*
Oxides (Wt. %)										
SiO_2	46.53	46.47	46.38	46.31	46.17	46.71	47.26	48.05	48.86	48.38
TiO_2	0.26	0.24	0.28	0.24	0.33	0.28	0.23	0.18	0.16	0.11
Al_2O_3	9.65	9.44	9.56	9.50	9.60	9.45	8.84	8.25	7.25	6.83
Cr_2O_3	0.06	0.02	0.00	0.06	0.01	0.00	0.01	0.01	0.00	0.03
FeO	25.07	25.58	24.67	24.87	24.82	24.79	24.40	24.28	24.84	23.92
MnO	0.45	0.46	0.40	0.48	0.42	0.47	0.38	0.36	0.35	0.33
MgO	17.78	17.53	17.88	17.42	18.05	17.71	18.07	18.92	19.13	19.69
CaO	0.07	0.07	0.05	0.04	0.05	0.05	0.02	0.05	0.04	0.04
Na_2O	0.00	0.01	0.00	0.04	0.05	0.01	0.02	0.01	0.04	0.00
Total	**99.87**	**99.80**	**99.21**	**98.96**	**99.50**	**99.49**	**99.24**	**100.12**	**100.67**	**99.32**
Formula(O=6)										
Si	1.75	1.76	1.76	1.76	1.74	1.77	1.79	1.80	1.82	1.82
Ti	0.01	0.01	0.01	0.01	0.01	0.01	0.01	0.01	0.00	0.00
Al(iv)	0.25	0.24	0.24	0.24	0.26	0.23	0.21	0.20	0.18	0.18
Al(vi)	0.18	0.18	0.19	0.19	0.17	0.19	0.19	0.16	0.14	0.13
Cr	0.00	0.00	0.00	0.00	0.00	0.00	0.00	0.00	0.00	0.00
Fe^{3+}	0.05	0.05	0.04	0.03	0.07	0.03	0.01	0.03	0.03	0.05
Fe^{2+}	0.74	0.76	0.74	0.76	0.71	0.76	0.76	0.73	0.75	0.71
Mn	0.01	0.01	0.01	0.02	0.01	0.02	0.01	0.01	0.01	0.01
Mg	1.00	0.99	1.01	0.99	1.02	1.00	1.02	1.06	1.06	1.11
Ca	0.00	0.00	0.00	0.00	0.00	0.00	0.00	0.00	0.00	0.00
Na	0.00	0.00	0.00	0.00	0.00	0.00	0.00	0.00	0.00	0.00
XMg	0.57	0.57	0.58	0.57	0.59	0.57	0.57	0.59	0.59	0.61
Xwo	0.00	0.00	0.00	0.00	0.00	0.00	0.00	0.00	0.00	0.00
Xen	0.56	0.55	0.56	0.55	0.56	0.56	0.57	0.58	0.58	0.59
Xfs	0.44	0.45	0.44	0.44	0.43	0.44	0.43	0.42	0.42	0.41

Tab. S3-5b: Representative analyses of garnet for sample ALR 13-58

Analysis	gt-4	gt-5	GtA-1	GtA-2	GtA-3	GtA-4	GtA-5	GtA-6	GtA-7	gt2-11
Texture	*Gt I*	*Gt I*	*Gt I*	*Gt I*	*Gt I*	*Gt I*	*Gt I*	*Gt I*	*Gt I*	*Gt II*
Oxides (Wt. %)										
SiO_2	39.16	38.59	39.13	38.79	38.76	38.81	38.70	38.65	39.35	38.77
TiO_2	0.01	0.01	0.02	0.04	0.03	0.03	0.03	0.05	0.01	0.00
Al_2O_3	22.06	21.70	21.76	21.74	21.92	21.97	22.08	22.07	22.06	21.85
Cr_2O_3	0.01	0.00	0.01	0.02	0.00	0.01	0.00	0.00	0.00	0.02
FeO	27.88	27.29	27.94	27.78	27.33	27.89	27.63	27.74	27.45	29.71
MnO	1.48	1.50	1.62	1.59	1.59	1.57	1.61	1.54	1.55	1.67
MgO	9.25	9.10	9.31	9.18	9.28	9.21	9.21	9.23	9.14	8.01
CaO	0.71	0.80	0.71	0.70	0.71	0.62	0.63	0.57	0.57	0.51
Total	100.55	98.99	100.54	99.94	99.76	100.12	99.93	99.88	100.18	100.54
Formula (O=12)										
Si	3.00	3.01	3.00	3.00	3.00	2.99	2.99	2.99	3.03	3.00
Ti	0.00	0.00	0.00	0.00	0.00	0.00	0.00	0.00	0.00	0.00
Al	1.99	1.99	1.97	1.98	2.00	2.00	2.01	2.01	2.00	1.99
Cr	0.00	0.00	0.00	0.00	0.00	0.00	0.00	0.00	0.00	0.00
Fe^{3+}	0.00	0.00	0.02	0.02	0.00	0.02	0.01	0.01	0.00	0.00
tot. cubic	2.00	1.99	1.99	2.00	2.00	2.02	2.02	2.03	2.00	2.00
Fe^{2+}	1.79	1.78	1.78	1.78	1.77	1.78	1.77	1.78	1.77	1.92
Mn	0.10	0.10	0.11	0.10	0.10	0.10	0.11	0.10	0.10	0.11
Mg	1.06	1.06	1.07	1.06	1.07	1.06	1.06	1.06	1.05	0.92
Ca	0.06	0.07	0.06	0.06	0.06	0.05	0.05	0.05	0.05	0.04
tot. oct	3.00	3.00	3.01	3.00	3.00	2.99	2.99	2.99	2.97	3.00
XMg	0.37	0.37	0.38	0.37	0.38	0.37	0.37	0.37	0.37	0.32
Xalm	59.61	59.24	58.73	59.01	58.86	59.16	59.08	59.24	59.61	64.12
Xpyr	35.25	35.22	35.25	35.09	35.66	35.15	35.32	35.39	35.38	30.82
Xgr	1.94	2.24	1.94	1.93	1.96	1.71	1.72	1.57	1.60	1.42
Xsps	3.20	3.30	3.48	3.45	3.47	3.41	3.50	3.34	3.41	3.65
Xand	0.00	0.00	0.60	0.52	0.05	0.57	0.37	0.45	0.00	0.00

Tab. S3-5b: continued

Analysis	gt2-15	gt2-12	13-058_c1-3	13-058_c1-6	13-58_GtII_1	13-58_GtII_2	13-58_GtII_3	13-058_c2-21	13-058_c2-23
Texture	*Gt II*	*Gt II*	*Gt II*	*Gt II*	*Gt II*	*Gt II*	*Gt II*	*sympl gt-opx*	*sympl gt-opx*
Oxides (Wt. %)									
SiO_2	39.10	38.71	38.41	38.60	38.46	38.77	38.60	38.15	38.20
TiO_2	0.00	0.00	0.03	0.02	0.04	0.04	0.06	0.03	0.07
Al_2O_3	22.11	21.96	21.96	21.94	21.50	21.82	21.51	21.71	21.95
Cr_2O_3	0.00	0.02	0.04	0.00	0.01	0.01	0.00	0.00	0.01
FeO	29.69	30.56	29.69	29.75	29.94	29.50	29.95	29.62	28.64
MnO	1.97	1.87	1.78	1.78	1.74	1.72	1.67	1.69	1.68
MgO	7.34	7.12	7.77	7.28	7.58	7.88	7.68	8.05	8.01
CaO	0.61	0.51	0.74	0.67	0.51	0.47	0.58	0.44	0.53
Total	100.82	100.75	100.42	100.05	99.82	100.24	100.05	99.69	99.09
Formula (O=12)									
Si	3.03	3.01	2.98	3.01	3.01	3.01	3.01	2.98	3.00
Ti	0.00	0.00	0.00	0.00	0.00	0.00	0.00	0.00	0.00
Al	2.02	2.01	2.01	2.02	1.98	2.00	1.98	2.00	2.03
Cr	0.00	0.00	0.00	0.00	0.00	0.00	0.00	0.00	0.00
Fe^{3+}	0.00	0.00	0.02	0.00	0.00	0.00	0.00	0.04	0.00
tot. cubic	2.02	2.01	2.03	2.02	1.99	2.00	1.98	2.04	2.03
Fe^{2+}	1.92	1.99	1.91	1.94	1.96	1.92	1.95	1.90	1.88
Mn	0.13	0.12	0.12	0.12	0.12	0.11	0.11	0.11	0.11
Mg	0.85	0.83	0.90	0.85	0.89	0.91	0.89	0.94	0.94
Ca	0.05	0.04	0.06	0.06	0.04	0.04	0.05	0.04	0.04
tot. oct	2.95	2.98	2.98	2.96	3.00	2.98	3.01	2.98	2.97
XMg	0.31	0.29	0.32	0.30	0.31	0.32	0.31	0.33	0.33
Xalm	65.18	66.73	63.39	65.54	65.25	64.28	65.01	62.75	63.22
Xpyr	28.73	27.71	29.93	28.58	29.46	30.60	29.71	31.03	31.51
Xgr	1.71	1.42	2.05	1.89	1.43	1.32	1.62	1.22	1.51
Xsps	4.38	4.14	3.90	3.98	3.85	3.80	3.67	3.71	3.76
Xand	0.00	0.00	0.73	0.00	0.00	0.00	0.00	1.30	0.00

Tab. S3-5c: Represeniafive analyses of spinel for sample ALR 13-58

Analysis	13-58a_hc1	13-58a_hc1b	13-58a_hc2	13-58a_hc2-1	13-58a_hc6	13-58a_hc1	13-58a_hc1b	13-58_c1-5	13-58_c1-1	13-58_c1-4	13-58a_hc2-1	13-58a_hc6	13-58a_hc2
Oxides (Wt. %)													
SiO_2	0.00	0.05	0.07	0.01	0.00	0.00	0.05	0.00	0.00	0.02	0.01	0.00	0.07
TiO_2	0.04	0.01	0.03	0.05	0.03	0.04	0.01	0.03	0.04	0.02	0.05	0.03	0.03
Al_2O_3	58.39	57.47	58.13	58.41	58.72	58.39	57.47	58.26	59.13	59.01	58.41	58.72	58.13
Cr_2O_3	0.10	0.10	0.10	0.08	0.07	0.10	0.10	0.11	0.13	0.13	0.08	0.07	0.10
FeO	32.12	33.19	32.25	32.03	32.45	32.12	33.19	32.24	30.99	32.03	32.03	32.45	32.25
MnO	0.13	0.15	0.17	0.12	0.15	0.13	0.15	0.16	0.17	0.20	0.12	0.15	0.17
MgO	8.58	8.42	8.23	8.32	8.30	8.58	8.42	8.54	8.94	8.38	8.32	8.30	8.23
ZnO	0.14	0.22	0.17	0.20	0.16	0.14	0.22	0.29	0.21	0.18	0.20	0.16	0.17
NiO	n.a.	n.a.	n.a.	n.a.	n.a.	0.03	0.08	n.a.	n.a.	n.a.	0.08	0.06	0.07
V_2O_3	n.a.	n.a.	n.a.	n.a.	n.a.	0.01	0.01	n.a.	n.a.	n.a.	0.06	0.00	0.06
Total	**99.50**	**99.60**	**99.15**	**99.22**	**99.87**	**99.55**	**99.73**	**99.63**	**99.60**	**99.97**	**99.36**	**99.93**	**99.27**
Formula (O=4)													
Si	0.00	0.00	0.00	0.00	0.00	0.00	0.00	0.00	0.00	0.00	0.00	0.00	0.00
Ti	0.00	0.00	0.00	0.00	0.00	0.00	0.00	0.00	0.00	0.00	0.00	0.00	0.00
Al(vi)	1.90	1.87	1.90	1.91	1.90	1.90	1.87	1.89	1.91	1.91	1.91	1.90	1.90
Cr	0.00	0.00	0.00	0.00	0.00	0.00	0.00	0.00	0.00	0.00	0.00	0.00	0.00
Fe^{3+}	0.10	0.13	0.10	0.09	0.10	0.10	0.13	0.11	0.09	0.09	0.09	0.10	0.10
Fe^{2+}	0.64	0.64	0.65	0.65	0.65	0.64	0.64	0.63	0.62	0.65	0.65	0.65	0.65
Mn	0.00	0.00	0.00	0.00	0.00	0.00	0.00	0.00	0.00	0.00	0.00	0.00	0.00
Mg	0.35	0.35	0.34	0.34	0.34	0.35	0.35	0.35	0.37	0.34	0.34	0.34	0.34
Zn	0.00	0.00	0.00	0.00	0.00	0.00	0.00	0.01	0.00	0.00	0.00	0.00	0.00
XMg	0.36	0.35	0.34	0.35	0.34	0.36	0.35	0.36	0.37	0.35	0.35	0.34	0.34

Tab. S3-5d: Representative analyses of osumilite for sample ALR 13-58

Analysis	osm_8	osm_9	osm_10	osm_11	osm_12	osm_13	osm_14	osm_15	osm_16	osm_17	osm_18
Oxides (Wt. %)											
SiO_2	61.67	61.95	61.36	61.95	62.33	62.18	62.36	62.03	61.92	62.50	62.42
TiO_2	0.04	0.05	0.06	0.03	0.05	0.03	0.08	0.05	0.06	0.09	0.07
Al_2O_3	22.38	22.22	22.24	22.52	22.46	22.44	22.51	22.22	22.23	22.35	22.24
FeO	3.79	3.94	3.93	3.86	3.85	3.82	3.98	3.15	3.44	3.39	3.28
MnO	0.04	0.10	0.05	0.10	0.14	0.06	0.16	0.03	0.00	0.05	0.03
MgO	7.06	6.82	6.83	6.76	6.95	6.78	6.75	7.58	7.29	7.69	7.34
K_2O	4.29	4.06	4.11	4.13	4.21	4.01	4.13	4.12	4.08	4.13	4.02
CaO	0.00	0.01	0.00	0.00	0.00	0.01	0.00	0.01	0.00	0.01	0.01
Na_2O	0.48	0.47	0.56	0.57	0.56	0.52	0.49	0.50	0.46	0.44	0.42
Total	**99.76**	**99.61**	**99.13**	**99.91**	**100.56**	**99.85**	**100.46**	**99.68**	**99.47**	**100.64**	**99.82**
Formula (O=30)											
Si	10.28	10.33	10.30	10.31	10.31	10.33	10.32	10.31	10.32	10.30	10.35
Al(T1)	1.72	1.67	1.70	1.69	1.69	1.67	1.68	1.69	1.68	1.70	1.65
sum	12.00	12.00	12.00	12.00	12.00	12.00	12.00	12.00	12.00	12.00	12.00
Al(T2)	2.68	2.70	2.69	2.72	2.69	2.73	2.71	2.66	2.69	2.64	2.69
Fe(tot)	0.53	0.55	0.55	0.54	0.53	0.53	0.55	0.44	0.48	0.47	0.45
Mn	0.01	0.01	0.01	0.01	0.02	0.01	0.02	0.00	0.00	0.01	0.00
Ti	0.01	0.01	0.01	0.00	0.01	0.00	0.01	0.01	0.01	0.01	0.01
Mg	1.76	1.69	1.71	1.68	1.71	1.68	1.67	1.88	1.81	1.89	1.81
sum	4.98	4.97	4.97	4.95	4.96	4.95	4.96	4.99	4.98	5.01	4.98
K	0.91	0.86	0.88	0.88	0.89	0.85	0.87	0.87	0.87	0.87	0.85
Ca	0.00	0.00	0.00	0.00	0.00	0.00	0.00	0.00	0.00	0.00	0.00
Na	0.15	0.15	0.18	0.18	0.18	0.17	0.16	0.16	0.15	0.14	0.14
sum	1.07	1.02	1.06	1.06	1.07	1.02	1.03	1.03	1.01	1.01	0.99
XMg	0.77	0.76	0.76	0.76	0.76	0.76	0.75	0.81	0.79	0.80	0.80
tot. Oxygen	30.00	30.00	30.00	30.00	30.00	30.00	30.00	30.00	30.00	30.00	30.00
tot. Cation	34.87	34.80	34.81	34.78	34.81	34.76	34.79	34.85	34.83	34.90	34.80

Tab. S3-5e: idem for cordierite

Analysis	13-64_crd1
Texture	*sympl. Crd-Kfs*
Oxides (Wt. %)	
SiO_2	49.82
TiO_2	0.00
Al_2O_3	32.84
FeO	4.71
MnO	0.03
MgO	10.52
CaO	0.01
Na_2O	0.36
K_2O	0.02
Total	**98.31**
Formula (O=10)	
Si	5.05
Al	3.92
Mg	1.59
Fe^{2+}	0.40
Ti	0.00
Mn	0.00
Cr	0.00
Ca	0.00
Na	0.07
K	0.00
XMg	0.80

Tab. S3-5f: Representative analyses of biotite for sample ALR 13-58

Analysis	bt-21	bt-22	bt-23
Oxides (Wt. %)			
SiO_2	39.23	40.18	41.56
TiO_2	5.11	4.83	4.07
Al_2O_3	13.90	13.01	18.19
Cr_2O_3	0.02	0.08	0.00
FeO	6.14	6.21	4.63
MnO	0.00	0.00	0.07
MgO	19.95	20.49	15.49
CaO	0.00	0.00	0.00
Na_2O	0.38	0.28	0.35
K_2O	9.64	9.47	8.07
BaO	0.10	0.13	0.11
F	6.47	2.04	4.64
Cl	0.00	0.01	0.00
Total	100.95	96.73	97.17
Formula (O=11)			
Si	2.84	2.89	2.97
Al(iv)	1.16	1.10	1.03
Al	0.02	0.00	0.50
Mg	2.15	2.20	1.65
Fe^{2+}	0.37	0.37	0.28
Ti	0.28	0.26	0.22
Mn	0.00	0.00	0.00
Cr	0.00	0.00	0.00
Ca	0.00	0.00	0.00
Na	0.05	0.04	0.05
K	0.89	0.87	0.74
Ba	0.00	0.00	0.00
Sr	0.00	0.00	0.00
Rb	0.00	0.00	0.00
F	1.48	0.46	1.05
Cl	0.00	0.00	0.00
OH*	0.52	1.54	0.95
XMg	0.85	0.85	0.86

Tab. S3-5g: Representative analyses of feldspar for sample ALR 13-58

Analysis	fld-8b	fld-3
Texture	*corrona around Gt I*	*corrona around Gt I*
Oxides (Wt. %)		
SiO_2	62.07	62.01
TiO_2	0.02	0.01
Al_2O_3	23.68	23.63
Cr_2O_3	0.02	0.01
FeO	0.08	0.14
MnO	0.02	0.00
MgO	0.00	0.01
CaO	5.65	5.81
Na_2O	8.12	8.23
K_2O	0.18	0.27
BaO	0.00	0.00
Total	99.83	100.11
Formula (O=8)		
Si	2.77	2.76
Ti	0.00	0.00
Al	1.24	1.24
Cr	0.00	0.00
Fe^{3+}	0.00	0.00
Fe^{2+}	0.00	0.01
Mn	0.00	0.00
Mg	0.00	0.00
Ca	0.27	0.28
Na	0.70	0.71
K	0.01	0.02
Ba	0.00	0.00
An (mol%)	27.5	27.6
Ab (mol%)	71.5	70.8
Or (mol%)	1.1	1.6

Tab. S3-5h: Ti in quartz temperature for sample ALR 13-58

Grain	TiO2	err 95%	Temperature (°C)*
B01029a_Q2-1	0.048	0.004	940
B01029a_Q2-2	0.050	0.004	948
B01029a_Q2-3	0.045	0.004	929
B01029a_Q2-4	0.054	0.004	961
B01029a_Q2-5	0.050	0.004	948
B01029a_Q2-6	0.044	0.004	925
B01029a_Q2-7	0.049	0.004	944
B01029a_Q3-centre	0.042	0.004	917
B01029a_Q3-bordure	0.045	0.004	929
B01029a_Q3-inclusion	0.047	0.004	937
B01029a_Q4	0.050	0.004	948
B01029a_scanq10	0.042	0.004	917
B01029a_scanq10	0.046	0.004	933
B01029a_scanq10	0.045	0.004	929
B01029a_scanq10	0.044	0.004	925
B01029a_scanq10	0.046	0.004	933
B01029a_scanq10	0.044	0.004	925
B01029a_scanq10	0.050	0.004	948
B01029a_scanq10	0.045	0.004	929
B01029a_scanq10	0.044	0.004	925
B01029a_scanq10	0.042	0.004	917
B01029a_scanq10	0.048	0.004	940
B01029a_scanq10	0.049	0.004	944
B01029a_scanq10	0.046	0.004	933
B01029a_scanq10	0.045	0.004	929
B01029a_scanq10	0.042	0.004	917
Mean	***0.046***		***934***
2SD	*0.006*		*23*
Max	*0.054*		*961*
Min	*0.042*		*917*

* Ti-in-quartz temperature calculated with the calibration of Thomas et al. 2010 at a nominal pressure of 5 kbar and Ti activity of 0.5

Tab. S3-6a: Representative analysis of garnet for sample ALR 14-19

Analysis	Gt1-1	Gt1-2	Gt1-3	Gt1-4	Gt1-5	Gt1-6	Gt1-7	Gt1-8	Gt1-9	Gt1-10	Gt1-11	Gt1-12	Gt1-13	Gt1-14	Gt1-15	Gt1-16
Oxides (Wt. %)																
SiO_2	38.15	37.99	37.95	38.06	37.65	37.67	37.57	37.54	38.00	37.74	37.71	38.06	38.34	38.05	38.19	38.03
TiO_2	0.03	0.02	0.03	0.01	0.03	0.05	0.04	0.01	0.03	0.05	0.04	0.04	0.03	0.04	0.06	0.05
Al_2O_3	21.39	21.33	21.25	21.52	21.02	21.06	21.09	21.14	21.47	21.55	21.39	21.57	21.61	21.46	21.46	21.29
Cr_2O_3	0.06	0.01	0.03	0.02	0.03	0.03	0.06	0.06	0.07	0.03	0.01	0.03	0.02	0.01	0.02	0.03
FeO	33.38	32.91	33.12	33.10	33.36	34.03	33.99	34.73	32.95	32.95	32.95	32.52	31.86	32.30	32.50	33.16
MnO	0.47	0.40	0.43	0.43	0.47	0.47	0.47	0.50	0.47	0.49	0.49	0.42	0.43	0.47	0.45	0.43
MgO	5.80	6.15	6.20	6.27	6.04	5.38	5.80	5.17	6.26	6.46	6.42	6.25	6.67	6.75	6.73	6.25
CaO	0.82	0.87	0.80	0.84	0.80	0.82	0.84	0.82	0.90	0.95	0.85	0.84	0.98	0.92	0.84	0.93
Total	**100.11**	**99.67**	**99.81**	**100.25**	**99.40**	**99.51**	**99.86**	**99.97**	**100.14**	**100.22**	**99.86**	**99.73**	**99.95**	**100.00**	**100.24**	**100.17**
Formula(O=12)																
Si	3.013	3.006	3.000	2.992	2.993	3.004	2.979	2.986	2.991	2.965	2.975	3.006	3.011	2.989	2.994	2.995
Ti	0.002	0.001	0.002	0.001	0.002	0.003	0.002	0.001	0.002	0.003	0.002	0.002	0.002	0.003	0.003	0.003
Al	1.992	1.990	1.980	1.994	1.970	1.980	1.972	1.982	1.992	1.996	1.989	2.007	2.001	1.987	1.983	1.976
Cr	0.004	0.001	0.002	0.001	0.002	0.002	0.004	0.004	0.004	0.002	0.000	0.002	0.001	0.001	0.001	0.002
Fe^{3+}	0.000	0.000	0.015	0.018	0.038	0.005	0.061	0.041	0.017	0.067	0.056	0.000	0.000	0.030	0.021	0.027
tot. cubic	1.997	1.991	1.999	2.014	2.012	1.989	2.039	2.027	2.015	2.067	2.047	2.011	2.004	2.020	2.008	2.007
Fe^{2+}	2.205	2.177	2.174	2.158	2.180	2.265	2.193	2.270	2.152	2.098	2.118	2.148	2.092	2.092	2.110	2.157
Mn	0.032	0.027	0.029	0.028	0.032	0.032	0.032	0.034	0.031	0.032	0.033	0.028	0.029	0.031	0.030	0.029
Mg	0.683	0.725	0.731	0.735	0.715	0.640	0.686	0.613	0.734	0.757	0.755	0.736	0.781	0.790	0.787	0.734
Ca	0.070	0.074	0.067	0.071	0.068	0.070	0.072	0.070	0.076	0.080	0.072	0.071	0.083	0.077	0.071	0.078
tot. oct	2.989	3.003	3.002	2.993	2.995	3.007	2.982	2.987	2.993	2.968	2.978	2.983	2.985	2.991	2.998	2.998
XMg	0.24	0.25	0.25	0.25	0.25	0.22	0.24	0.21	0.25	0.27	0.26	0.26	0.27	0.27	0.27	0.25
Xalm	73.76	72.50	72.07	71.68	71.87	75.21	72.07	74.99	71.49	69.15	69.83	72.01	70.09	69.25	69.91	71.32
Xpyr	22.85	24.14	24.23	24.42	23.58	21.25	22.53	20.25	24.39	24.94	24.89	24.68	26.18	26.17	26.06	24.26
Xgr	2.33	2.46	2.23	2.36	2.25	2.34	2.36	2.31	2.51	2.65	2.36	2.38	2.77	2.56	2.34	2.58
Xsps	1.05	0.90	0.96	0.94	1.05	1.05	1.04	1.12	1.04	1.07	1.09	0.94	0.96	1.04	0.99	0.95
Xand	0.00	0.00	0.51	0.60	1.26	0.15	2.01	1.34	0.57	2.20	1.84	0.00	0.00	0.99	0.69	0.89
tot. Oxygen	12.013	12.002	12.000	12.000	12.000	12.000	12.000	12.000	12.000	12.000	12.000	12.013	12.014	12.000	12.000	12.000
tot. Cation	8.000	8.000	8.000	8.000	8.000	8.000	8.000	8.000	8.000	8.000	8.000	8.000	8.000	8.000	8.000	8.000

Tab. S3-6b: Representative analysis of spinel for sample ALR 14-19

Analysis	13-19_Sp1	13-19_Sp2	13-19_Sp3	13-19_Sp4	13-19_Sp5
Oxides (Wt. %)					
SiO_2	0.063	0.008	0.06	0	0.012
TiO_2	0.028	0.006	0.097	49.764	0.033
Al_2O_3	57.046	56.687	56.996	0.023	82.016
Cr_2O_3	0.209	0.158	0.197	0.021	0.254
FeO	35.92	35.929	35.595	47.448	0.425
MnO	0.05	0.047	0.043	0.14	0.023
MgO	4.993	4.731	4.957	0.113	0.029
ZnO	0.482	0.57	0.486	0.052	0.072
Total	**98.791**	**98.136**	**98.431**	**97.561**	**82.864**
Formula(O=4)					
Si	0.00	0.00	0.00	0.00	0.00
Ti	0.00	0.00	0.00	1.45	0.00
Al(vi)	1.91	1.92	1.92	0.00	2.98
Cr	0.00	0.00	0.00	0.00	0.01
Fe^{3+}	0.09	0.09	0.08	0.00	0.00
Fe^{2+}	0.77	0.77	0.77	1.54	0.01
Mn	0.00	0.00	0.00	0.00	0.00
Mg	0.21	0.20	0.21	0.01	0.00
Zn	0.01	0.01	0.01	0.00	0.00
XMg	**0.22**	**0.21**	**0.21**	**0.00**	**0.11**
tot. Oxygen	4.005	4.006	4.005	4.450	4.493
tot. Cation	3.000	3.000	3.000	3.000	3.000

Tab. S3-6c: Representative analysis of biotite for sample ALR 14-19

Analysis	**13-19_Bt2**	**13-19_Bt3**	**13-19_Gt2-Bt4**	**13-19_Gt2-Bt5**	**13-19_Gt2-Bt6**	**13-19_Gt2-Bt7**	**13-19_Gt2-Bt8**	**13-19_Gt2-Bt8b**
Texture		*incl*	*incl*	*incl*	*incl*	*incl*	*dans melt*	*dans melt*
Oxides (Wt. %)								
SiO_2	36.38	36.77	36.99	36.84	37.24	36.64	34.92	34.59
TiO_2	7.27	4.31	5.28	3.87	4.73	5.07	3.46	4.01
Al_2O_3	15.02	15.66	16.18	15.03	15.76	14.71	14.26	14.39
FeO	16.80	12.68	12.53	14.40	12.64	12.79	22.25	23.54
MnO	0.00	0.00	0.00	0.01	0.02	0.01	0.01	0.02
MgO	10.11	14.73	14.03	14.16	14.39	14.45	8.88	7.72
CaO	0.00	0.00	0.00	0.00	0.01	0.03	0.05	0.03
Na_2O	0.16	0.18	0.41	0.11	0.14	0.19	0.16	0.13
K_2O	9.26	9.64	9.31	9.57	9.70	9.39	9.08	9.27
BaO	0.31	0.23	0.17	0.16	0.10	0.15	0.08	0.09
F	0.24	1.26	1.77	0.54	0.64	0.42	0.32	0.11
Cl	0.43	0.48	0.44	0.96	0.48	0.46	1.22	1.57
Total	**95.97**	**95.95**	**97.12**	**95.65**	**95.84**	**94.32**	**94.68**	**95.48**
Formula(O=11)								
Si	2.75	2.76	2.74	2.78	2.77	2.77	2.78	2.76
Al(iv)	1.25	1.24	1.26	1.22	1.23	1.23	1.22	1.24
Al	0.09	0.14	0.16	0.12	0.15	0.08	0.12	0.11
Mg	1.14	1.65	1.55	1.60	1.60	1.63	1.05	0.92
Fe^{2+}	1.06	0.80	0.78	0.91	0.79	0.81	1.48	1.57
Ti	0.41	0.24	0.29	0.22	0.26	0.29	0.21	0.24
Mn	0.00	0.00	0.00	0.00	0.00	0.00	0.00	0.00
Cr	0.00	0.00	0.00	0.00	0.00	0.00	0.00	0.00
Ca	0.00	0.00	0.00	0.00	0.00	0.00	0.00	0.00
Na	0.02	0.03	0.06	0.02	0.02	0.03	0.03	0.02
K	0.89	0.92	0.88	0.92	0.92	0.91	0.92	0.94
Ba	0.01	0.01	0.00	0.00	0.00	0.00	0.00	0.00
F	0.06	0.30	0.42	0.13	0.15	0.10	0.08	0.03
Cl	0.05	0.06	0.06	0.12	0.06	0.06	0.16	0.21
OH*	1.89	1.64	1.53	1.75	1.79	1.84	1.76	1.76
XMg	**0.52**	**0.52**	**0.67**	**0.64**	**0.67**	**0.67**	**0.42**	**0.37**
tot. Oxygen	11.000	11.000	11.000	11.000	11.000	11.000	11.000	11.000
tot. Cation	9.627	9.782	9.725	9.795	9.745	9.751	9.817	9.807

Tab. S3-6d: Representative analysis of cordierite for sample ALR 14-19

Analysis	13-19_Crd1	13-19_Crd2	13-19_Crd3	13-19_crd4	13-19_crd5	13-19_crd6
Oxides (Wt. %)						
SiO_2	48.56	48.45	46.82	48.28	48.48	48.82
TiO_2	0.02	0.01	0.02	0.01	0.01	0.00
Al_2O_3	31.97	31.95	30.78	31.57	31.34	32.06
FeO	7.58	6.92	7.50	7.04	6.53	6.90
MnO	0.07	0.00	0.08	0.04	0.06	0.05
MgO	8.67	8.79	9.66	8.50	8.40	8.95
CaO	0.02	0.03	0.00	0.00	0.08	0.00
Na_2O	0.08	0.38	0.63	0.27	0.38	0.06
K_2O	0.02	0.02	0.01	0.00	0.00	0.00
Total	**96.98**	**96.54**	**95.50**	**95.71**	**95.29**	**96.84**
Formula(O=18)						
Si	5.05	5.05	4.97	5.07	5.11	5.06
Al	3.92	3.93	3.85	3.91	3.89	3.92
Mg	1.34	1.37	1.53	1.33	1.32	1.38
Fe^{2+}	0.66	0.60	0.67	0.62	0.58	0.60
Ti	0.00	0.00	0.00	0.00	0.00	0.00
Mn	0.01	0.00	0.01	0.00	0.01	0.00
Cr	0.00	0.00	0.00	0.00	0.00	0.00
Ca	0.00	0.00	0.00	0.00	0.01	0.00
Na	0.02	0.08	0.13	0.05	0.08	0.01
K	0.00	0.00	0.00	0.00	0.00	0.00
XMg	**0.67**	**0.69**	**0.70**	**0.68**	**0.70**	**0.70**
tot. Oxygen	18.000	18.000	18.000	18.000	18.000	18.000
tot. Cation	10.998	11.026	11.164	10.996	10.986	10.982

Tab. S3-6e: Representative analysis of feldspar for sample ALR 14-19

Analysis	13-19_Kfs1	13-19_Pl1	13-19_Pl2-1	13-19_Pl3	13-19_Kfs2	13-19_Kfs3
Oxides (Wt. %)						
SiO_2	64.52	62.03	62.32	61.25	64.20	64.57
TiO_2	0.03	0.03	0.02	0.02	0.03	0.04
Al_2O_3	17.85	23.72	23.63	23.82	18.11	18.22
FeO	0.12	0.08	0.06	0.06	0.02	0.02
MnO	0.01	0.00	0.00	0.01	0.03	0.00
MgO	0.01	0.01	0.00	0.00	0.00	0.00
CaO	0.05	5.57	5.73	6.10	0.30	0.22
Na_2O	1.10	8.50	8.57	8.30	1.47	1.91
K_2O	14.79	0.12	0.08	0.18	14.10	13.35
BaO	0.51	0.00	0.00	0.00	0.41	0.48
Total	98.98	100.06	100.40	99.74	98.65	98.79
Formula(O=8)						
Si	3.016	2.752	2.756	2.728	3.003	3.011
Ti	0.001	0.001	0.000	0.001	0.001	0.001
Al	0.984	1.241	1.232	1.251	0.998	1.001
Cr	0.000	0.000	0.000	0.000	0.000	0.000
Fe^{3+}	0.000	0.000	0.000	0.020	0.000	0.000
Fe^{2+}	0.005	0.003	0.002	-0.018	0.001	0.001
Mn	0.000	0.000	0.000	0.000	0.001	0.000
Mg	0.001	0.000	0.000	0.000	0.000	0.000
Ca	0.002	0.265	0.272	0.291	0.015	0.011
Na	0.100	0.731	0.734	0.717	0.133	0.172
K	0.882	0.007	0.004	0.010	0.841	0.794
Ba	0.009	0.000	0.000	0.000	0.007	0.009
An (mol%)	0.23	26.42	26.88	28.56	1.50	1.12
Ab (mol%)	10.15	72.89	72.70	70.41	13.48	17.64
Or (mol%)	89.61	0.69	0.42	1.03	85.02	81.24
tot. Oxygen	8.018	8.005	8.003	8.000	8.015	8.029
tot. Cation	5.000	5.000	5.000	5.000	5.000	5.000

S3-7 : EDS maps

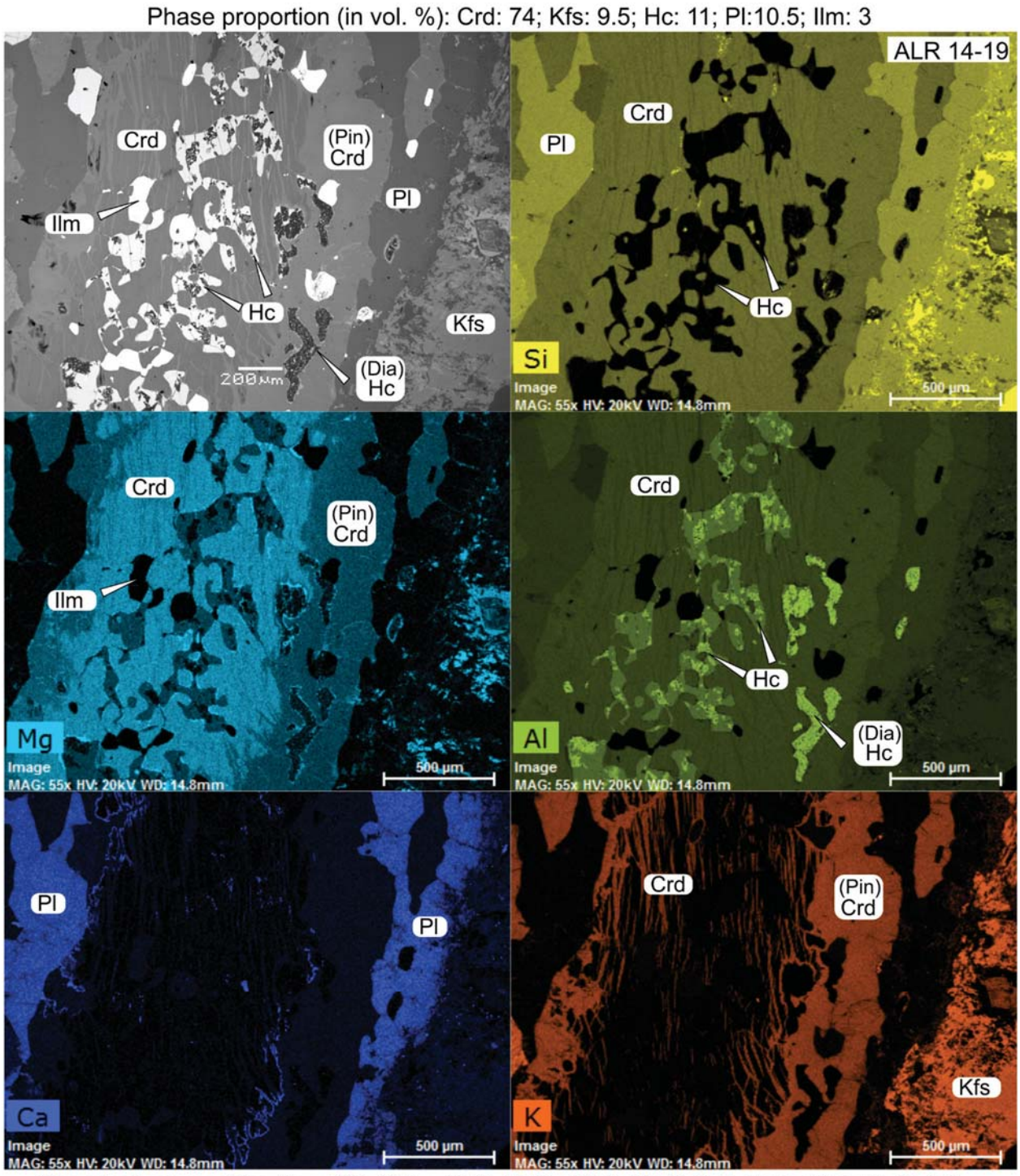

Chemical composition (in wt%): SiO_2: 40.9; Al_2O_3: 30.0; MgO: 6.5; FeO: 16.4; CaO: 0.6
Na_2O: 0.9; K_2O: 2.9; TiO_2: 1.2

Chapitre 4

The fate of zircon during polyphase granulite facies metamorphism in Rogaland, South Norway

ANTONIN T. LAURENT[1]*, BERNARD BINGEN[2], STEPHANIE DUCHENE[1], MARTIN J WHITEHOUSE[3], ANNE-MAGALI SEYDOUX-GUILLAUME[4], VALERIE BOSSE[5],

[1]GET, UMR 5563 CNRS–UPS–IRD, Université de Toulouse III, 14 av. E. Belin, 31400 Toulouse, France (*correspondence: antonin.laurent@get.obs-mip.fr)

[2]Geological Survey of Norway, 7491 Trondheim, Norway

[3]Departement of geoscience, Swedish Museum of Natural History, Stockholm, Sweden

[4]LMV, UMR 6524 CNRS–UBP–IRD, Université Jean Monnet, Saint-Etienne, France

[5]LMV, UMR 6524 CNRS–UBP–IRD, Université Blaise Pascal, Clermont-Ferrand, France

Keywords: zircon – U–Pb geochronology – ultra-high temperature metamorphism – Sveconorwegian

Résumé

Dans cet article, en cours de préparation, nous évaluons le comportement des zircons à basse pression (~5 kbar) dans un gradient de température apparent de 750 à 950 °C défini au Rogaland (Sud de la Norvège). Dans les échantillons de plus haut degré métamorphique, les cristaux de zircons sont systématiquement zonés. Il est possible d'identifier des domaines similaires de par leur signature en cathodoluminescence (CL), leur rapport Th/U et leur composition en terres rares. Les parties des cristaux formant ces populations chimiques bien identifiées conservent par contre des âges variables, s'étalant entre 1030 et 920 Ma. L'analyse *in-situ* des isotopes de l'O montre une forte homogeneité au sein du même échantillon suggérant une homogénéisation isotopique à haute température ou l'absence d'apport de fluides extérieurs. Il est possible de montrer que les grains hérités ayant dépassé le premier seuil de percolation (env. 25.10^{17} $\alpha.g^{-1}$) avant le début du métamorphisme Svéconorvégien sont sujets à la perte de Pb et à la remise à zéro partielle du chronomètre U–Pb. Nous proposons, en particulier, d'expliquer la zonation d'âge inverse, c'est-à-dire des cœurs plus jeunes que les bordures, par un processus de recristallisation à l'état solide des cœurs hérités structuralement instables, sans modifier la forme extérieure du grain. Nous explorons ensuite la mobilité différentielle U–Pb grâce à des cartes ioniques. Ces cartes ne révèlent pas de distribution hétérogène du Pb dans les échantillons de plus haut degré métamorphique. Par contre, nous observons des clusters de Pb radiogénique non associés à des concentrations en U dans le cœur hérité d'un zircon n'ayant pas recristallisé (échantillon non-UHT). L'absence de distribution hétérogène du Pb à ultra-haute température suggère que les néo-cristallisations et surcroissances conservent un âge primaire parfaitement valable et que la dispersion des données le long de la courbe *concordia* n'est pas dû à une discordance non résolue. Nous utilisons par conséquent ces surcroissances couplées à la thermométrie Ti-dans-le-zircon pour discuter des échelles de temps de présence de liquide silicaté dans les échantillons. L'analyse de ces résultats, associés à la comparaison des résultats obtenus sur les mêmes échantillons, par ailleurs, permet de mettre en évidence une variation systématique de l'enregistrement monazite/zircon au sein du gradient de température. Les roches appartenant au socle régional et ayant atteint des conditions *P–T* de 750°C à 5 kbar refroidissent sous le solidus à environ 1000 Ma, tandis que les roches à l'intérieur de l'isograde de l'orthopyroxène restent partiellement fondues jusqu'à au moins 971 ± 9 Ma. Les roches de UHT subissent, quant à elles, un second cycle thermique avec la cristallisation de nouvelles générations de zircon enregistrant un âge à environ 940–930 Ma. Par conséquent, cette étude suggère que certaines parties du domaine du Rogaland sont restées au-dessus de 800 °C pendant 100 Ma avec deux épisodes de UHT à environ 1030–1005 Ma et 940–930 Ma.

Abstract

In this contribution we evaluate the behaviour of zircon at low pressure (*c.* 0.5 GPa), in a thermal gradient ranging from 750 °C to 950 °C in Rogaland, S. Norway. In the highest grade samples, zircon crystals are systematically zoned. Within each crystal, it is possible to identify domains of consistent CL response, U/Th ratio and REE composition. These well characterized zircon domains however yield variable U–Pb dates, spreading along the concordia curve from c. 1030 Ma down to 920 Ma. *In-situ* O isotopic composition of zircon shows a strong homogeneity within single samples suggest high temperature isotopic homogenization or the absence of external fluid infiltration. It is possible to show that inherited zircon grains that have crossed the first percolation transition (25.10^{17} $\alpha.g^{-1}$) before the onset of Sveconorwegian metamorphism underwent Pb loss. Consequently, we propose a process to explain the inverse age zoning, i.e. younger cores than rims, observed in zircon grains. It involves solid-state recrystallization of structurally unstable old cores without changing the exterior shape of the grain. Scanning ion imaging, shows that some inherited zircon cores display a patchy distribution of unsupported radiogenic Pb. However, most of the grains seem unaffected by this process, implying that their apparent ages correspond to meaningful geological ages. The comparison of monazite and zircon U–Pb record through time and space, coupled to Ti-in-zircon thermometry provides firm evidence for protracted melting for some 110 My, from *c*. 1040 to 930 Ma, in the UHT samples. As a consequence, the Rogaland area did not cool below 750–800 °C between the two thermal maxima defined by monazite geochronology at *c*. 1030–1005 Ma and 940–930 Ma. In contrast, zircon and monazite record in the regional metamorphic basement are restricted to the 1040–990 Ma time span.

Introduction

Tracking the dynamics and duration of melting events within crustal rocks usually requires the use of the U–(Th)–Pb chronometer in zircon and monazite (Harley et al. 2007). Both minerals are able to preserve timely age information of long-lasting metamorphic events without suffering Pb-loss by diffusion, even at extreme crustal temperature (> 900 °C; Möller et al. 2002; Cherniak 2010; Kooijman et al. 2011). *In-situ* isotopic and micro-chemical investigations further allow to identify zircon growth processes and link them to the physico-chemical evolution of its crystallization environment like mineral paragenesis and *P–T*–fluids conditions (e.g. Ti in zircon, Ewing et al. 2013). Well characterized zircon growth processes include Ostwald ripening during prograde melting (Vavra et al. 1999), crystallization triggered by Zr saturation in the silicate melt (Watson and Harrison 1983; Kelly and Harley 2005; Kelsey et al. 2008) and sub-solidus growth in response to Zr release from other phases (Fraser et al. 1997; Degeling et al. 2001).

Metamorphic zircon thus show a wide diversity of internal textures that reflects the wide variety of P–T–fluid conditions under which growth is possible (Harley et al. 2007) but also largely reveals modification of pre-existing structures during metamorphism without changing the external shape of the grain (Corfu et al. 2003; Hoskin and Schaltegger 2003; Tichomirowa et al. 2005). Such zircon modification may result in complete resetting of U–Pb isotopic system through dissolution–precipitation which is characterized by transgressive front cross-cutting zircon internal structure (Tomaschek 2003; Geisler et al. 2007). Alternatively, subtle changes in zircon cathodoluminescence (CL) emission may hint to structural modification (Nasdala et al. 2002) in response to radiation damage accumulation in the crystal and to their subsequent annealing, resulting in incomplete Pb loss (Mezger and Krogstad 1997; Vavra et al. 1999; Hoskin and Black 2000; Ewing et al. 2003). Additionally, several recent studies document that chemical zoning (e.g. REE concentration) may actually be decoupled from U–Pb ages (Flowers et al. 2010; Taylor et al. 2014; Štípská et al. 2016). Extreme case is found in ultra-high temperature terrains, where patchily distributed radiogenic Pb at the nanoscale is the cause of reverse discordance (Kusiak et al. 2013; Whitehouse et al. 2014).

Interpretation of U–Pb *in-situ* analyses showing a range of concordant ages over several tens of million years is therefore not straightforward in granulite terrains. Such age spreads, exceeding analytical uncertainties, may reasonably be interpreted to result either from episodic zircon growth through time or to reflect post-crystallization disturbance of the U–Pb isotopic system that could remain almost unnoticed by *in-situ* techniques (Corfu 2013; Crowley et al. 2015). Wise geological interpretation of geochronological data therefore requires understanding

of the growth processes that can be tied to a specific *P–T* condition, but also evaluation of the response of U–Pb isotopic system to zircon textural changes through time.

In this contribution, we address the mineralogical and U–Pb isotopic response of zircon during repeated granulite facies events reaching ultra-high temperature in the Rogaland basement belonging to the Mesoproterozoic Sveconorwegian province (South Norway). The area is a well known occurrence of UHT metamorphism (Tobi et al. 1985; Maijer 1987) but the origin of its thermal heat source and duration – contact metamorphism vs regional metamorphism – has been controversial since then (Bingen 1998; Westphal 2003; Möller 2003; Druppel et al. 2013; Coint et al. 2015). Recent studies on zircon (Druppel et al. 2013) and monazite (Chp. 3) indeed suggest two distinct periods of UHT at *c*. 1030–1005 Ma and at *c*. 930 Ma. The thermal and rheological evolution of the orogen between these two maxima remains however unconstrained, and leaves open the question whether the crust sustained melt-present conditions during almost 100 My or cooled in between. To address this question we assess the evolution of zircon internal textures imaged by cathodoluminescence (CL) and back-scattered electron (BSE), REE chemistry and O isotopes through time in five key samples belonging to a unit of metasedimentary origin. We evaluate Pb mobilization via SIMS isotopic micro-mapping. Finally, zircon mineralogical and chemical record is compared to monazite age, chemistry and internal BSE textures from the same sample in order to discriminate between geological events affecting both minerals from those restricted to zircon.

Geological setting

The Sveconorwegian province (Fig. 1a) is made up of Mesoproterozoic crust reworked at the margin of Fennoscandia during the 1140–900 Ma Sveconorwegian orogeny (Bingen et al. 2008b). This study focuses on samples belonging to the Telemarkia terrane made up of *c*. 1520–1480 Ma magmatic rocks intruded by plutonic rocks and overlaid by sedimentary and bimodal volcanic rocks dated between *c*. 1500 and 920 Ma (Andersen et al. 2001; Laajoki et al. 2002; Roberts et al. 2013; Spencer et al. 2014). The Rogaland lithotectonic unit, which is located at the southwesternmost end of Telemarkia terrane, is composed of high-grade meta-igneous rocks of broadly granitic to tonalitic composition (granitic gneiss and meta-charnockite) interlayered with mafic rocks (amphibolite and banded gneiss) and metasedimentary rocks (Hermans et al. 1975; Fig. 1b). The UHT domain, delimited by the osumilite isograd (Fig. 1b), underwent two distinct granulite facies events peaking at *c*. 1030–1005 Ma and *c*. 930 Ma (Chp. 3). The first event (M1) is characterized by a clockwise *P–T* path reaching 940 °C at moderate pressure of *c*. 5–6 kbar (Chp. 3). *In-situ* U–Th–Pb geochronology on monazite and zircon provide a strong time bracket

between 1035 and 970 Ma for M1 regional metamorphism (Bingen and Van Breemen 1998; Bingen et al. 2008a; Druppel 2013; Coint et al. 2015; Chp. 3). The second stage of metamorphism (M2) dated at *c*. 930 Ma (Möller et al. 2002; Möller et al. 2003; Chp. 3) occurs at slightly lower *P* of *c*. 0.35–0.55 GPa and is associated with a geographical thermal gradient (850–1050 °C; Tobi et al. 1985) toward the contemporaneous massif-type anorthosite complex (Schärer et al. 1996; Westphal et al. 2003). Finally, zircon crystallization upon isobaric cooling of the terrain is dated at 908 ± 9 Ma (Möller et al. 2003). A regional scale average titanite U–Pb age of 918 ± 2 Ma also record regional fast cooling after M2 metamorphism (Bingen and van Breemen, 1998).

Analytical methods

Zircon crystals were separated using water table, heavy liquids and magnetic separator. Some 30 selected crystals for each sample were hand-picked under binocular, mounted in epoxy and polished to half thickness. All the crystals have been imaged individually to reveal their internal zoning with CL and BSE detector in a variable-pressure scanning electron microscope (SEM) hosted at the Geological Survey of Norway (Trondheim).

U–Th–Pb geochronology

Uranium–Pb and O isotopic composition were analysed by SIMS at the NORDSIM laboratory, Swedish Museum of Natural History, Stockholm. The oxygen isotopic analyses were performed before the U–Pb analyses, with a spot size of *c*. 10 µm. The mount was subsequently slightly repolished before U–Pb analyses so that the spot could be located at the same position. For U–Pb analyses the primary beam was adjusted to a diameter of either *c*. 10 µm (sample *ALR 13-22*; *ALR 13-05*; *ALR 13-58*) or *c*. 15 µm (sample *ALR 13-69*; *ALR 13-58*) depending on the size of internal CL zones. Detailed analytical protocol and data reduction for U–Pb and O analyses are described in Whitehouse and Kamber (2005) and Whitehouse and Nemchin (2009). The analysed grains were imaged again after SIMS analyses with BSE detector to check if any analytical spot overlapped two compositional domains or was located on a fracture.

Chemical micro-analyses

Microanalyses of zircon were collected by laser ablation inductively coupled plasma mass spectrometry (LA–ICP–MS), including the full suite of REE (^{139}La, ^{140}Ce, ^{141}Pr, ^{146}Nd, ^{147}Sm, ^{153}Eu, ^{157}Gd, ^{159}Tb, ^{163}Dy, ^{165}Ho, ^{166}Er, ^{169}Tm, ^{172}Yb, ^{175}Lu) along with ^{29}Si, ^{44}Ca, ^{49}Ti, ^{89}Y, ^{93}Nb, ^{178}Hf, ^{181}Ta, ^{208}Pb, ^{238}U and ^{232}Th. ^{90}Zr was used as internal standard and NIST 610 for external calibration. Repeated analyses of zircon reference material 91500 (Wiedenbeck et al. 1995) during

the session was used to monitor accuracy and reproducibility of the measurement and are reported in supplementary material S4-1. The spot size was 20 μm with a repetition rate of 1 Hz. Given the large difference in LA–ICP–MS and SIMS sampling volume, the data have been filtered for mixing between different chemical zones by comparing U and Th concentration measured by both techniques and discarding LA–ICP–MS analysis showing a deviation of more than 20 % of the SIMS value for any of the two elements. The precision is approximately ± 10 % relative.

Temperature of zircon crystallization was estimated using Ti-in-zircon thermometry, using the revised calibration of Ferry and Watson (2007) at a nominal pressure of 5 kbar. In the investigated samples rutile is absent but ilmenite and quartz are always present with additional titanite in sample *ALR* 13-*69*. The uncertainty presented in Tab. 1 was calculated by summing in quadrature the relative error on calibration of 2.2 % reported by Ferry and Watson (2007) with error resulting from the analytical uncertainty on Ti measurement.

Scanning ion imaging

The analytical protocol for scanning ion imaging closely follows that described by Kusiak et al. (2013). The Au-coating on the sample was removed over an 80 × 80 μm area using a rastered $O2^-$ primary beam (projected aperture of 200 μm corresponding to a spot diameter on the sample of *c*. 20 μm and beam current of *c*. 10 nA). For ion image acquisition over this same area, the spot diameter was reduced to *c*. 2 μm diameter (projected 20 μm aperture, nominal beam current of *c*. 100 pA). A secondary ion beam raster, synchronized with that of the primary beam, was applied using the deflectors of the dynamic transfer optical system (DTOS) on the IMS1270e7, located just above the sample extraction area. This so-called DTOS raster steers secondary ions emitted from any part of the analysed area onto the ion optical axis of the mass spectrometer, thus permitting high mass resolution analysis, while the image acquisition software reconstructs the sample image based on the primary beam position at a specific time. At the start of each image acquisition, the +10 kV secondary ion beam was centred in the field aperture by scanning across it using the x and y transfer deflectors and the ion energy was optimized in the 45 eV energy window by scanning the sample high voltage, in both cases using the large Zr_2O (or ZrO for some analyses) matrix peak. Pb-isotope ion imaging utilized simultaneous detection using four ion-counting electron multipliers to measure the species $^{90}Zr_2{}^{16}O$, ^{204}Pb, ^{206}Pb, and ^{207}Pb over a total of 100 cycles of 20 s integrations. Image analysis was performed using the CAMECA Winimage program to integrate all cycles and calculate isotope ratios from selected parts of the imaged area.

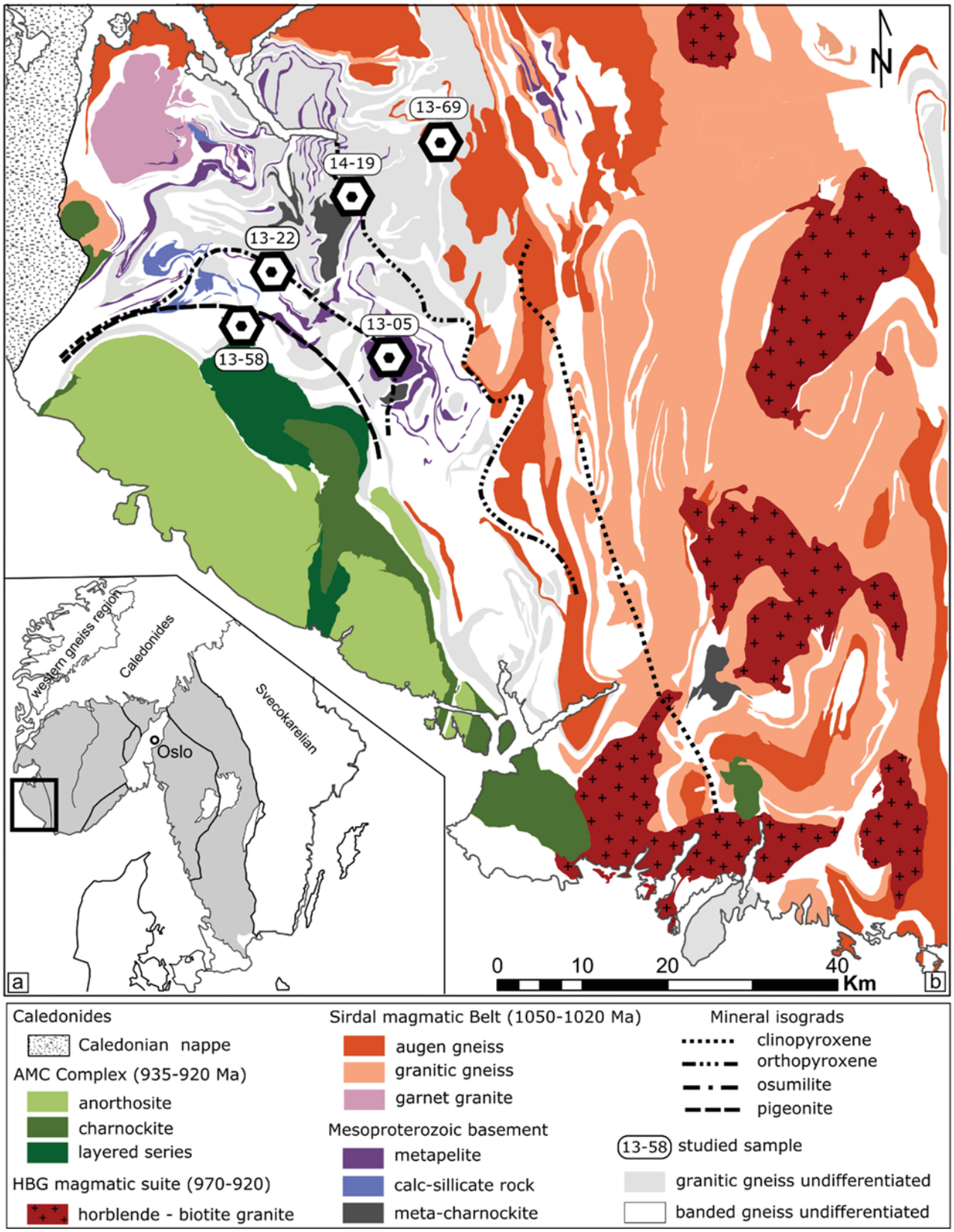

Fig. 4–1: – Geological maps. **a–** Sketch map of the Sveconorwegian Province in SW Scandinavia, black rectangle depicts the studied area. **b–** Simplified geological map of Rogaland-Vest Agder modified after (Falkum 1982; Coint et al. 2015) with mineral isograds drawn after (Tobi et al. 1985; Bingen et al. 1990) and localization of the studied samples.

Samples background

Five samples distributed in the granulite facies domain of Rogaland were chosen for the study. Sample *ALR 13-58* is taken within the mapped pigeonite isograd less than one kilometre of the exposed contact between the basement and the AMC complex (Fig. 1b; this sample is also studied in Chp. 2, Chp. 3). Sample *ALR 13-05* and *13-22* (also studied in Chp. 3) are taken within the osumilite isograd but differ in that *ALR 13-05* is a garnet leucosome whereas *ALR 13-22* represents a high Mg–Al restitic lithology. The garnet–hercynite–cordierite gneiss *ALR 14-19* (also studied in Chp. 3) is sampled at the limit of the mapped orthopyroxene isograd to provide a comparison point with previous work by Degeling et al. (2001) and Tomkins et al. (2005) who proposed specific zircon formation in the area, related to garnet breakdown into cordierite. Finally, sample *ALR 13-69* comes from the metamorphic basement outside of the mapped orthopyroxene isograd. Detailed petrological work and LA–ICP–MS monazite U–Th–Pb dating are presented for four out of five investigated samples in Chp. 3. For these samples, only key petrological and monazite geochronological features are summarized here. Additionnaly, we present new petrological constrains and U–Th–Pb monazite geochronology for distal sample *ALR 13-69* in supplementary material 4-2 and 4-3.

Sample ALR 13-69 (x = 355264; y = 6534649) is a migmatitic gneiss with garnet porphyroblast from a Gt–Bt-rich selvage zone. It was sampled in the Hunndendalen, some 35 km from the AMC contact and about 10 km beyond the mapped Opx-in isograd. The mineral assemblage comprises garnet (10 %), biotite (20 %), orthopyroxene (5 %), K-feldspar (20 %), plagioclase (10 %), quartz (27 %) magnetite (3%), ilmenite and minor secondary chlorite as well as accessory pyrrhotite, molybdenite, titanite, monazite, apatite and zircon. The main fabric is defined by ribbons of quartz and biotite wrapping around garnet with oriented inclusions of quartz, K-feldspar and biotite. The poikiloblastic garnets with inclusions of quartz, biotite and K-feldpar are interpreted to result from a fluid-absent dehydration melting such as Bt = Grt + Qz + Kfs (Le Breton and Thompson 1988). The appearance of orthopyroxene is related to terminal breakdown of biotite. Modelling of metamorphic phase equilibria, coupled with garnet chemistry indicates metamorphic peak conditions of c. 770–800 °C at 4–5 kbar (Supplementary material S4-2). Monazite crystals display BSE texture ranging from euhedral homogenous grains to rounded patchy crystals. The different chemical zones show a large variability in their Th and Y content (ThO_2 = 1.8–9.8 wt%; Y_2O_3 = 0.6–4.8 wt%), although no systematic correlation were found between grains. The dominant age group consist of both patchily-zoned rounded grains and euhedral homogenous grains that have individual $^{206}Pb/^{238}U$ scattering between 1072 ± 36 and

1000 ± 34 Ma. Additionally, one grain yields a younger age of 937 ± 9 Ma (Supplementary material S4-3).

Sample ALR 14-19 (x = 345793; y = 6517377) is a garnet–hercynite–cordierite migmatite from the Maudal locality. The dominant minerals are garnet (25 %), cordierite (15 %), spinel (5 %), perthite (25 %), plagioclase (10 %) quartz (15 %) with minor ilmenite, biotite, sillimanite and accessory monazite, zircon, pyrite, pyrrhotite. The rock texture is characterized by dark seams composed of cordierite + hercynite wrapping around sigmoid porphyroblastic garnet. Porphyroblastic garnets contain numerous inclusions of oriented sillimanite needles together with rounded biotite blades testifying of a prograde clockwise *P–T* path in the sillimanite stability field. Spinel hercynite with low Cr and Zn content is intergrown with cordierite and ilmenite, forming *c*. 250−500 μm thick bands that are interpreted to represent the peak temperature assemblage at 840 °C and 4.5 kbar (Chp. 3). A late hydrothermal event lead to spinel retrogression into diaspore while cordierite is in place replaced by pinite. Monazite retrieved from this sample typically show fine-scale patchy zoning but no systematic relationships between age and chemistry have been found (Chp. 3). Alternatively, two groups of monazite age are identified. The dominant age group defines a well constrained weighted $^{206}Pb/^{238}U$ age of 1035 ± 7 Ma while the youngest age group show some scatter along the concordia curve with a best estimate of the youngest cluster by a weighted $^{206}Pb/^{238}U$ age of 955 ± 22 Ma (Chp. 3).

Sample ALR 13-22 (x = 335550; y = 6510354) is a quartz undersaturated sapphirine–orthopyroxene gneiss enclosed in felsic garnet–orthopyroxene–spinel–cordierite migmatite. The dominant minerals are orthopyroxene (20%), sapphirine (15%), cordierite (15%), spinel (5%), biotite (20%), antiperthitic plagioclase (15 %), mesoperthite (10%) with accessory ilmenite, monazite, xenotime and zircon; quartz is absent. Prismatic sapphirine crystals are surrounded by a symplectite rim of cordierite and spinel toward orthopyroxene with occasional biotite replacing cordierite in the symplectite. Peak metamorphic conditions deduced from the initial sapphirine–orthopyroxene equilibrium corresponds to 940 °C at 0.6 GPa while the formation of the cordierite + spinel symplectite is predicted at 3.5 kbar and 900 °C (Chp. 3). This sample contains three generations of monazite crystals. The first generation consists of oscillatory zoned crystals rich in ThO_2 (up to 33.0 Wt. %) and Y_2O_3 (up to 7.15 Wt. %) defining a $^{206}Pb/^{238}U$ weighted average age of 1029 ± 9 Ma (Chp. 3). Thermometry based on the partitioning of Y between monazite and xenotime suggests crystallization temperature close to 900 °C, in accordance with peak metamorphic conditions. The second generation corresponds to patchy-zoned crystals rich in ThO_2 and Y_2O_3 which yields a $^{206}Pb/^{238}U$ weighted average age of 1006 ± 8 Ma and is interpreted as recrystallization of the first oscillatory-zoned monazite generation still at granulite facies temperature (Chp. 3). Finally, a third generation of low Y_2O_3 (< 1.5 Wt. %) and ThO_2 (< 5.5

Wt. %) grains that exsolved their xenotime and Th-component yields $^{206}Pb/^{238}U$ ages ranging from 985 ± 29 Ma down to 940 ± 28 Ma.

Sample ALR 13-05 (x = 348746; y = 6499700) is taken from a thick garnet-rich leucosome. The main constituents are garnet (35 %), micro- to mesoperthite (20 %), antiperthite (10 %), cordierite (10 %), orthopyroxene (10 %), quartz (5 %), hercynite (3 %), and biotite (10 %) with accessory monazite and zircon. The sample displays a well-developed cordierite–orthopyroxene–hercynite symplectite around porphyroblastic garnet which corresponds to UHT conditions of 900–950 °C at 5–3.5 kbar (Chp. 3). Investigation of monazite chemistry coupled to U–Th–Pb geochronology revealed three distinct monazite generations. The first generation consists of high-Th, low-Y cores yielding a concordia age of 1032 ± 5 Ma. The second population consists of low-Th, low-Y rims with individual $^{206}Pb/^{238}U$ ages ranging from 1017 ± 28 Ma down to 968 ± 28 Ma. The third generation carries a high-Y, low Th signature that is interpreted to reflect garnet breakdown and hence UHT conditions at 931 ± 6 Ma (Chp. 3).

Sample ALR 13-58 (x = 332482; y = 6503981) is an osumilite–hercynite gneiss from the Vikeså locality within the Pig-in isograd (Fig. 1b). The dominant minerals are garnet (20 %), orthopyroxene (15 %), hercynite (10 %), osumilite (15 %), mesoperthite (10 %), antiperthite (5 %), plagioclase (5 %) and quartz (15%) with minor cordierite, sillimanite and accessory monazite, zircon, pyrrhotite. The rock preserves porphyroblastic garnet enclosing needles of sillimanite together with F–Ti-rich biotite, providing evidence for a clockwise prograde evolution in the sillimanite stability field. Porphyroblastic garnet is in place pseudomorphosed by twinned cordierite. Alternatively garnet is replaced by a broad osumilite + hercynite domain enclosing numerous orthopyroxene blades. The latter assemblage is interpreted as the peak mineral paragenesis indicating a temperature of c. 910 °C at 4.5 kbar (Chp. 3). Secondary garnet rims occurring on hercynite point to an isobaric cooling path. Within this sample several monazite generations were identified. The oldest monazite domain is a S-rich core interpreted to reflect granulite facies sulphide breakdown at 1034 ± 6 Ma followed by a dissolution-precipitation episode forming secondary sulphate-bearing domains at 1005 ± 7 Ma. Finally, a S-free, high-Y population resulting from garnet breakdown at UHT is dated at 935 ± 7 Ma (Chp. 3).

Results

Zircon zoning and microchemistry

Zircon internal morphology was investigated with BSE and CL imaging and linked to trace elements chemistry. Because internal features are more visible in CL, only these images are presented here (Fig. 2). The trace element chemistry is reported in full in Tab. 1 with illustration of Th/U measured with the ion probe (Fig. 3) and REE spectra normalized to chondrite (Fig. 4).

In the distal garnet–biotite gneiss *ALR 13-69*, rounded zircon preserves partially resorbed cores (Fig. 2a) surrounded by a CL-dark featureless thick rim with very low Th/U ~ 0.01 (Fig. 3a). Additionally, one crystal displays a U-poor, CL-bright mottled zone that is interpreted as an annealed zone (Fig. 2a, grain 16). The chondrite normalized REE pattern of the different zones share a strong enrichment of HREE over LREE and a positive Ce anomaly typical of zircon (Fig. 4a). The CL-dark rims display moderate enrichment of HREE over MREE monitored by Gd/Lu normalized to chondrite (Gd_N/Lu_N) ranging from 0.3 to 0.5. The CL-dark rims has also rather high Y (856–1252 ppm) and lower concentration of HREE compared to the core (Y = 622–640 ppm) although their REE pattern are similar. The CL-bright area display a weaker Eu anomaly and steeper HREE pattern (GdN/LuN = 0.15) compared to the cores and CL-dark rims.

The orthopyroxene-zone sample (*ALR 14-19*) contains a large proportion of zircon crystals preserving prismatic oscillatory zoned core surrounded by a thick (> 30μm) CL-dark rim with faint oscillatory zoning. A second population lacking inherited cores consists of small (< 125 μm) stubby zircon with soccer-ball or sector zoning superimposed on faint oscillatory zoning (Fig. 2b). The chemical signature of CL-dark rims and stubby zircon are similar with moderate U (c. 600 ppm; Fig. 3b) rather high Hf (1.47–1.57 Wt. %) and low-Y content (< 197 ppm) whereas inherited core display moderate Hf (< 1.13 Wt. %) lower U content (<150 ppm) and higher Y content (561–913 ppm). Inherited cores display enrichment of HREE over MREE characterized by GdN/YbN = 0.05–0.11 (Fig. 4b) typical of magmatic zircon (Hoskin and Schaltegger 2003) whereas CL-dark rims and stubby zircon have slightly higher concentration of MREE than cores but show a marked negative slope from Gd to Lu (GdN/YbN = 1.9–8.4).

↓ **Fig. 4–2**: – Zircon cathodoluminescence image with $^{206}Pb/^{238}U$ age and $\delta^{18}O$ value in italics for each analysis spot **a–** sample ALR 13-69 displays CL-dark rims surrounding inherited cores **b–** sample ALR 14-19 shows CL-dark rims on inherited cores (grains 04, 03 & 01) and stubby sector-zoned zircon (grain 14); On grain 01, the white arrow points to CL-bright recrystallization at the core–rim interface **c–** sample ALR 13-22 displays sector-zoned inherited cores with blurred oscillatory rims **d–** sample ALR 13-05 consists of concentrically-zoned grains with a CL-dark external zone (grain 16 & 04), sector-zoned CL-bright zone (all grains), sector-zoned CL-grey zone (grain 01 & 04) and eventually, an inherited core surrounded by CL-dark moat (grain 05) **e–** sample ALR 13-58 display variable textures including CL-dark polygonal sector zoning (grain 09), CL-bright interior surrounded by CL-dark featureless exterior (grain 06), ghost of inherited core (grain 08) and an oscillatory CL-bright outer rim rich in Y (grain 12; also visible on grain 06).

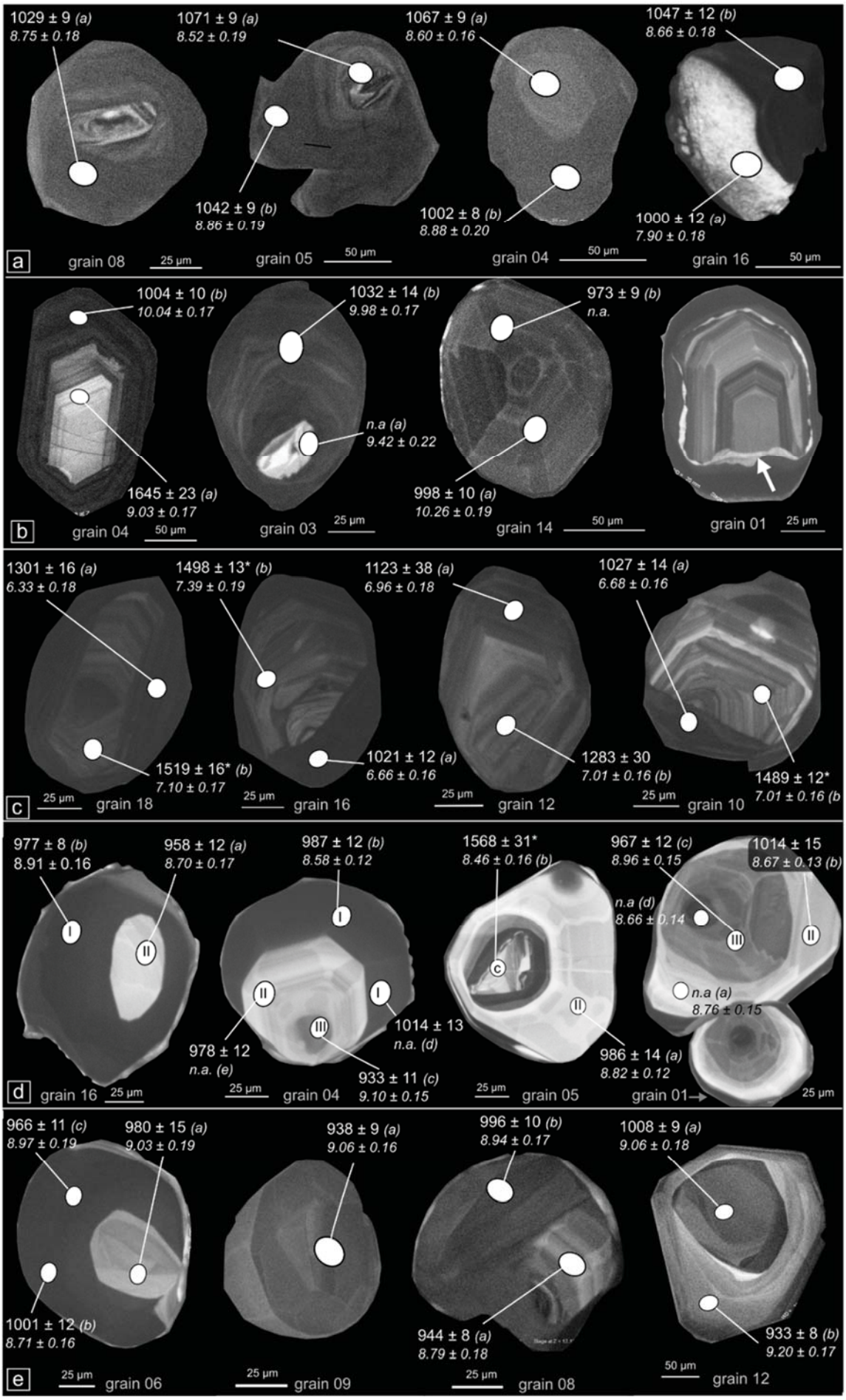
1029 ± 9 (a)
8.75 ± 0.18
1071 ± 9 (a)
8.52 ± 0.19
1042 ± 9 (b)
8.86 ± 0.19
1067 ± 9 (a)
8.60 ± 0.16
1002 ± 8 (b)
8.88 ± 0.20
1047 ± 12 (b)
8.66 ± 0.18
1000 ± 12 (a)
7.90 ± 0.18
a
grain 08
25 µm
grain 05
50 µm
grain 04
50 µm
grain 16
50 µm
1004 ± 10 (b)
10.04 ± 0.17
1645 ± 23 (a)
9.03 ± 0.17
1032 ± 14 (b)
9.98 ± 0.17
n.a (a)
9.42 ± 0.22
973 ± 9 (b)
n.a.
998 ± 10 (a)
10.26 ± 0.19
b
grain 04
50 µm
grain 03
25 µm
grain 14
50 µm
grain 01
25 µm
1301 ± 16 (a)
6.33 ± 0.18
1519 ± 16* (b)
7.10 ± 0.17
1498 ± 13* (b)
7.39 ± 0.19
1021 ± 12 (a)
6.66 ± 0.16
1123 ± 38 (a)
6.96 ± 0.18
1283 ± 30
7.01 ± 0.16 (b)
1027 ± 14 (a)
6.68 ± 0.16
1489 ± 12*
7.01 ± 0.16 (b
c
25 µm
grain 18
25 µm
grain 16
25 µm
grain 12
25 µm
grain 10
977 ± 8 (b)
8.91 ± 0.16
958 ± 12 (a)
8.70 ± 0.17
978 ± 12
n.a. (e)
987 ± 12 (b)
8.58 ± 0.12
1014 ± 13
n.a. (d)
933 ± 11 (c)
9.10 ± 0.15
1568 ± 31*
8.46 ± 0.16 (b)
986 ± 14 (a)
8.82 ± 0.12
967 ± 12 (c)
8.96 ± 0.15
n.a (d)
8.66 ± 0.14
1014 ± 15
8.67 ± 0.13 (b)
n.a (a)
8.76 ± 0.15
d
grain 16
25 µm
25 µm
grain 04
25 µm
grain 05
grain 01
25 µm
966 ± 11 (c)
8.97 ± 0.19
980 ± 15 (a)
9.03 ± 0.19
1001 ± 12 (b)
8.71 ± 0.16
938 ± 9 (a)
9.06 ± 0.16
996 ± 10 (b)
8.94 ± 0.17
944 ± 8 (a)
8.79 ± 0.18
1008 ± 9 (a)
9.06 ± 0.18
933 ± 8 (b)
9.20 ± 0.17
e
25 µm
grain 06
25 µm
grain 09
25 µm
grain 08
50 µm
grain 12

In the sapphirine granulite (sample ALR 13-22) zircon crystals are of small size (max. 150 µm) and mostly of prismatic shape with a pinkish colour. Imaging of zircon grains interior reveal systematic inherited cores with oscillatory zoning surrounded by a thin CL-dark rim with blurred oscillatory zoning (Fig. 2c). Oscillatory cores have distinctly lower U (< 600 ppm) and Th (< 180 ppm) compared to the CL-dark blurred rims (U up to 1400 ppm and Th up to 340 ppm; Fig. 3c). The REE pattern for both zones is characterized by steep HREE slope (Gd_N/Yb_N =0.02–0.09) with an overall higher Y+ Hf in blurred rims compared to the cores (Fig. 4c).

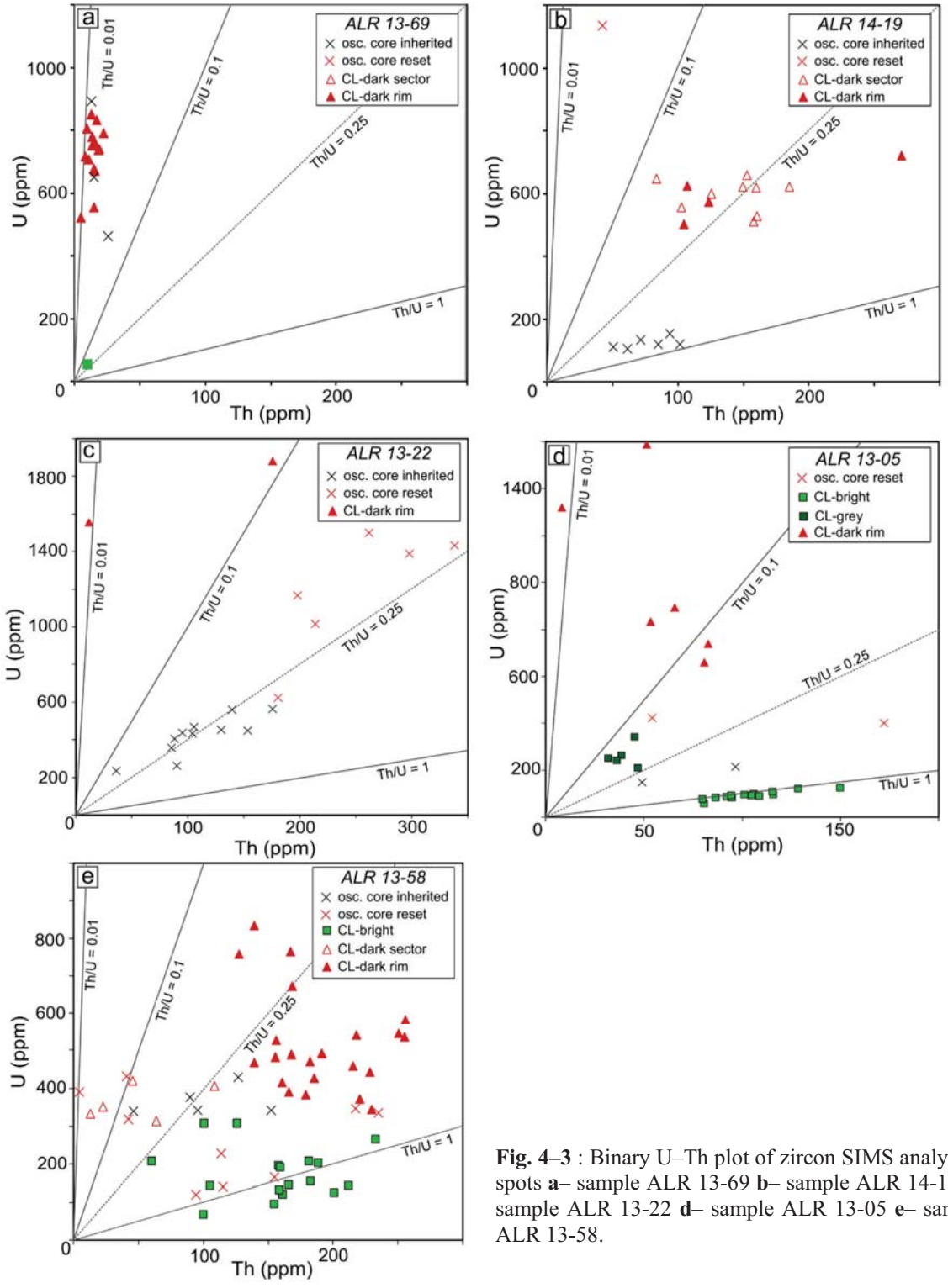

Fig. 4–3 : Binary U–Th plot of zircon SIMS analytical spots **a**– sample ALR 13-69 **b**– sample ALR 14-19 **c**– sample ALR 13-22 **d**– sample ALR 13-05 **e**– sample ALR 13-58.

In the garnet leucosome sample (ALR 13-05) zircon crystals have a moderate size (100–200 μm), rounded shape and a pale yellow colour. Inspection of their internal CL zoning pattern reveals a succession of four concentric zones (Fig. 2d) that correlates very well with micro-chemistry and particularly with U concentration (Fig. 3d). From the rim to the centre of the crystal we recognize: (I) a CL-dark area without distinguishable internal features correlated with high U content (660–1588 ppm) and low Th/U < 0.01 (II) a CL-bright zone that shows oscillatory zoning superimposed by sector or fir-tree zoning with Th/U ~ 1, (III) a CL medium-grey rounded zone displaying sector zoning with low Th (< 50 ppm) and intermediate Th/U = 0.13–0.23 (IV) corroded inherited core with variable Th/U surrounded by CL-black thin mantle (<15 μm). The CL-bright zone (II) displays the lowest content in HREE and Y (118–171 ppm) with a slightly negative HREE slope expressed by Gd_N/Yb_N = 1.6–2.8 (Fig. 4d). The medium-grey CL zone has somewhat higher Y (166–377 ppm) and HREE content with a flatter HREE pattern (Gd_N/Yb_N = 1.1–1.8). The analysed inherited core displays the highest Y (1060 ppm) and steepest HREE slope (Gd_N/Yb_N = 0.13).

In the osumilite gneiss (ALR 13-58) zircon are pale pink and rounded. They occasionally preserve corroded oscillatory-zoned cores surrounded by a CL-dark mantle and eventually a thin (< 5μm) CL-bright rim (Fig. 2e, grain 8). Alternatively, CL-bright zircon develops in the centre of CL-dark featureless crystals (Fig. 2e, grain 6). Some smaller grains (< 75 μm) display sector zoning (Fig. 2e, grain 9). The CL intensity of the different textural groups is again negatively correlated with U content (Fig. 3e), but not with CL activator elements like Dy and Gd that show similar concentration in all zones (Tab. 1). The CL-bright parts of the crystals are characterized by consistently high Th/U ~ 1, variable Y (186–707 ppm) and flat HREE pattern (Gd_N/Yb_N = 0.6–1.8; Fig. 4e). Featureless CL-dark zones also display flat HREE pattern (Gd_N/Yb_N = 1.1–1.8) and low Y (133–283 ppm) but have higher Th/U (0.18–0.69). The sector zoned zircon are distinguished from CL-dark zircon by their very low Th (< 110 ppm; Fig. 3e). The oscillatory zoned cores display variable Th/U signature that are again related to their CL luminescence with the brightest core yielding Th/U similar to the CL-bright sector-zoned part of the grains. One atypical crystal (Fig. 2e, grain 12) displays a thick oscillatory zoned CL-bright rim overgrowing a CL-dark central part of the grain, that has very high Y concentration (Y = 2763 ppm) and the steepest HREE slope (Gd_N/Yb_N = 0.6) compared to the other populations. This rim may correspond to the thin CL-bright rim observed on most of the grains that were too small (< 5 μm) to analyse (Fig. 2e).

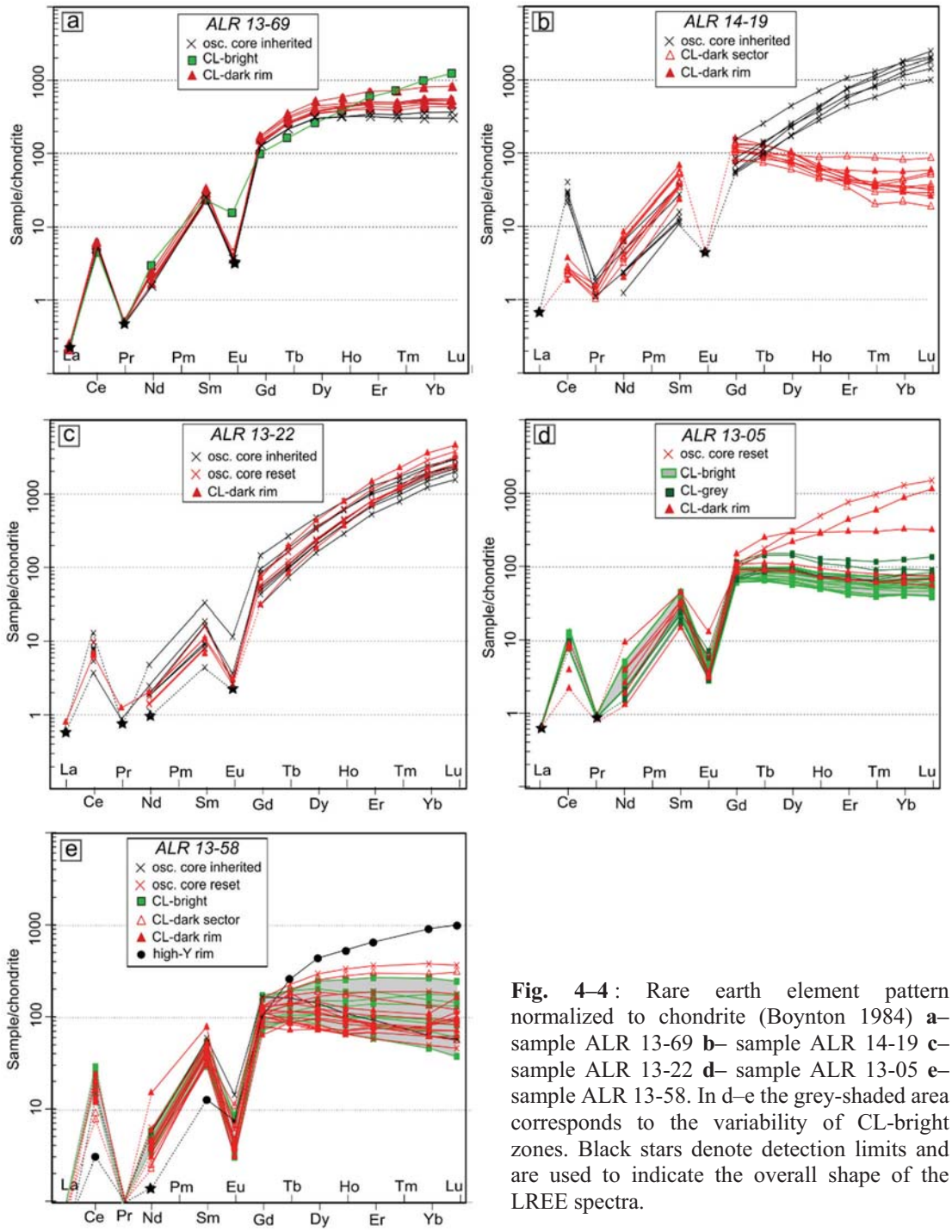

Fig. 4–4 : Rare earth element pattern normalized to chondrite (Boynton 1984) **a**– sample ALR 13-69 **b**– sample ALR 14-19 **c**– sample ALR 13-22 **d**– sample ALR 13-05 **e**– sample ALR 13-58. In d–e the grey-shaded area corresponds to the variability of CL-bright zones. Black stars denote detection limits and are used to indicate the overall shape of the LREE spectra.

Zircon U–Pb geochronology

Zircon U–Pb analyses (Tab. 2–6) are presented in Tera-Wasserburg plot (Fig. 5) and are complemented by selected binary plots illustrating variation of chemical parameters and radiation damage through time (Fig. 6). Radiation damage is calculated as a dose of α-decay events per gram since zircon crystallization given by its $^{206}Pb/^{238}U$ age, following the formula and procedure described in Ewing et al. (2003).

In sample *ALR 13-69*, 19 SIMS analyses in 14 grains, targeting metamorphic zones, were performed (Tab. 2; Fig. 2a). Partially resorbed oscillatory cores yield a weighted average

$^{206}Pb/^{238}U$ age of 1073 ± 10 Ma (Fig. 5a; MSWD = 0.6; n = 3) that may well represent the age of the protolith. The bulk of the CL-dark zone display excess scatter in $^{206}Pb/^{238}U$ age, ranging from 1042 ± 18 to 1002 ± 16 Ma. Thirteen analyses of CL-dark zones nevertheless yield a weighted average $^{206}Pb/^{238}U$ age of 1028 ± 7 Ma (Fig. 5a; MSWD = 1.3; n = 13) while the two remaining analyses yield a younger age equivalent to that of the CL-bright mottled zone at 1002 ± 10 Ma (MSWD = 0.1; n = 3; Fig. 5a). The CL-dark rims have accumulated an alpha dose of 19–32.10^{17} $\alpha.g^{-1}$ since their crystallization without obvious disturbance of U–Pb systematics (Fig. 6a).

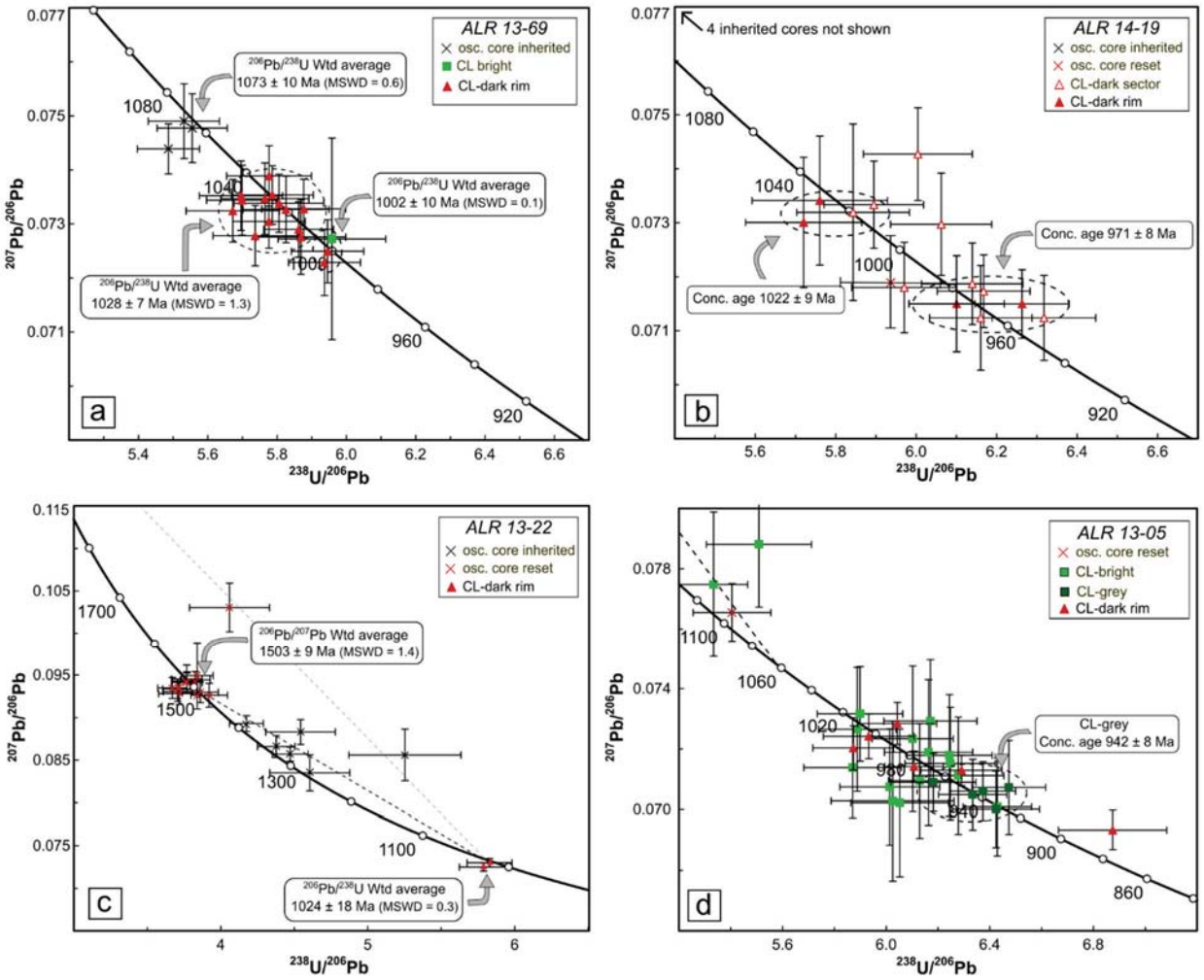

Fig. 4–5: Zircon U–Pb geochronology presented in Tera-Wasserburg diagrams **a**– sample *ALR 13-69* **b**– sample *ALR 14-19* **c**– In sample *ALR 13-22* **d**– sample *ALR 13-05* (inherited cores older than 1120 Ma not shown) All error crosses are 2σ, decay constant errors are included in the pooled ages.

In sample *ALR 14-19*, 20 analyses were collected in 16 grain (Tab. 3; Fig. 2b). Inherited cores have individual $^{206}Pb/^{207}Pb$ ages ranging from 2.69 to 1.47 Ga (Fig. 6b) with one younger spot at 1.00 Ga representing the high-U external margin of an oscillatory grain that has

accumulated an alpha dose over 40.10^{17} $\alpha.g^{-1}$. In contrast, inherited core that kept their presumably original U–Pb ratio did accumulate less than 4.10^{17} $\alpha.g^{-1}$ at the time of Sveconorwegian metamorphism (Fig. 6b). Four pristine core together with the high-U exterior define a loose discordia between 1577 ± 72 and 1027 ± 48 Ma (MSWD = 1.5; not shown). At least two Mesoproterozoic cores are characterized by unstable Pb signal resulting in large observed uncertainties in the $^{206}Pb/^{207}Pb$ ratio (> 2.0 %; σ) with one point (1419-09a) showing significant reverse discordance. Analyses retrieved from CL-dark rims and stubby zircon define a $^{206}Pb/^{238}U$ age spread between 1039 ± 28 Ma and 955 ± 17 Ma (Fig. 5b). Two modes may be identified, independently of the described CL textures, at 1022 ± 9 Ma (Fig. 5b; concordia age; 2σ; n = 4) and 971 ± 8 (Fig. 5b; concordia age; 2σ; n = 7).

In sample *ALR 13-22*, twenty SIMS analyses were performed on 14 grains (Tab. 4; Fig. 2c). Twelve spots in oscillatory zoned cores define a single population with a $^{207}Pb/^{206}Pb$ weighted average of 1503 ± 9 Ma (Fig. 5c; 2σ; MSWD = 1.4). One discordant analysis with a $^{207}Pb/^{206}Pb$ age of 1689 ± 52 Ma, corresponding to a CL-bright unzoned core surrounded by a thick oscillatory rim, testifies of older inheritance. Two blurred CL-dark rims with Th/U < 0.10 yields a weighted average $^{206}Pb/^{238}U$ age of 1024 ± 18 Ma (Fig. 5c; 2σ; MSWD = 0.3) interpreted as the age of crystallization of the rim. High-U blurred oscillatory cores define an array of apparent ages between *c*. 1400 and 1270 Ma

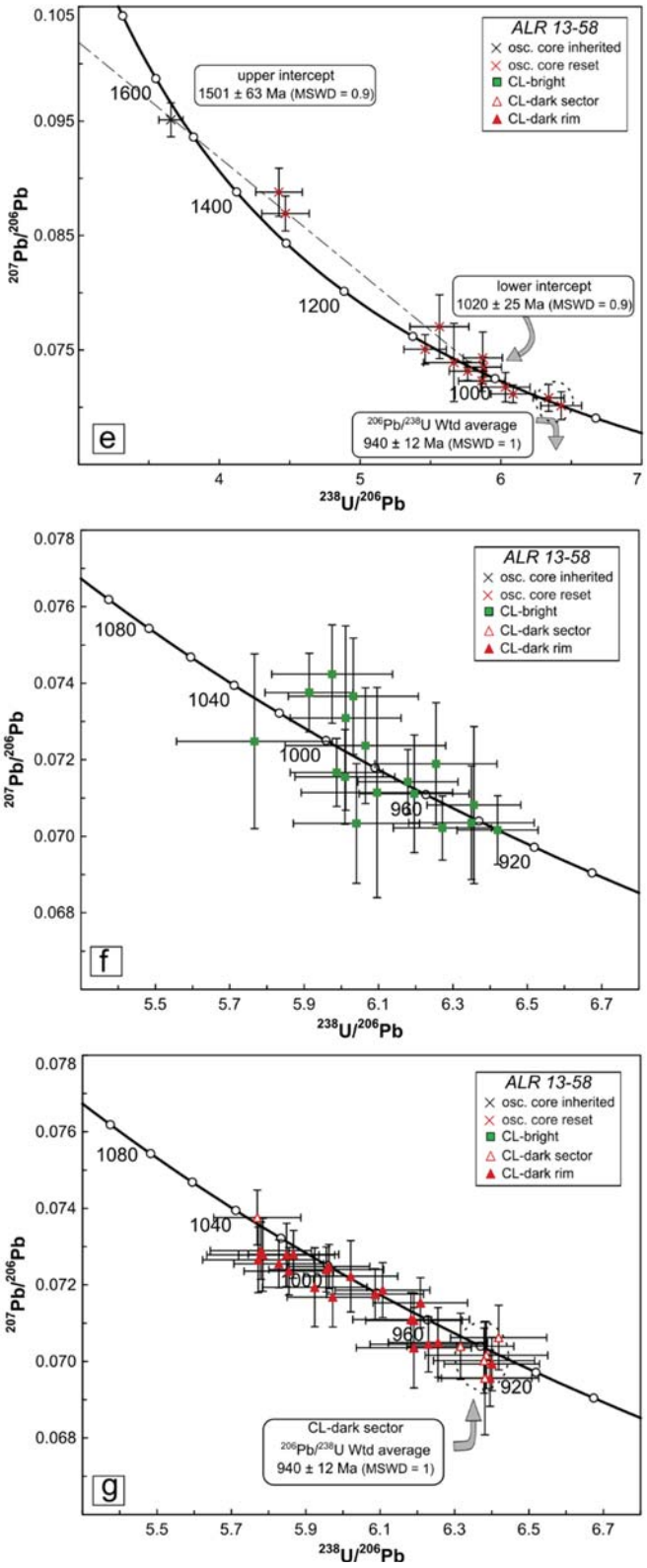

Fig. 4–5 : **e**– inherited cores in sample *ALR 13-58* **f**– CL-bright zones in sample *ALR 13-58* **g**– CL-dark featureless rims and CL-dark sector-zoned crystals in sample *ALR 13-58*.

lying along the discordia between 1500 and 1030 Ma. The alpha dose received by zircon crystals since their crystallization is negatively correlated with the apparent $^{206}Pb/^{238}U$ age (Fig. 6c). Uranium-rich parts of the crystals accumulated more than 50.10^{17} $\alpha.g^{-1}$ whereas oscillatory inherited cores are mostly below 30.10^{17} $\alpha.g^{-1}$ (Fig. 6c). We have also calculated the alpha dose received by zircon in the 1500–1030 time interval assuming a model age of 1500 Ma for all grains derived from the $^{207}Pb/^{206}Pb$ weighted average of 1503 ± 9 Ma from the oscillatory-zoned cores. In this model, the oscillatory-zoned cores accumulated less than 15.10^{17} $\alpha.g^{-1}$ whereas the blurred part of the grains accumulated mostly more than 24.10^{17} $\alpha.g^{-1}$.

In sample *ALR 13-05*, 33 analyses are reported in 19 grains (Tab. 5; Fig. 2d). Three analyses of inherited cores define a discordia line between 1475 ± 100 Ma and 1063 ± 91 Ma, with one additional analysis affected by severe reverse discordance (Fig. 5d). The three oldest spots retrieved from CL-dark zones of the crystals define a cluster with a concordia age of 1000 ± 9 Ma while the three youngest analyses from CL-dark zones correlate with higher alpha dose (up to 50 1017 α.g-1; Fig. 6d) suggesting post-crystallization disturbance. The CL-bright zone (II; Fig. 2d) displays a scatter of ages between 1014 ± 30 Ma and 932 ± 18 Ma with two older (> 1100 Ma) discordant spots. Individual ages are not correlated with the alpha dose (< 6.10^{17} $\alpha.g^{-1}$; Fig. 6d) and do not show covariation with any of the measured chemical parameters. Finally, five spots located in the innermost medium-grey CL zone yield a concordia age of 942 ± 8 Ma (Fig. 5d). In this sample, the apparent U–Pb age increases from the core to the rim in concentrically zoned grains (Fig. 2d). This is also evident when considering the pooled ages of the different zones.

In sample *ALR 13-58*, a total of 61 analyses were achieved in 43 grains (Tab. 6; Fig. 2e). Twelve oscillatory zoned cores define a discordia between 1501 ± 63 Ma and 1020 ± 25 Ma (Fig. 5e; MSWD = 0.9) although the apparent age of individual spots is not correlated with radiation damage (Fig. 6e). Two additional oscillatory cores with low U and high Th/U (> 0.8) yield a $^{206}Pb/^{238}U$ age of 940 ± 12 Ma (Fig. 5e; MSWD=1). Despite its homogenous chemistry, the CL-bright zone display $^{206}Pb/^{238}U$ ages spreading from 1031 ± 34 down to 942 ± 18 Ma with no clear age clustering (Fig. 5f). CL-dark part of the grain show a quasi-similar $^{206}Pb/^{238}U$ age spread ranging from 1030 ± 20 down to 936 ± 18 Ma (Fig. 5g). The 8 oldest spots retrieved from CL-dark zone yield a weighted $^{206}Pb/^{238}U$ average of 1022 ± 8 Ma (MSWD = 0.4) and the low-Th sector zoned zircon cluster at 940 ± 12 Ma (MSWD = 0.1), except one analysis yielding a $^{206}Pb/^{238}U$ age of 1030 ± 20 Ma.

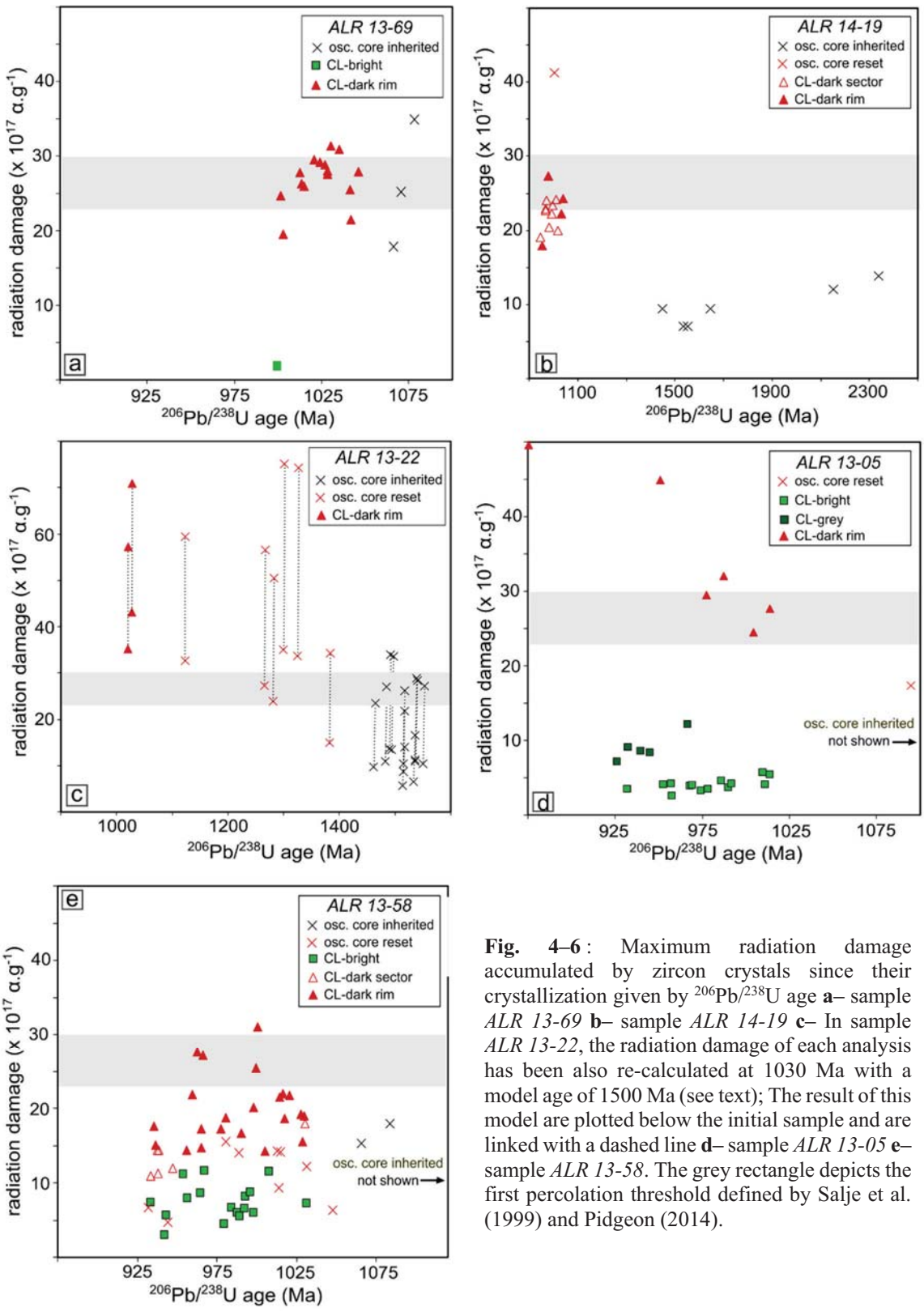

Fig. 4–6 : Maximum radiation damage accumulated by zircon crystals since their crystallization given by $^{206}Pb/^{238}U$ age **a**– sample *ALR 13-69* **b**– sample *ALR 14-19* **c**– In sample *ALR 13-22*, the radiation damage of each analysis has been also re-calculated at 1030 Ma with a model age of 1500 Ma (see text); The result of this model are plotted below the initial sample and are linked with a dashed line **d**– sample *ALR 13-05* **e**– sample *ALR 13-58*. The grey rectangle depicts the first percolation threshold defined by Salje et al. (1999) and Pidgeon (2014).

Comparing monazite and zircon age record through time and space

Sveconorwegian (metamorphic) zircon display flat HREE pattern in garnet-present samples (Fig. 4), suggesting garnet–zircon equilibrium from c. 1030 Ma down to 930 Ma (Whitehouse and Platt 2003; Hermann and Rubatto 2003; Kelly and Harley 2005). The apparent stability of zircon chemical signature through time strongly contrasts with that of monazite. Indeed, in samples *ALR 13-58* it has been shown that the high-Y population at 935 ± 7 Ma signs UHT garnet breakdown while two older S-bearing monazite generations, differing in their cheralite and huttonite content were identified (Chp. 2). As a consequence, we have plotted probability diagrams for sample *ALR 13-58* representing the different monazite chemical populations while CL-dark zircon are plotted as a single group for samples *ALR 13-69* and *14-19* and are split between CL-dark featureless rims and CL-dark sector-zoned zircon for sample *ALR 13-58*. Zircon analyses showing more than 3 % discordance, calculated as ([$^{206}Pb/^{207}Pb$ age – $^{206}Pb/^{238}U$ age]/ $^{206}Pb/^{238}U$ age) are not plotted in the probability diagrams (Tab. 2–6).

In the regional metamorphic basement represented by the garnet–biotite sample *ALR 13-69*, zircon and monazite display overall similar age distribution with a probability maximum in the c. 1040–1000 Ma time interval (Fig. 7a). In this titanite-present sample, Ti-in-zircon thermometry indicates crystallization temperature between 740–760 °C, in accordance with petrological constrains indicating a metamorphic peak at c. 750 °C at 5 kbar (Fig. 7b). We thus interpret the dominant zircon population at 1028 ± 7 Ma (Fig. 5a) to represent near peak conditions, with the crystallization of last melt and sporadic annealing occurring around 1002 ± 10 Ma (Tab. 2), in good agreement with the regional metamorphism timing proposed by Bingen and Van Breemen (1998) and Bingen et al. (2008a). The $^{206}Pb/^{207}Pb$ mean age of 1038± 9 Ma recorded by monazite is slightly older than that of zircon.

The cordierite–hercynite gneiss (*ALR 14-19*), sampled near the orthopyroxene isograd, displays a protracted zircon and monazite age record (Fig.7c). Monazite show a dominant age group at c. 1040–1020 Ma yielding a weighted $^{206}Pb/^{238}U$ age of 1035 ± 7 Ma (Chp. 3), with minor crystallization at 955 ± 22 Ma (Chp. 3). Zircon also displays two age groups at 1022 ± 9 Ma and 971 ± 8 Ma (Fig. 5b) with the youngest spot yielding 955 ± 17 Ma (Tab. 3). Ti-in-zircon thermometry above 760 °C defines a minimum crystallization temperature, given the lack of Ti-buffering assemblage (Fig. 7d). This temperature is consistent with crystallization of zircon in the presence of a silicate melt given the modelled solidus of c. 780 °C in this sample (Fig. 5a of Chp. 3).

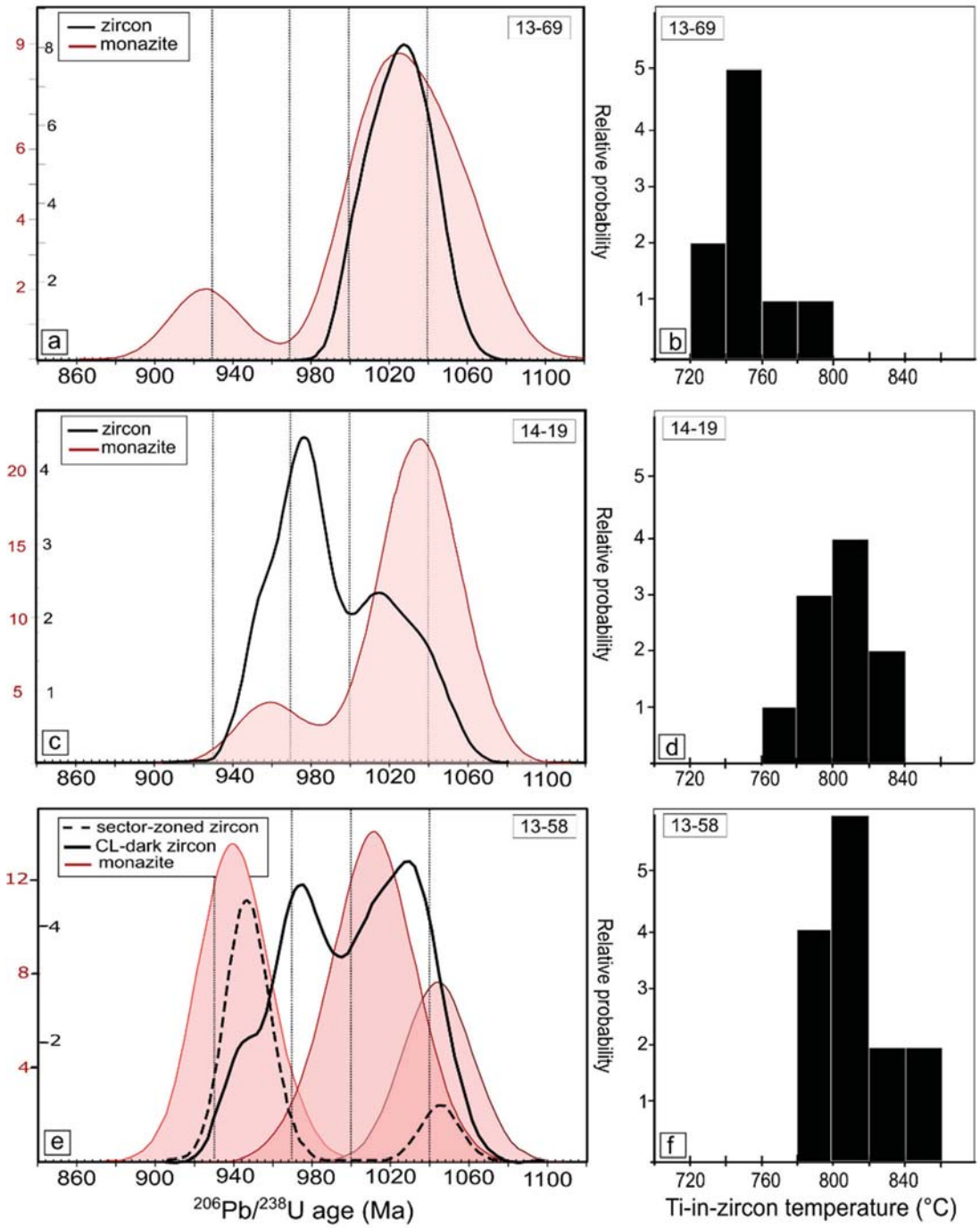

Fig. 4–7: Zircon and monazite U–Pb age record and Ti-in-zircon thermometry along the thermal gradient defined by various mineral isograd in Fig. 1b. The zircon dataset has been filtered out for discordant analyses (see text). **a**– Weighted probability diagram for monazite and CL-dark zircon in sample *ALR 13-69* representing the regional metamorphic basement outside the opx-isograd **b**– Frequency histogram of Ti-in-zircon thermometry in sample *ALR 13-69* **c**–Weighted probability diagram for monazite and CL-dark zircon in sample *ALR 14-19*, representative of the opx-in isograd **d**– Frequency histogram of Ti-in-zircon thermometry in sample *ALR 14-19* **e**–Weighted probability diagram for monazite, CL-dark zircon and CL-dark sector-zoned zircon in osumilite-bearing sample *ALR 13-58*, representative of the UHT area **f**– Frequency histogram of Ti-in-zircon thermometry in sample *ALR 13-58*. The weighted probability diagrams were generated with Isoplot/Ex v.3.75 (Ludwig 2008).

Within the UHT zone, the zircon record depends strongly on the investigated sample. In restitic lithologies that underwent early melt-loss such as the sapphirine gneiss (*ALR 13-22*; Chp. 3), zircon has only sparsely reacted at 1024 ± 18 Ma (Fig. 5c) and does not carry a record of younger events. Contrastingly, the osumilite gneiss (*ALR 13-58*) provides the most complete

record of the long-lasting metamorphic history (Fig. 7e). The onset of metamorphism in this sample is recorded by S-rich monazite crystals related to granulite-facies sulphide breakdown at 1034 ± 6 Ma (Chp. 2). It is also recorded by the zircon age distribution, in which the oldest population gives an age of 1022 ± 8 Ma (Fig. 5e), identical within the error. In this sample, zircon and monazite display an abundant U–Pb age record around 1000 Ma resulting in a probability peak (Fig. 7e). There is also a zircon probability peak at c. 970 Ma (Fig. 7e) similar to that observed in the opx-zone sample (Fig. 7c). Well identified monazite generation then grew at 935 ± 7 Ma (Chp. 3), together with the younger stubby sector zoned zircon at 940 ± 12 Ma (Fig. 5g).

Zircon oxygen isotopes

In sample *ALR 14-19*, c. 1.5 Ga zircon inherited cores preserve variable $\delta^{18}O$ between 5.70 ± 0.18 ‰ and 7.75 ± 0.17 ‰ with three older (> 1.6 Ga) cores displaying higher $\delta^{18}O$ values between 7.17 ± 0.16 and 9.41 ± 0.18 ‰ (Fig. 8a). In contrast, the Sveconorwegian CL dark group preserve a homogenous $\delta^{18}O$ value of 10.13 ± 0.14 ‰ (2σ; MSWD = 1.4; n = 12). The reset oscillatory cores display a $\delta^{18}O$ value of 10.04 ± 0.34 ‰ identical within the error to that of Sveconorwegian zircon.

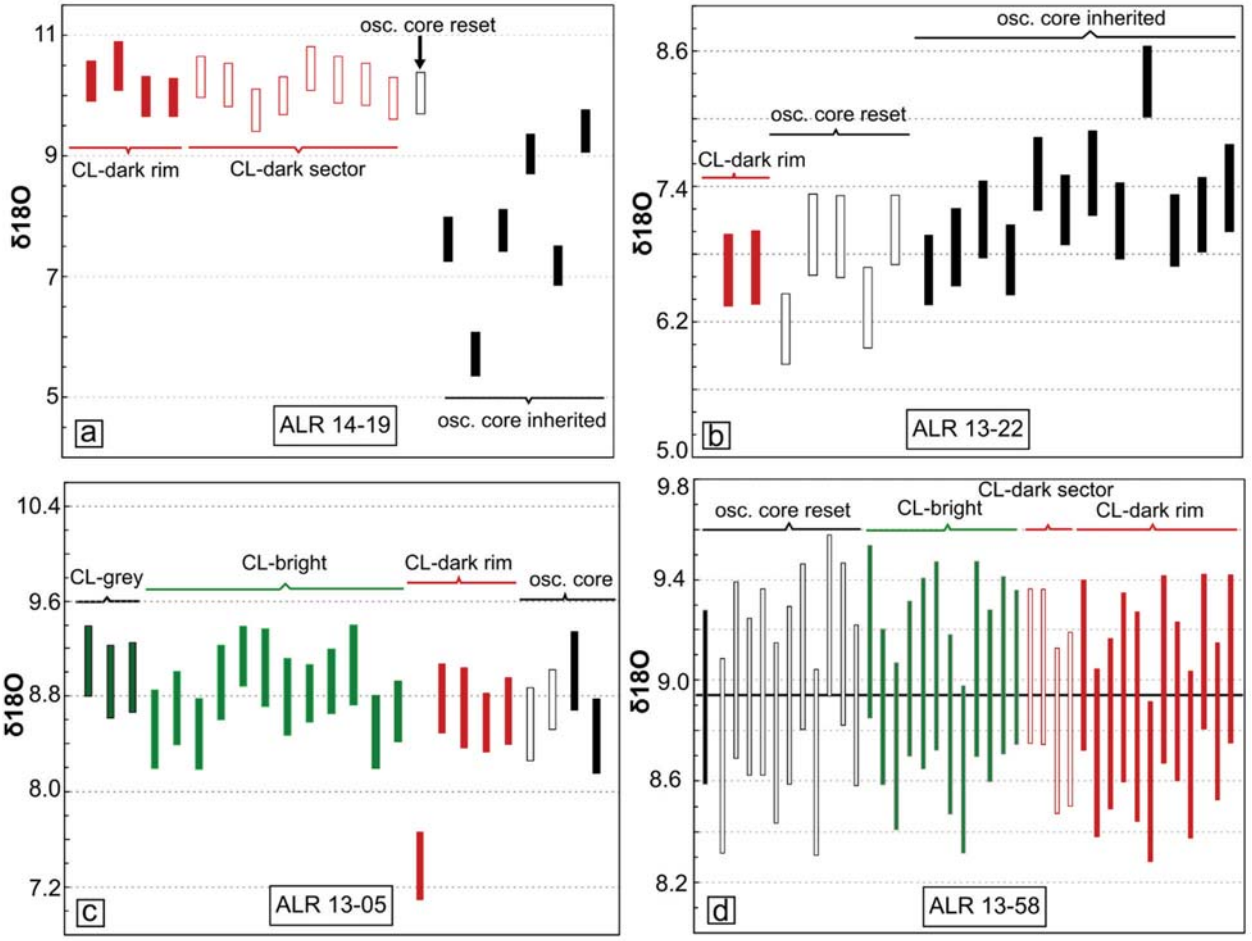

↑ **Fig. 4–8** : δ18O diagram for zircon in-situ analyses. **a–** sample ALR 14-19 **b–** sample ALR 13-22 **c–** sample ALR 13-05, the CL-dark outlier represents the U–Pb discordant analysis with apparent 206Pb/238U age younger than 900 Ma (see Fig. 5d) **d–** sample ALR 13-58. The analyses are sorted by textural groups defined in text and then by decreasing age from right to left.

In the sample *ALR 13-22*, the c. 1.50 Ga pristine oscillatory cores yield $\delta^{18}O$ values of 6.75 ± 0.16 ‰ to 8.33 ± 0.16 ‰ (Fig. 8b). When comparing $\delta^{18}O$ values in individual grains, the partially reset blurred oscillatory zones display consistently lower $\delta^{18}O$ values than the pristine cores (Fig. 2c).

In sample *ALR 13-05*, the $\delta^{18}O$ value for oscillatory zoned core ($\delta^{18}O$ = 8.93 ± 0.12 ‰; 2σ; MSWD = 1; n = 8) is equivalent within the error to that of the CL-bright and medium-grey zone yielding $\delta^{18}O$ values of 8.80 ± 0.14 ‰ (2σ; MSWD = 2.4; n = 12) and 8.99 ± 0.17 ‰ (2σ; MSWD = 0.4; n = 3), respectively (Fig. 8c). The CL-dark part of the grain shows the lowest $\delta^{18}O$ value of 8.67 ± 0.14 ‰ (2σ; MSWD = 0.4; n = 4).

Within the highest grade sample (*ALR 13-58*), no significant variation of oxygen isotopic composition is detected either between grains or between different textural zones of a single grain (Fig. 8d): $\delta^{18}O$ of inherited core = 8.93 ± 0.12 ‰ (2σ; MSWD = 1; n = 8); $\delta^{18}O$ of CL-dark zone = 8.91 ± 0.08 ‰ (2σ; MSWD = 0.9; n = 17); $\delta^{18}O$ CL-bright zone = 8.96 ± 0.10 ‰ (MSWD = 0.9; n = 12)

Scanning ion Imaging

Scanning ion images were acquired in three samples, *ALR 13-22* (1 grain), *ALR 13-05* (3 grains) and *ALR 14-19* (1 grain). Within the two highest grade samples (*ALR 13-22* and *13-05*) no micron-scale heterogeneities were imaged. The U map mirrors the BSE and CL images recording growth zoning (not shown). Within sample *ALR 14-19*, one inherited core ($^{206}Pb/^{238}U$ date = 1534 ± 27 Ma; grain 9; Fig. 9) with low U (109 ppm) and Th (50 ppm) concentration revealed heteregenous distribution of Pb at the micron scale (Fig. 9a). In the Sveconorwegian CL-dark rim Pb patchiness is absent or undetected.

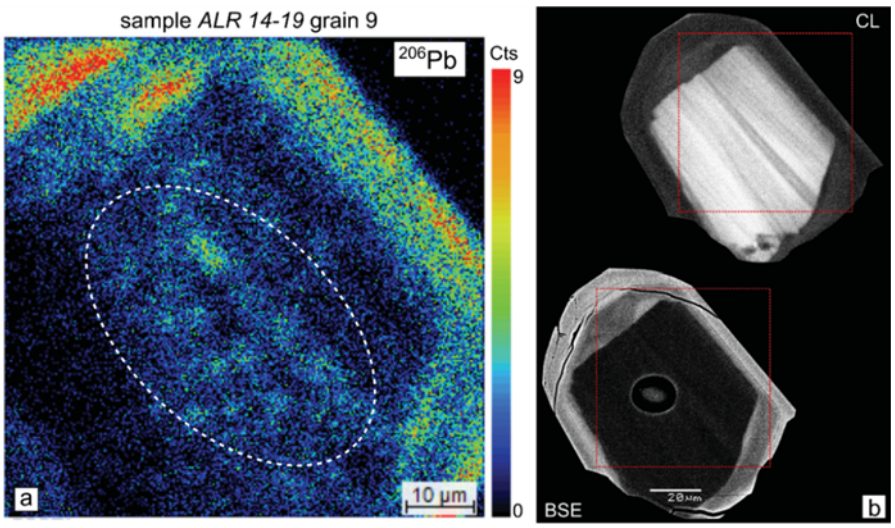

↑ **Fig. 4–9**: Patchy Pb distribution at the micron scale within sample *ALR 14-19*. **a–** ^{206}Pb SIMS map showing lumpy Pb distribution in zircon n°9 inherited core. **b–** high-contrast CL and BSE images of the same grain; note location of U–Pb spot 9a on the BSE image.

Discussion

Response of O isotopes

In sample *ALR 14-19* and *13-22,* inherited zircons clustering at c. 1.50 Ga display $\delta^{18}O$ value between c. 5.70 ‰ and 8.33 ‰ (n = 14). These values are similar to the $\delta^{18}O$ range (5.4 ± 0.9 to 8.7 ± 1.2 ‰) and U–Pb ages reported by Roberts et al. (2013) for meta-granitoids making up the Telemarkia basement. As a consequence, we postulate that these O isotopic compositions were not modified during granulite facies metamorphism temperature in excess of 800 °C. This observation suggests that the dry $\delta^{18}O$ diffusion coefficient of Watson and Cherniak (1997) is applicable to granulite facies rocks (Valley et al. 2003). Moreover, we expect that inherited cores coming from our samples *ALR 13-58* and *13-05* (same metasedimentary unit) would also display initial $\delta^{18}O$ values ranging from 5.4 ± 0.9 to 8.7 ± 1.2 ‰.

Within the highest grade samples *ALR 13-05* and *13-58*, O isotopic signature is equivalent within the error for all identified chemical domains including inherited core, suggesting either equilibrium at the sample scale and hence effective O diffusion during UHT metamorphism or intrinsically closed-system behaviour of $\delta^{18}O$ during recrystallization (Martin et al. 2008; see also discussion below). The first inference seems reasonable when comparing the petrological constrains of our samples with experimental data of Cherniak (2010; their Fig. 16) indicating that a grain of 120 µm is equilibrated for 1 My residence at 950 °C or 10 My at 900 °C. The rather high $\delta^{18}O$ values (8.67 ± 0.14 ‰ to 10.04 ± 0.34 ‰) retrieved from Sveconorwegian zircon in samples 13-58, 13-05 and 14-19 compared to the magmatic-like value of inherited zircon is consistent with equilibration in a melt derived from the anatexis of supracrustal material. Whole-rock O isotopic analyses from granitic gneiss and aluminous gneiss in the UHT zone yield similar $\delta^{18}O$ range of 7.1–9.8 ‰ (Demaiffe and Javoy 1980; Wilmart et al. 1994). A high $\delta^{18}O$ reservoir is represented in the area by marbles and quartzite from the Faurefjel unit, which are characterized by $\delta^{18}O_{quartz}$ in quartzite of 10.6–16.0 ‰ and $\delta^{18}O_{calcite}$ in marbles of 13.1–20.4 ‰ (Bol et al. 1995).

Processes of zircon U–Pb partial resetting

Within the studied samples, we identify two complementary processes that reset the U–Pb geochronometres of zircon during granulite facies metamorphism. The first resetting process is similar to the diffusion–reaction mechanism of Geisler et al. (2007). Indeed, zircon inherited cores from all investigated samples defines arrays of sub-concordant analyses between their

crystallization age at *c*. 1.50 Ga and the onset of Sveconorwegian metamorphism at *c*. 1030 Ma. The apparent U–Pb age of blurred oscillatory zones decreases with increasing alpha radiation damage along with an enrichment in Y+ Hf. These trends are best explained in term of Pb loss by diffusion in metamict connected volumes of the zircon during Sveconorwegian metamorphism (lower intercept). Zircon crystals that have accumulated radiation damage above a dose of *c*. 30.10^{17} $\alpha.g^{-1}$ (Salje et al. 1999; revised to 22.10^{17} by Pidgeon 2014) show an increasing amount of amorphous material leading to an interconnected percolating network enhancing Pb diffusion (Step 2 of Murakami et al. 1991). This process is best illustrated in sample *ALR 13-22* where zircon crystals with a model age of 1500 Ma that have crossed the first percolation transition of 22.10^{17} $\alpha.g^{-1}$ prior to the onset of Sveconorwegian metamorphism (c. 1035 Ma) have been partially reset, whereas crystals below this radiation dose kept their original U–Pb age (Fig. 6c). The presence of convex front cross-cutting the oscillatory core of totally reset crystals (Fig. 2c) together with their lower $\delta^{18}O$ isotopic signature (Fig. 2c) suggest the involvement of a fluid.

The second identified resetting process consists of a solid-state recrystallization of damaged parts of zircon crystals. In the highest grade samples *ALR 13-58* and *13-05* this process is evidenced by highly luminescent zones located in grain interior consisting either of prismatic inherited core displaying oscillatory zoning (e.g. Fig. 2d–e) or concentric zones with polygonal sector zoning superimposed on faint oscillatory zoning (e.g. Fig. 2d, grain 04). These bright zones show a consistent chemistry between the two samples with Th/U close to unity and flat HREE pattern (Fig. 4d–e), in strong contrast to that of inherited core and CL-dark metamorphic overgrowth. In sample *ALR 13-05*, and to a lesser extent in *ALR 13-58*, zircon crystals show inverse age zoning, i.e. younger cores than rims (Fig. 2d–e; Fig. 5d–g), which cannot be explained as simple overgrowth or volume diffusion. Such inconsistent relationships are well known in granulite facies zircon since the early work of Vavra et al. (1999) who described zircon population where the innermost zone characterized by faint relict of primary zoning is the most affected by age rejuvenation. Additionally, we do not find clear evidence of chemical reaction front cross-cutting previous zoning or infill with contrasting chemistry that would be expected in case of multiple events of dissolution precipitation in response to a changing chemical environment (Whitehouse and Platt 2003). Based on textural relationships and reverse age zoning observed both at the scale of individual grains and at the chemical population scale, we suggest that the CL bright zones represent recrystallization of older structurally instable part of the grain interior without changing its exterior shape.

We propose a three step process to explain the occurrence of concentrically zoned grain with inverse age zoning in sample *ALR 13-05* and *13-58* (Fig.9). The first step takes place during prograde melting of a rock package containing detrital zircon that will partly dissolve in silicate

melt (Kelsey et al. 2008; Yakymchuk and Brown 2014). Simultaneously, undissolved part of detrital grains that have accumulated enough radiation damage to reach the first percolation point of Salje et al. (1999) will suffer Pb loss as demonstrated for sample *ALR 13-22* and eventual recrystallization testified by thin CL-bright corona on detrital cores (Fig. 2b, grain 01). This zircon behaviour was also recognized by Kooijman et al. (2011) in UHT samples where anhedral CL-bright corona replacing detrital zircon core is interpreted as a recrystallization in response to chemical or structural instability. Depending on local saturation of the silicate melt in Zr, linked with transfer or trapping of melts, a U-rich zircon rim may growth on the partially reset cores. This first stage is recorded in sample *ALR 13-05* and *13-58* by the oldest CL-bright zone age at 1014 ± 30 Ma and 1031 ± 34 Ma respectively which overlaps with the oldest crystallization age of CL dark rims at 1009 ± 9 Ma in sample *ALR 13-05* and at c. 1022 ± 8 Ma in sample *ALR 13-58*.

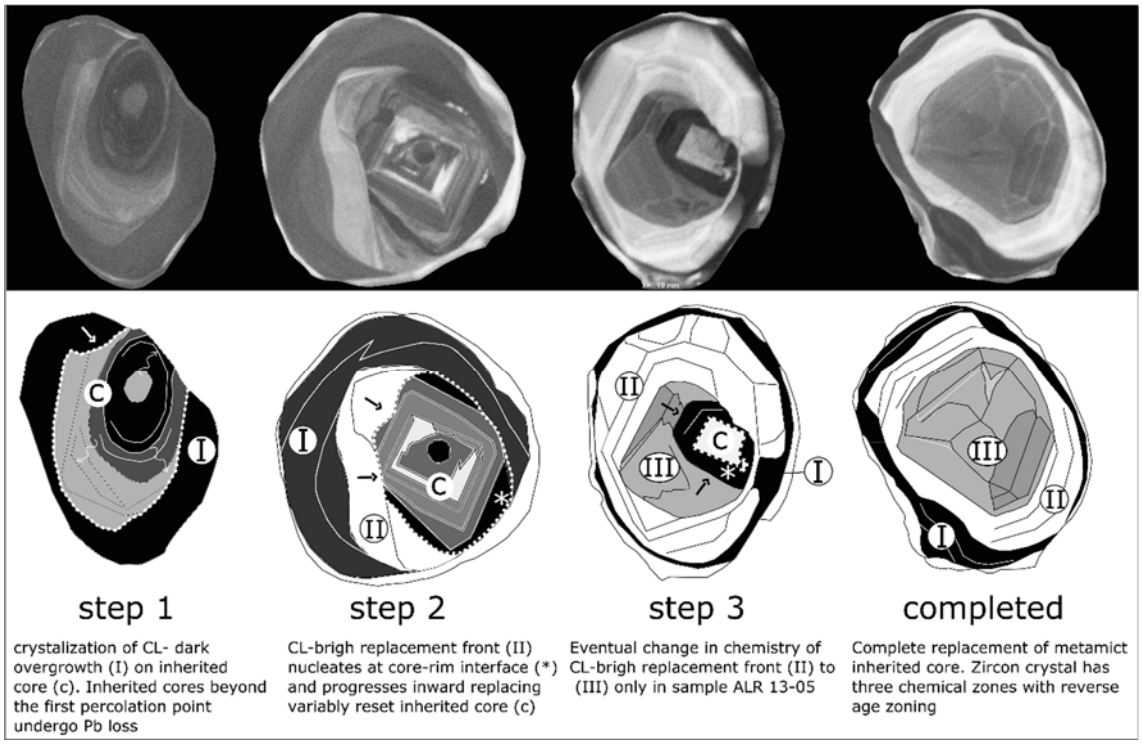

Fig. 4–10: Three step process to explain the occurrence of inverse age zoning in zircon

The second step consists in the development of a CL dark moat around the core remnant, a common feature in high grade zircon (Hoskin and Schaltegger 2003), that may act as reservoir interface for trace element exchange during recrystallization or recovery (Marsh and Stockli 2015). Third stage involves replacement of damaged part of the inherited core by CL-bright zircon following a gradual recovery probably controlled by epitaxial growth at the crystalline–amorphous boundaries as proposed by (Nasdala et al. 2005). The efficiency of this process would be essentially controlled by the interplay between temperature and time, i.e. heating or cooling rates and result in a zircon patchwork with various radiogenic Pb retention. In our samples, recrystallization is accompanied by unusual preferential expulsion of U over Th in the

recrystallized parts resulting in a very characteristic Th/U ~ 1 signature (Fig. 3d–e). This observation is different from many other studies where Th is preferentially expulsed from the recrystallized lattice over U cation because of its larger size (Hoskin and Black 2000) even though metamorphic zircons with high Th/U are not unusual (e.g. Vavra et al. 1999; Möller et al. 2002). The HREE pattern of the bright zones is flat whereas inherited cores mostly display very steep patterns. This observation may be interpreted either as a feature resulting of chemical equilibrium between garnet and zircon or by expulsion of REE from the recrystallized lattice.

The third step, is observed only in sample 13-05 where an inner CL-grey zone with contrasting chemistry nucleates at the interface between the metamict core and CL dark moat. In contrast with the CL-bright zone, the CL grey interior display Th/U < 0.1 and a consistent age of 942 ± 8 Ma. To explain the difference in U–Pb age record between CL-bright and CL-grey, we propose that fast heating at c. 940 Ma results in complete resetting of the U–Pb system with geologically instantaneous recovery while prolonged residence of zircon crystals at T > 750 °C (Geisler 2002) will promote slow recovery resulting in a patchwork of domains with different U–Pb closure age superimposed on variable reincorporation of unsupported radiogenic Pb. An alternative explanation is that the final heating stage allows to recrystallize even the most damaged zircon that have lost most of their radiogenic Pb.

Insight from Pb distribution

Within the highest grade samples, scanning ion imaging did not provide evidence of micrometric Pb heterogeneities in the CL-dark part of the investigated grains. As a consequence, the measured U–Pb dates may provisionally be interpreted as geological ages in the following discussion section. Besides, in the distal sample *ALR 14-19* that did not reach UHT conditions, ion mapping reveals heterogeneous distribution of radiogenic Pb in the inherited cores, the metamorphic rims being unaffected. The occurrence of Pb spots located in a low-U grain that has accumulated less than 3.10^{17} $\alpha.g^{-1}$ prior to the onset of Sveconorwegian metamorphism confirms the observation of Whitehouse et al. (2014) that zircon does not need to be metamict to display Pb heterogeneities, pointing to the operation of other mechanism, perhaps induced by rock deformation (Piazolo et al. 2016).

Tracking melt-present conditions in slow granulite

For our understanding of orogenic processes, it is crucial to decipher the timing of zircon population representing new growth. In fact, all the investigated samples contain stubby sector zoned zircon or CL-dark rims that are expected to crystallize from a silicate melt (Hoskin and Schaltegger 2003; Harley et al. 2007) and thus represents overgrowths. As a consequence, the U–

Pb age distribution of those parts of the crystals coupled to Ti-in-zircon thermometry may provide valuable information regarding crystallization temperature and presence of silicate melt through time (Fig. 7). Additionally, the comparison of the zircon and monazite U–Pb age records takes advantage of the contrasting strengths and weaknesses of these two minerals as geochronometer. Indeed, zircon is dramatically affected by radiation damage as described above, while monazite remains virtually unaffected, despite extremely high concentrations of U and Th resulting in alpha decay doses in the range of 10^{19}–10^{20} $\alpha.g^{-1}$ (Seydoux-Guillaume et al. 2004). On the other hand, monazite is very sensitive to U–Pb resetting as a result of dissolution–precipitation in the presence of alkali fluids, even at low-temperature (e.g. Rasmussen et al. 2006; Seydoux-Guillaume et al. 2012; Didier et al. 2013), whereas pristine zircon is much more resilient (e.g. Taylor et al. 2014). Finally, dissolution rate and saturation temperature of monazite and zircon in silicate melt are different (Watson and Harrison 1983; Kelsey et al. 2008; Stepanov et al. 2012) and controlled by elements (LREE; Zr) that are not incorporated in the same metamorphic minerals (Bea 1996). As a consequence, it is expected that monazite and zircon do not record identical U–Pb ages but rather provides complementary information.

All the investigated samples record widespread monazite and zircon growth in the c. 1040–990 Ma time interval (Fig. 7; Chp. 3), corresponding to regional granulite facies metamorphism (Bingen and Van Breemen 1998; Möller et al. 2002; Bingen et al. 2008a; Chp. 3). Although the range of individual U–Pb analyses of monazite and zircon largely overlap within the error, the statistical probability peak of CL-dark zircon is always younger than that of monazite by some 10–15 My (Fig. 7). It suggests that monazite keeps record of prograde or near-peak ages whereas zircon overgrowth occurs mostly near-peak and in the retrograde path (Harley et al. 2007).

The time interval 990–960 Ma is characterized by a scarcity of monazite U–Pb ages and absence of distinctive chemical composition, which may traduce monazite dissolution or lower reactivity. In contrast, CL-dark zircon crystallizes within the orthopyroxene isograd sample (*ALR 14-19*) and UHT sample (*ALR 13-58*) yielding a maximum probability peak of c. 970 Ma. This population is well identified in the sample *ALR 14-19* at 971 ± 8 Ma and is not likely to represent a "mixing" age, since this sample lacks any overprint at c. 950–930 Ma. The presence of CL-dark overgrowth and Ti-in-zircon temperature in excess of 760°C supports (episodic?) melt-present conditions over the entire period.

Finally, crystallization of sector-zoned stubby zircon in the UHT sample *ALR 13-58* at 938 ± 7 Ma (Fig. 5g) is coeval with crystallization of high-Y monazite at 935 ± 6 Ma that signs garnet breakdown into osumilite (Chp. 3). We thus consider that zircon T–t record defines a lower bound on possible thermal cooling between the two identified UHT events. Therefore, defining a time of residence above 800 °C (Δt_{800}) of 100 My for the present-day UHT zone samples.

Conclusion

The investigated zircons show a wide range of internal textures within the highest grade samples reaching UHT conditions. It is possible to identify consistent zircon populations on the basis of their CL-zoning and Th/U ratio. The identified populations, however, yield an age spread exceeding analytical uncertainties. This age spread results in part from the partial resetting of U–Pb system in inherited zircon cores in response to radiation damage through time. In particular, we propose that sector-zoned CL-bright zones represents recrystallization of older structurally instable part of the grain interior without changing its exterior shape. On the other hand, scanning ion imaging of CL-dark rims and overgrowth did not reveal unsupported radiogenic Pb suggesting that these CL-dark rims have meaningful geological ages. Investigation of oxygen isotopes did not reveal significant variations during Sveconorwegian metamorphism and did not prove useful in discriminating between different (metamorphic) zircon populations.

The comparison of monazite and zircon U–Pb record through time and space, coupled to Ti-in-zircon thermometry provides firm evidence of protracted melting event lasting some 110 My (1040–930 Ma) in the UHT samples. As a consequence, the Rogaland area did not cool below 750–800 °C between the two thermal maxima identified at c. 1030–1005 Ma and 940–930 Ma. In contrast, zircon and monazite record in the regional metamorphic basement are restricted to the 1040–1000 Ma time span.

References

Bingen B, Nordgulen Ø, Sigmond EMO, et al (2003) Relations between 1.19–1.13 Ga continental magmatism, sedimentation and metamorphism, Sveconorwegian province, S Norway. Precambrian Res 124:215–241.

Bingen B, Nordgulen O, Viola G (2008b) A four-phase model for the Sveconorwegian orogeny, SW Scandinavia. Nor Geol Tidsskr 88:43.

Bingen B, Van Breemen O (1998) U-Pb monazite ages in amphibolite- to granulite-facies orthogneiss reflect hydrous mineral breakdown reactions: Sveconorwegian Province of SW Norway. Contrib Mineral Petrol 132:336–353.

Cherniak DJ (2010) Diffusion in Accessory Minerals: Zircon, Titanite, Apatite, Monazite and Xenotime. Rev Mineral Geochem 72:827–869.

Corfu F (2013) A century of U-Pb geochronology: The long quest towards concordance. Geol Soc Am Bull 125:33–47.

Corfu F, Hanchar JM, Hoskin PW, Kinny P (2003) Atlas of zircon textures. Rev Mineral Geochem 53:469–500.

Crowley QG, Key R, Noble SR (2015) High-precision U–Pb dating of complex zircon from the Lewisian Gneiss Complex of Scotland using an incremental CA–ID–TIMS approach. Gondwana Res 27:1381–1391.

Degeling H, Eggins S, Ellis DJ (2001) Zr budgets for metamorphic reactions, and the formation of zircon from garnet breakdown. Mineral Mag 65:749–758.

Demaiffe D, Javoy M (1980) $^{18}O/^{16}O$ ratios of anorthosites and related rocks from the Rogaland Complex (SW Norway). Contrib Mineral Petrol 72:311–317.

Didier A, Bosse V, Bouloton J, et al (2015) NanoSIMS mapping and LA–ICP–MS chemical and U–Th–Pb data in monazite from a xenolith enclosed in andesite (Central Slovakia Volcanic Field). Contrib Mineral Petrol. doi: 10.1007/s00410-015-1200-1

Ewing RC, Meldrum A, Wang L, et al (2003) Radiation effects in zircon. Rev Mineral Geochem 53:387–425.

Ewing TA, Hermann J, Rubatto D (2013) The robustness of the Zr-in-rutile and Ti-in-zircon thermometers during high-temperature metamorphism (Ivrea-Verbano Zone, northern Italy). Contrib Mineral Petrol 165:757–779.

Flowers RM, Schmitt AK, Grove M (2010) Decoupling of U–Pb dates from chemical and crystallographic domains in granulite facies zircon. Chem Geol 270:20–30.

Fraser G, Ellis D, Eggins S (1997) Zirconium abundance in granulite-facies minerals, with implications for zircon geochronology in high-grade rocks. Geology 25:607–610.

Geisler T, Schaltegger U, Tomaschek F (2007) Re-equilibration of zircon in aqueous fluids and melts. Elements 3:43–50.

Harley SL, Kelly NM, Möller A (2007) Zircon behaviour and the thermal histories of mountain chains. Elements 3:25–30.

Hermans GAE, Tobi AC, Poorter RP, Maijer C (1975) The high-grade metamorphic Precambrian of the Sirdal-Ørsdal area, Rogaland/Vest-Agder, south-west Norway. Nor Geol Undersokelse 318:351–374.

Hoskin PW, Schaltegger U (2003) The composition of zircon and igneous and metamorphic petrogenesis. Rev Mineral Geochem 53:27–62.

Hoskin PWO, Black LP (2000) Metamorphic zircon formation by solid-state recrystallization of protolith igneous zircon. J Metamorph Geol 18:423–439.

Kelly NM, Harley SL (2005) An integrated microtextural and chemical approach to zircon geochronology: refining the Archaean history of the Napier Complex, east Antarctica. Contrib Mineral Petrol 149:57–84.

Kelsey DE, Clark C, Hand M (2008) Thermobarometric modelling of zircon and monazite growth in melt-bearing systems: examples using model metapelitic and metapsammitic granulites. J Metamorph Geol 26:199–212.

Kooijman E, Upadhyay D, Mezger K, et al (2011) Response of the U–Pb chronometer and trace elements in zircon to ultrahigh-temperature metamorphism: The Kadavur anorthosite complex, southern India. Chem Geol 290:177–188.

Kusiak MA, Whitehouse MJ, Wilde SA, et al (2013) Mobilization of radiogenic Pb in zircon revealed by ion imaging: Implications for early Earth geochronology. Geology 41:291–294.

Laajoki K, Corfu F, Andersen T (2002) Lithostratigraphy and U-Pb geochronology of the Telemark supracrustals in the Bandak-Sauland area, Telemark, South Norway. Nor Geol Tidsskr 82:119–138.

Ludwig KR (2008) Isoplot 3.7 a geochronological toolkit for Microsoft Excel. Berkeley Geochronology Center Special Publication 4:1–77

Marsh JH, Stockli DF (2015) Zircon U–Pb and trace element zoning characteristics in an anatectic granulite domain: Insights from LASS–ICP–MS depth profiling. Lithos 239:170–185.

Martin LAJ., Duchene S, Deloule E, Vanderhaeghe O (2008) Mobility of trace elements and oxygen in zircon during metamorphism: consequences for geochemical tracing. Earth Planet Sci Lett 267:161–174.

Mezger K, Krogstad EJ (1997) Interpretation of discordant U-Pb zircon ages: an evaluation. J Metamorph Geol 15:127–140.

Möller A, O'brien PJ, Kennedy A, Kröner A (2002) Polyphase zircon in ultrahigh-temperature granulites (Rogaland, SW Norway): constraints for Pb diffusion in zircon. J Metamorph Geol 20:727–740.

Möller A, O'Brien PJ, Kennedy A, Kröner A (2003) Linking growth episodes of zircon and metamorphic textures to zircon chemistry: an example from the ultrahigh-temperature granulites of Rogaland (SW Norway). Geol Soc Lond Spec Publ 220:65–81.

Murakami T, Chakoumakos B., Ewing RC, et al (1991) Alpha-decay event damage in zircon. Am Mineral 76:1510–1532.

Nasdala L, Hanchar JM, Kronz A, Whitehouse MJ (2005) Long-term stability of alpha particle damage in natural zircon. Chem Geol 220:83–103.

Nasdala L, Lengauer CL, Hanchar JM, et al (2002) Annealing radiation damage and the recovery of cathodoluminescence. Chem Geol 191:121–140.

Pidgeon RT (2014) Zircon radiation damage ages. Chem Geol 367:13–22.

Piazolo S, La Fontaine A, Trimby P, Harley S, Yang L, Armstrong R, Cairney JM (2016) Deformation-induced trace element redistribution in zircon revealed using atom probe tomography. Nat Commun 7:10490. doi: 10.1038/ncomms10490

Roberts NM, Parrish RR, Horstwood MS, Brewer TS (2011) The 1.23 Ga Fjellhovdane rhyolite, Grøss\a e-Totak; a new age within the Telemark supracrustals, southern Norway. Nor J Geol 91:239–246.

Roberts NMW, Slagstad T, Parrish RR, et al (2013) Sedimentary recycling in arc magmas: geochemical and U–Pb–Hf–O constraints on the Mesoproterozoic Suldal Arc, SW Norway. Contrib Mineral Petrol 165:507–523.

Salje EKH, Chrosch J, Ewing RC (1999) Is “metamictization” of zircon a phase transition? Am Mineral 84:1107–1116.

Schaltegger U, Fanning CM, Günther D, et al (1999) Growth, annealing and recrystallization of zircon and preservation of monazite in high-grade metamorphism: conventional and in-situ U-Pb isotope, cathodoluminescence and microchemical evidence. Contrib Mineral Petrol 134:186–201.

Schärer U, Wilmart E, Duchesne J-C (1996) The short duration and anorogenic character of anorthosite magmatism: U-Pb dating of the Rogaland complex, Norway. Earth Planet Sci Lett 139:335–350.

Štípská P, Powell R, Hacker BR, et al (2016) Uncoupled U/Pb and REE response in zircon during the transformation of eclogite to mafic and intermediate granulite (Blanský les, Bohemian Massif). J Metamorph Geol 34:551–572.

Taylor RJM, Clark C, Fitzsimons ICW, et al (2014) Post-peak, fluid-mediated modification of granulite facies zircon and monazite in the Trivandrum Block, southern India. Contrib Mineral Petrol. doi: 10.1007/s00410-014-1044-0

Tichomirowa M, Whitehouse MJ, Nasdala L (2005) Resorption, growth, solid state recrystallisation, and annealing of granulite facies zircon—a case study from the Central Erzgebirge, Bohemian Massif. Lithos 82:25–50.

Tobi AC, Hermans GAE., Maijer C, Jansen JBH (1985) Metamorphic zoning in the high-grade proterozoic of Rogaland-Vest Agder SW Norway. In: AC Tobi & JLR Touret (eds) The deep Proterozoic crust in the North Atlantic provinces, D. Reidel publishing company. pp 477–497

Tomaschek F (2003) Zircons from Syros, Cyclades, Greece – recrystallization and mobilization of zircon during high-pressure metamorphism. J Petrol 44:1977–2002.

Tomkins HS, Williams IS, Ellis DJ (2005) In situ U-Pb dating of zircon formed from retrograde garnet breakdown during decompression in Rogaland, SW Norway. J Metamorph Geol 23:201–215.

Valley J, Bindemann IN, Peck WH (2003) Empirical calibration of oxygen isotope fractionation in zircon. Geochim Cosmochim Acta 67:3257–3266.

Vavra G, Schmid R, Gebauer D (1999) Internal morphology, habit and U-Th-Pb microanalysis of amphibolite-to-granulite facies zircons: geochronology of the Ivrea Zone (Southern Alps). Contrib Mineral Petrol 134:380–404.

Watson EB, Cherniak DJ (1997) Oxygen diffusion in zircon. Earth Planet Sci Lett 148:527–544.

Watson EB, Harrison TM (1983) Zircon saturation revisited: temperature and composition effects in a variety of crustal magma types. Earth Planet Sci Lett 64:295–304.

Watson EB, Liang Y (1995) A simple model for sector zoning in slowly grown crystals: implications for growth rate and lattice diffusion, with emphasis on accessory minerals in crustal rocks. Am Mineral 80:1179–1187.

Whitehouse MJ, Platt JP (2003) Dating high-grade metamorphism – constraints from rare earth elements in zircon and garnet. Contib Mineral Petrol 145:61–74

Whitehouse MJ, Ravindra Kumar GR, Rimša A (2014) Behaviour of radiogenic Pb in zircon during ultrahigh-temperature metamorphism: an ion imaging and ion tomography case study from the Kerala Khondalite Belt, southern India. Contrib Mineral Petrol. doi: 10.1007/s00410-014-1042-2

Wiedenbeck M, Alle P, Corfu F, et al (1995) Three natural zircon standards for U-Th-Pb, Lu-Hf, trace element and REE analyses. Geostand Newsl 19:1–23.

Wilmart E, Pineau F, Réjou-Michel A, Duchesne JC (1994) Fluid transfer in anorthosites and related rocks from Rogaland (Southwest Norway): Evidence from stable isotopes. Earth Planet Sci Lett 125:55–70.

Yakymchuk C, Brown M (2014) Behaviour of zircon and monazite during crustal melting. J Geol Soc 171:465–479. doi: 10.1144/jgs2013-115

Tables

Tab. 1: LA-ICP-MS trace elements analysis of selected zircon grains

Sample ALR 13-05

Name	Domain	Ca	Y	Nb	Hf	Ta	La	Ce	Pr	Nd	Sm	Eu	Gd	Tb	Dy	Ho	Er	Tm	Yb	Lu	GdN/YbN	Ti	T° Ti (°C)
n5383-02c	osc. core reset	135.93	1060.7	2.5	10294.07	0.8	b.d.l	6.5	b.d.l	2.4	5.6	0.4	28.3	8.5	99.5	35.7	160.7	31.5	271.3	48.8	0.13	18	804
n5383-12a	osc. core inh.	276.49	1075.8	3.3	11884.86	1.1	116.9	693.1	109.6	550.1	138.2	4.8	96.9	12.9	108.3	36.9	176.1	37.3	345.8	68.5	0.35	24	835
n5383-08b	CL-dark rim	b.d.l	594.8	1.9	13925.73	1.0	b.d.l	3.3	b.d.l	0.8	3.0	0.2	24.8	7.5	71.3	20.6	93.3	19.3	184.2	37.3	0.17	17	800
n5383-06a	CL-dark rim	295.1	623.2	2.1	15131.73	1.4	b.d.l	1.8	b.d.l	1.2	6.6	0.3	39.0	12.0	97.5	21.2	64.2	9.9	68.9	10.4	0.70	16	791
n5383-02d	CL-dark rim	b.d.l	160.0	1.5	14236.70	0.5	0.3	7.3	0.7	5.8	8.9	1.0	24.0	4.5	28.6	5.2	13.9	2.0	13.8	2.2	2.15	15	786
n5383-16b	CL-dark rim	120.21	162.0	1.6	14790.98	0.5	b.d.l	6.4	b.d.l	1.6	6.3	0.2	21.9	4.2	28.4	5.3	14.6	2.0	12.5	1.8	2.16	14	780
n5383-04b	CL-dark rim	b.d.l	200.9	1.5	14278.75	0.4	b.d.l	6.8	b.d.l	2.4	8.8	0.3	28.4	5.4	35.5	6.9	18.1	2.6	16.0	2.5	2.19	17	801
n5383-01b	CL-dark rim	147.03	161.1	1.7	13925.58	0.4	b.d.l	8.7	b.d.l	2.5	7.2	0.4	23.1	4.5	28.1	5.4	14.4	2.1	14.5	2.3	1.97	21	822
n5383-03a	CL-bright	b.d.l	129.0	1.6	14037.96	0.4	b.d.l	7.6	b.d.l	2.5	7.5	0.2	21.0	3.7	23.1	4.4	11.3	1.6	9.8	1.5	2.65	24	833
n5383-04e	CL-bright	142.40	151.3	1.7	14079.82	0.5	b.d.l	8.3	0.1	2.3	5.5	b.d.l	19.9	3.9	25.8	5.0	13.5	1.8	12.7	1.7	1.93	21	821
n5383-05a	CL-bright	257.99	154.9	1.5	13858.92	0.5	b.d.l	7.7	0.1	2.9	8.9	0.2	25.3	4.5	29.7	5.4	13.7	1.8	11.3	1.6	2.76	22	825
n5383-06b	CL-bright	b.d.l	151.5	1.5	14074.91	0.5	b.d.l	9.4	b.d.l	2.7	6.6	0.3	20.6	4.0	26.9	5.0	14.1	2.0	13.4	2.0	1.91	15	788
n5383-08a	CL-bright	b.d.l	118.1	1.9	13998.71	0.6	b.d.l	8.5	b.d.l	1.6	4.3	0.3	16.0	3.2	20.9	3.9	10.8	1.6	11.1	1.8	1.78	21	820
n5383-10a	CL-bright	b.d.l	146.7	1.5	12496.90	0.5	b.d.l	8.1	b.d.l	2.2	6.4	0.4	18.5	3.3	22.1	4.3	12.5	1.8	10.6	1.7	2.15	19	810
n5383-11a	CL-bright	b.d.l	151.5	1.5	14227.38	0.4	b.d.l	8.2	0.1	3.1	8.4	0.2	23.7	4.3	27.1	5.1	13.4	1.9	11.8	1.9	2.48	21	820
n5383-12b	CL-bright	150.8	152.1	1.3	13901.28	0.4	0.0	7.7	0.2	2.6	7.5	0.4	23.5	4.2	28.6	5.1	13.0	1.7	11.0	1.7	2.64	19	809
n5383-14a	CL-bright	127.61	111.9	1.5	14064.19	0.3	b.d.l	7.2	0.1	2.0	6.3	0.2	18.1	3.2	18.7	3.7	9.7	1.4	8.6	1.3	2.60	18	804
n5383-15a	CL-bright	142.40	111.7	1.6	14087.84	0.4	b.d.l	7.4	b.d.l	2.3	6.4	0.3	18.3	3.3	20.2	3.7	9.5	1.4	8.9	1.3	2.54	20	814
n5383-16a	CL-bright	132.23	113.7	1.7	14087.87	0.4	b.d.l	8.3	0.1	2.7	7.1	0.3	19.0	3.4	20.2	3.7	8.9	1.3	8.8	1.3	2.67	21	820
n5383-20	CL-bright	172.92	140.8	2.0	14204.53	0.7	b.d.l	9.8	b.d.l	1.4	4.9	0.2	16.7	3.6	23.5	4.5	13.3	1.9	13.1	2.2	1.58	20	816
n5383-21	CL-bright	141.48	170.8	1.7	13918.69	0.5	b.d.l	10.5	0.1	2.9	7.8	0.3	24.0	4.6	31.1	5.8	16.0	2.4	16.2	2.5	1.83	18	806
n5383-14b	CL-grey	b.d.l	250.7	1.6	14030.04	0.8	b.d.l	6.9	b.d.l	1.2	4.7	0.4	27.7	6.8	46.6	8.1	21.8	2.9	19.6	2.9	1.75	17	795
n5383-17a	CL-grey	152.58	283.0	1.6	14016.63	0.7	b.d.l	8.0	b.d.l	1.3	5.4	0.5	30.1	7.3	49.4	9.3	26.0	3.8	26.4	4.4	1.41	23	829
n5383-04c	CL-grey	b.d.l	166.2	1.7	14408.66	0.8	b.d.l	6.6	b.d.l	0.9	3.3	0.2	18.3	4.5	30.8	5.4	14.4	2.2	16.3	2.7	1.39	16	789
n5383-19	CL-grey	152.58	167.8	1.6	14112.62	0.6	b.d.l	7.1	b.d.l	1.1	3.8	0.3	17.4	4.1	29.4	5.4	15.5	2.0	14.2	2.2	1.51	20	813

concentration are given in ppm

Tab. 1: continued

Sample ALR 13-22

Name	Domain	Ca	Y	Nb	Hf	Ta	La	Ce	Pr	Nd	Sm	Eu	Gd	Tb	Dy	Ho	Er	Tm	Yb	Lu	GdN/YbN	Ti	T° Ti (°C)
n5386-14a	osc. core inherited	155.9	1337	2.64	11708.22	1.21	-0.145	7.8	-0.119	1.18	3.21	0.267	21.67	7.82	107.1	43.2	222.8	49	462.2	93.69	0.06	10	742
n5386-10b	osc. core inherited	116.6	1003	2.76	11950.00	1.34	-0.127	6.03	-0.102	0.62	1.75	-0.175	13.93	5.16	75.19	31.84	169.6	38.84	382.7	76.06	0.04	14	775
n5386-18b	osc. core inherited	149.1	596.7	1.88	14081.66	1.06	-0.148	4.38	-0.13	-0.71	0.86	-0.221	7.99	3.46	51.21	20.69	111.2	25.72	258.1	50.64	0.04	16	789
n5386-20a	osc. core inherited	174.8	1577	1.89	12092.54	0.65	-0.15	6.59	-0.125	2.87	6.42	0.85	37.76	12.61	153.9	57.09	269.7	54.84	496.5	95.6	0.09	20	817
n5386-16b	osc. core inherited	-129	867.9	3.5	12591.49	1.67	-0.146	10.49	-0.118	-0.67	1.58	-0.204	11.24	4.54	65.67	27.7	150.6	35.34	344.7	69.81	0.04	10	741
n5386-15	osc. core inherited	210.2	821.8	2.11	11818.98	1.02	-0.146	6.25	-0.115	1.14	1.84	-0.199	12.41	4.76	66.18	27.24	142.2	31.59	311.7	63.28	0.05	14	778
n5386-01a	osc. core inherited	141.1	1297	1.632	11353.96	0.622	-0.126	2.99	0.106	1.49	3.64	0.198	24.52	8.72	115.4	43.6	209.6	43.6	401.7	76.1	0.08	11	752
n5386-18a	osc. core reset	176.8	1486	1.4	14044.64	0.758	-0.139	4.84	-0.114	1.06	3.11	0.224	20.35	7.68	111	45.33	243.4	57.44	588.2	120.5	0.04	15	783
n5386-12b	osc. core reset	-129	1020	2.98	13098.57	1.61	-0.139	5.5	-0.121	0.84	1.54	-0.21	13.13	5.04	72.89	30.88	169.6	39.51	396.2	81.44	0.04	12	763
n5386-11a	osc. core reset	128.4	981.4	2.53	12008.24	1.13	-0.114	7.99	-0.094	0.86	2.04	0.19	14.94	5.71	77.92	32.68	167.1	37.26	364	72.77	0.05	14	780
n5386-16a	CL-dark rim	203.2	830.4	1.66	16533.29	1.2	-0.142	5.57	-0.117	-0.64	1.32	-0.208	8.04	3.96	59.25	26.35	152.5	40.64	463.2	101.9	0.02	12	761
n5386-10a	CL-dark rim	130.5	1899	1.66	14402.63	0.836	0.246	5.27	0.151	1.23	2.14	0.223	18.33	9.25	140.2	57.24	308.9	72.25	739.7	146.5	0.03	16	791

Sample ALR 13-69

Name	Domain	Ca	Y	Nb	Hf	Ta	La	Ce	Pr	Nd	Sm	Eu	Gd	Tb	Dy	Ho	Er	Tm	Yb	Lu	GdN/YbN	Ti	T° Ti (°C)
n5389-05b	CL-dark rim	186	867	10	11896.86	3.9	-0.16	4.9	-0.13	1.38	5.7	0.25	38	12	119	30	104	16	108	16	0.43	11	751
n5389-10a	CL-dark rim	-134	888	10	11678.15	4.2	-0.16	5.1	-0.12	1.43	6.0	0.29	38	12	120	31	102	16	114	17	0.41	11	757
n5389-13b	CL-dark rim	184	797	10	11780.96	4.6	-0.14	4.2	-0.12	1.30	4.8	0.27	35	12	113	27	89	13	97	15	0.45	9.1	737
n5389-01a	CL-dark rim	-124	757	11	11777.72	4.5	-0.15	4.3	-0.12	0.98	4.7	0.34	34	12	110	27	83	12	88	14	0.48	11	756
n5389-07a	CL-dark rim	138	961	11	11469.82	5.3	-0.15	5.0	-0.12	1.47	6.2	0.24	44	15	140	34	104	16	111	17	0.49	11	752
n5389-08a	CL-dark rim	-133	916	10	11564.37	4.9	-0.15	4.6	-0.13	1.44	6.2	0.27	41	14	130	31	97	15	106	16	0.48	12	767
n5389-11c	CL-dark rim	241	857	8	11603.30	3.3	-0.15	5.1	-0.12	1.33	5.9	0.25	37	12	116	30	97	15	101	15	0.45	14	781
n5389-15b	CL-dark rim	177	1252	14	11773.16	6.1	-0.16	4.5	-0.13	1.39	5.6	0.29	44	16	160	41	145	23	165	26	0.33	-8	
n5389-03b	CL-dark rim	212	1002	17	12019	9.5	-0.15	3.2	-0.12	-0.70	3.0	-0.22	30	12	132	33	109	17	121	19	0.31	8.4	730
n5389-16a	CL-bright	-134	754	5	9500	0.6	-0.15	5.5	-0.13	1.78	4.3	1.08	25	7	83	27	120	23	202	39	0.15	-7.9	
n5389-04a	inherited core	-123	622	3	12369	1.3	-0.14	4.3	-0.11	0.93	4.5	0.24	31	10	93	23	71	11	73	12	0.53	9.62	742
n5389-05a	inherited core	-135	640	8	11699	3.8	-0.16	4.1	-0.13	0.92	4.1	0.28	31	10	95	22	65	9	62	10	0.62	-8.2	

concentration are given in ppm

Tab. 1: continued

Sample ALR 13-58

Name	Domain	Ca	Y	Nb	Hf	Ta	La	Ce	Pr	Nd	Sm	Eu	Gd	Tb	Dy	Ho	Er	Tm	Yb	Lu	GdN/YbN	Ti	T° Ti (°C)
n5387-04a	CL-bright	217.4	146.4	2.09	15521.47	1.04	b.d.l	16.13	0.16	3.45	9.98	0.65	28.98	4.61	27.50	4.87	12.71	2.51	9.86	1.24	2.94	15	782
n5387-06a	CL-bright	152.6	185.6	2.41	14602.64	0.87	b.d.l	17.27	b.d.l	2.78	7.24	0.23	21.73	4.25	30.84	6.09	17.14	2.43	15.06	1.99	1.44	21	818
n5387-01a	CL-bright	222.9	215.0	2.28	14372.94	0.86	b.d.l	20.11	b.d.l	2.93	7.84	0.34	25.19	5.01	35.27	7.01	21.39	1.96	19.79	2.95	1.27	16	794
n5387-13a	CL-bright	158.2	226.5	2.46	14623.39	1.02	b.d.l	15.60	b.d.l	2.21	5.83	0.32	19.13	4.58	35.05	7.36	21.32	2.93	18.22	2.69	1.05	18	804
n5387-20b	CL-bright	159.1	294.6	2.93	14107.02	1.04	b.d.l	13.07	b.d.l	2.47	7.75	0.24	23.77	5.43	43.17	9.52	29.69	3.31	28.61	4.33	0.83	18	805
n5387-10b	CL-bright	b.d.l	332.8	2.23	14426.56	0.83	b.d.l	14.73	b.d.l	3.07	8.58	0.36	29.52	6.49	49.66	10.82	33.59	4.21	32.81	4.67	0.90	20	817
n5387-15b	CL-bright	142.5	401.4	2.74	13784.04	0.91	b.d.l	23.94	0.14	3.54	10.79	0.62	45.08	9.36	66.31	13.64	39.84	4.56	37.55	5.63	1.20	19	811
n5391-17a	CL-bright	126	533	3.21	14510.11	1.5	b.d.l	17.13	b.d.l	2.15	8.09	0.58	41.1	1	80.18	18.56	57.2	5.96	56.4	8	0.73	11	752
n5387-05b	CL-dark rim	117.5	133.5	2.50	14345.00	0.97	b.d.l	11.25	0.11	2.92	10.05	0.30	30.06	4.30	24.42	4.77	14.77	2.46	23.12	5.34	1.30	18	806
n5391-07a	CL-dark rim	133	134	2	14557.11	0.66	b.d.l	10.76	b.d.l	2.35	9.84	0.3	27.01	4.05	23.97	4.88	14.83	2.32	18.17	3.7	1.49	21	818
n5391-10b	CL-dark rim	252	153	1.74	14243.46	0.37	b.d.l	13.34	b.d.l	2.5	7.83	b.d.l	20.98	3.52	24.63	5.33	17.02	2.59	17.46	3.28	1.20	15	784
n5387-17b	CL-dark rim	178.5	168.7	2.43	14719.71	0.94	b.d.l	10.24	b.d.l	1.86	7.23	0.24	23.45	4.20	26.61	5.19	16.34	2.35	17.30	2.98	1.36	17	798
n5387-17a	CL-dark rim	136.0	185.4	2.22	14715.58	0.82	b.d.l	9.77	b.d.l	2.28	7.87	0.29	26.15	4.75	30.85	6.09	17.06	2.41	18.21	3.11	1.44	20	813
n5391-21b	CL-dark rim	b.d.l	196	2.21	14548.31	0.98	b.d.l	19.85	0.551	9.28	15.57	0.272	28.12	5.56	37.32	6.87	17.76	2.25	15.69	2.36	1.79	28	852
n5387-13b	CL-dark rim	145.2	198.2	2.53	14392.82	0.92	b.d.l	13.51	0.13	2.71	5.99	0.23	17.03	4.19	31.91	6.54	18.09	2.43	15.26	2.36	1.12	21	818
n5387-06c	CL-dark rim	b.d.l	244.3	2.44	14655.48	0.82	b.d.l	16.35	0.10	2.78	8.90	0.32	28.46	8.83	40.56	8.08	21.96	2.85	18.33	2.73	1.55	22	827
n5387-06b	CL-dark rim	b.d.l	283.7	2.53	14710.61	0.84	b.d.l	17.33	0.12	3.60	10.43	0.28	33.50	6.70	48.01	9.16	25.16	2.29	20.83	2.98	1.61	17	797
n5387-02b	CL-dark sector	159.1	212.6	1.61	15231.79	1.14	b.d.l	7.44	b.d.l	1.54	7.77	0.81	33.72	6.86	41.04	7.06	16.95	2.44	13.30	1.85	2.53	18	802
n5391-11b	CL-dark sector	b.d.l	360	2.03	14323.56	0.81	b.d.l	6.38	b.d.l	1.4	6.57	0.289	34.02	8.28	61.42	12.7	34.17	2.51	28.22	3.94	1.21	18	806
n5391-30	CL-dark sector	149	549	2.19	14686.07	0.71	b.d.l	12.39	b.d.l	2.32	7.43	0.47	34.28	9.6	82.96	20.49	64.19	5.59	61.95	10.05	0.55	22	824
n5387-04b	osc. core inherited	b.d.l	244.4	1.90	15636.88	1.30	b.d.l	12.30	0.17	3.46	11.84	1.08	43.55	7.71	46.32	7.97	19.60	3.05	13.45	1.91	3.24	13	773
n5387-07a	osc. core reset	133.2	135.8	2.88	14031.22	1.39	b.d.l	19.99	0.17	3.87	10.94	0.46	26.60	4.31	25.18	4.84	12.53	2.38	10.64	1.52	2.50	14	780
n5387-18a	osc. core reset	198.9	388.1	2.61	14383.18	0.87	b.d.l	14.19	b.d.l	2.05	6.31	0.34	27.79	6.67	54.68	13.10	40.18	4.88	40.07	5.79	0.69	24	834
n5387-19b	osc. core reset	190.6	707.2	4.28	14492.13	1.87	b.d.l	15.27	b.d.l	2.19	8.27	0.54	41.69	10.88	96.33	24.29	76.97	8.34	80.46	11.96	0.52	13	774
n5387-14a	osc. core reset	189.6	296.9	1.81	14976.52	1.00	b.d.l	7.06	b.d.l	1.52	8.10	0.80	45.99	101.75	60.85	9.74	21.42	2.51	14.69	1.99	3.87	21	818
67-n5391-12b	high-Y rim	203.1	2763	12.27	13522.62	3.89	b.d.l	12.98	b.d.l	1.03	6.38	b.d.l	78.57	37.24	430.21	108.87	287.96	30.96	171.85	17.61	0.57	28	853

concentration are given in ppm

Tab. 1: continued

Sample ALR 14-19

Name	Domain	Ca	Y	Nb	Hf	Ta	La	Ce	Pr	Nd	Sm	Eu	Gd	Tb	Dy	Ho	Er	Tm	Yb	Lu	GdN/YbN	Ti	T° Ti (°C)
n8390-21a	CL-dark sector	163.7	111.1	2.0	15136.93	0.8	b.d.l	2.0	0.1	1.9	6.6	b.d.l	21.7	3.5	19.1	3.2	8.6	1.2	7.5	1.0	3.60	13.6	775
n8390-18a	CL-dark sector	136.9	138.0	1.9	15134.93	0.5	b.d.l	2.2	0.2	4.1	10.6	b.d.l	32.1	5.1	28.1	4.3	9.4	1.3	7.2	1.2	5.54	25.0	840
n8390-17a	CL-dark rim	b.d.l	161.0	2.1	14651.52	0.7	b.d.l	3.0	0.2	5.0	13.2	b.d.l	41.3	6.2	32.6	4.9	10.7	1.1	6.1	0.8	8.39	15.4	788
n8390-15a	CL-dark sector	162.8	142.2	1.6	15459.87	0.7	b.d.l	1.8	b.d.l	2.1	7.6	b.d.l	33.4	6.2	32.5	4.5	9.0	1.3	9.2	1.7	4.47	20.9	820
n8390-14b	CL-dark sector	b.d.l	123.5	1.8	15167.15	0.6	b.d.l	1.9	b.d.l	2.3	7.3	b.d.l	28.7	4.7	24.1	3.8	8.7	1.2	6.9	1.1	5.14	16.9	798
n8390-12b	CL-dark sector	212.8	197.0	1.8	14863.39	0.4	b.d.l	2.0	0.1	2.8	7.6	b.d.l	26.4	4.6	30.3	6.3	18.7	2.8	16.8	2.7	1.94	21.7	824
n8390-10a	CL-dark sector	b.d.l	122.1	1.8	15175.49	0.5	b.d.l	2.2	0.2	3.8	10.3	b.d.l	29.3	4.5	25.0	3.8	8.4	0.9	6.1	0.9	5.92	15.2	787
n8390-07a	CL-dark sector	135.1	106.3	1.7	15130.08	0.5	b.d.l	2.0	0.2	3.7	9.9	b.d.l	27.7	4.3	22.6	3.4	7.2	0.7	4.6	0.6	7.52	18.6	807
n8390-08a	osc. core inh.	148.9	686.1	1.6	11382.94	0.5	b.d.l	19.1	b.d.l	1.3	2.6	0.9	13.6	4.3	56.3	22.5	117.4	27.3	271.4	57.2	0.06	16.3	794
n8390-06a	CL-dark sector	174.8	160.0	1.7	15711.73	0.6	b.d.l	1.8	b.d.l	2.3	7.8	b.d.l	34.9	6.1	32.9	4.6	10.5	1.1	8.8	1.6	4.92	20.2	816
n8390-05b	osc. core inh.	142.5	809.4	2.3	11031.04	0.8	b.d.l	23.9	0.2	2.8	5.3	0.6	22.0	6.7	75.9	26.9	128.4	25.9	240.5	46.2	0.11	22.4	828
n8390-04a	osc. core inh.	130.4	907.9	3.3	11319.83	1.3	b.d.l	32.3	b.d.l	0.7	2.2	0.73	14.7	5.3	73.1	29.5	161.4	37.3	370.8	78.5	0.05	13.7	776
n8390-03b	CL-dark rim	b.d.l	145.5	1.6	15265.92	0.5	b.d.l	1.5	b.d.l	1.2	4.56	0.00	19.4	4.0	23.8	4.4	12.1	1.8	11.5	1.9	2.08	19.4	812
n8390-02a	osc. core inh.	b.d.l	912.9	3.1	11035.36	0.9	0.2	21.6	0.1	1.4	3.09	0.52	17.9	6.3	81.3	31.6	157.0	34.0	314.4	62.7	0.07	26.5	846
n8390-09a	osc. core inh.	257.2	1415.4	4.3	8114.01	1.2	b.d.l	17.3	0.2	3.8	7.06	1.22	39.3	12.0	142.6	50.7	224.1	42.4	361.2	65.9	0.13	20.1	816
n8390-20b	osc. core inh.	147.1	560.5	3.9	11114.43	0.9	b.d.l	22.98	b.d.l	1.4	2.31	0.42	14.3	4.7	55.0	20.1	93.0	18.9	172.3	32.4	0.10	17.0	798

concentration are given in ppm

Tab. 2: SIMS zircon U-Pb for sample *ALR 13-69*

		Isotope ratio										
Grain n°	**Texture**	**$^{207}Pb/^{206}Pb$**	**1σ %**	**$^{207}Pb/^{235}U$**	**1σ %**	**$^{206}Pb/^{238}U$**	**1σ %**	**Rho**	**$^{208}Pb/^{232}Th$**	**1σ %**	**f_{206} %**	**% disc.**
n5389-05b	CL-dark rim	0.073439	0.44	1.77676	1.00	0.17547	0.89915	0.90	0.054548	3.0	{0.01}	-1.5
n5389-10a	CL-dark rim	0.073889	0.38	1.76351	1.12	0.17310	1.05841	0.94	0.053020	3.3	{0.01}	0.9
n5389-06	CL-dark rim	0.073468	0.45	1.75719	1.19	0.17347	1.10120	0.93	0.053030	3.6	{0.00}	-0.4
n5389-13b	CL-dark rim	0.073536	0.37	1.75231	1.09	0.17283	1.02100	0.94	0.052273	3.2	{0.00}	0.1
n5389-16b	CL-dark rim	0.073245	0.40	1.78041	1.25	0.17630	1.18625	0.95	0.052758	11.3	{0.00}	-2.5
n5389-01a	CL-dark rim	0.073522	0.44	1.77977	1.14	0.17557	1.05227	0.92	0.056527	3.2	{0.00}	-1.4
n5389-02a	CL-dark rim	0.072759	0.48	1.70936	1.20	0.17039	1.10166	0.92	0.055481	3.7	{0.00}	-0.7
n5389-07a	CL-dark rim	0.073280	0.38	1.71928	1.10	0.17016	1.03060	0.94	0.052428	3.1	{0.00}	0.9
n5389-08a	CL-dark rim	0.073046	0.34	1.74352	0.96	0.17311	0.90372	0.94	0.053916	3.1	{0.00}	-1.4
n5389-09b	CL-dark rim	0.072898	0.35	1.71460	0.93	0.17059	0.85963	0.93	0.050811	3.3	{0.01}	-0.4
n5389-11b	CL-dark rim	0.072784	0.38	1.74935	1.13	0.17432	1.06060	0.94	0.054404	3.1	{0.01}	-2.7
n5389-11c	CL-dark rim	0.073381	0.37	1.74280	1.17	0.17225	1.11419	0.95	0.051823	2.9	{0.00}	0.0
n5389-15b	CL-dark rim	0.073268	0.42	1.73403	1.14	0.17165	1.06454	0.93	0.052044	3.6	{0.00}	0.0
n5389-03b	CL-dark rim	0.072288	0.42	1.67886	0.97	0.16844	0.87313	0.90	0.052052	4.4	{0.01}	-0.9
n5389-04b	CL-dark rim	0.072494	0.40	1.68117	0.97	0.16819	0.87872	0.91	0.050544	3.1	{0.00}	-0.2
n5389-16a	CL-bright	0.072723	1.28	1.68289	1.83	0.16783	1.30328	0.71	0.053409	3.9	{0.09}	0.6
n5389-04a	inherited core	0.074773	0.43	1.85595	1.01	0.18002	0.91065	0.91	0.055340	2.7	{0.00}	-0.4
n5389-05a	inherited core	0.074902	0.46	1.86712	1.04	0.18079	0.92915	0.90	0.054192	3.5	{0.00}	-0.5
n5389-03a	inherited core	0.074389	0.31	1.86946	0.88	0.18227	0.81890	0.93	0.059128	4.1	{0.00}	-2.5

Tab. 2: continued

		Dates								Chemical composition (ppm)			Radiation damage	Oxygen isotopes	
Grain n°	**Texture**	**$^{207}Pb/^{206}Pb$**	**1σ abs.**	**$^{207}Pb/^{235}U$**	**1σ abs.**	**$^{206}Pb/^{238}U$**	**1σ abs.**	**$^{208}Pb/^{232}Th$**	**1σ abs.**	**U**	**Th**	**Th/U calc.**	**(x10^{17} alpha/g)**	**δ18O**	**± ‰**
n5389-05b	CL-dark rim	1026.1	8.9	1037.0	6.5	1042.2	8.7	1073.5	31.8	668.9	15.3	0.02	25	8.86	0.19
n5389-10a	CL-dark rim	1038.4	7.6	1032.1	7.3	1029.2	10.1	1044.2	33.4	740.4	18.7	0.03	28	8.91	0.19
n5389-06	CL-dark rim	1026.9	9.1	1029.8	7.7	1031.2	10.5	1044.4	36.5	848.9	12.5	0.02	32	8.86	0.19
n5389-13b	CL-dark rim	1028.8	7.4	1028.0	7.0	1027.7	9.7	1029.9	32.3	778.7	13.2	0.02	29	n.a.	n.a.
n5389-16b	CL-dark rim	1020.7	8.0	1038.3	8.2	1046.7	11.5	1039.2	114.3	734.8	17.9	0.02	28	8.66	0.18
n5389-01a	CL-dark rim	1028.4	8.8	1038.1	7.4	1042.7	10.1	1111.4	34.3	553.8	14.9	0.03	21	8.83	0.20
n5389-02a	CL-dark rim	1007.3	9.6	1012.0	7.7	1014.3	10.3	1091.4	38.9	714.6	8.3	0.01	26	8.62	0.17
n5389-07a	CL-dark rim	1021.7	7.6	1015.8	7.1	1013.0	9.7	1032.8	31.4	758.9	15.4	0.02	28	8.77	0.17
n5389-08a	CL-dark rim	1015.2	6.8	1024.8	6.2	1029.2	8.6	1061.4	31.9	752.4	13.1	0.02	28	8.75	0.18
n5389-09b	CL-dark rim	1011.1	7.1	1014.0	6.0	1015.4	8.1	1001.8	31.8	704.9	11.0	0.02	26	8.79	0.16
n5389-11b	CL-dark rim	1007.9	7.8	1026.9	7.3	1035.9	10.2	1070.7	32.7	831.0	16.9	0.02	31	n.a.	n.a.
n5389-11c	CL-dark rim	1024.5	7.4	1024.5	7.6	1024.5	10.6	1021.2	28.9	789.4	21.9	0.03	29	n.a.	n.a.
n5389-15b	CL-dark rim	1021.4	8.5	1021.2	7.4	1021.2	10.1	1025.5	35.7	803.6	9.6	0.01	30	n.a.	n.a.
n5389-03b	CL-dark rim	994.0	8.6	1000.5	6.2	1003.5	8.1	1025.6	43.7	521.3	4.4	0.01	19	8.65	0.19
n5389-04b	CL-dark rim	999.8	8.2	1001.4	6.2	1002.2	8.2	996.6	29.9	676.5	15.1	0.02	24	8.88	0.20
n5389-16a	CL-bright	1006.3	25.8	1002.1	11.7	1000.2	12.1	1051.7	39.9	53.7	9.5	0.18	2	7.90	0.18
n5389-04a	inherited core	1062.4	8.5	1065.5	6.7	1067.1	9.0	1088.7	28.9	462.1	25.4	0.06	18	8.60	0.16
n5389-05a	inherited core	1065.9	9.3	1069.5	6.9	1071.3	9.2	1066.7	35.9	649.1	14.9	0.02	25	8.52	0.19
n5389-03a	inherited core	1052.0	6.2	1070.3	5.8	1079.3	8.1	1161.1	46.6	891.1	13.0	0.02	35	8.25	0.19

Tab. 3: SIMS zircon U-Th-Pb for sample *ALR 14-19*

		Isotope ratio										
Grain n°	**Texture**	**$^{207}Pb/^{206}Pb$**	**1σ %**	**$^{207}Pb/^{235}U$**	**1σ %**	**$^{206}Pb/^{238}U$**	**1σ %**	**Rho**	**$^{208}Pb/^{232}Th$**	**1σ %**	**f_{206} %**	**% disc.**
n5390-11a	CL-dark rim	0.0730	0.83	1.7597	1.51	0.1748	1.26	0.84	0.0532	2.6	{0.01}	2.6
n5390-20a	CL-dark rim	0.0715	0.44	1.5740	1.03	0.1597	0.93	0.90	0.0476	2.4	{0.00}	-1.9
n5390-03b	CL-dark rim	0.0734	0.81	1.7572	1.67	0.1736	1.46	0.87	0.0524	3.0	{0.00}	0.7
n5390-17a	CL-dark rim	0.0715	0.62	1.6161	1.15	0.1639	0.97	0.84	0.0493	2.2	{0.01}	0.8
n5390-21a	CL-dark sector	0.0743	0.58	1.7056	1.27	0.1666	1.13	0.89	0.0507	2.7	{0.00}	-5.7
n5390-10a	CL-dark sector	0.0732	1.12	1.7271	1.64	0.1711	1.20	0.73	0.0530	2.5	{0.01}	-0.1
n5390-15a	CL-dark sector	0.0733	0.55	1.7154	1.19	0.1696	1.05	0.89	0.0510	2.6	{0.00}	-1.4
n5390-06a	CL-dark sector	0.0730	0.65	1.6597	1.22	0.1650	1.04	0.85	0.0507	2.5	{0.00}	-3.1
n5390-07a	CL-dark sector	0.0712	0.68	1.5945	1.24	0.1623	1.03	0.84	0.0496	2.3	{0.01}	0.6
n5390-12b	CL-dark sector	0.0717	0.47	1.6036	1.05	0.1621	0.93	0.89	0.0502	2.4	{0.00}	-1.1
n5390-14a	CL-dark sector	0.0718	0.58	1.6582	1.24	0.1675	1.09	0.88	0.0505	2.4	{0.00}	2.0
n5390-14b	CL-dark sector	0.0719	0.53	1.6140	1.15	0.1629	1.03	0.89	0.0481	2.3	{0.01}	-1.0
n5390-18a	CL-dark sector	0.0712	0.55	1.5548	1.16	0.1583	1.02	0.88	0.0489	2.4	{0.01}	-1.9
n5390-04b	osc. core reset	0.0719	0.59	1.6697	1.21	0.1684	1.05	0.87	0.0542	5.6	{0.00}	2.3
n5390-04a	osc. core inh.	0.0994	1.09	3.9860	1.91	0.2907	1.57	0.82	0.0870	3.1	{0.01}	2.2
	osc. core inh.	0.1006	2.47	3.7792	3.63	0.2725	2.66	0.73	0.0802	4.4	{0.01}	-5.6
n5390-08a	osc. core inh.	0.0936	1.31	3.2522	2.60	0.2521	2.24	0.86	0.0741	3.7	{0.02}	-3.7
n5390-09a	osc. core inh.	0.0922	2.65	3.4152	3.31	0.2686	2.00	0.60	0.0808	3.6	{0.00}	4.7
n5390-20b	osc. core inh.	0.1840	0.61	11.0984	1.95	0.4376	1.85	0.95	0.1313	3.0	{0.01}	-15.5
n5390-05b	osc. core inh.	0.1264	1.91	6.9015	2.86	0.3961	2.13	0.74	0.1176	3.9	{0.00}	5.9

Pbc corrected isotopic ratios
** for partially reset oscillatory cores, a crystalization age of 1500 Ma is assumed*

Tab. 3: continued

		Dates								Chemical composition (ppm)			Radiation damage		Oxygen isotopes	
Grain n°	**Texture**	**$^{207}Pb/^{206}Pb$**	**1σ abs.**	**$^{207}Pb/^{235}U$**	**1σ abs.**	**$^{206}Pb/^{238}U$**	**1σ abs.**	**$^{208}Pb/^{232}Th$**	**1σ abs.**	**U**	**Th**	**Th/U calc.**	**(x10^{17} alpha/g)**	**at 1030 Ma***	**δ18O**	**± ‰**
n5390-11a	CL-dark rim	1014	17	1031	10	1039	12	1047	26	623	107	0.18	24.21		9.96	0.16
n5390-20a	CL-dark rim	972	9	960	6	955	8	940	22	501	105	0.20	17.87		10.24	0.17
n5390-03b	CL-dark rim	1025	16	1030	11	1032	14	1032	30	572	124	0.22	22.28		9.98	0.17
n5390-17a	CL-dark rim	972	13	976	7	979	9	973	21	721	271	0.38	27.36		10.49	0.20
n5390-21a	CL-dark sector	1049	12	1011	8	993	10	999	27	597	126	0.20	22.26		10.44	0.18
n5390-10a	CL-dark sector	1019	22	1019	11	1018	11	1044	25	510	158	0.32	19.93		9.95	0.17
n5390-15a	CL-dark sector	1023	11	1014	8	1010	10	1005	25	646	84	0.13	24.11		10.19	0.17
n5390-06a	CL-dark sector	1013	13	993	8	984	9	999	25	557	103	0.18	20.43		9.99	0.16
n5390-07a	CL-dark sector	964	14	968	8	970	9	978	22	619	160	0.26	22.71		9.75	0.18
n5390-12b	CL-dark sector	978	10	972	7	969	8	990	23	620	185	0.30	22.91		10.17	0.18
n5390-14a	CL-dark sector	980	12	993	8	998	10	996	23	620	150	0.25	23.39		10.26	0.19
n5390-14b	CL-dark sector	982	11	976	7	973	9	950	22	658	153	0.22	24.07			
n5390-18a	CL-dark sector	964	11	952	7	947	9	964	22	529	161	0.30	19.08		10.30	0.17
n5390-04b	osc. core reset	983	12	997	8	1004	10	1067	58	1136	42	0.04	41.26	25.74	10.04	0.17
n5390-04a	osc. core inh.	1614	20	1631	16	1645	23	1687	51	134	72	0.56	9.45	3.29	9.03	0.17
	osc. core inh.	1635	45	1588	30	1553	37	1559	66	106	61	0.55	7.07	2.63	7.75	0.17
n5390-08a	osc. core inh.	1499	25	1470	20	1449	29	1445	52	153	94	0.59	9.44	3.81	7.61	0.18
n5390-09a	osc. core inh.	1472	49	1508	26	1534	27	1570	55	109	50	0.49	7.01	2.66	5.70	0.18
n5390-20b	osc. core inh.	2689	10	2531	18	2340	36	2494	71	119	101	0.79	13.79	3.08	9.41	0.18
n5390-05b	osc. core inh.	2048	33	2099	26	2151	39	2248	83	118	85	0.79	12.01	3.00	7.17	0.16

Tab. 4: SIMS zircons U-Th-Pb for sample *ALR 13-22*

		Isotope ratio										
Grain n°	**Texture**	**$^{207}Pb/^{206}Pb$**	**1s %**	**$^{207}Pb/^{235}U$**	**1s %**	**$^{206}Pb/^{238}U$**	**1s %**	**Rho**	**$^{208}Pb/^{232}Th$**	**1s %**	**f_{206} %**	**% disc.**
n5386-06a	osc. core inh.	0.1030	1.39	3.5000	3.63	0.2463	3.35	0.92	0.0781	4.5	{0.00}	-17.2
n5386-01a	osc. core inh.	0.0928	0.69	3.4422	2.01	0.2690	1.89	0.94	0.0765	3.5	0.07	3.9
n5386-01b	osc. core inh.	0.0944	0.52	3.4034	1.43	0.2614	1.33	0.93	0.0772	3.0	{0.01}	-1.5
n5386-02a	osc. core inh.	0.0926	0.76	3.2569	1.76	0.2550	1.59	0.90	0.0771	4.1	{0.00}	-1.2
n5386-07a	osc. core inh.	0.0930	0.65	3.3203	1.72	0.2590	1.59	0.92	0.0769	4.8	{0.00}	-0.2
n5386-08a	osc. core inh.	0.0941	0.66	3.4430	1.53	0.2653	1.38	0.90	0.0800	3.3	{0.00}	0.5
n5386-10b	osc. core inh.	0.0930	0.62	3.4606	1.47	0.2697	1.34	0.91	0.0804	2.9	{0.00}	3.8
n5386-14a	osc. core inh.	0.0949	2.07	3.4088	2.50	0.2604	1.40	0.56	0.0797	3.5	{0.00}	-2.5
n5386-15	osc. core inh.	0.0943	0.51	3.4490	1.47	0.2653	1.38	0.94	0.0783	2.9	{0.00}	0.3
n5386-16b	osc. core inh.	0.0935	0.66	3.5119	1.51	0.2725	1.35	0.90	0.0781	3.1	{0.00}	4.2
n5386-18b	osc. core inh.	0.0945	0.88	3.4587	1.63	0.2654	1.38	0.84	0.0804	2.9	{0.01}	-0.1
n5386-20a	osc. core inh.	0.0934	0.62	3.4729	1.51	0.2698	1.37	0.91	0.0787	2.9	{0.02}	3.3
n5386-05a	osc. core reset	0.0835	1.27	2.5004	3.21	0.2172	2.95	0.92	0.0732	12.3	0.02	-1.2
n5386-11a	osc. core reset	0.0893	0.52	2.9493	1.47	0.2395	1.37	0.93	0.0724	3.1	{0.00}	-2.1
n5386-12a	osc. core reset	0.0856	1.77	2.2470	4.04	0.1904	3.63	0.90	0.0535	10.4	1.14	-16.9
n5386-12b	osc. core reset	0.0883	0.83	2.6798	2.74	0.2201	2.61	0.95	0.0692	4.8	{0.00}	-8.5
n5386-14b	osc. core reset	0.0866	0.74	2.7280	1.63	0.2285	1.45	0.89	0.0756	6.0	{0.00}	-2.1
n5386-18a	osc. core reset	0.0857	0.49	2.6424	1.45	0.2236	1.36	0.94	0.0715	3.9	{0.00}	-2.5
n5386-16a	CL-dark rim	0.0730	0.34	1.7272	1.36	0.1716	1.31	0.97	0.0563	4.9	{0.00}	0.7
n5386-10a	CL-dark rim	0.0725	0.33	1.7270	1.47	0.1728	1.43	0.97	0.0530	3.1	{0.01}	3.0

Pbc corrected isotopic ratios
** for partially reset oscillatory cores, a crystalization age of 1500 Ma is assumed*

Tab. 4: continued

		Dates								Chemical composition (ppm)			radiation damage		Oxygen isotopes	
Grain n°	**Texture**	**$^{207}Pb/^{206}Pb$**	**1s abs**	**$^{207}Pb/^{235}U$**	**1s abs**	**$^{206}Pb/^{238}U$**	**1s abs**	**$^{208}Pb/^{232}Th$**	**1s abs**	**U**	**Th**	**Th/U calc.**	**(x10^{17} alpha/g)**	**at 1030 Ma***	**δ18O**	**± ‰**
n5386-06a	osc. core inh.	1680	25	1527	29	1420	43	1520	66	117	48	0.37	6.82	2.83	6.66	0.15
n5386-01a	osc. core inh.	1484	13	1514	16	1536	26	1489	50	263	90	0.34	16.51	6.27	8.33	0.16
n5386-01b	osc. core inh.	1517	10	1505	11	1497	18	1504	44	560	140	0.25	33.52	13.15	7.51	0.16
n5386-02a	osc. core inh.	1480	14	1471	14	1464	21	1502	59	403	88	0.22	23.39	9.43	6.86	0.17
n5386-07a	osc. core inh.	1487	12	1486	13	1485	21	1498	70	453	130	0.29	27.08	10.72	7.11	0.17
n5386-08a	osc. core inh.	1511	12	1514	12	1517	19	1556	49	235	36	0.16	14.01	5.43	7.19	0.15
n5386-10b	osc. core inh.	1489	12	1518	12	1540	18	1563	43	470	106	0.24	28.92	10.99	7.01	0.16
n5386-14a	osc. core inh.	1527	38	1506	20	1492	19	1550	53	563	176	0.32	33.99	13.37	6.75	0.16
n5386-15	osc. core inh.	1514	10	1516	12	1517	19	1525	43	358	85	0.24	21.75	8.40	7.52	0.19
n5386-16b	osc. core inh.	1498	12	1530	12	1553	19	1519	45	437	95	0.22	27.15	10.21	7.39	0.19
n5386-18b	osc. core inh.	1519	16	1518	13	1517	19	1563	43	431	104	0.25	26.15	10.11	7.10	0.17
n5386-20a	osc. core inh.	1495	12	1521	12	1540	19	1531	43	449	153	0.35	28.31	10.72	7.15	0.16
n5386-05a	osc. core reset	1281	25	1272	24	1267	34	1427	169	1165	198	0.19	56.57	27.01	6.97	0.18
n5386-11a	osc. core reset	1410	10	1395	11	1384	17	1412	42	623	180	0.29	34.34	14.75	7.02	0.15
n5386-12a	osc. core reset	1329	34	1196	29	1123	38	1052	106	1390	298	0.17	59.45	32.46	6.14	0.16
n5386-12b	osc. core reset	1389	16	1323	20	1282	30	1353	62	1015	214	0.21	50.41	23.70	6.96	0.18
n5386-14b	osc. core reset	1352	14	1336	12	1326	17	1473	85	1431	338	0.26	74.26	33.56	n.a	n.a
n5386-18a	osc. core reset	1332	9	1313	11	1301	16	1396	52	1498	262	0.18	75.06	34.76	6.33	0.18
n5386-16a	CL-dark rim	1014	7	1019	9	1021	12	1107	52	1555	12	0.01	57.18	35.05	6.66	0.16
n5386-10a	CL-dark rim	1000	7	1019	9	1027	14	1043	32	1880	176	0.10	70.95	43.01	6.68	0.16

Tab. 5: SIMS zircons U-Th-Pb for sample *ALR 13-05*

		Isotope ratio										
Grain n°	**Texture**	**$^{207}Pb/^{206}Pb$**	**1s %**	**$^{207}Pb/^{235}U$**	**1s %**	**$^{206}Pb/^{238}U$**	**1s %**	**Rho**	**$^{208}Pb/^{232}Th$**	**1s %**	**f_{206} %**	**% disc.**
n5383-01b	CL-bright	0.0714	1.16	1.677	1.98	0.1703	1.60	0.81	0.0523	3.1	{0.00}	5.1
n5383-01c	CL-grey	0.0709	0.68	1.581	1.49	0.1618	1.33	0.89	0.0498	3.1	{0.00}	1.4
n5383-02c	inherited	0.0899	0.65	2.993	1.73	0.2414	1.61	0.93	0.0738	3.1	{0.01}	-2.3
n5383-02d	CL-dark rim	0.0713	0.35	1.563	1.29	0.1590	1.24	0.96	0.0621	10.9	0.02	-1.6
n5383-03a	CL-bright	0.0715	1.30	1.579	1.91	0.1601	1.39	0.73	0.0498	3.0	{0.00}	-1.7
n5383-03b	inherited	0.0765	0.63	1.953	1.52	0.1850	1.39	0.91	0.0598	3.4	{0.01}	-1.5
n5383-04b	CL-dark rim	0.0728	0.48	1.662	1.35	0.1655	1.26	0.94	0.0498	3.1	{0.00}	-2.4
n5383-04c	CL-grey	0.0700	0.90	1.503	1.59	0.1557	1.31	0.82	0.0490	3.7	{0.01}	0.5
n5383-04d	CL-dark rim	0.0720	0.51	1.691	1.42	0.1703	1.33	0.93	0.0537	3.2	{0.00}	2.9
n5383-04e	CL-bright	0.0723	1.66	1.635	2.10	0.1639	1.29	0.61	0.0509	2.9	{0.00}	-1.9
n5383-05a	CL-bright	0.0702	1.73	1.600	2.33	0.1652	1.56	0.67	0.0503	3.1	{0.00}	5.9
n5383-05b	inherited	0.0970	1.14	4.442	1.87	0.3320	1.49	0.79	0.0829	3.2	{0.02}	20.6
n5383-06a	CL-dark rim	0.0693	0.47	1.391	1.59	0.1455	1.52	0.96	0.0508	7.6	0.05	-3.9
n5383-06b	CL-bright	0.0729	1.39	1.629	2.02	0.1621	1.46	0.72	0.0515	3.0	{0.00}	-4.7
n5383-08a	CL-bright	0.0703	1.88	1.608	2.72	0.1660	1.97	0.72	0.0497	3.5	{0.00}	6.1
n5383-08b	CL-dark rim	0.0724	0.51	1.683	1.56	0.1686	1.47	0.94	0.0517	3.1	{0.00}	0.7
n5383-10a	CL-bright	0.0719	1.67	1.608	2.17	0.1623	1.38	0.64	0.0503	3.0	{0.00}	-1.5
n5383-11a	CL-bright	0.0707	1.35	1.622	2.10	0.1663	1.60	0.76	0.0505	3.3	{0.00}	4.7
n5383-12a	inherited	0.0939	1.54	3.524	4.01	0.2721	3.71	0.92	0.0773	5.7	0.30	3.4
n5383-12b	CL-bright	0.0710	1.34	1.596	1.66	0.1632	0.98	0.59	0.0499	2.6	{0.02}	2.1
n5383-13b	CL-bright	0.0711	1.36	1.562	1.95	0.1593	1.40	0.72	0.0497	3.0	{0.00}	-0.9
n5383-14a	CL-bright	0.0701	1.15	1.503	1.54	0.1555	1.03	0.67	0.0480	2.6	{0.00}	0.1
n5383-14b	CL-grey	0.0706	0.69	1.528	1.20	0.1569	0.99	0.82	0.0507	2.7	{0.01}	-0.8
n5383-15a	CL-bright	0.0727	1.41	1.701	1.90	0.1698	1.27	0.67	0.0521	2.8	{0.02}	0.7
n5383-16a	CL-bright	0.0718	1.40	1.585	1.92	0.1602	1.32	0.69	0.0490	2.7	{0.04}	-2.5
n5383-16b	CL-dark rim	0.0714	0.35	1.612	0.99	0.1637	0.93	0.93	0.0517	2.8	{0.00}	0.9
n5383-17a	CL-grey	0.0705	0.83	1.535	1.33	0.1579	1.04	0.78	0.0479	2.9	{0.00}	0.3
n5383-18a*	CL-bright	0.0788	1.32	1.973	2.26	0.1815	1.84	0.81	0.0514	3.4	{0.06}	-8.6
n5383-19	CL-grey	0.0707	1.09	1.507	1.55	0.1545	1.10	0.71	0.0492	8.3	{0.00}	-2.7
n5383-20*	CL-bright	0.0775	1.55	2.003	1.98	0.1875	1.23	0.62	0.0512	3.0	{0.05}	-2.5
n5383-21	CL-bright	0.0732	1.07	1.710	1.76	0.1695	1.40	0.79	0.0518	2.6	{0.05}	-1.0

Pbc corrected isotopic ratios

**Grains not used for age calculation*

Tab. 5: continued

		Dates								Chemical composition (ppm)		Radiation damage		Oxygen isotopes	
Grain n°	Texture	$^{207}Pb/^{206}Pb$	1s abs	$^{207}Pb/^{235}U$	1s abs	$^{206}Pb/^{238}U$	1s abs	$^{208}Pb/^{232}Th$	1s abs	U	Th	Th/U calc.	x10^{17} alpha/g	δ18O	± ‰
n5383-01b	CL-bright	968	23	1000	13	1014	15	1030	31	119	129	1.15	5.4	8.67	0.13
n5383-01c	CL-grey	955	14	963	9	967	12	983	30	340	46	0.14	12.1	8.96	0.15
n5383-02c	inherited	1424	12	1406	13	1394	20	1439	43	400	172	0.44	22.8	8.77	0.13
n5383-02d	CL-dark rim	966	7	956	8	951	11	1218	129	1320	8	0.01	44.9	8.78	0.15
n5383-03a	CL-bright	972	26	962	12	957	12	982	29	98	106	1.10	4.1	8.48	0.15
n5383-03b	inherited	1109	12	1099	10	1094	14	1174	39	424	54	0.14	17.3	8.57	0.15
n5383-04b	CL-dark rim	1010	10	994	9	987	12	983	29	892	66	0.07	32.1	8.58	0.12
n5383-04c	CL-grey	929	18	931	10	933	11	966	34	263	39	0.15	9.0	9.10	0.15
n5383-04d	CL-dark rim	987	10	1005	9	1014	12	1057	33	740	83	0.12	27.6	n.a.	n.a.
n5383-04e	CL-bright	996	33	984	13	978	12	1004	28	81	87	1.08	3.5	n.a.	n.a.
n5383-05a	CL-bright	935	35	970	15	986	14	993	30	106	116	1.16	4.6	8.82	0.12
n5383-05b	inherited	1568	21	1720	16	1848	24	1610	49	150	49	0.34	11.7	8.46	0.16
n5383-06a	CL-dark rim	909	10	885	9	876	12	1001	74	1588	52	0.04	49.6	7.38	0.14
n5383-06b	CL-bright	1012	28	982	13	968	13	1016	30	89	109	1.23	3.9	9.14	0.13
n5383-08a	CL-bright	937	38	973	17	990	18	981	34	82	95	1.23	3.6	8.93	0.14
n5383-08b	CL-dark rim	998	10	1002	10	1004	14	1018	31	661	81	0.12	24.5	8.68	0.14
n5383-10a	CL-bright	983	34	973	14	969	12	992	29	92	105	1.15	4.0	9.04	0.16
n5383-11a	CL-bright	950	27	979	13	992	15	996	32	95	102	1.12	4.2	9.07	0.17
n5383-12a	inherited	1507	29	1533	32	1552	51	1504	83	215	97	0.45	13.9	9.01	0.16
n5383-12b	CL-bright	956	27	969	10	974	9	984	25	77	80	1.07	3.3	8.79	0.16
n5383-13b	CL-bright	961	28	955	12	953	12	980	29	94	116	1.26	4.1	8.70	0.15
n5383-14a	CL-bright	931	23	932	9	932	9	947	24	84	92	1.12	3.5	8.52	0.16
n5383-14b	CL-grey	946	14	942	7	940	9	1000	27	248	32	0.14	8.6	8.92	0.15
n5383-15a	CL-bright	1004	28	1009	12	1011	12	1027	28	93	95	1.05	4.1	8.50	0.15
n5383-16a	CL-bright	980	28	964	12	958	12	967	26	58	81	1.37	2.6	8.91	0.16
n5383-16b	CL-dark rim	969	7	975	6	978	8	1020	28	832	54	0.07	29.5	8.70	0.17
n5383-17a	CL-grey	943	17	944	8	945	9	946	26	240	36	0.15	8.4	n.a.	n.a.
n5383-18a*	CL-bright	1167	26	1106	15	1075	18	1013	33	92	110	1.03	4.5	n.a.	n.a.
n5383-19	CL-grey	950	22	933	10	926	9	970	79	207	47	0.23	7.2	n.a.	n.a.
n5383-20*	CL-bright	1134	31	1117	14	1108	13	1009	30	104	146	1.25	5.5	n.a.	n.a.
n5383-21	CL-bright	1019	22	1012	11	1010	13	1020	26	124	150	1.21	5.7	n.a.	n.a.

Tab. 6: SIMS zircons U-Th-Pb for sample *ALR 13-58*

		Isotope ratio										
Grain n°	**Texture**	**$^{207}Pb/^{206}Pb$**	**1s %**	**$^{207}Pb/^{235}U$**	**1s %**	**$^{206}Pb/^{238}U$**	**1s %**	**Rho**	**$^{208}Pb/^{232}Th$**	**1s %**	**f_{206} %**	**% disc.**
n5391-14a	osc. core reset	0.0701	0.87	1.5043	1.43	0.1556	1.13	0.79	0.0476	2.4	{0.03}	0.0
n5391-08a	osc. core reset	0.0708	0.84	1.5403	1.21	0.1577	0.87	0.72	0.0477	2.4	{0.01}	-0.9
n5387-14a	osc. core reset	0.0712	0.55	1.6123	1.40	0.1643	1.29	0.92	0.0526	3.0	{0.01}	2.1
n5387-05a	osc. core reset	0.0718	0.90	1.6401	1.71	0.1658	1.45	0.85	0.0516	3.1	{0.00}	1.1
n5391-15a	osc. core reset	0.0735	0.58	1.7249	1.24	0.1702	1.09	0.88	0.0530	5.6	{0.03}	-1.6
n5387-19b	osc. core reset	0.0743	1.51	1.7453	1.92	0.1703	1.19	0.62	0.0512	2.7	{0.03}	-3.8
n5387-07a	osc. core reset	0.0723	0.63	1.6998	1.54	0.1705	1.40	0.91	0.0537	2.9	{0.00}	2.2
n5391-27	osc. core reset	0.0731	0.55	1.7496	1.26	0.1735	1.14	0.90	0.0569	3.0	{0.03}	1.4
n5387-18a	osc. core reset	0.0739	2.31	1.7985	2.99	0.1765	1.91	0.64	0.0526	3.2	{0.01}	0.9
n5387-04b	osc. core inh.	0.0770	1.81	1.9094	2.61	0.1797	1.88	0.72	0.0564	3.6	{0.02}	-5.5
n5391-25	osc. core inh.	0.0751	0.85	1.8947	1.63	0.1831	1.38	0.85	0.0493	5.7	{0.01}	1.4
n5391-05a	osc. core inh.	0.0869	0.88	2.6813	2.08	0.2237	1.89	0.91	0.0674	2.9	{0.00}	-4.7
n5387-16a	osc. core inh.	0.0888	1.18	2.7674	2.21	0.2261	1.86	0.84	0.0838	7.3	{0.00}	-6.8
n5391-13a	osc. core inh.	0.0951	0.78	3.5870	1.40	0.2735	1.17	0.83	0.0809	2.8	{0.00}	2.1
n5391-12b	CL-bright high-Y	0.0702	0.64	1.5074	1.07	0.1558	0.85	0.80	0.0469	2.6	{0.01}	0.0
n5387-15a	CL-bright	0.0708	1.45	1.5367	1.76	0.1574	0.99	0.56	0.0486	3.8	{0.01}	-1.1
n5387-04a	CL-bright	0.0704	1.06	1.5283	1.70	0.1575	1.33	0.78	0.0506	3.3	{0.00}	0.5
n5391-28	CL-bright	0.0702	0.60	1.5443	1.21	0.1595	1.05	0.87	0.0487	2.4	{0.00}	2.2
n5387-13a	CL-bright	0.0719	1.11	1.5857	1.72	0.1599	1.31	0.76	0.0507	3.0	{0.00}	-2.9
n5391-24	CL-bright	0.0711	1.08	1.5832	1.61	0.1615	1.20	0.74	0.0490	2.7	{0.02}	0.5
n5391-17a	CL-bright	0.0714	0.59	1.5946	1.24	0.1619	1.09	0.88	0.0497	2.4	{0.01}	-0.3
n5387-06a	CL-bright	0.0711	1.93	1.6100	2.56	0.1641	1.67	0.65	0.0501	3.4	{0.01}	2.0
n5387-10b	CL-bright	0.0724	1.04	1.6462	2.07	0.1650	1.78	0.86	0.0494	3.1	{0.03}	-1.3
n5387-01a	CL-bright	0.0703	1.11	1.6062	1.79	0.1656	1.41	0.78	0.0507	2.9	{0.00}	5.7
n5391-23a	CL-bright	0.0737	1.03	1.6845	1.78	0.1658	1.45	0.81	0.0507	2.7	{0.02}	-4.5
n5391-04a	CL-bright	0.0731	1.65	1.6773	2.06	0.1664	1.24	0.60	0.0539	2.7	{0.01}	-2.6
n5387-20b	CL-bright	0.0716	0.87	1.6425	1.42	0.1665	1.12	0.79	0.0500	2.9	{0.00}	2.1
n5391-08b	CL-bright	0.0717	0.62	1.6513	1.21	0.1671	1.04	0.86	0.0511	3.0	{0.01}	2.1
n5391-23b	CL-bright	0.0742	0.87	1.7141	1.61	0.1674	1.36	0.84	0.0508	2.6	{0.00}	-5.2
n5391-12a	CL-bright	0.0738	0.70	1.7207	1.22	0.1692	1.00	0.82	0.0516	2.4	{0.01}	-2.9
n5387-15b	CL-bright	0.0725	1.58	1.7342	2.41	0.1735	1.82	0.76	0.0527	3.8	{0.02}	3.4

Tab. 6 continued

		Dates								Chemical composition (ppm			Radiation damage		Oxygen isotopes	
Grain n°	Texture	$^{207}Pb/^{206}Pb$	1s abs	$^{207}Pb/^{235}U$	1s abs	$^{206}Pb/^{238}U$	1s abs	$^{208}Pb/^{232}Th$	1s abs	U	Th	Th/U calc.	($x10^{17}$ alpha/g) at 1030 Ma*		δ18O	± ‰
n5391-14a	osc. core reset	932	18	932	9	932	10	940	22	167.0	154.6	0.93	6.7	4.4	8.99	0.19
n5391-08a	osc. core reset	952	17	947	7	944	8	942	22	119.2	94.2	0.78	4.7	3.1	8.79	0.18
n5387-14a	osc. core reset	962	11	975	9	981	12	1036	31	432.2	41.0	0.10	15.5	9.9	8.94	0.18
n5387-05a	osc. core reset	979	18	986	11	989	13	1016	30	347.0	217.3	0.65	14.0	8.7	9.14	0.17
n5391-15a	osc. core reset	1028	12	1018	8	1013	10	1043	56	390.6	4.6	0.01	14.3	8.8	8.67	0.18
n5387-19b	osc. core reset	1050	30	1025	12	1014	11	1010	26	229.7	113.8	0.48	9.3	5.6	9.26	0.16
n5387-07a	osc. core reset	994	13	1008	10	1015	13	1057	30	335.5	235.2	0.75	14.1	8.5	9.15	0.16
n5391-27	osc. core reset	1018	11	1027	8	1031	11	1119	32	318.1	42.6	0.15	12.2	7.3	n.a.	n.a.
n5387-18a	osc. core reset	1039	46	1045	20	1048	18	1036	32	140.9	115.5	0.82	6.3	3.6	8.90	0.16
n5387-04b	osc. core inh.	1122	36	1084	18	1066	19	1108	39	376.3	89.5	0.23	15.2	8.8	8.93	0.16
n5391-25	osc. core inh.	1070	17	1079	11	1084	14	972	54	430.3	127.1	0.27	18.0	10.2	n.a.	n.a.
n5391-05a	osc. core inh.	1359	17	1323	16	1301	22	1319	37	341.3	152.2	0.43	18.1	8.3	8.70	0.19
n5387-16a	osc. core inh.	1400	22	1347	17	1314	22	1627	114	339.9	46.1	0.16	17.1	7.8	9.04	0.18
n5391-13a	osc. core inh.	1530	15	1547	11	1559	16	1573	42	341.8	95.9	0.29	21.6	8.1	8.95	0.17
n5391-12b	CL-bright high-Y	933	13	933	7	933	7	927	24	208.0	60.6	0.29	7.4		9.20	0.17
n5387-15a	CL-bright	952	29	945	11	942	9	959	36	66.3	100.5	1.53	3.0		8.89	0.15
n5387-04a	CL-bright	939	21	942	10	943	12	997	32	143.4	105.7	0.78	5.6		8.74	0.17
n5391-28	CL-bright	935	12	948	7	954	9	960	23	306.4	101.0	0.34	11.2		n.a.	n.a.
n5387-13a	CL-bright	983	22	965	11	956	12	1000	29	196.6	158.1	0.82	7.9		9.01	0.15
n5391-24	CL-bright	961	22	964	10	965	11	966	25	208.3	181.8	0.88	8.6		n.a.	n.a.
n5391-17a	CL-bright	970	12	968	8	967	10	981	23	306.1	126.3	0.42	11.6		n.a.	n.a.
n5387-06a	CL-bright	962	39	974	16	980	15	988	33	94.2	155.0	1.69	4.5		9.03	0.19
n5387-10b	CL-bright	997	21	988	13	984	16	974	29	142.6	212.0	1.45	6.7		9.10	0.19
n5387-01a	CL-bright	938	23	973	11	988	13	1000	28	124.6	200.9	1.72	6.0		8.83	0.18
n5391-23a	CL-bright	1032	21	1003	11	989	13	999	27	120.4	161.3	1.30	5.5		n.a.	n.a.
n5391-04a	CL-bright	1017	33	1000	13	992	11	1061	28	146.0	166.0	1.19	6.5		8.65	0.17
n5387-20b	CL-bright	973	18	987	9	993	10	986	28	192.6	159.2	0.84	8.1		9.09	0.19
n5391-08b	CL-bright	977	13	990	8	996	10	1008	30	204.3	189.0	0.96	8.8		8.94	0.17
n5391-23b	CL-bright	1048	17	1014	10	998	13	1002	25	131.2	159.1	1.16	6.0		n.a.	n.a.
n5391-12a	CL-bright	1035	14	1016	8	1008	9	1017	24	266.6	232.7	0.86	11.5		9.06	0.18
n5387-15b	CL-bright	1000	32	1021	16	1031	17	1038	39	155.6	182.8	1.22	7.3		9.05	0.15

Tab. 6 continued

		Isotope ratio										
Grain n°	**Texture**	**$^{207}Pb/^{206}Pb$**	**1s %**	**$^{207}Pb/^{235}U$**	**1s %**	**$^{206}Pb/^{238}U$**	**1s %**	**Rho**	**$^{208}Pb/^{232}Th$**	**1s %**	**f_{206} %**	**% disc.**
n5391-09a	CL-dark sector	0.0696	1.07	1.5024	1.45	0.1567	0.99	0.68	0.0483	4.0	{0.03}	2.7
n5391-02b	CL-dark sector	0.0704	0.61	1.5362	1.29	0.1583	1.14	0.88	0.0522	2.9	{0.00}	0.9
n5387-02b	CL-dark sector	0.0701	0.62	1.5144	1.43	0.1566	1.29	0.90	0.0498	3.2	{0.03}	0.6
n5391-11b	CL-dark sector	0.0706	0.60	1.5166	1.17	0.1558	1.01	0.86	0.0475	2.5	{0.01}	-1.5
n5391-14b	CL-dark sector	0.0700	0.61	1.5129	1.23	0.1567	1.07	0.87	0.0475	2.4	{0.00}	1.1
n5391-30	CL-dark sector	0.0737	0.49	1.7621	1.12	0.1733	1.01	0.90	0.0528	2.7	{0.01}	-0.5
n5387-06c	CL-dark rim	0.0711	0.50	1.5847	1.36	0.1617	1.27	0.93	0.0516	2.9	{0.00}	0.7
n5387-06b	CL-dark rim	0.0724	0.41	1.6758	1.36	0.1679	1.30	0.95	0.0533	2.8	{0.00}	0.4
n5391-22a	CL-dark rim	0.0711	0.51	1.5823	1.16	0.1615	1.05	0.90	0.0499	2.4	{0.00}	0.7
n5387-07b	CL-dark rim	0.0728	0.65	1.7342	1.46	0.1728	1.30	0.89	0.0538	2.9	{0.01}	2.2
n5387-11c	CL-dark rim	0.0717	0.54	1.6542	1.16	0.1674	1.03	0.88	0.0505	2.4	{0.00}	2.3
n5391-21b	CL-dark rim	0.0696	0.53	1.4992	1.15	0.1563	1.02	0.89	0.0475	2.4	{0.02}	2.5
n5387-13b	CL-dark rim	0.0703	0.75	1.5665	1.45	0.1615	1.25	0.86	0.0498	2.8	{0.00}	3.1
n5387-17b	CL-dark rim	0.0714	0.46	1.5851	1.12	0.1610	1.02	0.91	0.0490	2.3	0.02	-0.7
n5391-21a	CL-dark rim	0.0699	0.50	1.5060	1.12	0.1562	1.00	0.90	0.0472	2.4	{0.01}	1.1
n5387-17a	CL-dark rim	0.0725	0.40	1.6755	1.00	0.1677	0.92	0.92	0.0510	2.4	{0.00}	0.0
n5391-18a	CL-dark rim	0.0705	0.65	1.5532	1.25	0.1598	1.07	0.85	0.0486	2.5	{0.00}	1.5
n5387-11a	CL-dark rim	0.0726	0.59	1.7349	1.42	0.1732	1.29	0.91	0.0533	2.8	{0.01}	2.8
n5391-10b	CL-dark rim	0.0722	0.64	1.6534	1.23	0.1661	1.05	0.85	0.0506	2.4	{0.01}	-0.2
n5391-07a	CL-dark rim	0.0717	0.46	1.6251	1.17	0.1643	1.07	0.92	0.0518	2.3	{0.00}	0.2
n5391-20	CL-dark rim	0.0728	0.57	1.7153	1.24	0.1709	1.10	0.89	0.0487	2.4	{0.01}	1.0
n5391-26	CL-dark rim	0.0728	0.43	1.7102	1.12	0.1704	1.04	0.92	0.0517	2.3	{0.00}	0.7
n5391-03a	CL-dark rim	0.0729	0.51	1.7385	1.28	0.1730	1.18	0.92	0.0547	2.4	{0.01}	1.9
n5391-01b	CL-dark rim	0.0719	0.50	1.6220	1.16	0.1637	1.04	0.90	0.0514	2.4	{0.01}	-0.5
n5391-03b	CL-dark rim	0.0719	0.72	1.6738	1.38	0.1688	1.18	0.86	0.0515	2.4	{0.00}	2.4
n5391-16b	CL-dark rim	0.0723	0.43	1.7035	1.11	0.1708	1.03	0.92	0.0513	2.3	{0.00}	2.2
n5391-16a	CL-dark rim	0.0725	0.43	1.7159	1.12	0.1716	1.04	0.92	0.0521	2.3	{0.00}	2.1
n5387-05b	CL-dark rim	0.0704	0.51	1.5585	1.36	0.1605	1.26	0.93	0.0502	2.8	{0.01}	2.1

Tab. 6 continued

		Dates								Chemical composition (ppm)			Radiation damage	Oxygen isotopes	
Grain n°	**Texture**	**$^{207}Pb/^{206}Pb$**	**1s abs**	**$^{207}Pb/^{235}U$**	**1s abs**	**$^{206}Pb/^{238}U$**	**1s abs**	**$^{208}Pb/^{232}Th$**	**1s abs**	**U**	**Th**	**Th/U calc.**	**(x10^{17} alpha/g) at 1030 Ma***	**δ18O**	**± ‰**
n5391-09a	CL-dark sector	915	22	931	9	938	9	954	37	333.5	13.2	0.04	11.3	9.06	0.16
n5391-02b	CL-dark sector	940	13	945	8	947	10	1029	29	350.1	22.8	0.07	12.0	8.85	0.17
n5387-02b	CL-dark sector	933	13	936	9	938	11	983	31	419.2	45.5	0.11	14.3	9.06	0.15
n5391-11b	CL-dark sector	946	12	937	7	933	9	938	23	313.3	64.1	0.20	10.9	n.a.	n.a.
n5391-14b	CL-dark sector	929	12	936	8	939	9	938	22	406.3	108.6	0.27	14.4	8.80	0.16
n5391-30	CL-dark sector	1035	10	1032	7	1030	10	1040	28	460.3	102.4	0.22	17.9	n.a.	n.a.
n5387-06c	CL-dark rim	960	10	964	9	966	11	1016	29	757.8	127.5	0.18	27.2	8.97	0.19
n5387-06b	CL-dark rim	997	8	999	9	1000	12	1049	29	834.8	139.1	0.18	31.1	8.71	0.16
n5391-22a	CL-dark rim	959	10	963	7	965	9	985	23	468.9	139.4	0.31	17.2	n.a.	n.a.
n5387-07b	CL-dark rim	1008	13	1021	9	1028	12	1060	29	483.7	155.6	0.34	19.2	9.12	0.15
n5387-11c	CL-dark rim	977	11	991	7	998	9	995	23	526.8	156.2	0.30	20.1	n.a.	n.a.
n5391-21b	CL-dark rim	915	11	930	7	936	9	939	22	415.7	161.0	0.40	15.1	n.a.	n.a.
n5387-13b	CL-dark rim	938	15	957	9	965	11	982	27	390.0	165.9	0.45	14.7	8.83	0.17
n5387-17b	CL-dark rim	969	9	964	7	962	9	967	22	765.5	167.3	0.22	27.6	8.71	0.17
n5391-21a	CL-dark rim	926	10	933	7	936	9	932	21	490.5	168.0	0.34	17.6	n.a.	n.a.
n5387-17a	CL-dark rim	999	8	999	6	999	9	1005	23	671.1	168.5	0.25	25.4	8.92	0.16
n5391-18a	CL-dark rim	942	13	952	8	956	9	959	23	382.6	178.7	0.48	14.4	n.a.	n.a.
n5387-11a	CL-dark rim	1004	12	1022	9	1030	12	1049	29	470.4	182.0	0.40	18.9	9.09	0.17
n5391-10b	CL-dark rim	992	13	991	8	990	10	997	23	427.4	185.7	0.44	16.6	9.05	0.19
n5391-07a	CL-dark rim	979	9	980	7	980	10	1021	23	492.8	191.0	0.40	18.8	8.60	0.16
n5391-20	CL-dark rim	1008	11	1014	8	1017	10	961	23	460.6	215.4	0.45	18.6	n.a.	n.a.
n5391-26	CL-dark rim	1008	9	1012	7	1014	10	1019	23	541.4	218.1	0.41	21.5	n.a.	n.a.
n5391-03a	CL-dark rim	1011	10	1023	8	1029	11	1077	25	371.0	220.6	0.63	15.5	8.84	0.16
n5391-01b	CL-dark rim	982	10	979	7	977	9	1013	23	442.6	228.5	0.53	17.3	8.86	0.21
n5391-03b	CL-dark rim	984	15	999	9	1005	11	1014	24	343.6	230.0	0.69	14.2	n.a.	n.a.
n5391-16b	CL-dark rim	996	9	1010	7	1016	10	1010	23	544.4	250.8	0.47	21.9	n.a.	n.a.
n5391-16a	CL-dark rim	1001	9	1015	7	1021	10	1026	23	536.0	254.9	0.49	21.7	n.a.	n.a.
n5387-05b	CL-dark rim	941	10	954	8	959	11	990	27	581.0	255.8	0.46	21.9	9.06	0.17

Supplementary material

Tab. S4-1: Trace element analyses of the zircon reference material 91500 acquired alongside with unknown reported in Tab. 4-1

	Ti	Y	Nb	Hf	Ta	La	Ce	Pr	Nd	Sm	Eu	Gd	Tb	Dy	Ho	Er	Tm	Yb	Lu	Pb	Th	U
Session b																						
04-91500	<7.32	144	1.64	5731	0.37	b.d.l	2.47	b.d.l	b.d.l	b.d.l	b.d.l	2.21	0.76	11.23	4.44	25.3	5.94	61.8	12.87	2.57	26.94	77
05-91500	13	146	1.57	5807	0.50	b.d.l	2.54	b.d.l	b.d.l	b.d.l	0.25	2.13	0.80	10.70	4.57	25.2	5.99	63.5	13.12	2.77	27.35	78
28-91500	9	142	1.37	5640	0.41	b.d.l	2.52	b.d.l	b.d.l	b.d.l	0.28	1.66	0.74	10.76	4.41	24.3	5.75	59.4	12.64	2.45	25.70	74
29-91500	9	142	1.44	5911	0.46	b.d.l	2.60	b.d.l	b.d.l	b.d.l	b.d.l	2.00	0.86	10.86	4.71	25.2	6.10	63.3	13.13	2.79	27.04	78
51-91500	<7.81	144	1.33	6167	0.48	b.d.l	2.64	b.d.l	b.d.l	b.d.l	0.23	2.48	0.78	11.63	4.68	27.5	6.38	67.1	13.73	3.06	29.15	87
52-91500	11	142	1.29	6185	0.53	b.d.l	2.59	b.d.l	b.d.l	b.d.l	0.25	2.50	0.83	11.72	4.58	25.9	6.45	66.6	13.16	2.96	28.49	85
73-91500	8	145	1.32	5820	0.50	b.d.l	2.54	b.d.l	b.d.l	b.d.l	0.26	2.20	0.84	11.33	4.46	24.4	6.17	62.3	13.09	2.64	26.63	77
74-91500	9	141	1.31	5750	0.39	b.d.l	2.45	b.d.l	b.d.l	b.d.l	0.22	2.10	0.79	10.47	4.49	24.8	5.89	60.0	12.44	2.74	25.62	76
94-91500	7	118	1.32	6394	0.51	b.d.l	2.38	b.d.l	b.d.l	b.d.l	b.d.l	1.83	0.64	9.33	3.86	23.1	5.58	58.2	11.24	2.30	23.23	73
95-91500	8	122	1.35	6467	0.36	b.d.l	2.42	b.d.l	b.d.l	b.d.l	b.d.l	2.21	0.69	9.76	4.09	22.5	5.73	59.9	11.72	2.69	24.92	75
Mean	**9**	**139**	**1.39**	**5987**	**0.45**	**b.d.l**	**2.51**	**b.d.l**	**b.d.l**	**b.d.l**	**0.25**	**2.13**	**0.77**	**10.78**	**4.43**	**24.8**	**6.00**	**62.2**	**12.71**	**2.70**	**26.51**	**78**
sd	2	10	0.12	294	0.06	b.d.l	0.08	b.d.l	b.d.l	b.d.l	0.02	0.26	0.07	0.77	0.27	1.4	0.28	3.0	0.74	0.23	1.72	4
Session c																						
3-91500	<7.19	123	1.35	5653	0.48	b.d.l	2.36	b.d.l	b.d.l	b.d.l	b.d.l	1.40	0.66	8.80	3.44	20.5	4.91	50.5	10.44	2.15	20.96	60
30-91500	<7.86	129	1.14	5322	0.34	b.d.l	2.52	b.d.l	b.d.l	b.d.l	b.d.l	1.50	0.75	10.11	3.71	22.1	5.11	53.7	11.04	2.43	23.47	66
31-91500	10	126	1.19	5787	0.42	b.d.l	2.32	b.d.l	b.d.l	b.d.l	b.d.l	2.24	0.68	9.41	3.83	22.8	5.47	54.8	11.29	2.43	23.63	67
77-91500	12	157	1.28	5859	0.49	b.d.l	2.78	b.d.l	b.d.l	b.d.l	0.269	2.44	0.90	11.81	4.87	26.4	6.25	66.8	13.49	3.21	32.47	92
86-91500	<8.90	139	1.17	6801	0.45	b.d.l	2.55	b.d.l	b.d.l	b.d.l	b.d.l	2.81	0.81	12.29	5.04	27.7	6.96	73.6	14.21	3.50	32.86	99
4-91500	8	122	1.16	5909	0.34	b.d.l	2.33	b.d.l	b.d.l	b.d.l	b.d.l	2.03	0.69	8.61	3.63	21.8	5.07	52.5	11.02	2.18	21.63	63
Mean	**10**	**133**	**1.21**	**5888**	**0.42**	**b.d.l**	**2.48**	**b.d.l**	**b.d.l**	**b.d.l**	**0.27**	**2.07**	**0.75**	**10.17**	**4.09**	**23.6**	**5.63**	**58.6**	**11.92**	**2.65**	**25.84**	**75**
sd	2	12	0.08	451	0.06	b.d.l	0.16	b.d.l	b.d.l	b.d.l		0.50	0.08	1.42	0.63	2.6	0.74	8.5	1.41	0.52	4.92	15
Session b +c																						
Average	10	136	1.33	5950	0.44	b.d.l	2.50	b.d.l	b.d.l	b.d.l	0.25	2.11	0.76	10.55	4.30	24.3	5.86	60.9	12.41	2.68	26.26	77
sd	2	11	0.14	368	0.06	b.d.l	0.12	b.d.l	b.d.l	b.d.l	0.02	0.37	0.08	1.12	0.48	2.1	0.55	6.1	1.13	0.37	3.40	10
Accepted value	8	140	0.79	5900			2.56	0.024	0.24	0.5	0.24	2.21	0.86	11.80	4.84	24.6	6.89	73.9	13.10		29.90	80
sd	5	14		100			0.26		0.04	0.08	0.03	0.24	0.06	0.83	0.34	2.5	0.34	3.7	1.05		2.09	8
Difference	-0.19	0.03	-0.68	-0.01		b.d.l	0.02	b.d.l	b.d.l	b.d.l	-0.05	0.05	0.11	0.11	0.11	0.01	0.15	0.18	0.05		0.12	0.04

S4-2: Phase equilibria modelling for sample ALR 13-69

Methods

Phase equilibria of metamorphic assemblages were modelled using *P–T* and *T–X* pseudosections in the $MnO–Na_2O–CaO–K_2O–FeO–MgO–Al_2O_3–SiO_2–H_2O–TiO_2–O_2$ chemical system using Perple_X (version 6.7.2; Connolly 2009). All samples were modelled using the internally consistent thermodynamic database of Holland and Powell (2002) together with activity–composition models of White et al. (2007). The phases under consideration are garnet, silicate melt, plagioclase, K-feldspar, sillimanite, spinel, magnetite, ilmenite–hematite, rutile, orthopyroxene, sapphirine, cordierite, biotite, muscovite, quartz. The bulk rock composition have been determined by ICP–OES on the rock chips left over after thin section preparation at the CRPG (Nancy), following standard procedure described in Carignan et al. (2001). FeO has been measured by titration to estimate the oxidation state of the whole rock. Chemical composition used for modelling are reported as oxides weight percentage along with measured compositions are reported below:

Composition used for modelling (mol.%)										
SiO_2	TiO_2	Al_2O_3	FeO	Fe_2O_3	MgO	CaO	MnO	Na_2O	K_2O	H_2O
72.28	0.58	9.12	4.41	1.44	0.96	3.53	0.26	3.96	0.99	1.5
Measured composition (wt.%)										
66.30	0.71	14.20	4.84	3.51	0.59	3.02	0.28	3.75	1.42	0.68

Quantitative analysis of silicate and oxides were collected with the Cameca SX-Five microprobe with standard operating conditions of 15 kV and 20 nA. Representative analyses of mineral composition are reported in Tab.S4-2 below. The mineral formula of Garnet (Grt) and feldspar were calculated on the basis of 8 cations. Minerals belonging to the magnetite–ulvospinel–spinel–hercynite solid solution were calculated on the basis of 3 cations and 4 oxygens. Biotite (Bt) analyses were recalculated on the basis of 11 O. All mineral abbreviations follow Whitney and Evans (2010).

Results and interpretation

The sample ALR 13-69 is a migmatitic gneiss with garnet porphyroblast from a Gt-Bt–rich selvage zone. It has been sampled in the Hunndendalen, 35 km from the AMC contact and about 10 km beyond the mapped Opx-in isograd. The dominant structure in the area consists in large kilometric open folds with N-S trending vertical axial plane affecting a flat fabric characterized by alternating decimeter-thick bt-opx-rich melanosomes and q-pl-kfs-garnet leucosomes. Assemblage comprising Garnet (10 %) Biotite (20 %) Orthopyroxene (5 %) K-feldspar (20 %) plagioclase (10 %) quartz (30 %) magnetite (3 %) and minor secondary chlorite as well as accessory ilmenite, pyrrhotite, molybdenite, monazite, apatite and zircon. The main fabric is defined by ribbons of quartz and biotite wrapping around poikiloblastic garnet with oriented inclusions of quartz, K-feldspar and biotite. Garnets are unzoned with respect to Fe/Mg ratio (X_{Mg} = 0.19−0.20) but display a thin rim (<50 μm) richer in grossular than the core (Xgrs = 4.7−6.6). Several generations of biotite are present in the sample, (1) as inclusions in garnet poikiloblasts (X_{Mg} = 0.54–0.63; Ti = 0.23–0.30 apfu; F = 0.17–0.20 apfu), (2) in the matrix and in pressure shadows of garnets frequently associated with ilmenite along cleavage pointing to the exsolutions of the Ti-component upon cooling. (3) Flakes lacking preferential orientation in the matrix (X_{Mg} = 0.32–0.39; Ti = 0.25–0.26 apfu) and secondary growth along garnet cracks together with chlorite. Orthopyroxene is mostly replaced by a fine symplectite of biotite + quartz or appears strongly retrogressed into chlorite.

The calculated pseudosection for sample *ALR 13-69* is contoured with isopleths of X_{Mg} in garnet and X_{Grs} (grossular component in garnet). Overall the chosen rock composition shows only a limited number of reactions. The most prominent being the solidus located at a temperature of c. 670 °C and the terminal biotite breakdown into orthopyroxene recorded in a narrow field at c. 800°C. The garnet X_{Mg} and X_{Grs} isopleths indicate equilibrium at rather low pressure 4–5 kbar and some 775–800 °C in the stability field Bt + melt + Grt + Mag + Ilm and straddling the biotite-out reaction. This is consistent with petrographic inspection showing poikiloblastic garnets with inclusions of quartz, biotite, K-feldpar that are interpreted to result from a fluid-absent dehydration melting such as Bt = Grt + Qz + Kfs followed by the appearance of orthopyroxene. In the sample *ALR 13-69*, we interpret biotite + quartz symplectite to pseudomorph othopyroxene upon cooling of hydrous melt following Waters (2001).

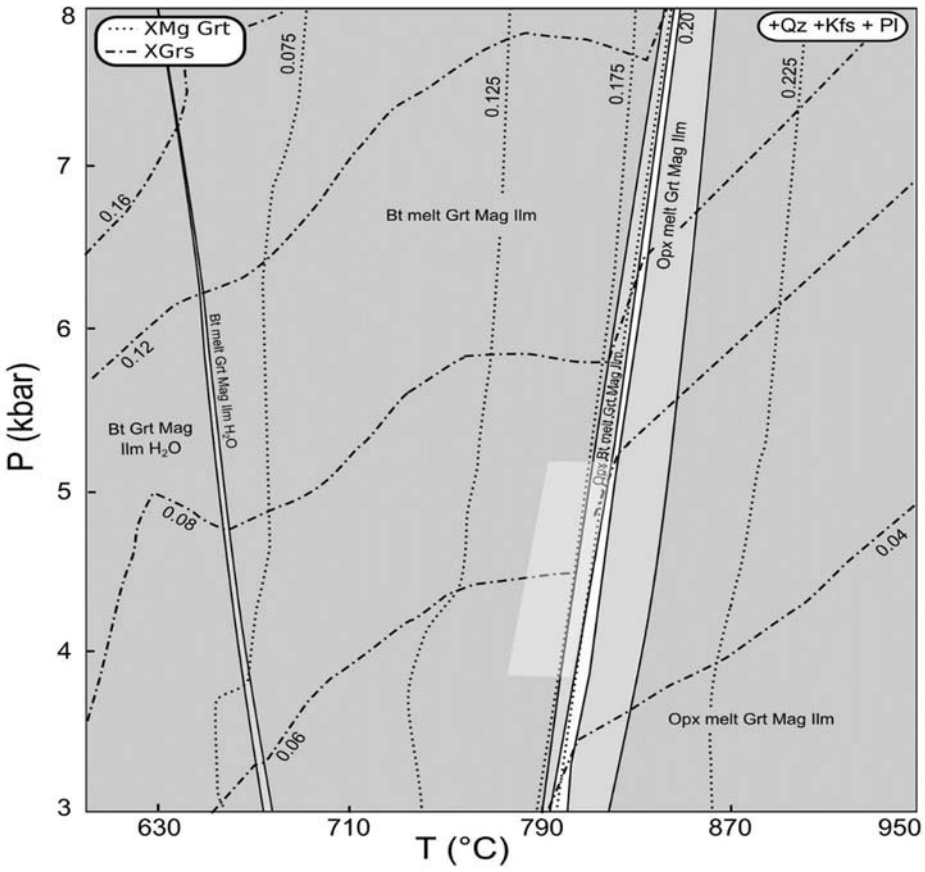

Pseudosection for sample ALR 13-69. The white-shaded field corresponds to the peak temperature field (see text)

Tab. S4-2a: Representative analyses of garnet for sample ALR 13-69

Analysis	13-69_Gt1_1	13-69_Gt1_2	13-69_Gt1_3	13-69_Gt1_4	13-69_Gt2_1	13-69_Gt2_2	13-69_Gt2_3	13-69_Gt2_4
Oxides (Wt. %)								
SiO_2	36.68	36.84	37.41	36.61	36.08	36.55	36.81	36.92
TiO_2	0.03	0.05	0.03	0.04	0.02	0.03	0.03	0.01
Al_2O_3	20.62	20.73	20.83	20.61	20.32	20.57	20.69	20.63
Cr_2O_3	0.02	0.00	0.01	0.00	0.01	0.00	0.01	0.00
FeO	31.21	31.64	31.66	31.34	31.42	31.24	31.45	31.00
MnO	4.13	3.92	3.87	3.98	4.09	3.86	3.87	3.90
MgO	3.65	4.14	4.05	3.86	3.98	4.34	4.34	4.32
CaO	2.22	1.70	1.65	2.15	2.07	1.86	1.79	2.22
Total	**98.56**	**99.01**	**99.52**	**98.58**	**97.98**	**98.44**	**98.99**	**98.99**
Formula(O=12)								
Si	2.981	2.975	3.006	2.972	2.947	2.964	2.969	2.975
Ti	0.002	0.003	0.002	0.002	0.001	0.002	0.002	0.001
Al	1.975	1.973	1.973	1.972	1.956	1.966	1.967	1.959
Cr	0.001	0.000	0.000	0.000	0.001	0.000	0.000	0.000
Fe^{3+}	0.058	0.072	0.010	0.080	0.146	0.104	0.092	0.090
tot. cubic	2.036	2.047	1.985	2.054	2.104	2.071	2.061	2.049
Fe^{2+}	2.063	2.065	2.117	2.047	2.000	2.014	2.030	1.999
Mn	0.284	0.268	0.264	0.273	0.283	0.265	0.265	0.266
Mg	0.442	0.498	0.485	0.467	0.485	0.524	0.522	0.518
Ca	0.193	0.147	0.142	0.187	0.181	0.161	0.155	0.192
tot. oct	2.983	2.978	3.008	2.974	2.949	2.965	2.971	2.976
XMg	0.18	0.19	0.19	0.19	0.20	0.21	0.20	0.21
Xalm	69.16	69.33	70.38	68.82	67.83	67.93	68.32	67.20
Xpyr	14.82	16.73	16.12	15.69	16.45	17.68	17.57	17.42
Xgr	6.48	4.94	4.73	6.29	6.13	5.44	5.20	6.44
Xsps	9.54	9.01	8.76	9.19	9.59	8.95	8.91	8.94
Xand	1.91	2.35	0.34	2.64	4.72	3.39	3.00	2.93
tot. Oxygen	12.000	12.000	12.000	12.000	12.000	12.000	12.000	12.000
tot. Cation	8.000	8.000	8.000	8.000	8.000	8.000	8.000	8.000

Tab. S4-2b: Representative analyses of biotite for sample ALR 13-69

Analysis *Texture*	13-69_Gt2_bt1-1	13-69_Gt2_bt1-2	13-69_Gt2_bt2-1	13-69_Bt3	13-69_Bt3-2	13-69_Bt4-1 *core*	13-69_Bt4-2 *rim*	13-69_Gt1-Bt5
Oxides (Wt. %)								
SiO_2	35.36	34.63	36.69	28.26	35.02	35.23	34.02	36.05
TiO_2	4.61	3.88	5.17	3.87	4.36	4.45	4.20	4.87
Al_2O_3	13.58	13.68	13.27	14.52	13.91	14.60	14.53	13.49
FeO	17.83	18.98	14.71	30.90	23.28	21.28	24.99	15.96
MnO	0.14	0.18	0.04	0.22	0.18	0.10	0.20	0.12
MgO	11.97	11.92	13.86	6.53	8.29	8.78	6.59	12.58
CaO	0.11	0.16	0.00	2.20	0.04	0.00	0.02	0.00
Na_2O	0.26	0.17	0.32	0.02	0.08	0.09	0.09	0.29
K_2O	8.44	7.55	9.20	2.29	9.09	9.52	8.94	9.13
BaO	0.12	0.13	0.14	0.03	0.11	0.12	0.09	0.07
F	0.81	0.66	0.74	0.10	0.37	0.56	0.31	0.67
Cl	0.27	0.25	0.27	0.05	0.11	0.12	0.12	0.22
Total	**93.49**	**92.19**	**94.41**	**88.97**	**94.83**	**94.86**	**94.12**	**93.43**
Formula(O=11)								
Si	2.77	2.75	2.81	2.44	2.77	2.77	2.74	2.80
Al(iv)	1.23	1.25	1.19	1.47	1.23	1.23	1.26	1.20
Al	0.03	0.04	0.00	0.00	0.06	0.12	0.11	0.04
Mg	1.40	1.41	1.58	0.84	0.98	1.03	0.79	1.46
Fe^{2+}	1.17	1.26	0.94	2.23	1.54	1.40	1.68	1.04
Ti	0.27	0.23	0.30	0.25	0.26	0.26	0.25	0.28
Mn	0.01	0.01	0.00	0.02	0.01	0.01	0.01	0.01
Cr	0.00	0.00	0.00	0.00	0.00	0.00	0.00	0.00
Ca	0.01	0.01	0.00	0.20	0.00	0.00	0.00	0.00
Na	0.04	0.03	0.05	0.00	0.01	0.01	0.01	0.04
K	0.84	0.77	0.90	0.25	0.92	0.95	0.92	0.90
Ba	0.00	0.00	0.00	0.00	0.00	0.00	0.00	0.00
Sr	0.00	0.00	0.00	0.00	0.00	0.00	0.00	0.00
Rb	0.00	0.00	0.00	0.00	0.00	0.00	0.00	0.00
F	0.20	0.17	0.18	0.03	0.09	0.14	0.08	0.16
Cl	0.04	0.03	0.03	0.01	0.01	0.02	0.02	0.03
OH*	1.76	1.80	1.79	1.97	1.89	1.84	1.90	1.81
XMg	0.54	0.53	0.63	0.27	0.39	0.42	0.32	0.58
tot. Oxygen	11.000	11.000	11.000	11.000	11.000	11.000	11.000	11.000
tot. Cation	9.771	9.768	9.772	9.703	9.789	9.780	9.787	9.772

Tab. S4-2c: Representative analyses of feldspar for sample ALR 13-69

Analysis	13-69_Pl1	13-69_Pl1-2	13-69_Pl2	13-69_Pl2-2	13-69_Pl3-1	13-69_Pl3-2
Texture	*core*	*rim*	*rim*	*core*		
Oxides (Wt. %)						
SiO_2	61.95	61.39	61.38	61.55	61.51	61.40
TiO_2	0.01	0.02	0.00	0.03	0.03	0.01
Al_2O_3	22.84	22.67	22.91	22.64	22.87	22.89
FeO	0.03	0.19	0.25	0.07	0.02	0.26
MnO	0.00	0.01	0.01	0.02	0.02	0.05
MgO	0.03	0.00	0.00	0.00	0.00	0.02
CaO	5.56	5.49	5.41	5.66	5.76	5.57
Na_2O	8.28	8.48	8.47	8.14	8.17	8.18
K_2O	0.46	0.34	0.43	0.44	0.42	0.50
BaO	0.00	0.00	0.00	0.00	0.00	0.00
Total	**99.16**	**98.59**	**98.87**	**98.56**	**98.80**	**98.88**
Formula(O=8)						
Si	2.777	2.764	2.755	2.779	2.769	2.762
Ti	0.000	0.001	0.000	0.001	0.001	0.000
Al	1.207	1.203	1.212	1.205	1.213	1.214
Cr	0.000	0.000	0.000	0.000	0.000	0.000
Fe^{3+}	0.000	0.029	0.039	0.000	0.000	0.003
Fe^{2+}	0.001	-0.021	-0.030	0.003	0.001	0.007
Mn	0.000	0.000	0.000	0.001	0.001	0.002
Mg	0.002	0.000	0.000	0.000	0.000	0.001
Ca	0.267	0.265	0.260	0.274	0.278	0.269
Na	0.720	0.741	0.738	0.712	0.713	0.714
K	0.026	0.020	0.025	0.026	0.024	0.029
Ba	0.000	0.000	0.000	0.000	0.000	0.000
Sr	0.000	0.000	0.000	0.000	0.000	0.000
Rb	0.000	0.000	0.000	0.000	0.000	0.000
An (mol%)	26.35	25.82	25.44	27.06	27.37	26.57
Ab (mol%)	71.05	72.25	72.14	70.41	70.25	70.59
Or (mol%)	2.60	1.92	2.43	2.53	2.39	2.84
tot. Oxygen	8.008	8.000	8.000	8.014	8.008	8.000
tot. Cation	5.000	5.000	5.000	5.000	5.000	5.000

S4-3: Monazite chemistry and U–Th–Pb geochronology for sample ALR 13-69

Methods

Monazite crystals were studied in mineral separate recovered by standard procedures, including crushing, heavy liquors and magnetic separation. Back Scattered Electron (BSE) images were taken at 20 kV with a SEM to guide *in-situ* chemical analysis acquired with a Cameca SX-FIVE electron probe micro-analyser (EPMA) hosted at the Raimond Castaing micro-characterization centre (Toulouse). The EPMA was operated with a focused beam at standard conditions of 15 kV and 20 nA

Uranium–thorium–lead isotopic analyses were performed by LA–ICP–MS in at the Laboratoire Magmas et Volcans (Clermont-Ferrand, France). Laser ablation spots were guided with BSE images, chemical composition previously acquired by EPMA together with reflected and transmitted light microphotograph. The laser ablation systems consists of a Resonetics Resolution M-50E system equipped with an ultra-short pulse (< 4 ns) ATL excimer 193 nm laser coupled to an Agilent 7500 cs ICP–MS. Detailed analytical procedures are reported in Paquette and Tiepolo (2007) and Didier et al. (2015). A spot diameter of 9 µm was used with 1 Hz repetition rate and a fluence of 6 J/cm². The ^{204}(Hg+Pb) signal was monitored but no common-Pb correction was applied. Raw data are corrected for U–Pb and Th–Pb fractionation during laser ablation and instrumental mass discrimination by standard bracketing with the C83-32 monazite (2681 ± 2 Ma; Corfu 1988). Repeated analysis during the run of Moacyr monazite (Seydoux-Guillaume et al. 2002a; Gasquet et al. 2010; Fletcher et al. 2010) and either Trebilcock monazite (272 ± 2 Ma; Tomascak et al. 1996) was used to monitor accuracy and reproducibility of the correction applied. During the analytical session 49 analyses of Trebilcock yielded a weighted ^{206}Pb/^{238}U age of 268 ± 3 Ma (MSWD = 1.3) and 8 analyses of Moacyr yielded a weighted ^{208}Pb/^{232}Th age of 502 ± 5 Ma (MSWD = 0.4). Data reduction was carried out using the Glitter software package (Van Achterbergh et al. 2001).

Results

In sample ALR *13-69*, monazite crystal display variable shape and BSE textures ranging from euhedral homogenous grains to rounded patchy crystals crowded with solid inclusions of Th-silicate. The different chemical zones show a large variability in their Th and Y content (ThO_2 = 1.8–9.8 wt%; Y_2O_3 = 0.6–4.8 wt%; Supplementary material S4-3), although no systematic

correlation were found between grains. Twenty-seven U–Th–Pb isotopic analyses have been carried out in 19 grain and are presented in Tera-Wasserburg diagram and reported in tables below along with corresponding monazite chemistry. The dominant age group consist of both zoned rounded grains and euhedral homogenous grain that have individual $^{206}Pb/^{238}U$ are scattering between 1072 ± 36 and 1000 ± 34 Ma. The $^{208}Pb/^{232}Th$ ages reveal similar scatter between 1078 ± 31 and 999 ± 30 Ma. Since no chemical tracer or textural features allows to distinguish different generations, we define a single $^{206}Pb/^{207}Pb$ weighted average of 1038 ± 9 Ma (MSWD = 0.4; n = 24) for this population. Individual crystals nevertheless suggests that several (re)crystallization events occurred between c. 1060 Ma and c. 1000 Ma, equivalent within the analytical errors. Finally, three younger spots retrieved from a single crystal yields a concordia age of 937 ± 9 Ma.

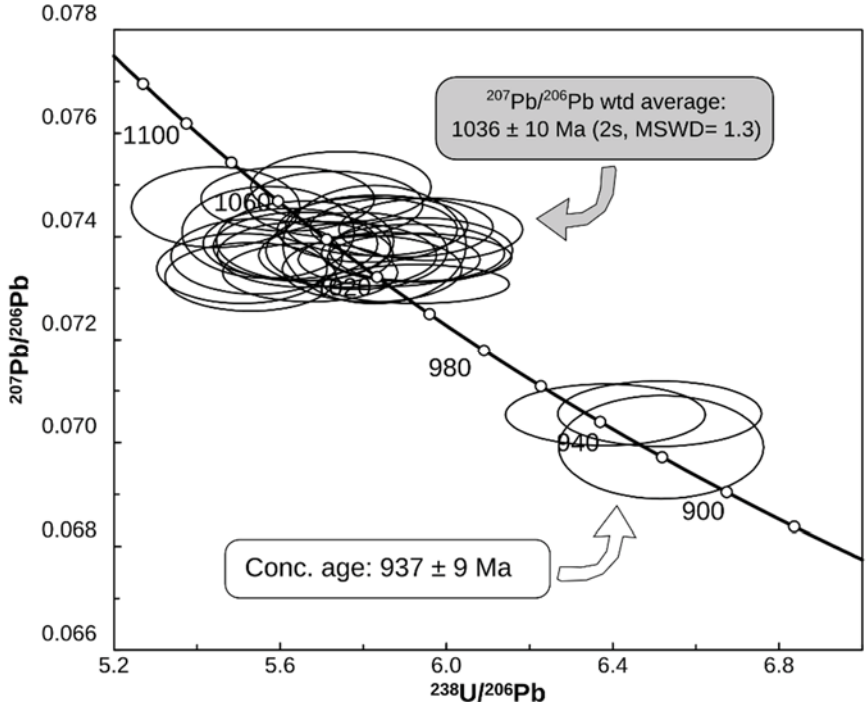

Monazite U–Th–Pb data presented in Terra-Wasserburg diagram for sample ALR 13-69. All error ellispses and quoted confidence interval are given at the 2σ level ;

Tab. S4-3: Monazite U-Th-Pb ratio and date measured by LA-ICP-MS for sample 13-69

	Isotope ratio									Dates								
Grain n°	Pb^{207}/Pb^{206}	**2s %**	Pb^{207}/U^{235}	**2s %**	Pb^{206}/U^{238}	**2s**	**rho**	Pb^{208}/Th^{232}	**2s**	Pb^{207}/Pb^{206}	**2s**	Pb^{207}/U^{235}	**2s**	Pb^{206}/U^{238}	**2s**	Pb^{208}/Th^{232}	**2s**	**% conc.**	**Th/U**
1369-03	0.0747	2.22	1.8341	3.45	0.1780	3.38	0.98	0.0548	2.88	1061.4	30.59	1057.7	36.51	1056.1	35.74	1077.6	31.05	99.5	8
1369-04a	0.0736	2.28	1.8311	3.48	0.1804	3.39	0.97	0.0528	2.87	1031.2	29.60	1056.7	36.81	1069.1	36.22	1039.6	29.84	103.5	13
1369-04b	0.0741	2.35	1.8335	3.53	0.1795	3.39	0.95	0.0534	2.88	1043.9	30.05	1057.5	37.33	1064.2	36.09	1050.5	30.24	101.9	16
1369-05	0.0738	2.25	1.8004	3.51	0.1769	3.43	0.97	0.0528	2.91	1036.5	30.13	1045.6	36.70	1050.1	36.03	1039.1	30.21	101.3	11
1369-06	0.0741	2.24	1.7594	3.46	0.1721	3.39	0.98	0.0527	2.87	1045.3	30.04	1030.6	35.69	1023.8	34.74	1038.3	29.84	97.9	8
1369-06b	0.0737	2.20	1.7163	3.45	0.1689	3.39	0.98	0.0524	2.89	1032.9	29.84	1014.7	34.98	1006.3	34.14	1032.4	29.82	97.4	9
1369-07	0.0742	2.21	1.7145	3.44	0.1677	3.38	0.98	0.0521	2.87	1045.5	29.97	1014	34.93	999.5	33.78	1027	29.44	95.4	6
1369-09	0.0732	2.24	1.8261	3.47	0.1809	3.39	0.97	0.0531	2.89	1020.3	29.47	1054.9	36.61	1071.7	36.34	1046.5	30.23	104.8	11
1369-100	0.0742	2.21	1.7545	3.48	0.1715	3.41	0.98	0.0517	2.89	1047.6	30.26	1028.8	35.75	1020.1	34.83	1018	29.41	97.3	8
1369-14	0.0737	2.23	1.7943	3.47	0.1767	3.39	0.97	0.0537	2.86	1032.3	29.54	1043.4	36.17	1048.7	35.60	1057.4	30.26	101.6	10
1369-17	0.0746	2.23	1.7954	3.45	0.1745	3.38	0.97	0.0528	2.87	1058.3	30.37	1043.8	35.99	1036.8	35.02	1040	29.84	97.9	4
1369-17	0.0737	2.23	1.7119	3.45	0.1684	3.38	0.98	0.0523	2.86	1034.4	29.57	1013	34.94	1003.2	33.91	1030	29.44	96.9	9
1369-21	0.0731	2.14	1.7000	3.45	0.1687	3.43	0.99	0.0520	2.91	1016.5	29.58	1008.5	34.83	1005	34.45	1024.1	29.80	98.9	21
1369-23	0.0737	2.26	1.7620	3.45	0.1735	3.38	0.98	0.0542	2.87	1031.8	29.63	1031.6	35.60	1031.6	34.89	1067.4	30.66	100.0	11
1369-24	0.0734	2.26	1.7380	3.45	0.1718	3.38	0.97	0.0526	2.84	1024.4	29.13	1022.7	35.31	1022	34.53	1035.9	29.46	99.8	5
1369-28a	0.0739	2.25	1.8107	3.48	0.1778	3.40	0.97	0.0525	2.88	1037.9	29.91	1049.3	36.52	1054.9	35.84	1034.9	29.82	101.6	11
1369-28b	0.0734	2.24	1.8370	3.47	0.1816	3.39	0.97	0.0526	2.88	1024.8	29.52	1058.8	36.77	1075.4	36.46	1035.5	29.83	104.7	11
1369-29a	0.0750	2.24	1.7987	3.51	0.1740	3.43	0.97	0.0520	2.91	1067.7	31.06	1045	36.64	1034.3	35.43	1024.3	29.79	96.8	14
1369-29b	0.0739	2.27	1.8007	3.53	0.1767	3.42	0.96	0.0512	2.91	1039.6	30.25	1045.7	36.90	1048.8	35.92	1009.9	29.39	100.9	12
1369-35a	0.0706	2.21	1.5238	3.49	0.1567	3.42	0.98	0.0486	2.89	944.3	27.33	940	32.82	938.3	32.11	959.3	27.76	99.4	20
1369-35b	0.0699	2.45	1.4793	3.63	0.1535	3.43	0.95	0.0459	2.88	926	26.65	921.9	33.43	920.3	31.60	907.9	26.13	99.4	6
1369-35c	0.0706	2.24	1.4938	3.50	0.1535	3.42	0.98	0.0470	2.90	945	27.42	927.8	32.45	920.8	31.50	928.1	26.93	97.4	23
1369-45	0.0736	2.18	1.7098	3.44	0.1685	3.40	0.99	0.0514	2.87	1030.8	29.54	1012.2	34.79	1003.7	34.12	1012.8	29.03	97.3	11
1369-46	0.0742	2.21	1.7359	3.46	0.1697	3.40	0.98	0.0519	2.88	1046.5	30.11	1021.9	35.36	1010.6	34.37	1022.6	29.42	96.4	12
1369-81	0.0736	2.18	1.7301	3.45	0.1706	3.40	0.98	0.0524	2.89	1029.7	29.74	1019.8	35.15	1015.3	34.49	1032.3	29.82	98.6	12
1369-89a	0.0737	2.28	1.7575	3.52	0.1729	3.42	0.97	0.0509	2.89	1034.2	29.87	1029.9	36.26	1028	35.19	1004	29.00	99.4	43
1369-89b	0.0739	2.51	1.7475	3.66	0.1716	3.43	0.93	0.0507	2.90	1037.5	30.11	1026.2	37.55	1021.1	35.06	998.7	28.99	98.4	21

Tab. S4-3: continued

	Chemical composition												
Grain n°	**SiO_2**	**ThO_2**	**UO_2**	**Ce_2O_3**	**Y_2O_3**	**La_2O_3**	**Pr_2O_3**	**Sm_2O_3**	**Nd_2O_3**	**Gd_2O_3**	**Dy_2O_3**	**SO_2**	**CaO**
1369-03	0.438	3.868	0.506	23.085	2.991	8.685	3.383	4.593	15.084	3.912	1.493	0.029	0.75
1369-04a	0.593	4.612	0.35	23.313	2.501	8.25	3.642	4.796	15.381	4.464	1.101	0	0.578
1369-04b	0.695	4.589	0.294	23.338	2.206	8.347	3.868	4.709	16.272	3.398	1.064	0.04	0.626
1369-05	1.012	5.701	0.537	26.084	1.589	11.264	3.508	2.974	14.787	2.057	0.594	0	0.479
1369-06	0.607	4.657	0.552	24.696	1.725	9.262	3.442	3.713	15.861	2.36	0.669	0.027	0.701
1369-06b	0.777	5.035	0.552	24.383	1.845	8.875	3.715	3.826	16.703	2.738	0.691	0.01	0.643
1369-07	0.683	5.602	0.994	22.461	2.812	8.16	3.119	4.127	14.618	3.446	1.354	0	0.801
1369-09	0.84	6.485	0.574	23.898	1.225	8.434	3.68	3.611	16.191	2.431	0.587	0	0.747
1369-100	0.554	3.738	0.471	23.987	2.329	9.98	3.668	4.139	14.335	3.657	1.401	0.004	0.477
1369-14	0.874	5.985	0.622	22.294	4.833	8.558	3.585	3.248	13.473	3.235	1.504	0.031	0.77
1369-17	0.22	1.793	0.413	27.057	3.087	10.356	3.34	3.196	14.032	2.707	1.32	0.018	0.439
1369-17	0.538	4.422	0.508	24.933	1.929	9.27	3.547	4.136	15.487	2.908	0.986	0	0.663
1369-21	0.642	4.962	0.242	23.656	2.276	9.588	3.46	3.554	14.516	3.098	0.939	0.004	0.631
1369-23	0.854	5.936	0.532	26.011	1.46	10.378	3.624	2.858	14.882	1.735	0.742	0.025	0.747
1369-24	0.401	2.565	0.568	26.521	2.523	10.543	3.359	3.058	14.357	2.195	0.991	0	0.428
1369-28a	0.836	5.136	0.471	26.527	1.33	11.394	3.52	2.834	13.919	2.059	0.836	0	0.534
1369-28b	0.845	5.163	0.458	26.53	1.617	11.188	3.61	2.942	13.68	2.281	0.738	0	0.566
1369-29a	0.546	4.153	0.296	22.912	2.843	8.352	3.171	4.309	15.375	4.132	1.311	0	0.567
1369-29b	0.657	4.62	0.397	22.963	2.343	7.623	3.363	4.5	16.703	3.574	1.174	0	0.609
1369-35a	1.722	9.227	0.459	26.866	0.62	11.372	3.652	2.045	13.585	0.766	0.09	0	0.57
1369-35b	0.085	2.476	0.42	27.479	2.575	18.268	2.43	1.827	9.547	1.885	0.948	0.001	0.516
1369-35c	1.408	9.752	0.426	26.296	0.599	11.305	3.235	2.486	12.596	1.37	0.25	0.001	1.189
1369-45	0.757	5.431	0.484	25.28	1.685	8.274	3.361	3.213	16.763	1.994	0.49	0.005	0.821
1369-46	0.583	4.686	0.388	24.188	2.247	9.202	3.421	4.025	14.891	3.465	1.277	0.016	0.602
1369-81	1.492	7.552	0.636	21.781	3.566	8.371	2.956	4.24	14.278	3.417	1.284	0.001	0.509
1369-89a	0.856	4.08	0.094	29.552	0.344	11.086	3.694	2.245	15.976	1.263	0.152	0.007	0.3
1369-89b	0.531	3.584	0.171	29.292	0.78	11.808	3.829	2.638	15.201	1.021	0.223	0	0.427

Chapitre 5

Discussion of temperature–time evolution of Rogaland and plausible heat sources for UHT metamorphism

Résumé

Ce chapitre se présente sous la forme d'une discussion thématique visant à fixer la durée du métamorphisme de ultra-haute température du Rogaland et à examiner ses relations avec le magmatisme crustal et mantellique afin de proposer un modèle géodynamique pour ce segment ultra-chaud de la chaîne Grenvillienne. Pour cela, nous présentons une coupe structurale du domaine étudié figurant les relations géométriques entre les différentes unités et les chemins *P–T–t* suivis. Il apparait que tous les échantillons ont suivi une boucle *P–T* assez resserrée dans un sens horaire avec une pression maximale enregistrée de l'ordre de 7 kbar puis une décompression vers 5 kbar. L'absence de mouvement vertical différentiel au cours du temps, et particulièrement entre les deux épisodes identifiés de UHT, suggère des taux d'exhumation très faibles (~ 0.05 km/Ma). La compilation des données géochronologiques présentées de manière thématique dans les chapitres 2, 3, 4 permet, par conséquent, d'examiner le trajet température–temps qui confirme un maintien de ce segment crustal à des températures supérieures à 800 °C pendant 60 à 100 Ma, ponctué de deux incursions à UHT à environ 1030–1005 Ma et 940–930 Ma. L'advection de magmas d'origine mantellique en base de croûte à environ 1050 Ma puis la mise en place des anorthosites ont apporté une chaleur indispensable à l'atteinte de la ultra-haute température dans la croûte moyenne. Le refroidissement très lent suivant le premier pic en température (env. 2 °C/Ma) contraste avec le refroidissement rapide suivant le second pic en température (env. 20 °C/Ma). Le Rogaland est donc une localité de ultra-haute température atypique par ses caractéristiques combinant un long temps de résidence dans le faciès granulite et une absence d'épaississement crustal. Cette dualité peut être expliquée en prenant en compte la différence dans la composition et la température du manteau Protérozoïque comparé à l'actuel, favorisant le développement d'orogènes ultra-chauds voir de phénomènes gravitaires dominants.

Abstract

This section defines the duration of ultra-high temperature metamorphism in Rogaland and discusses the interplay between magmatism and metamorphism. We begin by a study of Rogaland crustal architecture combined with the examination of *P–T* record of rock samples distributed along a well-defined thermal gradient. All samples underwent tight clockwise *P–T* loops with a maximum pressure of c. 6 kbar followed by a decompression toward 4–5 kbar. The absence of lateral pressure gradient suggests very low exhumation rates (~ 0.05 km/My). The compilation of geochronological data presented in chapter 2, 3, 4 moreover allows to draw a detailed temperature-time path for the whole Rogaland domain. Rogaland underwent protracted granulite facies metamorphism at crustal temperatures higher than 800°C for 60 to 110 My. This journey in the granulite facies was punctuated by two incursions in the UHT domain at c.1030–1005 Ma and 940–930 Ma. Advection of mantle-derived magmas at the base of the crust at c. 1050 Ma and the emplacement of massif-type anorthosites at c. 930 Ma provided decisive heat supply to reach UHT condition. Following the first UHT event, the Rogaland basement underwent a slow cooling (c. 2 °C/My) contrasting with the fast cooling following the second UHT event (c. 20 °C/My) This difference may be due to the presence of high-heat production elements in the underlying crust during the first cycle. Overall, Rogaland is an atypical UHT locality since it features both long-lived residence at granulite-facies conditions and limited evidences of crustal thickening. This specifity may be due to the different thermal and chemical properties of the Proterozoic mantle that was hotter. Indeed Precambrian orogens are characterized by ultra-hot tectonic styles and predominance of gravity driven processes.

Introduction

Secular evolution of mountain building from a gravity driven regime in the Archean to a regime dominated by horizontal plate motion in the Phanerozoic results from continuous changes in the earth thermal regime (Condie and Pease 2008). This secular change is recorded in the metamorphic archives, indicating that the Precambrian period was dominated by low-*P*/high-*T* metamorphism (Sandiford 1989) whereas the occurrence of ultra-high-pressure rocks is mostly restricted to the Phanerozoic (Brown 2007; Ganne et al. 2012). The style of orogens is also intrinsically linked to the strength of lithospheric plates and to internal heat production (Dewey and Bird 1970; England and Thompson 1984; Jamieson and Beaumont 2013). The presence of strong lithosphere will promote subduction and indentation tectonics (Gerya et al. 2008), giving birth to a spectrum of conceptual geological models ranging from small cold orogen to large hot orogen (Jamieson and Beaumont 2013). The occurrence of ultra-high temperature (UHT) crustal metamorphism is particularly abundant in Archean and Proterozoic eon and shows a remarkable coincidence with the formation of supercontinents (Nuna, Rodinia, Gondwana) implying that by that time localised sites of very high heat flow existed (Brown 2007). The inherently weaker and hotter lithosphere back in Archean and Proterozoic times, favoured shallow subduction with localised magmatism and deformation (Sizova et al. 2014) resulting in ultra-hot orogens (Chardon et al. 2009; Cagnard et al. 2011).

Models for UHT metamorphism

Accepted tectono-thermal numerical models to explain the occurrence of ultra-high temperature (> 900 °C) granulite facies metamorphism and associated sub-horizontal gneissic fabric are traditionally classified between two end-members corresponding to both extensional and compressional settings (Harley 2016). These corresponds to (1) arc, back-arc and accretionary systems (e.g. Brown et al. 2011) and (2) large hot collisional belts (e.g. Beaumont et al. 2006).

Arc and back-arc settings are expected to generate dominantly anti-clockwise *P–T* path followed by near isobaric cooling (Sandiford and Powell 1986; Ellis 1987; Brown and Korhonen 2009), although extensional accretionary systems that record transient thickening usually display tight clockwise *P–T* paths in the sillimanite stability field (Collins 2002; Brown 2007). The heat source in these models is provided by the upwelling asthenosphere and advection of magma beneath or within the crust (e.g. Wells 1980; Bohlen 1991). Brown (2009) proposed that thin and wide back-arc are prerequisite for granulite formation during subsequent arc–arc or arc–continent collision. Clark et al. (2011) nevertheless cautioned, on the basis of 1D modelling, that in the

absence of syn-metamorphic voluminous mafic magmatism, and for modern-like thermal parameters, the inversion of back arc is not likely to produce widespread and long-lived UHT granulite. In contrast, 2D thermomechanical investigation of back-arc thickening by Sizova et al. (2014) predicts that for Proterozoic thermal conditions (mantle hotter by 150–80 °C than at present day), UHT may be reached at shallow levels in association with abundant magmatism. The model is able to reproduce the tight clockwise *P–T* path followed by isobaric cooling, recorded by many UHT localities (Kelsey and Hand 2015), and predicts very short timescale of orogeny (c. 10 My). This short timescale in is in line with Cenozoic observation of UHT occurrences in back-arc basin of Seram (Indonesia; Pownall et al. 2014) as the result of mantle exhumation in a core complex and in a oceanic arc (Kemp et al. 2007). These observations point to two fundamental characteristics of UHT in modern arc/back-arc setting. First, U–Pb zircon and Ar–Ar dating of biotite demonstrates extremely fast cooling rate with exhumation to the surface less than 16 Ma after peak temperature (Pownall et al. 2014). Second, relatively juvenile magmatic rocks and freshly deposited sediments may be subject to HT metamorphism short after burial, highlighting the temporal link between crustal growth and UHT metamorphism in this particular setting.

Large hot orogens (LHO; Beaumont et al. 2006) are characterized by an elevated plateau underlain by 60–80 km of crust. The middle crust is composed of high-heat production material sandwiched between strong upper crust and decoupled lithospheric mantle (Royden 1996). Self-heating of the middle crust over long timescale leads to the establishment of a weak, partially molten, zone allowing ductile flow of the infrastructure in response to pressure gradients (Bird 1991; Vanderhaeghe 2009). In order to generate regional UHT conditions for rocks buried at 40 km depth, Clark et al. (2011) found that the following conditions should be met: (1) high upper-crustal radiogenic heat production (> 3 $mW.m^{-3}$) (2) slow erosion rates (< 0.05 $mm.My^{-1}$) (3) pre-conditioning of crust (*sensu* Vielzeuf et al. 1990; see also discussion in Chp. 3). The LHO model was further investigated *via* a numerical model designed for the Grenville orogen of Canada (Jamieson et al. 2010). This model displays rock packages that are buried during continental collision in the kyanite stability field and follow a clockwise *P–T* path with a near isothermal decompression from c. 10–13 kbar down to 6–7 kbar at UHT conditions lasting some 30–40 My. Comparison of this model with the *P–T–t* path recorded by numerous UHT terrain worldwide (e.g. Matter Paragneisses – Antarctica; Ouzzal – Algeria; Palni hills – India) lead Harley (2016) to propose that the LHO model provides the best setting for UHT generation during continental collision. Critical in this model is the timescale of thermal incubation after onset of crustal thickening, the longevity of UHT (30–100 My) and the typical clockwise *P–T* path yielding rather high pressure maxima of c. 10 kbar followed by isothermal decompression.

Deciphering the heat sources and tectonic setting of UHT metamorphism in Rogaland may thus be achieved by examination of (1) *P–T–t–D* path of rocks on the regional scale to constrain lateral extent of granulite facies metamorphism and associated structures; (2) the interplay between magmatism and metamorphism; (3) the heat production potential of the crust and finally (4) integrating observations from other parts of the Sveconorwegian province. The reader is refered to chapter 1 for detailed geological settings of the Sveconorwegian orogen and its integration in the broader framework of Rodina assembly. A synthetic table summing up the geochronological and petrological results presented in previous chapters is available in supplementary S5-3.

P–T–t–D paths of the Rogaland

Geometrical relationships

The geometrical relationships existing between the different rock units were deduced from previously published structural studies (Hermans et al. 1975; Huijsmans et al. 1981; Falkum 1985) and complemented by our own fieldwork. Geometrical relationships are visible on map view (Fig. 1) and illustrated on a geological cross-section (Fig.2a–f). The Rogaland basement is composed of high-grade meta-igneous rocks of broadly granitic to tonalitic composition (termed granitic gneiss) that may be interlayered with mafic rocks (thereafter termed banded gneiss) and metasedimentary rocks (Hermans et al. 1975). Metasedimentary rocks are divided in two formations, the "garnetiferous migmatite" representing Al-rich protolith such as greywacke and pelite and the "Faurefjel metasediments" comprising a succession of calc-silicate rocks, quartzite and minor marble of supracrustal origin (Bol et al. 1995; Fig. 1).

Granitic gneisses have a massive appearance with only limited evidence of penetrative deformation, although the transition from banded to massive facies is never sharp or discordant. In the same way, the transition between banded gneiss and garnetiferous migmatite is progressive, with most of the deformation localized in metasedimentary rocks. Indeed, garnetiferous migmatite display isoclinal folding resulting in the transposition of an early foliation defined by garnet- and sillimanite-rich layers (Fig. 2d–e; D1 of Huijsmans et al. 1981). Within the mapped banded gneiss, protracted partial melting lead to segregation of layers rich in ferromagnesian minerals relative to those rich in quartzo-feldspathic minerals creating a syn-migmatitic metamorphic layering (Fig. 2f). This layering is strongly reworked to form kilometric tight recumbent folds with N- to NW-striking axial plane dipping 25–50° eastwards that are seen in map view and form the dominant fabric visible on the cross-section (Fig. 2b; deformation phases D2 and D3 of Huijsmans et al. 1981). Leucocratic parts of garnetiferous migmatite (leucosome) may in turn segregate to form homogenous discordant bodies of small size (tens of meters) or large area of inhomogeneous

garnet-bearing metatexite ("garnet granite") concordant in the flat lying foliation (Fig. 1; Fig. 2b). The major N–S structure curve concordantly around the anorthosite massif resulting a c. 500 m thick sub-vertical re-foliation belt (Bolle et al. 2010). Finally, a last phase of deformation produced kilometric open folds with steep E–W trending axial plane (D4 of Huijsmans et al. 1981) that are well observed at the eastern end of the cross-section (Fig. 2b) where magmatic rocks belonging to the Sirdal–Feda magmatic belt alternate with banded gneiss (Falkum 1982; Coint et al. 2015; Fig. 1).

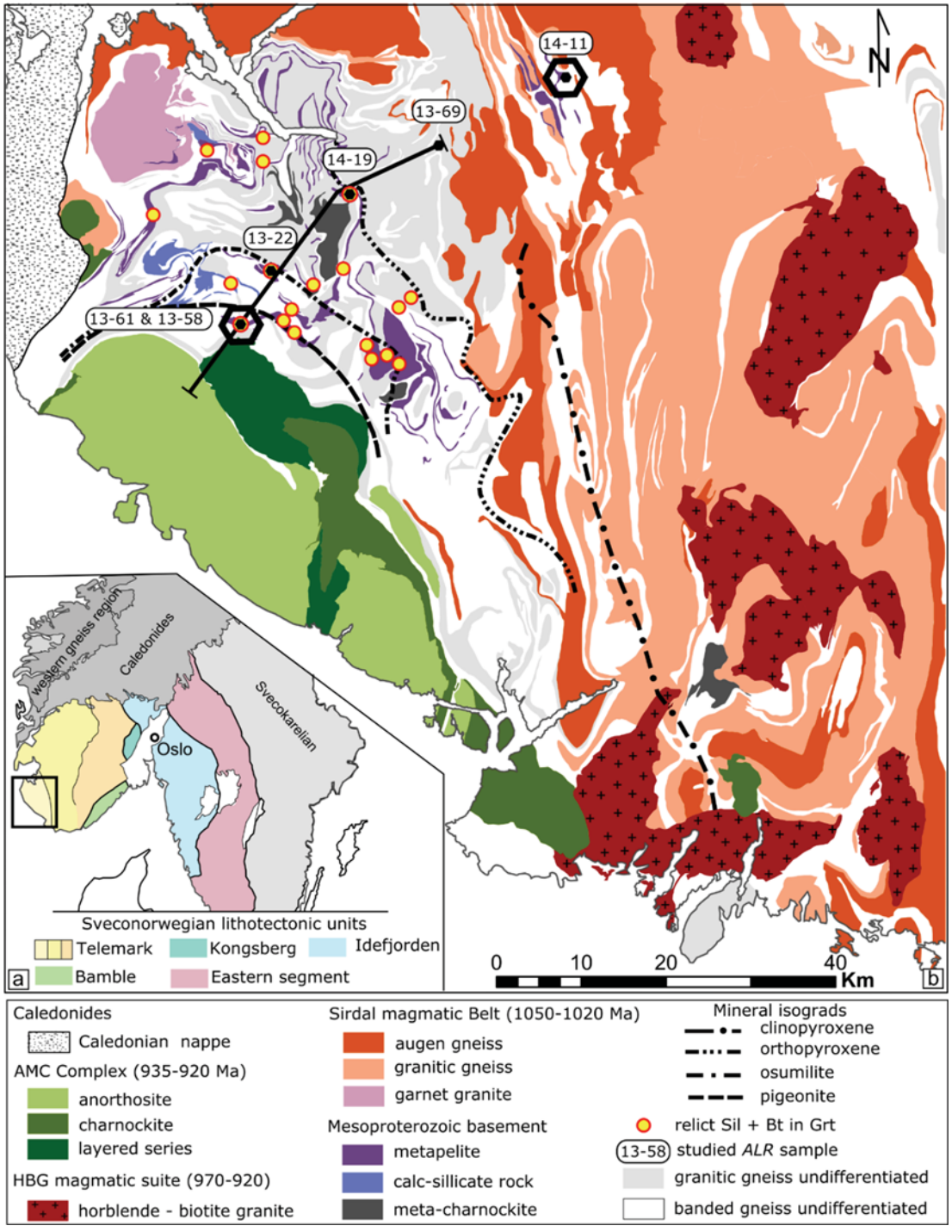

Fig. 5–1 : Geological maps. a– Sketch map of the Sveconorwegian Province in SW Scandinavia from Bingen et al. (2008b), black rectangle depicts the studied area. b– Simplified geological map of Rogaland-Vest Agder modified after (Falkum 1982; Coint et al. 2015) with mineral isograds drawn after (Tobi et al. 1985; Bingen et al. 1990) and localization of the studied localities. The bold A–A'–B line depicts the location of the cross section (Fig. 2b).

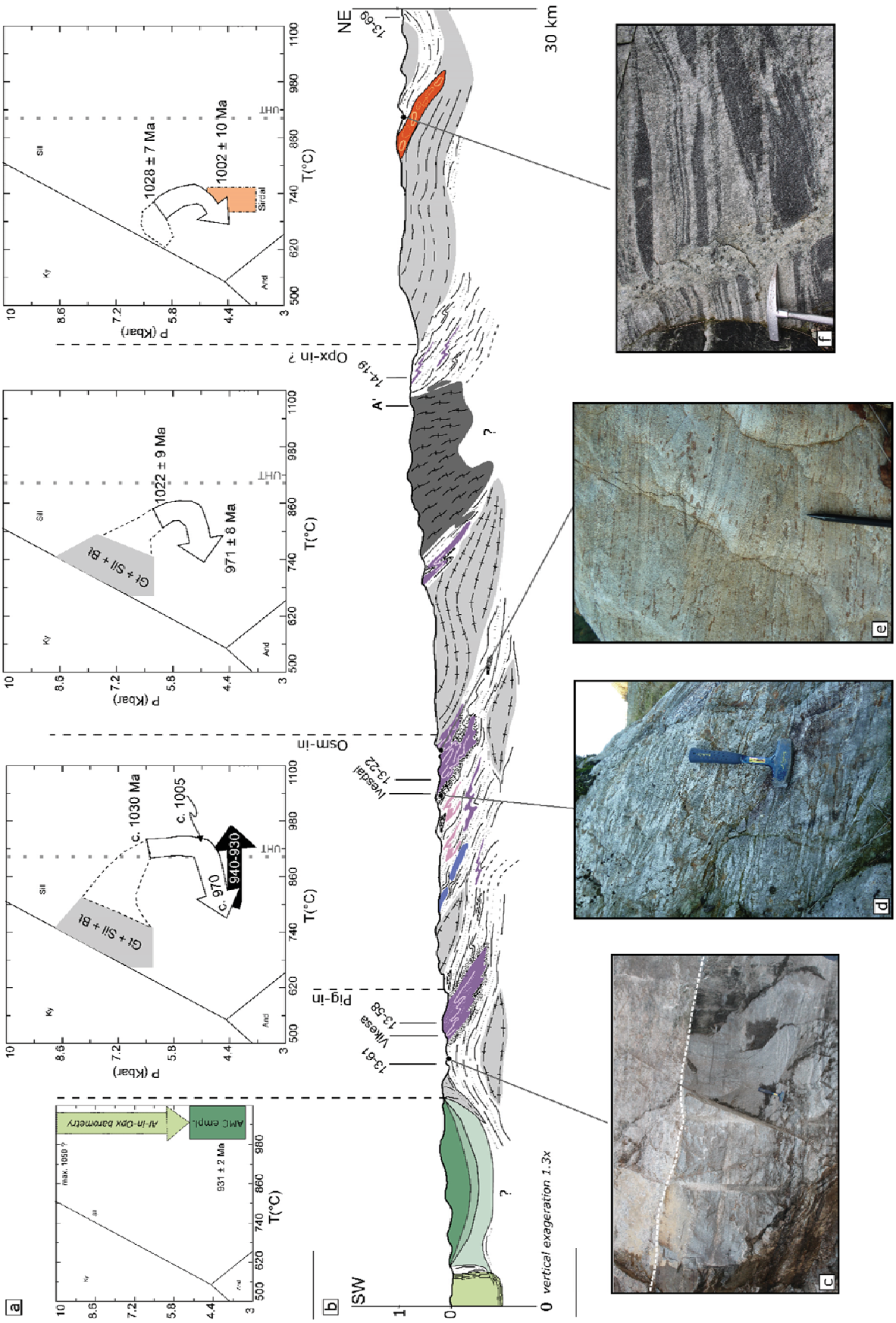
a
b
c
d
e
f
P (Kbar)
T(°C)
Ky
And
Sil
UHT
1028 ± 7 Ma
1002 ± 10 Ma
Sirdal
1022 ± 9 Ma
971 ± 8 Ma
Grt + Sil + Bt
c. 1030 Ma
c. 1005
c. 970
940-930
931 ± 2 Ma
AMC emplt.
Al-in-Opx barometry
max. 1050 °
NE
SW
30 km
13-69
A
A'
Opx-in ?
14-19
Osm-in
Vessdal
13-22
Pig-in
13-58
Vikese
13-67
vertical exaggeration 1.3x

↑ **Fig. 5–2** : Geological cross-section and field relationships along SW–NE thermal gradient a– P–T conditions deduced for the different metamorphic zones in Chp. 3 and Chp. 4 b– Geological cross-section of the high-grade basement of Rogaland, the location of cross-section is depicted on Fig.2b, the color-coding of the different units follows that of Fig. 2b. c–f Field photograph illustrating the major structures observed on the field

Significance of the Opx-isograd

In contrast to the osumilite and pigeonite isograd whose genetic link with the AMC is widely accepted (Möller et al. 2002; Möller et al. 2003; Bingen et al. 2008a; Chp. 3), the origin of the orthopyroxene isograd is still debated. In the past, this isograd has been suggested to be partly (Tobi et al. 1985) or totally related to the emplacement of the AMC complex (Maijer 1987; Westphal et al. 2003) despite its divergence toward the north. Alternatively, Coint et al. (2015) proposed that this isograd marks the boundary between an old Opx-bearing basement to the east and younger granitoids (Sirdal batholioth; c. 1070–1020 Ma) to the west, implying a pre- or early-Sveconorwegian metamorphic event in the basement. Although appealing, this last hypothesis is not supported by the large body of geochronological data gathered in Rogaland (Tab. 1–1), since there is no metamorphic age older than c. 1040 Ma. The new data presented in Chp. 4 supports previous conclusions presented by Möller et al. (2002) and Bingen et al. (2008a) demonstrating that low-pressure granulite facies conditions were reached in the vicinity of the Opx-in isograd at 1040–990 Ma synchronously with granitoid emplacement.

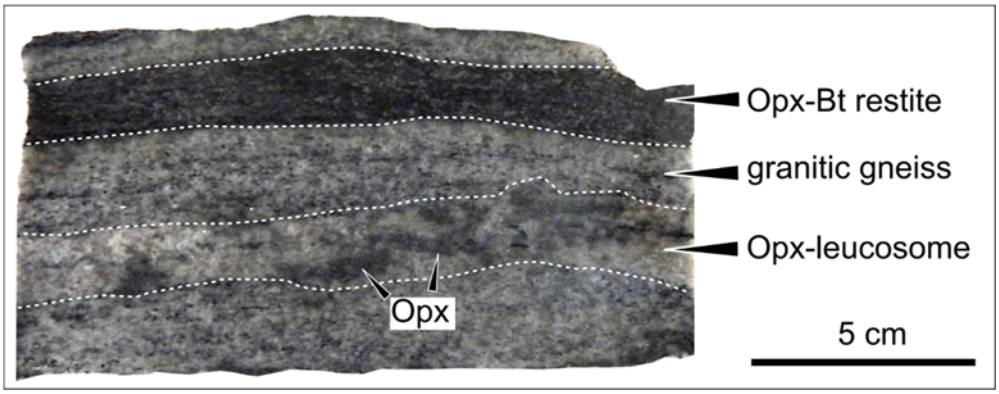

Fig. 5–3 : Rock-slab photograph of sample ALR 14-11.

Field reconnaissance in the metamorphic basement east of the mapped orthopyroxene isograd reveals that orthopyroxene can still be found in leucocratic parts of banded gneiss (Fig. 3).

A good example is provided by the *sample ALR 14-11 (x = 369981; y = 6532632)* taken some 20 km east of the mapped Opx-isograd. This sample is a banded gneiss with a well-defined foliation characterized by alternating dm-thick melanocratic layers composed of plagioclase, biotite and orthopyroxene with leucocratic layers composed of quartz, K-feldspar, plagioclase, minor biotite, magnetite and ilmenite. Biotite preferred orientation within the leucocratic layers also underline the gneissose foliation. Interestingly, leucocratic layers are intruded by a leucosome

composed of orthopyroxene, quartz and K-feldspar (Fig. 3). The occurrence of Opx-bearing leucosomes in the regional basement, well beyond the mapped isograd, thus suggests that the actual Opx-isograd was a moving boundary through time and runs subparallel to the present-day erosion level, i.e. do not have a dome shape.

Timing of deformation and vertical movement

The *P–T–t* path of individual rock samples that have been investigated in detail in Chp. 3 and Chp. 4 are reported on the cross-section extending from the anorthosite massif to the vicinity of the Opx-isograd (Fig. 2b). Examination of *P–T* paths shows that from southwest to northeast peak-pressure decreases slightly from *c*. 6–7 kbar to 4–5 kbar, while temperature decreases gradually from *c*. 920°C to *c*. 800 °C. There is no abrupt pressure or temperature drop along the cross-section pointing to the absence of late geological discontinuities (e.g. major faults). Additional petrographic observation of over 100 thin sections from the garnetiferous migmatite unit distributed along the cross section reveals the systematic presence of early sillimanite + biotite + quartz inclusions in garnet (spatial disctribution of this mineral assemblage is reported in Fig. 1). The occurrence of this relict mineral assemblage all over the Rogaland basement, together with the absence of kyanite, suggests burial along MP–HT gradient with a pressure peak in the order of 6–7 kbar and 750 °C (Jansen et al. 1985). The early syn-migmatitic isoclinal folding visible in garnetiferous migmatite may thus be tentatively linked to moderate crustal thickening at 1050–1030 Ma.

Pressure decrease (max. 2 kbar) is recorded for all samples between 1040 and 1000 Ma, but no significant pressure gradient is observed in space at a given time (Fig. 2a). This pressure decrease is probably synchronous with the development of flat-lying metamorphic fabric, since this deformation phase should have occurred prior to the intrusion of HBG granitoids at c. 970–950 Ma, that cross-cut in places the N–S trending foliation (Fig. 1). The presence of large scale recumbent folds in partially molten middle crust has been interpreted in numerous orogens to represent syn-convergence orogen-parallel flow (Chardon et al. 2009) or post-collisional orogenic collapse (Vanderhaeghe and Teyssier 2001). The Re–Os dating of molybdenite that crystallized in the N–S trending planar foliation confirms that the last increment of ductile deformation is older than c. 950 Ma to the east of the Cpx-in isograd whereas ductile deformation operates at least until c. 917 Ma close to the AMC complex (Bingen et al. 2006).

We conclude that the absence of differential vertical movement coupled with the sub-horizontal attitude of the Opx isograd indicates global uplift at very slow exhumation rates between M1 and M2 (e.g. Gapais et al. 2009). The spatial distribution of isotherms through time and space

further suggests focused heat input at the west of the mapped Opx-isograd but precludes the existence of a large scale geological structure juxtaposing two units with contrasted *P–T* record.

Interplay between magmatism and metamorphism

Timescale of AMC emplacement

Deciphering the timescale of massif-type anorthosite genesis and residence within the crust is challenging since zircon and baddeleyite are very rare in these rocks and their origin are not well understood (Schärer et al. 1996). In a recent contribution, Bybee et al. (2014) presented an internal Sm–Nd isochron for Al-rich orthopyroxene yielding an age of 1041 ± 17 Ma, that is some 100 My older than the age of the final emplacement of the plutons dated by U–Pb on zircon at 931 ± 2 Ma (Schärer et al. 1996). This age difference can imply the existence of a long-lived (80–100 My) magmatic system at the crust–mantle interface (Bybee et al. 2014). Alternatively, and in accordance with the Nd and Pb isotopic compositions, Vander Auwera et al. (2014b) suggest that Al-rich orthopyroxene megacryst belong to mafic underplates coeval or cogenetic with the Feda suite, that were re-melted some 100 My later to form the AMC complex. Both scenario acknowledge the presence of juvenile mafic magma underplating around 1050 Ma, but differs in the presence of a long-lived magma chamber (Bybee et al. 2014) versus re-melting of mafic underplates (Vander Auwera et al. 2011).

Our own geochronological data reveal that high-Y monazite related to UHT garnet breakdown yields U–Pb ages of 931 ± 6 Ma (*ALR 13-05*; Chp.3) and 935 ± 7 Ma (*ALR 13-58*; Chp 2) that fits well with the final emplacement of the anorthosite massifs at 931 ± 2 Ma (Schärer et al. 1996). In contrast, zircons yields somewhat older U–Pb ages of 942 ± 8 Ma (*ALR 13-05*; Chp.4) and 938 ± 7 Ma (*ALR 13-58*; Chp.4) suggesting that renewed UHT metamorphism may not be the consequence of anorthosite emplacement. To get further insight on the relative timing of anorthosite emplacement relative to M2 metamorphism, we investigated monazite and zircon geochronology from a sample lying some 150 m from the exposed anorthosite contact. The chosen sample is an orthopyroxene-bearing leucosome (*sample ALR 13-61)* associated with pigeonite granulite.

Within the Opx-bearing leucosome *ALR 13-61*, monazite crystals display fine scale patchy zoning on BSE images (Fig. 4a). The different chemical zones are rather U-rich (UO_2 > 0.6 wt%; Tab. 1) while the Th content is variable (ThO_2 = 4.6–24.4 wt%). Twenty-two U–Th–Pb analyses were achieved in 14 grains and are presented in Tera-Wasserburg diagrams. It is possible to distinguish two age groups on the basis of Y-content (Fig. 4b). The oldest group is composed of 5 analyses with Y_2O_3 < 4.5 wt% and yields a concordia age of 1011 ± 11 Ma (Fig. 4b; 2σ; n = 5). The youngest and dominant age-group is made up of Y-rich part of monazite crystals (Y_2O_3 = 4.2–6.2 wt%) and yields a concordia age of 936 ± 6 Ma (Fig. 4b; 2 σ; n = 18) representing individual $^{206}Pb/^{236}U$ ages ranging from 959 ± 30 Ma to 910 ± 28 Ma.

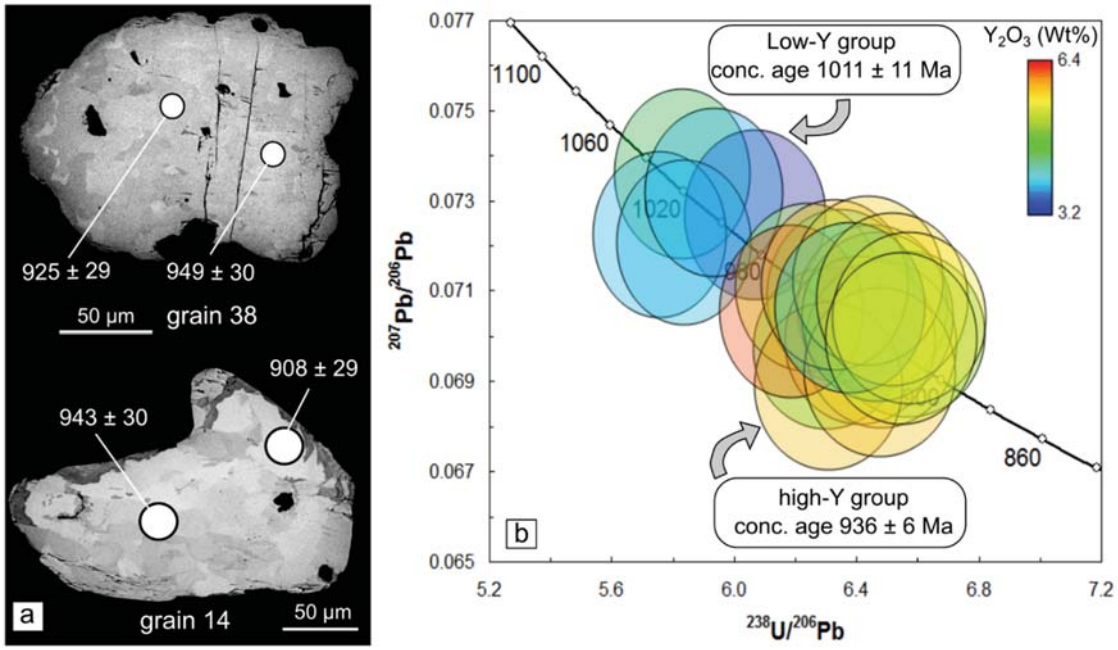

Fig. 5–4 : Monazite BSE zoning, U–Pb geochronology and micro-chemistry for sample ALR 13-61 **a–** BSE image of high-Y grains, note the extreme patchiness **b–** U–Pb monazite data in Tera-Wasserburg diagram, color-coded with Y2O3 concentration measured prior to laser ablation with EPMA. All error ellipses are 2σ, decay constant errors are included in the pooled ages.

Zircon crystals from this sample are of large size (> 200µm), very translucent and anhedral. CL imaging reveal rare rounded cores (not shown) surrounded by several growth zones displaying complex cross-cutting relationships (Fig. 5a). Twenty-three U–Pb analyses have been carried out in 20 grains and are presented in Tera-Wasserburg diagram (Tab. 2; Fig. 5b). The dataset divides in two age groups with one additional analysis yielding a significantly older $^{206}Pb/^{238}U$ age of 1066 ± 24 Ma. The oldest group consists of CL-dark zircon interior with three spots yielding a $^{206}Pb/^{238}U$ weighted average of 999 ± 13 Ma (MSWD = 1.4; *n* = 3). The youngest group consist of both CL-dark and CL-bright overgrowth yielding a consistent concordia age of 943 ± 4 Ma (Fig. 5b; 2σ; *n* = 19) with individual $^{206}Pb/^{238}U$ age ranging from 955 ± 18 Ma to 928 ± 19 Ma. *In-situ* O isotopic analyses of selected crystals defines a homogenous $\delta^{18}O$ of 6.56 ± 0.1 ‰ (MSWD = 1.06; *n* = 12).

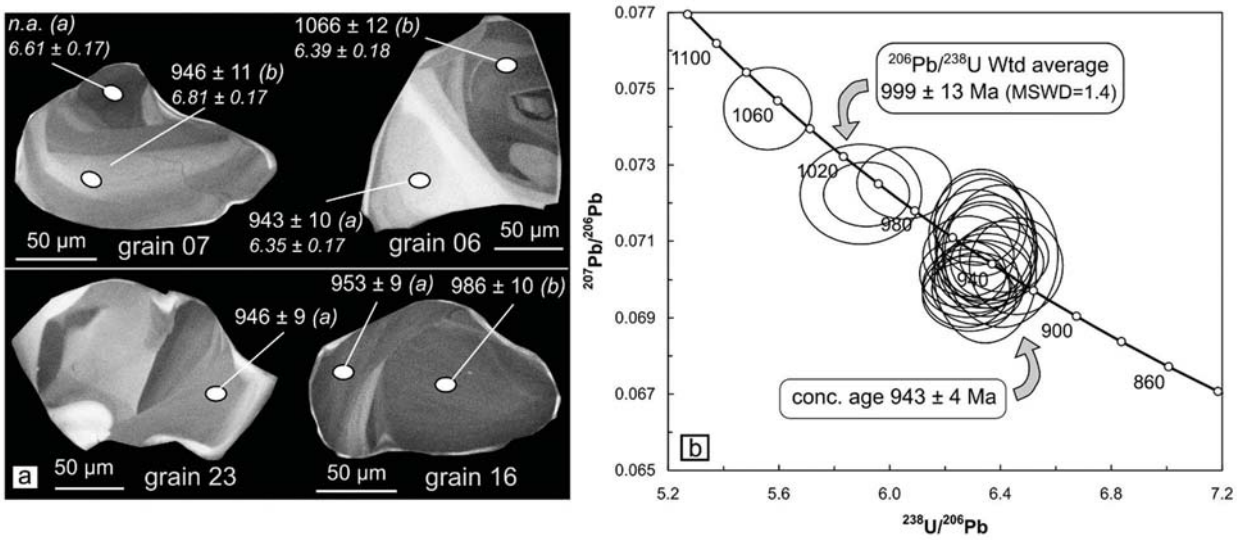

Fig. 5–5 : Zircon texture and U–Pb geochronology for sample ALR 13-61 **a–** Cathodo-luminsecence (CL) images of the investigated zircon grains with location and date U–Pb analytical spot and $\delta^{18}O$ value reported in Tab. 2. **b–** U–Pb zircon data in Tera-Wasserburg diagram. All error ellipses are 2σ, decay constant errors are included in the pooled ages.

The U–Pb geochronology on monazite and zircon thus suggests but do not demonstrate, given the uncertainties associated with SIMS analysis, that metamorphic crystallization of zircon occurred prior to zircon crystalisation in anorthosite at 931 ± 2 Ma (Schärer et al. 1996) interpreted to reflect AMC emplacement. This slight age difference is perhaps related to slow diapiric ascent of the plagioclase crystal mush in the ductile crust (Barnichon et al. 1999). This inference is supported by polybaric crystallization of high-Al orthopyroxene (Charlier et al. 2010) which favours a long timescale from source melting to magma emplacement and additionally constrains the maximum crustal thickness to c. 12 kbar.

Synthetic T–t diagram deduced from metamorphic rocks

Since no significant pressure gradient is observed in the Rogaland basement, we focus on Temperature–time evolution based on the new body of petrological and geochronological data discussed in Chp. 3 and Chp. 4. Additional cooling constrains following M2 metamorphism are derived from U–Pb titanite (Bingen and Van Breemen 1998) and amphibole Ar–Ar data reported by Bingen et al. (1998). The temperature–time curve for the different metamorphic zones are presented in Fig. 6. The oldest temperature constrain for all metamorphic zones comes from zircon and monazite growth in response to the onset of partial melting with minimum temperature of 750 °C recorded at 1040–1035 Ma (Chp. 3; Chp. 4). Outside the Opx isograd, last evidence of supra-solidus condition is provided by zircon crystallization at 1002 ± 10 Ma (Chp. 4). Within the Opx zone, supra-solidus conditions (c. 780 °C) are maintained until 971 ± 8 Ma (Chp. 4) suggesting a residence time above 800 °C (Δt_{800}; Harley 2016) of c. 50 My and slow cooling rate, below 2 °C/My. Rock samples belonging to present day UHT zone record two UHT events at 1030–1005

Ma and at 940–930 Ma (Chp. 3; Chp. 4). Thermal evolution between these maxima encompasses a Δt_{800} of at least 60 My and possibly as much as 100 My (Fig. 6). The uncertainty on the inflexion point between cooling and renewed UHT is largely due to the discrepancy between monazite and zircon record in response (or prior to) AMC emplacement. After the M2 UHT peak, regional cooling of the metamorphic basement below titanite closure temperature of c. 610 °C is documented by grouped U–Pb titanite data at 918 ± 2 Ma (Bingen and Van Breemen 1998). This extremely fast cooling rates of 20 °C/My stands in strong contrast with the slow thermal evolution during the previous 100 My.

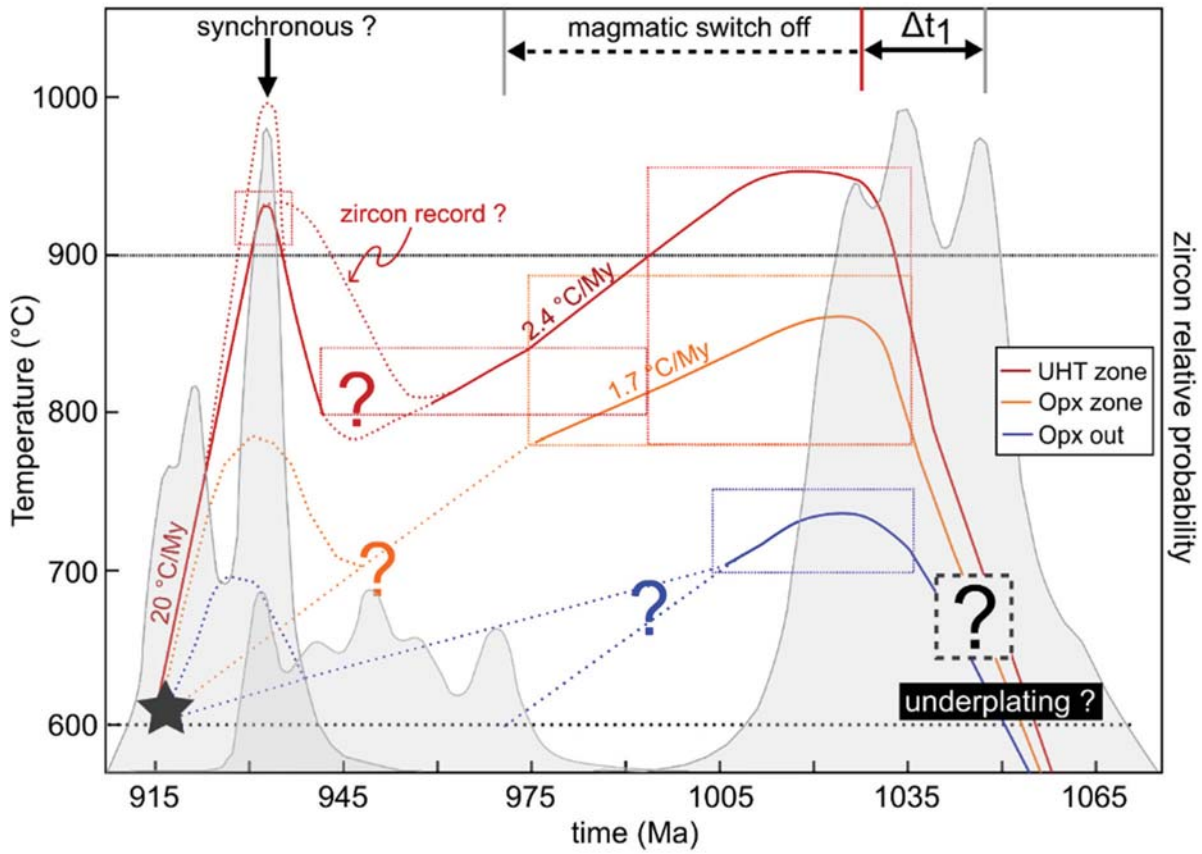

Fig. 5–6: Synthetic Temperature–time diagram. The figure was constructed with T–t data derived in Chp. 3 and Chp. 4 (see text). The colour-coding corresponds to the different metamorphic zones: Red curve depicts the thermal evolution of the present-day UHT zone; Orange curve depicts the thermal evolution of the present-day orthopyroxene zone; Blue curve depicts thermal evolution of the Rogaland basement outside the mapped Opx isograd. The full line denotes the portion of T–t diagram based on firm data whereas the dotted line represents extrapolated evolution. Zircon probability diagram is superimposed to represent the timing of magmatic activity; the geochronological data and their source used for plotting are compiled in Supplementary material S5–2.

Interplay between magmatism and metamorphism

The regional M1 and M2 thermal gradient of 150 to 200 °C.kbar^{-1} derived from Fig. 6, exceeds by far the conductive limit of crustal metamorphism of c. 100 °C.kbar^{-1} calculated for a mantle heat flow of 30 mW.m^2 (Stüwe 2007). It seems therefore necessary to consider advective

mantle heat source to generate these very high thermal gradient. The two identified (near-)UHT events nevertheless highlights two contrasting styles of magmatism–metamorphism interplay.

During the first thermal cycle leading to M1 UHT metamorphism, a latency time of at least c. 30 My (Fig. 6) is observed between the onset of magmatism at c. 1060 Ma (Coint et al. 2015) and the establishment of UHT temperatures at c. 1030–1005 Ma (Chp. 3). Most of the magmatic activity at this time and at the current erosion level is localized outside the hottest part of the basement corresponding to the Opx zone (Fig. 1) suggesting that there exist only limited spatial relationships between the intensity of magmatism and intensity of metamorphism. This assertion is not supported by the generalized mafic underplating postulated around 1050–1040 Ma on isotopic ground (see discussion above and Chp. 1 p.55). An enhanced mantle heat flow higher than c. 40 $mW.m^{-2}$ acting on a 35 km thick crust may initiate crustal melting after 4 My to 7 My, and create a partially molten layer in the lower crust in about 30 My following thermal modelling of Bea (2012). In contrast UHT metamorphism recorded during M2 is spatially related to anorthosite bodies and predates by a maximum of c.10 My the final AMC complex emplacement (Fig. 5b). We interpret the lack of latency between anorthosite emplacement and M2 peak metamorphism to results from crustal preconditioning (Chp. 3).

The second major difference between the two UHT events lies in the cooling rates following peak temperature. Indeed, cooling rates are less than 2–3 $°C.My^{-1}$ following M1 metamorphism whereas extremely fast cooling of c. 20 $°C.My^{-1}$ is achieved following M2 metamorphism (Fig. 6). The rapid cooling following anorthosite final emplacement indicates that the heat source vanishes as anorthosite crystallizes. Whether this is pure coincidence or whether there exists a causal relationship is intriguing. Indeed, massive-type anorthosite emplacement in the Western Gneiss Region are documented at 970–965 Ma (Lundmark and Corfu 2008), and are *followed* by a period of high-grade metamorphism between 950 and 920 Ma, in the Upper Jotun and Lindås nappes (Gothian affinity; Bingen et al. 2001; Lundmark et al. 2007; Roffeis and Corfu 2014). The beginning of AMC magmatism in the Sveconorwegian orogeny is thus significantly older than the Rogaland AMC complex and show contrasted temporal sequence of AMC magmatism and high-*T* metamorphism.

The slow cooling in Rogaland during the 990–950 Ma time span cannot be explained by protracted magmatism, since syn-metamorphic mafic magmas are absent between 1020 and 970 My. This absence may be related to the presence of a partially molten middle crust that acted as a filter which prevented mafic magma to rise further (e.g. Vielzeuf and Vidal 1990; Smithies et al. 2011). Alternatively, the presence of a moderately thickened crust with high heat production elements may be invoked to explain the slow cooling rates (< 2 $°C.My^{-1}$).

Radiogenic heat production of the crust

Whole rock geochemistry

In order to put quantitative constrains on the heat production potential of the exposed crust of Rogaland, we compiled available geochemical data and performed new whole-rock geochemical analyses on the "garnetiferous migmatite" group (Tab. 3). The heat production potential (*H*) of the different lithologies were all recalculated at 1 Ga and are presented in Tab. 4. Except for the banded and granitic gneiss, the investigated lithologies display high heat production in the range 1.5–5.2 $\mu W.m^{-3}$ (Tab. 4). Thermal modelling by Clark et al. (2011) showed that in a thickened crust, the presence of materiel with $H > 2.5$ $\mu W.m^{-3}$ at 40 km depths contribute significantly to the thermal budget of the orogen after 30–60 My of thermal incubation. In particular, the A-type meta-charnockite ($H = 5.2$ $\mu W.m^{-3}$) represent a very efficient heat source, as already noted by Bea (2012). Computing an average pre-Sveconorwegian *H* for the exposed crustal section in Rogaland is however hampered by the dynamic redistribution of U and Th in the course of metamorphism.

Redistribution of U and Th

The redistribution of U and Th in the course of metamorphism is principally controlled by the stability of their main carrier, i.e. monazite and zircon. Quantification of U–Th transfer through the crust may thus be critically assessed by studying monazite and zircon stability in the presence of a silicate melt. In fact, the presence of a silicate melt will favour the dissolution of accessory minerals as a function of *T*, *P*, abundance and composition of the silicate melt (Na, K, Ca, Al; H_2O; LREE; Zr). Experimental frameworks have been developed to quantify monazite (Montel 1993; Stepanov et al. 2012) and zircon solubility (Watson and Harrison 1983). Kelsey et al. (2008) proposed an approach to integrate these constrains to whole rock thermodynamic modelling in order to predict portion of *P–T* path were monazite/zircon is expected to dissolve or grow. We have tentatively applied this appealing approach to the case of UHT metamorphism in the Rogaland domain. A fully functional code (R language) to be used alongside with Perple_X are joined (Supplementary material S5–1) with the used algorithm.

Monazite and zircon solubility calculated with this model predicts that most zircon and monazite crystallization should take place in bulk on the down temperature *P–T* path when crossing back the solidus (Fig. 7; see also Yakymchuk and Brown 2014). This prediction is however very different from the observed continuous zircon and monazite age record over the whole metamorphic history as discussed in Chp. 4. The main limitation we find to such a modelling approach is that the dynamic nature of melting (e.g. melt loss, fractional crystallization) is not

taken into account. For example, in Chp. 3 we showed that small monazite crystallizes simultaneously to garnet breakdown, highlighting that some old monazite grains were shielded in garnet prior to M2 metamorphism. This shielding effects by major phases thus subtracts from the reactive medium a significant amount of LREE which is critical to compute monazite solubility. In Chp. 2 we also underline that the presence of efficient complexing agent for Th and U like S and the redox state of the magma, which may favour U mobilization as uranyl, are expected to have a strong influence on monazite solubility. Finally, the phase relationships between monazite–xenotime–zircon and Th–U oxides should be taken into account as shown in Chp.3. This last point was also demonstrated by Bingen et al. (1996) who studied the redistribution of Th–U in the course of Sveconorwegian within the Feda orthogenesis.

Our own observation during mineral separation of different rock types is that zircon and even more monazite tends to be concentrated in the melanosome and not in the leucosome. Whether this reflects gravity-induced segregation or actual low solubility cannot be elucidated. This behavior has the consequence to keep reasonable high heat producing material at depth during protracted metamorphism (e.g. Watt and Harley 1993; Bea and Montero 1999).

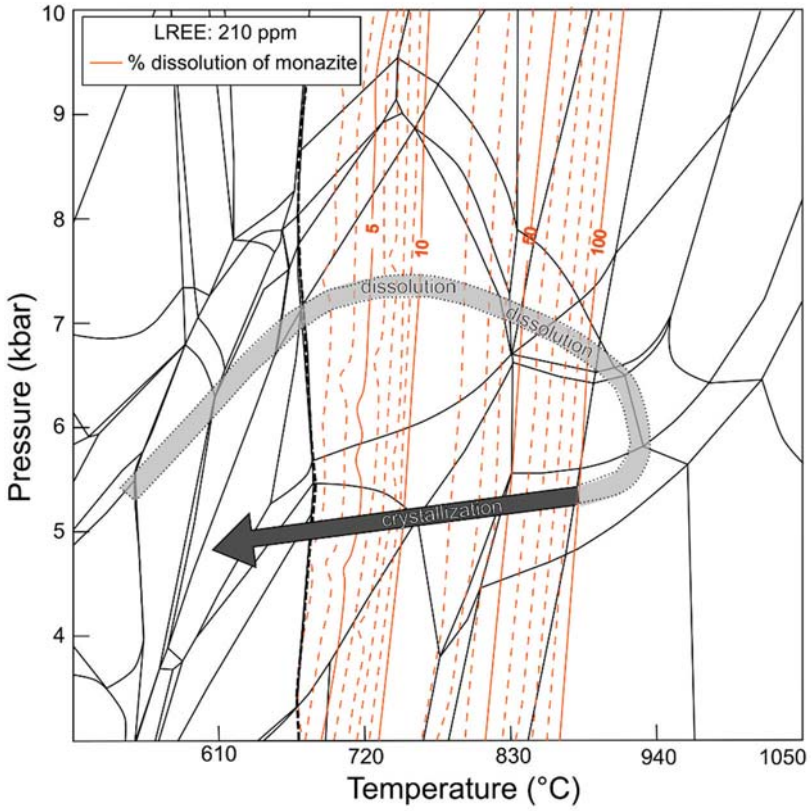

Fig. 5–7 : Calculated phase diagram for the metagreywacke composition presented in Kelsey et al. 2008 with superimposed contour of monazite solubility calculated for a bulk-rock LREE (La-Eu) content of 210 ppm (see text and Tab. 3). The *P–T* path drawn is only indicative of M1 loop in the UHT zone of Rogaland and does not take into account eventual melt loss.

Geodynamic speculation and conclusion

We start this section by summing up the prominent features observed in Rogaland:

- The Rogaland metamorphic crust underwent long-lived granulite facies metamorphism (Δt_{800} = 60–100 My) with two UHT excursions at 1030–1005 Ma and 940–930 Ma
- The *P–T* path is characterized by a maximum pressure of about 6–7 kbar at 750 °C and a tight (polyphase) clockwise *P–T* path down to a pressure of *c*. 4–5 kbar.
- The whole Sveconorwegian period is marked by the absence of differential vertical movement between the two (U)HT events (i.e. general uplift of the crustal segment) and very slow exhumation rates (*c*.0.05 km.My^{-1}).
- Advective heat source is provided by punctuated mantle-derived magma underplating or input within the crust through time.
- The presence of relatively high heat production material at mid-crustal depth may have provided a decisive contribution to maintain high temperature in the absence of magmatism.

Taken as whole, those observations highlight the apparent contradiction between the long-lived nature and low-pressure recorded by the Rogaland terrain when comparing our data with the accepted models for UHT metamorphism. Although no quantitative modelling exists at the moment, the UHO model of Chardon et al. (2009) for weak lithosphere may be reconciled with most of our observations (Fig. 8). Indeed, UHO are expected to develop as a result of lack of stiff lithospheric mantle due to higher mantle temperature in the Precambrian and abundant syn-metamorphic juvenile magmatism over long periods (> 60 My). This conceptual model also predicts limited homogenous thickening with horizontal flow of the middle and lower crust leading to negligible topography and hence very low-erosion and exhumation rates.

↓ **Fig. 5–8** : Orogen building modes in time and space **a–** Classification of Precambrian orogen proposed by Chardon et al. (2009) that emphasize the consequences of upper-mantle temperature in controlling plate interactions and continental growth; The ultra-hot-orogen (UHO) are characterized by distributed shortening and orogen-scale crustal flow combined with asthenosphere advection under long-lasting convergence; the hot orogen (HO) are representative of Cordilleran and wide mature collisional belt and may be compared to LHO of Beaumont (2013), they share the flow pattern with UHO but display less intense magmatic activity; the mixed-hot orogen (MHO) are representative of magmatic arcs and Proterozoic collisional belts; The modern cold orogen (CO) developed by shortening of lithosphere with a stiff upper-mantle **b–** Schematic cross-section illustrating different orogenic styles developed through time from Cagnard et al. (2011)

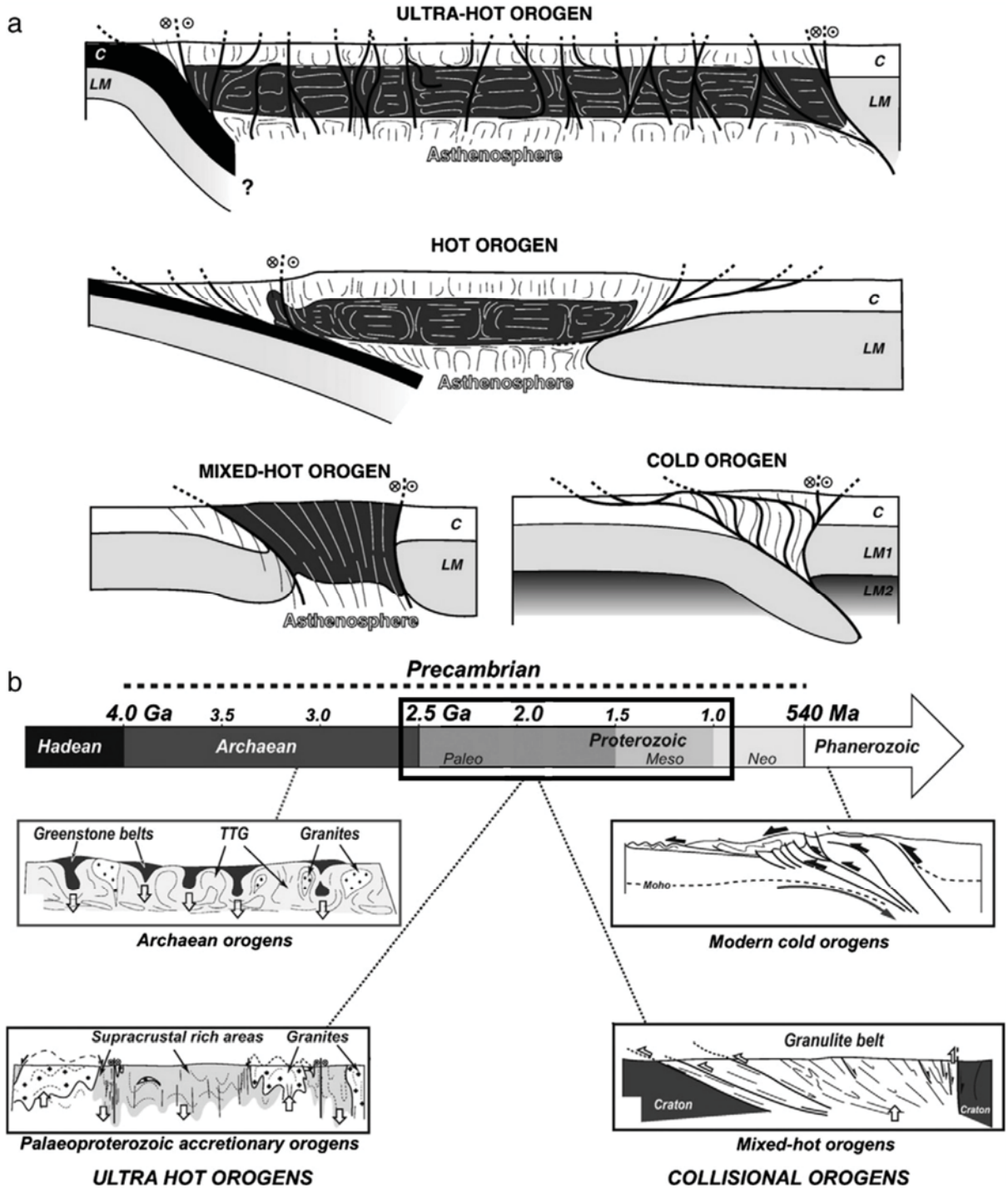

Ongoing thermal modelling will place new constrains on the interplay between the different heat sources and especially on lithosphere behaviour during Precambrian orogeny. Any orogen-scale thermo-mechanical model should in particular explain the presence of eclogites in the eastern segment at 990 Ma and their exhumation as hot migmatite nappe at c. 970 Ma (Möller et al. 2015) which is incompatible with a purely accretionary setting for the Sveconorwegian orogen. Besides, the absence of clear suture zone (Bingen et al. 2008), may suggest that intraplate processes are dominant in some part of orogenic development. Of particular relevance is the

lithosphere foundering or dripping off scenario which is favoured by the physical and thermal state of Proterozoic-like lithosphere (Djomani et al. 2001; Petitjean et al. 2006; Wang and Currie 2015).

References

Barnichon J-D, Havenith H, Hoffer B, Charlier R, Jongmans D, Duchesne J-C (1999) The deformation of the Egersund–Ogna anorthosite massif, south Norway: finite-element modelling of diapirism. Tectonophysics 303:109–130.

Bea F (2012) The sources of energy for crustal melting and the geochemistry of heat-producing elements. Lithos 153:278–291.

Bea F, Montero P (1999) Behavior of accessory phases and redistribution of Zr, REE, Y, Th, and U during metamorphism and partial melting of metapelites in the lower crust: an example from the Kinzigite Formation of Ivrea-Verbano, NW Italy. Geochim Cosmochim Acta 63:1133–1153.

Beaumont C, Nguyen MH, Jamieson RA, Ellis S (2006) Crustal flow modes in large hot orogens. Geol Soc Lond Spec Publ 268:91–145.

Bingen B, Austrheim H, Whitehouse MJ (2001) Ilmenite as a source for zirconium during high-grade metamorphism? textural evidence from the Caledonides of western Norway and implications for zircon geochronology. J Petrol 42:355–375.

Bingen B, Boven A, Punzalan L, Wijbrans JR, Demaiffe D (1998) Hornblende $^{40}Ar/^{39}Ar$ geochronology across terrane boundaries in the Sveconorwegian Province of S. Norway. Precambrian Res 90:159–185.

Bingen B, Davis WJ, Hamilton MA, Engvik AK, Stein HJ, Skar O, Nordgulen O (2008a) Geochronology of high-grade metamorphism in the Sveconorwegian belt, S. Norway: U–Pb, Th–Pb and Re–Os data. Nor Geol Tidsskr 88:13.

Bingen B, Demaiffe D, Hertogen J (1996) Redistribution of rare earth elements, thorium, and uranium over accessory minerals in the course of amphibolite to granulite facies metamorphism: the role of apatite and monazite in orthogneisses from southwestern Norway. Geochim Cosmochim Acta 60:1341–1354.

Bingen B, Demaiffe D, Hertogen J (1990) Evolution of feldspars at the amphibolite-granulite-facies transition in augen gneisses (SW Norway): geochemistry and Sr isotopes. Contrib Mineral Petrol 105:275–288.

Bingen B, Nordgulen O, Viola G (2008b) A four-phase model for the Sveconorwegian orogeny, SW Scandinavia. Nor Geol Tidsskr 88:43.

Bingen B, Stein HJ, Bogaerts M, Bolle O, Mansfeld J (2006) Molybdenite Re–Os dating constrains gravitational collapse of the Sveconorwegian orogen, SW Scandinavia. Lithos 87:328–346.

Bingen B, Van Breemen O (1998) U-Pb monazite ages in amphibolite- to granulite-facies orthogneiss reflect hydrous mineral breakdown reactions: Sveconorwegian Province of SW Norway. Contrib Mineral Petrol 132:336–353.

Bird P (1991) Lateral ectrusion of lower crust from under high topography, isostatic limit. J Geophys Res 96:10,275-10,286.

Bohlen SR (1991) On the formation of granulites. J Metamorph Geol 9:223–229.

Bol LC, Nijland TG, Sauter P, Jansen JBH, Valley JW (1995) Preservation of pre-metamorphic oxygen and carbon isotopic trends in granulite facies marbles from Rogaland, Southwest Norway. Am J Sci 295:1179–1219.

Bolle O, Diot H, Liégeois J-P, Vander Auwera J (2010) The Farsund intrusion (SW Norway): A marker of late-Sveconorwegian (Grenvillian) tectonism emplaced along a newly defined major shear zone. J Struct Geol 32:1500–1518.

Brown D, Ryan PD, Afonso JC, Boutelier D, Burg JP, Byrne T, Calvert A, Cook F, DeBari S, Dewey JF, Gerya TV, Harris R, Herrington R, Konstantinovskaya E, Reston T, Zagorevski A (2011) Arc–Continent Collision: The Making of an Orogen. In: Arc-Continent Collision. Springer Berlin Heidelberg, Berlin, Heidelberg, pp 477–493

Brown M (2007) Metamorphic Conditions in Orogenic Belts: A Record of Secular Change. Int Geol Rev 49:193–234.

Brown M (2009) Metamorphic patterns in orogenic systems and the geological record. Geol Soc Lond Spec Publ 318:37–74.

Brown M, Korhonen F (2009) Some remarks on melting and extreme metamorphism of crustal rocks. In: Physics and Chemistry of the Earth's Interior. Springer, pp 67–87

Bybee GM, Ashwal LD, Shirey SB, Horan M, Mock T, Andersen TB (2014) Pyroxene megacrysts in Proterozoic anorthosites: Implications for tectonic setting, magma source and magmatic processes at the Moho. Earth Planet Sci Lett 389:74–85.

Cagnard F, Barbey P, Gapais D (2011) Transition between "Archaean-type" and "modern-type" tectonics: Insights from the Finnish Lapland Granulite Belt. Precambrian Res 187:127–142.

Chardon D, Gapais D, Cagnard F (2009) Flow of ultra-hot orogens: A view from the Precambrian, clues for the Phanerozoic. Tectonophysics 477:105–118.

Charlier B, Duchesne J-C, Vander Auwera J, Storme J-Y, Maquil R, Longhi J (2010) Polybaric Fractional Crystallization of High-alumina Basalt Parental Magmas in the Egersund-Ogna Massif-type Anorthosite (Rogaland, SW Norway) Constrained by Plagioclase and High-alumina Orthopyroxene Megacrysts. J Petrol 51:2515–2546.

Clark C, Fitzsimons ICW, Healy D, Harley SL (2011) How Does the Continental Crust Get Really Hot? Elements 7:235–240.

Coint N, Slagstad T, Roberts NMW, Marker M, Røhr T, Sørensen BE (2015) The Late Mesoproterozoic Sirdal Magmatic Belt, SW Norway: Relationships between magmatism and metamorphism and implications for Sveconorwegian orogenesis. Precambrian Res 265:57–77.

Collins WJ (2002) Hot orogens, tectonic switching, and creation of continental crust. Geology 30:535–538.

Condie KC, Pease V (eds) (2008) When did plate tectonics begin on planet Earth? Special paper 440, Geological Society of America, Boulder. 295 pp

Dewey JF, Bird JM (1970) Mountain belts and the new global tectonics. J Geophys Res 75:2,625-2,647.

Djomani YHP, O'Reilly SY, Griffin WL, Morgan P (2001) The density structure of subcontinental lithosphere through time. Earth Planet Sci Lett 184:605–621.

Ellis DJ (1987) Origin and evolution of granulites in normal and thickened crusts. Geology 15:167–170.

England PC, Thompson AB (1984) Pressure—temperature—time paths of regional metamorphism I. Heat transfer during the evolution of regions of thickened continental crust. J Petrol 25:894–928.

Falkum T (1985) Geotectonic evolution of southern Scandinavia in light of a late-Proterozoic plate-collision. In: The Deep Proterozoic Crust in the North Atlantic Provinces. Springer, pp 309–322

Falkum T (1982) Geologisk kart over Norge, berggrunnskart Mandal, 1:250000, Norges Geologiske Undersøkelse.

Ganne J, De Andrade V, Weinberg RF, Vidal O, Dubacq B, Kagambega N, Naba S, Baratoux L, Jessell M, Allibon J (2012) Modern-style plate subduction preserved in the Palaeoproterozoic of West African craton. Nature Geoscience 5:60–65

Gapais D, Cagnard F, Gueydan F, Barbey P, Ballèvre M (2009) Mountain building and exhumation processes through time: inferences from nature and models. Terra Nova 21:188–194.

Gerya TV, Perchuk LL, Burg J-P (2008) Transient hot channels: Perpetrating and regurgitating ultrahigh-pressure, high-temperature crust–mantle associations in collision belts. Lithos 103:236–256.

Harley SL (2016) A matter of time: The importance of the duration of UHT metamorphism. J Mineral Petrol Sci 111:50–72.

Hermans GAE., Tobi AC, Poorter RP, Maijer C (1975) The high-grade metamorphic Precambrian of the Sirdal-Ørsdal area, Rogaland/Vest-Agder, south-west Norway. Nor Geol Undersokelse 318:351–374.

Huijsmans J, Kabel A, Steenstra S (1981) On the structure of a high-grade metamorphic Precambrian terrain in Rogaland, South Norway. Nor Geol Tidsskr 61:183–192.

Jamieson RA, Beaumont C (2013) On the origin of orogens. Geol Soc Am Bull 125:1671–1702.

Jamieson RA, Beaumont C, Warren CJ, Nguyen MH (2010) The Grenville Orogen explained? Application and limitations of integrating numerical models with geological and geophysical data. Can J Earth Sci 47:517–539.

Jansen JBH, Blok RJ, Bos A, Scheelings M (1985) Geothermometry and geobarometry in Rogaland and preliminary results from the Bamble area, S Norway. In: The deep Proterozoic crust in the North Atlantic provinces. Springer, pp 499–516

Kelsey DE, Clark C, Hand M (2008) Thermobarometric modelling of zircon and monazite growth in melt-bearing systems: examples using model metapelitic and metapsammitic granulites. J Metamorph Geol 26:199–212.

Kelsey DE, Hand M (2015) On ultrahigh temperature crustal metamorphism: Phase equilibria, trace element thermometry, bulk composition, heat sources, timescales and tectonic settings. Geosci Front 6:311–356.

Kemp AIS, Shimura T, Hawkesworth CJ, others (2007) Linking granulites, silicic magmatism, and crustal growth in arcs: Ion microprobe (zircon) U-Pb ages from the Hidaka metamorphic belt, Japan. Geology 35:807–810.

Lundmark A, Corfu F, Spurgin S, Selbekk R (2007) Proterozoic evolution and provenance of the high-grade Jotun Nappe Complex, SW Norway: U–Pb geochronology. Precambrian Res 159:133–154.

Lundmark AM, Corfu F (2008) Late-orogenic Sveconorwegian massif anorthosite in the Jotun Nappe Complex, SW Norway, and causes of repeated AMCG magmatism along the Baltoscandian margin. Contrib Mineral Petrol 155:147–163.

Maijer C, (1987) The metamorphic envelope of the Rogaland intrusive complex. In: Maijer C & Padget P (eds) The geology of southermost Norway: an excursion guide. Norges Geologiske undersokelse special publication 1, Trondheim, pp 68–72.

Möller A, O'brien PJ, Kennedy A, Kröner A (2002) Polyphase zircon in ultrahigh-temperature granulites (Rogaland, SW Norway): constraints for Pb diffusion in zircon. J Metamorph Geol 20:727–740.

Möller A, O'Brien PJ, Kennedy A, Kröner A (2003) Linking growth episodes of zircon and metamorphic textures to zircon chemistry: an example from the ultrahigh-temperature granulites of Rogaland (SW Norway). Geol Soc Lond Spec Publ 220:65–81.

Möller C, Andersson J, Dyck B, Antal Lundin I (2015) Exhumation of an eclogite terrane as a hot migmatitic nappe, Sveconorwegian orogen. Lithos 226:147–168.

Montel JM (1993) A model for monazite/melt equilibrium and application to the generation of granitic magmas. Chem Geol 127–146.

Petitjean S, Rabinowicz M, Grégoire M, Chevrot S (2006) Differences between Archean and Proterozoic lithospheres: Assessment of the possible major role of thermal conductivity. Geochem Geophys Geosystems 7 doi: 10.1029/2005GC001053

Pownall JM, Hall R, Armstrong RA, Forster MA (2014) Earth's youngest known ultrahigh-temperature granulites discovered on Seram, eastern Indonesia. Geology 42:279–282.

Roffeis C, Corfu F (2014) Caledonian nappes of southern Norway and their correlation with Sveconorwegian basement domains. Geol Soc Lond Spec Publ 390:193–221.

Royden L (1996) Coupling and decoupling of crust and mantle in convergent orogens: implications for strain partitioning in the crust. J Geophys Res 101:17,679-17,705.

Sandiford M (1989) Secular trends in the thermal evolution of metamorphic terrains. Earth Planet Sci Lett 95:85–96.

Sandiford M, Powell R (1986) Deep crustal metamorphism during continental extension: modern and ancient examples. Earth Planet Sci Lett 79:151–158.

Schärer U, Wilmart E, Duchesne J-C (1996) The short duration and anorogenic character of anorthosite magmatism: U-Pb dating of the Rogaland complex, Norway. Earth Planet Sci Lett 139:335–350.

Sizova E, Gerya T, Brown M (2014) Contrasting styles of Phanerozoic and Precambrian continental collision. Gondwana Res 25:522–545.

Smithies RH, Howard HM, Evins PM, Kirkland CL, Kelsey DE, Hand M, Wingate MTD, Collins AS, Belousova E (2011) High-Temperature Granite Magmatism, Crust-Mantle Interaction and the Mesoproterozoic Intracontinental Evolution of the Musgrave Province, Central Australia. J Petrol 52:931–958.

Stepanov AS, Hermann J, Rubatto D, Rapp RP (2012) Experimental study of monazite/melt partitioning with implications for the REE, Th and U geochemistry of crustal rocks. Chem Geol 300–301:200–220.

Stüwe K (2007) Geodynamics of the Lithosphere: an introduction, 2nd Edition. Springer, Berlin, Heidelberg

Tobi AC, Hermans GAE., Maijer C, Jansen JBH (1985) Metamorphic zoning in the high-grade proterozoic of Rogaland-Vest Agder SW Norway. In: The deep Proterozoic crust in the North Atlantic provinces, D. Reidel publishing compagny. A.C. Tobi & J.L.R. Touret, pp 477–497

Vander Auwera J, Bolle O, Bingen B, Liégeois J-P, Bogaerts M, Duchesne JC, De Waele B, Longhi J (2011) Sveconorwegian massif-type anorthosites and related granitoids result from post-collisional melting of a continental arc root. Earth-Sci Rev 107:375–397.

Vander Auwera J, Charlier B, Duchesne J-C, Bingen B, Longhi J, Bolle O (2014) Comment on Bydee et al. (2014): Pyroxene megacrysts in Proterozoic anorthosites: Implications for tectonic settings, magma source and magmatic processes at the Moho. Earth Planet Sci Lett 401:378–380.

Vanderhaeghe O (2009) Migmatites, granites and orogeny: Flow modes of partially-molten rocks and magmas associated with melt/solid segregation in orogenic belts. Tectonophysics 477:119–134.

Vanderhaeghe O, Teyssier C (2001) Partial melting and flow of orogens. Tectonophysics 342:451–472.

Vielzeuf D, Clemens JD, Moinet E (1990) Granites, granulites, and crustal differentiation. In: D. Vielzeuf and Ph. Vidal (eds.) Granulites and Crustal Evolution. Kluwer Academic Publishers, Dordrecht, pp 59–85

Vielzeuf D, Vidal P (eds) (1990) Granulites and Crustal Evolution. Springer Netherlands, Dordrecht

Wang H, Currie CA (2015) Magmatic expressions of continental lithosphere removal: magmatism induced by lithosphere removal. J Geophys Res Solid Earth 120:7239–7260.

Watson EB, Harrison TM (1983) Zircon saturation revisited: temperature and composition effects in a variety of crustal magma types. Earth Planet Sci Lett 64:295–304.

Watt GR., Harley SL (1993) Accessory phase controls on the geochemistry of crustal melts and restites produced during water-undersaturated partial melting. Contrib Mineral Petrol 114:550–566.

Wells PRA (1980) Thermal models for the magmatic accretion and subsequent metamorphism of continental crust. Earth Planet Sci Lett 46:253–265.

Westphal M, Schumacher JC, Boschert S (2003) High-temperature metamorphism and the role of magmatic heat sources at the Rogaland anorthosite complex in southwestern Norway. J Petrol 44:1145–1162.

Yakymchuk C, Brown M (2014) Behaviour of zircon and monazite during crustal melting. J Geol Soc 171:465–479.

Tables

Tab. 1: LA-ICP-MS monazite U-Th-Pb data for sample *ALR 13-61*

		Isotope ratio									Dates							(ppm)		
Grain n°	Texture	$^{207}Pb/^{206}Pb$	2s %	$^{207}Pb/^{235}U$	2s %	$^{206}Pb/^{238}U$	2s %	Rho	$^{208}Pb/^{232}Th$	2s %	$^{207}Pb/^{206}Pb$	2s abs	$^{207}Pb/^{235}U$	2s abs	$^{206}Pb/^{238}U$	2s abs	$^{208}Pb/^{232}Th$	2s abs	% disc. *	$^{232}Th^a$	$^{238}U^a$	Th/U
1361-09	2	0.0709	2.66	1.540	3.20	0.1576	3.10	0.96	0.0482	2.61	955	25	947	30	943	29	951	25	1.3	50538	4608	11.0
1361-11a	1	0.0736	2.57	1.742	3.13	0.1716	3.10	0.99	0.0522	2.61	1031	27	1024	32	1021	32	1029	27	1.0	34405	6021	5.7
1361-11b	1	0.0727	2.60	1.653	3.15	0.1649	3.10	0.98	0.0495	2.62	1006	26	991	31	984	31	976	26	2.3	35985	3951	9.1
1361-13	2	0.0706	2.65	1.527	3.21	0.1568	3.13	0.97	0.0477	2.63	947	25	941	30	939	29	941	25	0.8	117021	5988	19.5
1361-14a	2	0.0692	2.66	1.509	3.22	0.1545	3.13	0.96	0.0463	2.66	905	24	908	29	910	28	915	24	-0.5	209099	4620	45.3
1361-14b	2	0.0712	2.63	1.552	3.19	0.1580	3.12	0.97	0.0483	2.64	962	25	943	30	935	29	954	25	2.9	168527	5644	29.9
1361-17	2	0.0705	2.63	1.502	3.20	0.1546	3.13	0.97	0.0476	2.63	942	25	931	30	927	29	940	25	1.6	124253	5688	21.8
1361-25	2	0.0713	2.63	1.499	3.23	*0.1554*	3.12	0.96	0.0486	2.63	965	25	951	31	946	30	958	25	2.0	161729	8401	19.3
1361-29a	2	0.0689	2.67	1.529	3.20	0.1585	3.11	0.96	0.0473	2.65	896	24	912	29	918	29	934	25	-2.4	132724	3474	38.2
1361-29b	2	0.0706	2.67	1.596	3.16	0.1617	3.11	0.98	0.0462	2.62	945	25	922	29	913	28	913	24	3.5	80684	3392	23.8
1361-38a	2	0.0699	2.64	1.531	3.20	0.1560	3.13	0.97	0.0500	2.64	927	24	942	30	949	30	986	26	-2.3	76301	3599	21.2
1361-38b	2	0.0698	2.62	1.486	3.19	0.1544	3.12	0.97	0.0478	2.62	923	24	925	29	925	29	944	25	-0.2	96919	4765	20.3
1361-40a	1	0.0723	2.56	1.732	3.12	0.1738	3.10	0.99	0.0535	2.63	994	25	1021	32	1033	32	1054	28	-3.8	105327	8983	11.7
1361-40b	1	0.0721	2.56	1.704	3.13	0.1714	3.09	0.99	0.0532	2.64	989	25	1010	32	1020	32	1048	28	-3.0	72954	7428	9.8
1361-41	2	0.0707	2.60	1.510	3.17	0.1550	3.11	0.98	0.0480	2.61	948	25	934	30	929	29	948	25	2.0	114418	5214	21.9
1361-41b	2	0.0701	2.61	1.471	3.18	0.1523	3.10	0.97	0.0472	2.65	930	24	919	29	914	28	933	25	1.8	66874	4380	15.3
1361-58	2	0.0711	2.61	1.571	3.16	0.1603	3.11	0.98	0.0496	2.62	961	25	959	30	959	30	979	26	0.2	131226	5297	24.8
1361-66	1	0.0732	2.58	1.701	3.15	0.1686	3.10	0.98	0.0525	2.63	1020	26	1009	32	1004	31	1035	27	1.5	88711	6360	13.9
1361-71	2	0.0698	2.58	1.526	3.14	0.1587	3.10	0.98	0.0489	2.65	921	24	941	30	949	29	966	26	-3.0	76734	8140	9.4
1361-7a	2	0.0709	2.66	1.497	3.23	0.1535	3.12	0.96	0.0474	2.64	953	25	934	30	926	29	936	25	2.9	61287	4678	13.1
1361-7b	2	0.0704	2.68	1.480	3.22	0.1521	3.12	0.96	0.0472	2.65	941	25	929	30	924	29	932	25	1.8	54337	4420	12.3
1361-7c	2	0.0700	2.69	1.470	3.13	0.1528	3.10	0.99	0.0478	2.66	927	25	930	29	931	29	944	25	-0.4	64314	4796	13.4

No common Pb correction was applied

** disc. is calculated as (207/206 age - 206/238 age)/(206/238 age)*

Tab. 2: SIMS zircons U-Th-Pb for sample *ALR 13-61*

			Isotope ratio										
Grain n°	**Texture**	**Gp**	**$^{207}Pb/^{206}Pb$**	**1σ %**	**$^{207}Pb/^{235}U$**	**1σ %**	**$^{206}Pb/^{238}U$**	**1σ %**	**Rho**	**$^{208}Pb/^{232}Th$**	**1σ %**	**f_{206}%***	**% disc.**
1361-04b	CL-bright rim	*1*	0.070	1.05	1.524	1.58	0.158	1.18	0.75	0.049	2.4	{0.03}	-1.1
1361-05a	CL-bright rim	*1*	0.070	0.77	1.526	1.38	0.157	1.15	0.83	0.049	2.4	0.06	-0.6
1361-06a	CL-bright rim	*1*	0.071	1.04	1.539	1.57	0.158	1.18	0.75	0.050	2.5	{0.02}	1.0
1361-23a	CL-bright rim	*1*	0.071	0.80	1.557	1.34	0.158	1.08	0.80	0.048	2.4	{0.03}	2.7
1361-07b	CL-bright rim	*1*	0.071	0.96	1.549	1.55	0.158	1.22	0.79	0.050	2.5	{0.05}	1.6
1361-13a	CL-bright rim	*1*	0.071	1.08	1.521	1.69	0.156	1.31	0.77	0.048	2.6	{0.00}	1.2
1361-09b	CL-bright rim	*1*	0.071	0.86	1.533	1.39	0.157	1.10	0.79	0.049	2.5	{0.02}	0.9
1361-22	CL-bright rim	*1*	0.071	0.61	1.549	1.23	0.159	1.07	0.87	0.049	2.3	{0.00}	-0.6
1361-08c	CL-dark rim	*1*	0.071	0.56	1.558	1.15	0.158	1.01	0.87	0.049	3.2	{0.01}	2.1
1361-11a	CL-dark rim	*1*	0.070	0.53	1.526	1.16	0.157	1.03	0.89	0.050	3.2	{0.01}	-0.6
1361-03b	CL-dark rim	*1*	0.070	0.53	1.525	1.22	0.159	1.10	0.90	0.049	2.8	{0.01}	-3.8
1361-03c	CL-dark rim	*1*	0.070	0.73	1.502	1.30	0.155	1.07	0.82	0.049	2.4	{0.04}	1.1
1361-14b	CL-dark rim	*1*	0.070	0.54	1.531	1.15	0.159	1.01	0.88	0.050	2.9	{0.01}	-1.9
1361-16a	CL-dark rim	*1*	0.070	0.59	1.533	1.19	0.159	1.03	0.87	0.049	2.9	{0.02}	-3.3
1361-17	CL-dark rim	*1*	0.071	0.54	1.518	1.16	0.156	1.02	0.89	0.046	3.1	{0.00}	1.3
1361-18	CL-dark rim	*1*	0.070	0.56	1.520	1.21	0.157	1.07	0.89	0.049	2.4	{0.01}	0.3
1361-19a	CL-dark rim	*1*	0.070	0.55	1.523	1.20	0.158	1.07	0.89	0.049	2.7	{0.02}	-2.7
1361-20	CL-dark rim	*1*	0.070	0.47	1.533	1.13	0.159	1.03	0.91	0.049	2.6	{0.00}	-3.1
1361-21a	CL-dark rim	*1*	0.070	0.51	1.544	1.14	0.160	1.02	0.89	0.050	2.8	{0.01}	-2.3
1361-06a**	CL-dark interior		0.074	0.59	1.847	1.31	0.180	1.17	0.89	0.054	2.6	{0.00}	-1.1
1361-10a	CL-dark interior	*2*	0.072	0.74	1.689	1.69	0.170	1.52	0.90	0.052	2.8	{0.00}	-1.7
1361-16b	CL-dark interior	*2*	0.073	0.53	1.652	1.26	0.165	1.15	0.91	0.050	2.7	{0.01}	1.5
1361-12b	CL-dark interior	*2*	0.072	0.48	1.683	1.17	0.169	1.07	0.91	0.052	2.5	{0.00}	-1.4

Pbc corrected isotopic ratios

** {} denotes that no Pbc correction was applied*

*** not used for age calculation*

Tab. 2: continued

			Dates								Chemical composition			Oxygen isotopes	
Grain n°	**Texture**	**Gp**	**$^{207}Pb/^{206}Pb$**	**1σ abs.**	**$^{207}Pb/^{235}U$**	**1σ abs.**	**$^{206}Pb/^{238}U$**	**1σ abs.**	**$^{208}Pb/^{232}Th$**	**1σ abs.**	**Th**	**U**	**Th/U_{calc}**	**δ18O**	**± ‰**
1361-04b	CL-bright rim	*1*	933	21.4	940	9.7	943	10.4	967	22.7	179.8	258.0	1.49	6.33	0.19
1361-05a	CL-bright rim	*1*	937	15.7	941	8.5	943	10.0	962	22.5	218.0	219.8	1.04	6.73	0.18
1361-06a	CL-bright rim	*1*	953	21.1	946	9.7	943	10.4	977	23.4	110.6	199.0	1.85	6.35	0.17
1361-23a	CL-bright rim	*1*	971	16.2	953	8.3	946	9.5	952	22.2	173.6	223.3	1.26	n.a.	n.a.
1361-07b	CL-bright rim	*1*	960	19.4	950	9.6	946	10.7	985	23.6	169.7	164.4	0.99	6.81	0.17
1361-13a	CL-bright rim	*1*	946	21.9	939	10.4	936	11.4	954	24.4	87.3	153.7	1.78	6.88	0.18
1361-09b	CL-bright rim	*1*	950	17.4	944	8.6	941	9.6	968	23.6	186.0	126.7	0.69	6.39	0.17
1361-22	CL-bright rim	*1*	946	12.3	950	7.6	952	9.4	958	21.9	298.5	205.2	0.70	n.a.	n.a.
1361-08c	CL-dark rim	*1*	968	11.5	954	7.2	948	8.9	975	30.7	364.0	19.6	0.05	6.52	0.17
1361-11a	CL-dark rim	*1*	937	10.8	941	7.2	943	9.1	983	31.1	367.3	44.4	0.13	6.49	0.16
1361-03b	CL-dark rim	*1*	915	10.9	941	7.5	951	9.7	972	26.5	430.5	29.2	0.07	6.53	0.21
1361-03c	CL-dark rim	*1*	939	15.0	931	7.9	928	9.2	976	23.2	262.0	97.2	0.39	n.a.	n.a.
1361-14b	CL-dark rim	*1*	930	11.0	943	7.1	949	8.9	977	27.6	352.7	36.0	0.11	n.a.	n.a.
1361-16a	CL-dark rim	*1*	921	12.1	944	7.3	953	9.1	972	27.6	383.3	20.1	0.06	n.a.	n.a.
1361-17	CL-dark rim	*1*	946	10.9	938	7.1	934	8.9	915	27.5	379.4	23.8	0.06	n.a.	n.a.
1361-18	CL-dark rim	*1*	941	11.4	939	7.4	938	9.4	963	22.6	381.7	141.8	0.38	n.a.	n.a.
1361-19a	CL-dark rim	*1*	921	11.2	940	7.4	947	9.4	965	25.6	380.7	34.1	0.09	n.a.	n.a.
1361-20	CL-dark rim	*1*	923	9.5	944	7.0	952	9.1	970	24.5	497.7	46.3	0.10	n.a.	n.a.
1361-21a	CL-dark rim	*1*	933	10.4	948	7.0	955	9.0	981	27.1	417.0	22.9	0.06	n.a.	n.a.
1361-06a**	CL-dark interior		1054	11.9	1062	8.7	1066	11.5	1056	26.8	276.5	171.3	0.62	6.39	0.18
1361-10a	CL-dark interior	*2*	992	15.0	1004	10.8	1010	14.2	1032	28.3	363.4	210.4	0.60	6.66	0.17
1361-16b	CL-dark interior	*2*	1001	10.7	990	8.0	986	10.5	982	26.1	347.4	38.4	0.11	n.a.	n.a.
1361-12b	CL-dark interior	*2*	992	9.7	1002	7.5	1007	10.0	1023	25.0	483.9	64.9	0.14	6.62	0.18

Tab. 3: Major- and trace-elements whole-rock analysis for garnetiferous migmatites

		UTM coordinates		SiO_2	Al_2O_3	Fe_2O_3	FeO	MnO	MgO	CaO	Na_2O	K_2O	TiO_2	P_2O_5	PF	Total
Sample name	**Rock type**	**x**	**y**	**%**	**%**	**%**	**%**	**%**	**%**	**%**	**%**	**%**	**%**	**%**	**%**	**%**
ALR 13-063	Grt leucosome	321514	6516488	71.77	12.78	7.91	n.a	0.25	1.53	3.11	1.69	0.37	0.06	b.d.l	0.13	99.60
ALR 13-064	Grt-Spl-Crd gneiss	321547	6516474	65.71	16.62	0.22	5.5	0.05	1.82	1.73	2.16	3.38	0.91	b.d.l	1.46	100.17
ALR 14-060	Grt-Opx-Bt gneiss	321660	6516436	57.11	18.33	1.36	8.43	0.10	3.16	2.38	2.63	4.04	1.14	0.09	0.50	100.20
ALR 14-018	Grt-Opx-Bt-Hc	345794	6517366	41.14	20.53	2.05	18.38	0.21	4.83	2.75	2.18	2.17	1.72	b.d.l	2.71	100.72
ALR 14-019	Grt-Hc-Crd gneiss	345793	6517377	53.90	20.30	1.49	9.45	0.11	3.43	0.54	1.24	5.02	1.23	0.05	2.53	100.34
ALR 13-069	Grt-Bt gneiss	355264	6524649	66.30	14.20	3.51	4.84	0.28	0.59	3.02	3.75	1.42	0.71	0.24	0.68	100.06
ALR 13-005	Grt-Opx-Hc-Crd leucosome	348746	6499700	54.58	20.58	2.03	7.43	0.10	4.68	1.63	3.74	3.87	0.65	0.07	0.61	100.78
ALR 13-010	Gt-Hc-Qz gneiss	348434	6499583	62.80	17.49	3.68	3.97	0.08	1.10	0.92	2.23	6.07	0.89	0.06	1.39	101.13
ALR 13-006	Hc-Qz gneiss	348495	6499696	66.00	14.44	6.40	3.47	0.03	0.39	0.82	2.15	5.16	0.92	0.07	0.69	100.92
ALR 13-043	Hc-Qz gneiss	327962	6523881	76.3	10.9	3.24	n.a	0.04	0.19	0.65	1.73	4.51	0.38	0.03	0.28	98.35
ALR 13-045	Grt-Opx-bt gneiss	327720	6524288	69.1	13.55	7.02	n.a	0.11	1.38	1.66	2.68	4.3	0.78	0.05	0.29	100.99
ALR 13-056	Osm gneiss (Vikesa)	332535	6503984	67.1	14.1	9.56	n.a	0.11	3.37	0.7	1.37	1.47	1.01	b.d.l	1.3	100.12
ALR 13-057	Osm gneiss (Vikesa)	332496	6503977	72.2	12.55	7.63	n.a	0.08	2.16	1.29	2.54	1.85	1.14	0.04	0.34	101.86
B01029	Osm gneiss (Vikesa)	332472	6503971	52.8	16.5	5.11	12.9	0.31	6.93	0.46	1.05	1.52	0.49	0.17	b.d.l	99.56
ALR 13-058	Osm gneiss (Vikesa)	332482	6503981	62.5	15.8	3.48	6.27	0.15	3.87	0.68	2.38	4.18	0.53	0.07	0.16	100.87
ALR 13-017	Spr gneiss (Ivesdal)	335797	6510397	51.1	19.7	7.49	n.a	0.07	8.82	0.86	1.72	6.28	0.67	0.14	1.27	98.16
ALR 13-022	Spr gneiss (Ivesdal)	335550	6510354	51	21.8	2.03	4.55	0.06	9.78	1.71	2.3	5.98	1.01	0.08	0.94	101.85
ALR 13-023	Sp-Opx gneiss	335565	6510355	52.4	19.8	1.6	5.72	0.08	6.04	2.54	2.77	6.12	0.74	0.11	0.36	99.03
ALR 13-033	Grt-Bt-Hc-sill gneiss	334182	6525512	62.6	16.15	6.7	n.a	0.06	2.14	2.05	3.31	3.33	1.02	0.08	0.25	97.8
ALR 13-034	Gt-Opx-(bt) gneiss	334388	6522539	52.9	17.55	13.3	n.a	0.11	3.16	2.57	3.18	4.26	1.61	0.03	b.d.l	98.68
ALR 14-057	Osm gneiss (Bue)	324078	6505843	65.91	13.23	5.09	3.13	0.07	3.72	0.96	0.65	2.35	0.87	0.04	2.60	98.96
ALR 13-008	Hc-Qz gneiss	348495	6499696	72.47	13.52	2.18	2.3	0.02	0.38	0.83	2.07	4.04	0.43	0.06	0.84	99.41
ALR 13-044	Hc-Qz gneiss	327846	6523925	79.05	9.84	1.43	1.81	0.05	0.32	1.02	2.01	2.92	0.42	b.d.l	0.61	99.66
ALR 14-017	Grt-Opx-Bt gneiss	345809	6517358	61.36	16.70	7.93	n.a	0.10	3.18	3.57	2.83	1.59	0.95	b.d.l	1.52	99.74

Tab. 3: continued

Sample name	Rock type	La ppm	Ce ppm	Pr ppm	Nd ppm	Sm ppm	Eu ppm	Gd ppm	Tb ppm	Dy ppm	Ho ppm	Er ppm	Tm ppm	Yb ppm	Y ppm	Zr ppm	Th ppm	U ppm	Hf ppm
ALR 13-063	Grt leucosome	13.31	23.16	2.657	10.09	3.573	0.936	10.83	3.845	45.6	15.92	58.57	10.47	77.51	480.4	594.5	1.626	1.025	18.93
ALR 13-064	Grt-Spl-Crd gneiss	44.75	81.45	9.624	35.13	6.266	1.969	5.606	0.97	6.546	1.434	3.795	0.555	3.769	39.39	263.9	5.109	0.634	6.79
ALR 14-060	Grt-Opx-Bt gneiss	65.33	139	16.97	66.84	13.34	2.275	11.56	1.855	12.25	2.64	7.175	1.047	7.007	71.4	303.7	21.04	1.372	8.089
ALR 14-018	Grt-Opx-Bt-Hc	26.72	49.23	5.737	21.24	6.28	1.166	9.653	1.898	13.59	3.322	9.944	1.621	11.3	90.5	866.5	1.487	1.826	24.18
ALR 14-019	Grt-Hc-Crd gneiss	82.52	163.9	19.42	74.52	15.92	1.575	16.32	2.989	20.61	4.318	11	1.544	9.831	126.1	274.6	37.35	2.242	7.543
ALR 13-069	Grt-Bt gneiss	97.58	222.5	31.47	140.6	36.98	3.665	37.19	6.599	44.68	9.649	25.23	3.481	21.61	267.4	1287	18.85	6.343	35.94
ALR 13-005	Grt-Opx-Hc-Crd leucosome	48.73	94.51	11.1	41.28	8.404	2.615	9.668	1.733	10.24	1.838	4.387	0.619	4.019	50.21	416.9	5.544	0.809	9.91
ALR 13-010	Gt-Hc-Qz gneiss	68.54	142.5	16.97	65.17	13.21	1.957	12.16	1.992	13.42	3.01	8.413	1.272	8.479	83.54	316.3	22.69	1.315	8.352
ALR 13-006	Hc-Qz gneiss	68.02	131.3	17.61	70.02	14.32	2.259	12.71	1.994	12.8	2.637	6.63	0.933	5.921	69.82	565.2	24.83	1.332	14.75
ALR 13-043	Hc-Qz gneiss	57.7	114.5	13.45	52.6	8.21	1.38	6.77	0.99	6.03	1.39	4.9	0.74	5.19	40.9	428	14.6	2.04	12
ALR 13-045	Grt-Opx-bt gneiss	117.5	243	31	117	24.4	1.24	20.2	2.93	15.15	2.78	8.24	1.02	6.29	84.7	957	72.5	4.62	28.3
ALR 13-056	Osm gneiss (Vikesa)	44.1	82.3	9.98	40.2	7.18	0.91	9.75	1.5	9.51	1.97	5.78	0.96	5.73	56.2	305	3.18	0.28	8.6
ALR 13-057	Osm gneiss (Vikesa)	86.1	166.5	21.1	84.5	14.7	1.93	12.95	2.03	12.75	2.63	8.28	1.16	7.46	83.3	730	16.35	0.91	19.7
B01029	Osm gneiss (Vikesa)	508	1215	164	689	131.5	3.58	105.5	13.9	79.1	16.2	48.7	7.43	45	454	366	286	5.26	11
ALR 13-058	Osm gneiss (Vikesa)	70.4	159	21.4	94.2	18	1.79	18.5	3.03	20.2	4.42	13.8	1.95	12.5	138.5	276	40.3	0.49	7.8
ALR 13-017	Spr gneiss (Ivesdal)	17.3	38.5	5.17	21.7	5.12	0.53	5.19	0.92	6.43	1.28	3.98	0.56	3.68	33.9	341	24.8	6.11	10
ALR 13-022	Spr gneiss (Ivesdal)	11.9	21.6	2.58	11.3	3.68	1.19	7.53	1.76	13.05	3.14	9.94	1.41	8.68	112.5	366	4.59	3.34	10.2
ALR 13-023	Sp-Opx gneiss	24.5	44.4	5.58	22.6	4.8	1.12	5.27	0.93	5.62	1.1	3.43	0.54	3.31	30.4	357	19.7	2.96	10.8
ALR 13-033	Grt-Bt-Hc-sill gneiss	59.2	110.5	13.85	50.8	9.49	1.97	7.39	1.04	6.73	1.41	4.07	0.51	3.12	41.8	417	12.95	1.82	11
ALR 13-034	Gt-Opx-(bt) gneiss	59	95.9	11.1	42	8.5	1.51	14.85	2.86	18.15	3.39	9.7	1.39	8.3	98.6	677	12.45	1.18	19.6

Tab. 4: Overview of heat production potential (H) at 1.00 Ga of the different lithologies of Rogaland

Lithology	K_2O (wt%)	U (ppm)	Th (ppm)	H ($\mu W.m^{-3}$)	H min	H max	n	References
Garnetiferous migmatite	3.59	1.91	26.91	2.65	0.005	22.9	24	see Tab. 3
HBG suite	4.02	4.58	14.01	2.63	0.01	14.6	73	Vander Auwera et al. 2003
Sirdal suite (SMB)	4.88	3.91	22.29	3.45	0.85	12.1	52	Slagstad et al. 2013
Feda augen gneiss (SMB)	4.55	0.98	7.12	1.47	0.96	1.72	17	U and Th from Bingen et al. 1996, K_2O from Bingen et al. 1989
metacharnockite	4.49	1.06	8.97	5.18	0.014	11.2	10	Zhou et al. 1995
Amphibole granitic gneiss	4.43	1.04	7.46	3.12	0.014	10.1	12	Zhou et al. 1995
Banded gneiss - leucogneiss	3.93	0.58	2.77	0.43	0.016	2.09	8	Vander Auwera et al. 1993
Banded gneiss - metabasite	1.24	0.55	1.08	0.27	0.004	0.38	7	Vander Auwera et al. 1993
Banded gneiss (1/4 metabasite)	3.25	0.57	2.35	0.29	-	-	15	Vander Auwera et al. 1993

Supplementary materials

S5-1a: Algorithm R

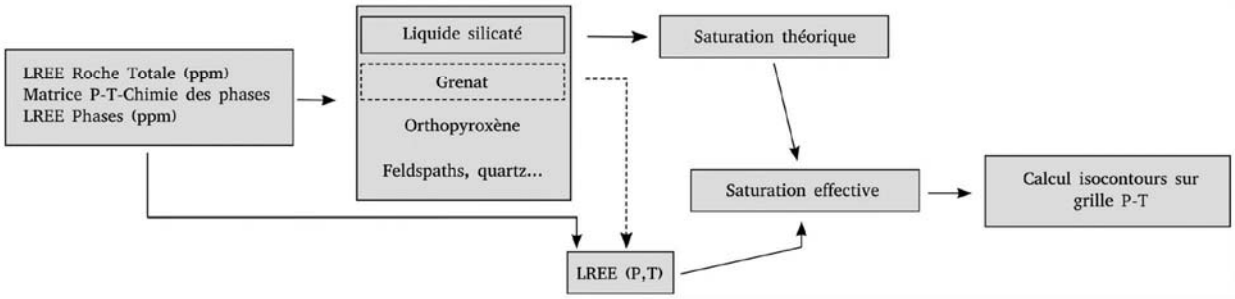

S5-1b : Code R de calcul de la solubilité de la monazite

```
#Monazite saturation
#renommer le fichier Perple_X en .txt puis effacer les premières lignes
#enlever les virgules, % et () dans le nom des colonnes

#charge les librairies
library(lattice,graphics)
install.packages("RColorBrewer")
library(RColorBrewer)
####

LREEwr = 210 # concentration LREE roche totale (ppm)
C2=10 # LREE dans Gt
C3=350 # LREE Kfs
C4=1000 # LREE PL
Xmz = 0.85
LREE = 210
original = read.table("1358_NCKFMASHO.txt",header = TRUE,as.is = TRUE,check.names = FALSE)
#nom du fichier Perple_X
MW = read.table("MW.txt",header = TRUE)
x.atoms = read.table("x.atoms.txt",header = TRUE)
```

```
cleaned <- subset(original, select = c(Name, T, P, wt, NA2O, CAO, FEO, MGO, AL2O3, SIO2, FE2O3, K2O, H2O))
melt <- subset(cleaned, Name == "melt(HP)")
GT <- subset(cleaned, Name == "Gt(WPH)")
KFS <- subset(cleaned, Name == "San")
PL<- subset(cleaned, Name == "feldspar_B")

###
# Saturation suivant Montel
###

#millications
oxides <- c("H2O", "NA2O", "CAO", "FEO", "MGO", "AL2O3", "SIO2", "FE2O3", "K2O")
oxides <- oxides[oxides %in% colnames(cleaned)] #teste quels sont les oxides présents
ee <- sapply(1:nrow(melt), function(f) {
                z <- melt[f, oxides]/MW[oxides] * x.atoms[oxides] * 1000
                return(z)})
milli <- t(ee) # matrice des millications
rownames(milli) <- rownames(melt)
cats <- matrix(unlist(milli), ncol = length(oxides), byrow = FALSE)

#normalisation à 100 des millications
tot <- apply(cats, 1, sum)
x <- t(sapply(1:nrow(cats), function(f) cats[f, ]/tot[f] * 100))
colnames(x) <- c("H2O", "NA2O", "CAO", "FEO", "MGO", "AL2O3", "SIO2", "FE2O3", "K2O")

#controle de la composition du melt
CFM <- (melt[,"CAO"]+melt[,"FEO"]+melt[,"MGO"])
ASI <- (x[,"AL2O3"]/(x[,"CAO"]+x[,"NA2O"]+x[,"K2O"]))
summary(CFM)
summary(ASI)

#calcul saturation
D<-(x[,"NA2O"]+x[,"K2O"]+2*x[,"CAO"])/x[,"AL2O3"]*1/(x[,"AL2O3"]+x[,"SIO2"])*100
sat <- 139*exp(9.50+2.34*D+0.3879*sqrt(melt[,"H2O"])-13318/melt[,"T"])

#####
#calcul LREE disponible i.e non piegé dans les minéraux
#Grenat
GmelT <- merge(GT,melt,by=c("P","T"),all.y = TRUE)
GmelT[is.na(GmelT)] <- 0
```

```
LREEM = (LREEwr - GmelT[,"wt.x"]/100*C2)/(GmelT[,"wt.y"]/100)
LREEM[LREEM<1] <- 1

#Kfs
KmelT <- merge(KFS,melt,by=c("P","T"),all.y = TRUE)
KmelT[is.na(KmelT)] <- 0
LREEM = (LREEwr - KmelT[,"wt.x"]/100*C3)
LREEM[LREEM<1] <- 1
#levelplot(wt~T*P, KFS, contour = TRUE, col.regions = heat.colors(100),at=c(seq(0,10,1),seq(20,100,10)), labels = TRUE) # tracer la proportion de Kfs en P-T

#Pl
PmelT <- merge(PL,melt,by=c("P","T"),all.y = TRUE)
PmelT[is.na(PmelT)] <- 0
LREEM = (LREEwr - PmelT[,"wt.x"]/100*C4)
LREEM[LREEM<1] <- 1
#levelplot(wt~T*P, PL, contour = TRUE, col.regions = heat.colors(100),at=c(seq(0,10,1),seq(20,100,10)), labels = TRUE)# tracer la proportion de Pl en P-T

####
solubility <- sat/LREEM*melt[,"wt"]
    #solubility <- sat/LREE*melt[,"wt"] #code sans minéraux (Gt, Pl, Kfs)
solubility <- round(solubility,1)
melt <- cbind(melt,D,solubility) #complete la matrice melt
solubility[solubility>100] <- 101
levelplot(solubility~T*P, melt, contour = TRUE, col.regions = heat.colors(100),at=c(seq(0,10,1),seq(20,100,10)), labels = TRUE) #trace les courbes d'iso-saturation suivant Montel

####
#Saturation suivant Stepanov
####
satS <- exp(16.16+0.23*sqrt(melt[,"H2O"])-11494/melt[,"T"]-19.4*melt[,"P"]*0.001/melt[,"T"]+log(Xmz))
solubilityS <- satS/LREEM*melt[,"wt"]
    #solubilityS <- satS/LREE*melt[,"wt"] #code sans minéraux (Gt, Pl, Kfs)
solubilityS <- round(solubilityS,1)
melt <- cbind(melt,solubilityS) #complete la matrice melt
solubilityS[solubilityS>100] <- 101
levelplot(solubilityS~T*P, melt, contour = TRUE, col.regions = heat.colors(100), at =c(seq(0,10,1),seq(20,100,10)),labels = TRUE)#trace les courbes d'iso-saturation suivant Stepanov
```

```
#levelplot(wt~T*P, melt, contour = TRUE, col.regions = heat.colors(100), at =c(seq(0,10,1),seq(20,100,10)),labels = TRUE)

###
# Saturation suivant Kelsey
###
FM<-((x[,"NA2O"]+x[,"K2O"]+2*(x[,"CAO"] +x[,"FEO"]+x[,"MGO"]))/(x[,"AL2O3"]*x[,"SIO2"]))

satK <- 566794*exp(310/melt[,"T"]+13.24*FM - 7.5852)
solubilityK <- satK/LREEM
    #solubilityK <- satK/LREE*melt[,"wt"] #code sans minéraux (Gt, Pl, Kfs)
solubilityK <- round(solubilityK,1)
melt <- cbind(melt,solubilityK)
solubilityK[solubilityK>100] <- 101
levelplot(solubilityK~T*P, melt, contour = TRUE, col.regions = heat.colors(100), at = c(seq(0,10,1),seq(20,100,10)), labels = TRUE) #trace les courbes d'iso-saturation suivant Kelsey
```

S5-2: Compilation of published geochronological data on igneous rocks in Rogaland

Rock description	Sample Id	Mineral	System	Method	type	Age	2s	x coordinate*	y coordinate	Reference
Sirdal- Feda suite										
Feda granodiorite suite, Mandal augen gneiss	B206	Zrn	U-Pb	TIMS	up.int	1049	8	413150	6440450	Bingen & van Breemen, 1998
Feda granodiorite suite, Veggja augen gneiss	B642	Zrn	U-Pb	TIMS	up.int	1051	8	391450	6454850	Bingen & van Breemen, 1998
Feda granodiorite suite, Feda augen gneiss	B113	Zrn	U-Pb	TIMS	up.int	1051	8	370650	6462000	Bingen & van Breemen, 1998
Feda granodiorite suite, Liland augen gneiss	B195	Zrn	U-Pb	TIMS	up.int	1051	4	356900	6470800	Bingen & van Breemen, 1998
Sparsely porphyritic granite (Sirdal magmatic belt)	73178	Zrn	U-Pb	LA-ICP-MS	207/206	1020	15	404000	6480981	Coint et al. 2015
medium-grained Bt granite (Sirdal magmatic belt)	MM02230	Zrn	U-Pb	SIMS	up. Int	1020	61	350409	6554133	Slagstad et al. 2013
Porphyritic granitoid (Sirdal magmatic belt)	MM026182	Zrn	U-Pb	LA-ICP-MS	conc	1021	10	335158	6587408	Slagstad et al. 2013
medium-grained granitoid (Sirdal magmatic belt)	R060350	Zrn	U-Pb	LA-ICP-MS	207/206	1022	13	374975	6485675	Coint et al. 2015
coarse-grained granitoid (Sirdal magmatic belt)	MM026183	Zrn	U-Pb	LA-ICP-MS	conc	1022	8	375014	6615718	Slagstad et al. 2013
porphyritic granite (Sirdal magmatic belt)	MM026302	Zrn	U-Pb	SIMS	conc	1022	6	342702	6570573	Slagstad et al. 2013
porphyritic granite (Sirdal magmatic belt)	MM057918	Zrn	U-Pb	LA-ICP-MS	conc	1024	6.5	350427	6592812	Coint et al. 2015
leucogranite (Sirdal magmatic belt)	MM026191	Zrn	U-Pb	SIMS	up. Int	1025	25	362621	6549102	Slagstad et al. 2013
medium-grained granitoid (Sirdal magmatic belt)	ROG33152	Zrn	U-Pb	LA-ICP-MS	up. Int	1027	23	365130	6479885	Coint et al. 2015
garnet granite	MM02277	Zrn	U-Pb	ID-TIMS	up. Int	1027	4	325424	6526915	Coint et al. 2015
massive granite (Sirdal magmatic belt)	MM026226	Zrn	U-Pb	ID-TIMS	up. Int	1027	9	315203	6513355	Coint et al. 2015
porphyritic granite (Sirdal magmatic belt)	ROG218	Zrn	U-Pb	SIMS	up. Int	1028	20	314258	6532437	Slagstad et al. 2013
porphyritic granite (Sirdal magmatic belt)	ROG033045	Zrn	U-Pb	LA-ICP-MS	conc	1030	10	371238	6472562	Coint et al. 2015
porphyritic granite (Sirdal magmatic belt)	ROG033044	Zrn	U-Pb	LA-ICP-MS	conc	1032	10	363750	6478250	Coint et al. 2015
porphyritic Bt granite (Sirdal magmatic belt)	73176	Zrn	U-Pb	LA-ICP-MS	207/206	1033	15	382099	6487939	Coint et al. 2015
porphyritic Bt granite (Sirdal magmatic belt)	73177	Zrn	U-Pb	LA-ICP-MS	conc	1033	7	406888	6481794	Coint et al. 2015
porphyritic granite (Sirdal magmatic belt)	NC080812	Zrn	U-Pb	LA-ICP-MS	conc	1033	7	384314	6514426	Coint et al. 2015
porphyritic granite (Sirdal magmatic belt)	ROG033129	Zrn	U-Pb	LA-ICP-MS	207/206	1033	14	376265	6487857	Coint et al. 2015
porphyritic Hbl-Bt granite (Sirdal magmatic belt)	MM02247	Zrn	U-Pb	SIMS	207/206	1035	9	338597	6572694	Slagstad et al. 2013
garnet granite	ROG275	Zrn	U-Pb	ID-TIMS	up. Int	1035	6	318862	6531428	Coint et al. 2015
porphyritic Bt granite (Sirdal magmatic belt)	73184	Zrn	U-Pb	LA-ICP-MS	conc	1036	9	406995	6477340	Coint et al. 2015
porphyritic granite (Sirdal magmatic belt)	ROG033124	Zrn	U-Pb	LA-ICP-MS	conc	1038	8	371003	6507925	Coint et al. 2015
porphyritic granite (Sirdal magmatic belt)	MM36470	Zrn	U-Pb	LA-ICP-MSA	conc	1040	10	335134	6553657	Coint et al. 2015
porphyritic granite (Sirdal magmatic belt)	SA3-01	Zrn	U-Pb	CA-LA-ICP-MS	207/206	1040	10	357948	6615161	Coint et al. 2015
porphyritic granite (Sirdal magmatic belt)	MM057845	Zrn	U-Pb	LA-ICP-MS	conc	1042	11	305958	6590515	Coint et al. 2015
porphyritic granite foliated (Sirdal magmatic belt)	ROG080	Zrn	U-Pb	SIMS	conc	1043	7	371806	6546058	Slagstad et al. 2013
porphyritic granite (Sirdal magmatic belt)	MM026306	Zrn	U-Pb	SIMS	conc	1047	6	340075	6579722	Slagstad et al. 2013
porphyritic granite foliated (Sirdal magmatic belt)	ROG076428	Zrn	U-Pb	LA-ICP-MS	conc	1047	9	383998	6458992	Coint et al. 2015
sparsely porphyritic granite (Sirdal magmatic belt)	ROG076442	Zrn	U-Pb	LA-ICP-MS	conc	1047	7	393173	6471857	Coint et al. 2015
porphyritic granite (Stropa granite)	SA7-58	Zrn	U-Pb	ID-TIMS	207/206	1049	5	359965	6596954	Coint et al. 2015
leucogranite (Sirdal magmatic belt)	MM026297	Zrn	U-Pb	SIMS	up. Int	1048	16	361312	6548784	Slagstad et al. 2013
Bt granite (Sirdal magmatic belt)	NC084354	Zrn	U-Pb	LA-ICP-MS	up. Int	1050	37	392759	6504616	Coint et al. 2015
porphyritic granite (Sirdal magmatic belt)	ROG032999	Zrn	U-Pb	LA-ICP-MS	conc	1050	9	355935	6475987	Coint et al. 2015
porphyritic granite (Sirdal magmatic belt)	ROG033000	Zrn	U-Pb	LA-ICP-MS	conc	1050	12	360535	6480446	Coint et al. 2015
Sirdal- Feda suite continued										
coarse-grained granitoid (Sirdal magmatic belt)	ROG033126	Zrn	U-Pb	LA-ICP-MS	207/206	1051	14	369013	6507064	Coint et al. 2015
porphyritic Bt granite (Sirdal magmatic belt)	73199	Zrn	U-Pb	LA-ICP-MS	?	1051	14	396456	6547682	Coint et al. 2015
porphyritic granite (Sirdal magmatic belt)	ROG032997	Zrn	U-Pb	LA-ICP-MS	conc	1052	9	356811	6471183	Coint et al. 2015
porphyritic granite (Sirdal magmatic belt)	ROG076439	Zrn	U-Pb	LA-ICP-MS	conc	1061	9	404642	6461267	Coint et al. 2015
porphyritic granite (Sirdal magmatic belt)	SA8-69	Zrn	U-Pb	CA-LA-ICP-MS	207/206	1066	10	370560	6607698	Coint et al. 2015

S5-3: Overview of the studied samples for each metamorphic zone. The complete sample set is presented in Tab. I-1

Isograd	Sample	Locality	Description & mineralogy	Monazite geochro.	Zircon geochro.	Thermodynamic modeling	Results
Opx-out	13-69	Hunnendal	Grt-Bt gneiss (+ Opx)	1036 = 10 ; 937 ± 9	1028 ± 9 ; 1002 ± 10	4-5 kbar; 775-800°C	chp.3 & chp. 4
Opx-in	13-64	Algard	aluminous gneiss (Grt, Sil, Hc, Crd, Bt)	1020 = 7 ; 1011 ± 7		4.5-5 kbar; 850-900°C	chp.3
	14-19	Maudal	aluminous gneiss (Grt, Sil, Bt, Crd, Hc, Kfs, Qtz)	1035 = 7; 955 ± 22	1002 ± 9 ; 971 ± 8	4.5-5 kbar; 850-900°C	chp. 4
Osm-in	13-05	Gyadal	Grt leucosome (Grt, Opx, Crd, Hc, Bt, Qz)	1032 = 5; 990 ± 9; 931 ± 6	age spread ; 942 ± 8	5-3.5 kbar; 900-950 °C	chp.3 & chp. 4
	13-06	Gyadal	fine grained leucocratic Hc + Qtz rock (+ Crd, Sil)	1040 = 9		c. 6 kbar; 910 °C	chp.3
	13-22	Ivesdal	Spr gneiss schlieren (Spr, Opx, Spl, Crd, Bt)	1029 = 9; 1006 ± 8;	1503 ± 9 ; 1024 ± 18	5-3.5 kbar; 900-950 °C	chp.3 & chp. 4
Pig-in	13-58	Vikesa	Osm gneiss (Grt, Sil, Hc, Qtz, Opx + Crd)	1034 ± 6; 1005 ± 7; 935 ± 7	age spread ; 940 ± 12	c. 5 kbar; 910 °C	chp.2, chp.3 & chp. 4
	13-61	Vikesa	Opx leucosome	1011 = 11; 936 ± 6	999 ± 13; 943 = 4		chp.5

Conclusion et perspectives

L'approche pluridisciplinaire (terrain, pétrologie, minéralogie, géochronologie, modélisation) appliquée à l'étude des roches de ultra-haute température du Rogaland (Norvège) a permis de mieux cerner le comportement de la monazite et du zircon. Le cœur du travail a consisté à lier géochronologie et géochimie des minéraux accessoires aux conditions quantitatives de pression et de température déduites de la modélisation thermodynamique, et plus largement, à l'évolution du domaine du Rogaland au sein de l'orogène Svéconorvégien. Ce travail de thèse est l'un des premier à placer des contraintes temporelles et de températures fortes quant à l'évolution des parties les plus chaudes des orogènes Précambriens et à discuter la nature polyphasée du métamorphisme de ultra-haute température.

L'évolution du Rogaland et causes du métamorphisme de UHT

L'étude pétrographique de plus de 150 échantillons, couplé à la modélisation thermodynamique de l'équilibre des phases et à la géochronologie sur une dizaine d'échantillons, montre que le domaine du Rogaland a subi un événement granulitique long avec un temps passé à plus de 800 °C compris entre 60 et 100 Ma. Cet événement est délimité par deux incursions à UHT à 1030–1005 Ma et à 940–930 Ma. L'étude de la distribution temporelle et spatiale du magmatisme et du métamorphisme suggère que l'advection de magmas d'origine mantellique en base de croûte à environ 1050 Ma puis la mise en place des anorthosites à 931 ± 2 Ma ont apporté une chaleur indispensable à l'établissement de la ultra-haute température dans la croûte moyenne. Le refroidissement très lent suivant le premier pic en température (env. 2 °C/Ma) contraste avec le refroidissement rapide suivant le second pic en température (env. 20 °C/Ma). Le maintien d'une température crustale élevée et d'un régime partiellement fondu dans la croûte peut être dû à la présence de matériel à forte production de chaleur par désintégration des éléments radioactifs.

Le Rogaland est donc une localité de ultra-haute température atypique par ses caractéristiques combinant un long temps de résidence dans le faciès granulite et une absence d'épaississement crustal. Ces observations ne sont pas expliquées par les modèles thermo-mécaniques actuellement acceptés pour expliquer le métamorphisme de UHT. Nous suggérons que les spécificités de composition et de température du manteau Protérozoïque favorisent le développement d'orogènes de type ultra-chaud où les mouvements gravitaires ont une importance particulière.

Apports à la compréhension du comportement de la monazite au cours du métamorphisme de UHT

Pour comprendre l'enregistrement chronométrique U–Th–Pb de la monazite, nous avons appliqué, au cours de ce travail de thèse, à la fois des corrélations texturales en lame mince et des corrélations chimiques, avec l'exploitation du partage des terres rares et de l'Y entre grenat et monazite de façon qualitative d'une part, et entre monazite et xénotime de façon quantitative, d'autre part. L'étude de la position texturale des grains de monazites en lame mince a permis de montrer en particulier que les monazites localisées dans des textures de déséquilibre, comme les symplectites issues de la déstabilisation du grenat, possèdent une signature chimique variable. Les monazites pour lesquelles nous pouvons au contraire démontrer l'équilibre avec les composants xénotime et huttonite sont capables d'enregistrer des âges à des températures supérieures à 880 °C.

La datation ponctuelle *in-situ* a été systématiquement combinée à l'analyse des éléments majeurs et traces contenus dans la monazite. Le grand nombre d'éléments chimiques qui peuvent être accommodés dans la monazite et la diversité des vecteurs de substitution mobilisant le site octaédrique seul ou les sites octaédrique et tétraédrique, rendent la monazite extrêmement utile. L'utilisation de traceurs chimiques simples (p. ex. S, Si, Ca, Th), ou une combinaison de traceurs, a permis dans la plupart des cas de discriminer des populations de cristaux. La présence d'un critère chimique permet d'identifier différentes populations parmi les cristaux dont les âges U–Pb se recoupent dans l'erreur analytique. Parmi ces traceurs chimiques, nous avons identifié le S comme un traceur pertinent, à la fois de la cristallisation de la monazite au cours du premier événement de fusion partielle, et de son évolution par dissolution–précipitation au cours de circulations fluides postérieures. Le changement de chimie des monazites est induit par des gradients de potentiel chimiques opérant à l'échelle de l'échantillon. L'existence de ces gradients entraine un mécanisme de dissolution–précipitation dans la monazite dont témoignent les multiples inclusions fluides et minérales secondaires.

Il est désormais évident que la température est un facteur cinétique favorisant les processus et mécanismes décrits ci-dessus, parfois de façon exponentielle, mais qu'elle n'est en rien l'unique paramètre régissant la remise à zéro des systèmes chronométriques. Dans les roches partiellement fondues, il est probable que ce soit la circulation de liquides silicatés, qui ne sont pas toujours à l'équilibre avec les roches traversées, qui contrôle des gradients de potentiel chimique à même de déclencher la dissolution ou la cristallisation des monazites. La nature dynamique de ce processus

empêche de le traiter de manière satisfaisante à l'aide de la conception thermodynamique classique « à l'équilibre ».

Finalement, nous montrons l'utilité de la caractérisation à l'échelle nanométrique des grains de monazite pour affiner l'interprétation géochronologique. Ainsi, des images à haute résolution au MET ont révélé la présence de nano-domaines de clino-anhydrite dans le réseau de la monazite riche en S. Cette observation suggère que les phénomènes d'oxydo-réduction doivent être considérés pour interpréter l'âge de cristallisation de la monazite en question. Cette approche est également pertinente lorsque les données analytiques U–Th–Pb se répartissent le long de la courbe *concordia* pour vérifier qu'il n'y ait pas de nano-inclusions à même de perturber le signal isotopique.

Apports à la compréhension du comportement du zircon au cours du métamorphisme de UHT

Le comportement des zircons décrits dans cette étude contraste fortement avec celui des monazites, qui de par leur flexibilité structurale sont capables d'accomoder un grand nombre de cations au sein de leur réseau cristallin. En effet, nous n'avons trouvé aucun traceur chimique adapté à la discrimination de plusieurs populations de zircons au cours du temps. Etant donné la variabilité chimique observée dans la monazite, nous excluons un environnement chimiquement stable de cristallisation pour les zircons durant plus de 60 Ma. L'absence de corrélation entre dates U–Pb et chimie des cristaux est pour une grande part liée aux processus de recristallisation à l'état solide à l'œuvre dans les zircons, en particulier sous l'effet du recuit des défauts induits par leur auto-irradiation. Nous suggérons que le processus de recristallisation des cœurs hérités, et structuralement instables, entraine la formation d'un patchwork de domaines structuraux (nanométriques ?) avec une rétention variable des âges U–Pb et une signature Th/U ~ 1 assez inhabituelle. De même, les isotopes de l'oxygène ne montrent pas de variation significative au cours du temps dans un même échantillon, suggérant un processus d'homogénéisation isotopique dans les roches de UHT.

La cartographie ionique de la répartition micrométrique du Pb à la SIMS n'a pas révélé d'hétérogénéités majeures dans les surcroissances et néo-cristallisations métamorphiques. Nous avons donc utilisé les âges de ces surcroissances pour estimer le temps que la roche a passé dans des conditions supra-solidus. La corrélation de la composition chimique en éléments majeurs et traces ainsi que des isotopes U–Th–Pb dans monazite et zircon entre différents échantillons a permis de construire un trajet température–temps synthétique du domaine du Rogaland. Il faut également noter que la comparaison de l'enregistrement temporel des monazites et des zircons

révèle une croissance tardive du zircon par rapport à la monazite lors du premier événement métamorphique. Cela peut traduire l'absence d'enregistrement du pic par les zircons avec une croissance essentiellement rétrograde. Paradoxalement, il semble que ce soit la résistance du zircon aux perturbations en tout genre (hormis l'irradiation) qui soit la cause de la rétention d'âge partielle.

La monazite : traceur des minéralisations ?

L'étude géochimique associée à la caractérisation nano-structurale *in-situ* de cristaux de monazite riche en S montre que le S y est incorporé en tant que sulfate (SO_4^{2-}) via la substitution clino-anhydrite ($Ca^{2+} + S^{6+} = REE^{3+} + P^{5+}$). Il a été montré pour le phosphate de Ca (apatite) que la quantité de S incorporé dans son réseau était proportionnelle à la concentration en S du magma à partir de laquelle elle cristallise. On peut raisonnablement supposer qu'il en est de même pour la monazite. Par conséquent, la mesure de l'âge isotopique U–Th–Pb couplé à la mesure par microsonde électronique de la concentration en S dans la monazite peut permettre de mieux contraindre le cycle du S dans les roches métamorphiques, c'est-à-dire son passage de l'état réduit dans les sulfures à l'état oxydé dans un fluide.

Au-delà de cet aspect purement théorique, nous montrons que les monazites riches en S sont typiques des environnements oxydés, ouvrant la possibilité de tracer les circulations de fluides oxydés riches en S dans des roches non minéralisées. Il est donc possible grâce à cet « outil » d'explorer le potentiel minéralisateur d'un événement géologique particulier au cours d'une orogenèse prolongée. Cette propriété de la monazite peut également permettre de dater le dépôt de gîtes minéraux oxydés, en distinguant le domaine du cristal de monazite co-génétique à la minéralisation des domaines résultant de recristallisations tardives.

Perspectives

De nombreuses perspectives s'ouvrent à la suite de cette thèse. Elles regroupent à la fois des questions connexes au sujet, qui n'ont pu être traitée faute de temps, mais aussi de nouvelles problématiques ou besoins méthodologiques émergeants.

Le prolongement le plus direct de ce manuscrit réside sûrement dans la modélisation thermique à effectuer pour valider numériquement la contribution des différentes sources de chaleur permettant d'expliquer le chemin température–temps établi dans ce manuscrit. Les conséquences de cette modélisation sur la genèse très débattue des massifs d'anorthosites protérozoïques seront analysées avec attention. Un code de diffusion de la chaleur 1D a été écrit

en prenant en compte la chaleur issue de la désintégration des éléments radioactifs contenus dans les roches, le flux de chaleur mantellique variable, la chaleur latente de fusion calculée à partir du code Perple_X. Il reste à implémenter l'érosion ainsi que le sous-placage de magmas basiques. Une fois le contexte 1D maitrisé, il serait envisageable de tester des modèles dynamiques pour tester la stabilité gravitaire de la croûte partiellement fondue sur des échelles très longues de temps et de tester si la délamination lithosphérique est un scénario géodynamique envisageable.

Les méthodes déployées pour comprendre le comportement des zircons se sont avérées limitées malgré leur nombre et leur complémentarité (imagerie optique, BSE et CL ; datation U–Pb, cartographie des isotopes du Pb en multi-collection, analyse des isotopes de l'oxygène ; analyse de la distribution des terres rares et autres éléments traces (Ti); vérification de la stœchiométrie ; cartographies à la nanoSIMS– non présenté). Il ressort de notre étude que certains domaines de zircons réincorporent partiellement du Pb radiogénique lorsqu'ils (re)cristallisent. Le mécanisme proposé pour expliquer nos données peut être testé par des observations structurales au microscope électronique à transmission ou à l'EBSD. De même, la nature minéralogique ou physique des points de Pb observés dans les cœurs de deux zircons hérités pourrait être précisée. Les avancées récentes en « nano-géochronologie » permises par la sonde atomique suggèrent que le Pb puisse s'accumuler dans des défauts cristallins planaires (Valley et al. 2015; Piazolo et al. 2016). Cette hypothèse mérite d'être confirmée et son effet sur les âges U–Th–Pb quantifiée.

Enfin, il sera nécessaire de compléter l'étude pétrologique de nos échantillons rares à osumilite puisque de nouvelles localités ont été échantillonnées en 2015 et qu'un nouveau modèle de solution solide prenant en compte le Na serait en développement pour être intégré à la base de données auto-cohérent utilisée dans ce manuscrit. Deux localités montrent, en particulier, des assemblages minéralogiques différents de ceux décrits dans ce manuscrit. A la première localité, l'osumilite apparaît en couronne entre orthopyroxène et cordiérite. Dans la seconde occurrence, la sillimanite est incluse dans de larges plages d'osumilite qui semble également à l'équilibre avec le hercynite. Enfin, du point de vu pétrologique, nous n'avons présenté que les roches alumineuses et felsiques dans ce manuscrit mais des roches carbonatées à wollastonite méritent d'être étudiées pour quantifier les flux de CO_2 dans la croûte profonde afin d'éclairer le paradigme de la prééminence des inclusions fluides de CO_2-CH_4 dans les granulites, alors que ces composants devraient être dissous dans le liquide sillicaté baignant ces roches.

Références

Piazolo S, La Fontaine A, Trimby P, Harley S, Yang L, Armstrong R, Cairney JM (2016) Deformation-induced trace element redistribution in zircon revealed using atom probe tomography. Nat Commun 7:10490. doi: 10.1038/ncomms10490

Valley JW, Reinhard DA, Cavosie AJ, Ushikubo T, Lawrence DF, Larson DJ, Kelly TF, Snoeyenbos DR, Strickland A (2015) Nano- and micro-geochronology in Hadean and Archean zircons by atom-probe tomography and SIMS: New tools for old minerals. Am Mineral 100:1355–1377. doi: 10.2138/am-2015-5134

A proximité de l'affleurement à sapphirine de Ivesdal. Octobre 2013, Rogaland

Remerciements

Je tiens en premier lieu, à adresser mes remerciements et ma sincère reconnaissance à mes directrices de thèse Stéphanie Duchene et Anne-Magali Seydoux-Guillaume, pour m'avoir proposé un sujet d'étude si riche et avoir su me guider, chacune à sa façon, durant ces trois années. L'équipe d'encadrement n'aurait pas été complète sans Bernard Bingen qui a été d'un soutien précieux et constant durant les moments clés de mon travail. Enfin, ma gratitude va à Valérie Bosse pour m'avoir accueilli à Clermont-Ferrand et m'avoir fait confiance pour les analyses LA-ICP-MS. Je suis reconnaissant à tous mes encadrants pour le cadre scientifique, matériel et humain exceptionel dans le lequel se sont déroulés mes travaux de thèse.

Je remercie ensuite les rapporteurs de cette thèse Simon Harley (université d'Edimbourg) et Philippe Goncalves (Université de Franche-Comté) pour avoir accepté de relire ce travail et pour les commentaires détaillés qu'ils y ont apporté. Les publications issues de cette thèse auront grandement bénéficié de leurs commentaires. Je remercie également Jean-Marc Montel (ENSG) et Fernando Corfu (Université d'Oslo) d'avoir accepté de faire partie du jury examinant ce travail. Olivier Vanderhaeghe (Université de Toulouse), président du jury, a animé une discussion très enrichissante lors de la soutenance et je l'en remercie. Les travaux de thèse présentés dans ce manuscrit ont en outre bénéficié des conseils d'un comité de thèse auquel ont pris part Julien Berger et Franck Poitrasson (Université de Toulouse).

Il faut aussi mentionner l'apport des personnels du laboratoire GET qui m'ont, de près ou de loin, aidé dans le travail de préparation ou dans la réalisation des nombreuses analyses présentées dans ce manuscrit. Je remercie, en particulier, les deux compères de l'atelier roche, Ludovic Menjot et Jean-François Mena, pour leur travail de grande qualité ainsi que toute l'équipe de micro-analyse, Thierry Aigouy, Sophie Gouy, Philippe de Parseval et Lucien Datas, pour leur aide, leur patience et tous les savoir-faire qu'ils ont su me transmettre.

Le rythme trépidant de la recherche a été ponctuée trois années durant d'enseignements en licence. Je tiens donc à remercier l'équipe pédagogique et notamment Damien Guillaume ainsi que Julien Berger pour avoir fait de mon monitorat une expérience extrêmement positive qui m'a donné l'appétit de l'enseignement.

Ce travail a également grandement profité de la bonne ambiance qui a régné au laboratoire entre doctorants. Je remercie chaleureusement les doctorants du GET, passés et actuels, persistants et passagers. Une mention spéciale revient à mes collègues de bureau et amis, Brian Cochelin, Thomas Leleu et Jing Ye.

Il en est d'autres qui ont œuvré à ce travail avant qu'il ne commence réellement, en me donnant le goût de la géologie lors de ma licence à Strasbourg, en particulier Yves Geraud. Je souhaite également remercier Karel Schulmann, Etienne Skrzypek (Université de Strasbourg) ainsi que Vojtěch Janoušek et Tomas Magna (Université de Prague) pour m'avoir encadré en master tout en me donnant l'envie et les moyens de poursuivre en thèse.

Il est temps de remercier mes parents Armand et Marie-Laure ainsi que toute la famille qui m'a soutenu. Enfin, je remercie Jessie Jusseaume pour autant de raisons qu'il y a de zircons dans les granulites du Rogaland.

Abstract

Understanding mountain building processes requires a better integration of petrological and geochronological data in order to link pressure-temperature paths to absolute ages. This work focuses on the behaviour of monazite and zircon, which are used as geochronometers, in ultra-high temperature granulites of Rogaland (South Norway). We show that linking *in-situ* U–Th–Pb dating of monazite with its major- and trace-element composition lead to the recognition of two ultra-high temperature (UHT) metamorphic events in Rogaland at c.1030–1005 Ma and c. 940–930 Ma. Indeed, the examination of monazite–xenotime–huttonite phase relationships suggests that monazite may record crystallization age at or near ultra-high temperature. Besides, the chemical and U–Th–Pb–O isotopic characterization of zircon neo-crystallization or overgrowths indicates that the Rogaland crust remains molten (> 800 °C at 0.7–0.4 GPa) at least during 60 My between the two identified UHT excursions. This manuscript also highlights the various factors responsible for U–Th–Pb (partial) resetting in the course of granulite facies metamorphism. Zircon behaviour is mostly controlled its level of amorphization, enhancing Pb loss during annealing, whereas monazite resetting is dominated by dissolution–precipitation processes in the presence of a melt or fluid phase. More specifically, we point out that monazite may be used to monitor the redox conditions of its crystallizing medium since monazite may incorporate the redox-sensitive element S in its lattice as sulphate. Finally, we demonstrate a spatial and temporal correlation between magmatism and UHT metamorphism in Rogaland. The timescale, *P–T* path and tectono-magmatic history however cannot be explained by currently accepted models for UHT. We suggest that physical and thermal specificities of Proterozoic mantle may explain the observed ultra-hot orogen style and the occurrence of gravity driven processes during orogeny.

Résumé

La compréhension des processus orogéniques nécessite un couplage toujours plus étroit entre données pétrologiques visant à contraindre le trajet pression-température des roches et les données géochronologiques donnant accès aux âges et durées absolues. Cette thèse vise en premier lieu à étudier le comportement des monazites et des zircons, utilisés en géochronométrie U-Th-Pb dans les granulites de ultra-haute température (UHT) du Rogaland (sud de la Norvège). Nous montrons que la datation ponctuelle *in-situ* U–Th–Pb, combinée à l'analyse des éléments majeurs et traces contenus dans la monazite permet d'identifier et de quantifier deux incursions à ultra-haute température du Rogaland à 1030–1005 Ma et à 940–930 Ma. En effet, l'examen des relations de phases à l'équilibre entre monazite, xénotime et huttonite a permis de démontrer que les monazites étaient capables de cristalliser et d'enregistrer des températures supérieures à 880 °C. D'autre part, la caractérisation chimique et isotopique U–Th–Pb–O des néo-cristallisations et surcroissances des zircons permet de définir un intervalle de temps de 60 Ma entre les deux pics de métamorphisme, au cours duquel la croûte moyenne était partiellement fondue à des températures supérieures à 800°C et à basse pression (0.7–0.4 GPa). Ces travaux de thèse soulignent par ailleurs la variété des facteurs susceptibles de conduire à la remise à zéro, partielle ou non, des âges U–Th–Pb dans les monazites et les zircons. Nous montrons que compte tenu de l'histoire *T-t* du domaine étudié, le système chronométrique U–Th–Pb est largement contrôlé dans le zircon par le degré d'amorphisation de ce dernier lié à son auto-irradiation, alors que dans la monazite, ce sont les processus de dissolution-recristallisation en présence de fluides silicatés ou aqueux qui sont prépondérants. Nous montrons également qualitativement l'influence des conditions d'oxydo-réduction dans l'incorporation du S comme sulfate dans le réseau cristallin de la monazite et par conséquent le potentiel que représente la monazite pour sonder l'état d'oxydo-réduction lié aux différents évènements géologiques, dans les roches métamorphiques. Finalement, nous mettons en évidence une corrélation spatiale et temporelle entre magmatisme mantellique et métamorphisme de ultra-haute température qui ne peut être expliquée avec les modèles actuellement acceptés pour la genèse du métamorphisme de UHT. Ces observations peuvent néanmoins être expliquées en prenant en compte la différence de composition et de température du manteau Protérozoïque comparé à l'actuel, favorisant le développement d'orogènes ultra-chauds et de phénomènes gravitaires.